The nature and co-behaviour of volatile and non-volatile elements in the sub-continental lithospheric mantle

James Clinton Crosby

Department of Earth Sciences
University of Cambridge

This dissertation is submitted for the degree of
Doctor of Philosophy

St Catharine's College

December 2021

Declaration

This thesis is the result of my own work and includes nothing which is the outcome of work done in collaboration except where specifically indicated in the text.

It is not substantially the same as any that I have submitted, or, is being concurrently submitted for a degree or diploma or other qualification at the University of Cambridge or any other University or similar institution. I further state that no substantial part of my thesis has already been submitted, or, is being concurrently submitted for any such degree, diploma or other qualification at the University of Cambridge or any other University or similar institution.

The total length does not exceed the 275 numbered page limit for the Degree Committee of Earth Sciences, including 225 pages of text, appendices, illustrations and bibliography

James Clinton Crosby
December 2021

“Life moves pretty fast. If you don’t stop and look around once in a while, you could miss it.”

Acknowledgements

I would first like to thank my supervisors, Professor Sally Gibson, Professor Fin Stuart and Dr Teal Riley. Their tireless, unwavering, and insightful guidance has made this PhD possible. I am grateful for the analytical assistance provided by Dr Luigia DiNicola at SUERC, Dr Iris Buisman and Dr Jason Day from the University of Cambridge, and Dr Cristina Talavera-Rodriguez and Dr Cees-Jan De Hoog from the University of Edinburgh.

I'd like to thank NERC for funding this PhD and additional support through the COVID-19 global pandemic. I am grateful to the VMSG community who have always made me feel welcome and I would like to thank St Catharines College for enhancing my experience. A special thanks to my happy hour partner, Dr Matthew Ball and his wonderful partner, Alice. I would also like to thank my excellent office mates and fellow PhD students Dr Matthew Gleeson, Dr Luke Grinham, Dr Penny Wieser, Dennis Mayk and Lizzy Steell.

I would like to thank my partner, Dr Alice Wrigley who has been my unfaltering pillar of support. Without her love, kindness and thoughtfulness, the past 4 years would not have been possible. I am incredibly grateful to my mother who has always provided a shoulder to lean on, a glass to drink from and a plate full of food. I grateful to my brothers, Buck and Richard, who have been excellent role models and provided insightful words of wisdom. I am grateful to my aunt and cousins who have always supported my educational journey and to the Wrigley who have provided excellent support. A special mention to my dogs, Marie and Abbey, who have always kept me grounded during difficult times.

Finally, this thesis is written with loving memory of my father, Robert Frank Crosby. Had he been here today, this would have made him prouder than words can describe.

Abstract

The lithospheric mantle represents a critical interface in global volatile cycles because it separates Earth's convecting mantle from the rigid crust. Nevertheless, the source, abundance and flux of volatiles stored in this reservoir are poorly constrained. In this work, the concentrations of volatiles stored both within the crystal lattice (H, Li, B, F, P and Cl) and fluid-inclusions (He and C) in mantle phases, together with their isotope compositions ($^{3}He/^{4}H$ and $^{13}C/^{12}C$), have been determined in 55 well-characterised peridotites and pyroxenites predominantly from off-craton mantle. The peridotites include spinel- and garnet-bearing lherzolites to harzburgites and are representative of the suites found at Kilbourne Hole, Colorado Plateau (SW USA), Tariat (Mongolia), West Eifel (Germany), Antarctic Peninsula, S. Patagonia, N.Tanzania and Ichinomegata (Japan). Their major and trace elements record a wide range in melt extraction (from 5 to 40%) but most xenoliths have undergone subsequent enrichment, via fluid or melt-related metasomatism. Fluid-inclusions are isotopically highly variable, with $^{3}He/^{4}He$ = 5.3 to 8.4 Ra and $\delta^{13}C$ = -25.0 to 5.6 ‰ (V-PDB).

$^{3}He/^{4}He$-major-trace-element systematics shows that the subcontinental lithospheric mantle dominantly reflects formation from a temporally evolving upper-mantle that has been overprinted by radiogenic processes. Furthermore, the influence of metasomatism is enhanced by $^{3}He/^{4}He$-$^{13}C/^{13}C$ systematics which show the dominant role of small-fraction volatile-rich upper-mantle melts with variable inputs from melts/fluids derived from recycled oceanic lithosphere containing organic material and carbonates. Coupled links between volatile and non-volatile elements suggest that the CO_2 hosted in fluid inclusions in the off-craton lithospheric mantle is approximately 41 ppm equating to an influx of 2.5 x 10^{19} g Myr^{-1}. The estimated concentration for CO_2 in off-craton mantle is lower than H_2O (85 to 100 ppmw), similar to P (40 ppm) add higher than for the halogen (F = 15 to 27 ppm; Cl = 3.4 to 5.4 ppm), B (0.09 to 0.22 ppm) and Li (1.77 ppm). In comparison with the depleted mantle, the off-craton mantle is more concentrated in Li, B and F has similar CO_2, P and Cl and lower amounts of H_2O. Finally, this study expands the importance of pyroxenites in the off-craton lithospheric mantle as important hosts for volatiles to including ^{3}He, CO_2, Li and P.

Overall, this study provides the first, fully internally-consistent appraisal of the petrography, mineral and calculated whole-rock major, trace and volatile element chemistry, and helium and carbon compositions of fluid-inclusions to advance the understanding of volatiles in the sub-continental lithospheric mantle on a global scale.

Table of contents

List of figures

Chapter 1

Chapter 2

Chapter 3

Chapter 4

Chapter 5

Chapter 6

Chapter 7

Chapter 8

Chapter 9

Chapter 10

Chapter 11

List of tables

Chapter 3

Chapter 7

Chapter 8

Chapter 1. Introduction

1.1. What is the lithospheric mantle?

The lithosphere transfers heat by conduction and is separated into the crust and lithospheric mantle (McKenzie & Bickle, 1988; Figure 1.1). It is separated from the overlying crust by the Moho, and the underlying convecting mantle (asthenosphere) by the lithosphere-asthenosphere boundary. The lithospheric mantle is compositionally and physically distinct beneath the oceanic crust (sub-oceanic lithospheric mantle) and the continental crust (sub-continental lithospheric mantle). The long term segregation of the asthenosphere and lithospheric mantle has enabled these reservoirs to have distinct chemical and isotopic compositions.

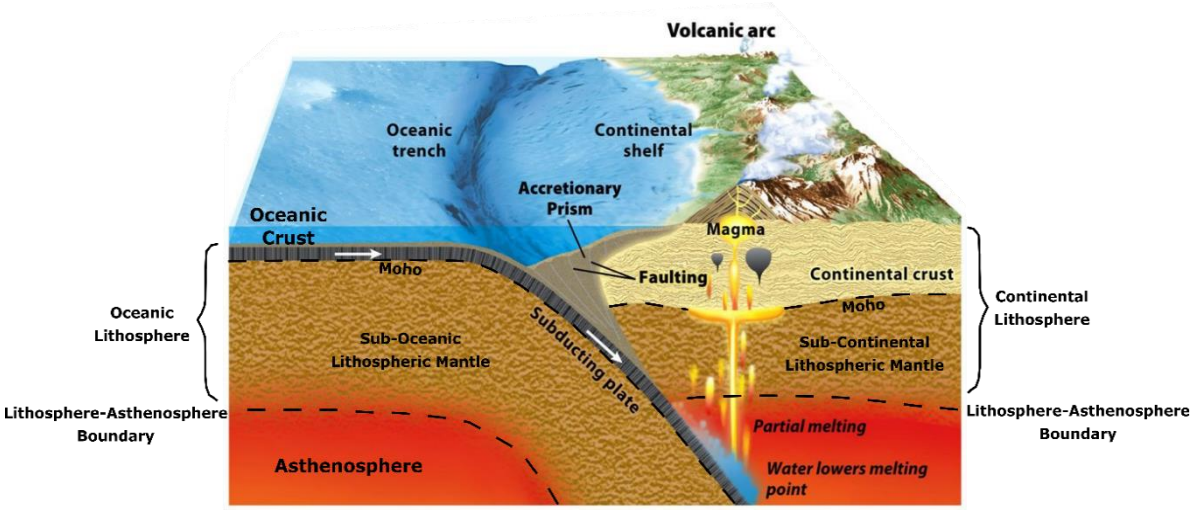

Figure 1.1. Cartoon schematic showing convergent boundary between oceanic and continental crust with lithospheric and asthenospheric reservoir boundaries illustrated. Not to scale.

The lithosphere consists of several major layers (Figure 1.2):

i) The mechanical boundary layer (MBL), which constitutes the upper most part of the lithosphere and is where heat is transported by conduction. This layer is rarely physically or chemically perturbed and is stable on geologically significant timescales. The conductive geotherm is commonly constrained by pressure-temperature estimates of ultramafic xenoliths and extrapolated to the average isentropic profile in the asthenosphere (this has a potential temperature of 1315 °C for present-day ambient mantle).

ii) The thermal boundary layer (TBL), which represents the region where heat transport in the mantle transitions from conduction to convection. Material within the thermal boundary layer convectively exchanges with the underlying asthenosphere and retains its geochemical signatures on very short timescales. Within the TBL is the lithosphere-

asthenosphere boundary, which is located where the conductive geotherm of the lithosphere intersects the isentrope in the asthenosphere.

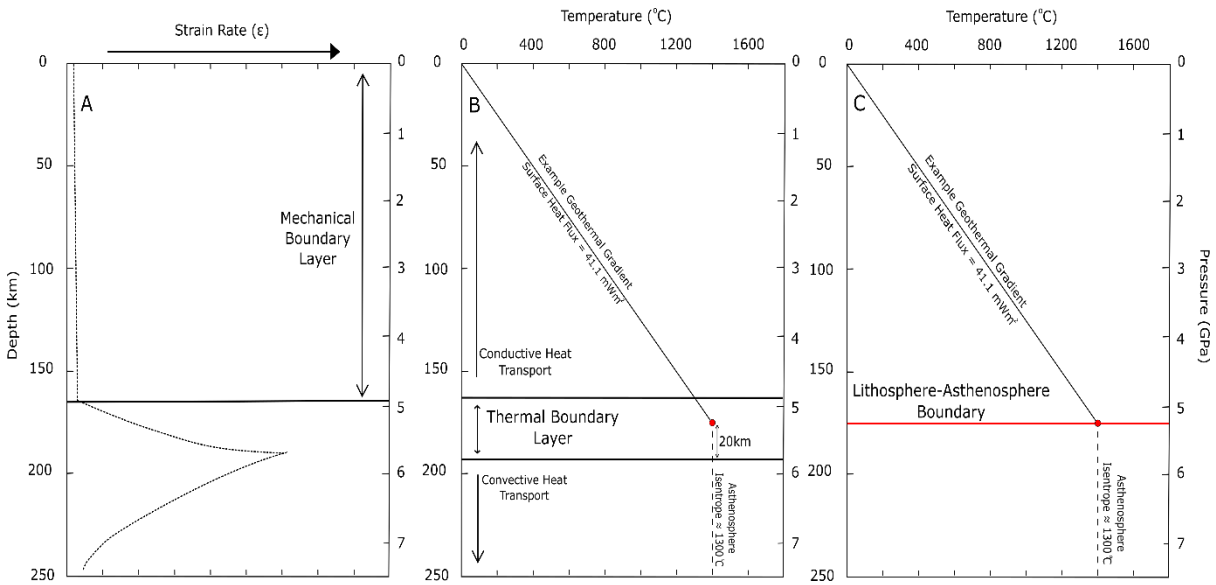

Figure 1.2. Schematic representation of; A) Mechanical Boundary Layer; B) Thermal Boundary Layer; C) Lithosphere-asthenosphere boundary following definitions from McKenzie & Bickle (1988). Figure adapted from Eaton et al. (2009).

The origin of the lithospheric mantle has been investigated through the compositions of small-fraction melts (kimberlites, lamprophyres, etc) generated during major heating and rifting events (e.g. McKenzie, 1989; Gibson *et al.*, 1995; Francis & Patterson, 2009), and also from their cargo of xenoliths and xenocrysts (e.g. Dawson, 1984; Pearson *et al.*, 1995; Witt-Eickschen *et al.*, 2003; Gibson *et al.*, 2013). Major- and trace-elements, together with Sr, Nd and Hf isotopic ratios of this entrained material show that the sub-continental lithospheric mantle initially formed as a residue of melting in the convecting mantle (e.g. Herzberg, 2004; Gibson *et al.*, 2008; Pearson & Wittig, 2008; Pearson *et al.*, 2021) but has typically also undergone subsequent metasomatic enrichment. This has involved the percolation and crystallisation or reaction of small-fraction volatile-rich melts or fluids, derived from the convecting mantle or subducted oceanic lithosphere (e.g. O'Reilly & Griffin, 2013). The subcontinental lithospheric mantle can be divided into the on- and off-craton lithospheric mantle. The former is older (>2.5 Ga), thicker (>150 km) and more depleted in magma-phile elements (such as Fe, Ca and Al) than the latter.

1.2. Why is the sub-continental lithospheric mantle important?

The physical attributes of the lithospheric mantle play a vital role in facilitating life at the Earth's surface. This is because this reservoir is able to provide vital thermal insulation and mechanical separation from the underlying hot convecting mantle (e.g. Griffin *et al.*, 2003). Furthermore, it is an excellent filter, and essentially able to modulate the flux of volatile elements from the convecting

mantle to Earth's surface (e.g. Gibson *et al.*, 2020). As a result, disruption to this layer may have dramatic consequences on biogeochemical cycles at Earth's surface with potentially catastrophic effects (e.g. Broadley *et al.*, 2018). Finally, the sub-continental lithospheric mantle plays an important role in producing mineral deposits which will be vital for a green future; when the lithospheric mantle becomes physically perturbed (e.g. during rifting) it may generate magmas that are enriched in key elements (e.g. Au and platinum group elements) that evolve and crystallise to form giant ore deposits (e.g. Wang *et al.*, 2020).

1.3. Petrology of the sub-continental lithospheric mantle

Mantle xenoliths entrained by magmas in cratonic (e.g. kimberlites) and off-craton settings (e.g. alkali basalts, nephelinities and basanites) reveal that the sub-continental lithospheric mantle is predominantly composed of olivine, orthopyroxene and clinopyroxene together with an aluminous phase (spinel and/or garnet). These phases occur in varying amounts so that the lithospheric mantle is lithologically heterogeneous. The various lithologies can broadly be distinguished into 3 groups according to the following methods of formation:

i) Crystallised channels of melts.
ii) Residues of upper-mantle melt extraction.
iii) Reactive infiltration of melts

Samples of mantle that are formed by crystallisation of channelised melts typically include dunites, wehrlites and pyroxenites. These melts may be sourced from the asthenosphere or recycled oceanic lithosphere (e.g. Downes, 2007). The composition of the mantle that forms as a result of channelised flow is controlled by both the composition of the incoming melts and the physical nature of the surrounding mantle. For example, clinopyroxene forms as a common reaction product while the formation of metasomatic olivine and orthopyroxene depend on the silica activity, pressure and temperature conditions (Lambart *et al.*, 2012 and references therein)

Mantle lithologies that formed as melt residues are dominated by harzburgites (and dunites in Archean times; Bernstein *et al.*, 2007). These formed in the convecting mantle via varying amounts of melt-extraction (e.g. Herzberg, 2004; Pearson & Wittig, 2014). By combining detailed petrological studies of abyssal peridotites with experimental run products valuable insights have arisen into the nature of enrichment and depletion of the lithospheric mantle. These have shown that samples with greater proportions of olivine relative to orthopyroxene and clinopyroxene are typical of more depleted melt residues. In contrast, samples that have greater proportions of orthopyroxene and clinopyroxene relative to olivine have experienced less depletion, or have become subsequently

enriched due to metasomatism, i.e. have been refertilised (Workman & Hart, 2005 and references therein). The effect of melt extraction on mantle lithology is shown on Figure 1.3.

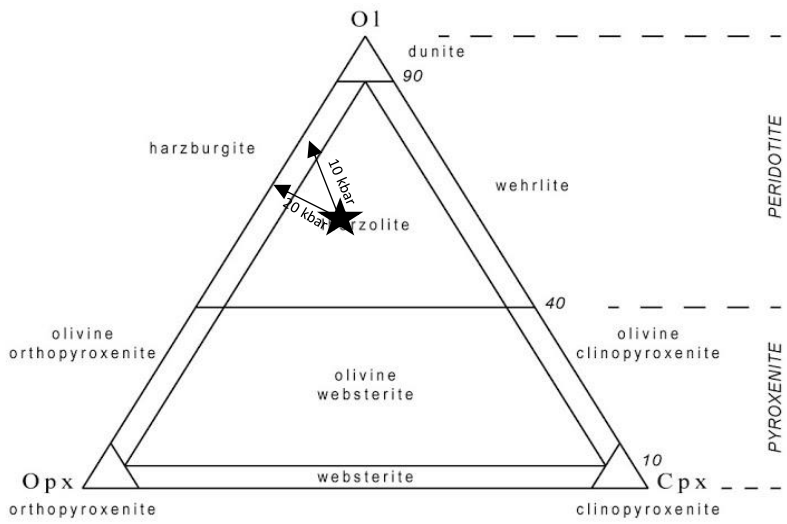

Figure 1.3. The IUGS ternary classification diagram for ultramafic rocks (Le Bas & Streckeisen, 1991). The black star shows the composition of fertile peridotite and the arrows indicate the effect of melting on modal compositions at 10 and 20 kbar. Melting model after Niu (1997).

The most common aluminous phase in mantle peridotites is spinel and/or garnet. This is because plagioclase is only stable in low pressure environments (typically <5 kbar), whereas spinel is stable at <15-20 kbar and garnet may occur with spinel at pressures >15-20kbar (Figure 1.4). Furthermore, mantle xenoliths also contain additional 'metasomatic' minerals, e.g. the MARID suite, which consists of mica (phlogopite), amphibole (K-richterite), rutile, ilmenite, diopside (Dawson, 1984). These metasomatic phases (and garnet and spinel) form in peridotites after the initial depletion process (Gregoire *et al.*, 2002; Fitzpayne *et al.*, 2018).

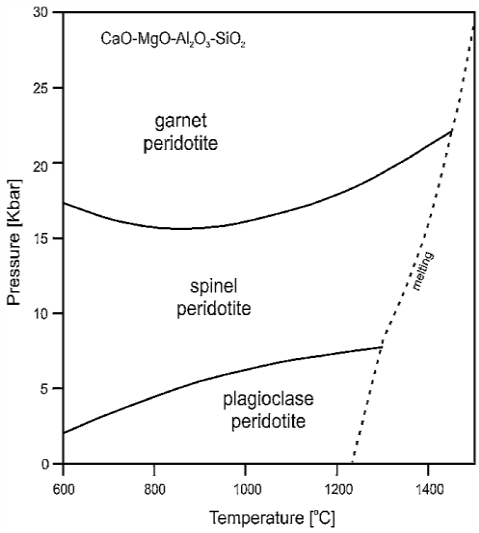

Figure 1.4. Stability fields of plagioclase, spinel and garnet in a CaO-MgO-Al_2O_3-SiO_2 system under varying pressure (0-30kbar) and temperature (600-1500°C). Figure from Perkins & Anthony using information from Gasparik (1984), Dixon (1980) and Presnall (1976).

Based on orogenic massifs and mantle xenolith suites, peridotite is by far the most dominant ultramafic composition in the upper mantle (accounting for 90 to 98%) while pyroxenite accounts for the remainder (Hirschmann & Stolper, 1996; Downes, 2007).

1.4 Fluid-Inclusions in sub-continental lithospheric mantle phases

Minerals in mantle xenoliths sometimes contain abundant CO_2-rich bubbles, which are the dominant reservoir for carbon in the off-craton mantle. These form as accidentally trapped fluids, which also contain minor quantities of CO, SO_2, H_2O and N_2 (Andersen & Neumann, 2001).

The lithospheric mantle varies in temperature (800 to ~1315 ^{o}C), pressure (1 to ~7 GPa) and oxygen fugacity (1 to ~-5 FMQ). Under the reducing conditions (< -1.6; FMQ) that are most typical for on-craton mantle (e.g. Hanger, 2014) carbon will exist as graphite at low pressures (<4.5 GPa) and diamond at high pressures (>4.5 GPa; Figure 1.5). Under the more oxidising conditions (>-1.6 FMQ) that are typical of off-craton mantle (e.g. Malaspina *et al.*, 2009) carbon will exist as a solid (carbonate) or as CO_2 fluids.

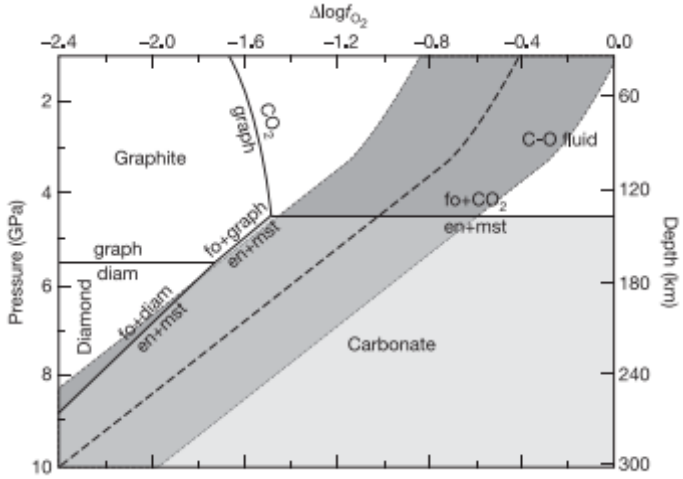

Figure 1.5. Carbon speciation at various pressures, temperatures and oxygen fugacities. Dark grey shaded region shows the typical adiabat for mid-ocean ridge mantle. Fo = forsterite, en = enstatite, graph = graphite, mst = magnesite, diam = diamond.

The CO_2 fluids observed in minerals found in peridotite and pyroxenite xenoliths are hypothesized to form by two main mechanisms. This first where carbonated peridotite becomes unstable at a given *P-T* point (termed the carbonate ledge; Figure 1.6) and decarbonation of dolomite-bearing peridotite occurs changing carbonate to CO_2-fluid (e.g. White & Wyllie, 1992; Moore & Wood, 1998; Equation 1.1). The second mechanism related to carbonate observed in fluid-inclusions. Frezzotti & Touret (2014) have proposed that these inclusions may also initially have hosted carbonate which has undergone complete or partial decarbonation during ascent.

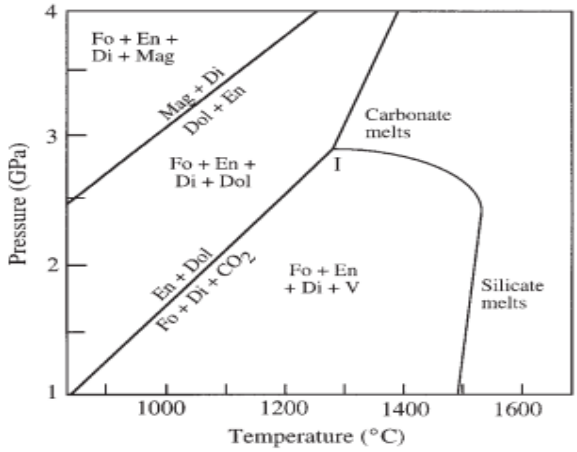

Figure 1.6. Stability of carbonated peridotite in oxidising upper-mantle conditions showing the carbonate-ledge at 2.5 to 2.75 GPa and the transition of dolomite to CO_2 fluid. Abbreviations are the same as Figure 1.5 with V= CO_2 vapour. Figure from Moore & Wood (1998).

$CaMg(CO_3)_2 + 4MgSiO_3 = CaMgSi_2O_6 + 2Mg_2SiO_4 + 2CO_2$ Equation 1.1

dolomite met + orthopyroxene = clinopyroxene + olivine + fluid

Fluid inclusions have been the subject of extensive investigations because they represent the dominant reservoir for many volatile species. These have included numerous micro-thermobarometry studies (e.g. Kobayashi *et al.*, 2019) to investigate CO_2-density. Estimates of CO_2 density in the global mantle xenolith database typically ranges from 0.6 to 1.2 g/cm^3 and correspond to trapping pressures of 0.5 to 1.5 Gpa. However, low-density inclusions sometimes co-exist in the same mineral. This has been inferred to result from either bubble volume expansion or decrepitation during transport to the surface (Andersen & Neumann, 2001). Expansion or decrepitation occurs as a result of the fluid inclusions experiencing a drop of external pressure while still maintaining high internal pressure. As the external and internal pressures becoming increasingly different, the fluid inclusions experience greater overpressure ($\Delta P > 0$), which causes the bubble to expand until it reaches a threshold and decrepitates (i.e. breaks). This concept is outlined in Figure 1.6.

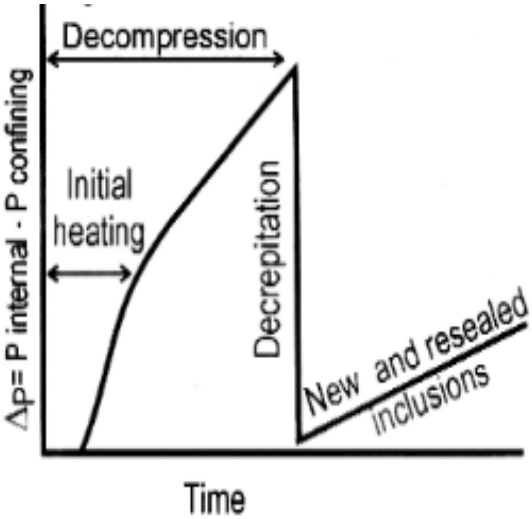

Figure 1.7. Relative quantitative relationship between overpressure and time. Figure from Andersen & Neuman (2001).

For the purposes of this study, bubble stretching and decompression are largely inconsequential because these processes permit fluid-inclusions to retain their primary compositions. However, the process of decrepitation is more significant because it may enable fluid-inclusions to re-equilibrate with the magmas hosting the mantle xenoliths. This would reset the fluids to be a hybrid of the primary and host-magma composition.

To investigate the response of CO_2-rich inclusions to deformation, Yamamoto *et al.* (2011) conducted annealing experiments on olivine, pyroxene and spinel. They found that these minerals showed clear evidence of volume expansion, but little to no sign of decrepitation. As a result, Yamamoto *et al.* (2011) concluded that these minerals would effectively retain their CO_2 signatures. This is further highlighted in models by Campione *et al.* (2015), which show that so long as fluid-inclusions are $\lesssim$ 5 µm, they are unlikely to experience decrepitation. Overall, given the small sizes of fluid-inclusions within mantle xenoliths, the evidence from Yamamoto *et al.* (2011) and Campione *et al.* (2015) indicates than fluid-inclusions within mantle minerals retain their primary signatures.

1.5 Chemistry of lithospheric mantle minerals

The main factor governing the distribution of the different elements on Earth is their geochemical behaviour/affinity. They can be broadly classified as 'lithophile', 'siderophile', 'chalcophile', 'atmophile', after Goldschmidt (1937). Lithophile (rock-loving) elements are preferentially partitioned into silicate minerals as oxides (Figure 1.7) and dominantly include O, Si, Fe, Ca, Mg, Mn, Ti, Na, K, REE (rare-rarth elements), U and Th. Siderophile (iron-loving) elements are preferentially partitioned into metals, such as in Earth's core, and are dominated by Fe, Ni, W, Co, noble metals (Pt, Pd, Ir, Ru, Rh and Os) as well as reduced Si and C. Chalcophile (copper-loving) elements are those that commonly form sulfide minerals, such as As, Te, Tl, Sn, Sb, Hg, Mo, Cd, Zn, Pb, Cu and some

noble-metals. Atmophile (air-loving) elements are highly volatile compounds mostly found in the atmospheres, such as O, C, H, N, S.

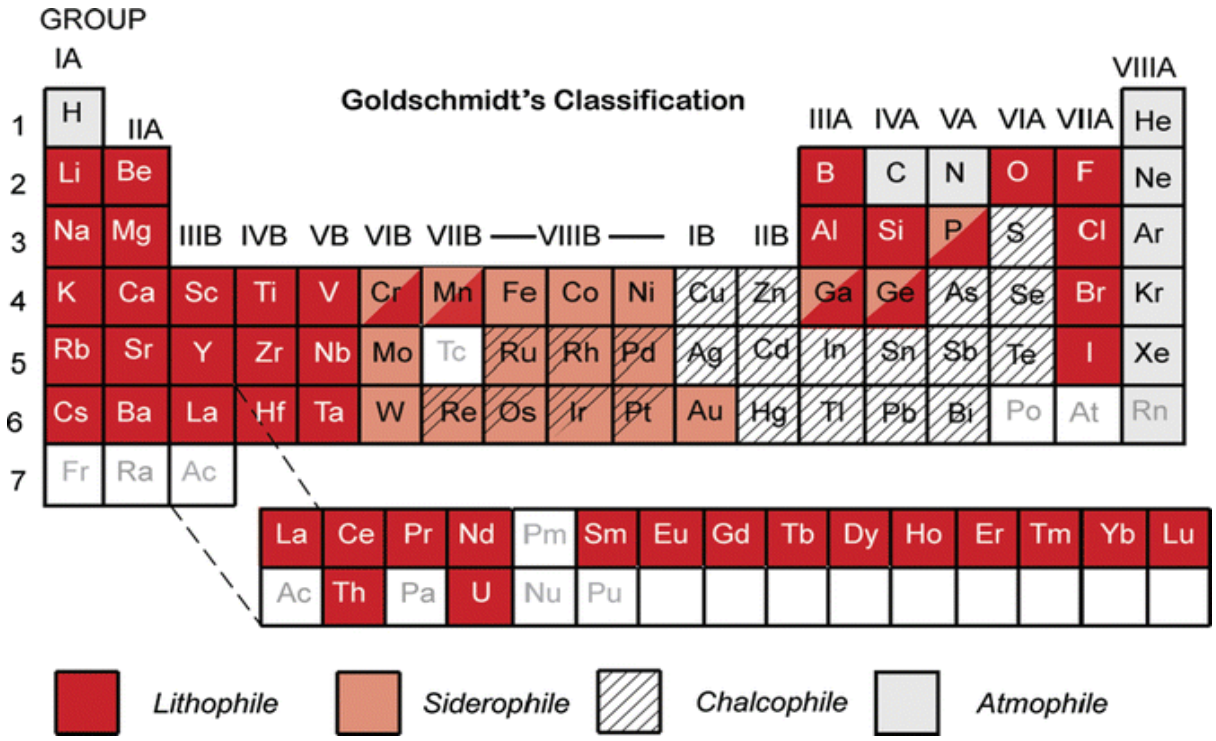

Figure 1.8. Periodic table of elements with Goldschmidt's classification superimposed with corresponding colours.

The lithospheric mantle is dominantly comprised of lithophile elements, with lesser amounts of siderophile, chalcophile and atmophile elements. The abundances of these elements in different phases can be classified into major, minor and trace amounts. The major elements comprise >0.4 wt% of a crystal lattice, while minor and trace elements comprise 0.1 to 0.4 wt% and <0.1 wt%, respectively.

The incorporation of elements into mantle phases from a melt can be described through the process of partitioning, i.e. the equilibrium of a chemical species between phases. The degree of this partitioning is described through a coefficient (*D*) outlined by Equation 1.2.

$$D_i^{a/b} = C_i^a / C_i^b \qquad \text{Equation 1.2}$$

Where C is the concentration of a species, *a* represents phase 1 and *b* is phase 2.

When applied to a mineral-melt system, an element which is in equilibrium has a *D* = 1. If this element preferentially partitions into a melt over a crystal it is incompatible (*D* <1), while if it preferentially partitions into a crystal over melt it is compatible (*D* >1). The partitioning of elements

together with the preference of large ionic radii elements for clinopyroxene>orthopyroxene>olivine is displayed in Figure 1.8

A summary of the factors controlling the chemistry of the lattice of each common mantle phase is presented:

Olivine has the formula M_2TO_4, where M is the octahedral site containing Mg^{2+} and Fe^{2+} and the T site comprises Si^{4+}, where Mg^{2+}, Fe^{2+} and Si^{4+} have ionic radii of 0.72Å, 0.78Å and 0.26Å, respectively. Because impurities of minor and trace elements typically have ionic radii similar to Mg^{2+} and Fe^{2+} (e.g. Ni^{2+} = 0.69Å, Mn^{2+} = 0.83Å), they commonly occupy the M site. Minor and trace cations with 1^+, 2^+, 3^+, 4^+ and 5^+ are incorporated into the olivine lattice through coupled substitution by replacing Mg^{2+}, Fe^{2+} and Si^{4+} with a differently charged element (e.g. Al^{3+} or Fe^{3+}) for charge balance. Small trivalent cations (e.g. Sc^{3+} = 0.745Å, V^{3+} = 0.64Å) may substitute into the M site, however REE (La to Lu) have significantly larger ionic radii (Lu = 0.861Å, La = 1.032Å) and are very incompatible in olivine. Thus, olivine is largely devoid of REE.

Pyroxene has the formula XYT_2O_6, with the T site accommodating tetrahedrally co-ordinated Si^{4+} and Al^{3+} and X and Y sites denote an M1 site (VI-fold typically for Mg^{2+}, Fe^{2+} and Al^{3+}) and a larger M2 site (e.g. Ca^{2+}, Na^+ and K^+). Smaller divalent cations (e.g. Ni^{2+} and Co^{2+}) with ionic radii similar to Mg^{2+} and Fe^{2+} will typically enter the M1 site. As larger cations (e.g. Ca^{2+}) enter the M2 site, the co-ordination number of this site increases from VI-fold to VIII-fold, generating larger ionic radius (e.g. $^{VIII}Ca^{2+}$ = 1.12Å v $^{VI}Ca^{2+}$ = 1.0Å), allowing greater incorporation of REE. In essence, because clinopyroxene has more Ca than orthopyroxene, it can incorporate more trace elements with large ionic radii (e.g. REE, Sr, Ba, Na). Akin to olivine, incorporation of varyingly charged elements requires coupled substitution. The most common type of clinopyroxene in the lithospheric mantle is a as a chromium-bearing diopside ($Ca(Mg,Cr)Si_2O_6$. The high calcium content mean that it can incorporate trace elements with large ionic radii (e.g. REE, Sr, Ba, Na).

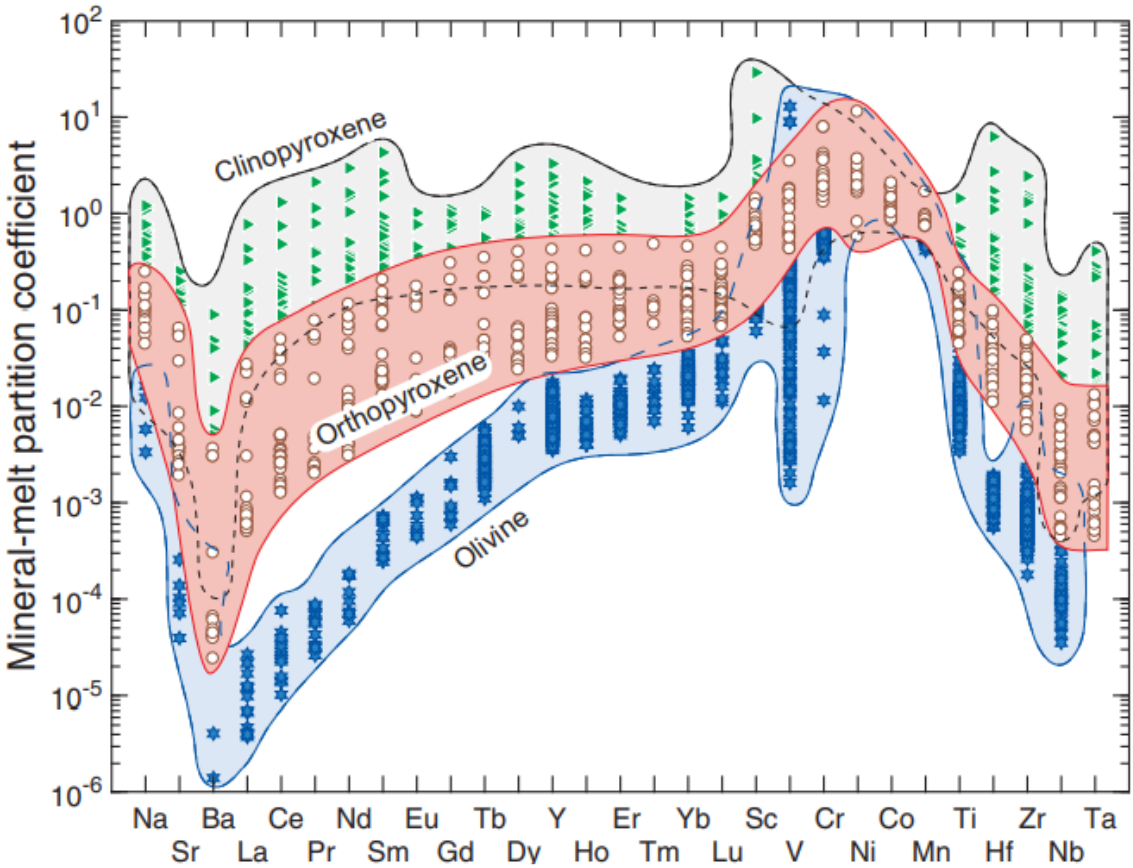

Figure 1.9. Mineral-melt partition coefficients of olivine, orthopyroxene and clinopyroxene for different elements. Partition coefficients for olivine, orthopyroxene and clinopyroxene from Sun (2018) and references therein.

Garnet has the general formula $X_3Y_2T_3O_{12}$, where the X site has VIII-fold coordinated divalent cations (Ca^{2+}, Fe^{2+}, Mg^{2+} and Mn^{2+}), the Y site has VI-fold coordinated smaller trivalent cations (Al^{3+}, Cr^{3+} and Fe^{3+}) and the T site is dominated by tetrahedral Si^{4+}. In general, X and Y sites incorporate trace element cations, with large ones (e.g. REE^{2+}, Na^{+}, Ba^{2+} and Sr^{2+}) favouring the X site and small ones (e.g. Ti^{5+}, V^{3+}, Cr^{3+}) the smaller Y site. Intermediate cations (e.g. Ni^{2+}, Co^{2+}, Zr^{4+}, Hf^{4+} and V^{3+}) can occupy either X or Y site. Like pyroxene, the greater amount of Ca^{2+} produces overall larger X sites, there enhancing the substitution of larger cations.

Spinel has the general formula XY_2O_4, with the X site typically comprising divalent cations (Mg^{2+} and Fe^{2+}) and the Y site comprising trivalent cations (Al^{3+}, Cr^{3+} and Fe^{3+}). Spinel structures occur with near-cubic packed oxygen atoms and cations (X and Y sites) occupying interstices in the lattice. Due to the small size of these X and Y sites, only equally-small minor elements (e.g. Ni^{2+}, Mn^{2+}, Sc^{3+}, V^{3+}) may be incorporated as impurities. Thus, like olivine, elements with larger ionic radii (e.g. REE, LILE) are highly incompatible with spinel-group minerals.

Mica ($XY_{2-3}Z_4O_{10}(OH)_2$ is composed of a tetrahedral (Si and Al), octahedral (Al, Cr, Fe^{3+}, Ti, Fe^{2+}, Mg, Mn), interlayer (K, Na, Ca, Ba) and hydroxyl (OH, F, Cl, O) site. It is most commonly observed in mantle xenoliths as phlogopite ($KMg_3[AlSi_3]O_{10}(OH)_2$. The diversity of the crystal structure allows a large range in cation charge, which enables a large range of trace elements (e.g. REE, LILE) to be incorporated into the structure.

Amphibole ($AB_2C_5T_8O_{22}(OH)_2$) is composed of a tetrahedral (Si and Al), small octahedron (Al, Cr, Fe^{3+}, Ti, Fe^{2+}, Mg), medium octahedral (Fe^{2+}, Mg, Mn), larger cation (Ca, Na, Mn, Fe^{2+}, Mg) and A (Na, K) site. It is most commonly observed in the mantle as kaersutite ($NaCa_2(Mg_3Ti^{4+}Al)(Si_6Al_2)O_{22}(OH)_2$), pargasite ($NaCa_2(Mg_4Al)(Si_6Al_2)O_{22}(OH)_2$) and K-richterite ($K(NaCa)Mg_5Si_8O_{22}(OH)_2$). Akin to mica, the diversity and range of cations enable a large range of cations to be incorporated.
Rutile is a TiO_2 polymorph in a tetragonal crystal lattice. Most common impurities are Fe, Ta, Nb, Cr, V, Sn, W and Sb.
Ilmenite is a titanium-iron oxide with the formula $FeTiO_3$, where Fe^{2+} and Ti^{4+} occupy alternating layers perpendicular to the C-axis. It most commonly contains impurities of Mn and Mg.

In the lithospheric mantle, clinopyroxene and garnet are the dominant hosts for REE (Figure 1.9) but have different styles of REE incorporation. The heavy-REE (e.g. Dy, Ho, Lu) have similar ionic radii to those in the garnet X site, making them more compatible than in clinopyroxene. Conversely, garnet has a much more 'rigid' lattice than clinopyroxene, enabling less substitution of the larger light-REE (e.g. La, Ce, Pr) and producing a tighter Onouma parabola (Figure 1.10). Thus, garnet is more highly incompatible for LREE relative to clinopyroxene.

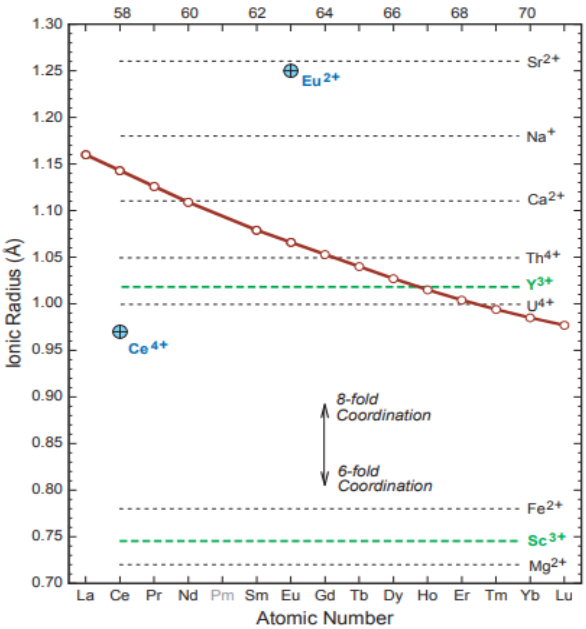

Figure 1.10. Plot of ionic radius (red line) versus atomic number with other trivalent rare-earth elements and other select cations after McLennan (2018).

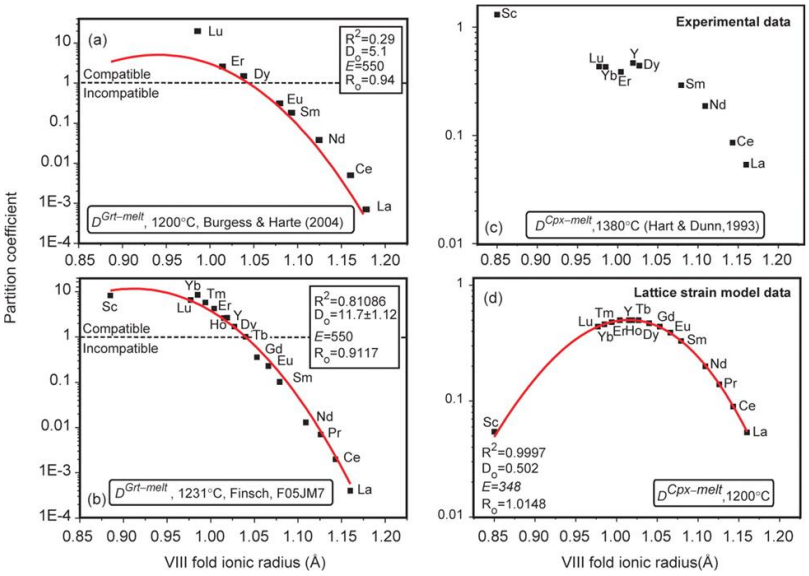

Figure 1.11. Lattice-strain models of mineral-melt partition coefficients (*D*) and ionic radii of given elemenets for; A+B) clinopyroxene; and C+D) garnet. Figures are adapted from Gibson et al. (2008) who used the experimental data from Hart & Dunn (1993) and Burgess & Harte (2004).

1.6 Isotope geochemistry

1.6.1 Helium isotopes

Helium is a noble gas with two stable isotopes, ^{3}He and ^{4}He. These are typically expressed as ^{3}He/^{4}He relative to atmospheric ^{3}He/^{4}He compositions (Ra) in Equation 1.3:

$$\frac{^3He}{^4He}Ra = \frac{\left(\frac{^3He}{^4He_{Sample}}\right)}{\left(\frac{^3He}{^4He_{Air}}\right)} \qquad \text{Equation 1.3}$$

Where the ^{3}He/^{4}He of air is 1.38x10^{-6}.

^{3}He is a primordial isotope formed during nucleosynthesis while ^{4}He is a radiogenic isotope formed by the decay of U and Th (e.g Pepin and Porcelli, 2002). Because of these different formation mechanisms the relative abundance of ^{3}He and ^{4}He varies within different Earth reservoirs. The crust is characterised by low ^{3}He/^{4}He, with an average of 0.02 Ra (Ballentine and Burnard, 2002), indicative of high U+Th/^{3}He environments (Figure 1.11). Mantle reservoirs have higher ^{3}He/^{4}He due to greater concentrations of ^{3}He and lower concentrations of U+Th. The upper-mantle (mid-ocean ridge basalt source) has ^{3}He/^{4}He 8 ± 1 Ra (Allegre *et al.*, 1995) whereas the deep primordial mantle has >10 Ra (e.g. Stuart *et al.*, 2003; Porcelli & Elliott, 2005).

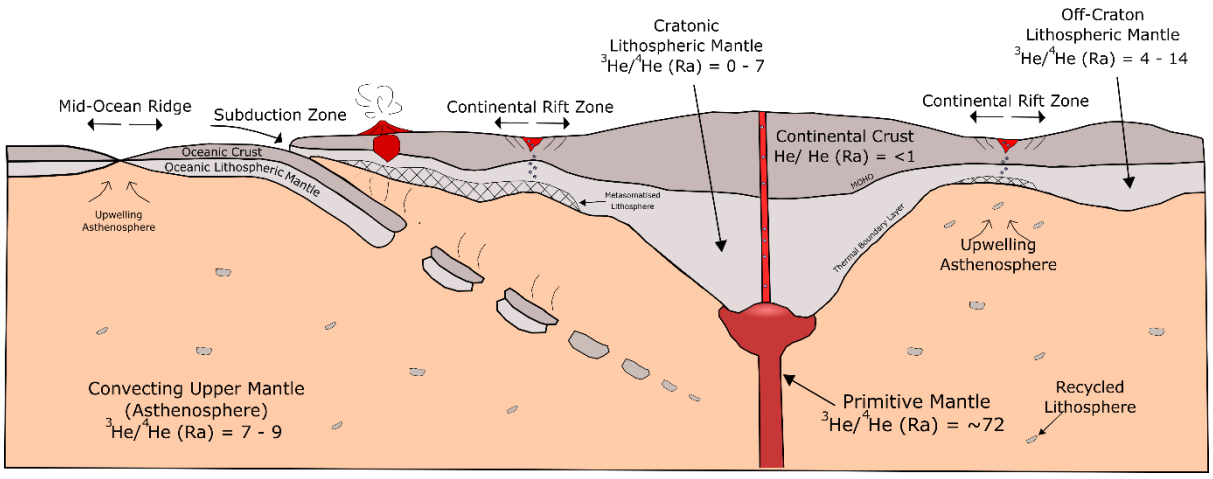

Figure 1.12. $^3He/^4He$ (Ra) compositions for different reservoirs of Earth with constraints mentioned in the text. Figure adapted from Goodneough et al. (2015).

The lithospheric mantle exhibits a range of $^3He/^4He$. In the of off-craton lithospheric mantle $^3He/^4He$ ranges from 0.5 to 14 Ra and from 0.05 – 7 Ra in on-craton lithospheric mantle (Halldorson *et al.*, 2014; Day *et al.*, 2015). This variation is thought to be the result of multiple processes, such as: i) radiogenic ingrowth from ambient U+Th decay; and ii) variable interaction with melts from recycled lithosphere, the convecting upper-mantle and primordial material. However, constraining these processes and the variable interaction of melts and fluids from different reservoirs remains an outstanding issue.

1.6.2 Carbon isotopes

On geological timescales, carbon has two isotopes: ^{12}C and ^{13}C. These are typically expressed as $\delta^{13}C$ shown in Equation 1.4:

$$\delta^{13}\mathrm{C}\ ‰ = \left(\frac{\left(\frac{^{13}\mathrm{C}}{^{12}\mathrm{C}}\mathrm{sample}\right)}{\left(\frac{^{13}\mathrm{C}}{^{12}\mathrm{C}}\mathrm{VPDB}\right)} - 1\right) \times 1000 \qquad \text{Equation 1.4}$$

Where VPDB $^{13}C/^{12}C$ is 0.0112372.

Carbon isotopes fractionate from each other due to equilibrium and kinetic effects. During a reaction under equilibrium conditions the heavier isotope (^{13}C) concentrates into the compound that is bound most strongly. An example of this is the exchange of CO_2 (g) and HCO_3 (aq) where the H-C bond in stronger than that of CO_2 as shown by Equation 1.4:

$$^{13}CO_2\ (g) + H^{12}CO_3^-\ (aq) = {}^{12}CO_2 + H^{13}CO_3^-\ (aq) \qquad \text{Equation 1.5}$$

Furthermore, kinetic effects occur due to different rates of reactions for ^{13}C and ^{12}C, where the activation energy for a reaction is smaller than that of the heavy isotope. As a result, the lighter (^{12}C)

isotope will react faster and become enriched relative to the heavier (^{13}C) isotope. This is schematically displayed by Figure 1.12.

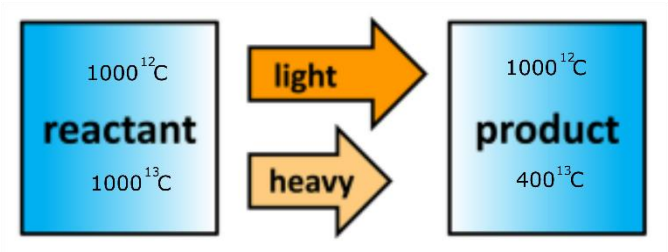

Figure 1.13. Schematic representation of kinetic isotope effect on ^{13}C and ^{12}C, where the lighter isotope will react faster and become preferentially enriched relative to the heavy isotope. Figure adapted from Wiederhold (2015).

Because these processes occur to varying degrees in different Earth reservoirs, the $^{12}C/^{13}C$ compositions have proven key in identifying their relative roles (Figure 1.12). Crustal reservoirs of carbonate have $\delta^{13}C$ of 0 to 5 ‰ (Gradstein *et al.*, 2012), organic carbon of < -20 ‰ (Planavsky *et al.*, 2011) and altered oceanic crust <-20 ‰ (e.g. Li *et al.*, 2019 and references therein). Additionally, the convecting upper-mantle has a $\delta^{13}C$ value of -5 ± 2‰ (Cartigny *et al.*, 2014; Figure 1.13).

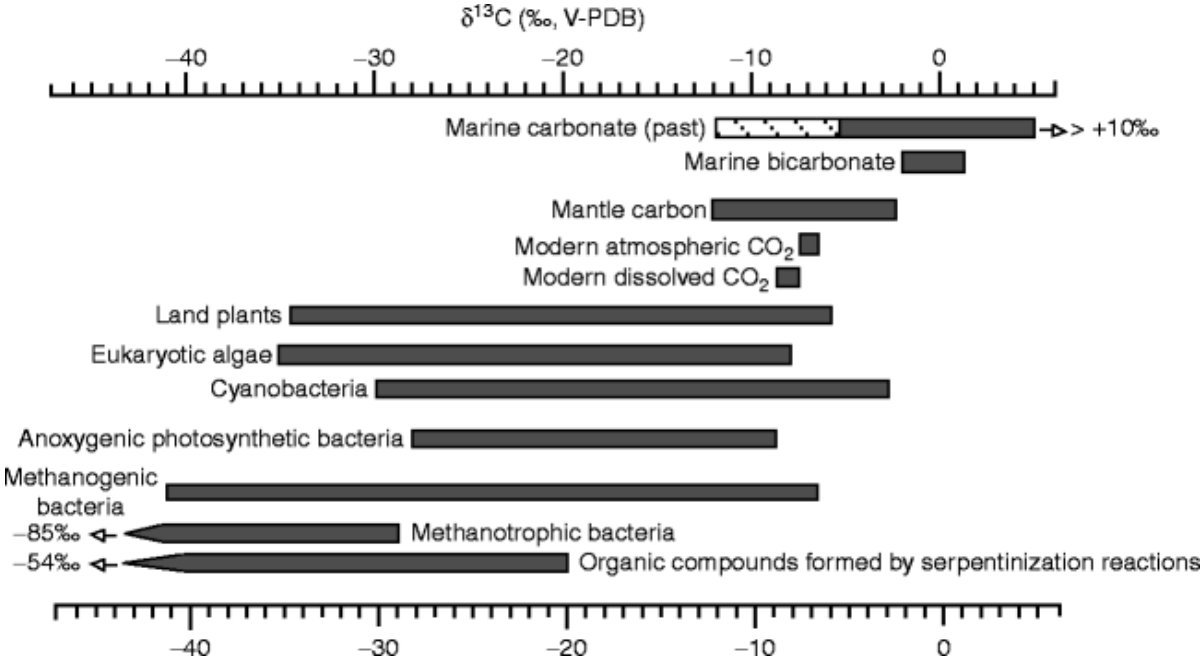

Figure 1.14. $\delta^{13}C$ range for significant carbon-bearing reservoirs of Earth. Figure from Planavsky et al. (2015).

These constraints for $\delta^{13}C$ have also provided key insights to understanding the origin of carbon in the cratonic mantle through diamond studies (e.g. Mikhail *et al.*, 2019; Li *et al.*, 2019) and off-craton mantle xenoliths (e.g. Deines, 2002).

1.7 Geochemical variability of the lithospheric mantle

The chemistry of the lithospheric mantle is exceptionally heterogeneous, primarily because it has formed in different melting regimes and been subjects to variable metasomatic processes. These are discussed below.

1.7.1 Melting

The lithospheric mantle is understood to have formed as a residue of melting in the convecting upper-mantle (see section 1.1). However, the extent of melt extraction experienced by the lithospheric mantle is spatially and temporally heterogeneous (e.g. Griffin *et al.*, 2003; Herzberg & Rudnick, 2012) and varies with age. An example of this is the young lithospheric mantle sampled beneath Kilbourne Hole in the Western USA that has experienced little melting (e.g. Harvey *et al.*, 2012) and the ancient lithosphere from Ubekendt Ejland in Greenland, which has experienced extensive melting over a prolonged geological history (e.g. Bernstein *et al.*, 2006).

Evidence for partial melting can be identified using various methods. The simplest is from the relative proportions of olivine and orthopyroxene to clinopyroxene (see section 1.3). However, more sophisticated and quantitative melting models have been developed. A common way of doing this is by comparison of elements with varying compatibility during melting. For example, in olivine and pyroxene Mg and Fe are very abundant yet they have different behaviours during melting. Whereby, Mg is more incompatible in a melt (i.e. has greater affinity to olivine and pyroxene during melting) than Fe. Therefore, as the mantle experiences greater degrees of partial melting, the residue (i.e. peridotite or pyroxenite) becomes more enriched in Mg compared to Fe (expressed as Mg# = 100 x (Mg/(Mg+Fe)). Experiments summarized by Bernstein *et al.* (2007) have quantified this relationship for olivine from the lithospheric mantle (Figure 1.14), which equates approximately to:

Melt Extraction (%) = 11.1 x Olivine Mg# - 990.

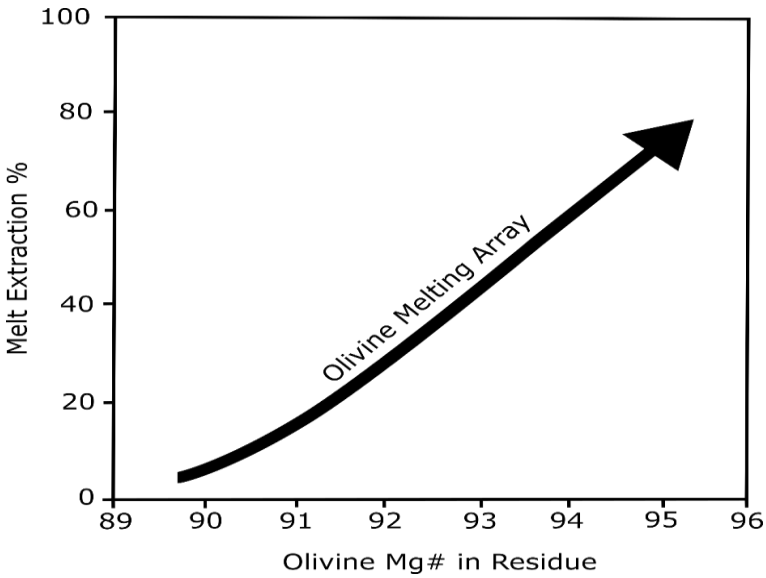

Figure 1.15. Experimentally constrained olivine Mg# and melt extraction (%) using data summarized by Bernstein et al. (2006).

This relationship has also been semi-quantified by Boyd (1989) who observed that the most olivine-rich abyssal peridotites have a more depleted chemistry (Figure 1.15A). This relationship between mineral chemistry and modal mineralogy has enabled the development of simple melting models that show the effect on whole-rock chemistry. These use abyssal peridotites to highlight the relationship between melting and whole-rock Al_2O_3 and CaO (Figure 1.15B; Boyd, 1989).

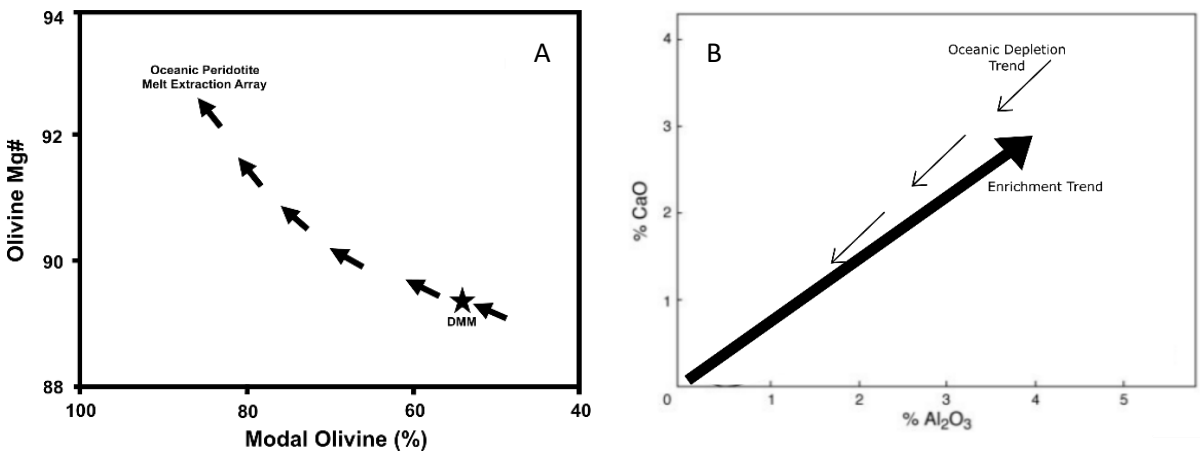

Figure 1.16. A) Modal olivine (%) and olivine Mg# with oceanic peridotite melt-extraction array overlain. B) Whole-rock Al_2O_3 (wt%) and CaO (wt%) with oceanic depletion trend and enrichment trend overlain. Both figures are after Boyd (1989).

The observations of Boyd (1989) have been built on by secular evolution models (e.g. Griffin *et al.*, 2003; Griffin *et al.*, 2009). This work has focussed on comparing the whole-rock Al_2O_3 and CaO (wt%) of Archean, Proterozoic and Phanerozoic and the asthenosphere (Figure 1.16). These authors showed that younger lithosphere preserves a less-depleted and more-fertile composition, and argued that this reflects progressive modification of relict and buoyant Archean lithosphere. In

contrast, other authors (e.g. Herzberg & Rudnick, 2012; Servali & Korenaga, 2018) have suggested that this relationship reflects decreasing upper-mantle temperatures through time, which would permit the generation of new lithospheric mantle with a less depleted chemistry.

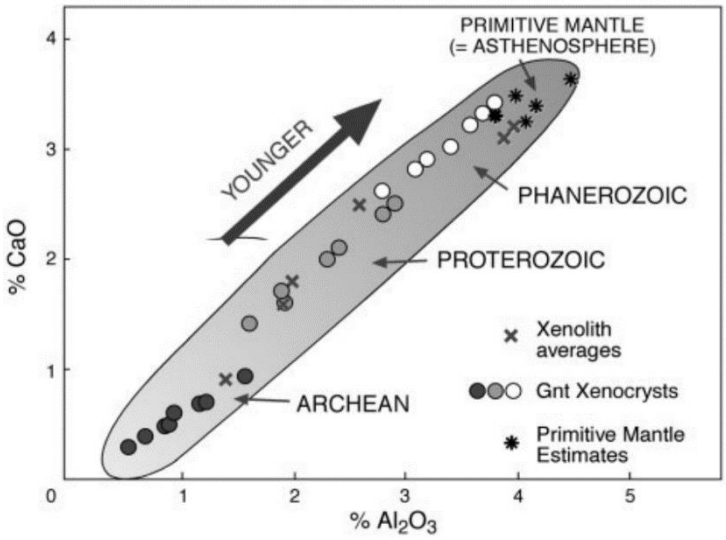

Figure 1.17. Whole-rock Al_2O_3 and CaO (wt%) of mantle of various ages using data outlined in Griffin et al. (1998; 1999; 2003; 2009).

These observations have developed into numerous parameterisations, which use the results of temperature sensitive experiments to model the variation in major element composition of the lithospheric mantle under different conditions (e.g. Walter, 2003; Herzberg, 2004; Figure 1.17). These parameterisations provide a more detailed understanding of peridotite chemistry.

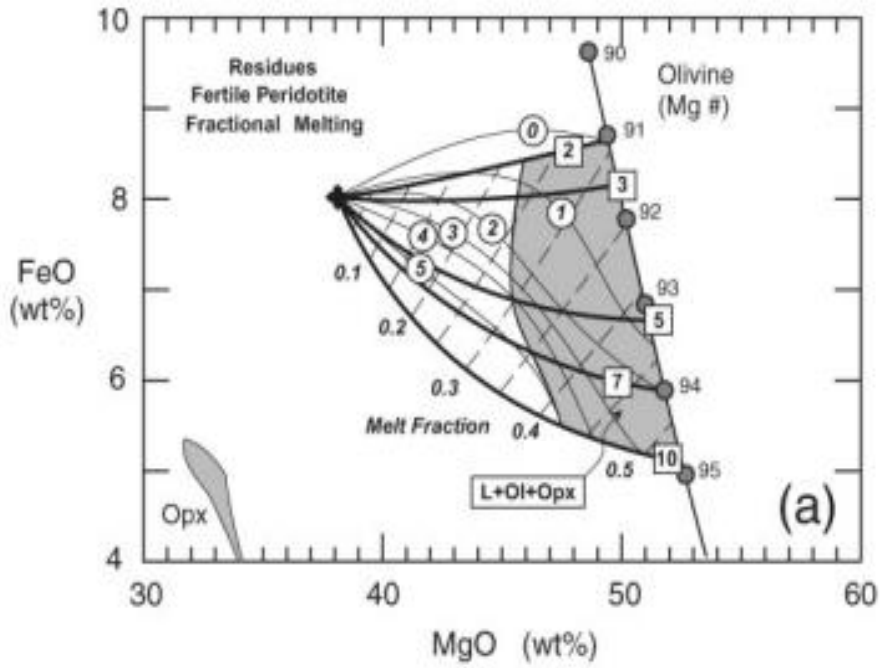

Figure 1.18. Whole-rock MgO and FeO (wt%) and olivine Mg# from various melting experiments and models using parameterisations of Herzberg (2004).

Finally, incompatible trace-elements have also been used to understand melting processes in the mantle. Particular focus has been made on lanthanide rare earth elements composed of Group 3 transition elements Y, La and f-block (inner transition elements), Ce, Pr, Nd, Pm, Sm, Eu, Gd, Tb, Dy, Ho, Er, Tm, Yb and Lu. These are trivalent, electropositive and incompatible in magmatic settings. Due to a phenomenon termed 'lanthanide contraction', the compatibility increases with increasing mass because of the increase in to the atomic radii of the elements (Figure 1.9). As a result, ions with the largest radii (e.g La, Ce) behave more incompatibly than small ones (e.g. Yb, Lu). This makes the lanthanides excellent at recording melting processes. Whereby, during melting the mantle will become preferentially depleted in La as opposed to Lu.

The model of Warren (2016) shows how increasing degrees of melting increasingly depletes lanthanides with small ionic radii (La and Ce) relative to those with larger ionic radii (e.g. Yb and Lu) (Figure 1.19A). This has been quantified by La/Yb (Figure 1.19B) and permits inferences about the degree of melt extraction experienced by residues found in the lithospheric mantle.

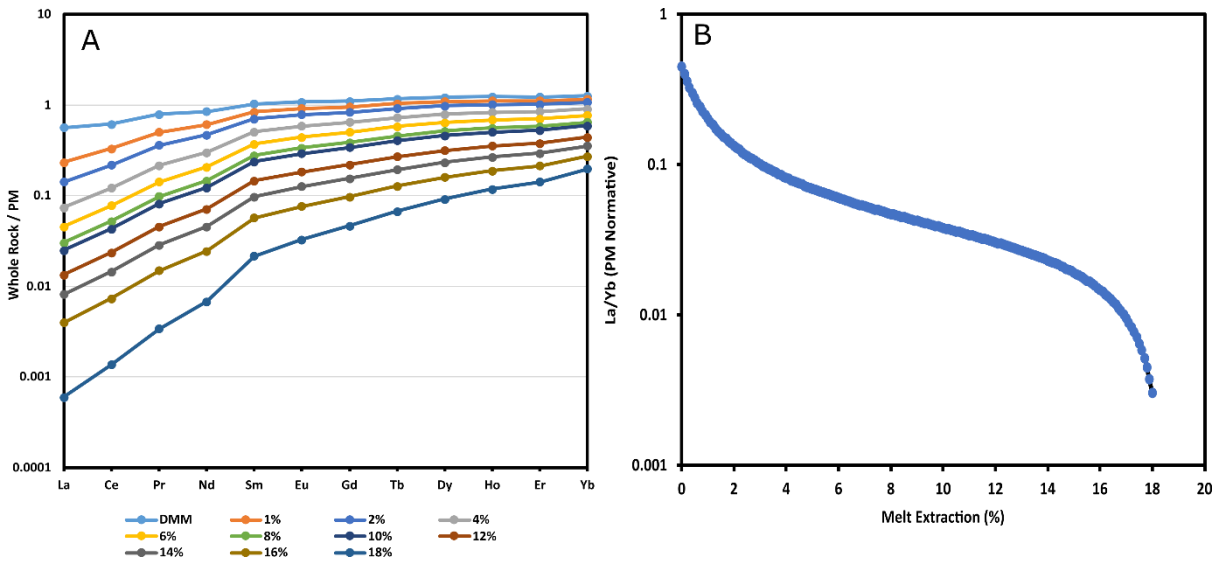

Figure 1.19. A) Whole-rock lanthanide concentration variation during increasing degrees of melt extraction. B) Whole-rock La/Yb_N composition at varying degrees of melt extraction (%).

1.7.2 Metasomatism

The sub-continental lithospheric mantle represents a reservoir that is geochemically isolated from the overlying crust and underlying convecting upper mantle (e.g. McKenzie & Bickle, 1988). Periodically, this closed reservoir becomes geochemically perturbed and enriched by a process called metasomatism. The process of mantle metasomatism was first hypothesized by Lloyd & Bailey (1975) and has since become the subject of extensive investigation. In essence there are two dominant mechanisms of mantle metasomatism as summarized by O'Reilly & Griffin (2013).

a) Grain-boundary infiltration. This is where fluids and/or melts infiltrate and along the grain

boundaries of minerals in the lithospheric mantle. During this infiltration, there are constant reactions which ultimately generate new geochemical compositions of the lithospheric mantle. Over geological timescales the lattice chemical variabilities equilibrate to generate locally homogeneous lithospheric mantle.

b) Crack propagation. This is where significant volumes of fluid and/or melt transfer through the lithospheric mantle due to overpressure of the parental lithospheric mantle.

Metasomatism of the lithospheric mantle is characterised into two distinct types.

1. Modal Metasomatism – where the primary mantle mineralogy of the lithospheric mantle has become modified to include more exotic 'MARID' minerals (see section 1.3).
2. Cryptic Metasomatism – where the primary mantle mineralogy is still present, but the geochemistry of the lithospheric mantle has been modified. This is typically observed in major and trace element contents and isotope geochemistry.

Modal metasomatism is a relatively straight forward process that is identified by examining a hand specimen or a thin section. Furthermore, it can also be observed when modal abundances are combined with olivine chemistry. For example, experiments have shown that the modal abundance of olivine and olivine Mg# are closely linked to the degree of melting. However, in the event of subsequent silica (SiO_2) enrichment, modal olivine and olivine Mg# become decoupled. This is due to an olivine-consuming orthopyroxene-forming reaction that has no significant effect on olivine chemistry. This effect was first outlined by Boyd (1989) and is illustrated in Figure 1.20 and Equation 1.6.

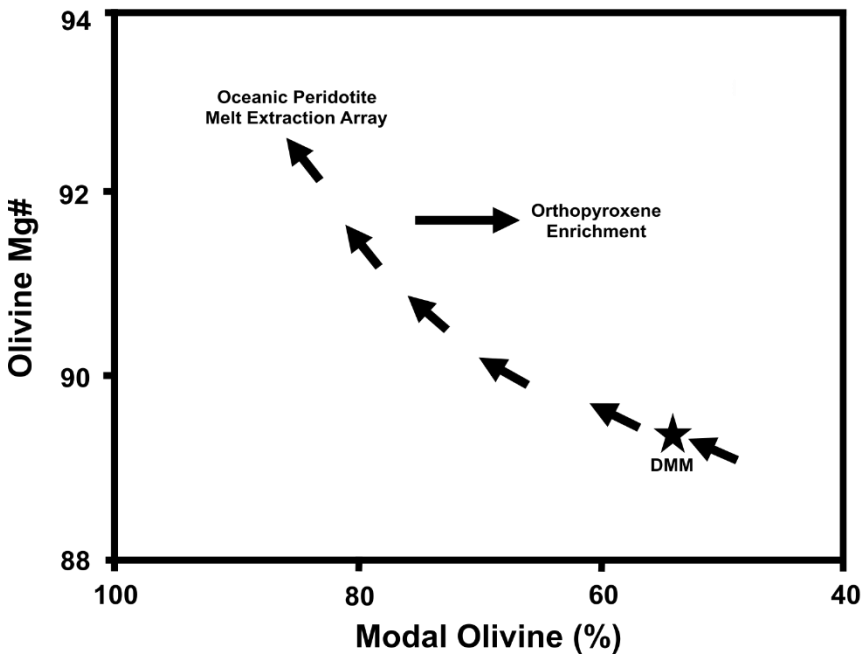

Figure 1.20. Modal olivine (%) compared to olivine Mg# outlining the effect of increasing degrees of melting extraction on and the influence of orthopyroxene enrichment from olivine-consuming SiO_2-enrichment. After Boyd (1989).

$[MgFe]_2SiO_4 + SiO_2 = [MgFe]_2Si_2O_6$ Equation 1.6

Olivine + Silicate Melt = Orthopyroxene

Cryptic metasomatism is determined by the composition of elements sensitive to enrichment. This is chiefly done by comparating melting and enrichment models. A whole-rock MgO and SiO_2 melting model using parameterizations from Herzberg (2004) is displayed in Figure 1.21. This shows that during partial melting, MgO and SiO_2 will behave akin to MgO and FeO at a given degree of melt extraction (Figure 1.16). However, these melting models are also sensitive to metasomatic perturbation by silica-enrichment (highlighted by the silicate enrichment vector on Figure 1.21).

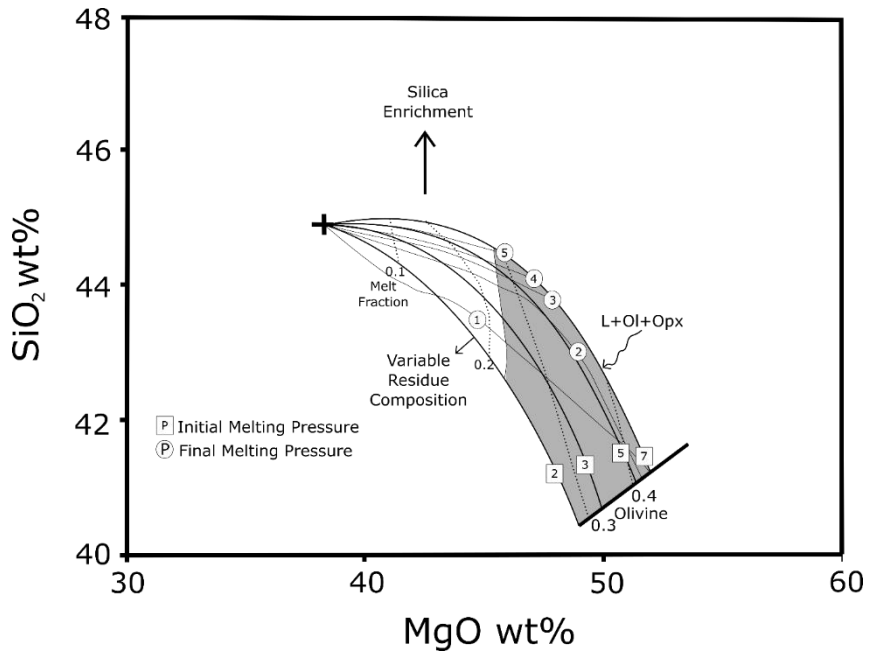

Figure 1.21. Whole-rock MgO and SiO_2 (wt.%) using various melting experiments and models using parameterisations of Herzberg (2004).

The incompatible trace-element chemistry of mantle xenoliths has proven unrivalled in detecting cryptic metasomatism. This is because during melting these will become preferentially depleted from the residue relative to HREE (Figure 1.19) but, during metasomatism by small fraction melts/fluids, they will be enriched in the lithospheric mantle will become enriched as they interact with LREE-enrichment small-fraction melts/fluids (Figure 1.22).

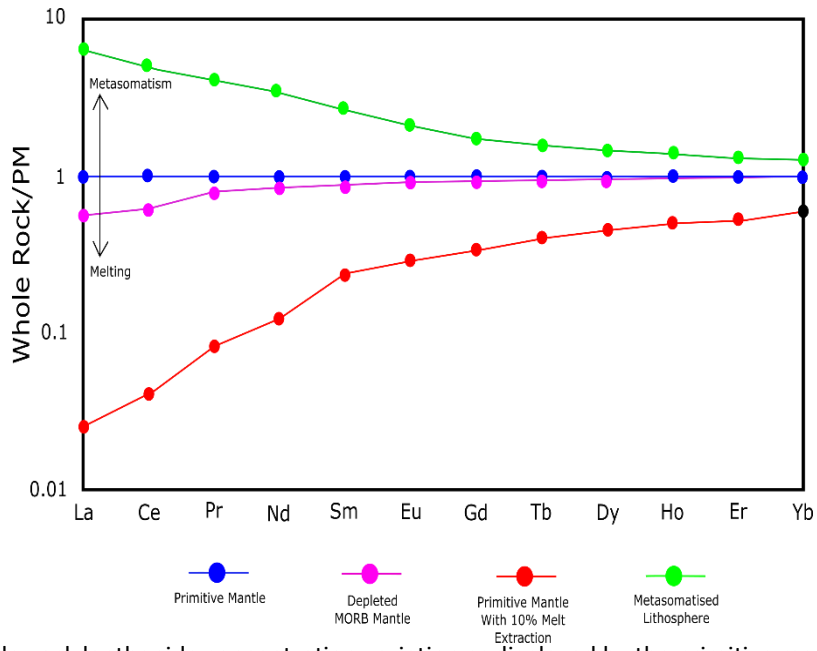

Figure 1.22. Whole-rock lanthanide concentration variation as displayed by the primitive mantle, depleted MORB mantle, primitive mantle with 10% melt extraction and metasomatised lithosphere.

The variability of incompatible trace elements has also been used to identify different styles of metasomatism. These relationships are divided into 4 distinct groups:

1. Lanthanide and rare earth elements.

These elements are excellent tracers of both depletion and enrichment due to more sensitive partitioning of LREE relative to HREE. Whereby, melt extraction would greatly reduce LREE relative to HREE (section 1.7.1), while enrichment would greatly increase LREE relative to HREE (Figure 1.22).

2. High Field Strength Elements (HFSE).

These are metal elements forming cations with a small radius and high charge, comprising Hf, Ti, Zr, Nb and Ta, that enable them to have a very low solubility in fluids. As a result, these elements are typically depleted relative to their neighbouring elements in subduction-zone settings because they are not fluxed into the overlying lithosphere and instead remain in the down-going slab.

3. Large-ion Lithophile Elements (LILE).

These elements have a large radius to charge ratio (large-ion) and have a strong geochemical affinity to silicates (lithophile). They comprise K, Rb, Sr, Cs, Ba, Eu and Pb and are very incompatible. During mantle melting the LILEs are enriched in intraplate basalts and island arc basalts but depleted in mid-ocean ridge basalts. Following the classification of Gast (1972) Th and U may also be included.

4. Actinide Elements.

These are composed of radioactive f-block elements of Actinium (Ac) to Nobelium (No). In mantle geochemistry, the actinide elements also include U and Th because they are the only nuclei stable enough to survive over the history of Earth and have a high affinity to silicates (lithophile).

The relationship of these incompatible trace-elements relative to melting and metasomatic enrichment is displayed by Figure 1.23A + B. The depleted upper-mantle (from Workman & Hart, 2005; Figure 1.23A) shows a consistent decrease of increasingly incompatible trace elements as a consequence of melt extraction. In contrast, regions of the lithospheric mantle that have undergone metasomatism show enrichment of incompatible trace elements (e.g. Class *et al.*, 1998). This is displayed using the the partition coefficients, starting compositions and melting model outliend by Ionov *et al.* (2002; Figure 1.23B).

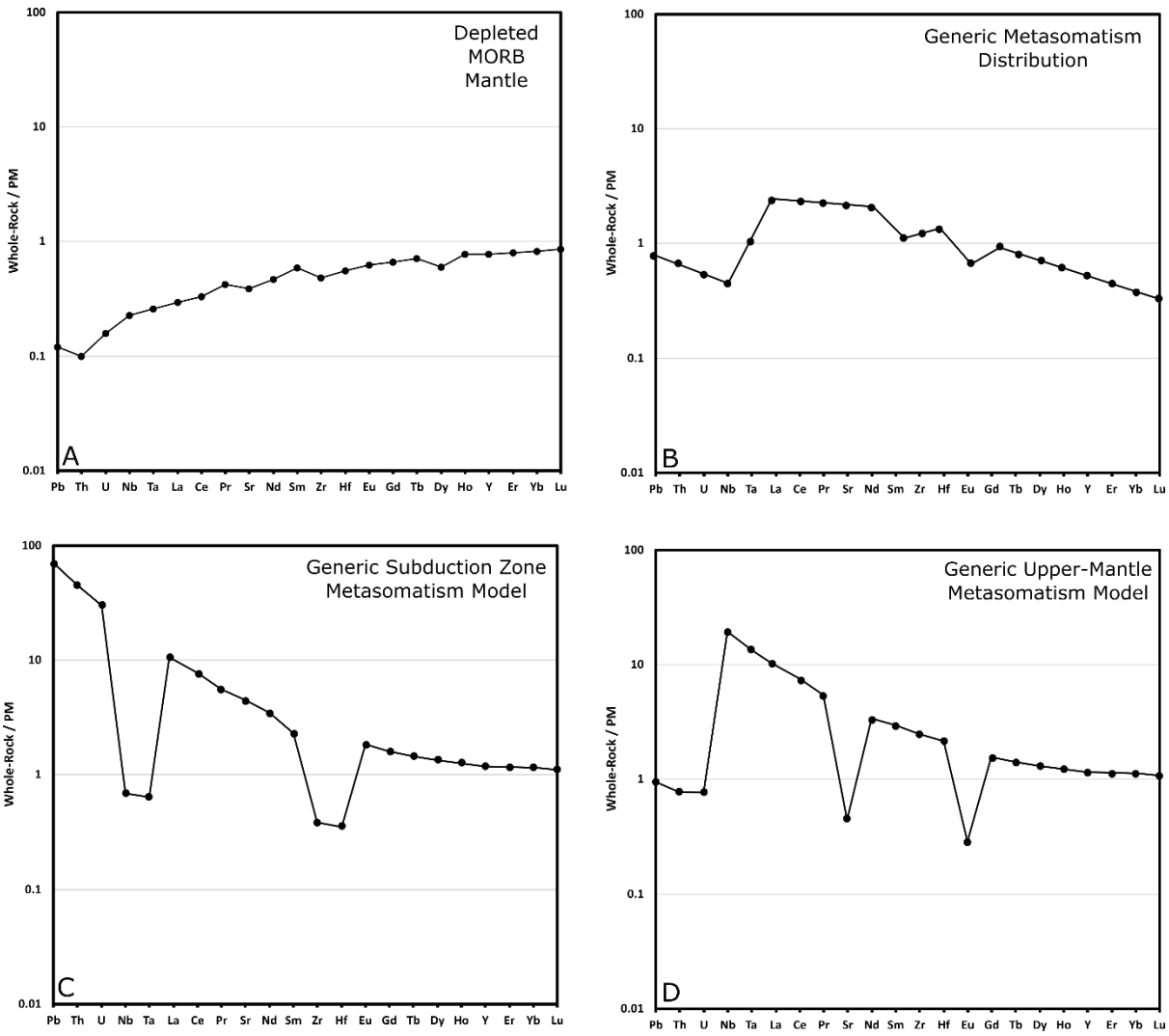

Figure 1.23. Schematic whole-rock primitive mantle normalised trace-element compositions for the A) Depleted MORB mantle B) Metasomatised lithospheric mantle C) Metasomatism by subduction zone melts D) Metasomatism by the upper mantle. These represent hypothetical idealised compositions to illustrate the unique compositions of different settings.

These concepts are also applied to metasomatism of the lithospheric mantle by subduction zone and upper-mantle metasomatic melts. Where on Figure 1.23C, metasomatizing melts from subduction zones are enriched in incompatible trace element but have distinct negative anomalies at HFSEs. Those from the MORB-source mantle are also enriched in incompatible trace elements but have prominent negative anomalies at LILEs (Figure 1.23D).

In addition to reservoirs having distinct trace element ratios, different metasomatic agents also have unique signatures. This relates to varying affinity of incompatible trace elements to different melts

and fluids. This relationship is shown in Figure 1.24.

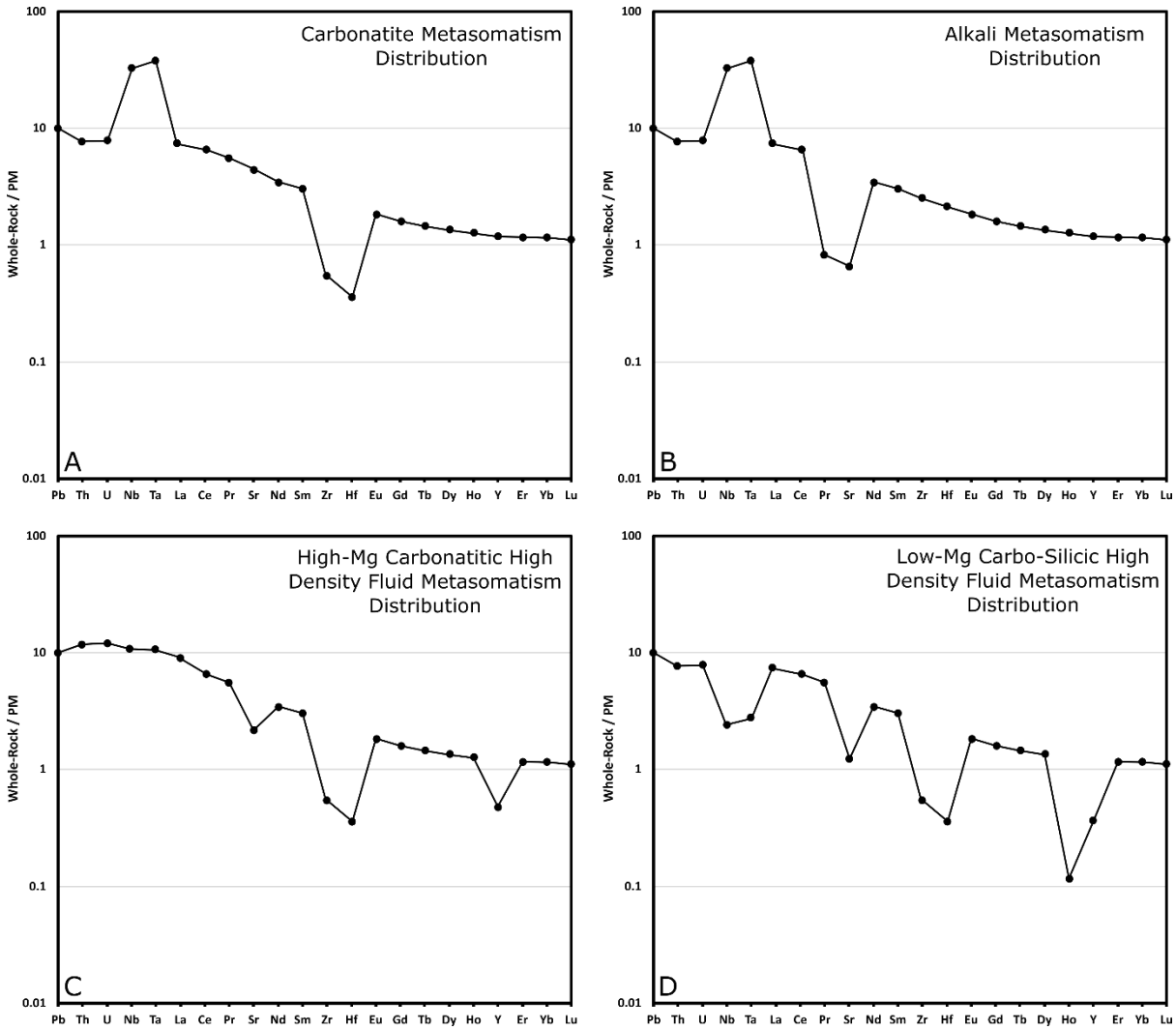

Figure 1.24. Schematics whole rock primitive normalised incompatible trace-element compositions for; A) Metasomatic enrichment by carbonatite melts; B) Metasomatic enrichment by alkali melts; C) Metasomatic enrichment by high-Mg carbonatite high-density fluids; and D) Metasomatic enrichment by low-Mg carbo-silicic high-density fluids. Patterns are from Gorring & Kay (2000), Coltorti et al. (2000) and Weiss et al. (2008).

Regions of the lithospheric mantle that have been metasomatised by carbonate-rich melts have an overall enriched pattern with clear negative anomalies at Zr and Hf but positive anomalies at Nb and Ta (e.g. Gorring & Kay, 2000). These are distinct from alkali metasomatic melts which record an overall enriched profile but negative anomalies at Sr and Pr and positive anomalies at U, Nb and Ta (e.g. Coltorti *et al.*, 2000). Lithospheric mantle that has been metasomatised by fluids records unique systematics (e.g. Weiss *et al.*, 2008). High-Mg carbonate high density fluids (HDFs) have an overall enriched profile but key negative anomalies at Y, Hf, Zr and Sr, whereas low-Mg carbo-silicate HFDs additionally have anomalies at Hf, Zr, Nb and Ta, Y, Ho and Sr. The presence of negative Y anomalies is key to distinguishing between metasomatism by melts and fluids.

1.8 Volatile elements

Volatility relates to the temperature at which an element condenses from a gas of solar compositions. Therefore, volatile elements are best defined as having condensation < ~1100 K (e.g. Wood et al., 2019; Figure 1.25). Examples of these include H_2O, B, F and Cl. Furthermore, a subset of elements (e.g. Li and P) have 'moderately volatile' nature (e.g. Wasson, 1985) that have condensation temperature of ~1100 to 1300 K.

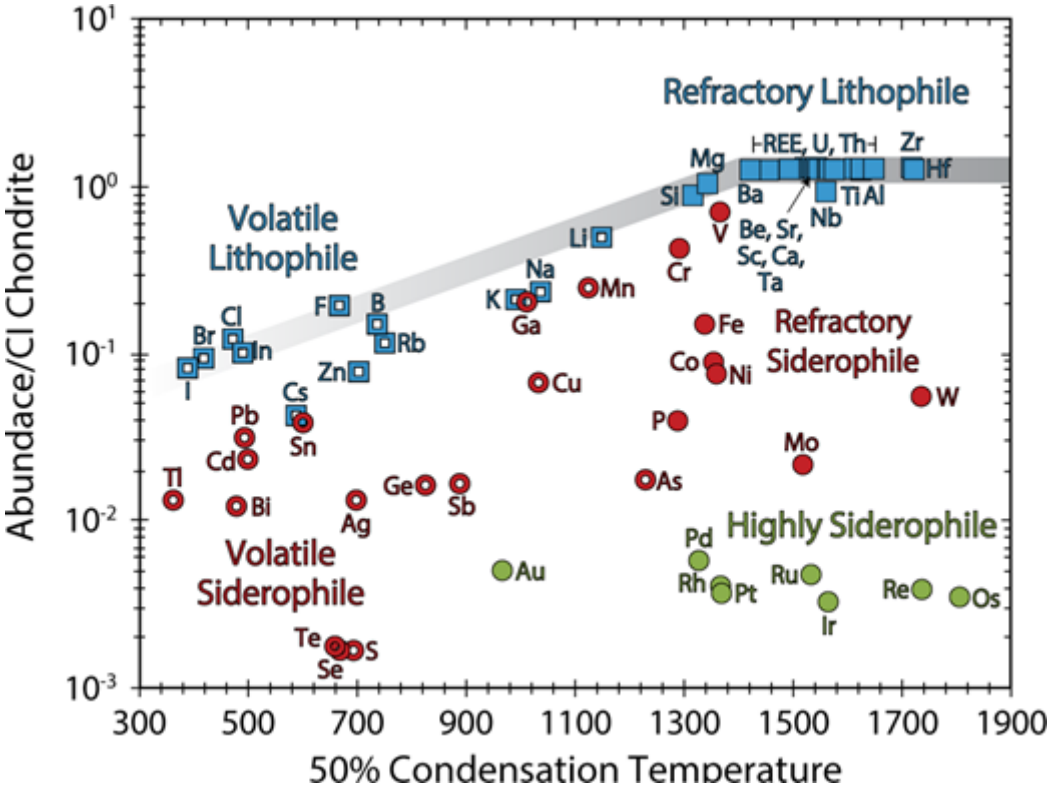

Figure 1.25. Abundances of elements in the silicate Earth relative to CI chondrite (Palme and O'Neill, 2014) compared to calculated temperature for 50% element condensation. Figure from Wood et al. (2019).

A key challenge has been understanding how these elements behave in the lithospheric mantle. This is because many of these element have unique ionic properties (radius and charge) compared to other major and trace-elements. This is illustrated in Figure 1.26 following the work of Shannon (1976) combined with determinations of co-ordination states of the analysed elements (Karki et al., 2020; Henry et al., 2011; Halenius et al., 2010; Dalou et al., 2012; Mallman et al., 2009), the atomic radii of H^+ = ~0.01 Å, Li^+ = 0.76 Å, B^{3+} = 0.4 Å, F^- = 1.33 Å, P^{5+} = 0.17 Å and Cl^- = 1.81 Å.

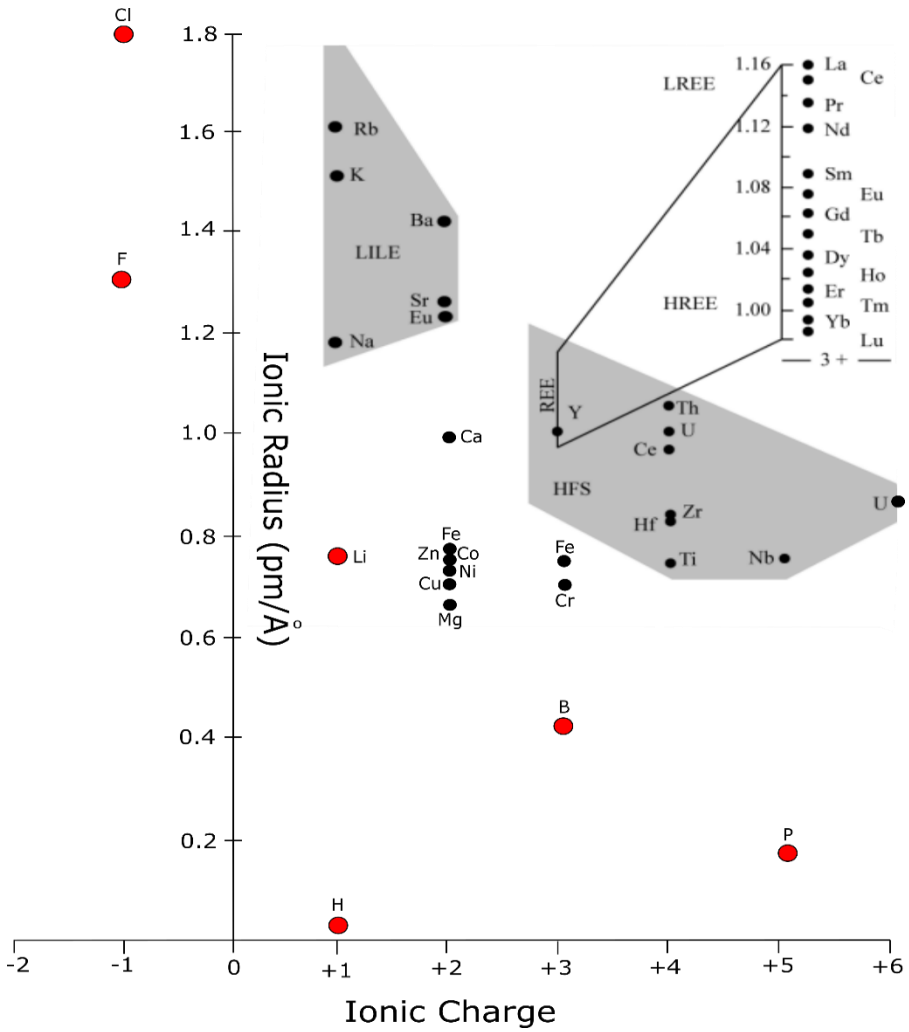

Figure 1.26. Comparison of ionic charge and ionic radius (pm) of LILE (Large Ion Lithophile Elements), HFS (High Field Strength) elements, selected lithophile elements and volatile elements (in red).

1.9 Thesis aims

This study analyses ultramafic xenoliths for their petrology, major and trace element chemistry together with fluid-hosted $^{3}He/^{4}He$ and $^{13}C/^{12}C$ and lattice-hosted H, Li, B, F and Cl volatile abundances. These coupled systematics are supplemented by data from previously published studies with intent to answer 4 key questions to advance the understanding of volatiles in the sub-continental lithospheric mantle.

Why does the $^{3}He/^{4}He$ composition of the sub-continental lithospheric mantle vary and what implications does this have on volatile cycles and intracontinental petrogenesis?

What is the source of CO_2-fluids in the lithospheric mantle, what is their concentration and how much is stored in the off-craton mantle?

What is the concentration and abundance of H_2O, Li, B, F, P and Cl in the off-craton mantle and what implications does this have to global volatile cycles?

Is there a significant distinction between peridotite and pyroxenites?

1.10 Thesis outline

Petrographic, major and trace element determinations combined with state of the art analyses of volatile elements have been undertaken on a large collection of ultramafic mantle xenoliths obtained from global locations. The findings of these are contextualised, presented and discussed in the following chapters.

Chapter 2 summarizes the geological setting of mantle xenoliths analysed in this study (Kilbourne Hole, Colorado Plateau, Tariat Volcanic Field, West Eifel Volcanic Field, Antarctic Peninsula, Southern Patagonia, Northern Tanzania and Ichinomegata). This has been inferred predominantly through previous geochemical and geophysical studies.

The petrography of 44 mantle xenoliths presented in this study is described in **Chapter 3** and includes details of the modal mineralogy, textures and fabrics.

Chapter 4 describes the variations in the major and minor element chemistry of olivine, orthopyroxene, clinopyroxene, spinel, garnet, phlogopite, amphibole and ilmenite using EMPA analyses. By comparing these compositions with the depleted mantle, four distinct groups are identified; i) highly depleted peridotites from Northern Tanzania; ii) fertile peridotites from Kilbourne Hole, Tariat Volcanic Field and Ichinomegata; iii) variably depleted and fertile peridotites from Colorado Plateau, West Eifel Volcanic Field, Antarctic Peninsula, Southern Patagonia; iv) pyroxenites.

Chapter 5 presents the trace element chemistry obtained by LA-ICP-MS analysis and volatile element chemistry from SIMS. These compositions, in combination with the major and trace element data, are discussed in relation to the various melting and metasomatic signatures of peridotite and pyroxenite xenoliths in **Chapter 6**. The major element data are also used in **Chapter 7** to calculate the final equilibration pressures and temperatures of the mantle xenoliths.

Chapter 8 summarizes the He and C (concentrations and isotopes) of the different mantle xenoliths presented in this study. The He compositions are used in combination with major-elements (from Chapter 4) and trace-elements (from Chapter 5) to improve constraints on the variability of $^{3}He/^{4}He$ in the sub-continental lithospheric mantle in **Chapter 9**. This highlights the dominant roles of melting and subsequent radiogenic ingrowth and the sub-ordinate role of metasomatism. These findings are used to understand the non-ubiquitous primordial noble-gas compositions of kimberlites and the importance of the lithospheric mantle as a host for fluid-hosted volatiles (e.g. CO_2, N_2) on geologically significant time-scales.

Chapter 10 builds on these findings by integrating CO_2 concentrations and isotope compositions with He, major elements and trace elements. It provides important constraints on the $CO_2/^3He$ composition of the lithospheric mantle which in turn enables CO_2 concentrations and budgets to be calculated. By integrating $\delta^{13}C$, $CO_2/^3He$ and $^3He/^4He$ it has been possible to demonstrate that the upper mantle is the ubiquitous source of volatiles with additional influence from recycled (carbonate and organic) and primordial carbon. Finally, this chapter shows how whole-rock CO_2/La can be used to calculate CO_2 concentrations and budgets in the off-craton sub-continental lithospheric mantle.

Chapter 11 integrates SIMS volatile data (H_2O, Li, B, F, P and Cl) with petrography, major-, minor-, trace-element and fluid-inclusion chemistry (from Chapters 3 to 8). This demonstrates the distinct partitioning of volatiles between mineral phases in on- and off-craton subcontinental lithospheric mantle. These volatile concentrations and bulk abundance in the off-craton mantle also provide exciting new insights on the metasomatic control of boron.

Chapter 12 summarizes how the findings from this study of global mantle xenoliths place improved constraints on the nature, source, abundance and flux of volatile elements stored within the lattice and fluid-inclusions of mineral phases in the sub-continental lithospheric mantle. It then uses these conclusions to suggest future work.

Chapter 2. Sample locations

2.1 Introduction

The mantle xenoliths examined in this project have been selected from global sites that are characterised by thin (<150 km) continental lithosphere in off-craton and circum-cratonic settings. The locations of the mantle xenoliths are shown on a map of global lithospheric thickness (Figure 2.1) that use the seismic tomography method from Priestley & McKenzie (2013). This is compared to other global seismic tomographic models in Figure 2.2). The horizontal and vertical resolution of the seismic tomography is approximately of Priestley & McKenzie (2013) 150 km and 30 km, respectively. While this method alone cannot be used to precisely estimate lithospheric thickness beneath xenolith locations, it does provide important regions settins (i.e. on or off craton). Overall, the selected mantle xenoliths provide both a broad spatial coverage from a range of geodynamic settings (continental rift, continental margin and craton margin), and permit a comprehensive analysis of the nature and behaviour of volatiles in off-craton sub-continental lithospheric mantle.

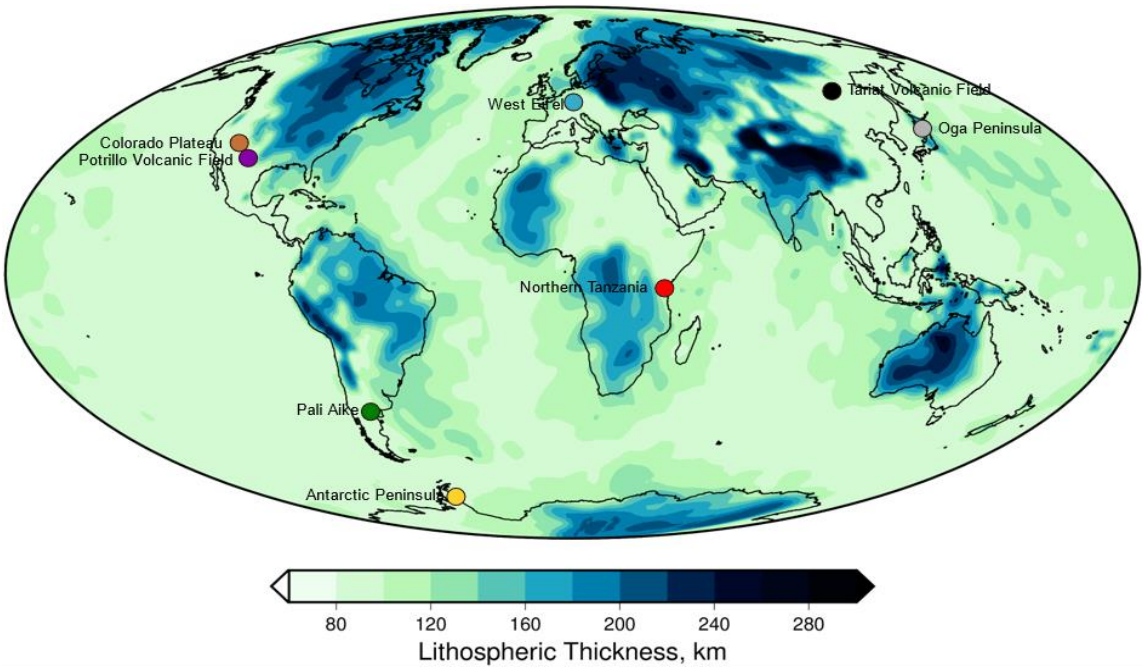

Figure 2.1 Mollweide global projection of seismic lithospheric thickness using the method of Priestley & McKenzie (2013). The locations of samples presented in this study are also shown. The map was generated by C O'Malley (pers. Comms.).

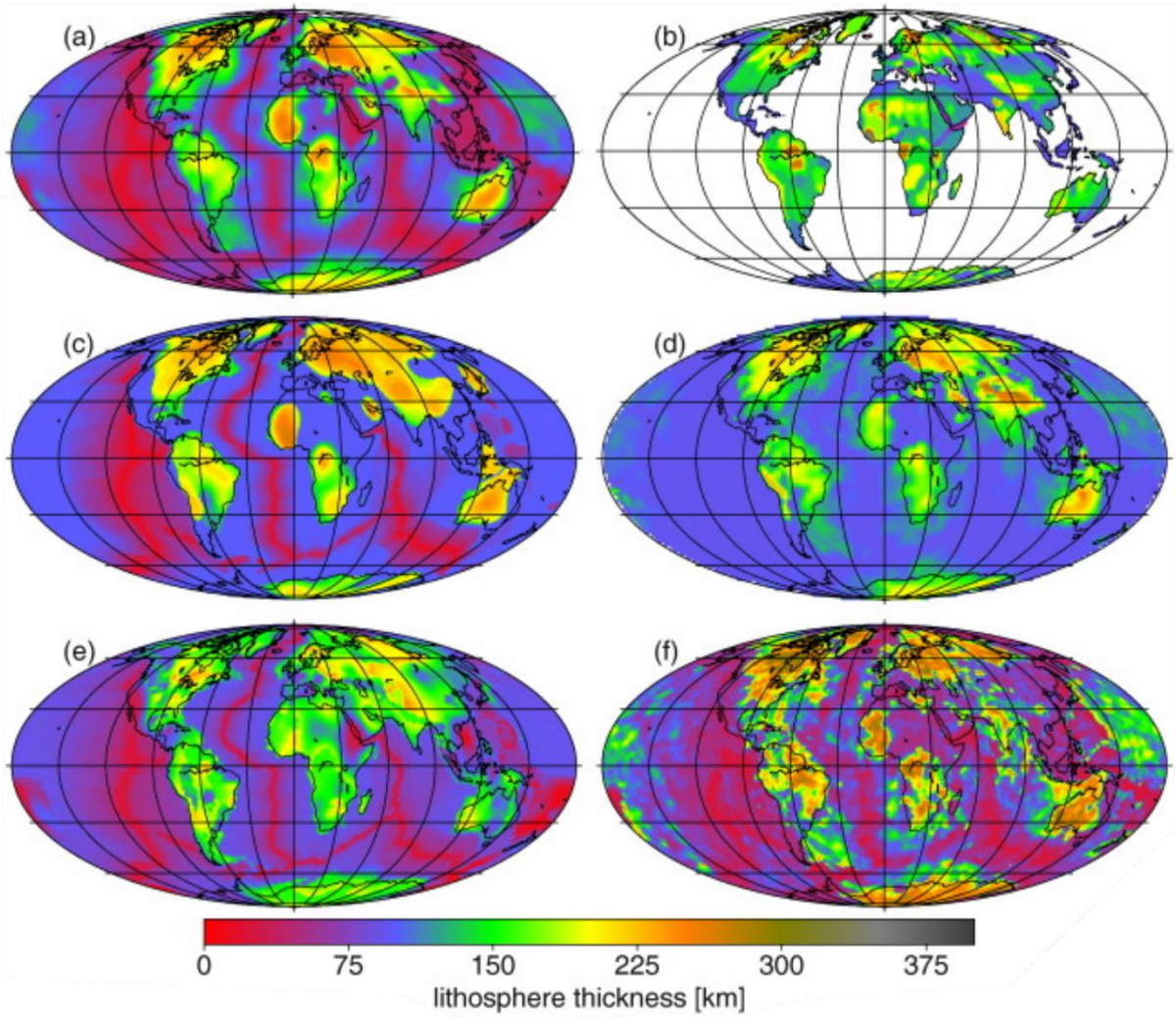

Figure 2.2. Mollweide global projections of lithospheric thickness showing the seismic tomography models of a) Steinberger & Becker, (2018); b) Artemieva (2006); c) Conrad and Lithgow-Bertelloni (2006); d) Priestley & McKenzie (2013); e) Bird *et al.* (2008); f) Pasyanos *et al.* (2014). Figure adapted from Steinberger & Becker (2018).

The mantle xenoliths used in this project are from the collections of SA Gibson, JB Dawson, DP McKenzie, FM Stuart, and the Natural History Museum. They are from the following locations:

1. Potrillo Volcanic Field (Kilbourne Hole) – W. USA.
2. Colorado Plateau (The Thumb and Buell Park) – W. USA.
3. Tariat Volcanic Field – Mongolia.
4. West Eifel Volcanic Field (Gees, Meerfelder, and Dreiser Weiher maars) – Germany.
5. Antarctic Peninsula (Bruce Nunatak and Rothschild Island).
6. Pali Aike Volcanic Field (Campo Picana, Laguna Timones, and Laguna de Los Cisnes) – S. Patagonia.

7. Northern Tanzania (Lashaine and Pello Hill).

8. Oga Peninsula (Ichinomegata) – Japan.

2.2. Location specific information

2.2.1 South West USA

2.2.2.1 Potrillo Volcanic Field:

The Potrillo Volcanic Field (PVF) in south-central New Mexico (Fig. 2.3), is located within the Rio Grande Rift, a major north-south extensional rift zone that separates the western margin of the North American Craton from the eastern margin of the Colorado Plateau. The early rift phase was initiated 20 – 30 Ma from intense low-angle normal faults and to lesser extent by high-angle normal faults (<10 Ma) (Keller *et al.*, 1990). This study examines samples from Kilbourne Hole, which is located approximately 35 km south-west of El Paso (Texas) and 45 km north-east of Las Cruces (New Mexico). Using DD co-ordinates (31.0, -107) Priestley & McKenzie (2013) show the lithosphere to be ~95 km thick. Further constraints from modelling the major and REE chemistry of basalts and basanites by Thompson *et al.* (2005) suggests that the mechanical and thermal boundary layers reside at ~70 km and ~90 km depth, giving an approximate lithosphere-asthenosphere boundary at 75 km depth. Additionally, Perkins & Anthony (2011) determined a moho at ~30 km.

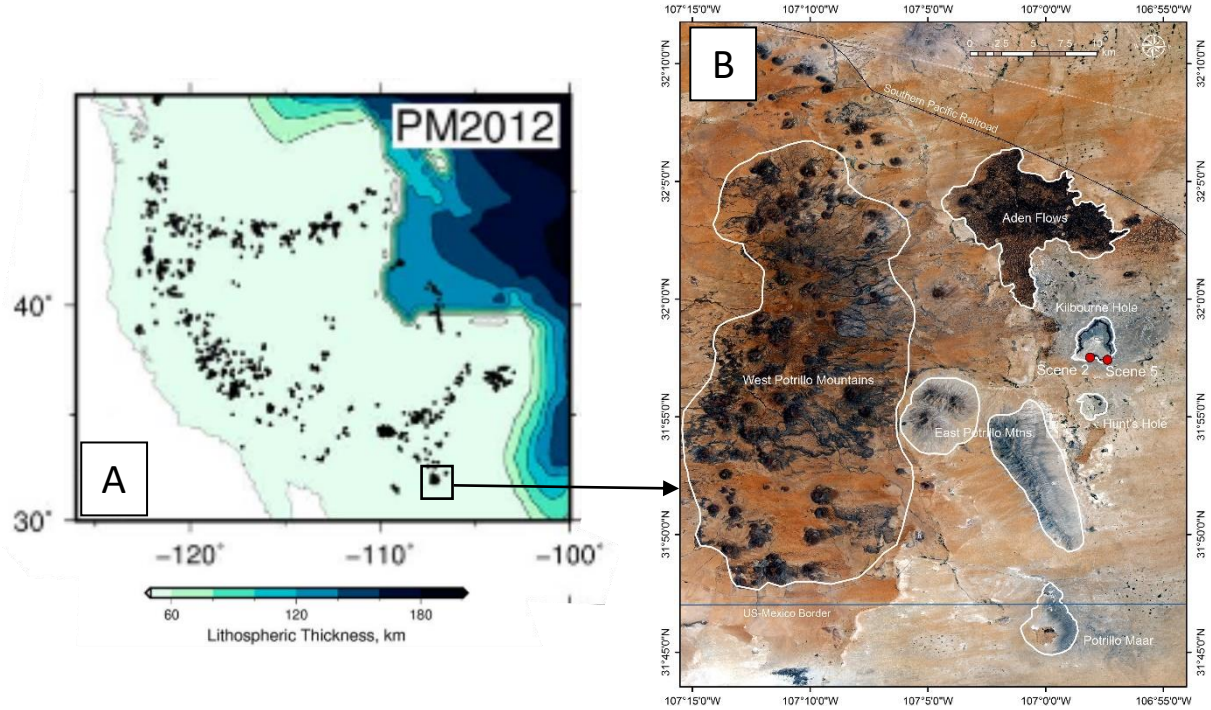

Figure 2.3. (A) Lithospheric thickness map of the Western USA after Klöcking *et al.* (2018) using the method of Priestley & McKenzie (2013; PM2012). Black dots show the locations of <10 Ma volcanic events. (B) Map of Potrillo Volcanic Field (right) after Ito *et al.* (2018), with red dots showing the location of Kilbourne Hole.

The PVF comprises approximately 100 volcanic vents that are dominated by maar-diatremes. These formed by hydrovolcanic activity of up-ward migrating magma and dikes interacting with groundwater (phreatomagmatic). In addition to mantle xenoliths, lower-crustal xenoliths (e.g. granulites, charnokites and anorthosites) and upper-crustal xenoliths (e.g. clastic sedimentary rocks, basaltic andesite and limestone) are found (Padovani & Reid, 1989). Volcanism within the PVF was triggered by lithospheric extension associated with the Mesilla Basin between Colorado and west Texas. This thinning produced two distinct types of lava – an alkaline suite of basanite, alkali basalt and trachybasalt; and a suite of sub-alkali basalts. The oldest PVF lavas erupted 28 Ma (based on K-Ar dates of Seager *et al.* (1984) and Ricketts *et al.* (2016), but those erupted at the Kilbourne Hole show much younger eruption ages of 20-10 Ka (based on ^{3}He surface exposure models of Anthony & Poths (1992) and Williams (1999)).

Basanite-hosted mantle xenoliths from the Kilbourne Hole were extensively investigated by Carter, (1965). They are predominantly peridotites with some clinopyroxenites. Previous studies of the major- and trace-element chemistry of the peridotites show that they are dominated by depleted signatures (Baker & Stopler, 1994; Baker *et al.*, 1995; Perkins & Anthony, 2011; Harvey *et al.*, 2012), inferred as being produced by approximately 20% melt

extraction from the asthenosphere. This interpretation is also consistent with BSE (bulk silicate Earth) and MORB- (mid-ocean ridge basalt) like Sr & Nd isotopic signatures (e.g. Roden *et al.*, 1988; Harvey *et al.*, 2012). Unlike the peridotite xenoliths, the clinopyroxenites are inferred to represent high-temperature cumulates that crystallised from ascending basaltic magmas (e.g. Irving 1980).

While peridotite samples from Kilbourne Hole are characterised by depleted major-, trace-, and isotopic signatures, consistent with their derivation from the convecting upper-mantle, caution must be placed on this simple generalisation for the underlying lithosphere. More detailed studies highlight small but important metasomatic characteristics ie. as clinopyroxene reaction textures, interstitial glasses, and decoupled Sr & Nd signatures. This metasomatism may be due reactive percolation of basanite host or melts and fluids released from or the 140 – 37 Ma Farallon Plate (Kil & Wendlandt, 2007; Harvey *et al.*, 2012; 2015).

2.2.2.2 Colorado Plateau

The Colorado Plateau (Fig 2.4) is located on the north Arizona/New Mexico border and forms part of the Rocky Mountain orogenic plateau. The Plateau formed from: a) low-angle subduction of the Farallon Plate in the interval 40 – 80 Ma; b) foundering of the Farallon Plate with an associated ignimbrite flare up at 25-50 Ma; or c) dynamic uplift by mantle convection at 0-25 Ma (Moucha *et al.*, 2009 and references therein). This investigation focusses on mantle xenoliths collected from The Thumb, and Buell Park (Fig. 2.4) in the eastern part of the Colorado Plateau. Integrative thermochemical tomography from Afonso *et al.* (2016) and peridotite thermobarmoetry from Li *et al.* (2008) suggest that the lithosphere-asthenosphere boundary beneath the Colorado Plateau resides ~140 km depth, the mechanical boundary layer is at ~110 km, and a thermal boundary layer is at ~160 km depth. Furthermore, these authors suggest that the moho is at approximately 45 km depth.

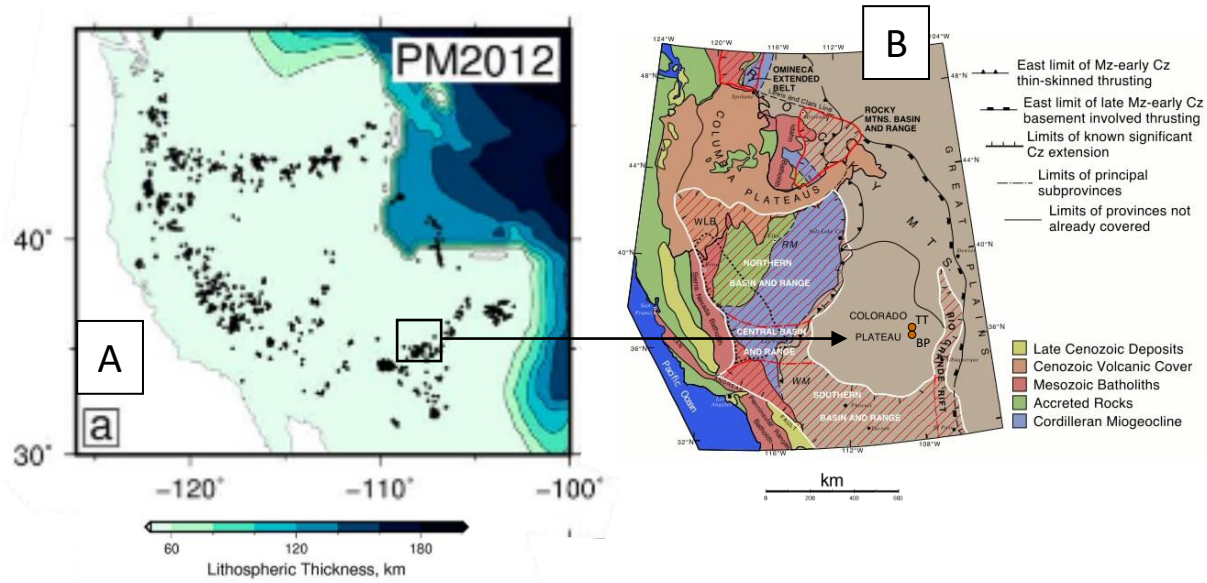

Figure 2.4. (A) Map of lithospheric thickness for western USA (after Klöcking *et al.* (2018)) using the method of Priestley & McKenzie (2013; PM2012), where black dots are <10 Ma volcanic events. (B) Location of the Colorado Plateau (right) adapted from Wernicke (1992) where brown dots show The Thumb (TT) and Buell Park (BP).

The Colorado Plateau comprises over 80 volcanoes dominated by maar-diatremes. The mantle xenoliths are mostly hosted by minettes (calc-alkaline lamprophyres) and serpentinized ultramafic microbreccia. The minettes contain variable amounts of phlogopite and diopside phenocrysts set in a matrix of sanidine, diopside, apatite and magnetite-ulvospinel. In addition to mantle xenoliths, both upper-crustal and lower-crustal xenoliths are found at these locations. K-Ar age dating of phlogopites suggest that the Buell Park diatremes were emplaced at 34.8 ± 0.5 to 21.1 ± 0.3 Ma (Naeser, 1971; Roden *et al.*, 1979; Laughlin *et al.*, 1986). Additional dates for other diatremes constrain eruption ages in the range 30 to 24 Ma (Helmstaedt & Doig, 1975; Smith *et al.*, 2004; Nybo, 2014).

Mantle xenoliths from the Navajo Volcanic Field were initially investigated by Smith & Levy (1976). Early insights determined that the lithospheric mantle beneath The Thumb and Buell Park was ancient and depleted but has undergone variable amounts of metasomatism (e.g. Roden *et al.*, 1990; Roden & Shimizu, 1993). Subsequent studies outlined the importance of metasomatic melts and fluids associated with the shallow flat slab subduction of the Farallon Plate (Fig 2.5) (e.g. Humphreys, 1995; Humphreys *et al.*, 2003; Chapman *et al.*, 2019; Smith, 2020). This has led to the formation of garnetites (Smith & Griffin, 2005), enrichment of fluid-mobile elements (Alibert, 1994; Lee, 2005), growth of Al-depleted

orthopyroxene porphryoblasts (Smith & Ritter, 1997; Smith *et al.*, 1999), oxygen isotopic signatures (Perkins *et al.*, 2006), H_2O-rich nominally anhydrous minerals (Li *et al.*, 2008; Marshall *et al.*, 2018), and the development of deformation textures (Behr & Smith, 2016). Overall, the samples from this location represent an excellent opportunity to investigate the influence of subduction-related metasomatic processes on the lithospheric mantle.

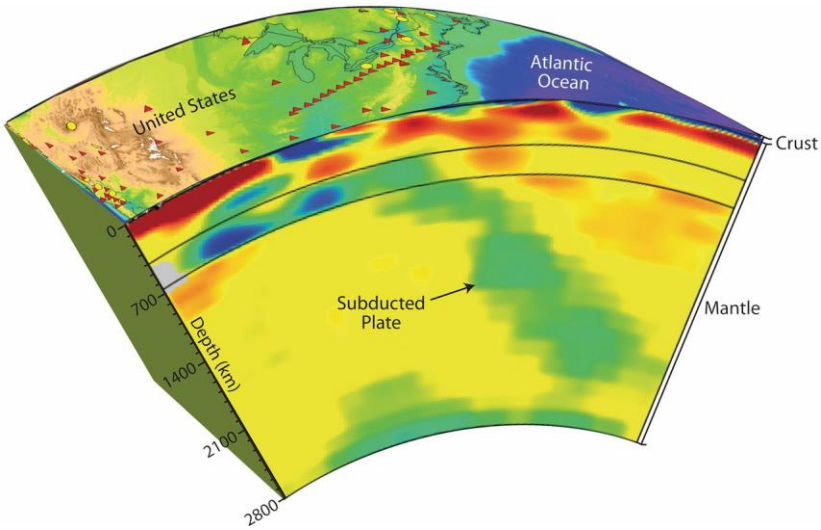

Figure 2.5 Illustration of the lithosphere and mantle underlying western USA based on seismic tomography. Colours show anomalies in rigidity which correlate with temperature – green and blue are relatively cool while orange and red are relatively hot. Labelled is a cold region inferred as the subducted Farallon plate (from Suzan van der Lee, 2021).

2.3 Tariat Volcanic Field (Mongolia)

The Tariat Volcanic Field (TVF) in north-central Mongolia forms part of the Hangai dome, within the Baikal rift zone of the Baikal-Sayan fold belt (Fig. 2.6). Volcanism developed in a mid-plate setting, with no obvious associated rifting (Ionov, 2002), and is linked to the diffuse Cenozoic volcanic belt encompassing southern Siberia and, SE Mongolia and NE China. This volcanism has been associated with upwelling of the asthenosphere (e.g. Barry *et al.*, 2007), crustal weakness along the Amur plate margin, and the combined effect of the Indian-Asian collision during the Eocene and upwelling mantle (Barry *et al.*, 2003). Nevertheless, the cause of the magmatism remains enigmatic. The exact location of samples used in this study are not precisely constrained, however deposits abundant in mantle xenoliths have been recorded from Horgo, Tsagan, Zala, Bosko, Haer, Shute and Shavaryn-Tsaram which are all within 20 km distance (Ionov, 2007). Ionov *et al.* (1998) determined the geotherm and lithospheric section for Tariat using pressure and temperature estimates from garnet-spinel lherzolites, garnet ± spinel pyroxenites, spinel lherzolites and granulites. These

authors suggest that the crust-mantle boundary (moho) is at 45 km depth (13 kbar) and the lithosphere-asthenosphere boundary is at ~90 km, the base of the mechanical and thermal boundary layer is at ~70 km and ~90 km depth, respectively. The heat flux in the lithosphere is ~60 mW/m^2.

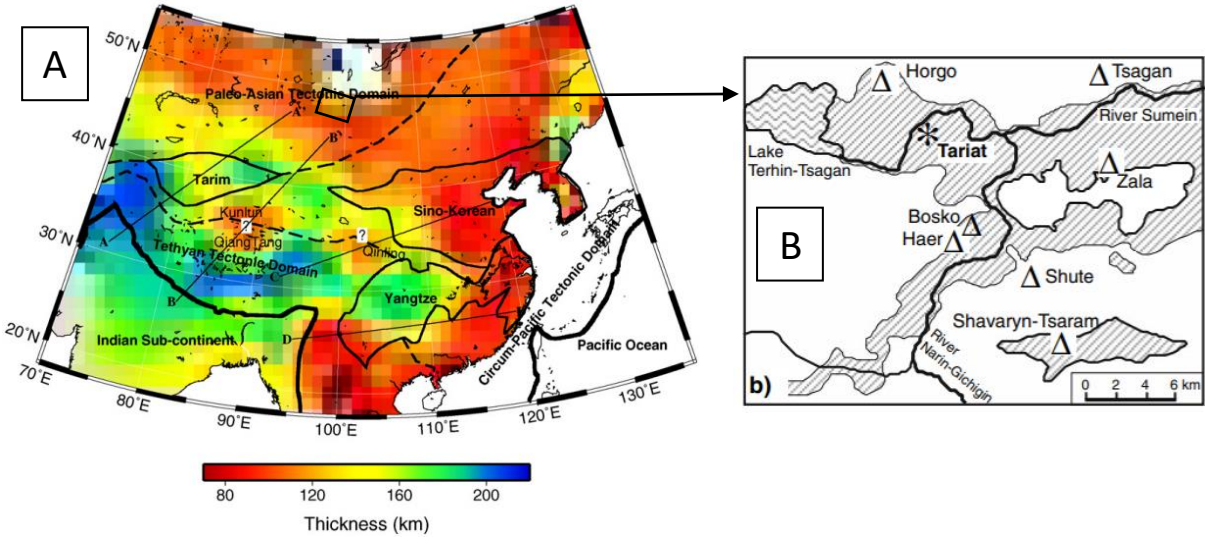

Figure 2.6. (A) Lithospheric thickness map of Eastern Asia from An & Shi (2006). The black box (b) shows the locations of the Tariat Volcanic Field and key locations within this (from Ionov (2007)).

The Tariat depression comprises multiple volcanic fields and is dominated by cinder cones. These cones are formed of loose pyroclastic fragments of basalt, phonotephrite, trachybasalt and basaltic trachyandesite. The basaltic lavas contain phenocrysts of olivine ± clinopyroxene with groundmass plagioclase, olivine, clinopyroxene and opaque oxides (Barry *et al.*, 2003). In addition to mantle xenoliths, the TVF also contains abundant lower-crustal xenoliths (e.g. Stosch *et al.*, 1995). Ages of volcanic eruption have been reviewed by Ivanov & Demonterova (2009) who suggest this activity began approximately 20 Ma and continued to very recent times (0.1 Ma). Barry *et al.* (2003) report Ar-Ar age specific to Hangai of 9.51 ± 0.02 to 0.55 ± 0.02 Ma.

The geochemistry and setting of the TVF was initially investigated by Preβ *et al.* (1986). This work was followed by extensive mineralogical, major- and trace-element, stable- and radiogenic-isotope studies on peridotite samples (e.g. Ionov, 1986; Ionov *et al.*, 1998; Ionov *et al.*, 2007; Barry *et al.*, 2007; Carlson & Ionov, 2019; Weyer & Ionov, 2007; Kang *et al.*, 2017; Qi *et al.*, 2019; Sauders *et al.*, 2020; Wang *et al.*, 2006; Carlson & Ionov, 2019). Overall, these investigations suggest that the lithospheric mantle consists of underplated, undifferentiated MORB-source mantle. Importantly, this makes mantle xenoliths from this

location ideal for examining the composition of the MORB-source and BSE (Carlson & Ionov, 2019).

2.4 West Eifel Volcanic Field (Germany)

The West Eifel Volcanic Field (WEVF) of south-west Germany forms part of the Central European Volcanic Field (Fig. 2.7). The WEVF has multiple xenolith-bearing vents and this study focusses on samples from the most frequently investigated locations; Gees, Meerfelder and Dreiser Weiher maars. The WEVF is located within the Palaeozoic Rhenish Massif. Pressure and temperature estimates for equilibrated mantle xenoliths from the WEVF (summarized in Witt-Eickschen, 2007) estimate a lithosphere-asthenosphere boundary at ~80 km depth, a mechanical boundary layer at ~55 km, and a thermal boundary layer at ~100 km depth. Furthermore, a moho was inferred at 30 km depth.

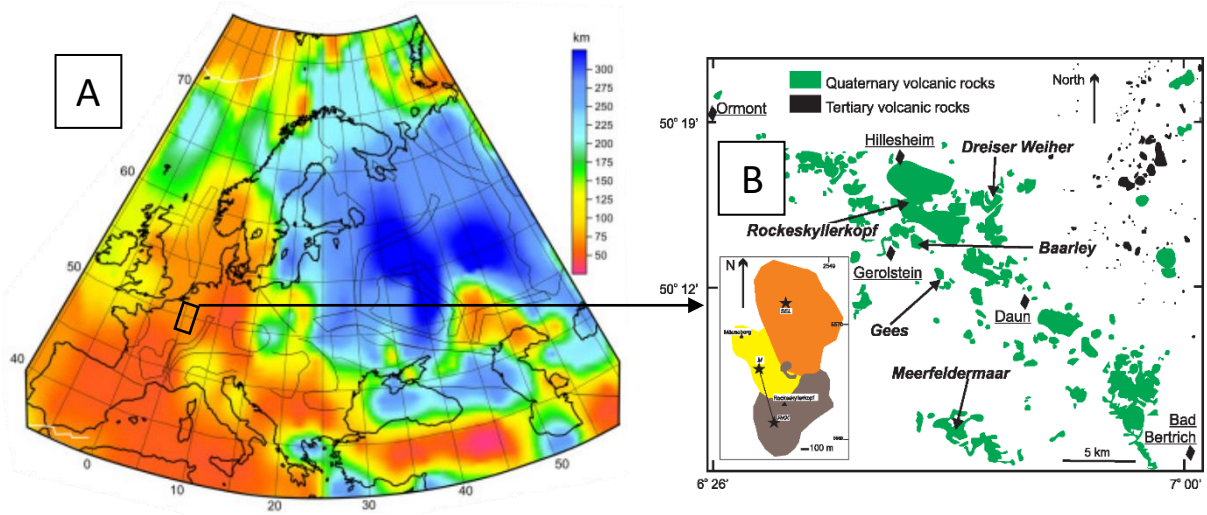

Figure 2.7. (A) Lithospheric thickness map of Europe from Artemieva, (2019). (B) Map of the West Eifel Volcanic Field showing the locations of Dreiser Weiher, Gees, and Meerfeldermaar (from Shaw *et al.*, 2018).

The Rhenish Massif which is the product of continuous uplift since the Eocene (e.g. Fuchs & Wedepohl, 1983) and its formation is most commonly attributable to upwelling of the upper mantle (Gautheron *et al.*, 2005; Bräuer *et al.*, 2013; Bekaert *et al.*, 2019). The magmatism in the WEVF has been dated to 700-600 ka (Schmincke, 2007) and consists of approximately 240 volcanic centres comprising 70 “dry” maar craters and 160 scoria cones (Shaw, 2004). These are classically interpreted as being formed by explosive water-magma interaction (e.g. Lorenz, 1984). In addition to mantle xenoliths, the volcanic centres in the WEVF also contain abundant crustal xenoliths (Schmincke, 2007). These are hosted by olivine and

melilite nephelinites and to a lesser extent basanites. These lavas have been widely investigated and are believed to come from a metasomatized mantle source.

Peridotite and clinopyroxenite xenoliths from the WEVF were first studied by Frechen (1963) and represent some of the first samples used to identify enrichment in the lithospheric mantle (Lloyd & Bailey, 1975). Since then there have been extensive mineralogical, major- and trace-, volatile-element, stable, and radiogenic isotope studies of the locations analysed as part of this study, most recently reviewed in Witt-Eickschen, 2007 (e.g. Stosch & Seck, 1980; Lloyd *et al.*, 1991; Zinngrebe & Foley, 1995; O'Connor *et al.*, 1996; Schmidt *et al.*, 2003; Shaw *et al.*, 2018; Denis *et al.*, 2013; Kempton *et al.*, 1988; Yokochi *et al.*, 2009; Stosch *et al.*, 1986; Stosch & Lugmair, 1986; Schmidt & Snow, 2002; Witt-Eickschen *et al.*, 1998; Witt-Eickschen 2003b). Overall, the mantle xenoliths display enriched geochemical signatures. Witt-Eickschen *et al.* (2003b) and Witt-Eickschen (2007) have divided them into 4 types:

1. High-temperature (1150 – 1250°C) peridotites that equilibrated at a depth of 60 – 65 km and have slightly depleted LREE and MORB-like Sr-Nd-Pb isotopes. These formed 2 Ga.
2. Amphibole-bearing porphyroclastic peridotites show enrichments in fluid mobile trace-elements (Ba, Sr, Pb) together with Th and U enrichments and depletions in Nb, Ta, Zr and Hf on normalised multi-element plots. These peridotites are therefore thought to be influenced by EM-like subduction-zone metasomatism.
3. Tabular recrystallised peridotites which have LREE-enriched clinopyroxenes and amphiboles with Nd-Sr-Pb isotope compositions akin to SCLM affected by melt of HIMU mantle. In this respect, they resemble Cretaceous nephelinite intrusions, which have melting attributed to ancient subducted crustal domains.
4. Composite xenoliths consisting of amphibole veins cross-cutting hydrous peridotite. They have similar Nd-Sr-Pb signatures to the most recent basaltic volcanism and are inferred as high-pressure cumulates.

2.5 Antarctic Peninsula

The Antarctic Peninsula (Fig. 2.8) extends from the main Antarctic continent into the Bellingshausen Sea and the Weddell Sea. The Antarctic Peninsula developed in a continental margin setting in West Gondwana and records an extensive volcano-sedimentary record from the Ordovician to the Miocene. The most recent volcanism is related to rifting. This

study focusses on mantle xenoliths from Bruce Nunatak (James Ross Island Volcanic Group), and from Alexander Island, and Rothschild Island (Bellingshausen Sea Volcanic Group). Pressure and temperature estimates by Gibson (2012) suggest a lithosphere-asthenosphere boundary at ~80 km and the thermal and mechanical boundary layers are at ~90 km and ~70 km, respectively. Geophysical constraints from Baranov & Morelli (2013) identify the Antarctic Peninsula to have a moho at approximately 40 km depth.

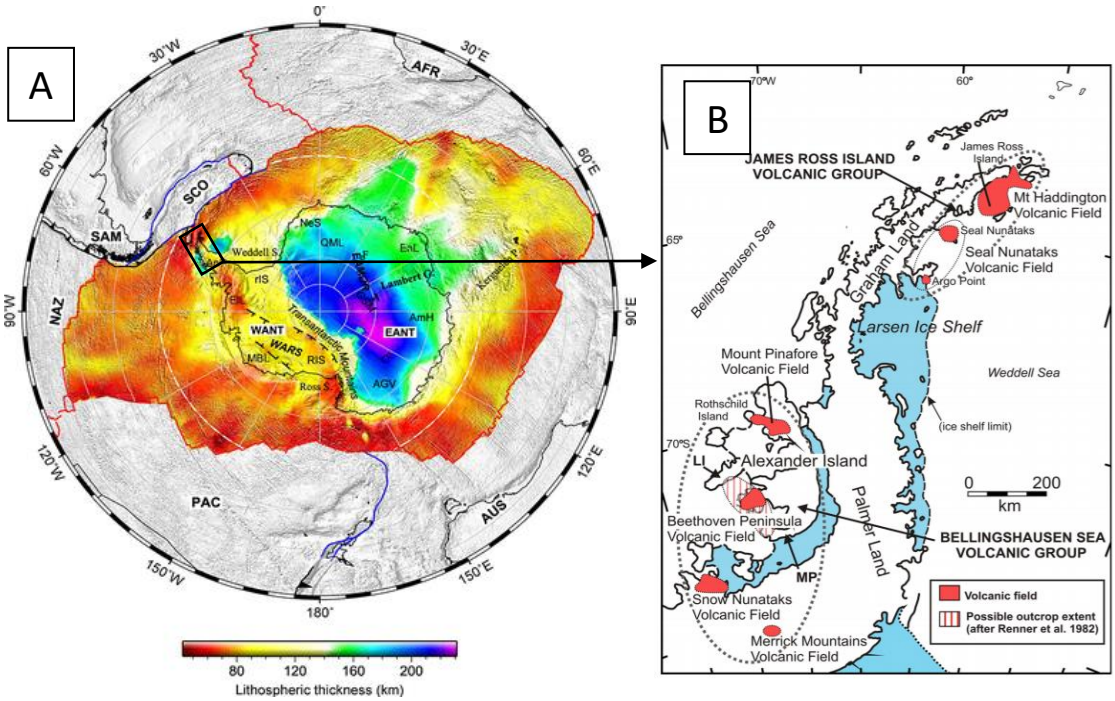

Figure 2.8. (A) Polar projection of lithospheric thickness for the Antarctic Continent after An *et al.* (2015). (B) Map of the Antarctic Peninsula with key geomorphological features (e.g. James Ross Island and Bellingshausen Sea Volcanic Group) from Smellie & Hole (2021).

Overall, this area is located in a fore-arc setting. Volcanism within the Antarctic Peninsula has been comprehensively summarized by Riley & Leat (2021a;b), Leat & Riley (2021a;b), Smellie & Hole (2021) and Hole (2021). The more recent volcanism is dominated by alkali basalts and basanites, where compositions show greatest affinity to an intraplate rift setting. The volcanism in the area is a result of post-subduction collisions between the Antarctic Peninsula, a trench and segments of an oceanic spreading centre during the last 7.7 my. These collisions caused locking of the spreading centre at the trench but continued subduction of the detached plate, resulting in the opening of 'slab windows'. This enabled upwelling and decompression melting of fertile mantle between the former subducted slab and overlying lithosphere. Lavas erupted at Bruce Nunatak, Alexander Island and Rothchild

Island have been dated using the K-Ar method to 1.5 ± 0.5, 7.7 ± 0.6 to 3.9 ± 0.4, and 5.4 ± 0.7 my, respectively (summarized by Smellie & Hole, 2021 and references therein).

The Antarctic Peninsula hosts abundant spinel-bearing peridotite and clinopyroxenite xenoliths. Although there are only a few publications (Gibson *et al.*, 2020; Ross, 2008, Gibson, 2012, and Rooks, 2016), the investigated samples are well characterised for mineralogical, major-, trace-, volatile-element, and isotope geochemistry. Overall, the peridotite xenoliths show a wide range in composition and are dominated by both enriched and depleted signatures (e.g. $(La/Yb)_N$, olivine Mg#). Radiogenic isotopes for the peridotites (e.g. $^{144}Nd/^{143}Nd$ v $^{87}Sr/^{86}Sr$, $^{187}Os/^{188}Os$ v $^{187}Re/^{188}Os$) show varying depletion ages and enrichment signatures. The samples which display enrichment are thought to have been metasomatized by agents derived from recycled oceanic lithosphere (e.g. Gibson, 2012).

2.6 Southern Patagonia

In Patagonia, Holocene volcanic plateaus were emplaced on Palaeozoic-Mesozoic continental margin successions (e.g. Ramos & Kay, 1992; Kay *et al.*, 2004). This study focusses on the Pali Aike Volcanic Field (PAVF), located in Southern Patagonia (Fig 2.9) and mantle xenoliths described in Gibson *et al.* (2020) and Rooks, (2016). The PAVF is composed of approximately 450 monogenic volcanoes on the border of Argentina and Chile, approximately 100 km south west of Rio Gallegos (Jalowitzki *et al.*, 2016). Pressure and temperature estimates using garnet-bearing peridotites (Stern *et al.* 1999) and Rooks (2016) indicate surface heat flux of 65 mW/m^2, with a lithosphere-asthenosphere boundary at ~90 km depth, a mechanical boundary layer at ~70 km depth and a mechanical and thermal boundary layer at ~70 km and ~100 km depth, respectively. Furthermore, the work of Stern *et al.* (1999) suggest that the a Moho depth is at ~30 km.

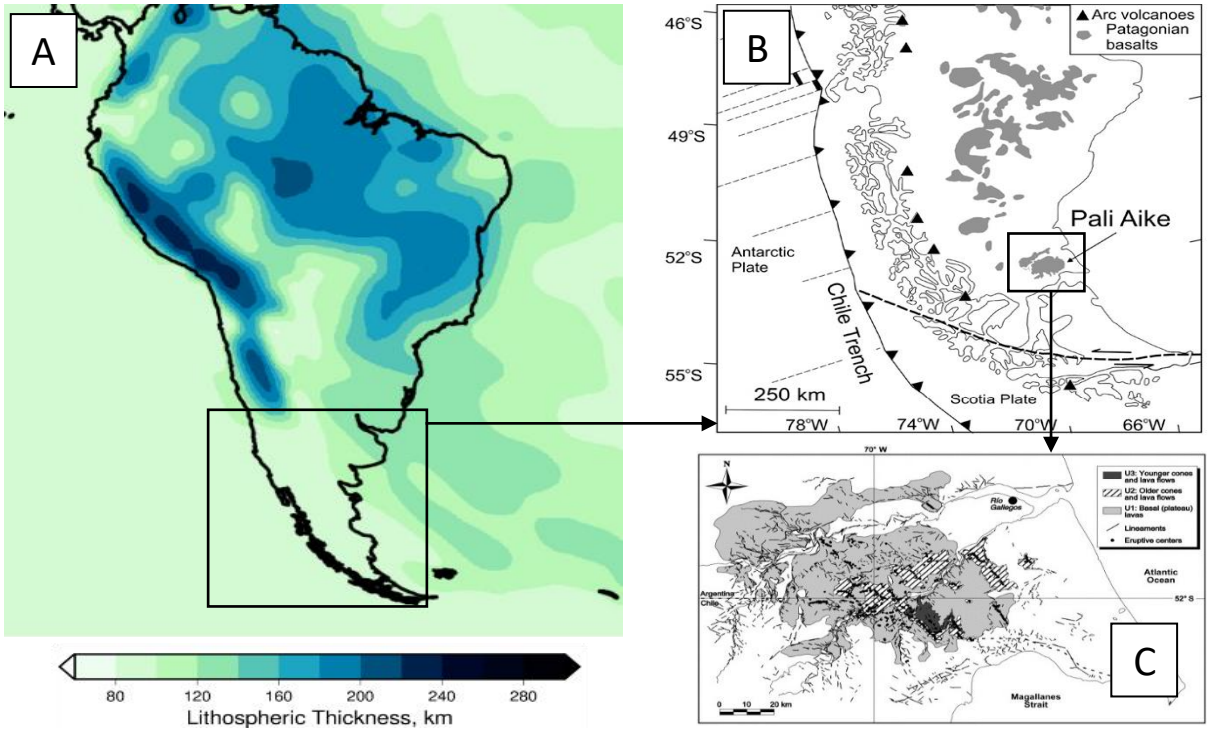

Figure 2.9. (A) Map of lithospheric thickness of the South American continent after Priestley & McKenzie (2013). (B) and (C) Maps of Southern Patagonia and the Pali Aike Volcanic Field with key geomorphological features (adapted from D'Orazio *et al.* (2000))

Southern Patagonia is a complex region in a back-arc setting that formed during several events related to the subduction of different oceanic plates (e.g. Pankhurst *et al.*, 2006). Currently, the western margin of Patagonia is characterised by the ongoing subduction of the Nazca and Antarctic oceanic plates forming the Andean volcanic arc. There have been four oblique active ridge segments that have subducted beneath South America since 12 Ma (SCR1 = 0.3 Ma, SCR0 = 3 Ma, SCR-1 = 6 Ma, and SCR-2 = 12 Ma; e.g. Cande & Leslie, 1986). This activity has produced xenolith-hosting lavas of alkaline basalts, basanites, and olivine basalts that erupted 3.78 to 0.17 Ma (D'Orazio *et al.*, 2000). These magmas lack clear 'subduction signatures' and are associated with the asthenospheric mantle upwelling in response to these subduction events (e.g. Gorring *et al.*, 1997; D'Orazio *et al.*, 2000). This has provided evidence for a of slab-window (e.g. D'Orazio *et al.*, 2000; Wang *et al.*, 2008) or slab rollback (Munoz *et al.*, 2000; de Ignacio *et al.*, 2001) of the subducted lithosphere generates magmatic activity in the area.

The mafic lavas of the PAVF contain abundant peridotite and pyroxenite xenoliths. Initial geochemical studies of these xenoliths were undertaken by Stern *et al.* (1986) following analysis of their host lavas by Skewes & Stern (1979). Subsequently, there has been

extensive mineralogical, major-, trace-, volatile-element, and radiogenic isotope studies (Kempton *et al.*, 1999a,b; Stern *et al.*, 1999; Gibson, 2012; Mundl *et al.*, 2015; Schilling *et al.*, 2017; Gibson *et al.*, 2020) which are summarized in Melchiorre *et al.*, (2020). Overall, the peridotite xenoliths from the PAVF are characterised by signatures that demonstrate they formed as residues of adiabatic decompression melting (up to 25%; Melchiorre *et al.*, 2020). However, some show slight enrichment signatures (e.g. $(La/Yb)_N$ and $^{144}Nd/^{143}Nd$ v $^{87}Sr/^{86}Sr$) due to metasomatism by alkaline fluids/melts. Overall, this provides evidence for the generation of the lithospheric mantle from MORB-sourced mantle (e.g. Jalowitzki *et al.*, 2016) which became overprinted by recycled components with EM1 or EM2 isotopic affinity (e.g. Wang *et al.*, 2008; Melchiorre *et al.*, 2020).

2.7 Northern Tanzania

Volcanism within Northern Tanzania has developed in the Eastern Branch of the East African Rift (Fig. 2.10). There are multiple volcanic centres, with kimberlite eruptions identified at Igiwisi Hills located on the Tanzania Craton (Dawson, 1994), and melilititic volcanic centres at Lashaine, Labait, Olmani and Pello Hill within the ajacent Mozambique Belts (Fig 2.10; see summary in Dawson, 2008). This study focusses on xenoliths from Lashaine and Pello Hill (within approximately 40 km of each other). Pressure and temperature estimates from garnet- and spinel-bearing peridotites outlined in Gibson *et al.* (2013) suggest a surface heat flux of ~40 mw/m^2, with the lithosphere-asthenosphere boundary at ~175 km depth and the mechanical and thermal boundary boundary layer at ~155 km and ~190 km depth, respectively. Geophysical constraints from Julia *et al.* (2005) estimate a Moho depth of 38 to 42km.

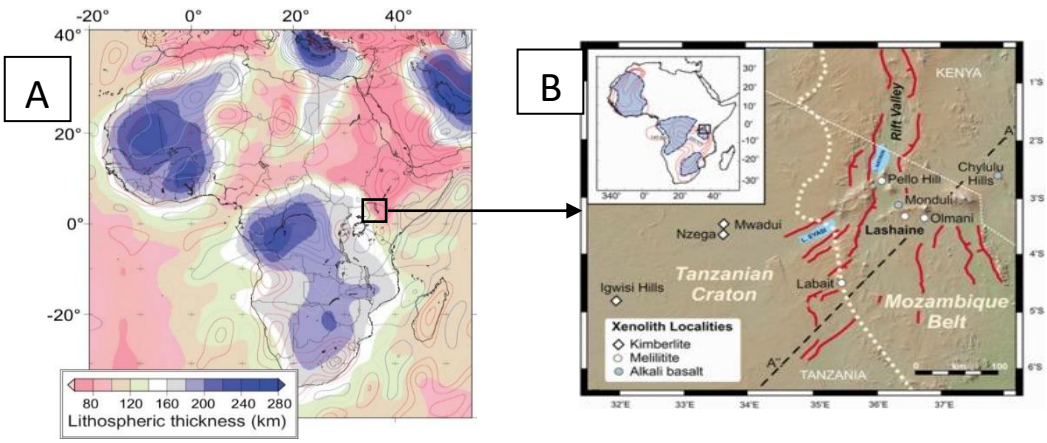

Fig 2.10. (A) Map of lithospheric thickness for the African continent from Fishwick & Bastow (2011). (B) Major volcanic and geographic locations on digital elevation map of Tanzania from Gibson *et al.* (2013).

The volcanism in Northern Tanzania began during a major phase of Tertiary faulting and extension associated with the East African Rift. Upwelling of the upper-mantle generated basaltic to trachytic magmas that have been radiometrically dated to approximately 4.5 to 1.2 Ma. Another major phase of rifting occurred post 1.2 Ma through the Pleistocene. This produced the Younger Extrusives, which comprise small-volume explosive nephelinite-phonolite-carbonatite volcanism (Dawson *et al.*, 2008 and references therein), including the Lashaine tuff cone.

2.7.1 Lashaine

Ultramafic xenoliths in the Lashaine tuff cone were first identified in 1961 (Dawson, 1964) and include peridotites and clinopyroxenites (e.g. Reid *et al.*, 1975; Rhodes & Dawson, 1975; Pike *et al.*, 1980), which are both garnet-bearing and garnet-free (e.g. Gibson *et al.*, 2013). The mantle xenoliths from Lashaine have been extensively investigated for their mineralogical, major- and trace-element, stable-, and radiogenic isotopes (Dawson *et al.*, 1970; Hutchison & Dawson, 1970; Reid & Dawson, 1972; Dawson & Smith, 1973; Reid *et al.*, 1975; Rhodes & Dawson, 1975; Ridley & Dawson, 1975; Pike *et al.*,1980; Dawson & Smith, 1992; Henjes-Kunst & Altherr, 1992; Gibson *et al.*, 2013; Aulbach & Rudnick, 2009; Savage et al, 2010; Saunders *et al.*, 2020; Cohen *et al.*, 1984; Burton *et al.*, 2000; Burton *et al.*, 2000; Dawson, 2002). Re-Os isotopes show that the xenoliths derived from a source depleted at ~3.4Ga and then experienced two episodes of metasomatism related to the invasion of low-temperature high-density fluids and high-temperature silicate-melts.

2.7.2 Pello Hill

Ultramafic xenoliths in the Pello Hill scoria cone were first described by Dawson & Smith (1988) and comprise peridotite xenoliths of olivine-mica-pyroxene veins (Dawson & Smith, 1992). Detailed petrographic investigations of their petrography and mineral chemistry suggests that these xenoliths represented metasomatic enrichment of a peridotite precursor (e.g. Dawson & Smith, 1992). Subsequently, xenoliths from this location have been subject to additional studies of major, trace, volatile element, stable isotope and radiogenic isotope studies (e.g. Cohen *et al.*, 1984; Porcelli *et al.*, 1992; Burton *et al.*, 2000; Lee *et al.*, 2000; Mattson, 2012; Baptiste *et al.*, 2015). Overall, the findings from these investigations point towards mantle metasomatism by melts from the MORB-source mantle (e.g Cohen *et al.*, 1984).

2.8 Oga Peninsula

The Oga Peninsula of north east Japan (Fig. 2.11) comprises five Quaternary volcanoes that form a 15 km-wide east-west oriented cluster (Yamamoto *et al.*, 2013). This peninsula forms the rear-arc of the greater northeast Japan Volcanic Arc (e.g. Yoshida *et al.*, 2014). This study focusses on a single mantle xenolith from Ichinomegata, approximately 20 km north-east of Oga. Pressure and temperature estimates from spinel-bearing peridotites (Sato & Ozawa, 2019) estimate the lithosphere-asthenosphere boundary to be ~75 km depth, and the base of the mechanical and thermal boundary layer to be at ~60 km and ~95 km, respectively. Furthermore, the Moho is estimated to be at 25-30 km depth based on geophysical constraints from Iwasaki *et al.* (2013).

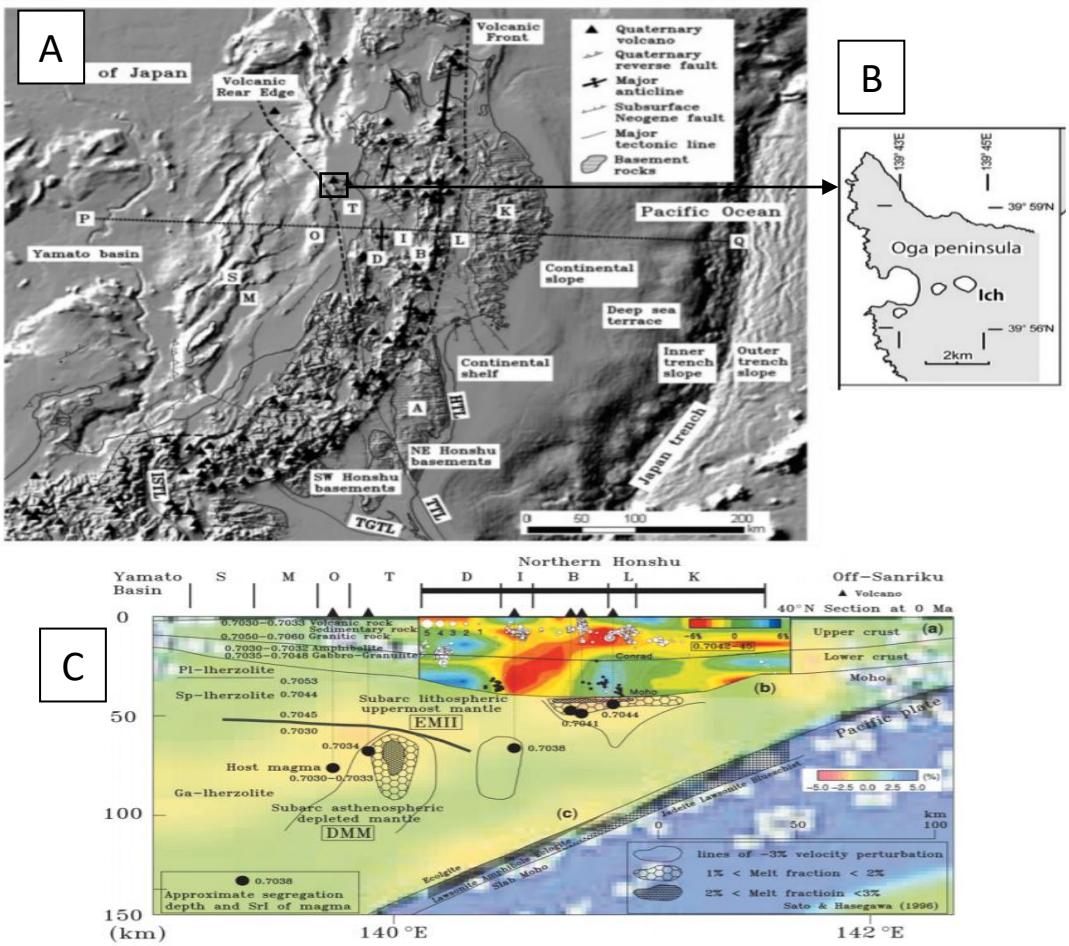

Figure 2.11. a) Major geological features of the Japanese Island Arc with cross section noted by P-Q along 40°N latitude and major regions defined by P, S, M, O, T, D, I, B, L, K and Q; b) Gographic location of Oga Peninsula in Japan relative for A; c) Annotated cross section profile of P-Q, note the close proximity to section T (Tobishima Basin (Akita-Niigata Basin). Figure adapted from Yoshida *et al.* (2014) and Takeuchi & Arai (2015).

Magmatism on the Oga Peninsula was initiated during the opening of the Japan Sea 28-18 Ma (e.g. Tamaki, 1995). There has been extensive magmatic activity in the area since the

onset of subduction, however, chronological and stratigraphic studies show Ichinomegata is a young volcano, forming between 80,000 and 60,000 years ago (Kitamura, 1990). During this time, Ichinomegata experienced three stages of volcanic activity: Stage-I involving ejected basal mud flow and air-fall deposits; Stage-II consisting of base surge deposits with calc-alkali andesite and dacite pumice; and Stage-III comprising tholeiitic basalt as lapilli (Takahashi, 1986). Sakuyama & Koyaguchi (1984) determined Stage-II and Stage-III magmas to come from the upper-mantle and be the product of variable mixing of fresh basalt with dacite formed from previously fractionated magmas. Typically, this geodynamic setting rarely retains mantle xenoliths, however volcanoes in north-east Japan are an exception (Arai *et al.*, 2007). The dacitic pumice and tholeiitic basalt lapilli from Stage-II and -III erupted 10,000 years ago contain abundant mantle and lower-crustal xenoliths (e.g. Abe *et al.*, 1998; Horie, 1964; Satsukawa *et al.*, 2017).

Mantle xenoliths from Ichinomegata were initially described by Kuno (1967) and comprise peridotite and clinopyroxenite, with peridotite compositions dominated by lherzolite and rarer harzburgite (Abe *et al.*, 1992; Abe & Arai, 1993; Abe *et al.*, 1998; Arai *et al.*, 2007; Satsukawa *et al.*, 2017; Sato & Ozawa, 2019). These peridotites can be veined by hornblendite with pargasite and phlogopite (Abe *et al.*, 1998; Sato & Ozawa, 2019). The peridotite xenoliths have been divided into low temperature and a high-temperature groups. The later have experienced recent heating (Takahashi, 1980). The peridotites have been extensively studied for thier major- and trace- element (Tanaka & Aoki, 1981; Abe *et al.*, 1998; Satsukawa *et al.*, 2017), radiogenic isotope (Brandon *et al.*, 1996; Abe & Yamamoto, 1999) and volatile element (Satsukawa *et al.*, 2017) characteristics. In general, the mantle peridotite are fertile, with low LREE relate to HREE contents and are enriched in Th-U-Pb by fluids from the dehydrating subducting Pacific plate (e.g. Satsukawa *et al.*, 2017).

Chapter 3. Petrography

3.1. Introduction

Of the 48 mantle xenoliths examined in this study, 44 of these xenoliths have their petrographic information constrained. The 4 unconstrained xenoliths are from the Antarctic Peninsula and Southern Patagonia are akin to xenoliths well characterised by previous work (Gibson *et al.*, 2020). Modal proportions were determined by point counting using the JMicroVision (www.jmicrovision.com/index.htm, version 1.2.7) image analysis toolkit.

The mantle xenoliths were classified based on the relative abundance of olivine, orthopyroxene and clinopyroxene using the IUGS ultramafic rock ternary classification diagram (Le Bas & Streckeisen, 1991; Figure 3.1). In this scheme, ultramafic rocks are broadly defined as peridotite where modal olivine >40% olivine and <60% orthopyroxene + clinopyroxene, and pyroxenites if modal olivine <40% and orthopyroxene + clinopyroxene >60%.

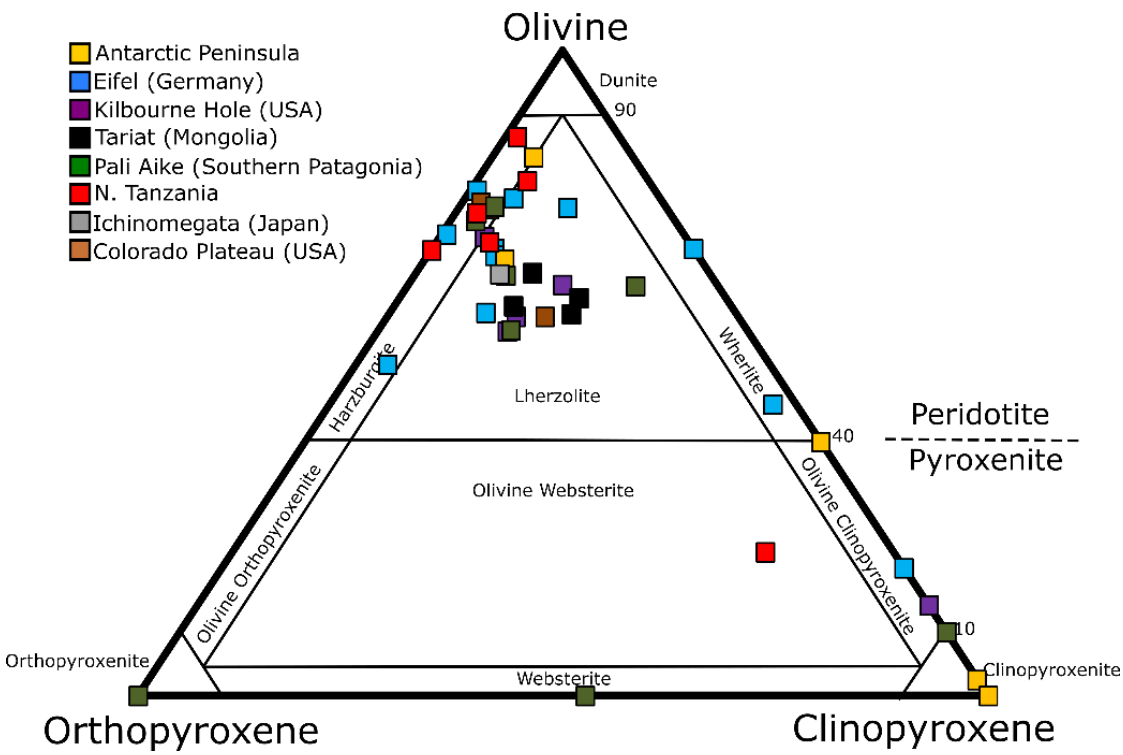

Figure 3.1 Modal petrology of mantle xenoliths displayed on an IUGS ternary classification diagram for ultramafic rocks (adapted from Le Bas & Streckeisen, 1991).

In addition to the modal mineralogy, the textures and fabrics of mantle peridotites are characterised using the terminology of Mercier & Nicolas (1975).

1. Protogranular – in which coarse grained (4 mm) olivine and orthopyroxene have curvilinear grain boundaries unless local recrystallization causes straight-lined boundaries. Clinopyroxene and spinels have a smaller grain size (1 mm) and are usually in contact with large enstatite grains, with spinel displaying a vermicular habit. The crystals display almost no elongation and the mantle xenoliths are devoid of any foliation or lineation.

2. Porphyroclastic – where there are two types of olivine and orthopyroxene; coarse grained (~4 mm), elongated, strained grains (porphyroclasts) and smaller, typically polygonal, strain-free grains (neoblasts). Clinopyroxene and spinels form small grains distributed throughout the mantle xenoliths, with the spinel displaying a xenomorphic (uncharacteristic) shape. Neoblasts must comprise >50% of rock to fulfil this criteria (Kil & Wendlandt, 2004).

3. Equigranular – in which there are two key components: tabular and mosaic. In both cases, the texture is fine grained (<1 mm), equally dimensioned and contains rare relic porphryroclasts. The grain boundaries are mostly straight and converge at 120° triple junctions. Clinopyroxene and spinel are scattered through the mantle xenolith, with spinel forming tiny spherical inclusions or along grain boundaries. Tabular textures consist of grains that are parallel/sub-parallel and define a strong foliation. In contrast, a mosaic texture shows little or no grain elongation and a weak or absent foliation.

4. Poikiloblastic – This texture is characterised by variable grain sizes and occurs in porphyroclastic, porphyroblastic and equigranular rocks. The distinction between poikiloblastic textures and those previously discussed is that spinel grains occur as inclusions in various different silicate phases (i.e. olivine, orthopyroxene and clinopyroxene) as opposed to only along grain boundaries.

Mercier & Nicolas (1975) outlined a sequence of deformation of mantle lithology from these textures (Figure 3.2): Initially, mantle rocks form residues with protogranular textures. These then become physically perturbed to produce a porphyroclastic texture, which becomes equigranular, then poikiloblastic. Poikiloblastic textures are now understood to be related to metasomatic reactions (e.g. Embey-Isztin *et al.*, 2014).

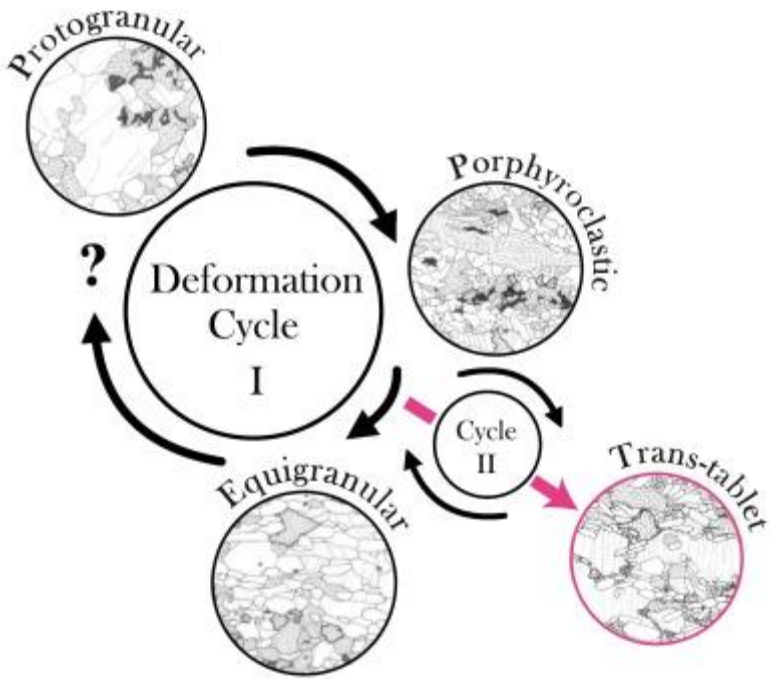

Figure 3.2. Schematic diagram showing the peridotite deformation cycle proposed by Mercier and Nicolas (1975).

Mantle lithologies may become altered syn- or post- entrainment and emplacement at the Earth's surface. This most commonly involves olivine, which breakdowns to serpentine, magnetite, and brucite due to the addition of water to its crystal structure below 250°C (e.g. Bach *et al.*, 2004). Decompression reactions also occur, such as the breakdown of garnet to spinel-bearing symplectites, i.e. kelphyphites (Godard & Martin, 2000).

3.2 Classification and description of mantle xenoliths used in this study

The complete modal mineralogy of the mantle xenoliths that form the basis of this investigation can be found in Table 3.1. These are also shown on the IUGS ternary classification diagram for ultramafic rocks (Figure 3.1).

Table 3.1. Modal petrology of mantle xenoliths examined in this study

Sample	Rock Type	Location	Volcanic Field	Olivine	Orthopyroxene	Clinopyroxene	Spinel	Garnet	Amphibole	Phlogopite	Calcite	Plagioclase	Ilmenite	Kelyphite	Serpentine
KH1	Olivine Clinopyroxenite	USA	Las Cruces (Kilbourne Hole)	9.7		60.0	30.3								
KH2	Lherzolite	USA	Las Cruces (Kilbourne Hole)	61.1	17.4	17.4	4.1								
KH3D	Lherzolite	USA	Las Cruces (Kilbourne Hole)	70.6	23.5	5.2	0.7								
KH4	Lherzolite	USA	Las Cruces (Kilbourne Hole)	54.0	27.1	14.6	4.3								
KH5	Lherzolite	USA	Las Cruces (Kilbourne Hole)	57.3	25.6	14.8	2.3								
TM1	Lherzolite	Mongolia	Khangai Rise (Tariat Depression)	63.1	20.0	13.1	3.8								
TM2	Lherzolite	Mongolia	Khangai Rise (Tariat Depression)	60.3	16.8	20.6	2.3								
TM3	Lherzolite	Mongolia	Khangai Rise (Tariat Depression)	56.0	18.3	20.3	5.4								
TM4	Lherzolite	Mongolia	Khangai Rise (Tariat Depression)	56.4	23.9	13.0	6.7								
DW3	Lherzolite	Germany	West Eifel (Dresier Weiher)	80.8	12.5	13.6	3.1								
DW5	Olivine Clinopyroxenite	Germany	West Eifel (Dresier Weiher)	18.9		76.8	4.3								
DW7	Harzburgite	Germany	West Eifel (Dresier Weiher)	50.6	44.3	3.7	1.4								
DW8	Lherzolite	Germany	West Eifel (Dresier Weiher)	66.5	22.4	7.1	4.0								
DW10	Wehrlite	Germany	West Eifel (Dresier Weiher)	66.0	0.0	29.4	2.0		2.6						
MM5	Lherzolite	Germany	West Eifel (Meerfelder Maar)	67.0	23.5	7.8	1.7								
MM6	Composite	Germany	West Eifel (Meerfelder Maar)	44.0	2.7	50.8	2.5								
MM8	Harzburgite	Germany	West Eifel (Meerfelder Maar)	77.8	20.8	0.6	0.9								
MM11	Lherzolite	Germany	West Eifel (Meerfelder Maar)	55.0	27.3	10.4	2.0		5.4						
G17	Lherzolite	Germany	West Eifel (Gees)	74.9	16.8	5.5	2.8								
G18	Harzburgite	Germany	West Eifel (Gees)	69.4	27.0	0.6	3.0								
TH17	Harzburgite	USA	Colorado Plateau (The Thumb)	73.1	20.4	3.5		0.6		0.2		0.9		1.6	
TH33	Harzburgite	USA	Colorado Plateau (The Thumb)	75.0	21.0	2.0		0.2	1.8						
BP1	Lherzolite	USA	Colorado Plateau (Buell Park)	50.7	19.6	16.0		4.0							9.8
KG3609.21	Peridotite	Antarctica	Alexander Island												
KG3610.10A	Harzburgite	Antarctica	Alexander Island	81.6	11.4	4.7		2.2							
KG3619.7	Pyroxenite	Antarctica	Rothschild Island												
KG3719.25	Peridotite	Antarctica	Rothschild Island												
L7.201.1.41	Lherzolite	Antarctica	Rothschild Island	65.6	22.4	9.0		2.8							
L7.201.1.74c	Olivine Clinopyroxenite	Antarctica	Rothschild Island	2.1		79.6		18.3		0.1					
R5194.2I	Olivine Clinopyroxenite	Antarctica	Adelaide Island	33.0		50.7		8.0			6.7	0.4			
R5194.2M	Clinopyroxenite	Antarctica	Adelaide Island			84.9		5.7			4.3	0.2			
BN	Peridotite	Antarctica	Bruce Nunatak												
CP31	Lherzolite	Chile	Pali Aike (Campo Picana)	60.4	22.4	10.0		1.5		5.7					
CP33	Lherzolite	Chile	Pali Aike (Campo Picana)	59.6	9.1	25.3		0.9		5.1					
LT1	Lherzolite	Chile	Pali Aike (Laguna Timones)	55.0	27.0	15.0		3.0							
LT16	Harzburgite	Chile	Pali Aike (Laguna Timones)	73.0	23.3	3.0		0.7							
PA3-5	Harzburgite	Chile	Pali Aike (Laguna de Los Cisnes)	75.0	20.0	4.0		1.0							
CP62	Orthopyroxenite	Chile	Pali Aike (Campo Picana)		72.0			2.0		20.0					
LT14	Websterite	Chile	Pali Aike (Laguna Timones)		46.3	51.4		2.3					1.0		
LT15	Olivine Clinopyroxenite	Chile	Pali Aike (Laguna Timones)	9.8		90.2									
BD730	Lherzolite	Tanzania	Lashaine Volcano	64.4	21.5	5.6				8.5					
BD738	Lherzolite	Tanzania	Lashaine Volcano	72.0	12.9	5.4				8.2			1.4		
BD794	Harzburgite	Tanzania	Lashaine Volcano	70.4	21.4	2.3				5.9					
BD797	Harzburgite	Tanzania	Lashaine Volcano	64.4	28.9			0.4		4.9					
BD822	Harzburgite	Tanzania	Lashaine Volcano	84.2	11.8	1.2		0.4							
BD816	Olivine Clinopyroxenite	Tanzania	Lashaine Volcano	22.0	15.0	62.0							1.0		
BD3847	Composite	Tanzania	Pello Hill												
JI	Harzburgite	Japan	Ichinomegata	72.9	24.7	1.2		1.2		Trace					

3.2.1 South West USA

3.2.1.1 Kilbourne Hole

Five mantle xenoliths in this study are from the Kilbourne Hole. Three are lherzolites (KH2, KH4, KH5), with modal olivine contents of 54 to 61%, orthopyroxene at 17 to 27%, and clinopyroxene from 15 to 17%. One is a harzburgite (KH3D) with 70% olivine, 24% orthopyroxene, and 5% clinopyroxene and one is an olivine clinopyroxenite (KH1) with 10%

olivine and 60% clinopyroxene. The aluminous phase present in these samples is spinel and forms 2 to 4% of lherzolites, <1% of the harzburgite and 30% of the olivine clinopyroxenite. The variable modal mineralogy of the mantle xenoliths from the Kilbourne Hole observed in this study is consistent with previous studies (e.g. Perkins & Anthony, 2011; Harvey *et al.*, 2012).

All of the peridotite mantle xenoliths from the Kilbourne Hole have varying grain sizes (~1 to ~4 mm) at varying proportions. The olivine clinopyroxenite sample (KH1) has very coarse (5-15 mm) grains with spinel often enclosed by clinopyroxene. Samples KH3D, KH4, and KH5 display protogranular textures, sample KH2 displays a marginal protogranular/porphyroclastic texture (Figure 3.3) and sample KH1 has a poikiloblastic texture.

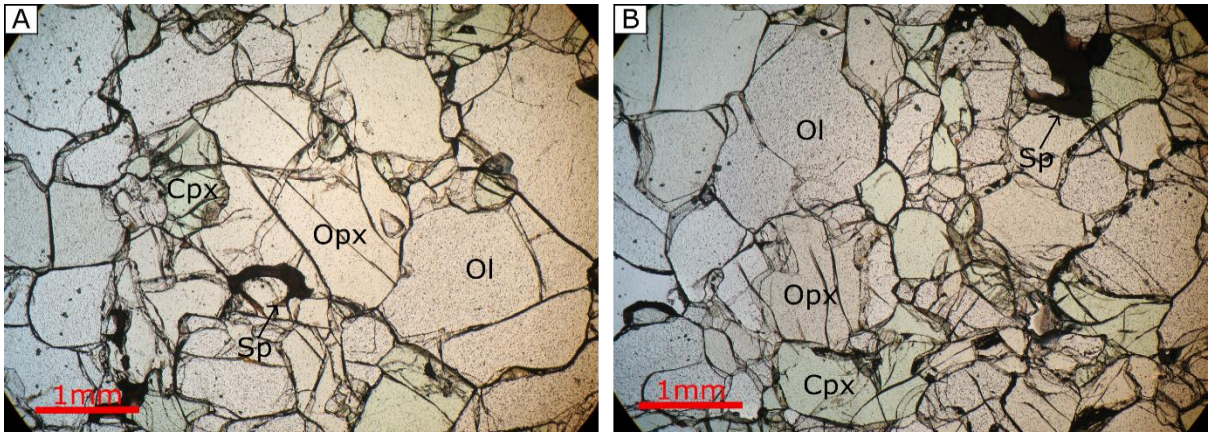

Figure 3.3. Photomicrographs of samples a) KH2 and b) KH4. Abbreviations: ol = olivine, opx = orthopyroxene, cpx = clinopyroxene, sp = spinel. The scale is shown in the bottom left of each photomicrograph.

3.2.1.2 Colorado Plateau

Of the mantle xenoliths examined from the Colorado Plateau, two from the Thumb (TH17 and TH33) are harzburgites with 73 to 75% olivine, 20 to 21% orthopyroxene, and 2 to 4% clinopyroxene. The other mantle xenolith is from Buell Park (BP1) and is a lherzolite with 51% olivine, 20% orthopyroxene, and 16% clinopyroxene. The dominant aluminous phase in TH17 is garnet which has kelyphite texture rims, both garnet and spinel are present in TH33, and only spinel occurs in BP1. Additionally, TH17 contains trace amounts of phlogopite and ilmenite, while BP1 contains abundant serpentine.

TH17 and TH33 have varying grain sizes but most grains are coarse (1-4 mm). Other parts of these mantle xenoliths are dominated by finer grains (<1 mm) with no foliation or lineation,

and have small amounts of kelyphite along grain boundaries. Overall, TH17 and TH33 display both protogranular and mosaic equigranular textures. BP1 is dominated by coarse (1-4 mm) grains with abundant spinel and serpentine along grain boundaries and cracks in olivine. BP1 likely had a protogranular texture, which has undergone significant serpentinization (Figure 3.4). The mineralogy and texture of these three mantle xenoliths from the Colorado Plateau are consistent with previous studies (e.g. Marshall *et al.*, 2017).

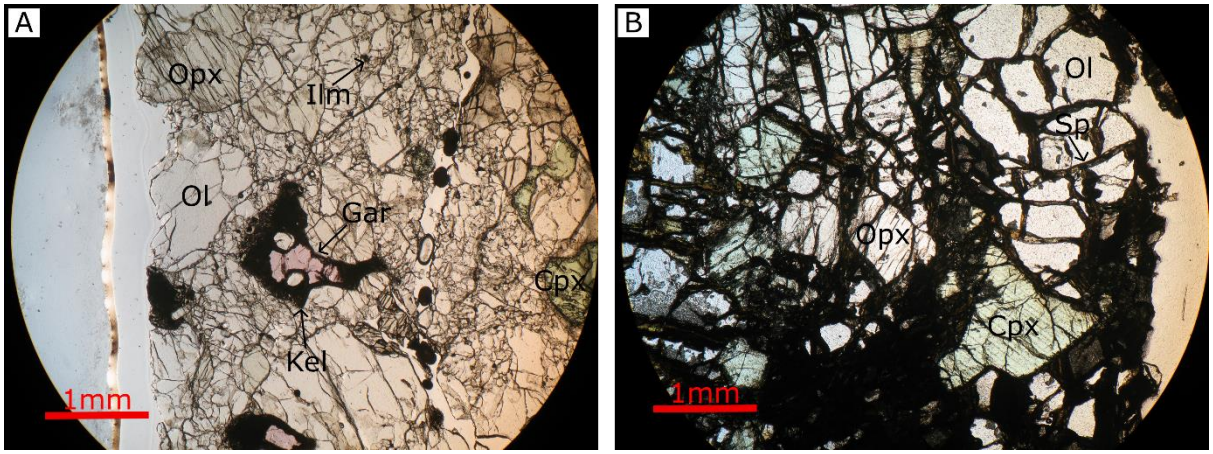

Figure 3.4. Photomicrographs of samples a) TH17; b) BP1. Abbreviations: ol = olivine, opx = orthopyroxene, cpx = clinopyroxene, sp = spinel, gar = garnet, ilm = ilmenite, kel = kelyphite. Scale in bottom left of each picture.

3.2.2 Tariat Volcanic Field (Mongolia)

Four of the mantle xenoliths examined in this study are from the Tariat Depression in Mongolia (TM1, TM2, TM3, and TM4). All of these are lherzolites, which is the dominant lithology found at this location (e.g. Ionov, 2007). They contain 56 to 63% olivine, 17% to 24% orthopyroxene, and 13% to 21% clinopyroxene. The aluminous phase present in these samples is spinel, which varies from 2% to 7%, together with trace amounts of phlogopite in TM2.

All of theTariat mantle xenoliths exhibit varying grain sizes, which range from fine (~1 mm) to coarse (~4 mm) and at different proportions. Samples TM1, TM2, and TM4 display protogranular textures while sample TM3 displays a marginal protogranular/porphyroclastic texture (Figure 3.5).

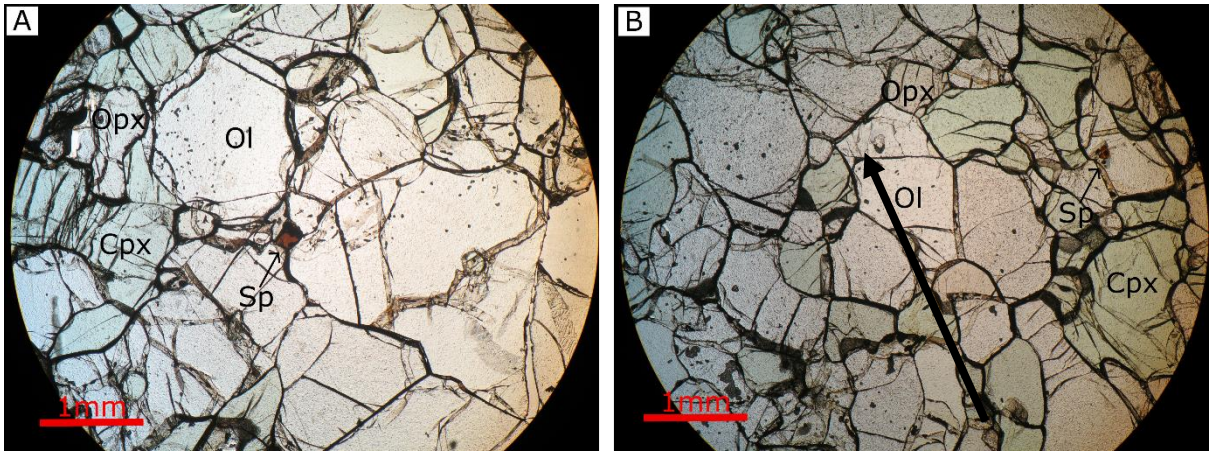

Figure 3.5. Photomicrographs of samples a) TM2 and b) TM3. Abbreviations: ol = olivine, opx = orthopyroxene, cpx = clinopyroxene, sp = spinel. Scale in bottom left of each picture. Strain alignment of TM3 minerals indicated by the black arrow which is more obvious in hand specimen and greater field-of-view thin-section observations.

3.2.3 West Eifel Volcanic Field (Germany)

Eleven of the mantle xenoliths are from the West Eifel Volcanic Field. Five of these are from Dreiser Weiher, where two are lherzolites (DW3 and DW8) with 67 to 81% olivine, 13 to 22% olivine, and 7 to 14% clinopyroxene. Another is a harzburgite (DW7) with 51% olivine, 44% orthopyroxene, and 4% clinopyroxene. A wehrlite (DW10) with 66% olivine and 30% clinopyroxene and also an olivine clinopyroxenite (DW5) with 19% olivine and 77% clinopyroxene were also studied. In all of the xenoliths examined from the West Eifel, the aluminous phase is spinel and represents 1% to 4% of the rock. Minor amounts (3%) of amphibole are present in the wehrlite (DW10).

Four of the mantle xenoliths are from Meerfelder Maar. Two are lherzolites (MM5 and MM11) with 55 to 67% olivine, 24 to 27% orthopyroxene, and 8 to 10% clinopyroxene. One is a harzburgite (MM8) with 78% olivine, 21% orthopyroxene, and <1% clinopyroxene. Lastly, one is a composite sample consisting of a harzburgite with a clinopyroxenite vein (MM6). The bulk composition of this is 44% olivine, 3% orthopyroxene, and 51% clinopyroxene. In all of the mantle xenoliths from Meerfelder Maar, the aluminous phase is spinel, which ranges from 1 to 3%. Minor amounts of amphibole (5%) are present in MM11.

Finally, two mantle xenoliths are from Gees, one is a harzburgite (G18) with 70% olivine, 27% orthopyroxene and 16% clinopyroxene, and another is a lherzolite (G17) with 75% olivine, 17% orthopyroxene and 6% clinopyroxene. In both samples the aluminous phase is spinel at 3%.

A wide variety of textures are displayed by mantle xenoliths from the West Eifel (Fig 3.4). Of the samples from Dreiser Weiher, two show coarse-grained (~4 mm) textures (DW5 and DW7), one shows no clear fabric (DW7), while four show distinctly tabular grains that define a foliation (DW3, DW5, DW8 DW10; Figure 3.6). According to the scheme of Mercier & Nicolas (1975), one sample is classified as protogranular (DW7), another has a coarse-grained (~4 mm) tabular equigranular texture (DW5), and three show fine-grained (~1 mm) tabular equigranular textures (DW3, DW8, and DW10). Of the samples from Meerfelder Maar, three show variable (1-4 mm) grain sizes (MM5, MM6, and MM8), with the composite xenolith (MM6) having smaller olivine (<1 mm) grains enclosed by larger clinopyroxene (1-4 mm) grains of the pyroxenite vein. Furthermore, one sample displays a fine-grained (<1 mm) texture (MM11). While sample MM11 has some tabular grains, all of the samples lack a distinct foliation. Two samples have protogranular textures (MM5, MM8), one is characterised as mosaic equigranular (MM11) and the composite xenolith (MM6) consists of protogranular harzburgite that is poikilitically enclosed within pyroxenite veins. Finally, mantle xenoliths from Gees (G17 and G18) consist most of fine-grained (<1 mm) crystals and a few coarse grains of mosaic equigranular orthopyroxene (>5 mm). Overall, these two samples (G17 and G18) are porphyroclastic. This wide variety of textures observed in the West Eifel xenolith suite are consistent with those discussed in Witt-Eickschen *et al.* (2003).

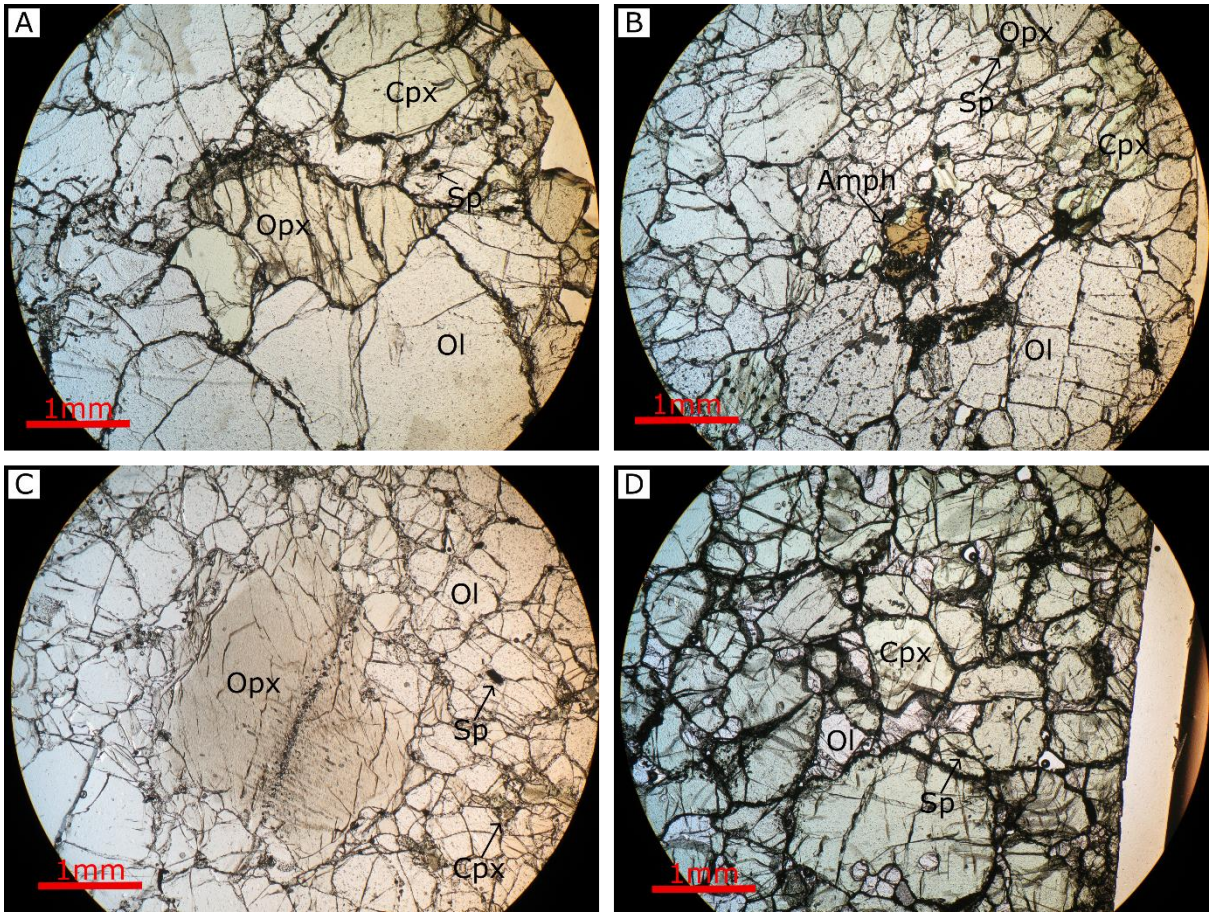

Figure 3.6. Photomicrographs of samples a) DW7; b) MM11; c) G17; and d) MM6. Abbreviations: ol = olivine, opx = orthopyroxene, cpx = clinopyroxene, sp = spinel, amph = amphibole. Scale in bottom left of each picture.

3.2.4 Antarctic Peninsula

The mantle xenoliths from the Antarctic Peninsula that are examined here have previously been extensively characterised by Ross (2008), Gibson (2012) and Gibson *et al.* (2020). Of the eight samples studied, two are from Alexander Island (KG.3609.21 and KG.3610.10A), four are from Rothschild Island (KG.3619.7, KG.3719.25, L7.201.1.41 and L7.201.1.74c), two are from Adelaide Island (R.5194.2I and R.5194.2M) and one is from Bruce Nunatak (BN).

KG.3610.10A is a harzburgite with 82% olivine, 11% orthopyroxene, and 5% clinopyroxene. L7.201.1.41 is a lherzolite with 66% olivine, 22% orthopyroxene, and 9% clinopyroxene. L7.201.1.74c and R5194.2I are both olivine clinopyroxenites with 2% to 33% olivine and 51% to 80% clinopyroxene. Lastly, R.5194.2M is a clinopyroxenite dominated by clinopyroxene (85%), calcite (4%) and trace amounts of plagioclase (<1%). The common aluminous phase in the Antarctic Peninsula mantle xenoliths is spinel (ranging from 2 to 18%) with trace amounts of amphibole and phlogopite in L7.201.1.41.

According to the information presented in Gibson *et al.* (2020), harzburgite KG.3610.10A and lherzolite L7.201.1.41 have varying crystal sizes (<1 mm to 12 mm), with clinopyroxene occurring as smaller crystals (<1 mm) often included along with olivine and spinel in large (up to 12 mm) poikilitic orthopyroxene crystals. The olivine clinopyroxenites (L7201.1.74c and R.5194.2I) and clinopyroxenite (R.5194.2M) are coarse grained and have protogranular textures.

3.2.5 Pali Aike (Southern Patagonia)

Eight mantle xenoliths in this study are from Pali Aike and have previously been extensively characterised and studied by Kempton *et al.* (1999a,b), Rooks (2016) and Gibson *et al.* (2020). Four are from Laguna Timones (LT1, LT14, LT15, and LT16), three are from Campo Picana (CP31, CP33, and CP62), and one is from Laguna de Los Cisnes (PA3-5).

Two of the Pali Aike mantle xenoliths are harzburgites (LT16 and PA3-5) with 73 to 75% olivine, 20 to 23% orthopyroxene, and 3 to 4% clinopyroxene. Three are lherzolites (CP31, CP33, and LT1) with 55 to 60% olivine, 9 to 27% orthopyroxene, and 10 to 25% clinopyroxene. One is an orthopyroxenite (CP62) with 72% orthopyroxene, another is a websterite (LT14) with 46% orthopyroxene and 51% clinopyroxene, and one is an olivine clinopyroxenite (LT15) with 10% olivine and 90% clinopyroxene. In LT1 and LT16 the aluminous phase is spinel at 15% and 3%, respectively. Samples CP31, CP33, and CP62 contain both spinel and garnet, which ranges from 1 to 2% and 5% to 20%, respectively. Orthopyroxenite CP62 contains a minor amount of (1%) phlogopite.

According to the information presented in Gibson *et al.* (2020), the harzburgites and lherzolites from Pali Aike are all medium- to coarse-grained but display complex textures (Fig 3.6). The large olivine grains (up to 3 mm) are strained, display curvilinear grain boundaries, and have 120° angles between each other (as do orthopyroxenes), indicative of textural equilibration. Orthopyroxenes occur as large porphyroblasts (up to 5 mm) and may fully enclose rounded grains of olivine and occur proximally to olivine neoblasts. Garnet ranges from 0.5 to 3 mm in diameter and contains spinel inclusions. Overall, these mantle xenoliths display porphyroclastic-poikilitic textures. The orthopyroxenite, websterite, and clinopyroxenites (CP62, LT14, LT15) are coarse-grained. CP62 has garnets occurring in

clusters and orthopyroxene with small (<1 mm) inclusions of spinel. Overall, all show a protogranular-poikiloblastic texture (Figure 3.7).

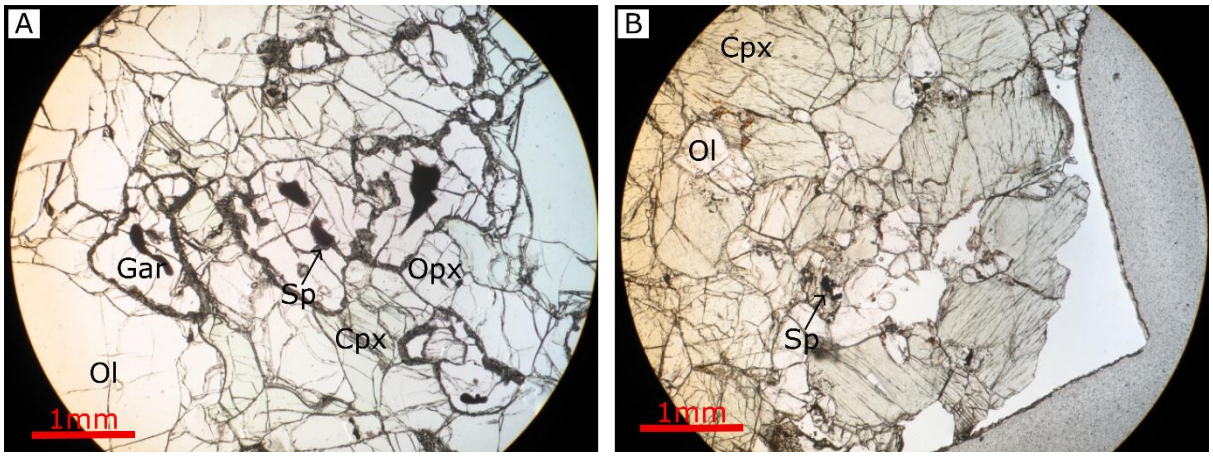

Figure 3.7. Photomicrographs of samples a) CP33; b) CP62. Abbreviations: ol = olivine, opx = orthopyroxene, cpx = clinopyroxene, sp = spinel, gar = garnet. Scale in bottom left of each picture.

3.2.6 Northern Tanzania

3.2.6.1 Lashaine

The mantle xenoliths from Lashaine (BD730, BD738, BD794, BD797, BD822, BD816) and Pello Hill (BD3847) have been extensively studied and characterised by Dawson & Smith (1973), Reid *et al.* (1975), Ridley & Dawson. (1975), Dawson & Smith (1988) and Gibson *et al.* (2013).

Of the six mantle xenoliths from Lashaine, three are harzburgites (BD794, BD797 and BD822) with 64 to 84% olivine, 12 to 29% orthopyroxene and 0 to 2% clinopyroxene. Two are lherzolites (BD730 and BD738) with 64 to 72% olivine, 9 to 22% orthopyroxene, and 10 to 25% clinopyroxene. One (BD816) is an olivine clinopyroxenite with 22% olivine, 15% orthopyroxene, and 62% clinopyroxene. Spinel forms a small proportion of in BD822 (<1%). Both spinel and garnet are present in BD797 at <1% and 5%, respectively, whereas garnet is the only aluminous phase found in BD370, BD738 and BD794 at 6 to 9%. Trace amounts of phlogopite are present in BD738 and BD816.

The textures of these mantle xenolith have been summarized by Gibson *et al.* (2013). The harzburgites are dominated by medium to coarse grained (1-3 mm), subhedral olivine and orthopyroxene, with some coarse grains of olivine (up to 9 mm). The garnets are medium to coarse grained (1 to 5 mm) and have reaction rims producing red-brown spinel,

orthopyroxene and clinopyroxene. The lherzolites are coarse grained with crystals typically 3 mm in diameter. They have 120° dihedral angles and show textual equilibrium. Clinopyroxenes are similar sized to olivine and orthopyroxene and the garnets frequently have reaction rims producing spinel and orthopyroxene. Phlogopite-bearing peridotite samples (e.g. BD822) are typically finer grained (<1 mm) than phlogopite-free samples, which is indicative of recrystallisation. Pyroxenite BD816 has small to medium grains showing indistinct banding. BD730, BD794, BD797 and BD822 have protogranular textures with poikilitic garnet. BD738 has a mosaic equigranular texture and BD816 shows a tabular equigranular texture (Figure 3.8).

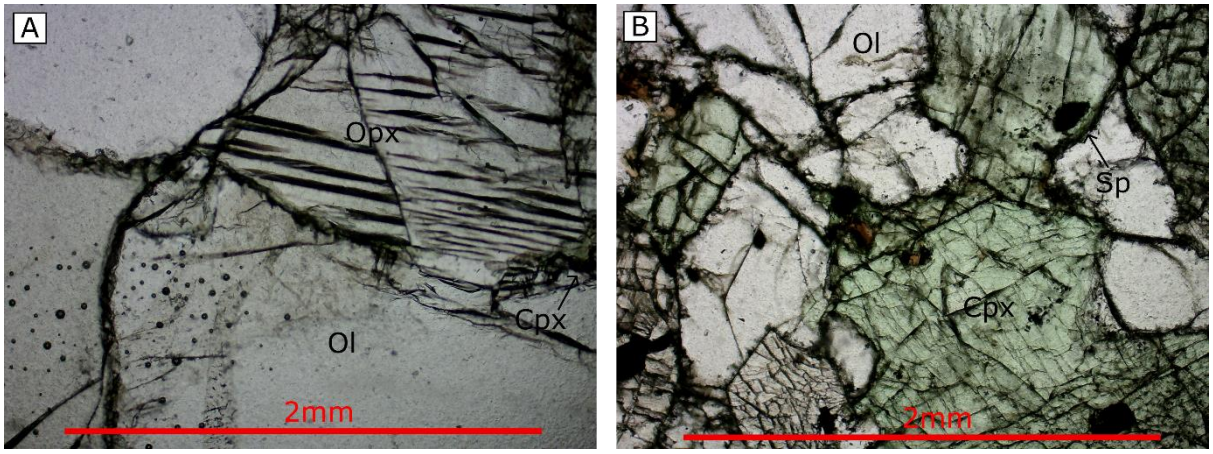

Figure 3.8. Thin section image of a) BD794 and b) BD816. Abbreviations: ol = olivine, opx = orthopyroxene, cpx = clinopyroxene, sp = spinel. The scale bar is shown to the right of A.

3.2.6.2 Pello Hill

According to information from Dawson & Smith (1988), the xenolith from Pello Hill (BD3847) is a composite xenolith with three distinct features of peridotite wall-rock, a mica-amphibole-pyroxene vein and metasomatized peridotite. The wall rock comprises olivine with minor clinopyroxene and phlogopite. The vein is composed of amphibole and phlogopite plus minor amounts of clinopyroxene with olivine likely from the wall-rock. The central metasomatized peridotite is dominated by olivine with subordinate amounts of phlogopite, amphibole and diopside.

The texture of composite xenolith BD3847 from Pello Hill is described in detail by Dawson & Smith (1988). It contains a distinct foliation, with the peridotite wall-rock having coarse grains of olivine (>1 mm) with isolated grains of clinopyroxene and phlogopite and amphibole replacing olivine displaying a porphyroclastic texture. The mica-pyroxenite vein

contains 3 mm amphibole grains with 2mm phlogopite, with very fine (<0.1 mm) diopside indicative of a protogranular texture. Finally, the central metasomatized peridotite contains equant and tabular 4 mm olivine with small (0.3 mm) inclusions of anhedral ilmenite and phlogopite. Clinopyroxene, amphibole and phlogopite are also found throughout this zone occurring as intergranular grains to the dominant olivine. Overall, BD3847 has a poikiloblastic texture.

3.2.7 Oga Peninsula

One mantle xenolith (J1) in this study is from Ichinomegata in the Oga Peninsula. It is a harzburgite with 73% olivine, 25% orthopyroxene and 1% clinopyroxene. It contains spinel (1%) and trace amounts of amphibole. The xenolith is fine grained (<1 mm) and has a mosaic equigranular texture. The mineralogy and texture is similar to those previously discussed by Satsukawa *et al.* (2017).

3.2.9 Summary of mantle xenolith petrography

The mantle xenoliths presented in this study include both peridotites and pyroxenites. In total, there are: 23 lherzolites, 13 harzburgites, 6 olivine clinopyroxenites, 1 wehrlite, 1 clinopyroxenite, 1 orthopyroxenite, 1 websterite, and 2 composite peridotite-pyroxenite rocks (Table 3.1). 9 of the peridotites contain garnet.

Furthermore, a wide variety of textures have been observed in these mantle xenoliths. According to the terminology of Mercier & Nicolas (1975), 17 are protogranular, 2 are prophryoblastic, 5 are equigranular-tabular, 3 are equigranular-mosaic, 5 are poikiloblastic, 2 are transitional protogranular-porphyroblastic, 2 are transitional protogranular-equigranular, 5 are hybrid prophyroblastic-poikiloblastic and 3 are hybrid protogranular-poikiloblastic.

3.3 Fluid inclusion petrography

The textural classification for fluid inclusions within igneous rocks was proposed by Roedder (1984) and outlined ‘primary’, pseudosecondary’ and ‘secondary’ appearances:

Primary: Isolated individual high-density bubbles.

Pseudosecondary: Isolated individual low-density bubbles.

Secondary: Inclusions that formed along healed fracture plains of minerals.

However, this classification criteria is determined to be unsuitable for mantle xenoliths because the fluid inclusions rarely occur in clusters and are typically situated along healed fractures (Figure 3.9). This does not however, make them secondary with respect to their formation (Andersen & Neumanm, 2011). This is because metasomatic reactions and dynamic tectonic processes operating in the lithospheric mantle will generate abundant fracturing, thus producing 'secondary' fluid inclusions of primary mantle origin.

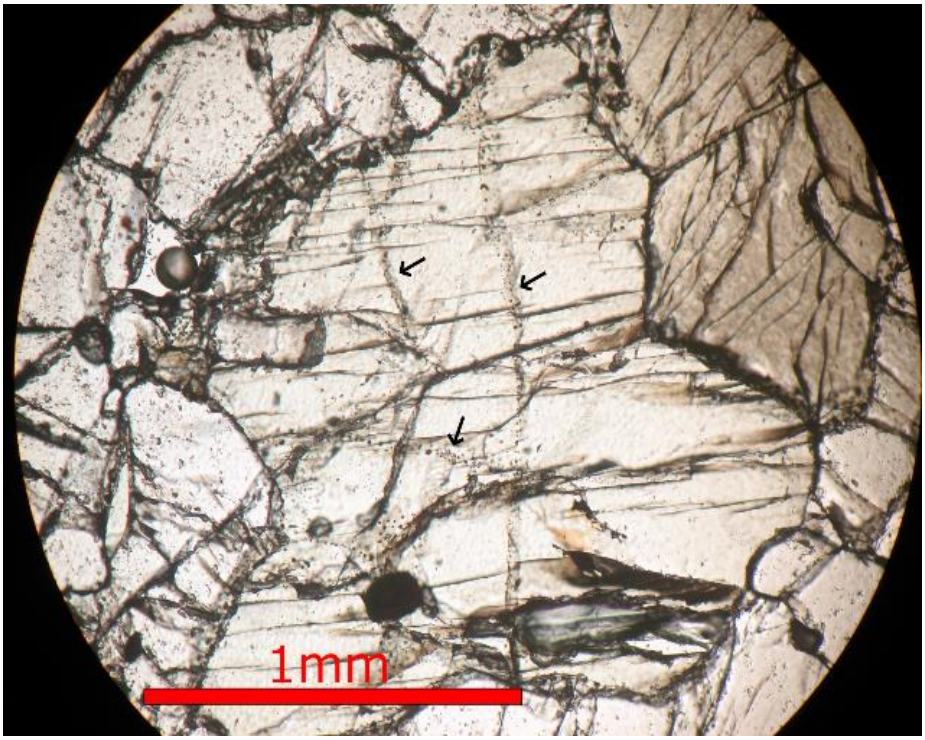

Figure 3.9. Thin section photomicrograph of MM5. Arrows point to CO_2-rich inclusions along healed fracture plane of orthopyroxene

The fluid-inclusion bubbles presented in this study are all very small (1-5 µm) relative to their host minerals. Therefore, following the work of Yamamoto *et al.* (2011) and Campione *et al.* (2015), they should retain the same ^{3}He, ^{4}He, ^{12}C and ^{13}C compositions as when they first formed in the continental lithospheric mantle.

Chapter 4. Major and minor element chemistry of on- and off-craton mantle peridotites and pyroxenites

4.1 Introduction

The relative amounts of different major and trace elements present in Earth's lithospheric mantle provide valuable insights into the melting and enrichment regimes that were involved in its formation and subsequent evolution (e.g. Herzberg, 2004; Bernstein *et al.*, 2006; Griffin *et al.*, 2009). A common method of tracing some of these processes is through comparison of major elements that exhibit varying compatibility during mantle melting. For example, Mg is more compatible than Fe in both olivine and pyroxene and so as peridotite melts, Mg becomes more concentrated in the residue. The relationship between these elements is commonly expressed as Mg# (100 x (Mg/(Mg+Fe)). Likewise, for spinel and garnet, Al and Ca partition more readily into the melt than the residue. The relationship between Cr and Al is typically expressed as Cr# (100 x (Cr/Cr+Al)). In the depleted MORB-source mantle (DMM), the Mg# of olivine (89.5) is similar to orthopyroxene (89.7), slightly less than clinopyroxene (90.8) and higher than spinel (73.2; Workman & Hart, 2005). Additionally, in DMM the Cr# for spinel and clinopyroxene is 10.7 and 9.3, respectively, and the estimated CaO/Al_2O_3 for orthopyroxene (0.34) is lower than for clinopyroxene is (2.48).

In the following sections, the compositions of minerals found in xenoliths from the individual locations examined in this study are presented. The dataset includes major and minor elements that were determined by Electron Micro-Probe Analysis (EMPA) operating at 15keV and 20nA with a beam size of 1µm. Further details are available in the Appendix C. The major and minor element concentrations of 44 olivines, 39 orthopyroxenes, 43 clinopyroxenes, 37 spinels, 8 garnets, 6 phlogopites, 4 amphiboles and 2 ilmenites were determined. These analysis are presented in Appendix Tables 1 to 8.

4.2 Location specific information

4.2.1 South West USA

4.2.1.1 Kilbourne Hole

4.2.1.1.1 Olivine

The Mg# of olivines in three spinel lherzolites from Kilbourne Hole (KH2, KH4, and KH5) range from 89.2 to 89.3 (Figure 4.1A) and resemble those measured in the same location by

Harvey *et al.* (2012). They are also similar to DMM (olivine Mg# = 89.5; Workman & Hart, 2005). The Kilbourne Hole sample with only 5% clinopyroxene (KH3D; Table 3.1 in Chapyer 3) contains olivine with a slightly higher Mg# (90.9) and is similar to those in the harzburgites analysed by Perkins & Anthony. (2011). All of the Kilbourne Hole olivines contains trace amounts of MnO (0.13 to 0.15 wt.%) and CaO (0.06 to 0.13 wt.%). The olivine in the spinel pyroxenite from Kilbourne Hole (KH1) has a much lower Mg# (79.9), and greater amounts of MnO (0.25 wt.%) and CaO (0.16 wt.%) than those in the peridotites and similar NiO (Figure 4.1B).

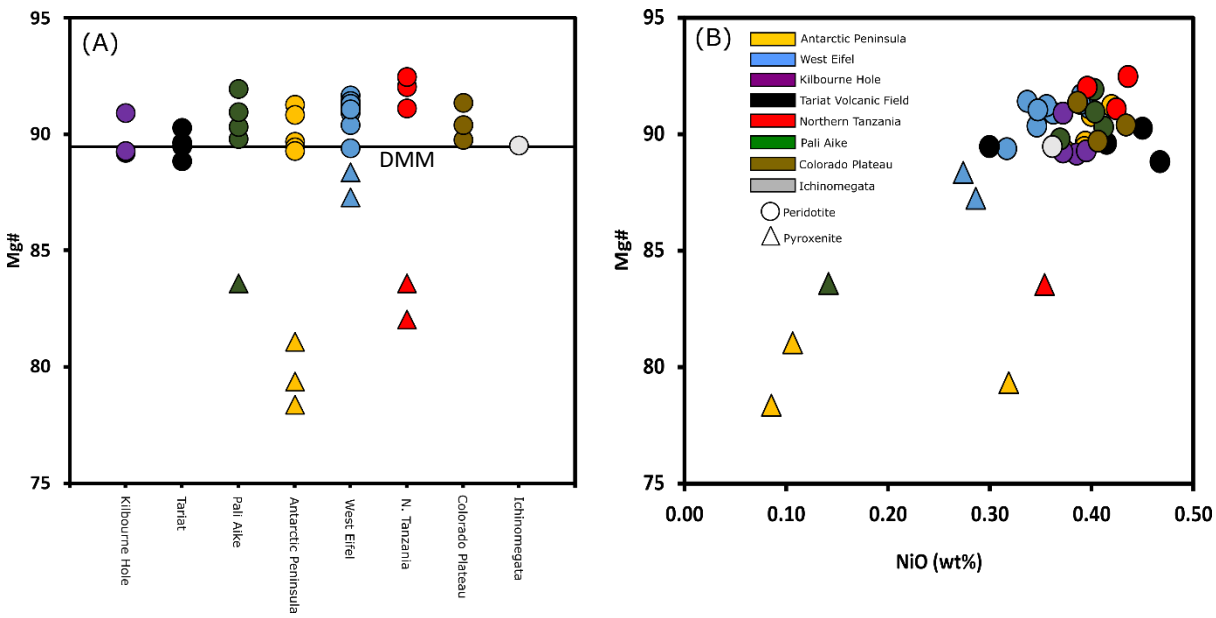

Figure 4.1. A) Olivine Mg# for different xenolith locations. B) Olivine Mg# and NiO (wt.%) compositions.

4.2.1.1.2 Orthopyroxene

The orthopyroxenes in the Kilbourne Hole peridotites have a similar Mg# to the co-existing olivine. Those in the three spinel lherzolites (KH2, KH4 and KH5) have moderate Mg# values of 89.2 to 89.7 (Figure 4.2A) and are comparable to those in Kilbourne Hole lherzolites analysed by Harvey *et al.* (2012), i.e. they are representative of this lithology. They are also similar to the orthopyroxene in DMM (Mg# = 89.7; Workman & Hart, 2005). Orthopyroxenes in xenolith KH3D have a higher Mg# = 91.3 and akin to olivine in the harzburgites analysed by Perkins & Anthony (2011). Orthopyroxenes in the less depleted samples (KH2, KH4 and KH5) have lower Cr_2O_3 (0.35 to 0.40 wt.%) and CaO (0.82 to 0.84 wt.%) but higher Al_2O_3 (4.88 to 4.92 wt.%) then KH3D (Cr_2O = 0.85 wt.%, CaO = 0.85 wt.%, and Al_2O_3 = 4.31 wt.%;

Figure 4.2B). Trace amounts of TiO_2 (0.06 to 0.15 wt.%), MnO (0.13 to 0.16 wt.%), NiO (0.09 to 0.12 wt.%) and NiO (0.10 to 0.11wt.%) are present in the Kilbourne Hole orthopyroxenes.

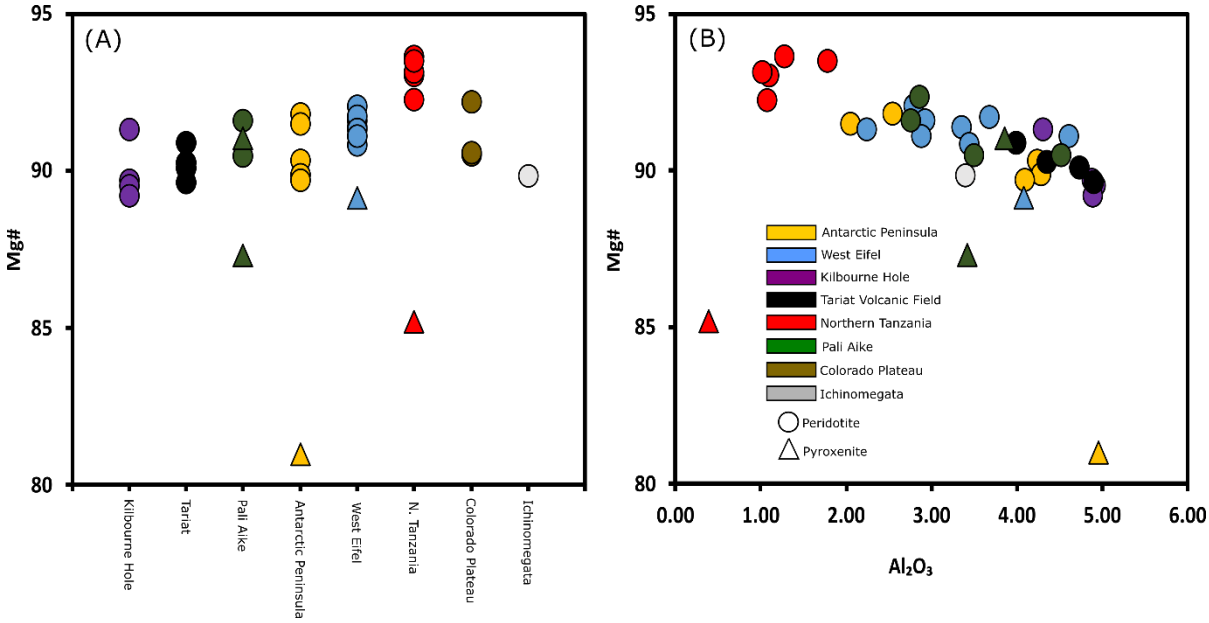

Figure 4.2 A) Variation in orthopyroxene Mg# for different locations. B) Orthopyroxene Mg# and Al_2O_3 (wt.%) compositions.

The orthopyroxenes are all enstatites (Figure 4.3) and the detailed classification of Morimoto *et al.* (1988) show that they are all aluminian-chromian-enriched (Figure 4.3). The spinel pyroxenite (KH1) does not contain any orthopyroxene for comparison.

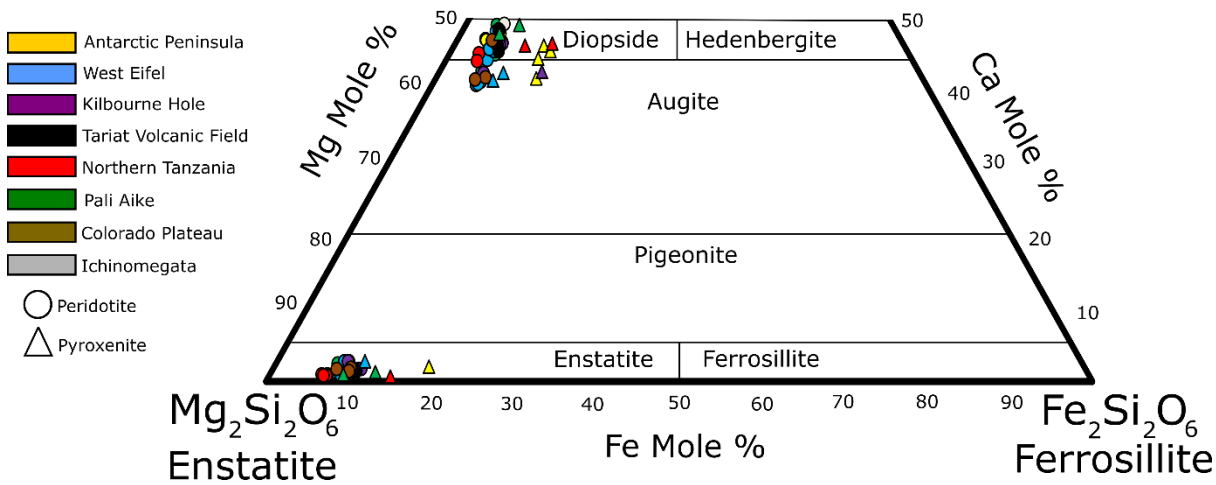

Figure 4.3. Samples from this study displayed in a pyroxene ternary diagram.

4.2.1.1.3 Clinopyroxene

Akin to olivines and orthopyroxenes, clinopyroxenes in KH2, KH4 and KH5 have lower Mg# (89.6 to 90.0) than KH3D (Mg# = 90.8), and resemble those analysed in lherzolites by Harvey *et al.* (2012) and harzburgites by Perkins & Anthony (2011), respectively (Figure 4.4).

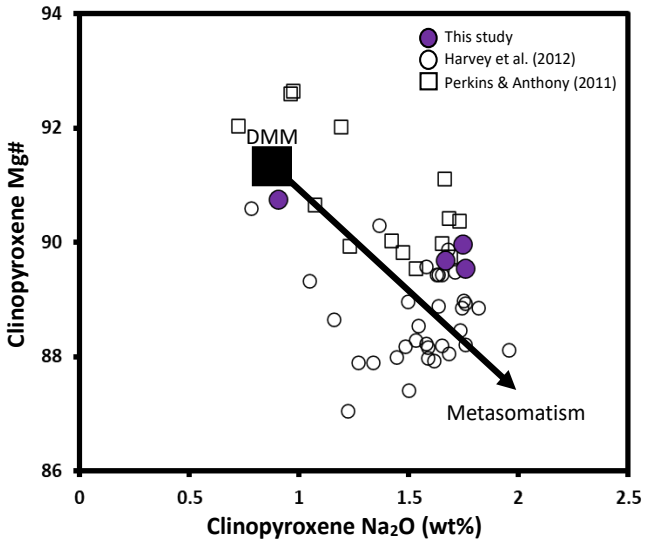

Figure 4.4. Variation in Na_2O (wt.%) and Mg# for clinopyroxene from Kilbourne Hole analysed in this study compared to those from Harvey et al. (2012) and Perkins & Anthony (2011).

The clinopyroxenes in KH2, KH4, and KH5 are diopsides. They have higher Al_2O_3 and TiO_2 compared to KH3D, whilst KH3D has a much greater Cr_2O_3 content (1.38 compared to 0.71 to 0.81 wt.%) and similar CaO concentrations (19.21 to 19.7 wt.%). However, unlike olivine and orthopyroxene, the Mg# of the clinopyroxene in KH3D is imilar to that in the DMM (90.8; Workman & Hart, 2005). The lower-than-expected Mg# and elevated Na_2O contents of clinopyroxene in KH2, KH4 and KH5 relative to the DMM may be the result of metasomatic enrichment (Fig 4.8). The more detailed clinopyroxene classification scheme of Morimoto *et al.* (1988) shows that the clinopyroxenes in KH2, KH4, and KH5 are chromian-aluminian-diopsides and that KH3D contains chromian-aluminian-augite.

The clinopyroxene in the Kilbourne Hole spinel pyroxenite (KH1) has a lower Mg# (78.7) than those in the associated peridotites, and are more Fe-rich than those in the DMM (90.8) of Workman & Hart (2005). Additionally, the clinopyroxenes have higher TiO_2 (1.14 wt.%) and Al_2O_3 (8.74 wt.%), together with lower Cr_2O_3 (0.02 wt.%) and CaO (18.15 wt.%), than clinopyroxenes in the DMM. Based on Morimoto *et al.* (1998), these are aluminian-augites.

4.2.1.1.4 Spinel

Three of the peridotite xenoliths (KH2, KH4, and KH5) contain spinels with a low Cr# (9.0 to 10.2) and Mg# (76.6 to 78.2) and are classified as Fe-spinels (Figure 4.5A). As with the olivine and pyroxenes in these samples, the compositions of the spinels are comparable to those in DMM (Cr# = 10.7; Workman & Hart, 2005). The spinels in KH3D have higher Cr# (31.2) and are Cr-spinels. The spinel in the pyroxenite from Kilbourne Hole (KH1) has a very low Cr# (<0.01) and Mg# (61).

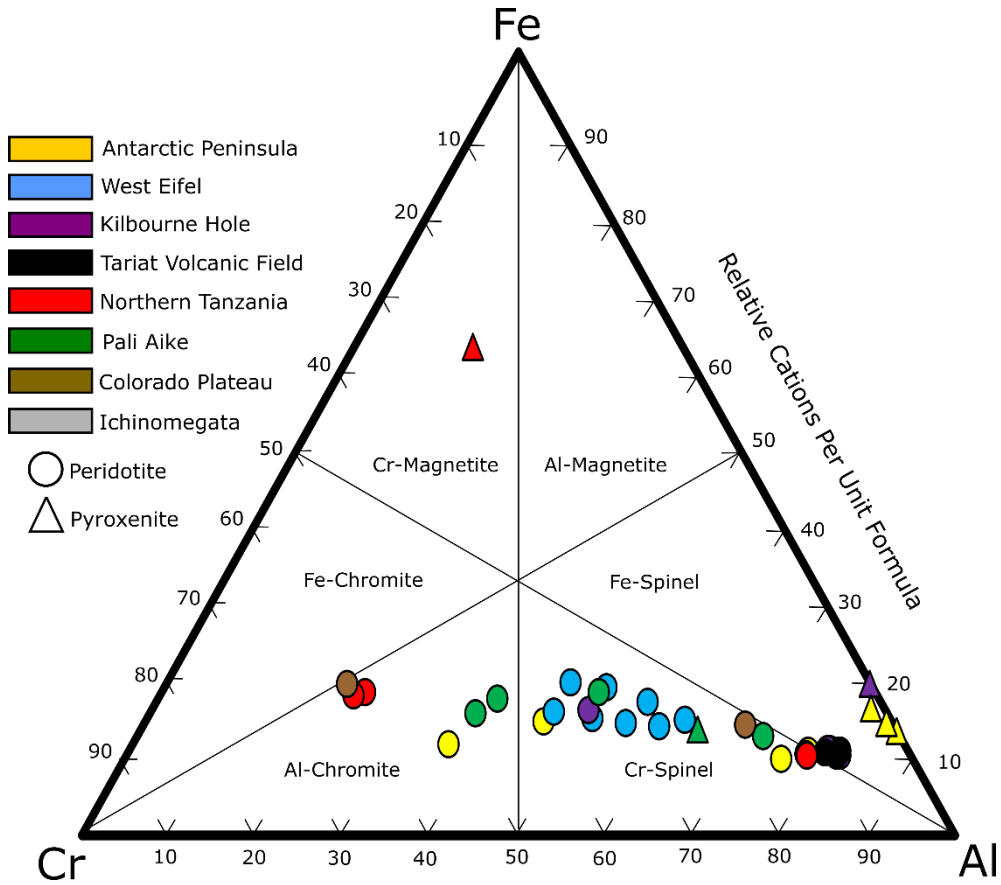

Figure 4.5 Spinel composition classification ternary diagram (After Stevens, 1994).

4.2.1.2 Colorado Plateau

4.2.1.2.1 Olivine

Olivines in the garnet harzburgites from the The Thumb have Mg# that range from 89.7 (TH17) to 91.4 (TH33). The olivines from the Buell Park spinel lherzolite (BP1) have an intermediate Mg# (90.4). The MnO contents of these olivines range from 0.09 to 0.13 wt.%, NiO contents range from 0.39 to 0.43 wt.% and CaO from 0.02 to 0.08 wt%. These values fall within the range of previous investigations of the Colorado Plateau (e.g. Li *et al.*, 2008).

4.2.1.2.2 Orthopyroxene

Orthopyroxenes in TH17, BP1 and TH33 have Mg# of 90.5, 90.6 and 92.2, respectively, and so are more depleted than orthopyroxene in the DMM. Additionally, SiO_2 ranges from 54.38 to 57.51 wt.%, Cr_2O_3 from 0.58 to 0.80 wt.%, TiO_2 from 0.03 to 0.32 wt.%, MnO from 0.11 to 0.14 wt.%, CaO from 0.74 to 0.95 wt.% and Na_2O from 0.05 to 0.24 wt.%. Finally, orthopyroxenes in the garnet-bearing harzburgite from the Thumb (TH17 and TH33) have lower Al_2O_3 (1.52 to 1.63 wt.%) than those in the garnet-free peridotite from Buell Park (BP1, 4.53 wt.%). These compare well with the results from previous investigations (e.g. Smith, 2000; Li *et al.*, 2008). Using the classification of Morimoto *et al.* (1998), all of the orthopyroxenes in these three peridotite xenoliths are enstatites (Figure 4.3).

4.2.1.2.3 Clinopyroxene

Garnet harzburgites TH17 and TH33 contain clinopyroxene with Mg# of 90.0 and 91.9, respectively. Those in spinel lherzolite BP1 have a higher Mg# (92.1). The clinopyroxene in TH17 is slightly more Fe-rich than those in the DMM (Workman & Hart, 2005), while clinopyroxenes in TH33 and BP1 are slightly more magnesian, i.e. depleted. The clinopyroxenes in the garnet-bearing peridotites from the Thumb have SiO_2 from 53.67 to 53.71 wt.%, TiO_2 from 0.12 to 0.66 wt.%, Al_2O_3 from 2.01 to 2.25 wt.%, Cr_2O_3 from 0.09 to 0.10 wt.%, CaO from 18.11 to 18.15 wt.% and Na_2O from 1.57 to 1.90 wt.%, respectively. Diopsides in the spinel-bearing peridotite (BP1) have lower SiO_2, TiO_2, Cr_2O_3 and Na_2O at 52.37 wt.%, 0.09 wt.%, 1.04 wt.% and 1.24 wt.%, respectively, but higher Al_2O_3, MnO and CaO at 5.73 wt.%, 0.11 wt.% and 20.50 wt.%. The more detailed clinopyroxene classification of Morimoto *et al.* (1988) shows that clinopyroxenes in TH17 are titanian-chromian-augites, chromian-augites in TH33 and aluminian-chromian-diopsides in BP1.

4.2.1.2.4 Spinel

The lherzolite from Buell Park (BP1) contains spinels with Cr# of 19.65 and Mg# of 70.75. The spinels in TH33 have a much higher Cr# (74.27) and Mg# (59.79), i.e. are more depleted. According to the classification of Stevens (1944), BP1 contains Cr-spinel while TH33 contains Al-chromite.

4.2.1.2.5 Garnet

The harzburgites from The Thumb (TH17 and TH33) contain garnets with FeO contents of 6.45 to 7.77 wt.% and MgO of 20.25 to 21.00 wt.%, producing an Mg# ranging from 82.3 to

85.3. Additionally, these garnets have Al_2O_3 contents varying from 16.93 to 19.51 wt.% and Cr_2O_3 from 4.49 to 7.49 wt.%, producing a range in Cr# from 13.4 to 22.9. Finally, SiO_2 contents vary from 40.99 to 41.49 wt.%, TiO_2 from 0.19 to 0.73 wt.%, MnO from 0.31 to 0.33 wt.% and CaO from 5.31 to 6.24 wt.%. These are all therefore pyrope garnets (Figure 4.6A) with a lherzolitic paragenesis (Figure 4.6B). When compared to previous studies, these garnets have higher Mg# and Cr# than those investigated by Li *et al.* (2008).

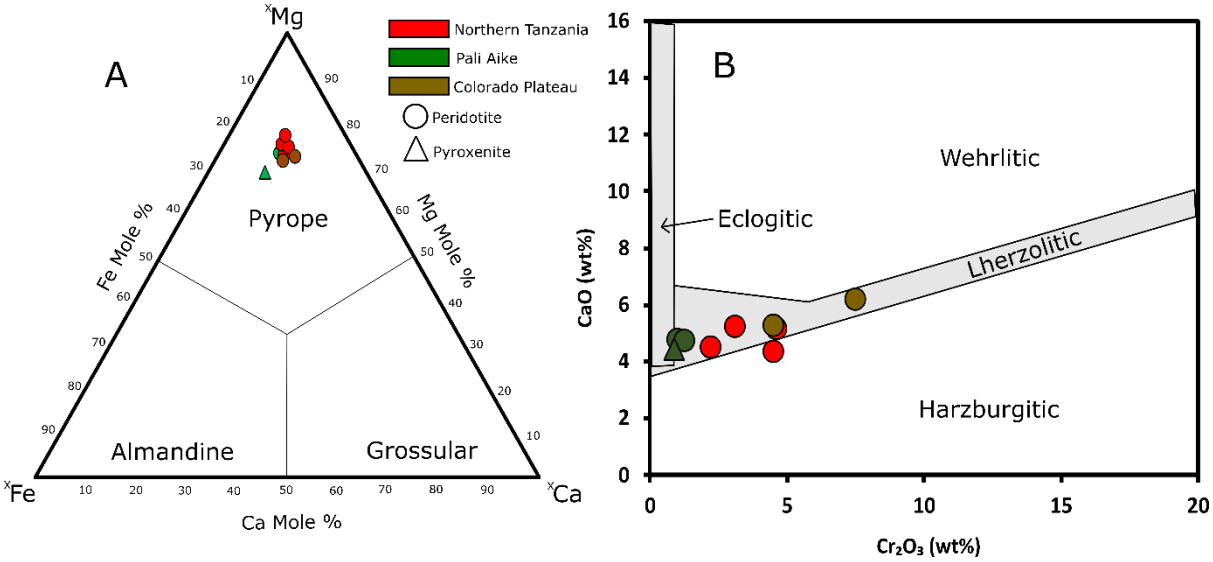

Figure 4.6 A) Ternary diagram showing the various classifications of garnets (after Grew et al., 2013). B) Classification using Cr_2O_3 and CaO (wt.%) to distinguish garnets of harzburgitic, lherzolitic, wehrlitic and eclogitic paragenesis (after Sobolev et al., 1973).

4.2.1.2.6 Accessory Minerals

TH17 has a minor amount of mica. This has an FeO content of 4.30 wt.% and MgO of 23.06 wt.%, producing an Mg# of 90.52. The mica also contains 13.60 wt.% Al_2O_3 and 1.33 wt.% Cr_2O_3, generating a Cr# of 13.3. SiO_2 is 40.17 wt.%, TiO_2 is 3.26 wt.%, K_2O is 10.45 wt.%, MnO is 0.03 wt.% and NiO 0.23 wt.%. Using the classification of Tischendorf *et al.* (2004) this is a phlogopite (Figure 4.7).

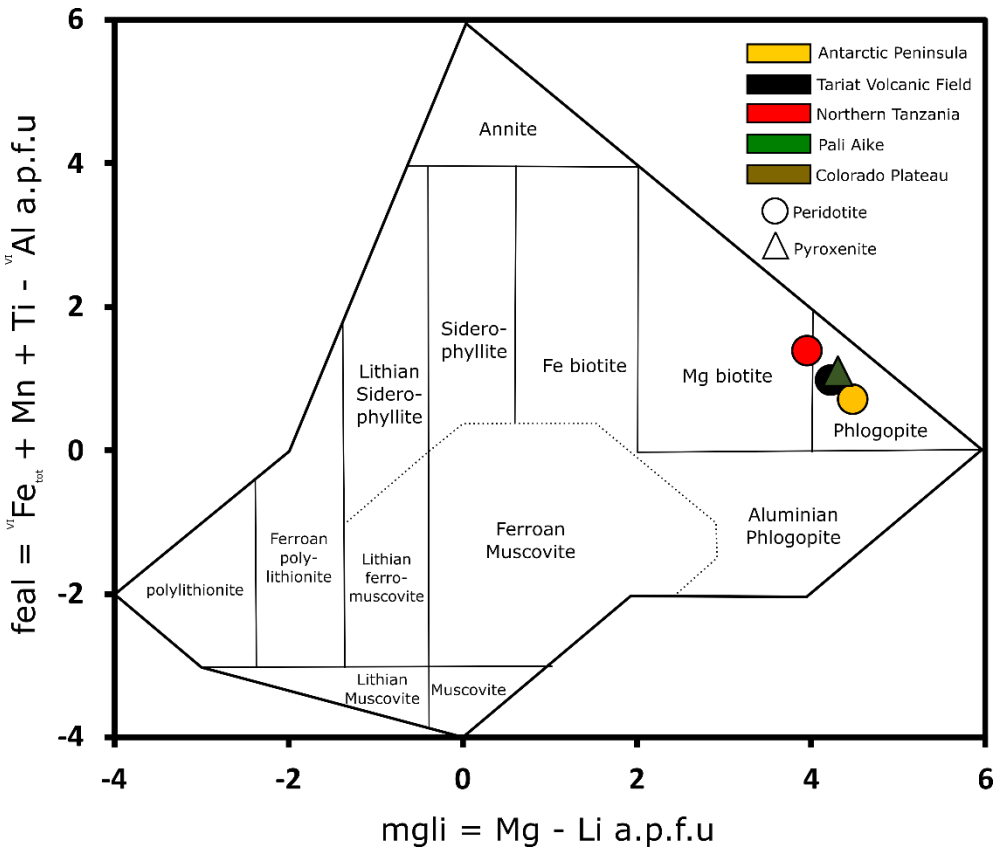

Figure 4.7 Mica classification diagram (after Tischendorf et al., 2004).

TH17 contains a minor amount of ilmenite. This has 49.97 wt% TiO_2 (47.97 wt.%), 26.43 wt.% of FeO and 13.57 wt.% of MgO, generating an Mg# of 47.8. Additionally, the ilmenite contains 1.68 wt.% Al_2O_3 and 9.28 wt.% Cr_2O_3, producing a Cr# of 1.6. Finally, TH17 has 0.21 wt.% MnO and 0.30 wt.% NiO.

4.2.2 Tariat Volcanic Field

4.2.2.1 Olivine

The four spinel lherzolites analysed from the Tariat Volcanic Field (TM1, TM2, TM3 and TM4) contain olivine that has a very restricted range in Mg# (89.5 to 90.3). This is similar to olivine in DMM (Workman & Hart, 2005). The olivines with the lower Mg# (89.5 to 89.9) are from TM1, TM2 and TM3 and resemble those in the lherzolites analysed by Ionov (2007), while the slightly more depleted olivine in TM4 (Mg# = 90.3) is marginally higher than previously published values.

4.2.2.2 Orthopyroxene

All of the Tariat spinel lherzolites contain orthopyroxene with a similar Mg# (89.6 to 90.9) and these are comparable to those in DMM (Workman & Hart, 2005). Akin to olivine, TM1, TM2 and TM3 record slightly lower Mg# (89.6 to 90.3) than TM4 (Mg# = 90.9) and are similar to those published by Ionov (2007). Consistent with their Mg#, the orthopyroxenes in TM4 have slightly lower Al_2O_3 (4.0 wt.%) and higher Cr_2O_3 (0.40 wt.%) compared to TM1, TM2 and TM3 (Al_2O_3 = 4.35 to 4.90 wt.%; Cr_2O_3 = 0.31 to 0.40 wt.%). The detailed classification scheme of Morimoto *et al.* (1988) indicates that orthopyroxenes in TM1 and TM4 are enstatites while those in TM2 and TM3 are aluminian-enstatites.

4.2.2.3 Clinopyroxene

All of the xenoliths analysed from the Tariat Volcanic Field contain diopside with Mg# values of 89.6 to 92.0, and are similar to DMM of Workman & Hart (2005). The Mg# of these diopsides (88.5 to 93.8) in similar to peridotites previously analysed from Tariat (e.g. Carlson & Ionov, 2019, Preß *et al.*, 1986; Figure 4.8). The variable Mg# of the diopsides correlate with other elements (e.g. Al_2O_3, Na_2O, CaO; Figure 4.8). The classification of Morimoto *et al.* (1988) shows that the clinopyroxenes in TM1, TM2, TM3 and TM4 are all aluminian-chromian-diopsides.

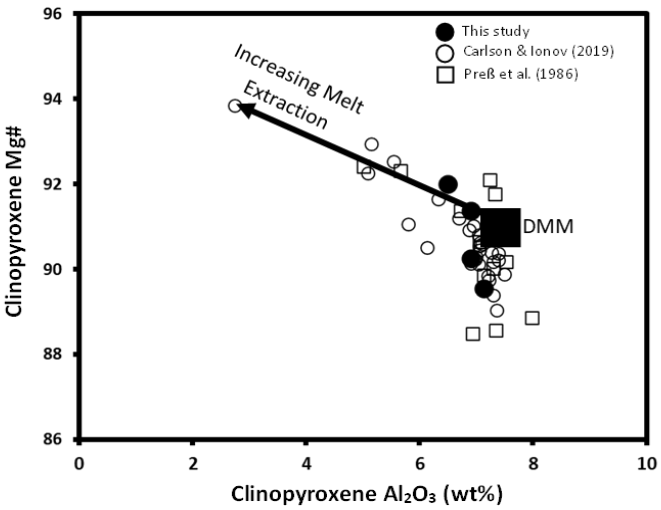

Figure 4.8. Al_2O_3 (wt.%) versus Mg# for clinopyroxenes from Tariat xenoliths analysed in this study compared to those from Carlson & Ionov (2019) and Preß et al. (1986).

4.2.2.4 Spinel

Spinels in TM1, TM2, TM3 and TM4 exhibit a small range in Cr# values (8.7 to 13.3), which is very similar to the range estimated for the DMM by Workman & Hart (2005). Consistent

with olivine, orthopyroxene, and clinopyroxene, the spinels in TM4 record a slightly depleted mineral chemistry (Cr# = 13.7). The classification of Stevens (1944) indicates that these are all Fe-spinels.

4.2.2.5 Accessory Minerals

TM2 has a minor amount of mica. This has an FeO content of 3.57 wt.% and MgO of 19.93 wt.%, producing an Mg# of 88.96. The mica also contains 16.54 wt.% Al_2O_3 and 0.88 wt.% Cr_2O_3, producing a Cr# of 3.4. Furthermore, SiO_2 is 37.87 wt.%, TiO_2 is 5.77 wt.%, K_2O is 10.07 wt.%, MnO 0.05 wt.% and NiO is 0.25 wt.%. Using the classification scheme of Tischendorf *et al.* (2004; Figure 4.6) this is a phlogopite.

4.2.3 West Eifel Volcanic Field

4.2.3.1 Olivine

The olivines in the spinel lherzolites and harzburgites from the West Eifel Volcanic Field have Mg# = 90.4 to 91.7, while olivine in the wehrlitic sample (DW10) has a slightly lower Mg# = 89.5, and is similar to the DMM (Figure 4.10). Olivines in the lherzolites and harzburgites have lower MnO (0.12 to 0.14 wt.%) than those in the wehrlite (0.22 wt.%), while NiO contents are very slightly higher in olivine in the lherzolites and harzburgites (0.34 to 0.40 wt.%) than the wehrlite (0.32 wt.%). The olivines analysed from the West Eifel Volcanic Field in this study have similar composotions to those from previous investigations (Figure 4.9).

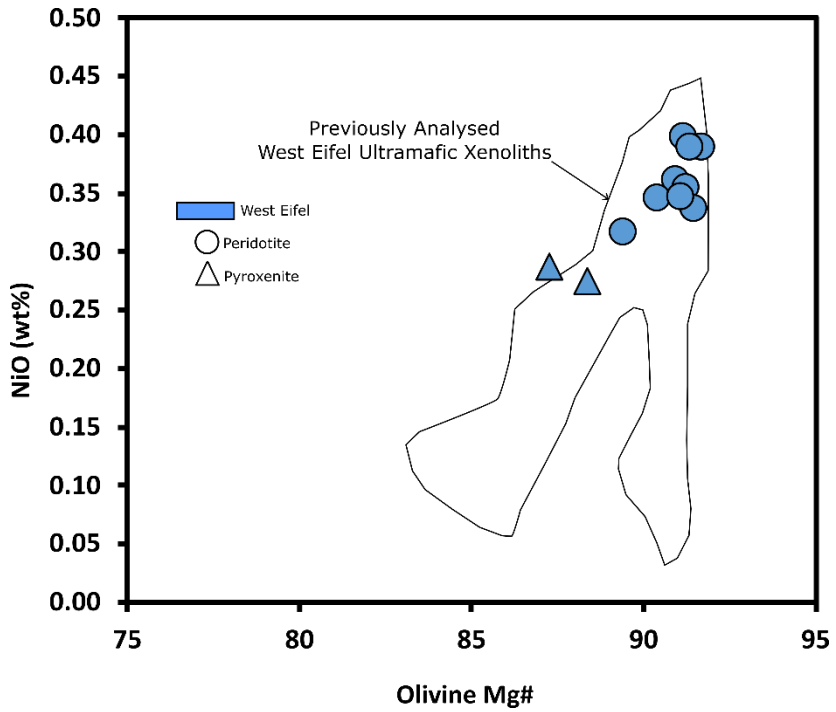

Figure 4.9 Mg# and NiO (wt.%) of West Eifel olivines analysed in this study. The field of olivines previously analysed from the West Eifel is from Rizzo et al. (2021).

Olivines in the spinel pyroxenite xenoliths from the West Eifel Volcanic Field (DW5 and MM6) have lower Mg# (87.3 to 88.4) than the associated peridotites. They have MnO contents of 0.16 to 0.17 wt.%, NiO contents of 0.27 to 0.29 wt.% and CaO contents of 0.15 wt.%.

4.2.3.2 Orthopyroxene

All of the West Eifel spinel peridotites contain orthopyroxenes with Mg# = 90.8 to 92.1, which is slightly more depleted than that of the DMM (Workman & Hart, 2005). Orthopyroxene have SiO_2 of 55.15 to 56.73 wt.%, Cr_2O_3 of 0.31 to 1.01 wt.%, CaO of 0.32 to 1.45 wt.% and Al_2O_3 of 2.24 to 4.61 wt.%. Trace amounts of TiO_2 (0.04 to 0.12 wt.%), MnO (0.13 to 10.5 wt.%), NiO (0.06 to 0.25 wt.%), and Na_2O (0.02 to 0.15 wt.%) are also measured. The detailed classification of Morimoto *et al.* (1988) shows the orthopyroxene in G17 as an enstatite, DW3, DW7, DW8, MM5, MM11, G17 and G18 as aluminian-chromian-enstatites, and MM8 as an aluminian-chromian-sodian-enstatite. These orthopyroxene compositions are akin to those previously observed in peridotites from the West Eifel Volcanic Field (e.g. Witt-Eickschen *et al.*, 2003; Rizzo *et al.*, 2021).

Orthopyroxene in the West Eifel spinel pyroxenite (MM6) has a slightly lower Mg# = 89.1 than those in the peridotites. It has a Cr_2O_3 content of 0.77 wt.%, CaO of 1.43 wt.% and

Al_2O_3 of 4.08 wt.%. Based on the classification scheme of Morimoto *et al.* (1998), this is an aluminian-chromian-enstatite.

4.2.3.3 Clinopyroxene

The clinopyroxenes from the West Eifel display a wide range in Mg# (varying from 90.4 to 92.1). Samples DW3, DW7, MM5, MM8 and G17 contain augite and DW8, DW10, MM11 and G18 contain diopside. The augite has Cr_2O_3, CaO and Na_2O that range from 0.74 to 1.78 wt.%, 18.11 to 20.37 wt.% and 1.01 to 1.28 wt.%, respectively. The diopside has similar Cr_2O_3 (0.76 to 1.22 wt.%) and Na_2O (0.76 to 1.29 wt.%) but higher CaO (20.16 to 22.08 wt.%). The detailed classification of Morimoto *et al.* (1988) shows that the clinopyroxenes in DW3, DW7, MM5, MM8 and G17 are aluminian-chromian-augites and those in DW8, DW10, MM11 and G18 are aluminian-chromian-diopsides.

Spinel pyroxenites DW5 and MM6 contain augite with Mg# of 88.0 and 86.7, respectively. These augites have Cr_2O_3 contents of 1.13 to 1.23 wt.%, CaO of 18.46 to 18.80 wt.% and Na_2O from 0.97 to 1.04 wt.%. The detailed classification of Morimoto *et al.* (1988) shows the clinopyroxenes as as aluminian-chromian-augites.

4.2.3.4 Spinel

Spinels in the West Eifel Volcanic Field peridotites have Al_2O_3 contents that range from 29.90 to 44.73 wt.% and Cr_2O_3 ranges from 21.12 to 36.67 wt.%, which produces Cr# ranging from 24.1 to 42.5. FeO varies from 13.21 to 18.14 wt.% and MgO from 15.83 to 18.11 wt.%, with a Mg# of 60.9 to 71.1. Following the classification of Stevens (1944), all of these are chrome-spinels.

4.2.3.5 Amphibole

Sample lherzolite MM11 and wehrlite DW10 contain a minor amount of amphibole. These have 42.66 to 43.20 wt.% SiO_2, 0.39 to 0.93 wt.% TiO_2, 13.15 to 14.21 wt.% Al_2O_3, 1.84 to 1.85 wt.% Cr_2O_3, 4.03 to 4.13 wt.% FeO, 0.07 to 0.1 wt.% MnO, 3.00 to 2.87 wt.% Na_2O and 1.22 to 1.55 wt.% K_2O. Both have 17.86 wt.% MgO, 10.89, 11.13 wt.% CaO and 0.12 wt.% NiO. Following the classification scheme of Hawthorne *et al.* (2012), amphiboles in both these xenoliths are pargasites.

4.2.4 Antarctic Peninsula

4.2.4.1 Olivine

Olivines in the spinel peridotites from the Antarctic Peninsula have Mg# that vary from 89.4 to 91.3 (Figure 4.1). The Mg# of olivines in KG3719.25 (89.7) and L7.201.1.41 (89.4) are similar to those in the DMM (Workman & Hart, 2005), while those in samples KG3610.10A (91.3) and KG3609.21 (90.8) are more depleted (Fig. 4.11). SiO_2 contents range from 40.48 to 41.53 wt.%, MnO from 0.12 to 0.15 wt.%, NiO from 0.39 to 0.42 wt.% and CaO from 0.03 to 0.07 wt.%.

The spinel pyroxenites (KG3619.7, L&201.1.74c and R5194.2I) contain olivines with Mg# ranging from 78.4 to 81.1, respectively. These are all significantly more Fe-rich than those in the DMM proposed by Workman & Hart (2005). Additionally, SiO_2 ranges from 38.78 to 39.15 wt.%, MnO from 0.21 to 0.26 wt.%, NiO from 0.09 to 0.32 wt.% and CaO from 0.09 to 0.20 wt.%.

4.2.4.1 Orthopyroxene

The spinel peridotites contain orthopyroxene with an Mg# of 89.9 to 91.8, which is slightly more depleted than the DMM (Workman & Hart, 2005). Furthermore, these orthopyroxenes have SiO_2 of 55.08 to 55.72 wt.%, Cr_2O_3 of 0.39 to 0.55 wt.%, CaO of 0.43 to 0.77 wt.% and Al_2O_3 of 2.05 to 4.28 wt.%. Trace amounts of TiO_2, MnO and Na_2O are present and range from <0.03 to 0.10 wt.%, 0.12 to 0.16 wt.% and 0.05 to 0.11 wt.%. The detailed classification of Morimoto *et al.* (1988) shows the orthopyroxene in KG3609.21 is an enstatite while those in KG3610.10A, KG3719.25 and L7.201.1.41 are Al-enstatites.

Orthopyroxene is present in one pyroxenite – KG3719.7. It has an Mg# of 81.0 and much more Fe-rich than in the peridotites and the DMM. Concentrations of SiO_2, Al_2O_3, Cr_2O_3 and CaO in the orthopyroxene are 58.27 wt.%, 4.95 wt.%, 0.23 w%, 0.99 wt.%, respectively. Minor amounts of TiO_2 (0.32 wt.%), MnO (0.19 wt.%) and Na_2O (0.15 wt.%) are present. The detailed classification scheme of Morimoto *et al.* (1988) shows this to be an Al-enstatite.

4.2.4.3 Clinopyroxene

All of the Antarctic Peninsula spinel peridotites analysed in this study are diopside-bearing. They have an Mg# of 90.3 to 93.8, Cr# of 5.6 to 18.7 and CaO/Al_2O_3 of 3.1 to 10.3. Those in spinel peridotites KG3719.25, L7.201.1.41 and BN have a lower Mg#, Cr# and CaO/Al_2O_3

than the DMM (Workman & Hart, 2005), while peridotites KG3610.10A and KG3609.21 have higher Mg#, Cr# and CaO/Al_2O_3 than the DMM, i.e. are more depleted. Additionally, SiO_2 ranges from 51.57 to 54.59 wt.%, with the more depleted peridotites having <52 wt.%. Contents of TiO_2, MnO and Na_2O range from 0.03 to 0.61 wt.%, 0.07 to 0.10 wt.% and 0.57 to 2.03 wt.%, respectively. Using the classification of Morimoto *et al.* (1988), the clinopyroxenes in spinel peridotites KG3719.25, L7.201.1.41 and BN are Al-Ca-diopsides while those in KG3610.10A and KG3609.21 are all Ca-diopsides.

Pyroxenites KG3619.7 and L7.2010.1.74c are augite-bearing while R5195.2I and R5194.2M are diopside-bearing. Mg# ranges from 78.3 to 80.4, Cr# from 1.1 to 3.5 and CaO/Al_2O_3 from 2.0 to 2.5, which are all higher than the DMM. SiO_2 ranges from 48.2 to 50.44 wt.%, TiO_2 from 1.26 to 1.58 wt.%, MnO from 0.14 to 0.17wt.% and Na_2O from 1.02 to 1.67 wt.%. Using the classification of Morimoto *et al.* (1988), all of these are Al-diospides.

4.2.4.4 Spinel

Spinels in the Antarctic Peninsula peridotites exhibit a wide range of Al_2O_3 (22.68 to 58.22 wt.%) and Cr_2O_3 contents (8.82 to 48.49 wt.%), which produces Cr# of 9.2 to 58.9. Concentrations of FeO range from 9.48 to 13.60 and MgO from 15.74 to 20.44, so that Mg# range from 67.4 to 78.6. Following the classification from Stevens (1944), Al-chromite is present in KG3610.10A, Cr-spinels occur in KG3609.21 and L7.201.141, and Fe-spinels in KG3719.25 and BN.

In the pyroxenite, the spinels have 58.05 to 61.35 wt.% of Al_2O_3 and 0.03 to 1.55 wt.% of Cr_2O_3, producing Cr# of <0.1 to 1.76. FeO ranges from 13.22 to 16.19 wt.% and MgO from 16.36 to 19.18 wt.%, producing an Mg# of 62.2 to 72.1. Following the classification from Stevens (1944) all of these are Fe-spinels.

4.2.4.5 Accessory Minerals

Trace amounts of amphibole are present in lherzolite L7.201.1.41. This contains 42.18 wt.% of SiO_2, 2.29 wt.% of TiO_2, 14.36 wt.% of Al_2O_3, 1.45 wt.% of Cr_2O_3, 4.18 wt.% of FeO_T, 16.63 wt.% of MgO and 3.15 wt.% of Na_2O. It is therefore a pargasite.

Sample L7.201.1.41 also contains trace amounts of phlogopite. This has 37.31 wt.% of SiO_2, 3.57 wt.% of Cr_2O_3, 3.57 wt.% of TiO_2, 16.81 wt.% of Al_2O_3, 4.43 wt.% of FeO, 20.92 wt.% of

MgO and 9.44 wt.% of K_2O. Minor amounts of MnO (0.02 wt.%), NiO (0.22 wt.%), CaO (0.13 wt.%) and Na_2O (0.89 wt.%) are also present.

4.2.5 Southern Patagonia

4.2.5.1 Olivine

The olivine in lherzolites and harzburgites from Southern Patagonia have Mg# of 89.8 to 92.0 (Fig 4.12). Sample CP33 has Mg# of 89.8, which is akin to DMM (Workman & Hart, 2005), while samples LT1, LT16 and PA3-5 have higher Mg# of 90.3, 91.0 and 92.0, respectively. SiO_2 ranges from 40.94 to 41.28 wt.%, MnO from 0.09 to 0.13 wt.%, NiO from 0.37 to 0.41 wt.% and CaO from 0.03 to 0.11 wt.%. They are comparable to olivines previously investigated from this location (Figure 4.10; Rooks, 2016; Melchiorre *et al.*, 2020).

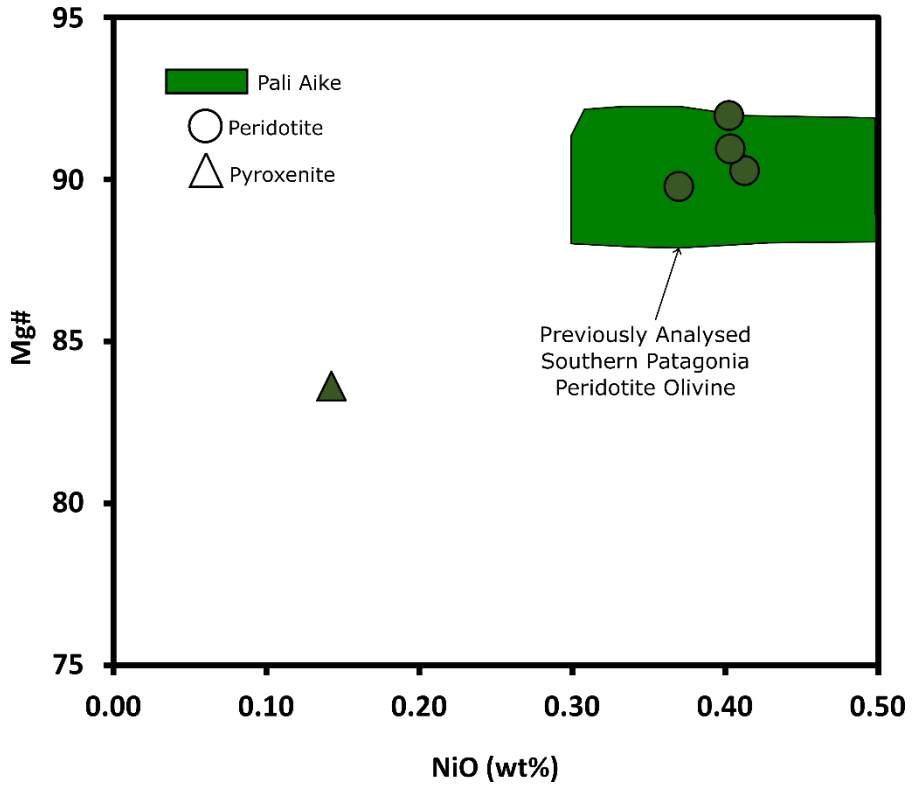

Figure 4.10. Plot of NiO versus Mg# for the olivines from Southern Patagonia analysed in this study. The field of previously analysed peridotite olivine compositions is from Melchiorre et al. (2020).

The olivine in the spinel pyroxenite (LT15) has an Mg# of 83.6, which is much lower than that present in the peridotites and DMM (Workman & Hart, 2005). It contains low SiO_2 (39.88 wt.%), high MnO (0.22 wt.%), low NiO (0.14 wt.%) and 0.04 wt.% of CaO.

4.**2**.**5**.2 **Orthopyroxene**

Orthopyroxene in the peridotites has a Mg# ranging from 90.5 to 92.4, which is slightly more depleted than the DMM of Workman & Hart (2005). Furthermore, these orthopyroxenes have 0.42 to 0.99 wt.% of Cr_2O_3, 0.62 to 1.26 wt.% of CaO and 2.75 to 4.52 wt.% of Al_2O_3. Trace amounts of TiO_2 (0.06 to 0.18 wt.%), MnO (0.12 to 0.14 wt.%) and Na_2O (0.05 to 0.16 wt.%) are presented. The detailed classification of Morimoto *et al.* (1988) shows that the orthopyroxenes in CP31, CP33, LT1 and LT16 are all Al-enstatites.

Pyroxenites CP62 and LT14 contain orthopyroxene with an Mg# of 87.3 and 91.0, respectively. Those in CP62 are slightly less depleted than DMM compositions, while the orthopyroxenes in LT14 are slightly more depleted. Cr_2O_3 ranges from 0.25 to 0.34 wt.%, CaO from 0.47 to 0.66 wt.% and Al_2O_3 from 3.42 to 3.86 wt.%. Trace amounts of TiO_2, MnO, NiO and Na_2O are present and range from 0.06 to 0.31 wt.%, 0.09 to 0.12 wt.%, 0.13 to 0.14 wt.% and 0.11 wt.%, respectively. The detailed classification of Morimoto *et al.* (1988) shows that the orthopyroxenes in CP62 and LT14 are all Al-enstatites.

4.**2**.**5**.3 **Clinopyroxene**

Of the peridotites, LT1 is diopside-bearing while CP33 and LT16 are augite-bearing. Mg# ranges from 90.1 to 92.7, Cr# from 10.6 to 23.27 and CaO/Al_2O_3 from 5.9 to 9.7. These are all more depleted than the DMM of Workman & Hart (2005). Additionally, SiO_2 ranges from 52.18 to 52.91 wt.%, TiO_2 from 0.21 to 0.66 wt.%, MnO from 0.07 to 0.10 wt.% and Na_2O from 1.20 to 2.12 wt.%. Using the classification of Morimoto *et al.* (1988), the clinopyroxene in LT1 is an Al-Ca-diopside, CP33 an Al-Ca-augite and LT16 a Ca-augite.

Of the pyroxenites, both LT14 and LT15 are diopside-bearing. Mg# ranges from 87.6 to 91.2, Cr# from 5.9 to 6.2 and CaO/Al_2O_3 from 2.7 to 4.9. LT14 is more depleted than the DMM while LT15 is less depleted. SiO_2 ranges from 51.47 to 52.66 wt.%, TiO_2 from 0.27 to 0.34 wt.%, MnO from 0.07 to 0.12 wt.% and Na_2O from 0.44 to 2.32 wt.%. Using the classification of Morimoto *et al.* (1988), the clinopyroxenes in both LT14 and LT15 are Al-Cr-diopsides.

4.**2**.**5**.4 **Spinel**

The peridotites contain spinels with a wide range of Al_2O_3 (23.45 to 48.48 wt.%) and Cr_2O_3 (15.77 to 44.08 wt.%), giving a Cr# of 17.9 to 55.8. Contents of FeO range from 12.16 to 15.47 wt.% and MgO from 15.91 to 18.01 wt.%, producing a Mg# of 64.9 to 72.5. Based on

the classification of Stevens (1944), Al-chromites are present in LT16 and PA3-5 and Cr-spinels in CP33 and LT1.

Pyroxenites CP62 and LT14 have high Al_2O_3 (41.44 to 43.69 wt.%) and moderate Cr_2O_3 (19.35 to 23.23 wt.%), producing Cr# of 23.8 to 26.3. Contents of FeO range from 13.00 to 19.96 wt.% and MgO from 15.88 to 17.55 wt.%, producing a Mg# of 58.6 to 70.6. Following the classification of Stevens (1944) both samples of pyroxenite contain Cr-spinel.

4.2.5.5 Garnet

The garnet in peridotites CP31 and CP33 contain 7.40 to 7.72 wt.% of FeO and at 20.49 to 20.91 wt.% of MgO, producing an Mg# of 82.8 to 83.2. Additionally, these garnets have 22.91 to 23.02 wt.% of Al_2O_3 and 0.97 to 1.25 wt.% of Cr_2O_3, producing a Cr# of 2.7 to 3.5. Finally, SiO_2 ranges from 42.52 to 42.52 wt.%, TiO_2 0.17 from 0.19 wt.%, CaO from 4.77 to 4.81 wt.% and MnO is 0.32 wt.%.

Peridotite CP62 contains pyrope garnet with 10.31 wt.% of FeO and 19.54 wt.% of MgO producing a Mg# at 77.2. Concentrations of Al_2O_3 is 22.74 and Cr_2O_3 is 0.87 wt.%, producing a lower Cr# (2.5) than in the other peridotites from this locality. Finally, SiO_2 is 41.94 wt.%, TiO_2 is 0.28 wt.%, MnO is 0.34 wt.%, CaO is 4.45 wt.% and Na_2O is 0.03 wt.%. All of these garnets have a lherzolitic paragenesis (Figure 4.6).

4.2.6 Northern Tanzania

4.2.6.1 Lashaine

4.2.6.1.1 Olivine

The olivine in the garnet peridotites from Lashaine have some of the highest Mg# (91.1 to 92.5) of the samples analysed in this study (Figure 4.11). The least depleted sample is BD730 (Mg# = 91.1) and the most depleted sample is BD822 (Mg# = 92.5). These are all significantly more depleted than olivine in the DMM of Workman & Hart (2005). Additionally, contents of SiO_2 range from 41.01 to 41.40 wt.%, MnO from 0.08 to 0.11 wt.%, NiO from 0.40 to 0.44 wt.% and CaO from 0.03 to 0.09 wt.%.

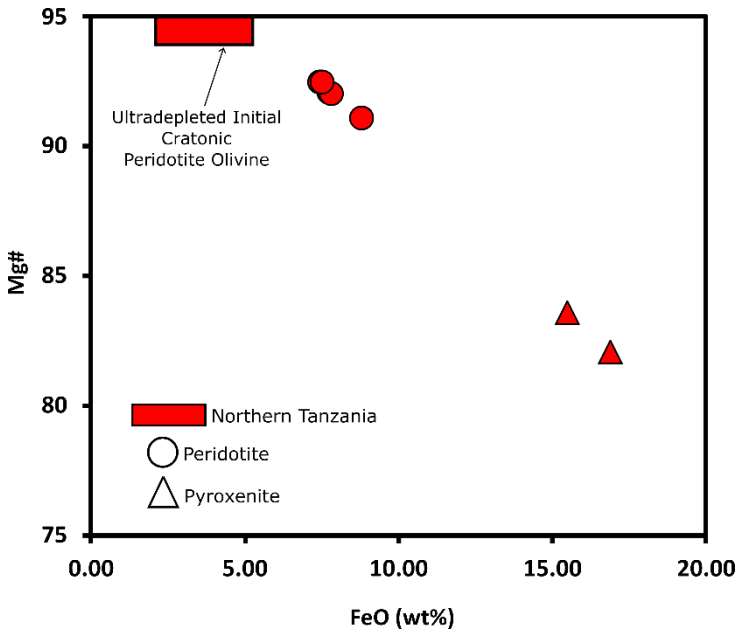

Figure 4.11. FeO (wt.%) versus Mg# for Tanzanian olivines presented in this study. The field of hypothetical ultra-depleted olivine that formed in the peridotite initially accreted to the sub-cratonic mantle is from Herzberg & Rudnick (2012).

Olivine in pyroxenite sample BD816 has a Mg# of 83.6, significantly more Fe-rich than the DMM of Workman & Hart (2005). This also contains lower SiO_2 (39.40 wt.%), MnO (0.21 wt.%), NiO (0.35 wt.%) and CaO (0.05 wt.%).

4.2.6.1.2 Orthopyroxene

The Lashaine peridotites contain orthopyroxene with Mg# of 92.2 to 93.6 which, akin to olivine, is significantly more depleted than the DMM. Furthermore, SiO_2 ranges from 57.68 to 58.21 wt.%, Cr_2O_3 from 0.19 to 0.57 wt.%, Al_2O_3 from 1.01 to 1.78 wt.% and CaO from 0.41 to 0.55 wt.%. The orthopyroxene contains minor amounts of TiO_2 (up to 0.15 wt.%), MnO (0.10 to 0.12 wt.%) and Na_2O (0.08 to 0.12 wt.%). The detailed classification scheme of Morimoto *et al.* (1988) shows that orthopyroxenes in the Lashaine peridotites (BD730, BD738, BD794, BD797 and BD822) are all Al-enstatites.

Pyroxenite sample BD816 contains orthopyroxene with a Mg# of 85.2, far more Fe-rich than the DMM. SiO_2 is 56.8 wt.%, Cr_2O_3 is 0.25wt.%, Al_2O_3 is 0.39 wt.% and CaO is 0.66 wt.%. Minor amounts of TiO_2 (0.09 wt.%), MnO (0.24 wt.%), NiO (0.03 wt.%) and Na_2O (0.04wt.%) are also present. The detailed classification scheme of Morimoto *et al.* (1988) shows that the orthopyroxene in pyroxenite BD816 is an Al-enstatite.

4.2.6.1.3Clinopyroxene

Peridotite BD730 is diopside-bearing while BD738 and BD794 are augite-bearing. Mg# ranges from 92.9 to 93.4, Cr# is 17.5 to 35.6 and CaO/Al_2O_3 is 5.2 to 9.0, all more depleted than the DMM of Workman & Hart (2005). SiO_2 ranes from 54.79 to 55.10 wt.%, TiO_2 is 0.09 to 0.42 wt.%, MnO is 0.08 to 0.09 wt.% and Na_2O is 1.56 to 2.21 wt.%. Using the classification of Morimoto *et al.* (1988) all samples are Al-enriched.

Pyroxenite BD816 is diopside-bearing with Mg# of 93.6, Cr# of 33.9 and CaO/Al_2O_3 of 8.8, all more depleted than the DMM. SiO_2 is 54.03 wt.%, TiO_2 is 0.14wt.%, MnO is 0.06 wt.% and Na_2O is 1.62 wt.%. The classification of Morimoto *et al.* (1988) indicates this is a Ca-diopside.

4.2.6.1.4 Spinel

Some of the Lashaine mantle peridotites (BD730, BD797 and BD822) are spinel-bearing. Large ranges are present in the contents of Al_2O_3 (13.70 to 55.83) and Cr_2O_3 (12.59 from 54.90), producing a large range in Cr# (13.1 to 72.9) in the spinels. The FeO contents of the spinels range from 10.29 to 15.90 and MgO from 15.10 to 20.74 wt.%, producing a Mg# of 62.9 to 78.2. The spinels in BD730 are much more depleted (Mg# = 78.2 and Cr# = 13.1) than BD797 (Mg# = 62.9 and Cr# = 71.4) and BD822 (Mg# = 63.6 and Cr# = 72.9). Using the classification of Stevens (1944), Cr-spinel is present in BD730 and Al-chromites occur in BD797 and BD82.

4.1.6.1.5 Accessory Minerals

BD738 contains small amounts of mica. It has 40.00 wt.% SiO_2, 9.13 wt.% TiO_2, 13.50 wt.% Al_2O_3, 0.71 wt.% Cr_2O_3, 3.57 wt.% FeO, 18.70 wt.% MgO and 9.64 wt.% K_2O. Minor amounts of MnO (0.04 wt.%) and NiO (0.06 wt.%) are also present. Following Hawthorne *et al.* (2012), the mica in BD738 is a Mg-biotite.

4.1.6.1.6 Garnet

Mantle peridotites BD730, BD738, BD794 and BD797 contain pyrope garnet with 6.15 to 7.52 wt.% of FeO and 20.76 to 21.94 wt.% of MgO, producing a Mg# of 83.1 to 86.4. Concentrations of Al_2O_3 vary from 20.70 to 22.30 wt.% and Cr_2O_3 from 2.18 to 4.49 wt.%, producing Cr# ranging from 6.2 to 12.7. Finally, concentrations of SiO_2 vary from 41.50 to 42.90 wt.%, TiO_2 from 0.10 to 0.42 wt.%, MnO from 0.32 to 0.37 wt.%, CaO from 4.39 to

5.25 wt.% and Na_2O from 0.02 to 0.05 wt.%. The CaO and Cr_2O_3 contents indicate that the Lashaine garnets have a lherzolitic paragenesis (Figure 4.6).

4.2.6.2 Pello Hill, N. Tanzania

4.2.6.2.1 Olivine

The xenolith from Pello Hill contains a vein of mica pyroxenite (BD3847) and the olivine composition varies depending on proximity to the vein. The olivine located 8 mm away from the vein has an Mg# of 89.0, akin to the DMM of Workman & Hart (2005). Furthermore, SiO_2 is 40.9 wt.%, NiO is 0.37 wt.%, CaO is 0.10 wt.% and MnO is below detection limits. Olivine located 2mm from the vein has a lower Mg# of 0.86, and much lower than the DMM. SiO_2 is 40.7 wt.%, NiO is 0.29 wt.%, CaO is 0.11 wt.% and MnO is below detection limits. Finally, olivine located within the mica-pyroxenite vein has an even lower Mg# (0.80 to 0.82). The content of SiO_2 is low (38.3 to 39.6 wt.%), NiO is low (0.05 to 0.22 wt.%), high CaO (0.13 to 0.18 wt.%) and MnO is below detection limits to 0.29 wt.%.

4.2.6.2.2 Clinopyroxene

The clinopyroxenes within both the peridotite and the pyroxenite vein are of uniform composition. They have Mg# of 84.4, Cr# of 33.9 and CaO/Al_2O_3 of 8.8, all less depleted than the DMM. The SiO_2 content is 54.03 wt.%, TiO_2 is 0.14 wt.%, MnO is 0.06 wt.% and Na_2O is 1.62 wt.%. Using the classification of Morimoto *et al.* (1988) the clinopyroxene in BD3847 is a diopside.

4.2.6.2.3 Spinel

BD3847 contains spinel with low Al_2O_3 (6.84 wt.%) and high Cr_2O_3 (58.70 wt.%) producing a Cr# of 63.7. FeO is 32.0 wt.% and MgO is 7.7 wt.%, generating a Mg# of 30.0. Following the classification from Stevens (1944) the spinel in this xenolith is a Cr-magnetite (Figure 4.5).

4.2.6.2.4 Accessory Minerals

In BD3847, amphibole is present within the pyroxenite vein and at the contact of the peridotite and pyroxenite. Concentrations of SiO_2 range from 43.2 to 44.wt.%, TiO_2 from 3.50 to 3.58 wt.%, Al_2O_3 from 10.3 to 10.6 wt.%, FeO from 5.74 to 7.42 wt.% (higher FeO in the vein), MgO from 16.4 to 17.6 wt.% (higher MgO in the peridotite), CaO from 11.00 to 11.10 wt.% and Na_2O from 3.19 to 3.22 wt.%. Minor amounts of Cr_2O_3 (0.05 to 0.15 wt.%)

and MnO (0.07 to 0.11 wt.%) are also present. According to the classification of Hawthorne *et al.* (2012) these amphiboles are Ti-pargasites.

Two types of mica are present in BD3847–a phlogopite within the peridotite and an Mg-biotite in the pyroxenite vein. These micas have 37.2 to 39.1 wt.% of SiO_2, 2.87 to 4.18 wt.% of TiO_2, 14.2 to 15.0 wt.% of Al_2O_3, 0.11 to 1.69 wt.% of Cr_2O_3, 3.04 to 7.51 wt.% of FeO, 20.1 to 22.1 wt.% of MgO and 0.90 to 1.14 wt.% of Na_2O. The mica in the peridotite contains higher SiO_2, Al_2O_3, Cr_2O_3 and MgO and lower TiO_2 and Na_2O. Minor amounts of MnO are also present (0.02 to 0.06 wt.%) in the mica.

BD3847 also contains small amounts of ilmenite. This has 49.9 to 50.2 wt.% of TiO_2, 0.46 to 0.46 wt.% of Al_2O_3, 0.53 to 0.60 wt.% of Cr_2O_3, 10.0 to 10.6 wt.% of Fe_2O_3, 27.1 to 27.4 wt.% of FeO, 0 to 0.38 wt.% of MgO and 9.8 to 9.93 wt.% of NiO.

4.2.7 Oga Peninsula

4.2.7.1 Olivine

The olivine in spinel peridotite J1 has Mg# of 89.5, SiO_2 of 40.95 wt.%, MnO of 0.14 wt.%, NiO of 0.36 wt.%, and CaO of 0.06 wt.%, all of which are similar to that of the DMM of Workman & Hart (2005).

4.2.7.2 Orthopyroxene

In spinel peridotite J1, the orthopyroxene has an Mg# of 89.8, which is comparable to that of the DMM. SiO_2 is 55.30 wt.%, Al_2O_3 is 3.40 wt.%, Cr_2O_3 is 0.41 wt.%, and CaO is 0.53 wt.%. The SiO_2 content of the orthopyroxene is higher than that of the DMM, but the contents of Al_2O_3, Cr_2O_3 and CaO and CaO/Al_2O_3 (0.15) are lower. Minor amounts of TiO_2 (0.11 wt.%) and NiO (0.09 wt.%) are present. Using the classification of Mirmoto *et al.* (1998), this orthopyroxene is an aluminian-enstatite.

4.2.7.3 Clinopyroxene

The clinopyroxene in J1 is a diopside with an Mg# of 91.1, which is similar to, albeit slightly higher than that of the DMM. It contains significantly more CaO (22.49 wt.%) than clinopyroxene in the DMM but lower Al_2O_3 (4.61 wt.%) and Cr_2O_3 (1.02 wt.%). The CaO/Al_2O_3 (4.88) is also high relative to the DMM. Minor amounts of TiO_2 (0.51 wt.%), MnO (0.09 wt.%), NiO (0.04 wt.%) and Na_2O (0.50 wt.%) are also present. The detailed

classification scheme of Morimoto *et al.* (1988) shows that the clinopyroxene in J1 is an aluminian-chromian-diopside.

4.3 Summary

Overall, ultramafic xenoliths from the six different locations presented in this study can be broadly defined into four groups.

1. The most 'depleted' peridotites are found at Lashaine in N. Tanzania, which is the only xenolith location in this study that is in an on-craton setting (Chapter 2). The Lashaine harzburgites contain the most magnesian olivines (92.5; Fig 4.1A), orthopyroxenes (Mg# = 93.0 to 93.5) and clinopyroxenes (Mg# = 91 to 93.5; Fig 4.3A). Because they co-exist with the highest amounts of garnet in our sample suite, these orthopyroxenes also have the lowest Al_2O_3 (1 to 2 wt.%; Fig 4.1B) and the highest SiO_2 contents (57 to 58 wt.%).

2. The most 'fertile' peridotites are spinel lherzolites from the Kilbourne Hole, the Tariat Volcanic Field and Oga Peninsula (olivine Mg# = 89 to 91, orthopyroxene Mg# = 89 to 92 and clinopyroxene Mg# = 89 to 92). The orthopyroxenes from these locations are in equilibrium with spinel and have the highest Al_2O_3 contents (3 to 5 wt%) and lowest SiO_2 contents (54 to 56 wt%).

3. The variably depleted and fertile peridotites are from the Antarctic Peninsula, Southern Patagonia, West Eifel Volcanic Field and Colorado Plateau. Where, olivines have Mg# which range from ~ 89.5 to 91.5, orthopyroxene Mg# ~ 90 to 92 and clinopyroxene at ~ 90.5 to 93.5.

4. The minerals in the pyroxenites typically have lower Mg# (olivine = 78.4 to 88.4, orthopyroxene = 85.2 to 91 and clinopyroxene Mg# = 78.7 to 90.0; with BD816 being the exception with Mg# = 93.6). Furthermore, they have uniquely Fe-rich clinopyroxene and spinel Cr# at 0.1 to 13.4 and <0.1 to 26 (with the exception being clinopyroxene from BD816 and spinel from BD3847).

Chapter 5. Trace and volatile element mineral contents of on- and off-craton mantle peridotites and pyroxenites

5.1 Trace Element Mineral Chemistry

Trace elements are typically defined as occurring at ppm and ppb concentrations and have been determined by LA-ICP-MS. The results for clinopyroxene, garnet, amphibole and mica are presented in Appendix A (Tables 9 to 16). The analysis was undertaken on a New Wave UP193 Solid State laser ablation system coupled to a Perkin-Elmer Nexion ICP-MS and processed using the Glitter Software as described in Appendix B.

5.1.1 South West USA

5.1.1.1 Kilbourne Hole

5.1.1.1.1 Clinopyroxene

Clinopyroxenes in the Kilbourne Hole spinel lherzolites have varying LREE/HREE ratios, with $[La/Yb]_N$ (where $_N$ denotes primitive-mantle normalised) values of 0.06 to 0.80 (Figure 5.1). When compared to the $[La/Yb]_N$ of DMM (0.36; Workman & Hart, 2005), the diopsides in KH2, KH4 and KH5 are more depleted (0.06 to 0.19), while the analysis in KH3D is slightly more enriched (0.80). All samples have negative Ti, Hf, and Zr relative to neighbouring elements and KH2 also has a negative Nb anomaly. LILE vary, with KH2, KH3D and KH4 showing negative Sr anomalies and KH2 has elevated U + Th concentrations. Uranium concentrations range from 0.007 to 0.027 ppm and Th concentrations from 0.020 to 0.054 ppm.

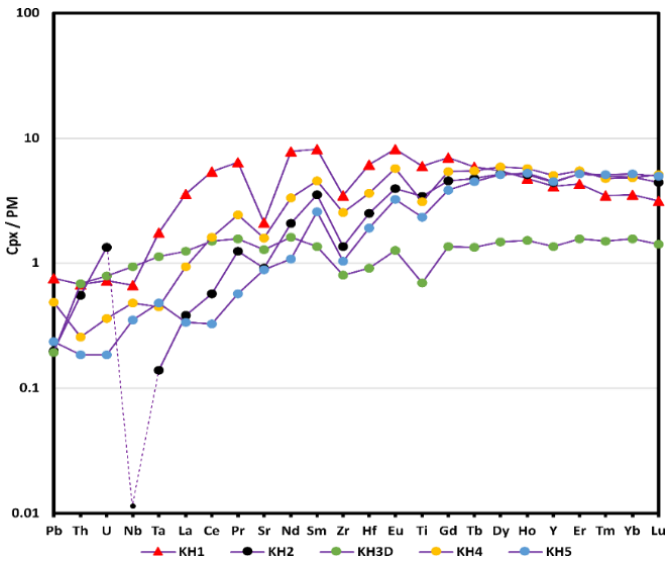

Figure 5.1. Primitive-mantle-normalized trace element patterns clinopyroxene of peridotite and pyroxenite from the Kilbourne Hole. Normalization factors are from McDonough & Sun (1995). Circles are analyses for peridotite and triangles for pyroxenites.

Clinopyroxenes in pyroxenite KH1 are significantly more enriched in LREE relative to HREE ($[La/Yb]_N$ = 1.01) than those in the spinel lherzolites. On normalised multi-element plots negative anomalies are present at Ti, Zr and Sr. The clinopyroxenes contain moderately low U (0.004 ppm) and Th of U (0.015 ppm).

5.1.1.2 Colorado Plateau, Southern USA

5.1.1.1.2 Clinopyroxene

Peridotites from the Colorado Plateau contain clinopyroxene with two distinct incompatible trace element compositions (Fig. 5.2). The augites in the garnet harzburgites from the Thumb (TH17 and TH33) have very strong LREE enrichment relative to HREE, with $[La/Yb]_N$ of 13.9 to 23.1 and have distinct negative anomalies at Ti, Zr, Ta and Nb. The fractionated HREE patterns ($[Ho/Yb]_N < 1$) are consistent with these clinopyroxenes are in equilibrium with garnet. Their LILE and U+Th compositions show no distinct signatures, and Uranium (0.011 to 0.030 ppm) and thorium (0.047 to 0.131 ppm) are relatively high. The diopside in the spinel lherzolite from Buell Park (BP1) has a very noticeable depletion in LREE relative to HREE and $[La/Yb]_N$ = 0.003 (Figure 4.13). Overall, the trace-element concentrations in clinopyroxenes from BP1 are very low, and below are close to detection limits. Uranium (0.001 ppm) and thorium concentrations (0.0014 ppm) are also low.

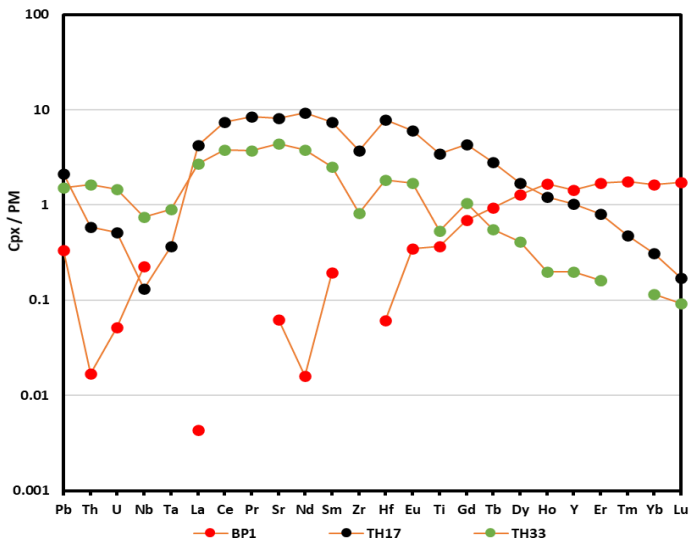

Figure 5.2. Primitive-mantle-normalized trace element patterns of peridotite clinopyroxene from the Colorado Plateau. Normalization factors are from McDonough & Sun (1995).

5.1.1.1.2 Garnet

The garnets analysed in this study from The Thumb exhibit a strong enrichment in HREE relative to LREE ($[La/Yb]_N$ at 0.005 to 0.09) and so display 'normal' REE patterns for mantle garnets (Fig 5.3A; Stachel *et al.*, 1998). They have negative anomalies at Nb, Ta and Ti. Contents of uranium (0.006 to 0.028 ppm) and thorium (0.003 to 0.017 ppm) are low and are akin to the depleted mantle. The partitioning of trace elements between clinopyroxene and garnet observed in samples TH17 and TH33 (Fig 5.3B) match with those observed in experiments undertaken at 2.5 to 7 GPa and 1080 to 1200 °C from Green *et al.* (2000). Overall, this highlights the equilibrated nature of these peridotites.

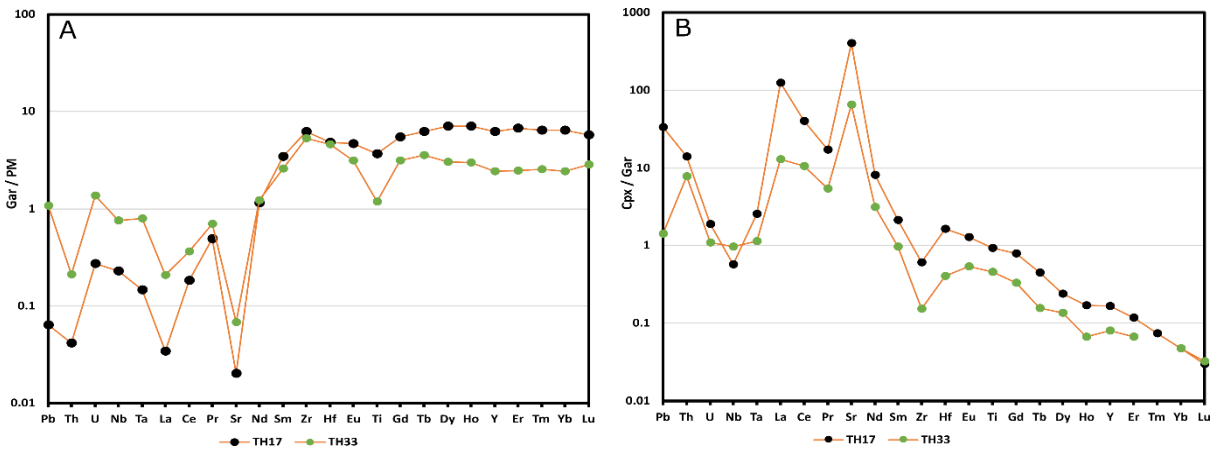

Figure 5.3 A) Primitive-mantle-normalized trace element patterns of garnets in peridotites from the The Thumb, Colorado Plateau. Normalization factors are from McDonough & Sun (1995). B) Clinopyroxene-garnet partitioning for given samples.

5.1.2 Tariat Volcanic Field

5.1.2.1 Clinopyroxene

Diopsides in the spinel lherzolite xenoliths from the Tariat Volcanic Field all have similar normalised incompatible trace-element patterns (Fig 5.4). They are depleted in LREE relative to HREE, with $[La/Yb]_N$ values of 0.27 to 0.57; those of samples TM2 and TM3 are slightly higher than the DMM and TM1 and TM4 are slightly more depleted. All of the clinopyroxenes show slight negative anomalies at Ti, Zr and Hf. TM3 has slightly elevated U + Th concentrations relative to Ta, with U concentrations ranging from 0.007 to 0.03 ppm and Th from 0.016 to 0.105 ppm.

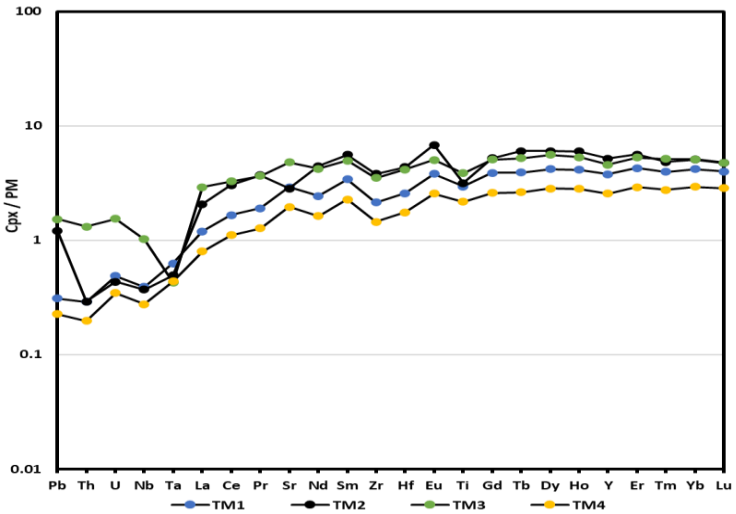

Figure 5.4 Primitive-mantle-normalized trace element patterns of clinopyroxene from Tariat peridotites. Normalization factors are from McDonough & Sun (1995). Circles are peridotite.

5.1.2.2 Accessory Minerals

The phlogopite in TM2 has a greater abundance of Th and U, a lower abundance of rare-earth elements, and a varying distribution of HFSE relative to co-existing clinopyroxenes (Figure 5.5A). The distribution coefficients of cpx/phlogopite from this study compare well with those obtained by Krmicek *et al.* (2014) from a calc-alkaline lamprophyre (Figure 5.5B).

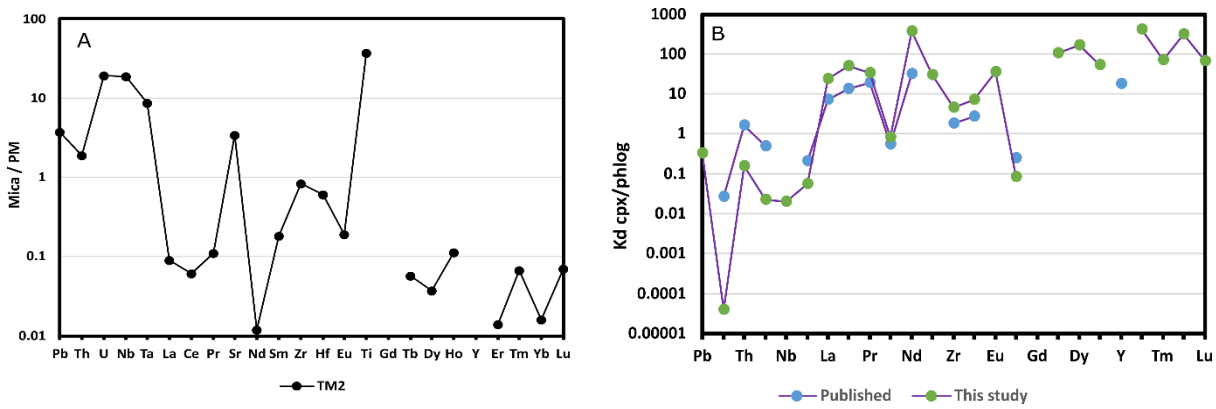

Figure 5.5 A) Primitive-mantle-normalized trace element patterns of phlogopite from a Tariat peridotite (TM2). B) Partition coefficients for clinopyroxene and phlogopite compared to published values for a clac-alkaline lamprohyre (Krmicek *et al.*, 2014).

5.1.3 West Eifel Volcanic Field

5.1.3.1 Clinopyroxene

Diopsides in all of the mantle xenoliths analysed in this study from the West Eifel Volcanic Field are characterised by enriched LREE/HREE signatures, with $[La/Yb]_N$ in the pyroxenites ranging from 1.3 to 19.8 and peridotites ranging from 2.9 to 3.1. However, they display highly-variable normalised multi-element patterns (Fig 5.6).

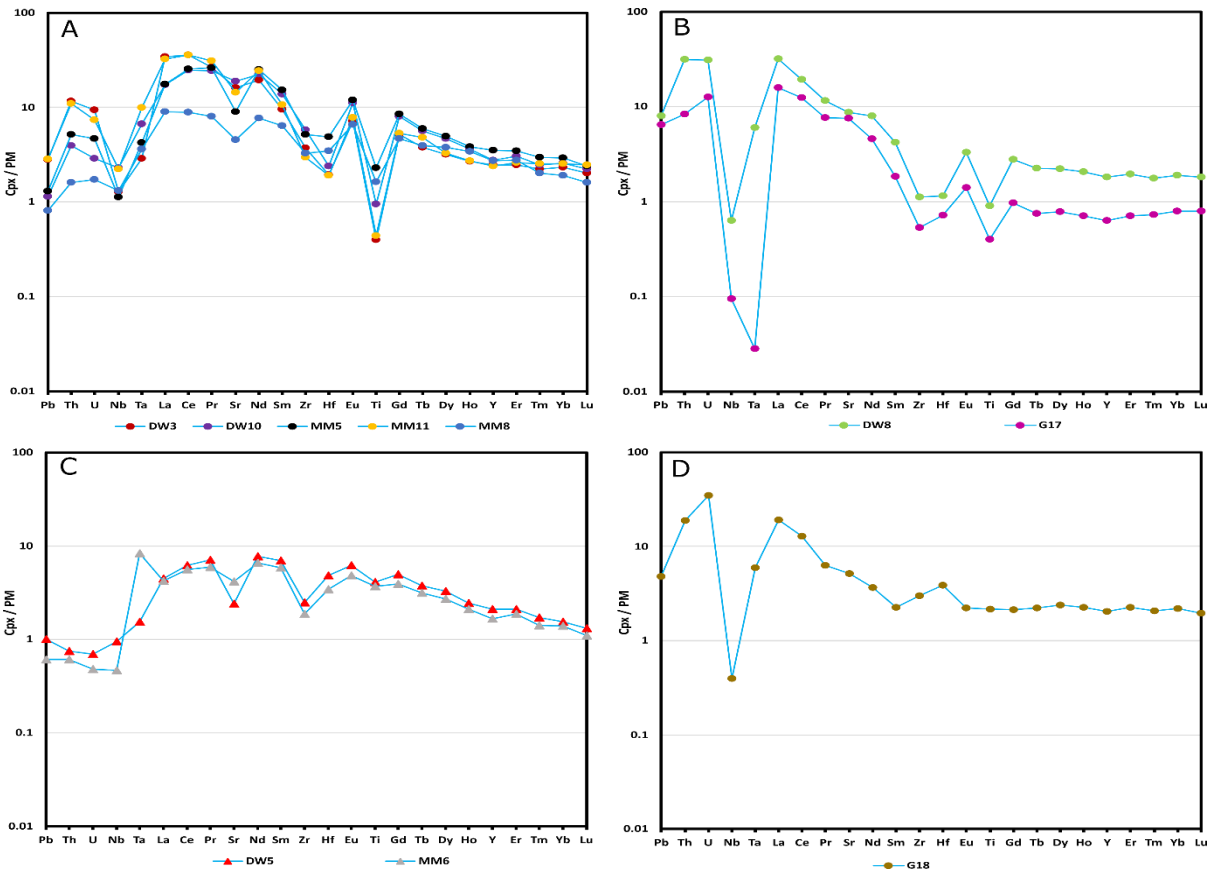

Figure 5.6 Primitive-mantle-normalized trace element patterns of clinopyroxenes from the West Eifel peridotites. Normalization factors are from McDonough & Sun (1995). A) Group 2 peridotites, B) Group 3 peridotites, C) Group 4 pyroxenites and D) is a novel group 5 signature.

Using the grouping from Witt-Eickschen *et al.* (2003), the samples are classified as follows:

Group 1 clinopyroxenes have a depleted LREE/HREE chemistry (e.g. [La/Yb]N< 1). There are no samples presented in this study with these characteristics.

Group 2 clinopyroxenes are enriched in MREE relative to HREE, have negative Ti, Zr, Hf, Sr, Nb and Ta anomalies and positive U & Th anomalies. Analysis in spinel peridotites DW3, DW10, MM5, MM11 and MM8 fall into this group (Fig 5.6A).

Group 3 clinopyroxenes have V-shaped REE, flat MREE/HREE, clear negative Ti, Zr, Hf, Ta and Nb anomalies and positive Th and U anomalies. Spinel lherzolites DW8 and G17 fall into this group (Fig 5.6B).

Group 4 clinopyroxenes exhibit MREE/HREE enriched and have negative Ti, Hf, Sr, Ta, Nb, U, Th and Pb anomalies. These are limited to augites in the pyroxenites DW5 and MM6 (Fig 5.6C).

A previously unrecognised trace-element signature is observed by diopside in spinel harzburgite G18 (Fig 5.6D). The clinopyroxene is LREE/HREE enriched, has flat MREE/HREE signatures, displays negative Nb anomalies and has unique positive Hf and Zr anomalies.

5.1.3.2 Amphibole

Pargasites in wehrlite DW10 and spinel lherzolite M11 are enriched in LREE relative to HREE, with $[La/Yb]_N$ of 7.0 and 14.0, respectively. On normalised muti-element plots, they have prominent negative anomalies at Ti and Hf (Fig 5.7A). In MM11, the pargasite has positive Nb, Ta and Ba anomalies unlike those in DW10 which lack Nb-Ta anomalies and are depleted in Ba. Uranium (0.045 to 0.195 ppm) and thorium (0.207 to 0.934 ppm) are present in moderate amounts. DW10 and MM11 show distinct partitioning of trace elements between co-existing amphibole and clinopyroxene (Fig 5.7B). Those in MM11 preferentially partitioning into amphibole, while in DW10 they preferentially partition into clinopyroxene, and are comparable with previous studies (e.g. Witt-Eickschen & Harte, 1994; Chazot *et al.*, 1995).

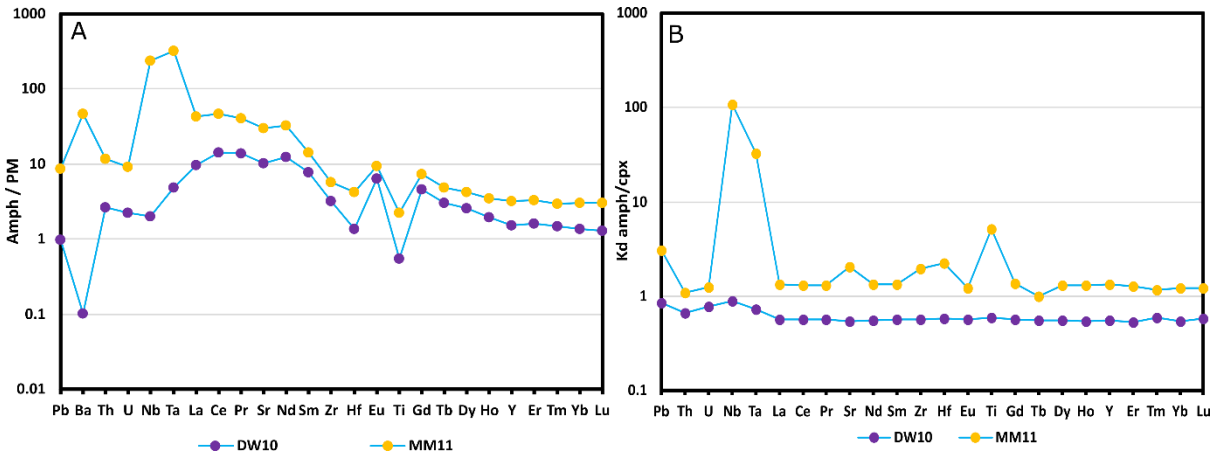

Figure 5.7 A) Primitive-mantle-normalized trace element patterns of amphiboles from the West Eifel peridotites. Normalization factors are from McDonough & Sun (1995). B) Partition coefficients for amphibole and clinopyroxene.

5.1.4 Antarctic Peninsula

5.1.4.1 Clinopyroxene

Diopsides in the spinel peridotites and pyroxenites from the Antarctic Peninsula have highly variable incompatible trace-element compositions. These may be classified into four groups (Figure 5.8):

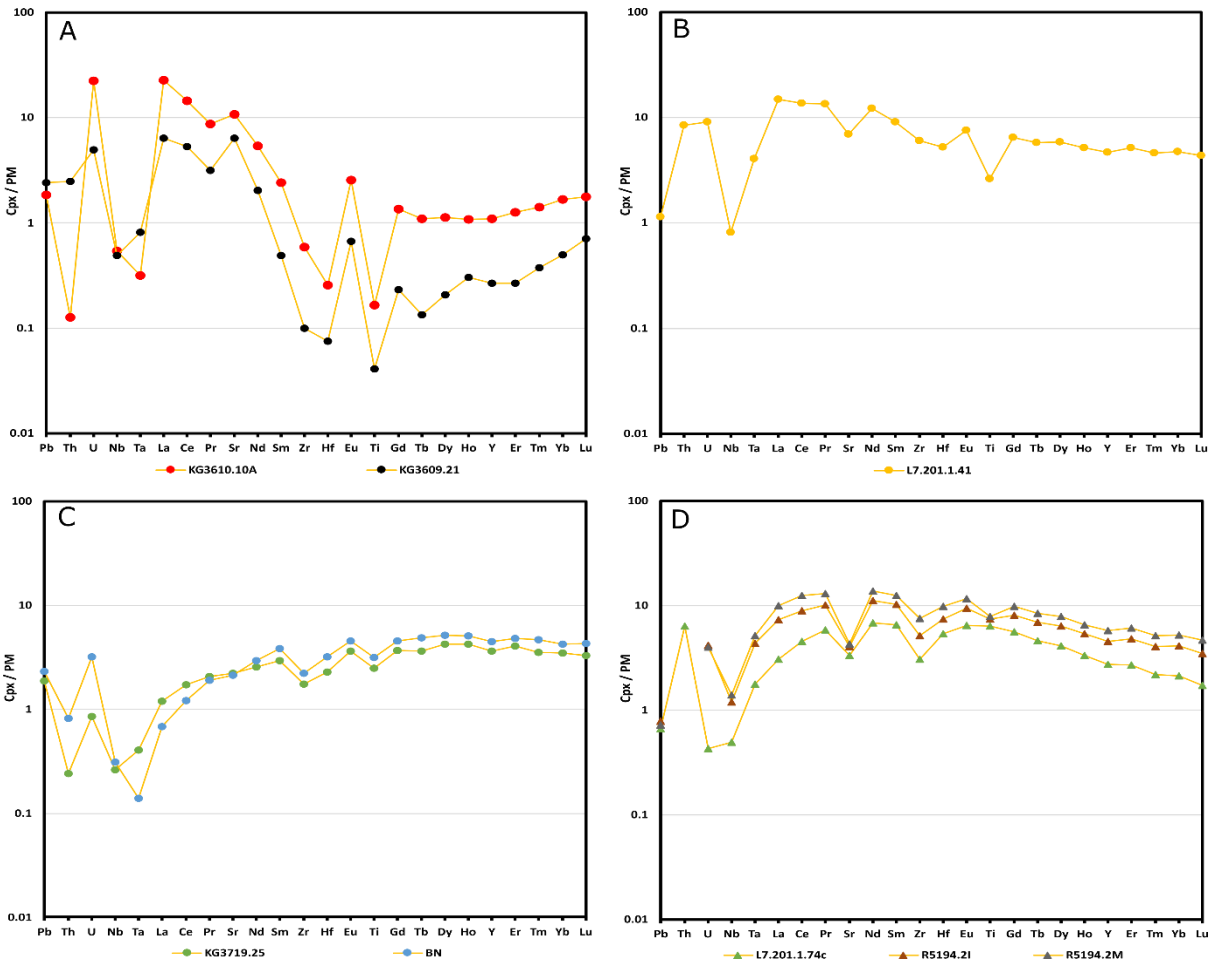

Figure 5.8. Primitive-mantle-normalized trace element patterns of clinopyroxenes in peridotites from the Antarctic Peninsula. Normalization factors are from McDonough & Sun (1995). A) Group 1 peridotites, B) Group 2 peridotites, C) Group 3 peridotites and D) Pyroxenite signature.

Group 1 clinopyroxenes exhibit strong enrichment in LREE relative to HREE ([La/Yb] > 10) and are depleted in MREE relative to HREE (Figure 5.8A). Furthermore, they have distinct negative HFSE anomalies at Ti, Zr, Hf, Nb and Ta. Uranium is 0.100 to 0.460 ppm and thorium is 0.01 to 0.198 ppm. These clinopyroxenes are found in spinel peridotites KG3610.10A and KH3609.21

Group 2 clinopyroxenes are slightly enriched in LREE relative to HREE ($[La/Yb]_N > 1$) but have similar normalised MREE/HREE ratios (Figure 5.8B). Furthermore, these have slightly negative anomalies at Ti, Zr, Hf, Nb and Ta. Actinides are enriched, with uranium at 0.18 ppm and thorium at 0.67 ppm. These clinopyroxenes are present in spinel peridotite L7.201.1.41.

Group 3 clinopyroxenes are depleted in LREE relative to HREE ($[La/Yb]_N < 1$) but have similar MREE/HREE ratios (Figure 5.8C). They have slight anomalies at Ti, Zr, Hf, Ta and Nb.

Normalised uranium is enriched relative to thorium, with uranium at 0.017 to 0.065 ppm thorium at 0.019 to 0.065 ppm. These clinopyroxenes are present in spinel peridotites KG3619.25 and BN

Group 4 clinopyroxenes are slightly enriched in LREE and MREE relative to HREE (Figure 5.8D; [La/Yb] and [Ho/Yb] > 1). They have prominent negative anomalies at Zr and Ta and slight negative anomalies at Ti and Hf. For LILE, there is a distinct negative anomaly at Sr. Uranium is 0.01 to 0.08 ppm and thorium is below detection limit to 0.508 ppm. These clinopyroxenes are ubiquitous in the pyroxenites (L7.20101.74c, R5194.2I and R5194.2M)

5.1.5 Southern Patagonia

5.1.5.1 Clinopyroxene

The trace-element compositions of the clinopyroxenes from the Pali Aike Volcanic Field can also be broadly classified into four groups (Figure 5.9).

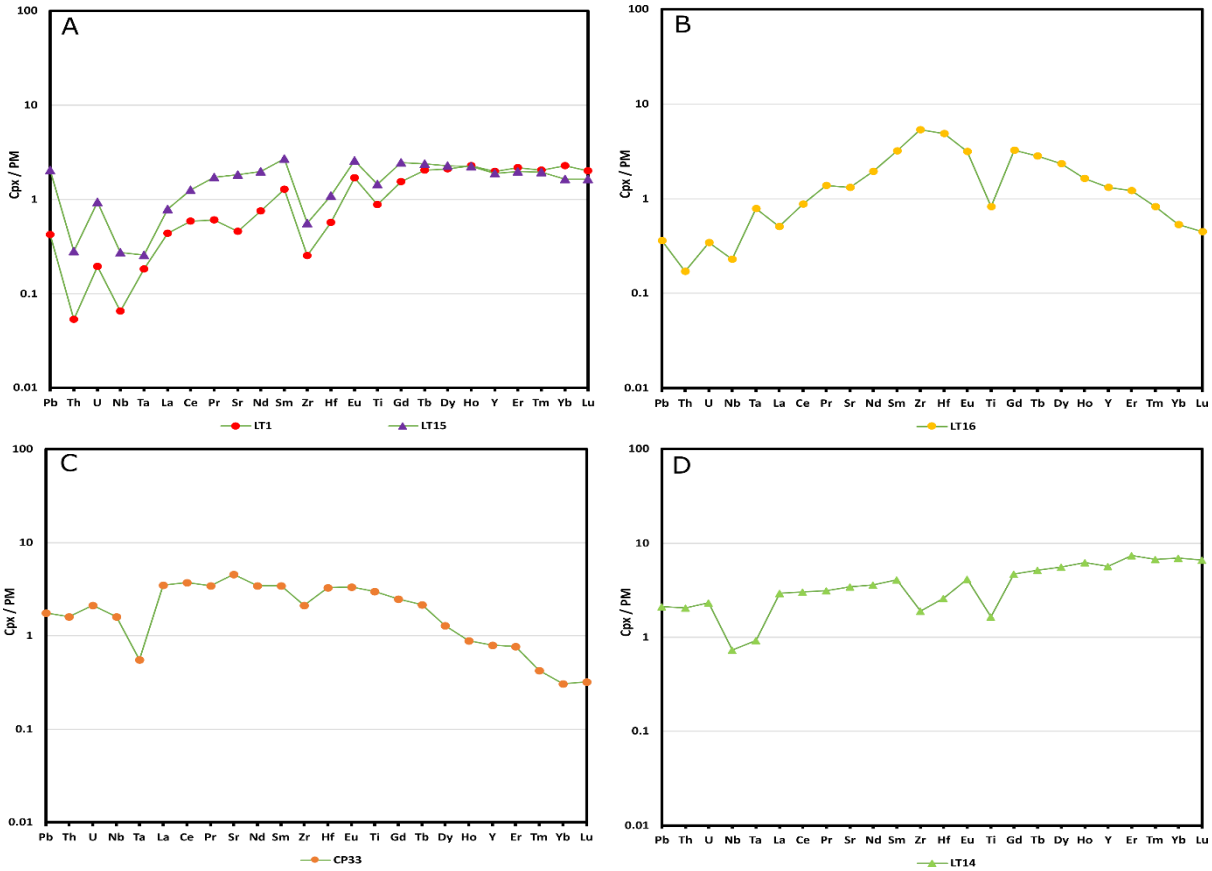

Figure 5.9 A) Primitive-mantle-normalized trace element patterns of clinopyroxene in peridotites from Southern Patagonia. Normalization factors are from McDonough & Sun (1995). Circles are peridotites and triangles are pyroxenites. A) Group 1, B) Group 2, C) Group 3, D) Group 4.

Group 1 clinopyroxenes (diopsides) are slightly depleted in LREE relative to HREE ([La/Yb] > 1) but have similar MREE/HREE compositions (Fig 5.9A). They have distinct negative anomalies at Ti, Hf and Zr. Furthermore, they have slightly negative anomalies at Sr. Variable amounts of uranium (0.004 to 0.019 ppm) and thorium (0.004 to 0.022 ppm) are present. These clinopyroxenes occur in spinel peridotite LT1 and pyroxenite LT15

Group 2 clinopyroxenes (augites) are slightly enriched in LREE relative to HREE, with $[La/Yb]_N$ = 0.95, and exhibit a strong MREE enrichment relative to LREE and HREE (Fig 5.9B). Furthermore, these clinopyroxenes have positive anomalies at Zr, Hf and Ta but negative Ti. Low amounts of uranium (0.007 ppm) and thorium (0.014 ppm) are present. These clinopyroxenes occur in spinel peridotite LT16.

Group 3 clinopyroxenes (augites) show clear enrichment in LREE relative to HREE ($[La/Yb]_N$ of 11.4) and have slight depletion at Ta (Fig 5.9C). Moderate amounts of uranium (0.043 ppm) and thorium (0.128 ppm) are present. These clinopyroxenes coexist with garnet and are found in peridotite CP33.

Group 4 clinopyroxenes (augites) are slightly depleted in LREEs relative to HREEs and MREEs (Fig 5.9D). They have clear negative anomalies at Ti, Zr, Hf, Ta and Nb. Uranium (0.048 ppm) and thorium (0.163 ppm) are present in moderate amounts. These clinopyroxenes are found in pyroxenite LT14

5.1.5.2 Garnet

Garnets in peridotites analysed from the Pali Aike Volcanic Field are depleted in LREEs relative to HREEs and MREEs and so show 'normal' trace-element patterns (Fig 5.10A). They have similar U (0.011 to 0.014 ppm) and Th concentrations (0.004 to 0.008 ppm). A distinction between the garnets in peridotite CP33 and pyroxenite CP62 is the Zr and Hf enrichment in the latter. Trace-element partitioning between clinopyroxene and garnet (Fig 5.10B) is consistent with experimental data from Green *et al.* (2000).

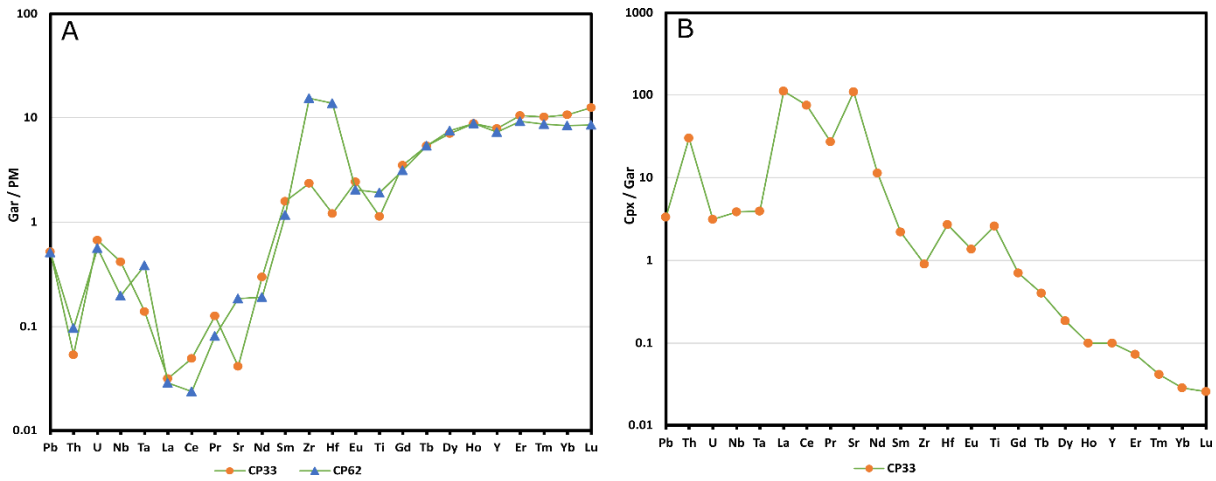

Figure 5.10. A) Primitive-mantle-normalized trace element patterns of garnet from Pali Aike peridotite and pyroxenite and; B) Partition coefficients for clinopyroxene and garnet.

5.1.5.3 Accessory Minerals

A trace-element analysis of phlogopite in orthopyroxenite CP62 is shown in Figure 5.11A and a plot showing the partitioning of trace elements between garnet and co-existing phogopite is provided in Figure 5.11B. Overall, the LREEs, HFSEs and many LILEs preferentially partition into phlogopite relative to garnet. In contrast, the HREEs and MREEs preferentially partition into garnet. This is consistent with the experimental data from Green *et al.* (2000).

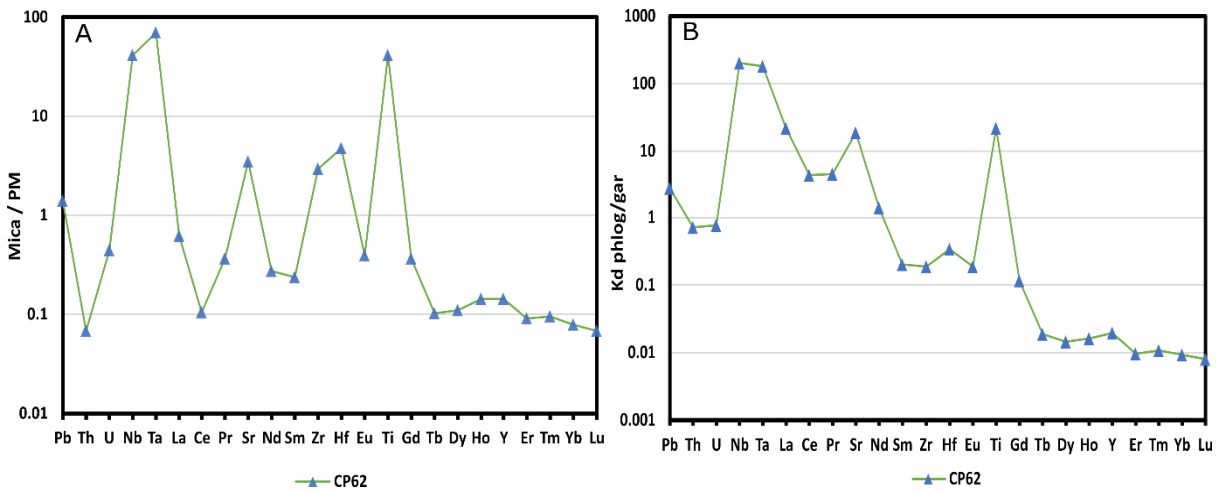

Figure 5.11 A) Primitive-mantle-normalized trace element patterns of phlogopite from a Pali Aike pyroxenite (CP62). Primitive mantle normalization factors are from McDonough & Sun (1995). B) Partition coefficients for phlogopite and garnet.

5.1.6 Lashaine, Northern Tanzania

5.1.6.1 Clinopyroxene

Trace-element compositions for clinopyroxenes (diopsides and augites) analysed in Lashaine peridotites and pyroxenites are displayed in Figure 5.12. They are all strongly enriched in LREE relative to HREE and MREE, but $[La/Yb]_N$ varies hugely from 8.7 to 153. Furthermore, they show negative anomalies at Ti, Hf, Zr, Ta and Nb and positive anomalies at Sr and Pb. Uranium concentrations range from 0.010 to 0.298 ppm and thorium from 0.043 to 0.148 ppm; clinopyroxene in BD794 is distinctly more enriched in U relative to the other samples.

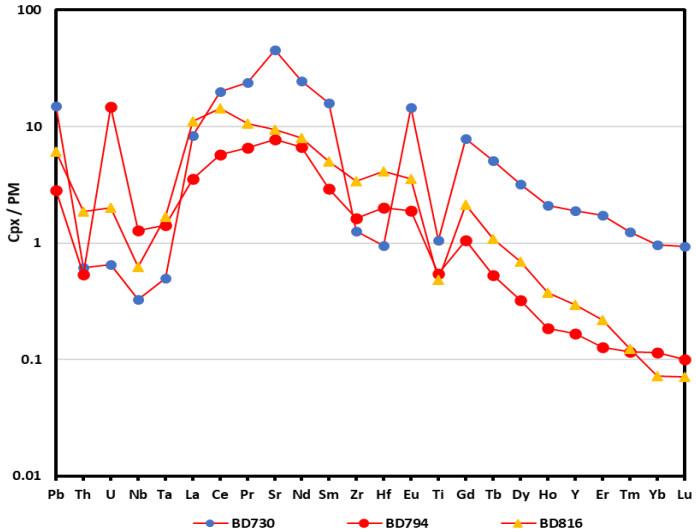

Figure 5.12. Primitive-mantle-normalized trace element patterns of clinopyroxene from Lashaine. Circles are peridotites and triangles are pyroxenites.

5.1.6.2 Garnet

The garnet in BD730 is significantly more depleted in the LREE than MREE and HREE (Figure 5.13A) and so has a 'normal' trace-element pattern for mantle garnet. It has a U concentration of 0.01 ppm and Th concentration of 0.05 ppm. Trace-element partitioning between clinopyroxene and garnet (Figure 5.13B) is consistent with experimental data from Green *et al.* (2000).

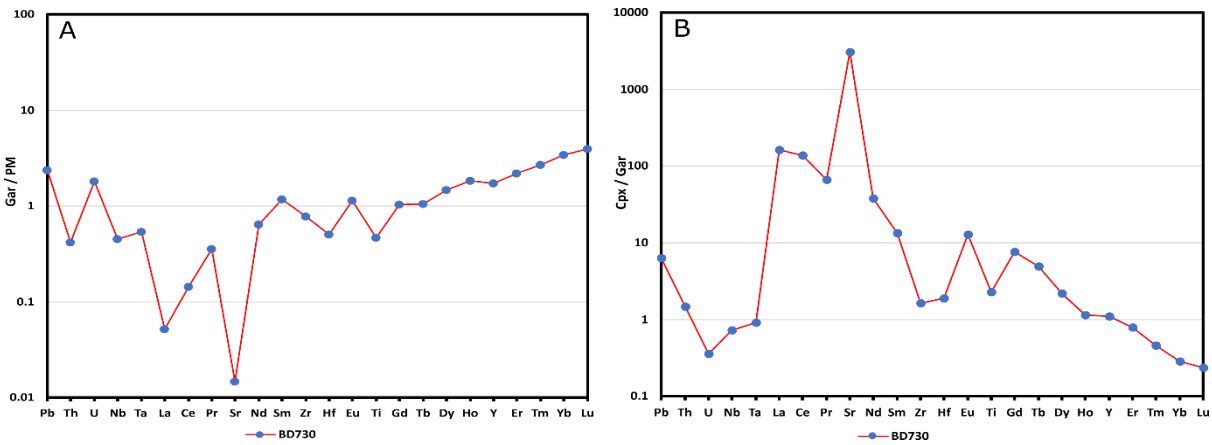

Figure 5.13. A) Primitive-mantle-normalized trace element patterns of garnet from Lashaine. B) Garnet-clinopyroxene partition coefficients for trace elements Circles are for peridotites and triangles are for pyroxenites.

5.1.7 Oga Peninsula

5.1.7.1 Clinopyroxene

The clinopyroxene analysed in the spinel harzburgite from the Oga Peninsula is strongly depleted in LREE relative to HREE ($[La/Yb]_N$ = 0.014; Figure 5.14), and so significantly more depleted than the DMM. Furthermore, the clinopyroxene shows negative anomalies at Y, Ti, Hf, Sr and Ba, with Nb and Ta below detection limits. U and Th concentrations are 0.015 and 0.031 ppm, respectively.

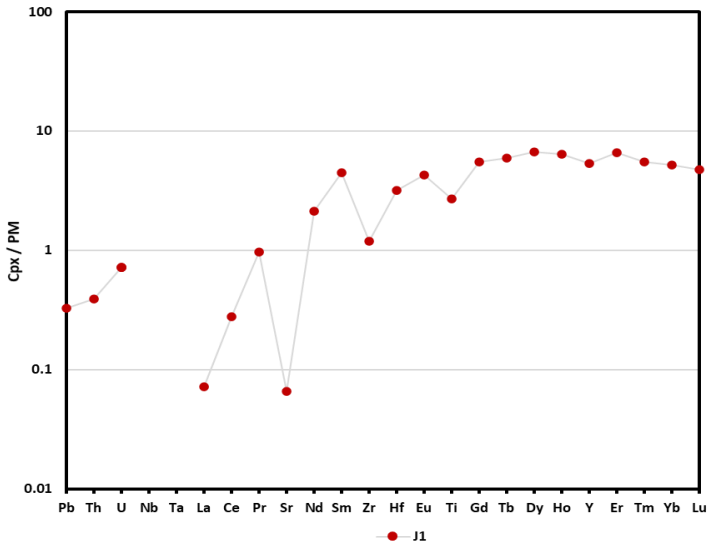

Figure 5.14. Primitive-mantle-normalized trace element patterns of clinopyroxene from the Oga Peninsula peridotite. Normalization factors are from McDonough & Sun (1995).

5.2 Volatile element chemistry from SIMS

5.2.1 Mineral chemistry

Unlike major- and trace-elements, the composition, affinity and factors controlling the distribution of volatile elements in mantle olivine, orthopyroxene, and clinopyroxene remain key outstanding issues. In this study, concentrations of H_2O, Li, B, F, P and Cl were determined in olivine, orthopyroxene and clinopyroxene from seventeen mantle xenoliths from six different volcanic fields (Kilbourne Hole, Tariat, West Eifel, Colorado Plateau and Lasahaine). This data was obtained by secondary ion mass spectrometry (SIMS) at the NERC Edinburgh Ion Microprobe Facility during three different sessions (November 2019, May 2021 and June 2021). In the first session H_2O, Li, B, F and Cl were determined, while in the second session H_2O, B, F, P and Cl were determined which is summarized in Figure 5.16 and provided in the Appendix (Tables 18 to 20).

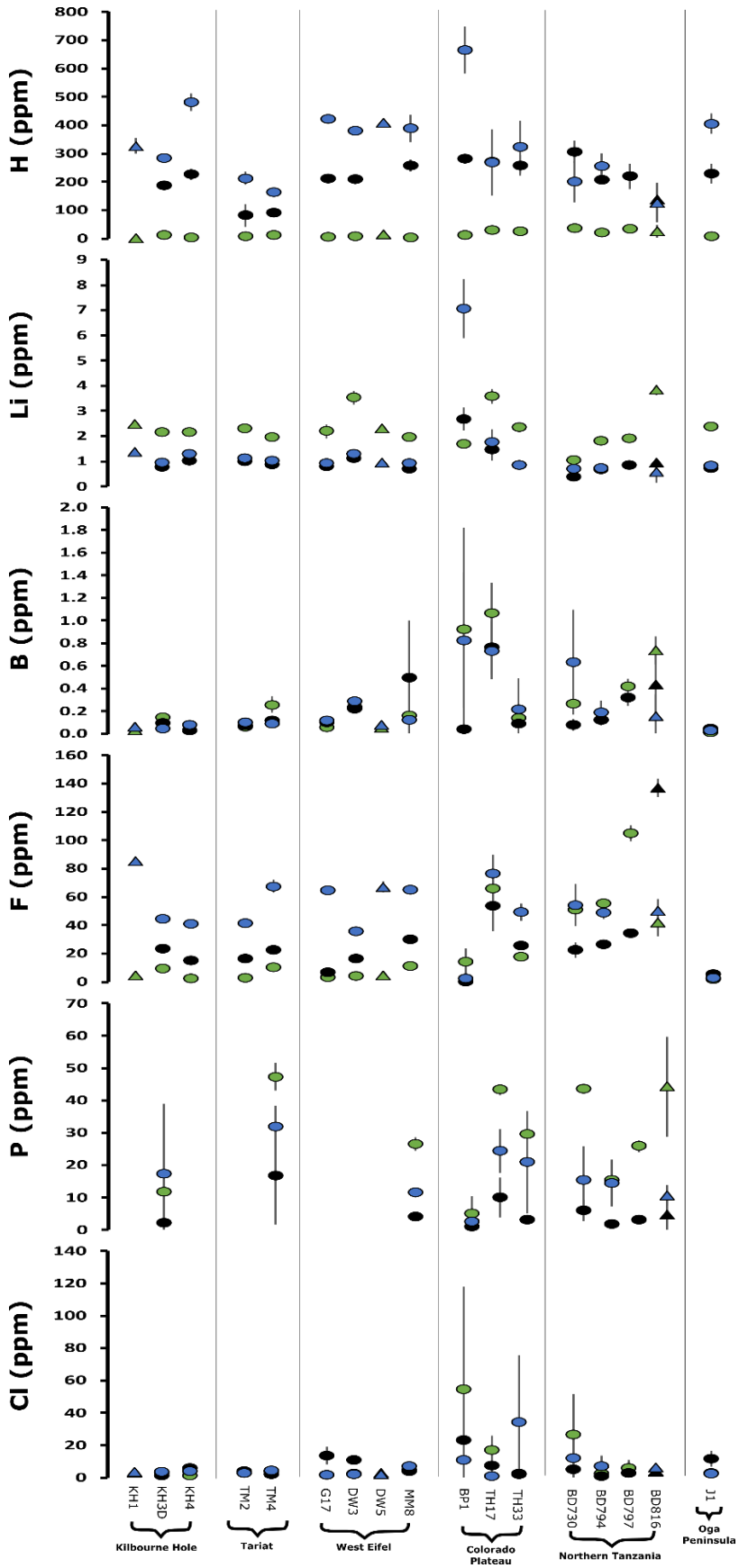

Figure 5.15. Hydrogen, lithium, boron, fluorine, phosphorous and chlorine concentrations in olivine (green), orthopyroxene (black) and clinopyroxene (blue). Minerals analysed in peridotites are shown by circles and in the pyroxenites by triangles.

5.2.1.1 South West USA

5.2.1.1.1 Kilbourne Hole

Two spinel lherzolites xenoliths were analysed from the Kilbourne Hole (KH3D and KH4). In these peridotites, olivine contains a low amount of H_2O (4 to 11 ppm), moderate Li (2.1); low B (0.05 to 0.15 ppm); low F (2.6 to 9.4); Low P (12 ppm) of P; and low Cl (2 to 3 ppm). Additionally, orthopyroxene contains moderate H_2O (188 to 227 ppm); low Li (0.8 to 1.0 ppm); low B (0.03 to 0.10 ppm); low F (15 to 23 ppm), low P (2.2 ppm), and low Cl (2 to 6 ppm). Finally, clinopyroxene contains moderate H_2O (284 to 481 ppm); moderate Li (1.0 to 1.3 ppm), low B (0.05 to 0.08 ppm), moderate F (41 to 45 ppm), moderate P (17.2 ppm of P); and low Cl (4 ppm).

Mineral phases were also analysed in one pyroxenite xenolith (KH1). The olivine in this xenolith contains low H_2O (2 ppm), high Li (2.5 ppm), low B (0.03 ppm), low F (5 ppm) and low Cl (3 ppm). Additionally, the clinopyroxene contains low H_2O (326 ppm), moderate Li (1.37 ppm), low B (0.07 ppm), high F (85 ppm) and low Cl (4 ppm).

H_2O, F and P have previously been determined by SIMS in orthopyroxene and clinopyroxene from two Kilbourne Hole peridotites presented in Kumamoto *et al.* (2017). For orthopyroxene, concentrations of H_2O (182 to 216 ppm), F (15 to 25 ppm), P (1.5 to 10.6 ppm) and clinopyroxene, H_2O (367 to 427 ppm), F (40 to 65 ppm) and P (5.3 to 37 ppm) fall within the range of this study. Furthermore, F and Cl contents from a single sample were also analysed in Urann *et al.* (2017). For olivine, this produced higher F (17 ppm) but lower Cl (0.15 ppm), for orthopyroxene this produced similar F (18 ppm) and lower Cl (~0.1 ppm), and for clinopyroxene this produced similar F (43 ppm) and lower Cl (~0.1 ppm) than results presented in this study. Overall, the H_2O, F and P contents from previous studies align well with this study, but this study produces much higher Cl contents.

5.2.1.1.2 Colorado Plateau

The mineral phase in three peridotite samples from the Colorado Plateau were analysed by SIMS. The olivine in the garnet harzburgite xenoliths from the Thumb (TH17 and TH33) contains: 26 to 29 ppm of H_2O; 2.4 to 3.6 ppm of Li; 0.1 to 1.1 ppm of B; 18 to 66 ppm of F; 29.5 to 43.3 ppm of P; and 3 to 18 ppm of Cl. The orthopyroxene contains 258 to 270 ppm of H_2O; 0.8 to 1.5 ppm of Li; 0.1 to 0.8 ppm of B; 26 to 54 ppm of F; 3.2 to 10.0 ppm of P;

and 2 to 8 ppm of Cl. Lastly, clinopyroxene contains 269 to 322 ppm of H_2O, 0.85 to 1.76 ppm of Li; 0.2 to 0.7 ppm of B; 49 to 77 ppm of F; 20.9 to 24.4 ppm of P; and 12 ppm of Cl.

Olivine in the highly-serpentinized spinel lherzolite from Buell Park (BP1) contains 12 ppm of H_2O, 1.69 ppm of Li, 0.93 ppm of B; 14 ppm of F; and 5.1 ppm of P. Cl is very imprecise, recording 54 ± 63 ppm. Orthopyroxene contains: 281 ppm of H_2O, 2.7 ppm of Li; 0.04 ppm of B; <1 ppm of F; and 1.0 ppm of P. Cl is again very imprecise, recording 23 ± 35 ppm. Finally, clinopyroxene contains 664 ppm of H_2O, 7.1 ppm of Li; 0.83 ppm of B; 2 ppm of F; 2.6 ppm of P; and 11 ppm of Cl.

Volatiles analysed in peridotites from the Colorado Plateau by Marshall *et al.* (2017) focussed on H_2O. These authors produced orthopyroxene concentrations at 53 to 588 ppm and clinopyroxene concentrations at 36 to 581 ppm. Furthermore, the work of Urann *et al.* (2017) constrained the F and Cl content of peridotites. Where, olivine has F at 31 ppm and Cl at ~0.2 ppm, orthopyroxene had F at 35 ppm and Cl at 0.12 ppm, and clinopyroxene has F at 86 ppm and Cl at ~0.3 ppm. Overall, the H_2O and F contents of previous studies align well with this study, but the Cl contents presented here are much higher.

5.2.1.2 Tariat Volcanic Field

Mantle phases in two spinel lherzolites from the Tariat Volcanic Field (TM2 and TM4) have been analysed for volatiles. The new data show that olivine contains: low H_2O (8 to 13 ppmw), moderate Li (2.0 to 2.3 ppm), high B (0.07 to 0.26 ppm); low F (3 to 10 ppm of F), high P (47.3 ppm) and moderate Cl (3 to 4 ppm). The orthopyroxene contains low H_2O (82 to 90 ppm), low Li (0.9 to 1.0 ppm); moderate B (0.07 to 0.12 ppm), moderate F (16 to 23 ppm of F), low P (16.83 ppm) and moderate Cl (2 to 4 ppm). The clinopyroxene contains low H_2O (164 to 212 ppm), moderate Li (1.0 to 1.1 ppm), moderate B (0.09 to 0.11 ppm), moderate F (42 to 68 ppm), moderate P (31.9 ppm of P) and moderate Cl (3 to 5 ppm).

Previously, SIMS analysis of orthopyroxene H_2O contents were determined for 3 samples by Wenzel *et al.* (2021). These range from 78 to 137 ppm and align well with the results from this study.

5.2.1.3 West Eifel Volcanic Field

The volatile contents of phases in three spinel peridotites from the West Eifel Volcanic Field were analysed (lherzolites DW3, G17 and harzburgite MM8) in this study. In these

peridotites, olivine contains low H_2O (3 to 7 ppm), high Li (2.0 to 3.1 ppm), variable B (0.06 to 0.24 ppm), low F (4 to 11 ppm), moderate P (29.5 ppm); and moderate Cl (2 to 5 ppm). Additionally, orthopyroxene contains high H_2O (208 to 258 ppm), low Li (0.7 to 1.1 ppm), high B (0.10 to 0.51 ppm), low F (7 to 30 ppm of F) low P (4.07 ppm) and variable Cl (4 to 13 ppm) of Cl. Finally, clinopyroxene (augite) contains high H_2O (379 to 421 ppm), moderate Li (0.9 to 1.3 ppm), high B (0.12 to 0.29); high F (36 to 65 ppm), low P (11.6 ppm), and moderate Cl (2 to 7 ppm).

One pyroxenite (DW5) was analysed. The olivine in this sample has low H_2O (13 ppm), moderate Li (2.3 ppm), low B (0.05 ppm), low F (5 ppm) and moderate Cl (3 ppm). Additionally, the clinopyroxene (augite) has high H_2O (408 ppm), moderate Li (0.9 ppm), low B (0.08 ppm), high F (67 ppm) and low Cl (2 ppm).

Previously, SIMS constraints on orthopyroxene H_2O contents for a 2 samples were determined by Wenzel *et al.* (2021). These authors determined H_2O contents at 241 to 256 ppm and these align with the results from this study.

5.2.1.4 Lashaine, Northern Tanzania

The volatile contents of minerals in three peridotites (lherzolite BD730 and harzburgites BD794, and BD797) from Lashaine were analysed in this study. No previously published volatile analyses are available for this location. The new data show that the olivines contain high H_2O (20 to 34 ppm), 1.0 to 1.9 ppm of Li; 0.13 to 0.42 ppm of B; 51 to 105 ppm of F; and 15 to 43 ppm of P. The concentration of Cl is imprecise, ranging from 2.4 ± 2.0 to 26 ± 25 ppm. Orthopyroxene contains: 208 to 305 ppm of H_2O; 0.4 to 0.8 ppm of Li; 0.08 to 0.32 ppm of B; 22 to 35 ppm of F; and 1.8 to 5.9 ppm of P. Cl is imprecise, ranging from 0.8 ± 0.8 ppm to 15.1 ± 5.8 ppm. Finally, the clinopyroxene contains: 201 to 255 ppm of H_2O; 0.70 to 0.73 ppm of Li; 0.2 to 0.6 ppm of B; 49 to 54 ppm of F; 14.5 ppm of P; and 7.2 ± 6.6 to 12.1 ± 3.7 ppm of Cl.

A pyroxenite (BD816) from Lashaine was analysed. The olivine in this xenolith contains: 25 ppm of H_2O; 3.82 ppm of Li; 0.7 ppm of B; 42 ppm of F; 44.3 ppm of P; and 4 ppm of Cl. For this sample, orthopyroxene was analysed over two different runs (November 2019 and May 2021). Similar concentrations were determined for each run with: 101 ± 14 and 134 ±37 ppm of H_2O, 0.9 ± 0.1 and 1.0 ± 0.1 of Li; 0.22 ± 0.13 and 0.44 ± 0.27 of B; 15 ± 2 and 17 ± 7

of F; 5 ± 5 and 4 ± 3 of Cl, from November 2019 and May 2021, respectively. Finally, clinopyroxene (diopsides) contains: low H_2O (123 ppmw), Li (0.16 ppm) and P (10.7 ppm), moderate B (0.16 ppm) and high F (50 ppm) and Cl (6 ppm).

5.2.1.5 Oga Peninsula

The minerals in one spinel harzburgite (J1) from the Oga Peninsula were analysed for volatiles. No previously published volatile analyses obtained by SIMS are available for this location. The new data show that the olivine contains low H_2O (8 ppm), high Li (2.4 ppm), low B (0.01 ppm), low F (2 ppm) moderate Cl (3 ± 2 ppm). Furthermore, orthopyroxene contains high H_2O (230 ppm), moderate Li (0.7 ppm), low B (0.05 ppm), low F (5.5 ppm) and high Cl (12 ± 5). Finally, clinopyroxene (diopside) contains high H_2O (405 ppm), low Li (0.8 ppm) and B (0.03 ppm), and moderate Cl (3 ± 2 ppm).

5.2.2 Whole rock calculations

Whole rock concentrations are calculated by integrating the modal abundances of a sample (see Chapter 3 and Table 3.1) as X^{min}, with the volatile composition of a mineral (this chapter and Appendix Tables 18 to 20) as C_i^{min}. This is shown by Equation 5.1.

$$C_i^{whole\ rock} = \left(X^{ol} \times C_i^{ol}\right) + \left(X^{opx} \times C_i^{opx}\right) + \left(X^{cpx} \times C_i^{cpx}\right) \qquad \text{(Equation 5.1)}$$

Where: X is modal abundance in % and C is concentration in ppm.

5.2.2.1 South West USA

5.2.2.1.1 Kilbourne Hole

Spinel lherzolites KH3D and KH4 have H_2O from 67 to 134 ppm, Li from 1.6 to 1.7 ppm, B from 0.04 to 0.13 ppm, F from 11.6 to 14.4 ppm, P at 9.7 ppm and Cl from 2.5 to 3.1 ppm. Pyroxenite KH1 has higher H_2O (196 ppm), lower Li (1.1 ppm), lower B (0.04 ppm), higher F (51.7 ppm) and similar Cl (2.6 ppm).

5.2.2.1.2 Colorado Plateau

Garnet harzburgites TH17 and TH33 have moderate H_2O (80 to 85 ppm), high Li (2.0 to 3.0) ppm, B of 0.13 ppm, F of 19.7 to 61.8 ppm, P from 23.2 to 34.6 ppm and Cl from 3.0 to 14.1 ppm. This is distinct from the highly serpentinized BP1, which has lower H_2O (61 ppm), Li (1.4 ppm), F (7.4 ppm) and P (2.8 ppm) and higher but very imprecise Cl (32.3 ± 39.0 ppm).

5.2.2.2 Tariat Volcanic Field

Spinel lherzolites TM2 and TM2 have low H_2O (50 to 62 ppm), moderate Li (1.5 to 1.8 ppm), high B (0.07 to 0.19 ppm), low F (13.0 to 20.0 ppm), high P (34.8 ppm) and moderate Cl (3.1 to 3.2 ppm).

5.2.2.3 West Eifel Volcanic Field

Spinel peridotites from the West Eifel Volcanic Field (DW3, MM8 and G17) have varying whole-rock volatile compositions. With H_2O from 58 to 84 ppm, Li from 1.7 to 3.2 ppm, B from 0.07 to 0.26 ppm, F from 7.4 to 15.4 ppm, P at 21.6 ppm and Cl from 3.6 to 4.6 ppm. The pyroxenite (DW5) has much higher H_2O (316 ppm), lower Li (1.2 ppm), low B (0.07 ppm), high F (52.5 ppm) and lower Cl (2.4 ppm).

5.2.2.4 Northern Tanzania

Peridotites from Lashaine (Northern Tanzania) have moderate to high contents of H_2O (65 to 100 ppm), Li (0.8 to 1.5), B (0.12 to 0.36 ppm), F (40.9 to 77.7 ppm), P (11.5 to 30.2 ppm) and Cl (2.0 ppm to 18.9 ppm). The pyroxenite (BD816) has higher H_2O (105 ppm), similar Li (1.3 ppm), similar B (0.33 ppm), lower F (42.9 ppm), similar P (17.1 ppm) and similar Cl (5.4 ppm).

5.2.2.5 Ichinomegata

The spinel harzburgite has low H_2O (67.4 ppm), moderate Li (1.9 ppm), low F (2.8 ppm) and high Cl (5 ppm).

5.3 Summary

The 4 groups of xenoliths identified in Chapter 4 are further expanded here to include their trace and volatile element chemistry.

1. The most ‘depleted’ peridotites that are found at Lashaine in N. Tanzania are all strongly enriched in LREE relative to HREE with $[La/Yb]_N$ varying widely (from 8.7 to 153) and typical of those previously described from Lashaine (e.g. Gibson *et al.*, 2020). Relative to other whole-rock calculations for on-craton xenoliths (e.g. Jackson, 2020), there is moderate H_2O (65 to 105 ppm), and Li (0.8 to 1.5 ppm), the first analysed B (0.12 to 0.36 ppm), high F (41 to 78 ppm), the first analysed P (11.5 to 30.2 ppm) and high Cl (2 to 19 ppm).

2. The most 'fertile' peridotites are spinel lherzolites from the Kilbourne Hole, the Tariat Volcanic Field and Oga Peninsula, and paradoxically have clinopyroxene compositions with low enrichments in incompatible trace elements ($[La/Yb]_N$ = 0.01 to 0.8). For whole rocks, the H_2O ranges from 50 to 134 ppm, Li from 1.45 to 1.92 ppm, B from 0.02 to 0.19 ppm, F from 3 to 20 ppm, P is 9.7 to 34.0 ppm and Cl is 3 to 5 ppm. Compared to other peridotites, these encompass the range of H_2O (total range of 37 to 137 ppm), have moderate Li (total range of 1.00 to 3.17 ppm), low to moderate B (total range of 0.02 to 0.33 ppm), low F (total range of 2.8 to 126 ppm), the range for P (9.7 to 34.8 ppm) and moderate to high for Cl (total range of 2 to 5 ppm).

3. The variably depleted and fertile peridotites from the Antarctic Peninsula, Southern Patagonia, West Eifel Volcanic Field and Colorado Plateau are dominated by metasomatically enriched signatures ($[La/Yb]_N > 1$) with some depleted exceptions (e.g. BN, KG.3719.25 and CP62). Whole-rock H_2O ranges from 37 to 124 ppmw, Li from 1.00 to 3.17 ppm, B is 0.04 to 0.26 ppm and F is 7 to 62 ppm, P from 3 to 34 ppm and Cl from 3 to 32 ppm. Relative to other peridotites, these encompass the range of H_2O, Li, B, P and Cl but have low F.

4. Pyroxenite samples with exception of orthopyroxenite CP62 all have enriched trace-element compositions, with La/Yb_N at 0.4 to 152. The calculated bulk volatile contents of the pyroxenites are very high, measuring up to 317 ppmw H_2O, 1.7 ppm Li, 0.21 ppm B, 126 ppm F, and 3 ppm Cl.

Chapter 6. Melting and Metasomatism

6.1 Introduction

The effect of melting and metasomatism on the mantle xenoliths investigated in this study can be constrained using their petrography, major element and trace element chemistry.

6.2 Petrography

The influence of melting on modal mineralogy of peridotites has been investigated by numerous experiments, including at 6.5 GPa (Brey et al., 1990; Takahashi et al., 1991); 2 GPa (Kinzler, 1997; Walter *et al.*, 1995) and 1 GPa (Kinzler & Grove, 1992; Baker & Stolper, 1994). These studies highlighted that increasing degrees of melting lead to increased modal proportions of orthopyroxene and olivine, relative to clinopyroxene in the residue during polybaric melting. Although they were unable to quantify the degree of melt extraction, the experimental results indicate which xenoliths are depleted based on their petrography (Figure 6.1).

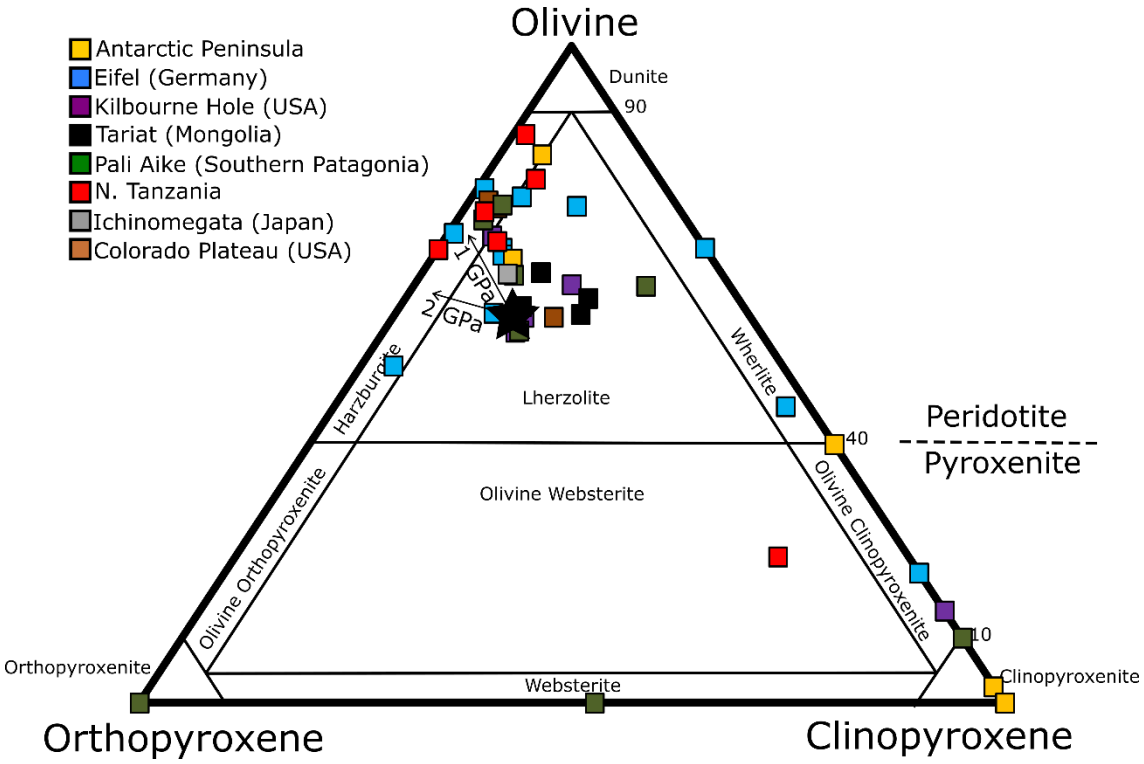

Figure 6.1. Ultramafic ternary classification diagram with compositions of samples with this study overlayed by a melting model from Niu et al. (1997).

Using data from Table 3.1 projected onto an ultramafic ternary with melting models from Niu *et al.* (1997; Figure 6.1), qualitative insights are provided on the depleted nature of

xenoliths examined in this study. Peridotites KH2, KH4 and KH5 from Kilbourne Hole, preserve fertile lherzolite compositions while KH3D is a more depleted composition. For the Colorado Plateau, BP1 preserves a fertile composition while TH17 and TH33 are depleted. From the West Eifel, samples DW3, DW8 and MM11 have fertile compositions while DW7, MM5, MM8, G17 and G18 have depleted compositions. From the Antarctic Peninsula, sample L7.201.1.41 has a fertile composition while KG.3610.10A is depleted. Of peridotites from Pali Aike, CP31, CP33 and LT1 are fertile while LT16 and PA3-5 are depleted. All peridotites from Northern Tanzania (BD370, BD738, BD794, BD797 and BD822) have depleted compositions while the harzburgite from the Oga Peninsula (J1) is fertile.

The pyroxenites and wehrlites are also displayed in Figure 6.1. These cannot be explained by simple melt-extraction from fertile mantle sources. Instead, they are interpreted to represent channelised melts in the lithospheric mantle derived from either the asthenospheric or recycled lithospheric reservoirs (e.g. Lambart *et al.*, 2012).

6.3 Mineral major element chemistry

Olivine Mg# and spinel Cr# are important phases because they are sensitive to the degree of melting experienced. Based on co-existing olivine and spinel compositions, the degree of partial melting has been quantified at 0% to 40% melting by Jaques and Green (1980) using anhydrous experiments on fertile peridotite at 1.5 GPa. Using these insights, the extent of partial melting on peridotites examined in this study can be quantified (Figure 6.2).

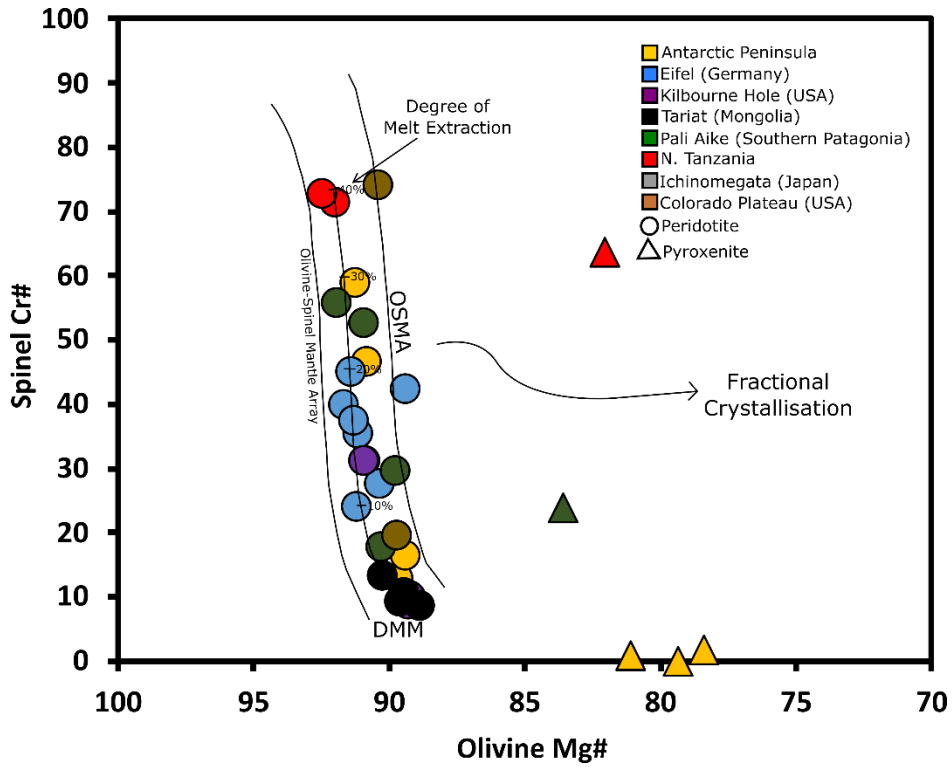

Figure 6.2. Olivine Mg# and Spinel Cr# compositions of samples with this study overlayed by the melting model of Jaques & Green (1980). Data from Chapter 4 and Appendix Tables 1 and 4. Samples KH1, KH2 and KH4 are behind TM1, TM2, TM3 and TM4.

Based on Figure 6.2, Kilbourne Hole spinel peridotites record 0 to 10% partial melting for KH1, KH2 and KH4, while KH3D represents the residue of approximately 13% melt extraction. Spinel-bearing peridotites TH33 and BP1 from the Colorado Plateau record varying degrees of melting, from ~8% to ~40%, respectively. Spinel lherzolites from the Tariat Volcanic Field have similar olivine and spinel compositions to the fertile upper mantle and have experienced up to 4% melt extraction. The West Eifel peridotites all have olivine-spinel compositions that are more depleted than the MORB-source mantle, with melting extraction ranging from 10 to 20%. Some of Antarctic Peninsula spinel peridotites (KG.3719.25, L7.201.1.41 and BN) have fertile olivine-spinel signatures indicative of ~4 – 6% melt extraction, while other samples (KG.3610.10A and KG.3609.21) have more depleted signatures indicative of 20 to 30% melt extraction. The spinel-bearing Pali Aike peridotites have varying olivine-spinel signatures, with LT1 and CP62 at <10% melt extraction, CP33 at ~13% melt extraction and LT16 and PA3-5 at 25 to 30% melt extraction. The spinel-bearing peridotites from Northern Tanzania (BD794 and BD797) have very depleted signatures indicative of ~40% melt extraction. Finally, the peridotite from the Oga Peninsula is spinel free, but given the olivine compositions and published spinel compositions from the same

location, it likely represents a melt residue that has experienced approximately 10% melt extraction.

6.4 Mineral chemistry and petrography

As previously outlined, both the mineralogy and mineral chemistry are sensitive to melting; increasing degrees of partial melting lead to a more depleted mineral chemistry (i.e. increasing spinel Cr# and increasing olivine Mg#) and compositions (i.e. lower clinopyroxene and higher orthopyroxene and olivine). These coupled effects have been modelled for mineral chemistry and modal compositions at varying degrees of partial melting (e.g. Walter, 2003; Herzberg, 2004). However, these systematics are also sensitive to metasomatic perturbation, such as Si-enrichment (e.g. Boyd, 1989). This Si-enrichment enables olivine-consuming reactions that produce excess orthopyroxene at a given olivine Mg# compared to the array for melt residues (e.g. Modal olivine = 0.513 + 0.167 x Melt Fraction; Niu, 1997).

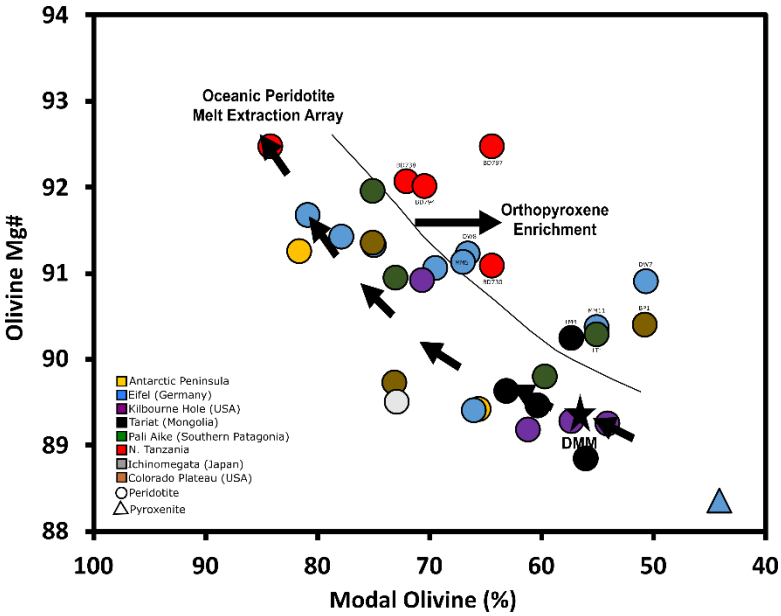

Figure 6.3. Modal olivine and olivine Mg# of samples from this study compared to the melting model proposed by Boyd (1989) and quantified by Niu as Modal olivine = 0.513 + 0.167 x Melt Fraction. Samples from this study from Table 3.1 in Chapter 3 and Appendix Table 1.

Figure 6.3 shows that samples which display evidence for Si/orthopyroxene enrichment are BP1 from the Colorado Plateau, TM4 from the Tariat Volcanic Field, DW7, DW8, MM5 and MM11 from the West Eifel, LT1 from Pali Aike and BD738, BD794 and BD797 from Northern Tanzania. All other samples plot along the mantle melt extraction array of Boyd (1989).

6.5 Whole-rock major element chemistry

Because the mineral chemistry and modal mineralogy of peridotites are directly related to the degree of partial melting involved in the residues that form the lithospheric mantle, the whole-rock compositions are also sensitive to this process. Various melting systematics are outlined below and compared to the calculated whole-rock major element chemistry of samples presented in this study (Appendix Table 21). These are calculated by integrating the modal mineralogy of a sample (Table 3.1) with their corresponding major-element mineral chemistry (see Chapter 4 and Appendix Tables 1 to 8). This is shown by Equation 6.10 and an example is given for CaO.

Equation 6.1

$$C_i^{whole\ rock} = \left(X^{ol} \times C_i^{ol}\right) + \left(X^{opx} \times C_i^{opx}\right) + \left(X^{cpx} \times C_i^{cpx}\right) + \left(X^{spinel} \times C_i^{spinel}\right) + \left(X^{garnet} \times C_i^{garnet}\right) \text{ etc...}$$

Where: X^{min} is the abundance in % and C_i^{min} is the concentration of a mineral for a given element.

Boyd (1989) observed the relationship between whole-rock Al_2O_3 and CaO in mantle peridotites. Whereby, fertile mantle has high Al_2O_3 and CaO, which progressively decreases during melting and becomes enriched in more refractory elements (e.g. FeO). This relationship is highlighted in Figure 6.4 and matches the observations made by the chemistry of co-existing olivine and spinel (Figure 6.2). The xenoliths from Kilbourne Hole and Tariat are dominated by fertile compositions, with the Colorado Plateau, Antarctic Peninsula, West Eifel, Southern Patagonia, Northern Tanzania and the Oga Peninsula all preserving compositions consistent with greater degrees of partial melting.

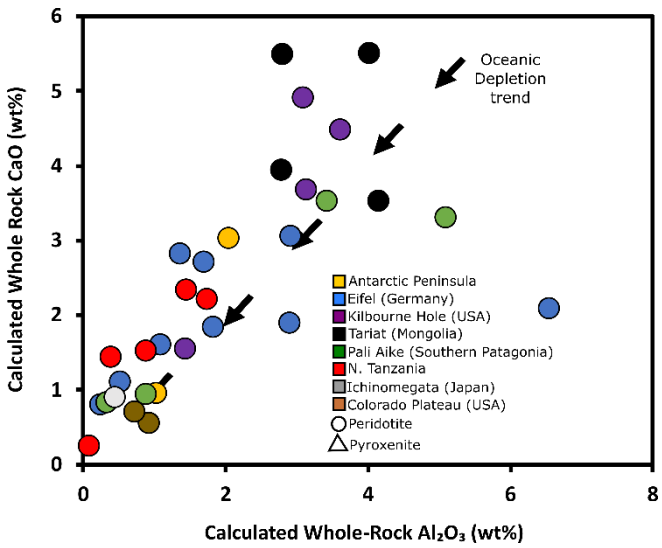

Figure 6.4. Whole rock Al_2O_3 (wt%) and CaO (wt%) of samples from this study compared to the melting array from abyssal peridotites of Boyd (1989). Data are from Appendix C table 22.

Since the findings of Boyd (1989), more sophisticated whole-rock melting models have been developed for peridotites (e.g. Waters, 2003; Herzberg, 2004). These have provided important insights to the secular evolution of the lithospheric mantle (e.g. Griffin *et al.*, 2003; Herzberg & Rudnick, 2012) and the upper mantle (e.g. Herzberg *et al.*, 2010) together with metasomatic reactions in the lithospheric mantle (e.g. Tomlinson & Kamber, 2021). Figure 6.5 compares the whole-rock compositions of samples from this study to those in melting models of Herzberg (2004).

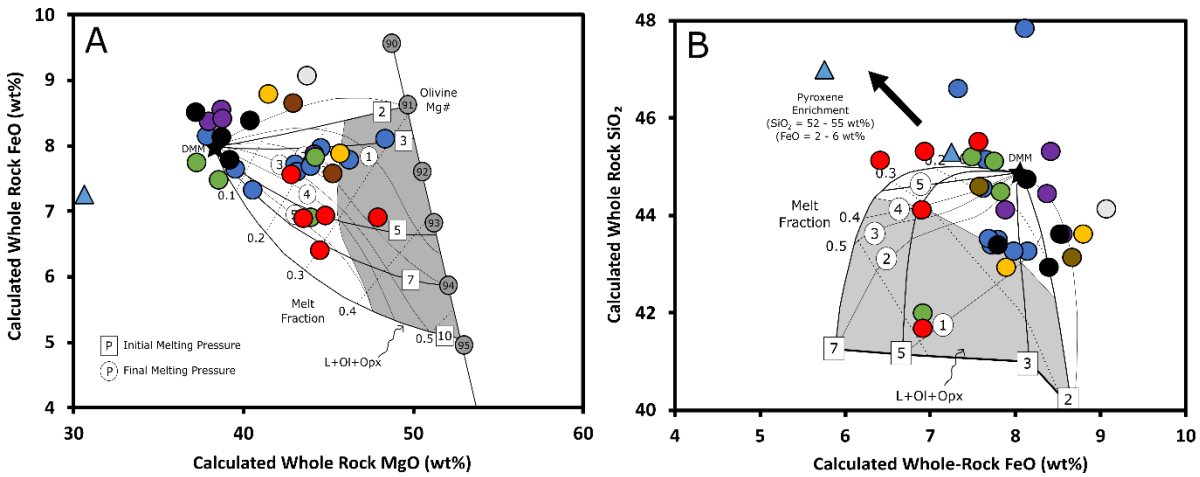

Figure 6.5. Samples from this study overlain on melting models A) Whole rock MgO (wt%) and FeO (wt%) and B) FeO and SiO_2 from Herzberg (2004).

Overall, these results are consistent with interpretations from petrography, mineral and whole-rock chemistry. Furthermore, Figure 6.5 shows that some peridotites plot outside the

predicted compositions of melt residues and highlights the role of SiO_2/orthopyroxene enrichment from metasomatism.

6.6 Whole-rock trace-element chemistry

Insights from petrography, mineral compositions, and whole-rock chemistry provide vital information on the melting history of the residues that formed the lithospheric mantle. However, except for identifying Si/orthopyroxene enrichment, the extent of subsequent metasomatism within the lithospheric mantle is more challenging to estimate. This section investigates calculated whole-rock (and clinopyroxene if whole-rock information is not available) trace element compositions (Chapter 5 and Appendix Table 23) to constrain the role of partial melting and metasomatism within the lithospheric mantle. These are calculated using the same method presented in Equation 6.10.

6.2.3.1 Southern USA

6.2.3.1.1 Kilbourne Hole

Ultramafic xenoliths from the Kilbourne Hole has low whole-rock $[La/Yb]_N$ of 0.07 to 0.95. Where peridotite KH3D $[La/Y]b_N$ = 0.92) have a composition indicative of metasomatic enrichemt. Comparatively, KH2, KH4 and KH5 have more depleted compositions. Following the methods of Warren (2016; see Chapter 1), these compositions equate to 1.5 to 5% melt extraction (Figure 6.6). Pyroxenite KH1 has $[La/Yb]_N$ of 0.95 indicative of crystallisation of a small-fraction melt.

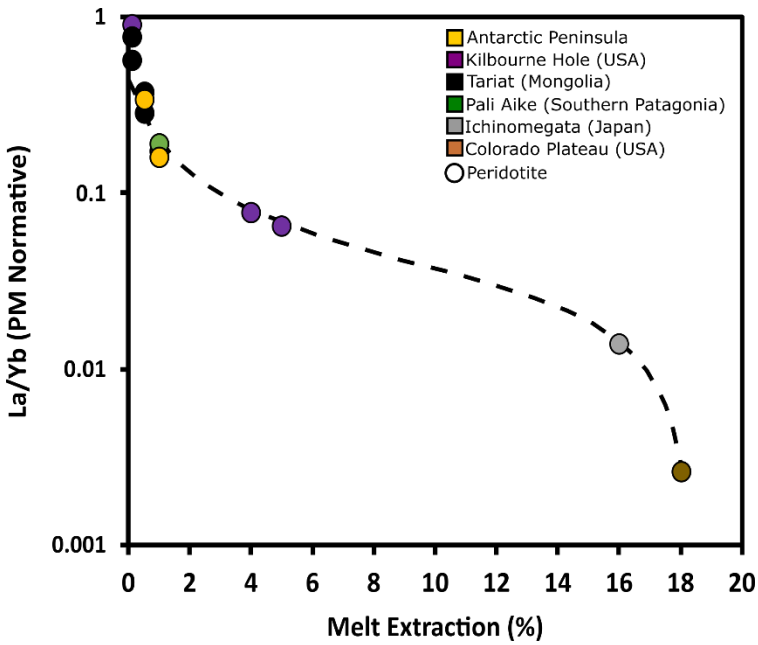

Figure 6.6. $[La/Yb]_N$ of peridotites with melt extraction (%) constraints from melting model of Warren (2016).

Extended incompatible trace element compositions of spinel peridotites (Figure 6.6) provide important insights into the metasomatic history of the lithospheric mantle beneath Kilbourne Hole. The most distinctive composition is displayed by KH5. Overall, this xenolith has a depleted signature with distinct negative Hf, Zr and Y anomalies and positive Nb and Ta anomalies. Negative Hf, Zr and Y anomalies are observed in all samples in addition to negative Sr in KH1 and KH2. These observations coupled with those from major elements are consistent with the interpretation that the lithospheric mantle beneath Kilbourne Hole formed as a residue from the convecting upper mantle and has undergone minor amounts of metasomatic enrichment by low-Mg carbo-silicic high-density fluids, akin to those proposed by Weiss *et al.* (2008). The fluids are likely sourced from a subduction zone related to the Farallon Plate.

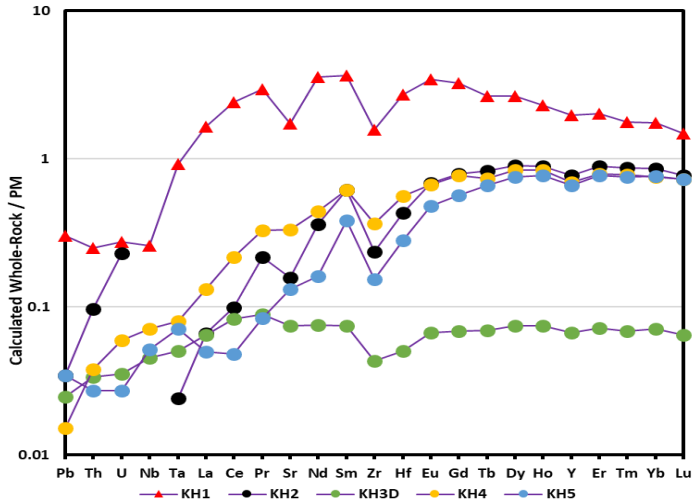

Figure 6.6. Extended whole-rock trace element systematics for peridotite and pyroxenite samples analysed from the Kilbourne Hole.

6.2.3.1.2 Colorado Plateau

Peridotite xenoliths from the Colorado Plateau have whole-rock $[La/Yb]_N$ values of 0.003 to 3. The garnet-bearing peridotites (TH17 and TH33) record evidence of metasomatic enrichment whilst the spinel lherzolite (BP1) has a very depleted signature. Using the melting model of Warren (2016), BP1 $[La/Yb]_N$ represents a residue of 18% melt extraction.

Determining the metasomatic signature recorded by xenoliths from the Colorado Plateau is challenging due to the general absence of distinctive geochemical anomaloies in the REE, LILE and HFSE (Figure 6.7). However, garnet-bearing harzburgite, TH17, exhibits negative anomalies at Zr, Nb and Ta and TH33 also shows negative anomalies in Nb and Ta. Such geochemical characteristics are recognised in xenoliths derived from subduction zone settings and previously been attributed to metasomatism of the lithosphere beneath the Colorado Plateau (e.g. Li *et al.*, 2008).

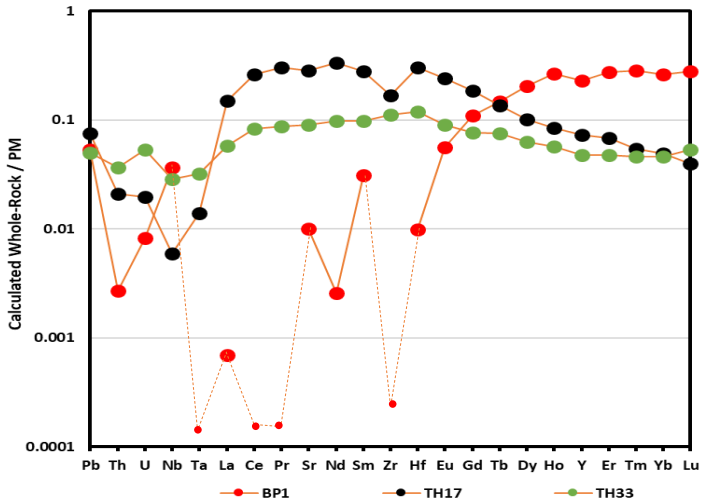

Figure 6.7. Extended whole-rock trace element systematics for peridotite samples analysed from the Colorado Plateau.

6.2.3.2 Tariat Volcanic Field

Spinel lherzolites from the Tariat Volcanic Field all have low whole-rock $[La/Yb]_N$ values (0.3 to 0.8). These compositions are similar to the depleted MORB mantle (Workman & Hart, 2005) and according to the melting model of Warren (2016) represent <1% melt extraction.

The normalised trace element abundances of the spinel lherzolites (Figure 6.8) are characterised by negative Y, Zr, Hf, Nd, Ta and Nb abundances. Based on these properties it is likely that the lithospheric mantle beneath Tariat formed as a depleted residue from the convecting mantle and has undergone only a minor amount of metasomatism by small fraction carbonate-rich melts and fluids and is consistent with previous studies (e.g. Carlson & Ionov, 2019; Kourim *et al.*, 2021).

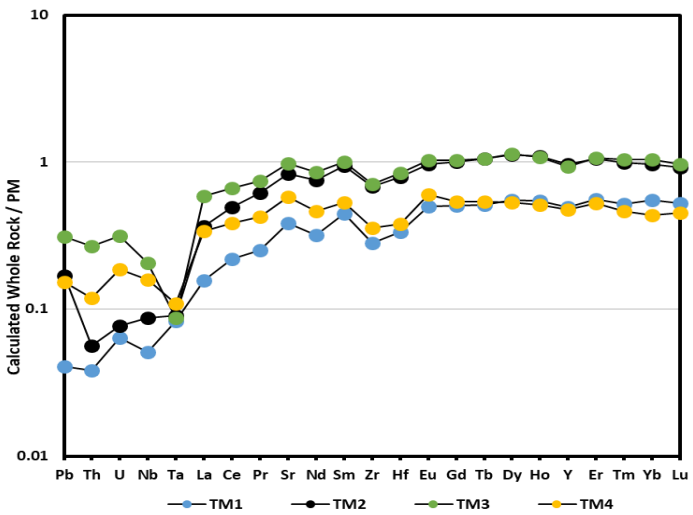

Figure 6.8. Extended whole-rock trace element systematics for peridotite samples analysed from the Tariat Volcanic Field.

6.2.3.3 West Eifel Volcanic Field

Ultramafic xenoliths from the West Eifel Volcanic Field have whole-rock $[La/Yb]_N$ of 1.3 to 14.8, which suggest that they have undergone varying levels of metasomatic enrichment. The normalised elemental abundances of the xenolith suite from the West Eifel are shown in Figure 6.9 and are separated into groups building on the trace-element characteristics outlined by Witt-Eickschen et al. (2003).

Group 2 xenoliths are characterised by an overall enriched LREE/HREE signature with negative HFSE anomalies at Hf, Zr, Nb and Ta anomalies and include samples DW3, DW10, MM5, MM8 and MM11 (6.9A). These HFSE depletions are most consistent with metasomatism by subduction-zone derived fluids or melts. However, the presence of negative Sr anomalies are more consistent with upper-mantle metasomatism. Therefore, these samples likely represent metasomatism by a melt from a mixed upper-mantle and recycled lithosphere reservoir. MM11 is anomalous because it has positive Ta and Nb signatures. These may be indicative of a carbonatite melt, but are more likely to be the product of over-representative amphibole abundances which would increase Nb and Ta abundances.

Group 3 xenoliths include samples DW8 and G17, which have very distinctive depletions at Zr, Hf, Ta and Nb (6.9B). These strong Nb and Ta anomalies are indicative of subduction-zone metasomatism.

Group 4 includes pyroxenite xenoliths MM6 and DW5, with LREE/HREE enrichment (6.9C). Their distinct negative anomalies at Sr and Zr were recognised by Witt-Eickschen *et al.* (2003)

and linked these to high-pressure cumulates from the most recent volcanism in the area.

Finally G18 has moderate LREE/HREE but is unusual because it has positive Zr and Hf and negative Nb and Ta anomalies. Furthermore, it is enriched in Sr, U and Th. These signatures have previously been observed in alkaline rocks from the Calatrava Volcanic Field and have been linked to melts that have fractionated titanian pargasite and kaersutite (Tiepolo *et al.*, 2001).

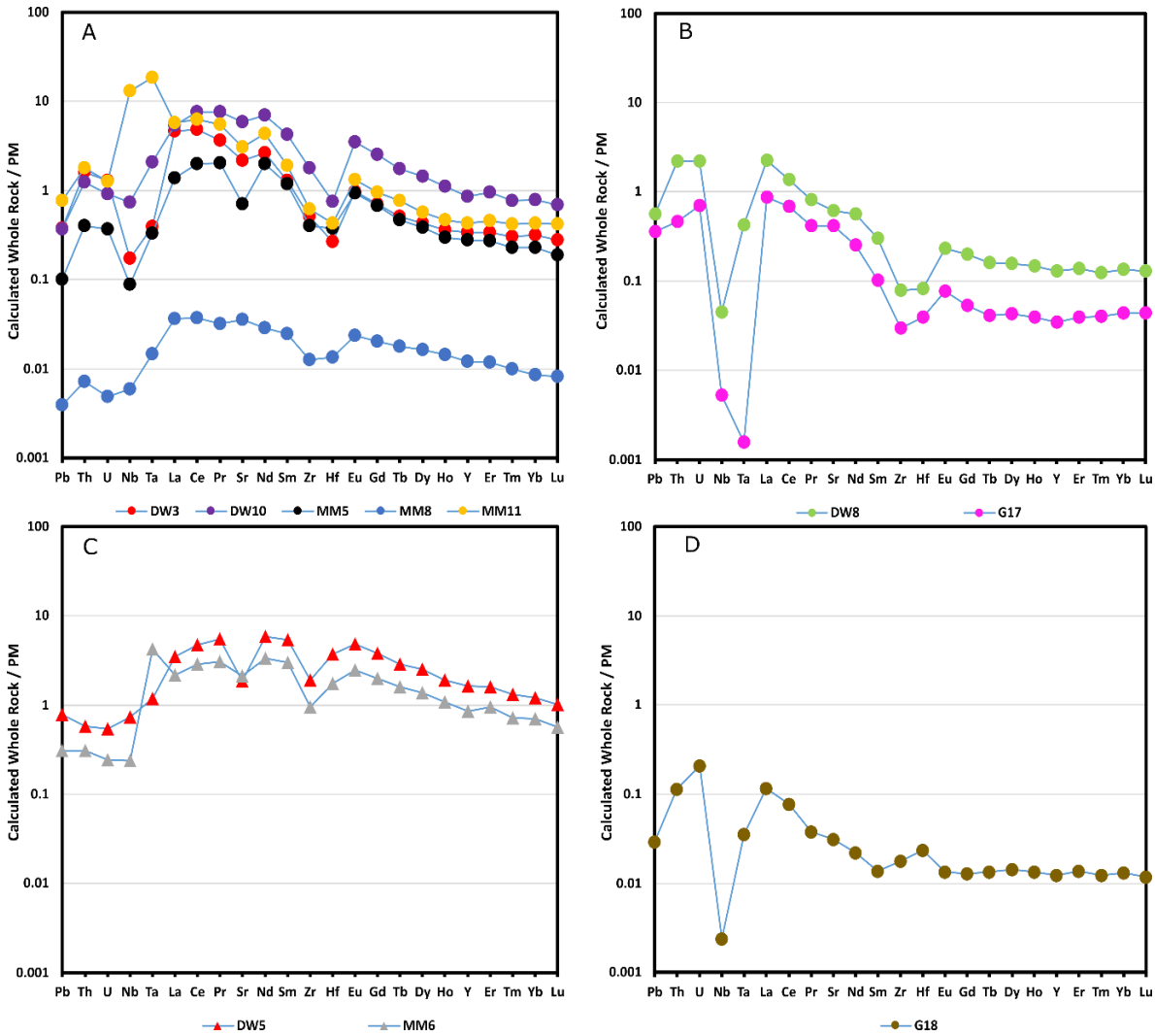

Figure 6.9. Primitive mantle normalised trace element patterns for peridotites analysed from the West Eifel Volcanic Field. A) Group 2; B) Group 3; C) Group 4; D) Novel Group 5.

6.2.3.4 Antarctic Peninsula

Ultramafic xenoliths from the Antarctic Peninsula have whole-rock $[La/Yb]_N$ of 0.16 to 13.5. Four separate groups of metasomatised xenoliths have been identified based on their trace element characteristics:

Group 1: Spinel peridotites KG.3610.10A and KG.3609.21 have LREE/HREE enrichment and depleted MREE relative to HREE (6.10A). Furthermore, they have distinct negative HFSE anomalies at Ti, Zr, Hf, Nb and Ta. These signatures are most consistent with metasomatism by melts from a subduction zone and their continental margin arc setting.

Group 2: L7.201.1.41 has slightly enriched LREE relative to HREE (6.10B). Furthermore, it has slightly negative anomalies at Ti, Zr, Hf, Nb and Ta and negative Y, Sr and Pb. These features are most consistent with metasomatism by low-Mg carbo-silicic high-density fluid likely from a subduction zone.

Group 3: Spinel peridotites KG.3719.25 and BN have depleted LREE relative to HREE and similar MREE/HREE signatures. Furthermore, they have slight HFSE anomalies at Ti, Zr, Hf, Ta and Nb. Using the melting model of Warren (2016), KG.3719.25 and BN have low $[La/Yb]_N$ indicative of <1 and 1% melt extraction, respectively. These peridotites appear to have formed as a depleted residues in the upper-mantle that has undergone a small amount of metasomatism by melts from the recycled lithosphere.

Group 4: Pyroxenites (L7.201.1.74c, R.5194.2I and R.5194.2M) are slightly enriched in LREE and MREE relative to HREE (6.11C). They exhibit clear negative anomalies at Zr and Sr and enrichment in Th and U. These compositions are indicative of a carbonatite melt likely sourced from the convecting upper mantle.

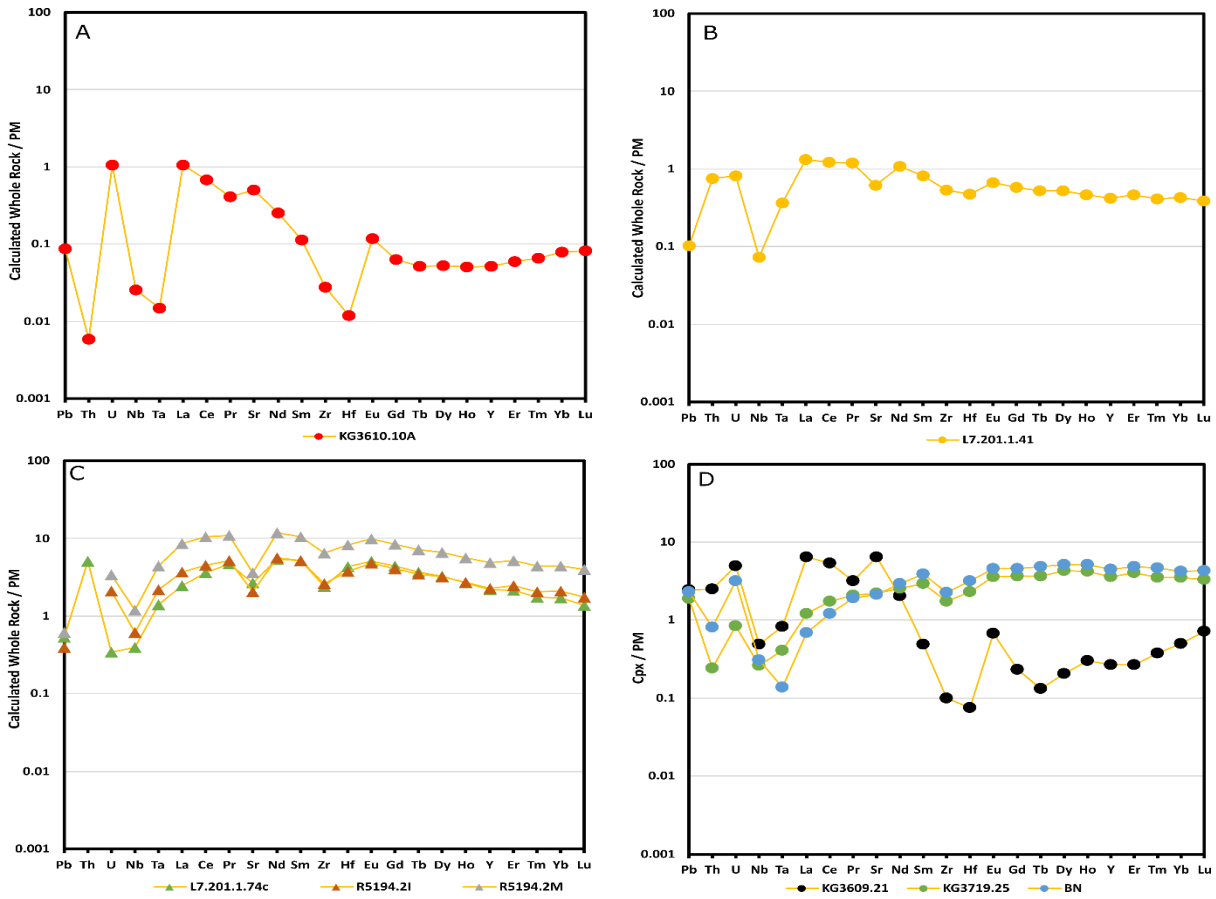

Figure 6.10. Primitive mantle normalised whole-rock trace element systematics for peridotite samples analysed from the Antarctic Peninsula. A) Group 1; B) Group 2; C) Group 3; D) Cpx analysis.

6.2.3.5 Southern Patagonia

Ultramafic xenoliths from southern Patagonia have whole-rock $[La/Yb]_N$ values of 0.005 to 10.3. A garnet lherzolite (CP33) and harzburgite (LT16) record metasomatic enrichment while lherzolites LT1 and CP62 have depleted signatures. Using the melting model of Warren (2016), LT1 has a $[La/Yb]_N$ value indicative of <1% melt extraction while orthopyroxenite sample CP62 has $[La/Yb]_N$ indicative of 17.5% melt extraction. Five separate groups have been identified based on their distinctive trace element characteristics:

Group 1: Peridotite LT1 is slightly depleted in LREE relative to HREE, similar MREE to HREE (6.11A), has distinctive negative anomalies at Ti, Hf and Zr and a slightly negative anomaly at Sr. These are indicative of metasomatic enrichment from a melt from the subducted lithosphere mixed with the upper-mantle.

Group 2: Harzburgite LT16 shows slightly enriched LREE relative to HREE and strong MREE enrichment relative to LREE and HREE (6.11B). Furthermore, this xenolith has positive

anomalies at Zr, Hf and Ta. This sample is akin to that observed by Ionov *et al.* (2002) from Spitsbergen and may indicate metasomatic enrichment by carbonatite melts.

Group 3: Garnet-bearing peridotite CP33 is enriched in LREE relative to HREE (6.11C) and has distinctive negative anomalies at Hf, Nb and Ta along with a positive Sr anomaly. This composition is most consistent with metasomatic enrichment by melts sourced from a subduction zone.

Group 4: Pyroxenites LT14 and LT15 have similar compositions with negative HFSE anomalies at Hf, Eu, Zr and Hf (6.11D). Overall, this trace-element signature is most akin to a hypothetical subduction zone metasomatic model.

Group 5: Orthopyroxenite CP62 is a phlogopite-bearing garnet pyroxenite. Overall, it has a very depleted signature but notable positive anomalies at Zr and Hf (6.11F). This likely relates to strong partitioning of Hf and Zr into mica. Determining source and type of metasomatic enrichment is challenging.

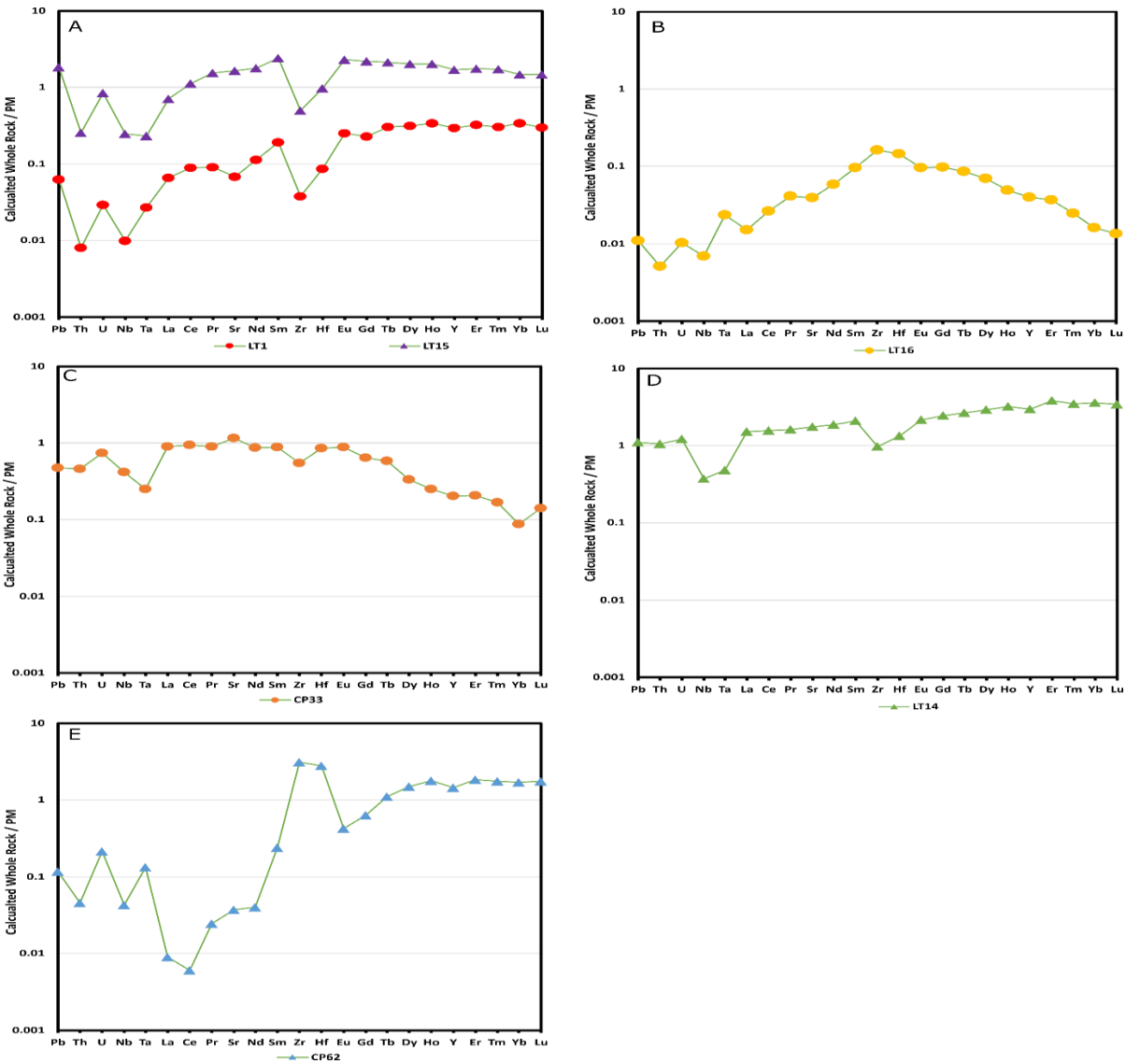

Figure 6.11. Extended whole-rock trace element systematics for peridotite samples analysed from Southern Patagonia. A) Group 1; B) Group 2; C) Group 3; D) Group 4; E) Group 5.

6.2.3.6 Northern Tanzania

Ultramafic xenoliths from northern Tanzania exhibit large ranges in their $[La/Yb]_N$ (1.4 to 145.2) indicative of variable metasomatic enrichment. The nature of these metasomatic signatures are outlined by Figure 6.12.

Samples BD794 has a strong LREE/HREE enrichment with negative Dy, Sm and U anomalies. Overall, this signature is most consistent with metasomatic enrichment by an upper-mantle melt. In contrast, garnet lherzolite BD730 and olivine clinopyroxenite BD816 have a more complex trace-element patterns. Both have negative anomalies at Zr, Ta, Nb and positive anomalies at Th. These are consistent with metasomatic enrichment from a hybrid

metasomatic melt from the convecting upper-mantle and recycled oceanic lithosphere.

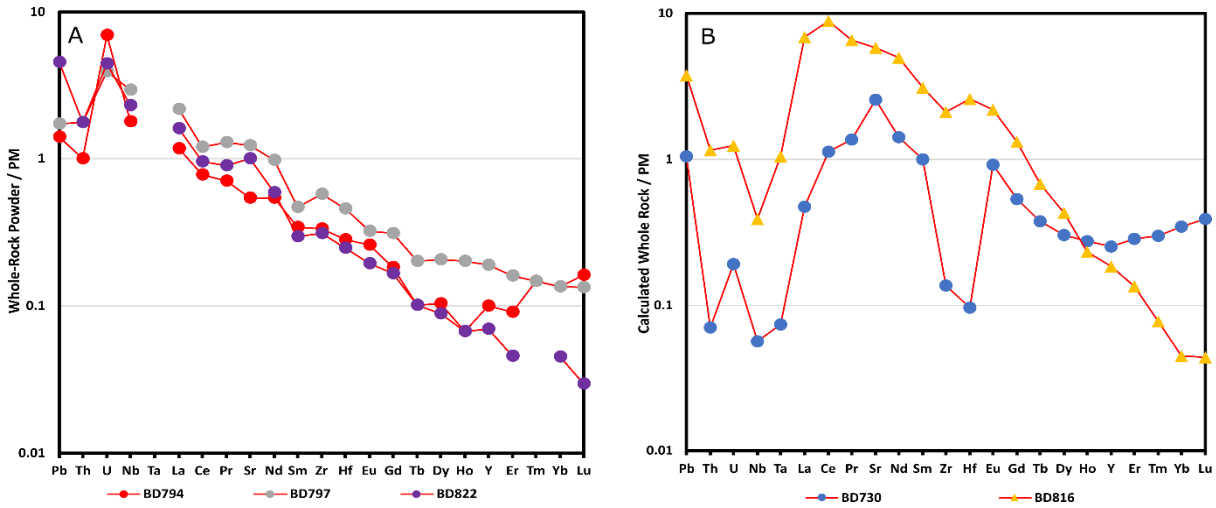

Figure 6.12. Extended whole-rock trace element systematics for peridotite samples analysed from Northern Tanzania. A) whole-rock powder calculations B) calculated whole-rock compositions.

6.2.3.7 Oga Peninsula

The spinel harzburgite (J1) from the Oga Peninsula has a low whole-rock $[La/Yb]_N$ (0.014). Based on the melting model of Warren (2016), J1 has values indicative of 16% melt extraction. The normalised trace-element pattern for this xenoliths exhibits negative anomalies at Zr, Hf, Nb, Ta, Sr and Y (Figure 6.13). Overall, this signature is consistent with this sample forming from the depleted upper-mantle with a small amount of metasomatic enrichment from a low-Mg carbo-silicic high-density fluid.

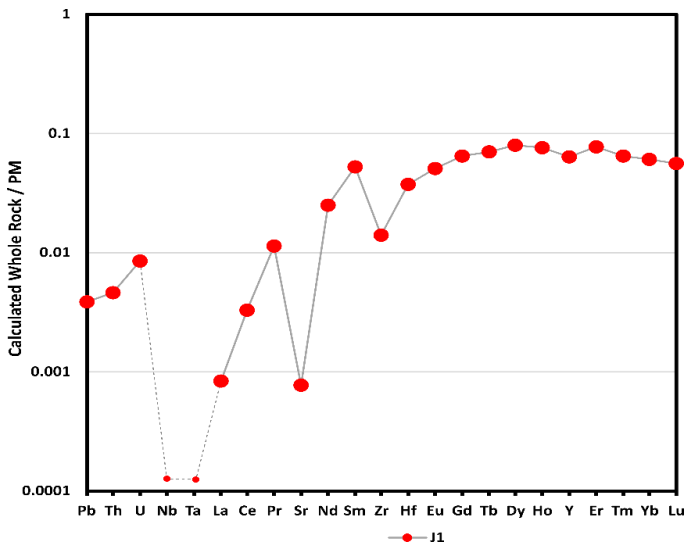

Figure 6.13. Extended whole-rock trace element systematics for peridotite samples analysed from the Oga Peninsula.

6.7 Comparison of melting and metasomatism signatures

Outlined previously is the sensitivity of olivine Mg#, spinel Cr# and whole-rock $[La/Yb]_N$ to melting. These are compared in Figure 6.14 to evaluate the interplay of melting and metasomatism. Hypothetically, melting should decrease [La/Yb] and increase olivine Mg# and Cr#. However, observations from the peridotites presented in this study are inconsistent with these models. This is because peridotites with higher $[La/Yb]_N$ have higher co-existing olivine Mg# and spinel Cr#. This must be explained by metasomatic enrichment of incompatible trace elements not affecting the major-element composition of a peridotite. Whereby, peridotites may undergo metasomatic enrichment but retain highly-depleted major element mineralogy (e.g. Gibson *et al.*, 2013).

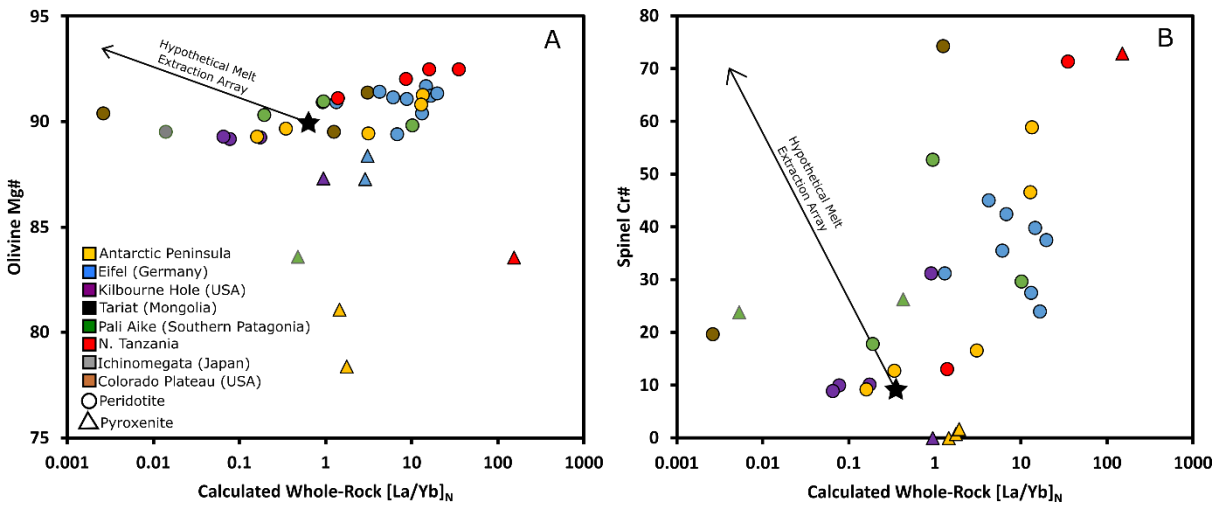

Figure 6.14. Comparative chemistry indicative of melting and metasomatism; A) Calculated bulk xenolith $[La/Yb]_N$ and Olivine Mg# and; B) Calculated bulk xenolith $[La/Yb]_N$ and spinel Cr#.

6.8 Summary of investigated samples

Using the insights displayed here combined with previous observations displayed in Chapters 4 and 5, 4 important groups of mantle xenoliths are identified here.

The most 'depleted' peridotites from Northern Tanzania. These have the most depleted major element compositions which represent mantle residues that have experienced approximately 40% melt extraction. In contrast, they have highly enriched trace-element signatures which are indicate interaction with melts from the convecting upper-mantle and recycled oceanic lithosphere.

The most 'fertile' peridotites are from the Kilbourne Hole, Tariat Volcanic Field and

Ichinomegata. These have the most fertile major element compositions indicative of <10% melt extraction, with Kilbourne Hole and Tariat Volcanic Field dominated by DMM-like olivines (Mg# = 89.5). They also have the most depleted incompatible trace-element chemistry ($[La/Yb]_N$ = 0.01 to 0.8) indicative of their formation as a residue from melting in the convecting upper-mantle with slight influence by low-Mg carbo-silicic high-density fluids.

Variably depleted and fertile peridotites occur in the Antarctic Peninsula, Southern Patagonia, West Eifel Volcanic Field and Colorado Plateau. These samples record varying melting regimes within a single location, ranging from ~1% to ~30% melt extraction. They also record highly variable metasomatic signatures that indicate variable melt and fluid compositions from mantle and recycled lithosphere sources.

Pyroxenite samples which are channelised melts with olivine (Mg# = 78.4 to 88.4) and clinopyroxene (Mg# = 78.7 to 90) which are more Fe-rich than the DMM (olivine Mg# = 89.5, clinopyroxene # = 90.8). Furthermore, they are crystallised from small fraction melts and fluids.

Chapter 7. Thermo-barometry

7.1 Introduction

The temperatures (*T*) and pressures (*P*) in Earth's lithospheric mantle range from ~ 800 °C to 1300 °C and ~ 1 to 8 GPa, respectively (McKenzie 8 Bickle, 1988; Figure 1.2). In continental off-craton settings the pressure interval is typically between 1 and 4 GPa (30 to 125 km) but within the sub-cratonic mantle this extends to ~ 7 GPa (230 km).

Geothermobarometry represents the most important tool for examining compositional variations in the lithospheric mantle and also its physical properties, e.g. geothermal gradients, the depths of the mechanical and thermal boundary layers and also the lithosphere-asthenosphere boundary. Here, the pressure-temperatyre (*PT*) of a given sample is estimated using the major element compositions of clinopyroxene, orthopyroxene and garnet compositions that were presented in Chapter 4.

7.2 Garnet-bearing peridotites

Several methods have been employed to calculate the final equilibration pressures of garnet-bearing mantle xenoliths. The most widely used involve the Al-in-orthopyroxene barometers of Nickel & Green (1985; NG85), Brey *et al.* (1990) and Brey *et al.* (2008). These are all based on the pressure-dependence of the Mg-tschermak ($MgAl_2SiO_2$) component of orthopyroxene and pyrope (Equation 7.1).

$$Mg_2Si_2O_6 + MgAl_2SiO_6 = Mg_3Al_2Si_3O_{12} \qquad \text{(Equation 7.1)}$$

Nimis & Grutter (2010) argued that the most accurate barometer for garnet peridotites is that of Nickel & Green (1985). This is due to the overestimates in pressure in the formulation by Brey *et al.* (1990) and the low precision of Brey at al. (2008) at moderate pressures. In this work, the final equilibration pressures of garnet-bearing peridotites are therefore calculated using the NG85 method, which produces an error of ± 0.3 GPa (Equation 7.2).

$$P_{NG85}^{Al-opx-gt} = \left(\frac{1}{-[1.83.3+1.78.98X_{Al}^{M1}(1-X_{Al}^{M1})]}\right) \times \left(-RTln\left[\left[1 - X_{gt}^{Ca})^3(X_{al}^{gt})^2\right] \times \left[X_{Mg,Fe}^{M1}\left(X_{Mg,Fe}^{M2}\right)^2 X_{Al}^{M1}\right]^{-1}\right] - 900\left(X_{Ca}^{gt}\right)^2 - 3400(2\left(2(X_{Ca}^{gt})^2 - X_{Mg}^{M1}X_{Cr}^{opx}\right] - X_{Ca}^{gt}X_{Cr}^{gt}(90853 - 52.1T) - 7590X_{Fe}^{gt}X_{Ca}^{gt} + 5157X_{Mg}^{M1}X_{Fe}^{M1} + 6047 - 3.23T\right) \qquad \text{(Equation 7.2)}$$

In which:

$$X_{Al}^{M1} = (Al - Cr - 2Ti + Na)/2$$

$$X_{Mg,Fe}^{M1} = 1 - X_{Al}^{M1} - Cr - Ti$$

$$X_{Mg,Fe}^{M2} = 1 - Ca - Na - Mn$$

$$X_{Mg}^{M1} = [Mg/Mg + Fe]X_{Mg,Fe}^{M1}$$

$$X_{Ca}^{gt} = [Ca/(Ca + Mg + Fe + Mn)]^{gt}$$

$$X_{Al}^{gt} = [Al/(Al + Cr)]^{gt}$$

$$X_{Cr}^{gt} = [Cr/(Al + Cr)]^{gt}$$

Nimis & Grutter (2010) also evaluated the most suitable thermometers for garnet-bearing peridotites. They found that the most accurate results were obtained using the two-pyroxene thermometer of Taylor (1998; TA98 shown by Equation 7.3), which has an accuracy of ΔT = +6 °C and a precision of 1σ = 31 °C.

$$T_{TA98}^{cpx-opx}(K) = \frac{24.787 + 678P(GPa)}{15.67 + 14.37Ti^{cpx} + 3.69Fe^{cpx} - 325X_{ts} + (lnKd)^2} \quad \text{(Equation 7.3)}$$

Where: lnKd = ln[a(EN)^{cpx}]-ln[a(En)^{cpx}]; X_{ts} = (Al+Cr+Na)^{cpx}; a(En) = (1-Ca-Na).(1-Al^{VI}-Cr-Ti).(1-Al^{IV}/2)^2

The Ca-in-enstatite thermometer of Brey & Kohler (1990; BKN90) has also been widely used for harzburgites (Equation 7.4). However, Nimis & Grutter (2010) found that this method is only accurate above 1000°C, with a strong bias at lower temperatures and therefore less reliable. In this work, the thermobarometry for garnet-bearing peridotites is therefore calculated using the Taylor (1998) two-pyroxene thermometer combined with the Nickel & Green (1985) Al-in-Opx barometer.

$$T_{BKN90}^{Ca-in-opx}(K) = \frac{6425 + 26.4P}{-\ln(Ca^{opx}) + 1.843} \quad \text{(Equation 7.4)}$$

7.3 Garnet-free peridotites and pyroxenites

Currently, the available barometers for garnet-free peridotites and pyroxenites are very imprecise (e.g. D'Souza *et al.* 2020). This is primarily a result of the poor pressure-dependent relationship between olivine-orthopyroxene-clinopyroxene-spinel and the

absence of garnet as a pressure sensitive indicator (e.g. Nickel & Green, 1985). Therefore, pressure estimates are based on the stability field of coexisting minor minerals (i.e. spinel or plagioclase). Under upper-mantle conditions (800 to 1300 °C) spinel is stable between 0.5 and 2.5 GPa and plaiogclaise at <0.5 GPa (e.g. Gasparik, 1984; Ziberna *et al.* , 2013). Garnet-free peridotites and pyroxenites analysed in this study have minor spinel (Chapter 3), therefore a pressure of 1.5 GPa is assumed in thermometers.

In this study, the Taylor (1998) two-pyroxene thermometer is used for spinel peridotites with coexisting orthopyroxene and clinopyroxene with assumed pressure of 1.5 GPa. For clinopyroxene-only (Equation 7.5), or orthopyroxene-only pyroxenites (Equation 7.6), the temperatures are calculated using the formulas from Mercier (1980; M80) also assuming 1.5 GPa.

(Equation 7.5)

$$T_{M80}^{cpx} = \frac{(-7537.5 \times \ln(XKw) + 61152)}{D} - 273.16$$

Where: XKw = (1-2 x W)/(1-2 x W); XKa = A/(1-A)/(1-2.87xFCR)^2; D = ln(XKa) x (ln(XKw) – 11.2724 x ln(XKw) + 2.2595 x ln(XKw) +32.371; W = XCa/(XCa + XMg + XFe + XMn); A = (XAl – XNa)/2; FCR = XCr/(XAl + XCr – XNa).

XAl, XCr, XFe, XMn, XMg, XCa and XNa represent atom fractions for six-oxygens per formulae.

$$T_{M80}^{opx} = \frac{-6308.5 \times \ln(XKw) + 45549}{D} - 273.16$$

(Equation 7.6)

Where: XKw = (1-2 x W)/(0.667 + 0.667 x W); XKa = A/(1-A)/(102.87 x FCR)^2; D = ln(XKa) x ln(XKw) – 8.6751 x ln(XKw) + 2.2595 x ln(XKa) + 24.568; W = XCa/(XCa + XMg + XFe + XMn); A = (XAl – XNa)/2; FCR = XCr/(XAl + XCr – Xna)

XAl, XCr, XFe, XMn, XMg, XCa and XNa represent atom fractions for six-oxygens per formulae.

The challenge with using temperature estimates from clinopyroxene or orthopyroxene based on the formulation of Mercier (1980) is that they are frequently overestimates. In order to obtain internally consistent temperatures, the estimates from Mercier (1980) are corrected by using a coefficient calculated from samples that have both TA98 and M80

estimates (Figure 7.1). For clinopyroxene-only samples, this equates to a correction factor of 0.9468 and for orthopyroxene-only samples of 0.8411 (Equations 7.7 and 7.8).

$$T_{T98-M80}^{cpx} = T_{M80}^{cpx} \times 0.9469 \qquad \text{(Equation 7.7)}$$

$$T_{T98-M80}^{opx} = T_{M80}^{opx} \times 0.8411 \qquad \text{(Equation 7.8)}$$

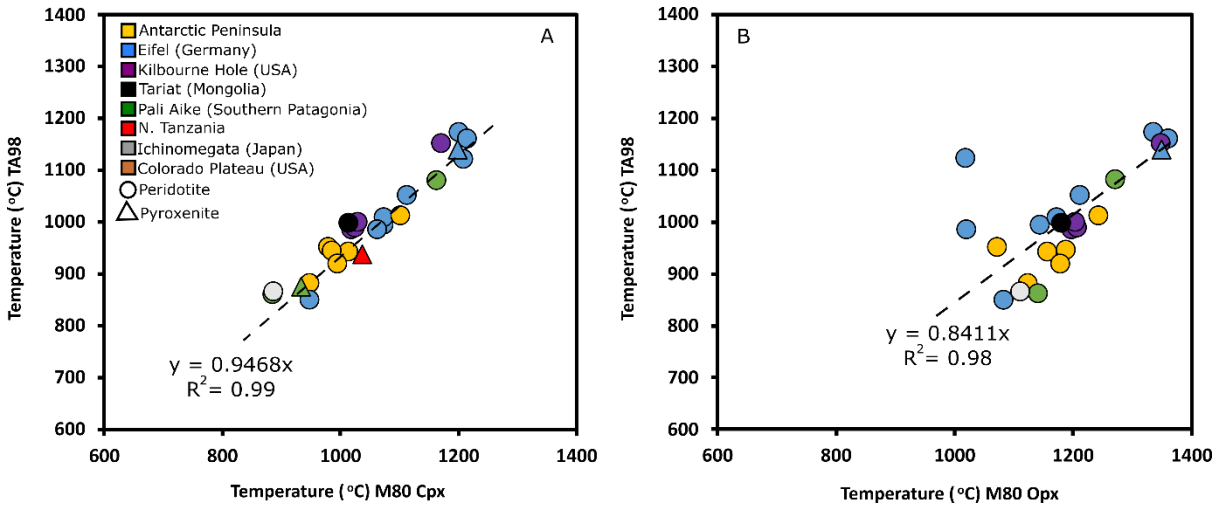

Figure 6.1 A) Final equilibrium temperatures of samples determined using both Mercier (1980) clinopyroxene-only and Taylor (1998) clinopyroxene-orthopyroxene formulas. B) Temperature estimates of samples using both Mercier (1980) orthopyroxene-only and Taylor (1998) clinopyroxene-orthopyroxene formulas.

Using the equations presented in sections 7.2 and 7.3 are difficult to reconstruct, therefore to reproduce these calculations the reader is advised to use a programme titled PTQuick (http://www.dimadd.ru/en/Programs/ptquick).

7.4 Geotherm extrapolations

More accurate final equilibration pressure estimates for mantle xenoliths can be quantified by extrapolating final equilibration temperatures to modelled geotherms through the *FITPLOT* program (McKenzie et al., 2005; Mather et al., 2011). This program uses equations for the thermal properties of the lithospheric mantle with input parameters for i) pressure-temperature estimates of xenoliths; ii) mantle potential temperature; iii) crustal thickness; iv) heat production. In addition to the geotherm, this program also calculates the thickness of the mechanical boundary layer, thermal boundary layer and Moho. Temperatures calculated using TA_{98} and corrected M_{80} are then applied to calculated geotherms and extrapolated to infer pressure estimates. Fortunately, the temperature estimates of TA_{98} are

very insensitive to pressure, with large variations in pressure (0.5 GPa) producing minor changes in temperature (± 20 ^{o}C).

Estimates of geothermal gradients, mechanical boundary layer and thermal boundary layer thickness are shown in Figure 6.2 and 6.3 with temperatures extrapolated to geotherms for individual locations. Using these observations, peridotites and pyroxenites from Ichinomegata, Tariat Volcanic Field, Southern Patagonia (Pali Aike), Northern Tanzania (Lashaine) and Colorado Plateau sample the mechanical boundary layer. Peridotites and pyroxenites from the Kilbourne Hole, West Eifel Volcanic Field (Eifel) are derived from both the mechanical boundary layer and thermal boundary layer, while in the Antarctic Peninsula peridotites come from the mechanical boundary layer while pyroxenites sample the thermal boundary layer.

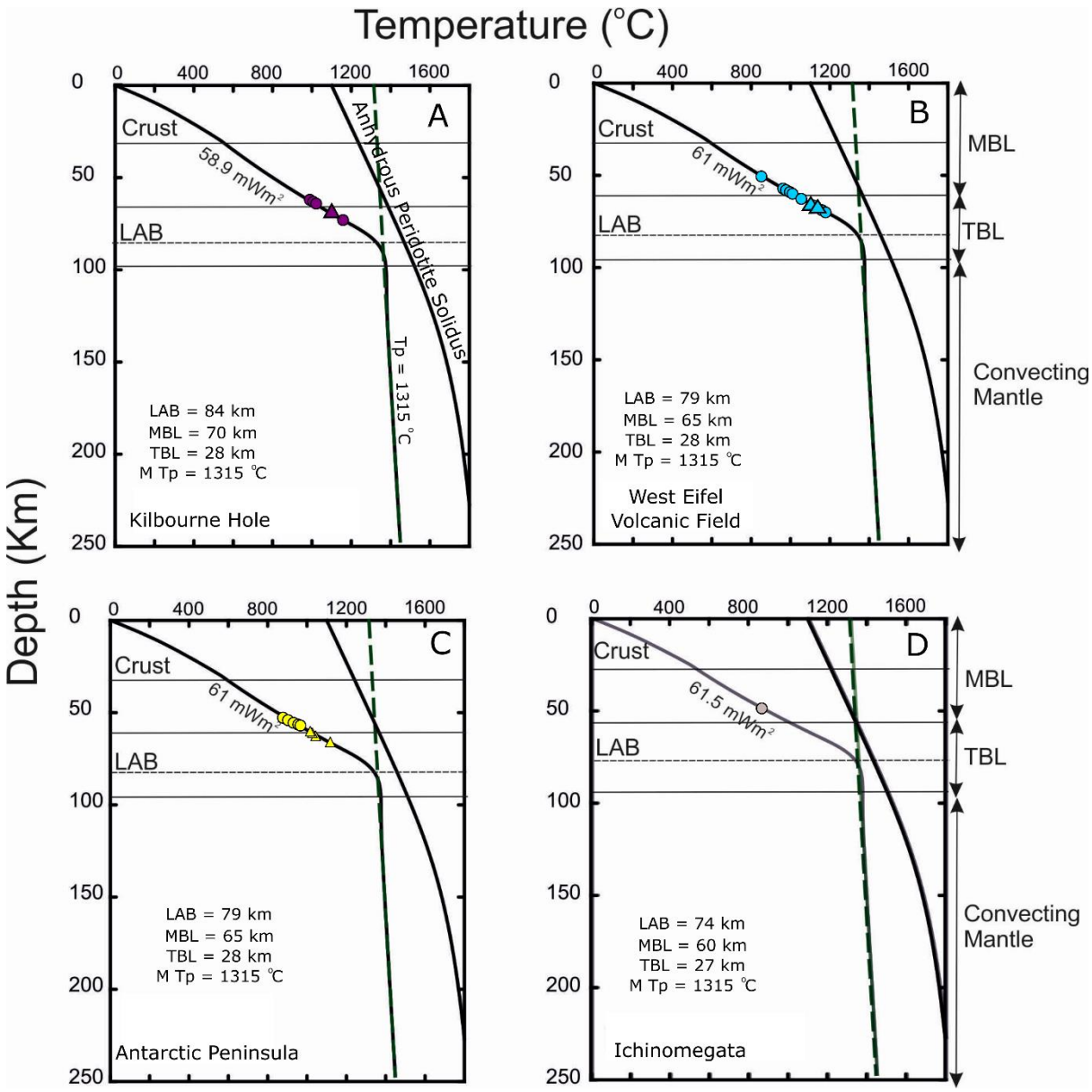

Figure 6.2 Geothermal gradient with pressure and temperature estimates of peridotite and pyroxenite xenoliths for; a) Kilbourne Hole; b) West Eifel Volcanic Field; c) Antarctic Peninsula; and d) Ichinomegata.

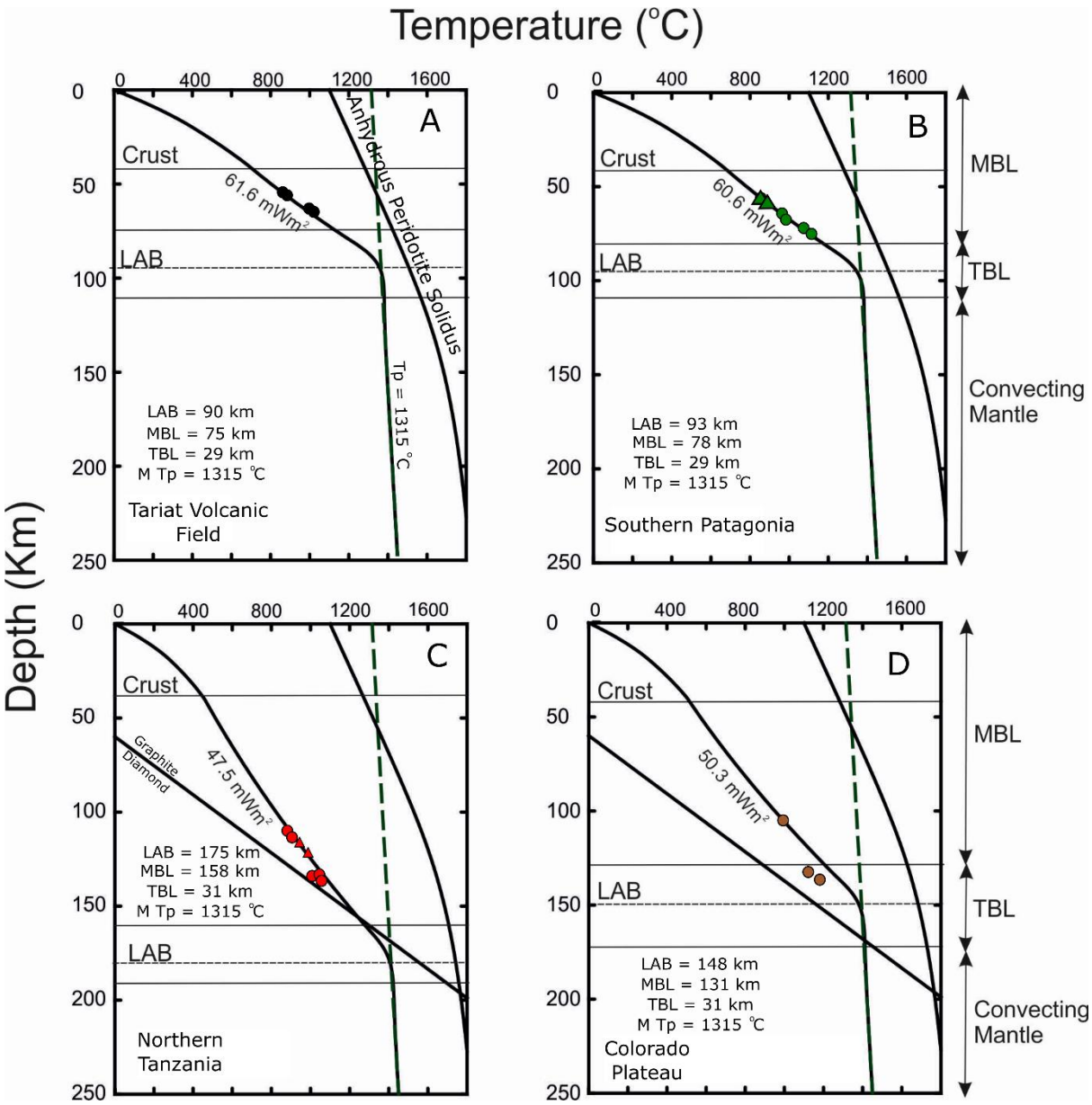

Figure 6.3 Geothermal gradient with pressure and temperature estimates of peridotite and pyroxenite xenoliths for; a) Kilbourne Hole; b) West Eifel Volcanic Field; c) Antarctic Peninsula; and d) Ichinomegata.

7.5 Summary and conclusions

The final equilibration pressures and temperatures calculated using the parameterisations described above are reported in Table 7.1, with preferred values highlighted in green.

Table 7.1 Calculated temperatures and pressures of ultramafic xenoliths presented in this study. Depth from geothermal gradient extrapolations converted to GPa using 33km = 1GPa approximation.

	Temperature							Pressure (GPa)			
Method	TA98	BK90	M80a	M80b	M80a-corr	M80b-corr	Preferred	Assumed	FITPLOT	NG85	Preferred
KG3610.10A	951	910	979	1070	927	900	951	1.5	1.7		1.7
KG3609.21	943	957	1014	1156	960	972	943	1.5	1.7		1.7
KG3719.25	945	996	985	1186	933	998	945	1.5	1.7		1.7
L7.201.1.41	919	973	995	1177	942	990	919	1.5	1.7		1.7
BN	882	943	947	1122	897	944	882	1.5	1.6		1.6
DW3	994	1060	1074	1143	1017	961	994	1.5	1.8		1.8
DW7	1173	1219	1200	1334	1136	1122	1173	1.5	2.1		2.1
DW8	850	876	948	1081	898	909	850	1.5	1.5		1.5
DW10			1031		976		976	1.5	1.8		1.8
MM5	1051	1119	1112	1211	1053	1019	1051	1.5	1.9		1.9
MM8	1161	1216	1215	1359	1150	1143	1161	1.5	2.1		2.1
MM11	1008	1056	1073	1171	1016	985	1008	1.5	1.8		1.8
G17	1122	1195	1209	1018	1145	856	1122	1.5	2.0		2.0
G18	985	1020	1063	1019	1006	857	985	1.5	1.8		1.8
KH2	986	1044	1019	1196	965	1006	986	1.5	1.9		1.9
KH3D	1151	1187	1170	1346	1108	1132	1151	1.5	2.2		2.2
KH4	989	1048	1024	1206	970	1014	989	1.5	1.9		1.9
KH5	999	1050	1030	1202	975	1011	999	1.5	1.9		1.9
TM1	856	922	922	1075	873	904	856	1.5	1.7		1.7
TM2	989	1062	1034	1176	979	989	989	1.5	1.9		1.9
TM3	1002	1071	1059	1161	1003	977	1002	1.5	1.9		1.9
TM4	861	930	904	1105	856	929	861	1.5	1.7		1.7
CP31											
CP33	994						994		2.1	2.2	2.2
LT1	861	901	885	1140	838	959	861	1.5	1.8		1.8
LT16	1081	1137	1162	1270	1100	1068	1081	1.5	2.3		2.3
PA3-5				1327		1116	1116	1.5	2.4		2.4
CP62				1156		972	972	1.5	2.1		2.1
BD730	1011						1011		3.8	4.1	4.1
BD738	1055						1055		4.0	4.1	4.1
BD794	1047						1047		4.0	4.1	4.1
BD797				1056		888	888	1.5	3.4		3.4
BD822				1071		901	901	1.5	3.4		3.4
TH17	1121						1121		3.6	4.0	4.0
BP1	998	1022	1013	1179	959	992	998	1.5	3.2		3.2
TH33	1176						1176		3.8	4.1	4.1
J1	865	878	886	1110	839	934	865	1.5	1.5		1.5
KG3619.7	1012	1046	1102	1241	1043	1044	1012	1.5	2.0		2.0
L7201.1.74c			1181		1118		1118	1.5	2.2		2.2
R5194.2I			1045		989		989	1.5	1.9		1.9
R5194.2M			1075		1018		1018	1.5	2.0		2.0
MM6	1139	1189	1199	1348	1135	1134	1139	1.5	2.1		2.1
DW5			1170		1108		1108	1.5	2.0		2.0
KH1			1159		1097		1097	1.5	2.1		2.1
LT14	875	962	934		884		875	1.5	1.9		1.9
LT15			901		853		853	1.5	1.8		1.8
BD816	937	971	1037		982		937	1.5	3.5		3.5
BD3847			1037		982		982	1.5	3.7		3.7

The temperature and pressures estimates of mantle xenoliths analysed in this study cover a large interval, ranging from ~850 to ~1175 ^{o}C and ~1.5 to ~4.1 GPa, respectively. The most depleted samples, from the margin of the Tanzania craton have low to moderate temperature estimates at 888 to 1055 ^{o}C and from the highest pressure estimates, ranging from 3.2 to 4.1 GPa.

The most fertile peridotites, i.e. those from Kilbourne Hole, the Tariat Volcanic Field and

Ichinomegata, equilibrated at relatively low temperatures, ranging from 856 to 1002 ^{o}C, with exception of KH3D where *T*= 1151 ^{o}C. Furthermore, they all occur in the mechanical boundary layer (except KH3D) with temperatures of 1.5 to 1.9 GPa.

The variably depleted and enriched samples from the West Eifel, Antarctic Peninsula, Southern Patagonia and Colorado Plateau have final equilibration temperatures ranging from 850 to 1176 ^{o}C and pressures from 1.5 to 4.1 GPa. Those from the Antarctic Peninsula all have low final equilibration temperatures (882 to 951 ^{o}C) while the xenoliths from the other locations are highly variable.

The pyroxenites encompass a large range in temperature (875 to 1118 ^{o}C) and pressure (1.8 to 3.7 GPa), with final equilibration pressures for Eifel, Kilbourne Hole and Antarctic Peninsula occurring within the thermal boundary layer while those from Pali Aike and Northern Tanzania in the mechanical boundary layer.

Chapter 8. Fluid Inclusion Chemistry

8.1 Helium isotopes

8.1.1 Introduction

Helium isotopes have proved unrivalled as reservoir tracers due to the unique $^3He/^4He$ signatures of the continental crust (<0.1 Ra; Ballentine & Burnard, 2002), the convecting mantle (8 ± 1 Ra; Allegre *et al.*, 1995) and primitive mantle (>10 Ra; Stuart *et al.*, 2003). To try and improve constraints on the $^3He/^4Her$ of the sub-continental lithospheric mantle, mineral separates from peridotite and pyroxenite xenoliths have been analysed for their ^3He and ^4He concentrations.

8.1.2 Data reporting of ^3He- and ^4He-concentrations and $^3He/^4He$ values

$^3He/^4He$ (R) is reported as a normalised factor to the $^3He/^4He$ of air (Ra = 1.38 x 10^{-6}) given as R/Ra (Equation 8.1). All of the mineral separates were subjected to *in vacuo* crushing to avoid secondary lattice-hosted cosmogenic ^3He or radiogenic ^4He (e.g. Timmermann *et al.*, 2019; Yokochi *et al.*, 2005). High ^3He and ^4He concentrations (^3He > 1x10^{-14} ccSTP/g & ^4He > 5x10^{-9} ccSTP/g) are required to avoid extensive overprinting by secondary radiogenic and cosmogenic He ingrowth (e.g. Martelli *et al.*, 2011) the xenolith need to have been entrained within the last 100 Ma (Day *et al.*, 2015).

$$^3He/^4He\ (Ra) = \frac{\frac{^3He}{^4He}sample}{\frac{^3He}{^4He}air} \qquad \text{(Equation 8.1)}$$

Where: $^3He/^4He$ of Air is 1.38x10^{-6}.

$^3He/^4He$ and ^3He-concentrations for 86 separates of olivine, orthopyroxene and clinopyroxene together with single garnet were analysed in this study (Figure 8.1 and Appendix Table 24). These are from mantle xenoliths from the Southern USA, Tariat Volcanic Field, West Eifel Volcanic Field, Antarctic Peninsula, Southern Patagonia, Northern Tanzania and Ichinomegata.

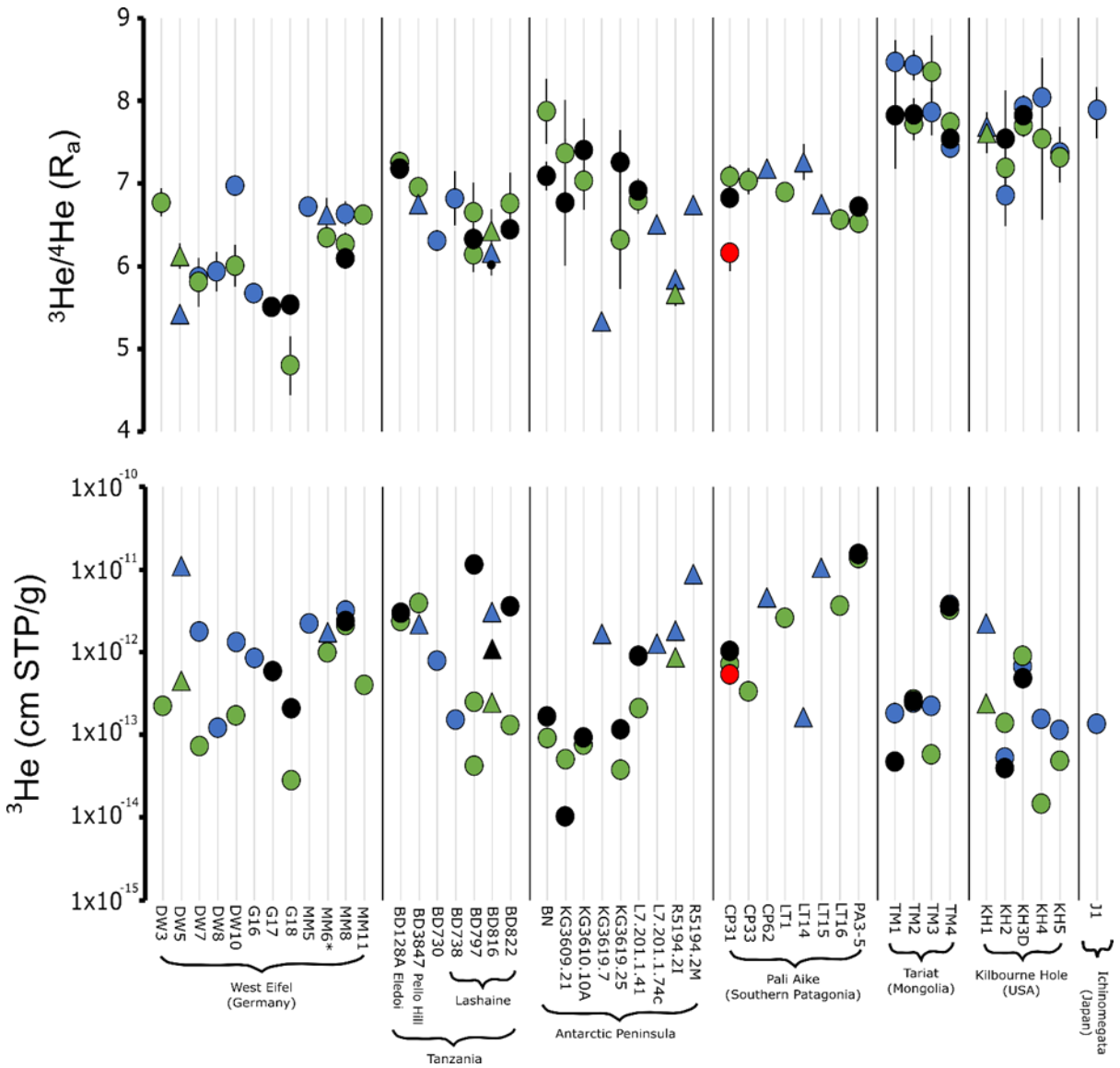

Figure 8.1 $^3He/^4He$ and ^3He-concentrations (ccSTP/g) in all minerals analysed in this study. If error bars (1 standard deviation) are not shown they are smaller than the symbols. Circles are peridotites and triangles are pyroxenites. Green fill corresponds to olivine, blue to clinopyroxene, black to orthopyroxene and red to garnet. * = composite xenolith of peridotite and pyroxenite.

8.1.3 Results

8.1.3.1 Southern USA

8.1.3.1.1 Kilbourne Hole

The ^3He and ^4He contents of four spinel lherzolites and one pyroxenite from the Kilbourne Hole were determined. In two samples olivine, orthopyroxene, and clinopyroxene were analysed ((KH2 and KH3D), while the remaining three (KH4, KH5, and KH1) only olivine and clinopyroxene were analysed. Figure 8.1 shows no clear variation in $^3He/^4He$ between different mineral phases or rock types (i.e. peridotite or pyroxenite). Furthermore, the mineral separates display very similar He concentration between different phases (with the

exception of KH1, which has slightly higher ^3He and ^4He for clinopyroxene compared to co-existing olivine). Calculated bulk rock $^3He/^4He$ range from 7.1 (± 0.4) to 7.9 (± 0.4) Ra.

These measurements overlap the $^3He/^4He$ of a single sample from the Kilbourne Hole presented in Day *et al.* (2015), which has $^3He/^4He$ of 7.23 ± 0.2 Ra. Lavas from the Potrillo Volcanic Field have also been analysed (Anthony & Potts, 1992; Williams, 1999) but yield imprecise ratios (errors >0.5 Ra) and provide no useful constraint for this study.

8.1.3.1.2 Colorado Plateau

Mineral separates form one spinel lherzolite were analysed from Buelle Park (BP1) and one garnet harzburgite from the Thumb (TH17). Orthopyroxene from BP has a moderate $^3He/^4He$ of 7.1± 0.9 Ra, while olivine from TH17 has a low $^3He/^4He$ 5.7 ± 0.6 Ra. In both samples, ^3He are above the concentration threshold ($1x10^{-14}$ ccSTP/g) but ^4He falls below the threshold ($5x10^{-9}$ ccSTP/g). This causes imprecise $^3He/^4He$ and the data are not further discussed.

8.1.3.2 Tariat Volcanic Field

Mineral separates from four spinel lherzolites from Tariat were analysed for ^3He and ^4He. In two samples (TM2 and TM4) olivine, orthopyroxene, and clinopyroxene were analysed whereas TM1 had orthopyroxene and clinopyroxene analysed and TM3 was analysed for olivine and clinopyroxene. Figure 8.1 shows there is no clear variation in He concentration or $^3He/^4He$ values between different mineral phases. Calculated bulk xenolith $^3He/^4He$ (ranges from 7.6 (± 0.1) to 8.3 (± 0.4) Ra.

Two mantle xenoliths have previously been analysed for $^3He/^4He$ from Tariat (Barry *et al.* 2007). These results are more imprecise (8.8 ± 0.9 and 8.26 ± 2.0 Ra) that the data produced in this study.

8.1.3.3 West Eifel Volcanic Field

Mineral separates from thirteen xenolith from the West Eifel were analysed; five from the Dreiser Weiher (DW3, DW5, DW7, DW8, DW10), four from Meerfelder Maar (MM5, MM6, MM8, and MM11) and three from Gees (G16, G17, G18). Olivine, orthopyroxene and clinopyroxene were analysed in MM8 while all other samples had two mineral (of either olivine, orthopyroxene or clinopyroxene) analysed. In peridotites and pyroxenites from the West Eifel Volcanic Field there is no clear variation in $^3He/^4He$ between different mineral

phases, but clinopyroxene appears to record slightly higher He concentrations than co-existing olivine in 3 of 5 samples analysed (DW5, DW7, and DW10; Figure 8.1). Calculated bulk xenolith $^3He/^4He$ is relatively low and ranges from 5.3 (± 0.2) to 6.8 (± 0.2) Ra, with large ranges in ^4He concentrations (7.3 x 10^{-9} to 1.9 x 10^{-7} ccSTP/g). While $^3He/^4He$ values show no distinction between peridotite and pyroxenite, the pyroxenites consistently produce higher He concentrations.

Samples from the West Eifel Volcanic Field have been previously analysed for $^3He/^4He$ (Dunai & Baur, 1995; Gautheron & Moreira, 2002; Gautheron *et al.*, 2005; Buikin *et al.*, 2005). The helium isotope values of samples obtained by crushing (Gautheron & Moreira, 2002; Gautheron *et al.*, 2005; Buikin *et al.*, 2005) $^3He/^4He$ ranges from 5.5 to 6.8 Ra and overlap the values reported here.

Numerous mantle xenoliths from the West Eifel have been the subject of extensive Nd-Sr-Pb-isotopes and trace element analysis as well as He-Ne-Ar isotopes investigations (see review by Trieloff & Altherr, 2007). The low $^3He/^4He$ (~6 Ra) appeared to conflict with the Nd-Sr-Pb signatures, which are similar to enriched and MORB-type mantle. The Ne and Ar signatures enable high model-dependent $^3He/^4He$ values (~20 Ra) which are indicative of a deep primordial mantle plume. However, more recent Xe data (Moreira *et al.*, 2018) are consistent with un-modelled noble-gas compositions reflecting MORB/SCLM signatures. Therefore, the current balance of evidence indicates West Eifel (and Central European) volcanism and the chemistry observed in mantle xenolith to be from an upper-mantle source as opposed to a deep mantle source enriched in primordial noble gases.

8.1.3.4 Antarctic Peninsula

Mineral separates from nine mantle xenoliths from the Antarctic Peninsula were analysed; four from Rothschild Island (KG3719.25, L7.201.1.41, KG3619.7, and L7201.1.74c), two from Alexander Island (KG3619.10A and KG3609.21), two from Adelaide Island (R5194.2I and R5194.2M), and one from Bruce Nunatak (BN). In spinel peridotites olivine and orthopyroxene were analysed, in pyroxenite (R5194.2I) clinopyroxene and olivine were analysed and remaining pyroxenites had clinopyroxene analysed. The data shows no clear variation in He concentration or $^3He/^4He$ values between different mineral phases. The peridotites record a large range of $^3He/^4He$ (5.6 (± 0.1) to 7.4 (± 0.2) Ra), which encompass the more radiogenic pyroxenites (5.8 (± 0.1) to 6.8 (± 0.2) Ra).

No samples from the Antarctic Peninsula have previously been analysed.

8.1.3.5 Southern Patagonia

Eight peridotite and pyroxenite sample from Pali Aike in Southern Patagonia were analysed for ^{3}He and ^{4}He; four from Laguna Timones (LT1, LT14, LT15, and LT16), three from Campo Picana (CP31, CP33, and CP62), and one from Laguna de Los Cisnes (PA3-5). Garnet, olivine, and orthopyroxene were analysed from CP31, olivine and orthopyroxene from PA3-5, and olivine from CP33, LT1 and LT16. Only clinopyroxene was analysed from pyroxenites (LT14, LT15, and CP62). Figure 8.1 shows no clear variation in He-concentration or $^{3}He/^{4}He$ between different mineral phases. Furthermore, there is no clear difference between the peridotites and pyroxenites and the calculated whole-rock $^{3}He/^{4}He$ (Ra) ranges from 6.6 (± 0.1) to 7.3 (± 0.2) Ra.

Mantle xenoliths from Southern Patagonia have previously been analysed for ^{3}He and ^{4}He by Jalowitski *et al.* (2016), and have $^{3}He/^{4}He$ in the range of 6.9 (± 0.1) to 7.4 (± 0.1) Ra. This is similar to $^{3}He/^{4}He$ ranges from this study. Furthermore, Jalowitski *et al.* (2016) concluded from helium isotope data combined with Ne-Ar-Kr-Xe and Sr-Nd-Pb isotope systematics that the Pali Aike mantle is dominantly influenced by metasomatism by melts from MORB-like mantle.

8.1.3.6 Northern Tanzania

Eight samples from Northern Tanzania were analysed for their ^{3}He and ^{4}He concentrations. They include five peridotites (BD128A, BD730, BD738, BD797 and BD822), one pyroxenite (BD816), and one composite peridotite and pyroxenite (BD3847). Olivine, orthopyroxene, and clinopyroxene analysed in BD816, while the composite xenolith (BD3847) had the clinopyroxene from the vein and olivine from the wall-rock analysed. In the peridotites, BD128A, BD738, BD797, and BD822 had olivine and either orthopyroxene or clinopyroxene analysed, while BD730 had clinopyroxene were analysed. There is no clear variation in $^{3}He/^{4}He$ values between different mineral phases from the peridotites. However, there appears to be a slight increase in ^{3}He and ^{4}He concentration for some orthopyroxenes (BDBD797 and BD822) and clinopyroxenes (BD816) relative to co-existing olivines. The calculated xenolith $^{3}He/^{4}He$ (Ra) ranges from 6.2 (± 0.1) to 7.0 (± 0.1), and ^{3}He and ^{4}He concentrations from $6.5x10^{-14}$ to $3.9x10^{-12}$ and $6.8x10^{-9}$ to $4.0x10^{-7}$ ccSTP/g, respectively.

Some of these xenoliths (BD128, BD738, BD816 and BD3847) have previously been analysed for ^{3}He and ^{4}He, however this was done using a laser heating technique (Porcelli *et al.*, 1986). As expected, the samples analysed by laser-heating release more ^{3}He and ^{4}He (Figure 8.2 A+B) from lattice-hosted radiogenic and cosmogenic sources. All of the samples with the exception of BD738 have similar $^{3}He/^{4}He$ values to those from this study (Figure 8.2C). Sample BD738 from Lashaine produces high $^{3}He/^{4}He$ (9.3 and 15.3 Ra) in Porcelli *et al.* (1986) but is similar to other samples in this study (6-7 Ra). This anomalously high $^{3}He/^{4}He$ likely reflects overprinting of secondary cosmogenic ^{3}He accumulated into the lattice of low concentration crystals of BD738 ($^{3}He = 6.5x10^{-14}$ and $^{4}He = 6.8x10^{-9}$ ccSTP/g; this study). This cosmogenic ^{3}He becomes released during heating experiments but not crushing and so generates elevated $^{3}He/^{4}He$ values.

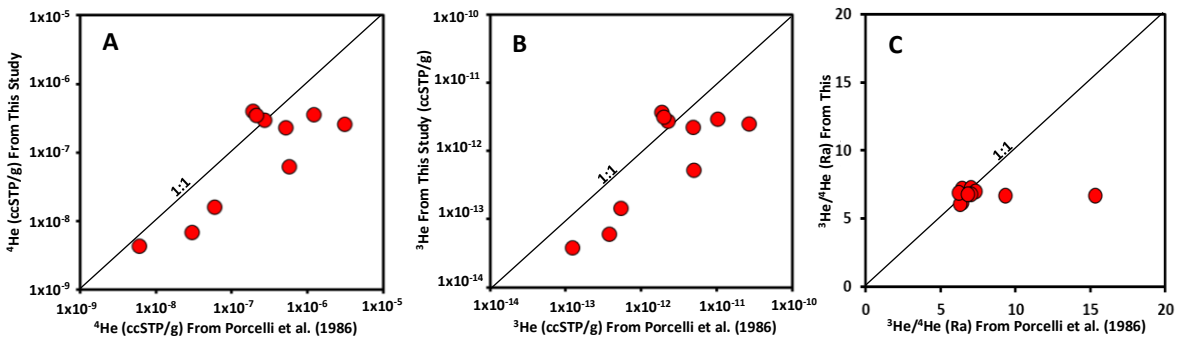

Figure 8.2 a) ^{4}He-concentration (ccSTP/g), b) ^{3}He-concentration (ccSTP/g), c) $^{3}He/^{4}He$ (Ra) of whole-rock and mineral compositions of BD128, BD738, BD816, and BD3847 from this study and Porcelli et al. (1986). Analytical errors are smaller than the symbols.

8.1.3.7 Oga Peninsula

One sample (J1) from the Oga Peninsula (Ichinomegata) had olivine, orthopyroxene and clinopyroxene analysed for ^{3}He or ^{4}He concentrations. There were clear distinctions between mineral phases, with orthopyroxene and clinopyroxene producing low He compared to olivine. As a result, the orthopyroxene and clinopyroxene have imprecise $^{3}He/^{4}He$ (6.3 ± 0.9 and 4.2 ± 1.0 Ra), which may have been overprinted by ingrowth of radiogenic ^{4}He. Olivine produced reasonably precise results (8.5 ± 0.4 Ra), which show affinity towards MORB-like mantle (8 ± 1 Ra).

8.2 Carbon Isotopes

8.2.1 Introduction

Carbon isotopes have proven very powerful in constraining different reservoirs. Where, crustal signatures vary from carbonate compositions ($\delta^{13}C$ > 0‰) and organic compositions ($\delta^{13}C$ < -20‰; Gradstein *et al.*, 2012) and mantle carbon is dominated by $\delta^{13}C$ = -5 ± 2‰ (e.g. Cartigny *et al.*, 2014). To establish the origin of CO_2 stored within the lithospheric mantle, mineral separates of peridotite and pyroxenites have been analysed for their CO_2 concentrations and $^{13}C/^{12}C$. Furthermore, ^{3}He and CO_2 are known to be closely related (e.g. Marty & Tolsikhin, 1998), therefore ^{3}He and CO_2 determined on the same xenoliths offer a unique opportunity to constrain the volatile evolution of the lithospheric mantle.

8.2.2 Data reporting of $^{12}C/^{13}C$ and CO_2

$\delta^{13}C$ is reported relative to $^{13}C/^{12}C$ of the Vienna Pee Dee Belemnite (VPDB = 0.0112372) standard by Equation 8.2:

$$\delta^{13}\mathrm{C}\ ‰ = \left(\frac{\left(\frac{^{13}\mathrm{C}}{^{12}\mathrm{C}}\mathrm{sample}\right)}{\left(\frac{^{13}\mathrm{C}}{^{12}\mathrm{C}}\mathrm{VPDB}\right)} - 1\right) \times 1000 \qquad \text{(Equation 8.2)}$$

CO_2 concentrations are reported as ccSTP/g and mol/g as shown by equation 8.3 and 8.4.

CO_2 ppm to cm^3/g at STP = $\frac{(\mathrm{ppm} \times \mathrm{CO_2\ molecular\ weight} \times \mathrm{Moles\ per\ L\ in\ air})}{1000}$

(Equation 8.3)

cm^3/g at STP to mol/g at STP = CO_2 cm^3/g STP x Conversion Factor (Equation 8.4)

Where: CO_2 molecular weight = 44.01, Moles per L in air = 0.00409, Conversion factor = 4.4032×10^{-5} (after Balco, 2019).

$\delta^{13}C$ and CO_2-concentrations were also obtained using *in vacuo* crushing technique (e.g. Abernethy *et al.*, 2013; see Appendix C). This was done to ensure internal consistency with ^{3}He and ^{4}He analyses.

8.2.3 Results

CO_2 concentrations were obtained for mineral separates from 15 mantle xenoliths, of which 13 contained enough CO_2 to obtain $\delta^{13}C$ (‰; Figure 8.3 and Appendix C Table 26). These comprise samples from the Kilbourne Hole, Tariat Volcanic Field, West Eifel Volcanic Field,

Pali Aike Volcanic Field and Antarctic Peninsula. Samples from Lashaine Volcano in Northern Tanzania (BD816, BD3827) were also analysed, but the CO_2 concentrations were below detection limit and are not considered further.

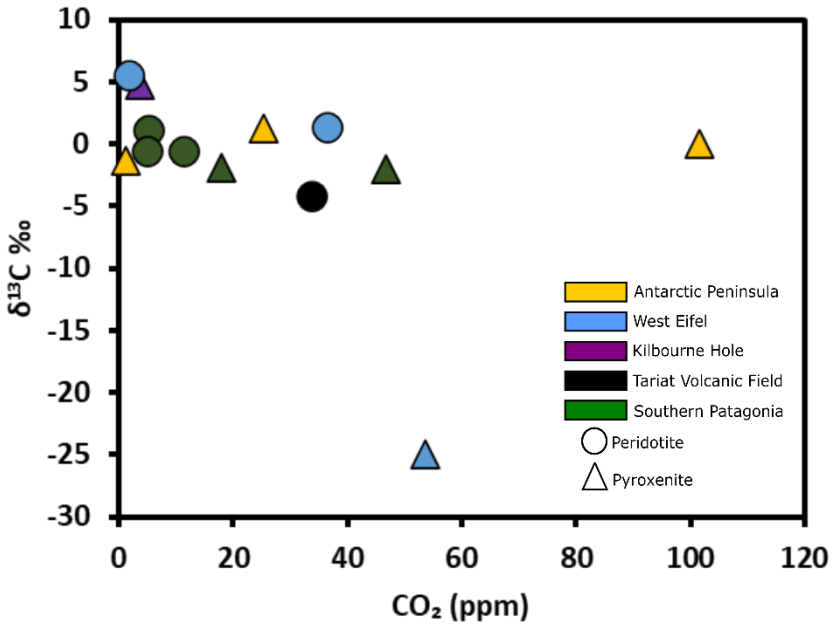

Figure 8.3. $\delta^{13}C$ in ‰ and CO_2-concentration (ppm) for different mineral phases presented in this study. Error bars are shown for $\delta^{13}C$ in ‰ and are smaller than the symbols. Circles are peridotites and triangles are pyroxenites.

8.2.3.1 Kilbourne Hole

Three mineral separates of mantle xenoliths from the Kilbourne Hole were analysed for $\delta^{13}C$ and CO_2-concentrations. These comprised clinopyroxene from pyroxenite KH1 and two spinel lherzolites (KH2 and KH3D). The CO_2 concentrations range from 0.8 to 4.8 ppm, with the pyroxenite having the highest concentrations. Only sample KH1 released enough gas to accurately constrain its isotopic composition ($\delta^{13}C$ = 3.6 ± 1 ‰).

8.2.3.2 Tariat Volcanic Field

Clinopyroxene separates from one spinel lherzolite (TM4) from Tariat were analysed for CO_2 concentration and $\delta^{13}C$ composition. This produced a relatively high CO_2 concentration of 33.7 ppm CO_2 and moderate $\delta^{13}C$ of -4.14 ± 1 ‰.

8.2.3.3 West Eifel

Mineral separates from four xenoliths from the West Eifel were analysed for $\delta^{13}C$ and CO_2 concentration. These comprise clinopyroxene from a pyroxenite (DW5), olivine from one spinel harzburgite (MM8), and clinopyroxene from a spinel harzburgite (DW7) and wehrlite

(DW10). The CO_2 concentrations range from 0 to 53.6 ppm, with sample MM8 producing values below detection limit and the pyroxenite sample having the highest concentration. $\delta^{13}C$ compositions are highly variable, with pyroxenite (DW5) having very low $\delta^{13}C$ = -24.99 ± 1.4 ‰ and peridotites (DW7 and DW10) having very high $\delta^{13}C$ = 1.4 to 5.6 ± 1.4 ‰.

8.2.3.4 Antarctic Peninsula

Clinopyroxene was analysed in four mantle xenoliths (KG3719.25, R5194.2M, R5194.2I, and L7.201.1.74c) from the Antarctic Peninsula for $\delta^{13}C$ and CO_2. CO_2 concentrations range from 0 to 101.7 ppm, with spinel peridotite KG3719.25 producing values below detection limit and pyroxenite R5194.2M retaining the highest concentration. Samples R5194.2M, R5194.2I and L7.201.1.74c have a narrow range in $\delta^{13}C$ compositions, ranging from -1.3 to 1.3 ± 1.2 ‰.

8.2.3.5 Southern Patagonia

Five mantle xenoliths from Southern Patagonia were analysed for $\delta^{13}C$ and CO_2. These comprise clinopyroxene from two pyroxenites (LT15 and CP62) and olivine from three peridotites (LT1, LT16, PA3-5). CO_2 concentrations range from 4.8 to 46.6 ppm, with clinopyroxene from pyroxenites having the higher concentrations (46.6 and 18.0 ppm, respectively) than olivine from peridotite samples (LT1 = 5.1 ppm, LT16 = 4.8 ppm, PA3-5 = 11.4 ppm). All of the samples have a narrow range in $\delta^{13}C$ compositions, ranging from -2.0 to 1.2 ± 1.2 ‰.

8.2.3.6 Northern Tanzania

Two pyroxenites (BD816 and BD3827) from Northern Tanzania were analysed for $\delta^{13}C$ and CO_2. Clinopyroxene was analysed in BD816 and olivine in BD3827. Both analyses produced CO_2 concentrations below detection limit and no $\delta^{13}C$ compositions were obtained.

8.2.4 Comparison with previous investigations

The carbon concentrations obtained using crushing methods for samples from the Kilbourne Hole, West Eifel and Tanzania are significantly lower than those obtained by Mathez *et al.* (1984) and Porcelli *et al.* (1992). For example, CO_2 concentrations in the Kilbourne Hole ranged from 0.8 to 4.8 ppm, while those from Mathez *et al.* (1984) range from 15 to 78 ppm. For the West Eifel ranged from 0 to 53.6 ppm, while those from Mathez *et al.* (1984) range from 19 to 67 ppm, and results from Northern Tanzania are below detection limit for

this methodology (approximately 0.2 ppm) while those from Porcelli *et al.* (1992) range from 7 to 13 ppm. The most obvious reason for this discrepancy is the difference in methodology. This study has employed a crushing rather than a heating technique, which only releases fluid- and gas-phases of carbon from mantle xenoliths as opposed to trapped carbonate and graphite. X-ray photoelectron spectroscopy investigations (e.g. Mathez, 1987) show that many of these solid species are found as particles in prominent cracks and semi-continuous carbonaceous films on microcracks and are attributed to host lavas. Additionally, solid secondary carbon may also be inherited from the host-magma and carbonate-rich surface water during alteration (e.g. serpentinization). While many of the carbonates released by heating techniques are undoubtably of mantle origin, they are unlikely to be indicative of upper-mantle lithology. Therefore, by employing this crushing technique, this work provides the best estimate on carbon concentration and $^{13}C/^{12}C$ of the diamond- and graphite-free lithospheric mantle.

8.3 Summary of data

8.3.1 Helium isotopes

There is no statistically significant relationship between $^{3}He/^{4}He$ and ^{3}He- or ^{4}He-concentration in xenoliths presented here (Figure 8.4). The decision to discard results with $^{3}He < 1x10^{-14}$ ccSTP/g and $^{4}He < 5x10^{-9}$ ccSTP/g minimises the effect of secondary processes on the measured $^{3}He/^{4}He$, and results with $^{3}He/^{4}He$ uncertainties > 0.4 Ra being excluded. Furthermore, the results display a general similarity of $^{3}He/^{4}He$ for all coexisting mineral phases, with no systematic differences.

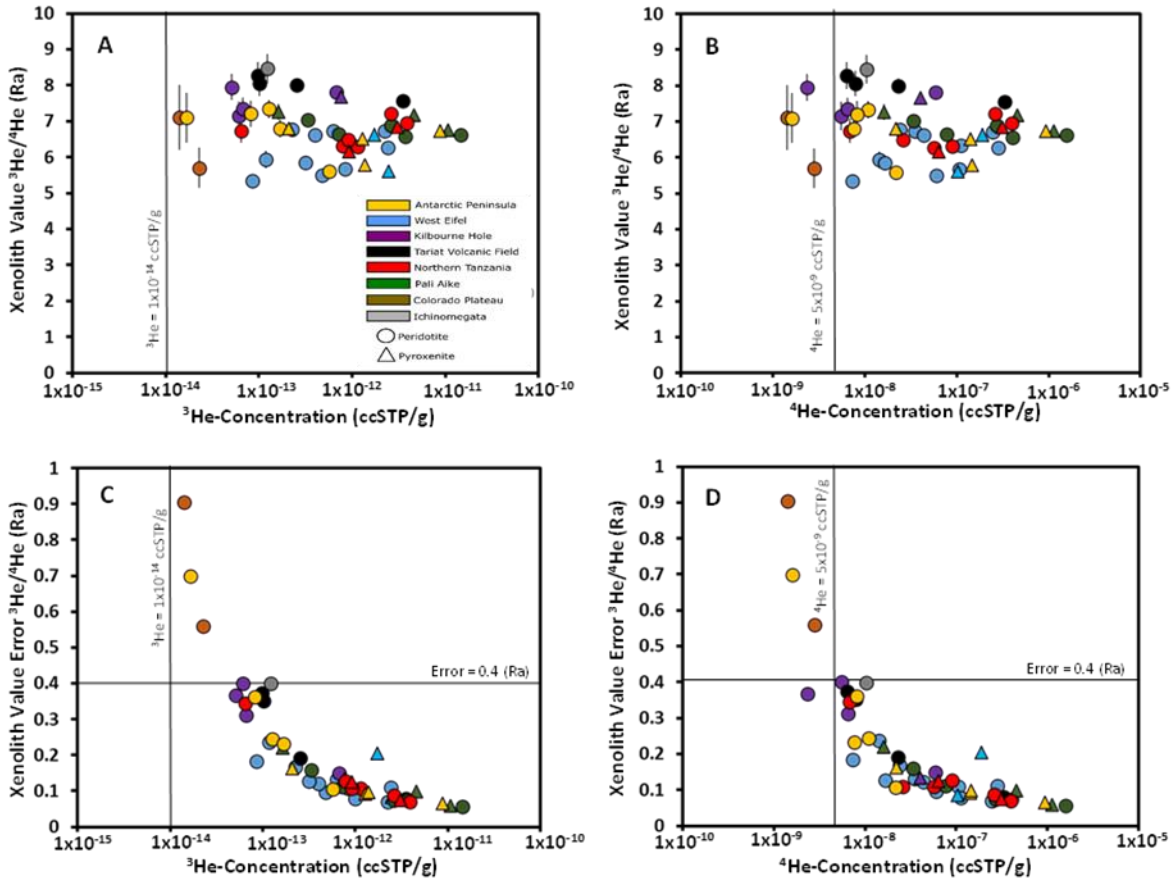

Figure 8.4 Xenolith ^{3}He/^{4}He compared to a) xenolith value ^{3}He-concentration and b) xenolith value ^{4}He-concentration, and xenolith value ^{3}He/^{4}He error compared to c) xenolith value ^{3}He-concentration and b) xenolith value ^{4}He-concentration. Error bars are displayed for A + B and key for symbols displayed in A.

When comparing the He concentrations of coexisting mineral phases (Figure 8.5), there is a subtle tendency for higher He concentrations in clinopyroxene (DW5, DW7, DW10, KH1, BD816) and orthopyroxene (BD797 and BD822) compared to olivine. This is consistent but less obvious than the findings presented in the review by Dunai & Porcelli (2002) and may indicate a greater ability of clinopyroxene and orthopyroxene to resist degassing during ascent to the surface (e.g. Yamamoto *et al.*, 2011). Furthermore, this may also be a product of the stronger cleavage in clinopyroxene and orthopyroxene allowing planes of weakness for micro-bubbles of helium to accumulate.

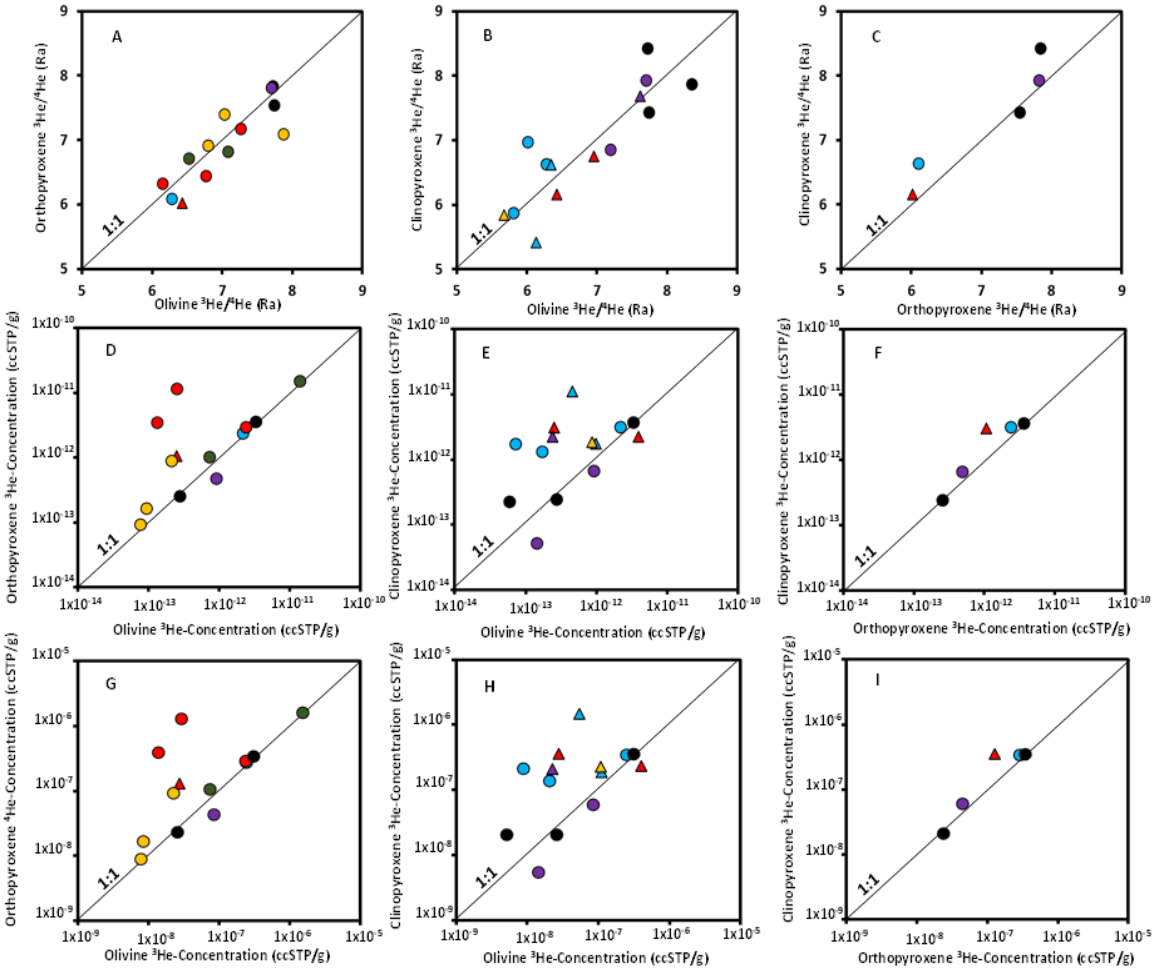

Figure 8.5. Comparison of He concentration and $^3He/^4He$ between a) olivine-orthopyroxene, b) olivine-clinopyroxene, and c) orthopyroxene-clinopyroxene. ^3He-concentration (ccSTP/g) are compared between d) olivine-orthopyroxene, e) olivine-clinopyroxene, and f) orthopyroxene-clinopyroxene. Finally, ^3He-concentration (ccSTP/g) ared compared between g) olivine-orthopyroxene; h) olivine-clinopyroxene; and i) orthopyroxene-clinopyroxene. Symbols are the same as Fig. 8.1.

The $^3He/^4He$ and He concentration of xenoliths with multi-mineral analyses are used to obtain a weighted average. An example is shown in Table 8.1 for a Kilbourne Hole xenolith (KH2) below, and the results for all samples provided in Appendix C (Table 24):

Table 8.1. Outline of method used to calculate whole-rock $^3He/^4He$. Cpx = clinopyroxene, opx = orthopyroxene and ol = olivine

Sample	Mineral	$^3He/^4He$ (Ra)	$^3He/^4He$ (Ra) Error	Sum Error	$^3He/^4He$ Error/Sum Error	Sum F	Weighted %	Contribution	$^3He/^4He$ Value Total
KH2	Cpx	6.85	0.4	1.3	3.48	9.6	42%	2.9	7.15
KH2	Opx	7.54	0.6	1.3	2.18		39.48%	2.96	
KH2	Ol	7.18	0.3	1.3	3.94		18.53%	1.33	

Using these estimates, the highest $^3He/^4He$ compositions are typically observed from Kilbourne Hole (SW USA; 7.1 ± 0.4 to 7.9 ± 0.4 Ra) and the Tariat Volcanic Field (Mongolia; 7.6 ± 0.1 to 8.3 ± 0.4). Furthermore, the one sample analysed from Ichinomegata also has

relatively high $^3He/^4He$ at 8.5 ± 0.5 Ra. These all fall within the range proposed for the MORB-source (e.g. Allegre *et al.*, 1995). The $^3He/^4He$ of ultramafic xenoliths from the West Eifel Volcanic Field (5.3 ± 0.2 to 6.6 ± 0.2 Ra), Antarctic Peninsula (5.8 ± 0.1 to 7.3 ± 0.2 Ra), Southern Patagonia (6.6 ± 0.1 to 7.3 ± 0.2 Ra) and Northern Tanzania (6.3 ± 0.1 to 7.0 ± 0.1 Ra) is lower than that proposed for the MORB source. Finally, the calculated bulk xenolith ^3He concentrations range from 1.7 x 10^{-14} to 1.4 x 10^{-11} ccSTP/g and ^4He from 1.1 x 10^{-9} to 1.6 x 10^{-6} ccSTP/g, with higher concentrations typically found in the pyroxenites (Figure 8.6). The peridotite ^3He-concentration mean is 1.2x10^{-12} and the median is 1.0x10^{-13}, while the pyroxenite ^3He-concentration mean is 3.0x10^{-12} and the median is 1.6x10^{-12}.

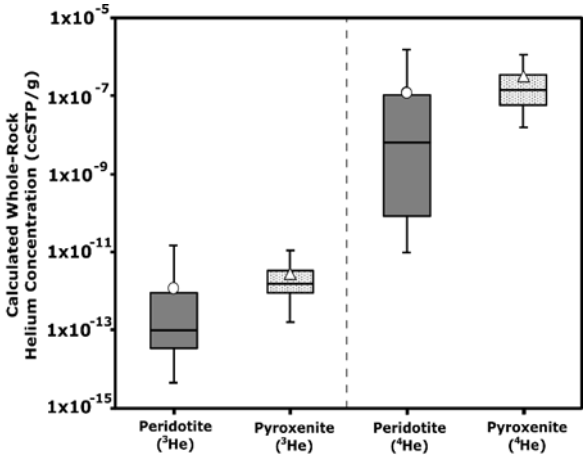

Figure 8.6. Variations in calculated bulk ^4He and ^3He concentrations of mantle peridotites and pyroxenites presented in this study as a box and whisker diagram with minimum, maximum, median, inter-quartile and outer-quartile. The circles and triangles show the mean of peridotite and pyroxenites, respectively.

8.3.2 Carbon isotopes

For peridotite and pyroxenite xenoliths analysed for $\delta^{13}C$ and CO_2, the 13 results for $\delta^{13}C$ compositions are dominated by a small range (-4.1 ± 1 to 5.6 ± 1.4 ‰) with an anomalously low result for olivine clinopyroxenite DW5 from the West Eifel. When compared to estimates for global reservoirs, the xenoliths display strongest affinity to the upper-mantle (-5 ± 2 ‰) and recycled carbonate (>0 ‰). However, the very light $\delta^{13}C$ from DW5 shows the greatest affinity to recycled organic carbon. Finally, CO_2-concentrations have a large range from 0.8 to 102 ppm, with pyroxenites typically recording elevated concentrations.

Chapter 9. Relative role of melting and metasomatism on $^3He/^4He$ in the sub-continental lithospheric mantle

This chapter has been prepared for submission to *Earth and Planetary Science Letters*

Author contributions are as follows: J Crosby designed the study, undertook the analytical work with I. Buismann, J. A. Day and L. DiNicola, developed the numerical models and drafted the manuscript. SA Gibson, F. Stuart and T.R. Riley edited the manuscript and contributed to the discussion.

9.1 Introduction

Helium isotopes have proved to be unrivalled as tracers of the structure and evolution of the convecting mantle (e.g. Graham, 2002; Stuart *et al.*, 2003; Porcelli & Elliott, 2008), as well as being crucial for tracking the inventory of major volatile species such as CO_2 (e.g. Marty & Tolstikhin, 1998). The He isotope composition of the lithospheric mantle has, however, attracted far less attention and so is less constrained. Initial studies considered that the lithospheric mantle displayed a rather narrow range in $^3He/^4He$ (5–8 Ra; e.g. Dunai *et al.*, 2002; Gautheron & Moreira, 2002) with a mean value lower than that of the convecting upper mantle, i.e. the MORB source (7-9 Ra; Graham, 2002). It has been suggested that this is a consequence of higher U+Th contents in the sub-continental lithospheric mantle (e.g. Dunai & Porcelli, 2002). As the $^3He/^4He$ dataset for global sub-continental lithospheric mantle has expanded to include material from a wider range of tectonic settings, so has the range (0.07 to 13.9 Ra, e.g. Halldórsson *et al.*, 2014; Day *et al.*, 2015). The important role of melts and fluids that have enriched the sub-continental lithospheric mantle (e.g. subducted lithosphere, MORB-source mantle, primordial mantle) is now recognised, as is the effect of radiogenic He ingrowth in ancient lithosphere (Day *et al.* 2015).

To advance the understanding of how well $^3He/^4He$ tracks the origin and metasomatic history of the sub-continental lithospheric mantle this study focusses on the relationship of whole-rock $^3He/^4He$ values (Chapter 8) with major and trace elements (Chapter 4 and 5) that act as proxies for long-term melt depletion and enrichment (Chapter 6). These are supplemented by previous studies of $^3He/^3He$, major- and trace-elements in off-craton mantle xenoliths from Yemen, Saudi Arabia, NW Libya, Hyblean Plateau, West Eifel, Siebengebirge, Eastern Transylvanian Basin, West Antarctica, North East Australia, Korean Peninsula and the Eastern

Block of the North China craton (Thornber, 1992; Kim *et al.*, 2005; Beccaluva *et al.*, 2008; 2011; Czuppon *et al.*, 2009; Konrad *et al.*, 2016; Correale *et al.*, 2012; 2016; 2019; Su *et al.*, 2014; Sgualdo *et al.*, 2015; Berkesi *et al.*, 2019; Xu *et al.*, 2019; Faccini *et al.*, 2020; Rizzo *et al.*, 2021) and sub-cratonic mantle xenoliths from Somerset Island (Canada), Diavik (Canada), Bultfontein (South Africa) and Obnazhennaya (Howarth *et al.*, 2014; Day *et al.*, 2015; Barry *et al.*, 2015; Bragagni *et al.* 2017). All of which were entrained within the past 100 million years.

9.2 Origin of $^3He/^4He$ variability in the sub-continental lithospheric mantle

9.2.1 Time-dependent melt extraction

A striking relationship between olivine and orthopyroxene compositions and $^3He/^4He$ of peridotite xenoliths is shown in Figure 9.1. The mantle xenoliths from cratonic settings with the most depleted major-element mineral compositions (i.e. harzburgites with high Mg# olivine and orthopyroxene, high Cr# spinel, and orthopyroxene with low Al_2O_3 content) have $^3He/^4He < 7\ R_a$. While there is some overlap, peridotites from off-craton settings tend to have less depleted compositions (i.e. relatively low Mg# olivine and orthopyroxene (88 to 92.5), low Cr# spinel (<20) and high Al_2O_3 orthopyroxene contents (>2 wt. %), and $^3He/^4He > 7\ R_a$. Note that on Figure 9.1 the strongly-metasomatised, amphibole-bearing xenoliths from the Eastern Transylvanian Basin have anomalously high Al_2O_3 and FeO contents (Faccini *et al.*, 2020) and plot away from this global trend.

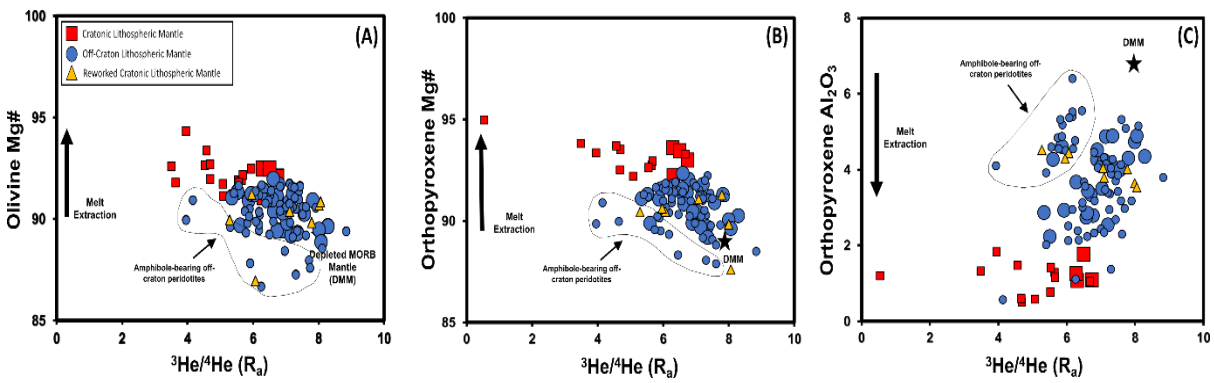

Figure 9.1. Calculated bulk xenolith $^3He/^4He$ plotted against; a) olivine Mg#; b) orthopyroxene Mg#; and c) orthopyroxene Al_2O_3 content. Solid black star shows the composition of depleted MORB-source mantle (DMM) based on the $^3He/^4He$ from Allegre et al. (1995) and olivine Mg# from Workman & Hart (2005).

A similar relationship for $^3He/^4He$ is evident with the calculated whole-rock major element compositions (Figure 9.2); the least-depleted peridotites (FeO > 7 wt%) typically have higher $^3He/^4He$ (> 7 R_a) than more-depleted peridotites (FeO < 7 wt%; $^3He/^4He$ = 5-7 R_a; Figure 9.2A). By superimposing the calculated whole-rock compositions of mantle peridotite xenoliths onto

the fractional mantle melting models of Herzberg (2004) it is possible to interrogate the relationship between $^3He/^4He$ and the amount of melt-extraction. Figure 9.2A shows that off-craton mantle xenoliths, which have experienced <25% fractional melting at <4 GPa, typically have $^3He/^4He$ >7 R_a. In contrast, mantle xenoliths with compositions that reflect greater amounts of fractional melting (>25%) at higher pressures typically record $^3He/^4He$ <7 R_a. This relationship can be further scrutinised for spinel-bearing peridotites by examining the co-variation of $^3He/^4He$ with spinel Cr# and olivine Mg#. Peridotites with depleted spinel (Cr# >25) and olivine compositions (Mg# >91), and hence have experienced greater degrees of melt extractions (>10%; Arai, 1994), have more radiogenic $^3He/^4He$ than those with less-depleted mineral signatures (Figure 9.2B). These observations compare well with the findings of Rizzo *et al.* (2021), which illustrated this concept by comparing olivine and orthopyroxene Mg# with $^4He/^{40}Ar^*$ from the West Eifel and Siebengebirge (east Transylvanian Basin).

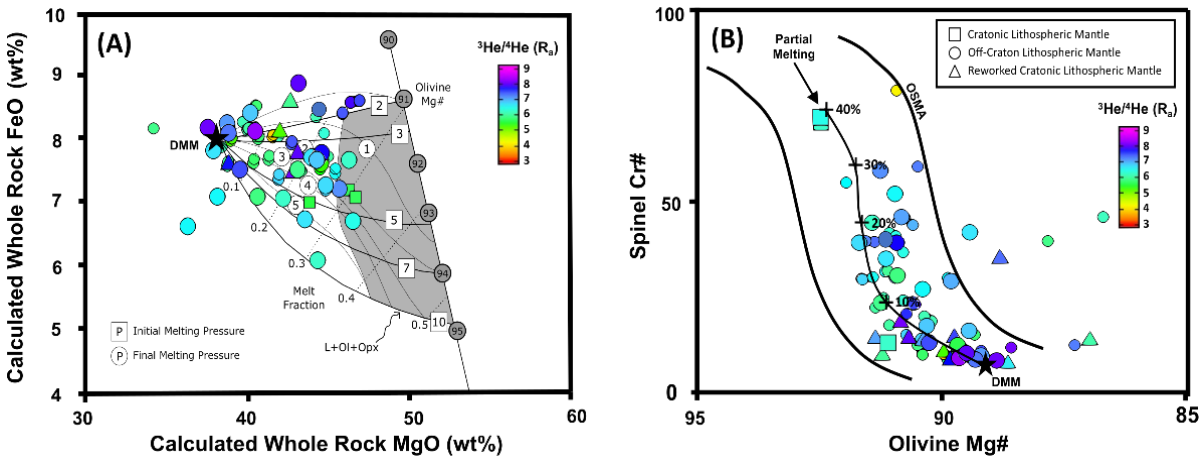

Figure 9.2. Variation of calculated bulk xenolith $^3He/^4He$ with extent of melting and metasomatism in on- and off-craton mantle xenoliths. Variations in $^3He/^4He$ are shown together with: A) calculated whole-rock MgO and FeO; B) Olivine Mg# and spinel Cr#. In plot (A) the melting model from Herzberg (2004) is included to illustrate the variation of $^3He/^4He$ with the pressure of adiabatic decompression melting, i.e. before the melt residues separated from the convecting mantle. Similarly, plot (B) shows how $^3He/^4He$ varies with the melt-extraction arrays of Boyd (1989) and Arai (1994). In all plots, the solid black star shows the composition of the Depleted MORB Mantle (DMM) source based on the $^3He/^4He$ from Allegre *et al.* (1995) and olivine Mg# from Workman & Hart (2005). FeO is calculated using the FeO:Fe_2O_3 method from Canil *et al.* (2004).

The degree of melt depletion recorded by peridotites from the sub-continental lithospheric mantle is primarily controlled by the temperature of the convecting mantle at the time of formation of the residue, i.e. prior to aggregation in the lithospheric mantle (see Chapters 1 and 6). The upper mantle has undergone significant secular cooling from the Archean (~1650°C) to the present day (~1330°C; e.g. Richter, 1988) and this is evident in primitive mantle melts where MgO contents have progressively decreased from the Archean (~30

wt.%) to the present day (~10 wt.%; Herzberg *et al.*, 2010). This cooling of Earth's convecting mantle has been widely attributed to be one of the causes of the compositional difference between ancient cratonic and younger off-craton continental mantle; peridotites with time-integrated model ages (i.e. from Re-Os and Lu-Hf isotopic systems) show a decrease in olivine Mg# from the Archean (94) to modern times (89.7; Servalli & Korenaga, 2018). The $^3He/^4He$ of the convecting mantle has also reduced in the last 3.5 Ga, likely from 80 to 8 R_a (Porcelli & Elliott, 2008). Consequently, the initial $^3He/^4He$ of the newly formed sub-continental lithospheric mantle would have been higher in the past. The absence of the expected high $^3He/^4He$ in cratonic mantle xenoliths implies that radiogenic He generated by U and Th decay (Day *et al.*, 2015) has been released by *in vacuo* crushing.

To test whether ^4He ingrowth in the lithospheric mantle explains the low $^3He/^4He$ in cratonic xenoliths, a model has been developed in this work that integrates the evolution of mantle $^3He/^4He$ and radiogenic He ingrowth with temperature-dependent melt-extraction (Herzberg *et al.*, 2010; Servali & Korenaga, 2018). This model allows the calculation of $^3He/^4He$ and the Mg# of the olivine in the lithospheric mantle that formed between the present day and the Archean (0 and 3.5 Ga). The time-resolved $^3He/^4He$ is calculated by integrating the $^3He/^4He$ of the upper mantle outlined in Porcelli & Elliott (2008) with the radiogenic ingrowth equation:

$$[He] = \sim 2.8 \times 10^{-8} (4.35 + Th/U) \times [U].t \qquad \text{(Equation 9.1)}$$

where Th and U concentrations are in ppm, [He] is 1×10^{-6} cm^3/g of ^4He at STP, and *t* is time in millions of years (see Day *et al.* 2015 and references therein).

Using the data from this study, the model assumes a ^3He starting concentration in the lithospheric mantle of 1×10^{-13} cm^3STP/g, and that the radiogenic component contains 0.138 ppm of U and 0.537 ppm of Th (Rudnick et al., 1998). Fluid-ingrowth efficiency is set at 0.1% (akin to assumptions in previous investigation, e.g. Barry *et al.*, 2014). The amount of ^3He-loss from degassing and ingrowth via thermal neutron reactions in fluid-inclusions are assumed to be negligible. The corresponding time-resolved olivine Mg# content was obtained using the calculations of Korenaga (2008) and integrated with the pressure and temperature dependent melting models of Herzberg *et al.* (2010). Previous studies have used a melting regime based on mantle temperatures influenced by a Urey ratio (*Ur*) between 0.38 and 0.23 but here the model has elected to use a *Ur* of 0.2, as this is more consistent with the

geochemistry of the lithospheric mantle (this work; Servali & Korenaga, 2018; Pearson *et al.*, 2021).

The melting model in Figure 9.3 shows that the more depleted compositions of Archean (3.5 to 2.5 Ga) sub-cratonic mantle would evolve to lower $^3He/^4He$ than off-craton sub-continental mantle which formed since 2.5 Ga. Using the parameters from previous studies (Herzberg, 2004; Herzberg *et al.*, 2010; Porcelli & Elliot, 2008; Servali & Korenaga, 2018), and assuming that the sub-continental lithospheric mantle is derived from melting of peridotite in the convecting upper mantle, this model predicts that the $^3He/^4He$ of fluids trapped in inclusions in the ancient sub-cratonic mantle (olivine with Mg# = 92.5 to 94) has evolved to values in the range 2.9-4.5 R_a. Off-craton mantle with olivine Mg# = 89.7 to 92.5 should have $^3He/^4He$ ranging from 4.5 to 8 R_a (Figure 9.3A). These results largely match the observed global trend shown in Figure 9.3B.

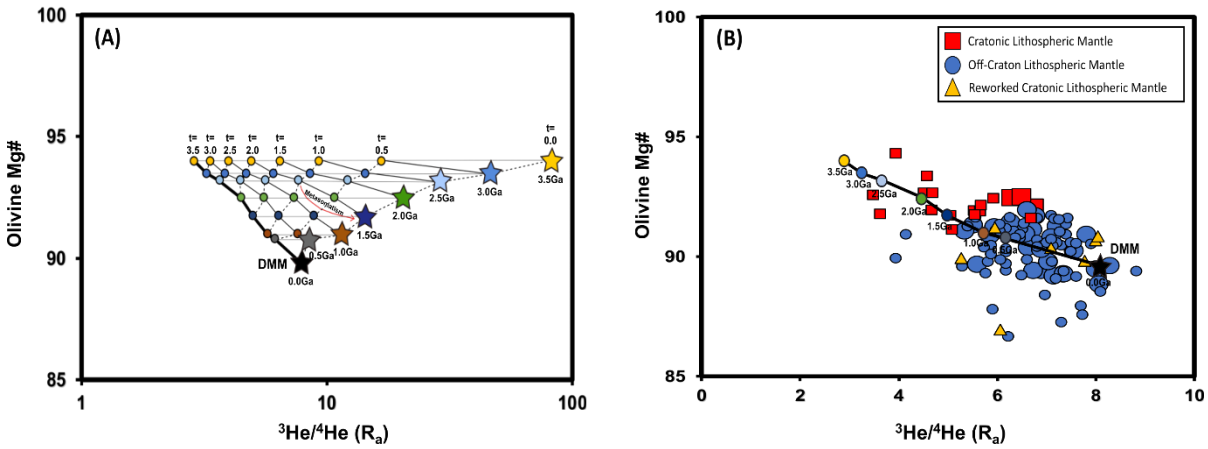

Figure 9.3. (A) Time-dependent lithosphere evolution diagram comparing bulk xenolith $^3He/^4He$ with olivine Mg#. Stars show the composition of the MORB source mantle at different time intervals, where $^3He/^4He$ at 3.5 Ga = 81.4 Ra, 3 Ga = 45.8 Ra, 2.5 Ga = 28.8 Ra, 2 Ga = 20.2 Ra, 1.5 Ga = 14.3 Ra, 1 Ga = 11.4 Ra, 0.5 Ga = 8.4 Ra, 0 Ga = 8 Ra (Porcelli & Elliott, 2007). The closed circles show the time-dependent sub-continental lithospheric mantle composition in billions of years, (B) Variation in olivine Mg# and bulk xenolith $^3He/^4He$ (from this study) and the published literature overlain on the results of time-dependent lithosphere evolution models shown in (A).

This work provides little evidence for the involvement of either high $^3He/^4He$ deep mantle or low $^3He/^4He$ derived from subduction-modified mantle. Instead, the range of xenolith $^3He/^4He$ (typically from 3.5 to 8.8 R_a) predominantly reflects time-dependent change in the $^3He/^4He$ of melts derived from the convecting mantle and variability in the incorporation of radiogenic He. Superimposed on this are the effects of metasomatism by percolating small-fraction melts derived from the depleted upper-mantle, which would overprint the pre-

existing lithospheric mantle (see below). This process might account for mantle peridotites from N. Tanzania that retain Archean Re-Os sulfide ages (up to 3 Ga; Burton *et al.*, 2000) but have olivine with moderate Mg# (91-92.5) and $^3He/^4He$ (6.3-6.7 R_a; Table 1). This interpretation is consistent with multiple phases of metasomatic enrichment of the lithospheric mantle in this region (e.g. Gibson *et al.*, 2013).

9.2.2 $^3He/^4He$ constraints on the formation and evolution of off-craton mantle

Off-craton mantle peridotites with the lowest enrichments in incompatible trace-elements ($[La/Yb]_N$ <0.36) and $[Th/Yb]_N$ <0.12) typically have $^3He/^4He$ that overlap with modern MORB-source mantle (7–9 R_a; Figure 9.4). These characteristics are well established in the mantle xenolith suites from Tariat (Mongolia) and Kilbourne Hole (SW USA) and are common, albeit not ubiquitous, in published datasets for the Yemen and western Saudi Arabia xenolith suites (Sgualdo *et al.*, 2015; Konrad *et al.*, 2016). This relationship suggests that these xenoliths are recording: (i) recent underplating by MORB-source mantle; or (ii) an ancient depletion event that has been overprinted by He derived from the host magma during entrainment. The young Re-Os ages of peridotite xenoliths from Kilbourne Hole (Harvey *et al.* 2011) and Tariat (Carlson & Ionov, 2019) support recent underplating, as reactive infiltration of the host alkali basalt/basanite magma would tend to increase both $^3He/^4He$ and incompatible trace-element concentrations of the peridotite xenoliths. The preferred interpretation of the $^3He/^4He$ determined in off-craton mantle xenoliths from Kilbourne Hole and Tariat is also supported by the similarity of mineral and whole-rock chemistry of the xenoliths to depleted MORB source mantle (see Chapter 4, 5, 6 and 8), and implies that this lithospheric mantle formed from modern-day upper-mantle. With the exception of the Ethiopian Rift region (Halldórsson *et al.*, 2014), there is no significant evidence in the existing database to suggest that mantle peridotites, entrained by <100 Ma magmas, form as a residue of deep mantle melting (i.e. $^3He/^4He$ > 10 R_a).

The correlations outlined above imply that the $^3He/^4He$ trapped in fluid inclusions in sub-continental lithospheric mantle phases remains largely unaffected by subsequent events. (Figure 9.3). This is inconsistent with the abundant evidence from trace element and isotopic signatures for metasomatism (e.g. Dawson, 1984). This study demonstrates that metasomatised peridotites with high SiO_2 and low FeO have the most radiogenic $^3He/^4He$ (<7 R_a; Figure 9.4A). Furthermore, mantle xenoliths with a relatively low modal amount of olivine

at a given olivine Mg#, and which plot outside the oceanic peridotite melt-extraction array (Figure 9.4B), also record more radiogenic $^3He/^4He$ (<7 R_a). The low modal olivine is compensated for by excess orthopyroxene, which is commonly interpreted as silicate-enrichment associated with melts or fluids from subducted oceanic lithosphere (e.g. Kelemen *et al.*, 1998).

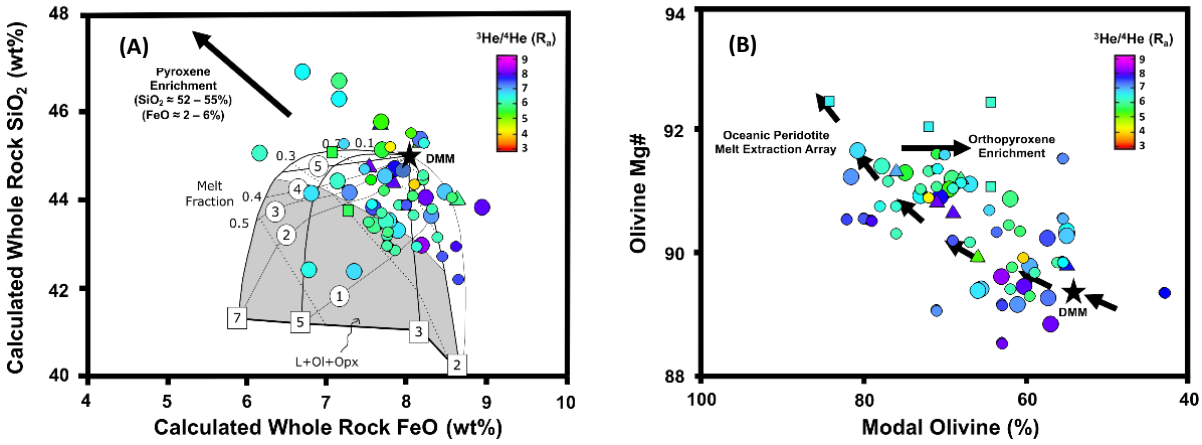

Figure 9.4. A) calculated whole-rock FeO* and SiO_2; B) modal olivine and olivine Mg#. Melting model from Herzberg (2004) is included to illustrate the variation of $^3He/^4He$ with the pressure of adiabatic decompression melting, i.e. before the melt residues separated from the convecting mantle. Similarly, (B) shows how $^3He/^4He$ varies with the melt-extraction arrays of Boyd (1989) and Arai (1994).

The mantle xenoliths with incompatible trace element signatures indicative of enrichment by small-fraction melts (e.g. $[La/Yb]_N$ > 0.36) have $^3He/^4He$ that ranges from 5 to 8 R_a (Figure 9.5A). Those with the higher $^3He/^4He$ (> 7 R_a) include off-craton samples from the Antarctic Peninsula, Southern Patagonia, Yemen, Hyblean Plateau, Western Saudi Arabia, and the Southern Main Ethiopian Rift. The off-craton enriched mantle xenoliths with lower $^3He/^4He$ (<7 R_a) include those from the W. Eifel, the Antarctic Peninsula, NW Libya and E. Transylvanian Basin. In the Antarctic Peninsula xenolith suite, the peridotites have the highest $^3He/^4He$ and more the radiogenic signatures are present in clinopyroxenites.

To resolve the cause of the local variations in the $^3He/^4He$ of sub-continental mantle, this study investigates relationships of $^3He/^4He$ with signatures indicative of: (i) different metasomatic agents, i.e. carbonatite and silicate melts or fluids; and (ii) melts or fluids derived from different reservoirs, e.g. recycled oceanic crust and the MORB source mantle. Incompatible trace-element ratios such as $[Ti/Eu]_N$ and $[La/Yb]_N$ of clinopyroxenes are widely used to distinguish between silicate and carbonatite metasomatic agents (Coltorti *et al.*, 1999), but Figure 9.5B shows that the $^3He/^4He$ of clinopyroxenes does not vary systematically

with either $[Ti/Eu]_N$ or $[La/Yb]_N$. A relationship between $^3He/^4He$ and LILE/HREE (e.g.$[Th/Yb]_N$) should discriminate between small-fraction melts of MORB source mantle and those from melts or fluids from recycled oceanic lithosphere. Figure 9.5C shows that xenoliths with $^3He/^4He$ >7 R_a tend to have been enriched by small-faction melts of the MORB-source mantle, whereas, xenoliths with lower $^3He/^4He$ (<7 R_a) have higher $[Th/Yb]_N$ that are characteristic of melts and fluids from ancient recycled oceanic lithosphere. These low $^3He/^4He$ xenoliths are also dominated by high $[La/Yb]_N$ and intermediate $[Ti/Eu]_N$ (0.1 -1), which are typical of subduction-zone fluids (Kessel *et al.*, 2005). While this model favours the input of recycled material, the more radiogenic $^3He/^4He$ and high LILE/HREE could reflect an ancient metasomatic event that became isolated and has experienced ^4He ingrowth. This hypothesis cannot rule out, however, the contribution of metasomatic melts derived from 'streaks' of ancient enriched (pyroxenite) material in the convecting upper mantle. These would have elevated U and Th contents relative to those from the surrounding peridotite mantle. Over time, this type of metasomatism would result in a lower $^3He/^4He$. The variations of $^3He/^4He$ with major and trace elements displayed in Figure 9.5D reflect these different mechanisms, and show that many of the peridotites with elevated LILE/HREE and lower $^3He/^4He$ also have a depleted chemistry (e.g. olivine Mg# >92), consistent with ancient lithosphere formation and substantial ^4He-ingrowth.

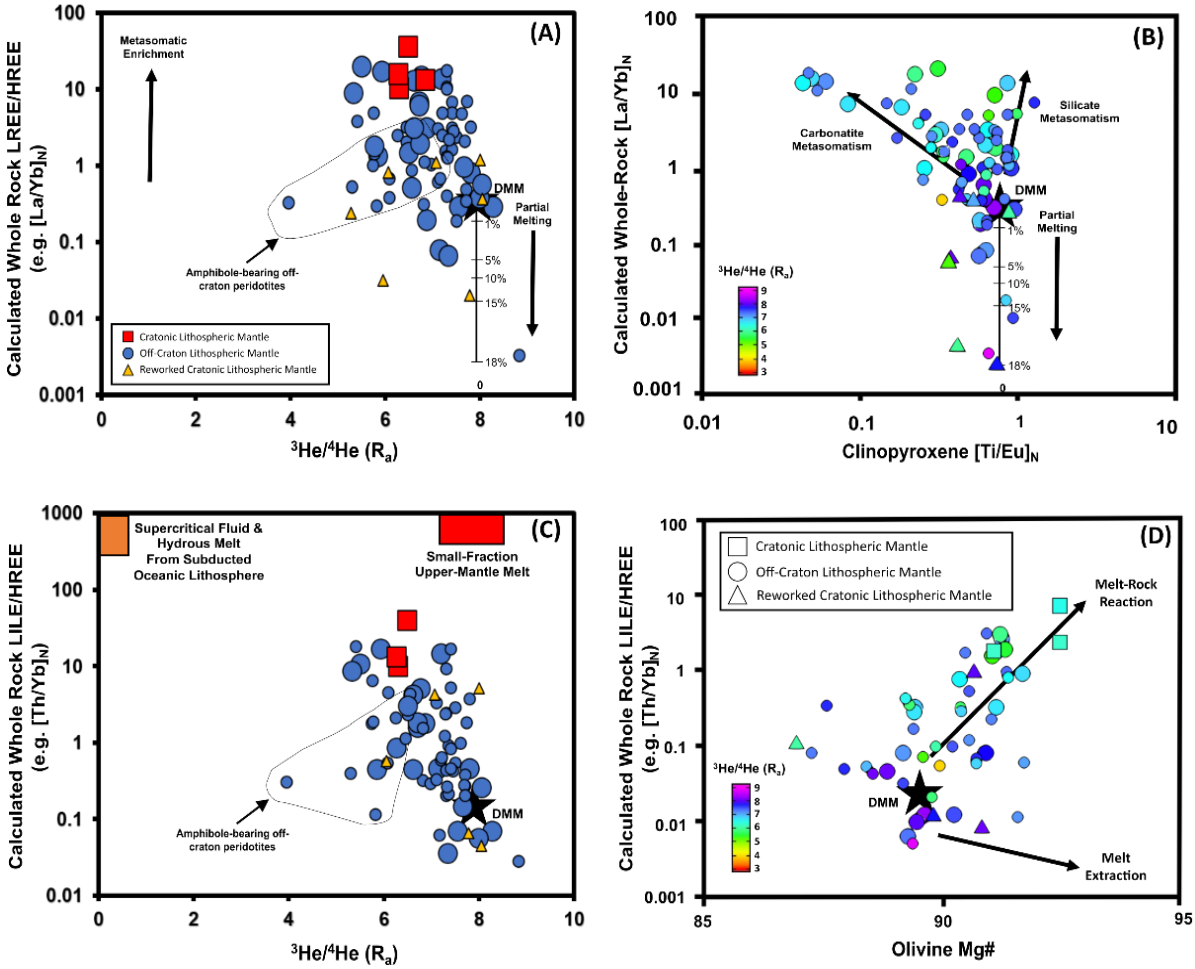

Figure 9.5 Variation of $^3He/^4He$ with different indices of metasomatism in mantle xenoliths. (A) Shows the variation between calculated bulk xenolith $^3He/^4He$ and $[La/Yb]_N$ for mantle peridotites and pyroxenites. (B) Illustrates the variations in clinopyroxene $^3He/^4He$ with $[Ti/Eu]_N$ and $[La/Yb]_N$, where $_N$ denotes normalised to primitive mantle (McDonough & Sun, 1998). (C) Shows calculated whole-rock $^3He/^4He$ and $[Th/Yb]_N$. The compositions of supercritical fluids derived from subducted oceanic lithosphere is from Kessel *et al.* (2005), hydrous melt from recycled oceanic lithosphere is from Hermann & Rubatto (2009) and small-fraction upper-mantle melt from Blundy & Dalton (2000). (D) Illustrates the variation in olivine Mg# and calculated bulk xenolith $[Th/Yb]_N$, colour coded for $^3He/^4He$. On all panels, the solid black star represents Depleted MORB Mantle (DMM; Workman & Hart, 2005; Allegre *et al.,* 1995). The radiogenic ingrowth and partial melting models are based on Day et al. (2015) and Warren (2016), respectively.

Enrichment of the lithospheric mantle from silicate or carbonatitic melts can both increase or decrease $^3He/^4He$ depending, on the age and source of the metasomatic melts and the age of the lithospheric mantle with which they are interacting. Based on SiO_2 and LILE/HREE systematics, the more radiogenic $^3He/^4He$ signatures (<7 R_a) may reflect the involvement of melts from recycled oceanic lithosphere, while less radiogenic signatures (>7 R_a) show a greater affinity to small-fraction melts sourced from the MORB source mantle. However, the effects of the metasomatic melts appear to be modest and not the primary control on $^3He/^4He$ in the sub-continental lithospheric mantle.

9.3 Implications for intra-continental magmatism

The wide range of $^3He/^4He$ in fluid inclusions trapped in lithospheric mantle phases, and the distinct signatures of on- and off-craton mantle (this work, Day *et al.*, 2015), indicate that the $^3He/^4He$ of the sub-continental lithospheric mantle is considerably more variable than earlier studies conceived (e.g. Dunai & Porcelli, 2002; Gautheron & Moreira 2002). This has broader implications for the variability of $^3He/^4He$ in magmas erupted through continental lithosphere. The thick cratonic lithosphere (up to 240 km) limits the amount of mantle melting and the only magmas to reach surface are small-fraction melts, i.e. proto-kimberlites, lamproites and ultramafic lamprophyres (Dawson, 1980). Despite the proposed origin of some kimberlites in the deep convecting mantle (Woodhead *et al.*, 2019), these relatively small-volume magmas typically have $^3He/^4He$ that are lower than depleted mantle (Figure 9.6A). This is probably because they contain a large cargo of lithospheric mantle derived olivine xenocrysts (typically 20-30 vol % or more), which are characterised by radiogenic $^3He/^4He$ (this work; Day *et al.*, 2015). Moreover, the ascent of proto-kimberlites through this thick ancient lithospheric mantle is fuelled by the preferential digestion of orthopyroxene from entrained wall-rocks, that decreases melt MgO content and drives exsolution of CO_2 (Russell *et al.*, 2012). Since orthopyroxene from ancient sub-cratonic mantle is also characterised by low $^3He/^4He$ (this work; Day *et al.*, 2015) and $^{143}Nd/^{144}Nd$ (e.g. Pearson & Wittig, 2014), the assimilation of a large amount of this phase during kimberlite ascent (approximately 20-30 %; Russell *et al.*, 2012) may significantly decrease the melt $^3He/^4He$, Mg/Si, and $^{143}Nd/^{144}Nd$. Olivine subsequently crystallising from this melt will also have relatively low $^3He/^4He$, Mg# and $^{143}Nd/^{144}Nd$. These observations suggest that the incorporation of olivine and assimilation of orthopyroxene from the sub-cratonic mantle are responsible for the rarity of kimberlite olivines (xenocrysts or phenocrysts) with high $^3He/^4He$ in certain locations (Figure 9.6B).

Olivines with high $^3He/^4He$ (up to 26.2 R_a; Gaffney *et al.* 2005; Tachibana *et al.*, 2006) are found in CO_2-rich, high-MgO magmas with similarities to kimberlites (aillikites; Tappe *et al.*, 2011). These ultramafic lamprophyres were emplaced as dykes at Sarfartoq in West Greenland, on the northern margin of the North Atlantic craton. The olivines analysed by Tachibana *et al.* (2006) are small (0.5 mm to 1 mm) and appear to have crystallised directly from the aillikite melt. The aillikites have higher bulk-rock Mg/Si ratios (1.53; Gaffney *et al.*

2005) than global kimberlites (1.31 ± 0.16; Giuliani *et al.*, 2020), which suggests that the parental melts ascended without assimilating large amounts of mantle orthopyroxene.

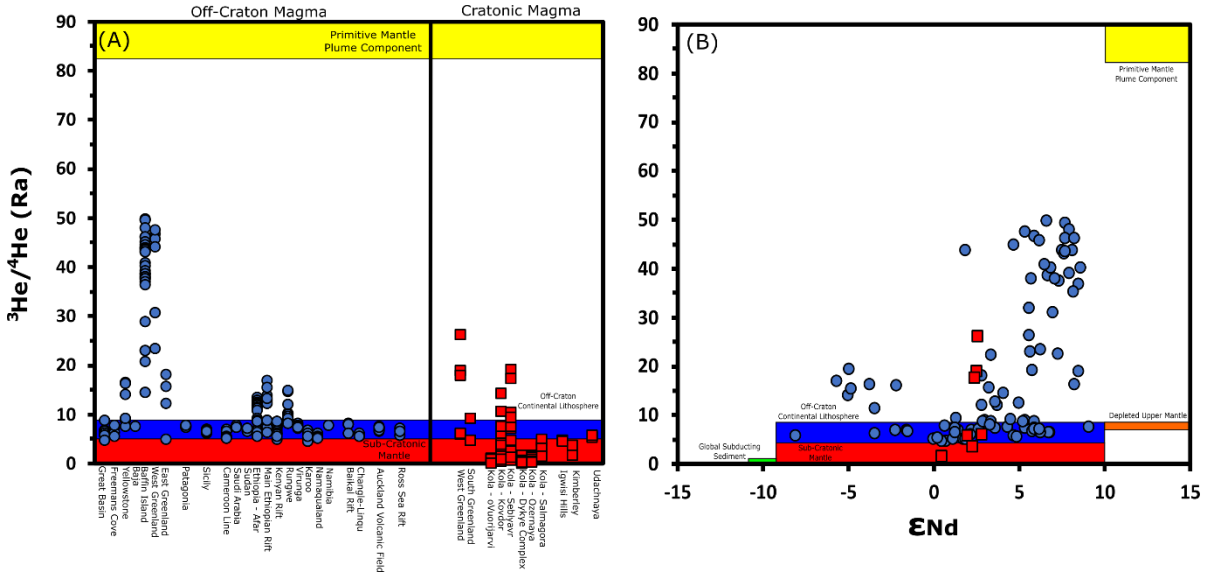

Figure 9.6. A) Comparison of $^3He/^4He$ in on- and off-craton continental magmas and mantle xenoliths. B) $^3He/^4He$ versus $^{143}Nd/^{144}Nd$ (normalised to chondritic uniform reservoir value of 0.512638, expressed as εNd) of off-craton and on-craton magmas. On-craton lava from Udachnaya (Sumino *et al.*, 2006); Kimberley (Giuliani *et al.*, 2020); Igwisi Hills (Brown *et al.*, 2012; Willox *et al.*, 2015); West & South Greenland (Tachibana *et al.*, 2006; Gaffney *et al.*, 2007); Kola Peninsula (Marty *et al.*, 1998; Tolstikhin *et al.*, 2002). Off-craton data from Great Basin (Reid *et al.*, 1996); Canadian Cordillera (Day *et al.*, 2005); Yellowstone (Graham *et al.*, 2009); Baja, California (Schmitt *et al.*, 2010); Nicaragua (Shaw *et al.*, 2006); Patagonia (Ackert *et al.*, 2003); Baffin Island (Stuart *et al.*, 2003; Starkey *et al.*, 2009; Willhite *et al.*, 2019; Jackson *et al.*, 2010); East Greenland (Jackson *et al.*, 2010; Marty *et al.*, 1998); West Greenland (Starkey *et al.*, 2009; Graham *et al.*, 1998); Sicily (Marty *et al.*, 1994; Coulson *et al.*, 2011; Nuccio *et al.*, 2008); Cameroon Line (Barfod *et al.*, 1999); Saudi Arabia (Konrad *et al.*, 2016); Sudan (Franz *et al.*, 1999); Ethiopia (Pik *et al.*, 2006; Scarsi & Craig, 1996; Halldorsson *et al.*, 2014; Rooney *et al.*, 2012); Kenyan Rift (Pik *et al.*, 2006; Halldorson *et al.*, 2014; Mollex *et al.*, 2018); Rungwe, Tanzania (Hilton *et al.*, 2011 Halldorsson *et al.*, 2014); Virunga (Day *et al.*, 2005; Pik *et al.*, 2006; Halldorson *et al.*, 2014); Karoo (Heinonen *et al.*, 2015); Namaqualand (Day *et al.*, 2005); Namibia (Stroncik *et al.*, 2017); Baikal Rift (Barry *et al.*, 2007); China (Li *et al.*, 2002; Chen *et al.*, 2007; Xu *et al.*, 2014); New Zealand (Rowe *et al.*, 2020); Antarctica (Nardini *et al.*, 2009). Reservoir constraints from Depleted mantle from Ito *et al.* (1987) and Allegre *et al.* (1995); primitive mantle from Ito *et al.* (1987) and Class & Goldstein (2005); on- and off-craton mantle from Fan *et al.*, 2000 and this study; global subducted sediment from Plank & Langmuir, (1988) and Oxburgh & O'Nions (1983); Proto-kimberlite from Guiliani *et al.*, (2021) and Willox *et al.*, (2015).

Figure 9.7 provides an initial appraisal of this, indicating a relationship between kimberlite Mg/Si and $^3He/^4He$ and the important role for orthopyroxene assimilation. Notably, the lithospheric mantle beneath the North Atlantic craton has less excess orthopyroxene than other cratons and so the $^3He/^4He$ of melts traversing through this region are less susceptible to overprinting. More work is required, however, to determine the full extent of the variability of $^3He/^4He$ in well-characterised kimberlites and associated high MgO magmas (lamproites and ultramafic lamprophyres). This would place improved constraints on the He-concentrations in the cratonic mantle and proto-kimberlites (outlined by 1:1 to 1:100 mixing

lines) and the role of ^{4}He-ingrowth from host-kimberlite (shown by secondary ^{4}He-ingrowth vector). Future studies also needed involve: fresh unaltered olivine; phenocrystic (as opposed to xenocrystic) olivine; and an appraisal of the role of secondary ^{4}He overprinting from the host kimberlite.

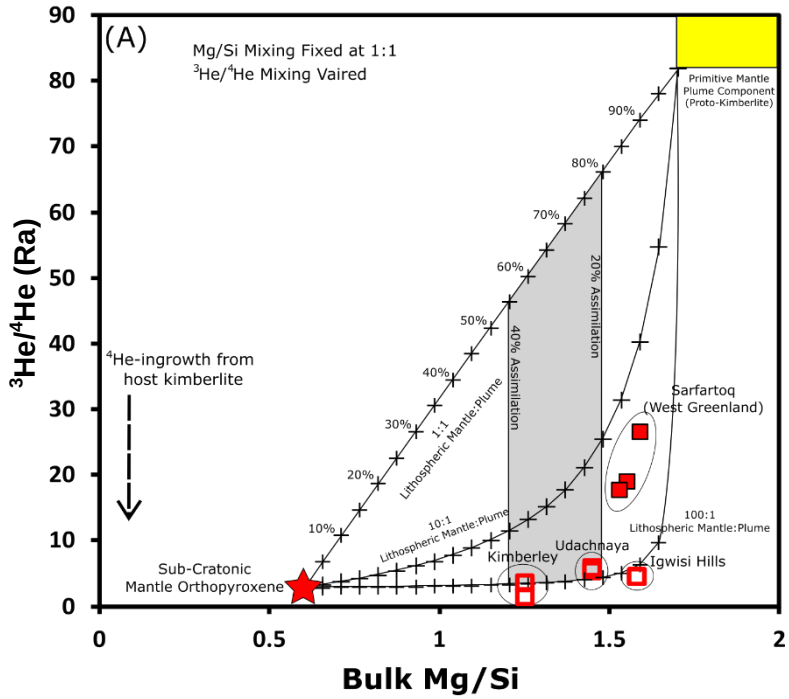

Figure 9.7. Binary mixing model of sub-cratonic mantle orthopyroxene with proto-kimberlite ^{3}He/^{4}He and Mg/Si. Data sources same as Figure 9.6 with additional sub-cratonic mantle orthopyroxene from Gibson *et al.* (2008).

9.4 Conclusions

This study has observed systematic differences within the ^{3}He/^{4}He of off-craton mantle and also between on- and off-craton mantle. The ^{3}He/^{4}He of off-craton mantle varies, with some locations exclusively retaining ^{3}He/^{4}He signatures > 7 R_a (e.g. Kilbourne Hole), others have more radiogenic signatures < 7 Ra (e.g. West Eifel Volcanic Field), and the remainder preserving a wide range of ^{3}He/^{4}He (4 to 8.8 R_a e.g. Antarctic Peninsula; Figure 9.8). The ^{3}He/^{4}He signatures of off-craton mantle xenoliths are largely distinct from those found in on-craton settings (0.5 to 6.7 R_a). These findings are consistent with: (i) the local variability in ^{3}He/^{4}He in off-craton mantle, which in combination with varying U+Th concentrations will produce globally heterogeneous ^{3}He flux rates (e.g. Sandoval-Velasquez *et al.*, 2021); and (ii) the systematic difference in the ^{3}He/^{4}He of on- and off-craton continental mantle noted by Day *et al.* (2015). An important finding from these previous studies, and supported by this

work, is that a single mean $^3He/^4He$ cannot be attributed to the lithospheric mantle at different tectonic settings as suggested by Gautheron & Moreira (2002).

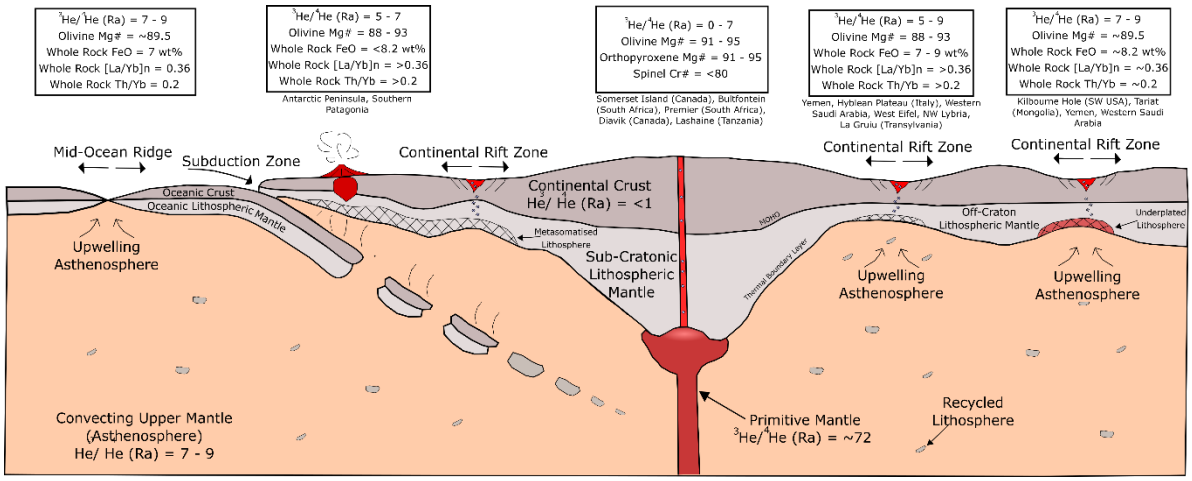

Figure 9.8. Summary diagram showing variations in $^3He/^4He$ of the lithospheric mantle at different tectonic settings, based on data from mantle xenoliths presented in this study (Table 1) and the published literature. The $^3He/^4He$ of various reservoirs in the convecting mantle are shown for comparison.

An important new finding from this work is that $^3He/^4He$ exhibits systematic relationships with the major- and trace-element composition of mantle olivines and pyroxenes. While there is some evidence that metasomatism may affect the $^3He/^4He$ of the lithospheric mantle, this appears be a sub-ordinate process that results in some minor scatter to global correlations. In off-craton mantle, the more radiogenic $^3He/^4He$ signatures (<7 R_a) may reflect the involvement of melts or fluids from recycled oceanic lithosphere, whereas less radiogenic signatures (>7 R_a) show a greater affinity to small-fraction melts sourced from the depleted upper-mantle (Figure 9.8). Overall, the variations in $^3He/^4He$ and Mg# exhibited by on- and off-craton mantle largely reflect the amount of melt-extraction in the convecting mantle, and the different amounts of radiogenic ingrowth occurred after the melt residues had been incorporated into the sub-continental lithospheric mantle.

These new findings also highlight the role of material derived from the sub-continental lithospheric mantle reservoir on the $^3He/^4He$ of small-fraction, deep-sourced mantle melts. The low $^3He/^4He$ signatures observed for many kimberlites that have ascended through the ancient sub-cratonic lithospheric mantle reflect the high propensity of their parental melts to assimilate and digest orthopyroxene; in many cases this has resulted in overprinting of the initial high $^3He/^4He$ expected for kimberlites. This is distinct from basaltic magmas that have erupted through off-craton lithosphere and preserve the melt source $^3He/^4He$ more clearly.

Finally, this study highlights the complex series of melt extraction and enrichment events which influence the volatiles stored in the lattice of crystals (C, H, S, B, halogens) and trapped in fluid inclusions (He, CO_2, CH_4, H_2O). Further advancement on understanding these volatiles is most evident through the variability of $^3He/^4He$ of fluid inclusions trapped in lithospheric mantle phases. Overall, this indicates these reservoirs remain largely undisturbed unless metasomatically perturbed by mantle melts.

Chapter 10. Coupled variations of He & C isotopes with major & trace elements in mantle xenoliths

10.1 Introduction

The origin and abundance of carbon in the off-craton sub-continental lithospheric mantle is poorly constrained (e.g. Kelemen & Manning, 2015; Foley & Fischer, 2017; Hirschmann, 2018) and the extent to which it acts as a reservoir in global carbon cycles is unclear. Determinations of CO_2 and He systematics in peridotite and pyroxenite xenoliths have yielded important insights into the regional variations within the subcontinental lithospheric mantle (Correale *et al.*, 2015; Rizzo *et al.*, 2018; 2021; Halldorson, 2014; Sandoval-Velasquez *et al.*, 2021; Gennaro *et al.*, 2017; Porcelli *et al.*, 1992; and Bianchini & Natali, 2017). The influence of melts/fluids from the primitive mantle was identified by Halldorson (2014), the convecting upper-mantle by Sandoval-Velasquez (2021) and recycled lithosphere by Gennaro *et al.* (2017). However, there remain outstanding uncertainties in the $CO_2/^3He$ of global lithospheric mantle and the extents to which different melts and fluids from different reservoirs contributed to these variations.

This work combines the new C and He (concentrations and isotope ratios) from peridotites and pyroxenites from Kilbourne Hole, Tariat Volcanic Field, West Eifel, Pali Aike and the Antarctic Peninsula (Chapter 8) with the global database for off-craton mantle. This builds on previous studies by integrating mineral and whole-rock major and trace element chemistry with CO_2 analysis in order to improve constraints on the variability of CO_2 in the off-craton mantle.

10.2 CO_2 and ^3He concentrations

To evaluate the co-variation of CO_2 and ^3He in off-craton mantle, $CO_2/^3He$ is compared with CO_2 and ^3He concentrations of olivine, orthopyroxene, clinopyroxene, as well as calculated whole-rock values for peridotite and pyroxenites in Figure 10.1. This reveals a linear positive relationship between $CO_2/^3He$ and CO_2 (Figure 10.1A). This linear trend, however, cannot be explained by a fixed ^3He-concentration (from $1x10^{-15}$ to $1x10^{-10}$ ccSTP/g) with variable CO_2 input ($1x10^{-6}$ to $1x10^{2}$ ccSTP/g). Instead, the $CO_2/^3He$ array is a product of 3 distinct groups with their own processes (Figure 10.1B). Group 1 consists of olivine-hosted fluids with low $CO_2/^3He$ that range from approximately 5×10^6 to 1×10^9; Group 2 consists of

orthopyroxene, clinopyroxene and some peridotite whole-rocks that have $CO_2/^3He$ mostly within 5 x 10^9 to 1 x 10^{11} and Group 3 is a subset of whole-rock analysis from Bianchini & Natali (2017) that have very high $CO_2/^3He$ at 1 x 10^{14} to 1 x 10^{16} from the Iberian Peninsula.

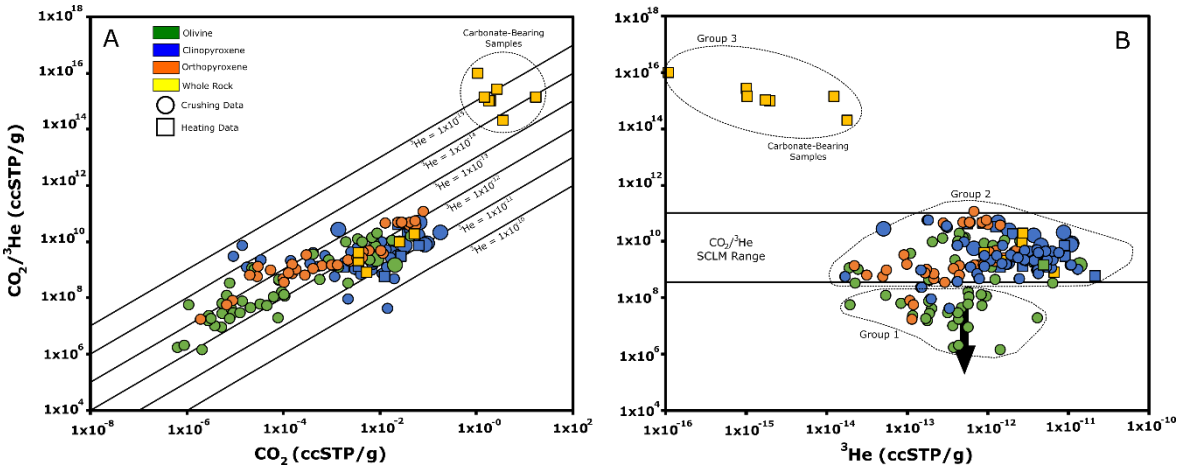

Figure 10.1. Variations in olivine, orthopyroxene, clinopyroxene and whole-rock CO_2 and ^3He concentrations displayed as: a) CO_2 vs $CO_2/^3He$ with modelled array for a fixed ^3He-concentration. b) ^3He vs $CO_2/^3He$. $CO_2/^3He$ and range for lithospheric mantle proposed using insights from this study. Symbols for data from this study larger than those from the published database. Data from Correale *et al.* (2015); Rizzo *et al.* (2015; 2021); Halldorson, (2014); Sandoval-Velasquez *et al.* (2021); Gennaro *et al.* (2017); Porcelli *et al.* (1992); and Bianchini & Natali (2017).

The $CO_2/^3He$ from Group 1 correlates positively with the CO_2 concentration of olivine (Figure 10.1A) but not with ^3He (Figure 10.1B). In contrast, the Group 2 samples (mainly orthopyroxene and clinopyroxene including data from this study) have constant $CO_2/^3He$ at given ^3He and CO_2 concentrations. The variation in olivine $CO_2/^3He$ observed in Group 1 is explained by ^3He-equilibrium and CO_2-disequilibrium between mantle phases analysed by Rizzo *et al.* (2021). The ^3He is evenly distributed between olivine, orthopyroxene and clinopyroxene but olivine is CO_2-poor relative to other minerals.

The high $CO_2/^3He$ of Group 3 reflects the mineralogy of these peridotites and the method used for the CO_2-analysis. These are rare carbonate-bearing peridotites from Bianchini & Natali (2017) that were analysed by heating experiments. This method releases carbonates and so produces very high whole-rock CO_2 concentrations relative to crushing techniques, which only release CO_2 from fluid inclusions. Since carbonates are accessory phases in the off-craton lithospheric mantle, with most carbon occurring as CO_2-bearing fluid inclusions, the high $CO_2/^3He$ recorded by samples presented by Bianchini & Natali (2017) are unrepresentative.

Based on these insights, the $CO_2/^3He$ of the off-craton mantle is calculated using only the analysis of Group 2 minerals. Figure 10.2 shows that the concentrations of ^3He and CO_2 are closely correlated and $CO_2 = 8 \times 10^{11} \times {}^3He^{1.20}$ (with CO_2 and ^3He in ccSTP/g) and $R^2 = 0.74$. This equates to a $CO_2/^3He$ ratio of roughly 1.3×10^9 (where $^3He = 1 \times 10^{-14}$), 2.0×10^9 (where $^3He = 1 \times 10^{-13}$), 3.2×10^9 (where $^3He = 1 \times 10^{-12}$), 5.1×10^9 (where $^3He = 1 \times 10^{-11}$) and 8.0×10^9 (where $^3He = 1 \times 10^{-10}$). This range encompasses the median $CO_2/^3He$ ratio of 2.2×10^9 and 1.67×10^9 of the MORB-source mantle proposed by Marty & Tolstikhin (1998) and Tucker *et al.* (2018).

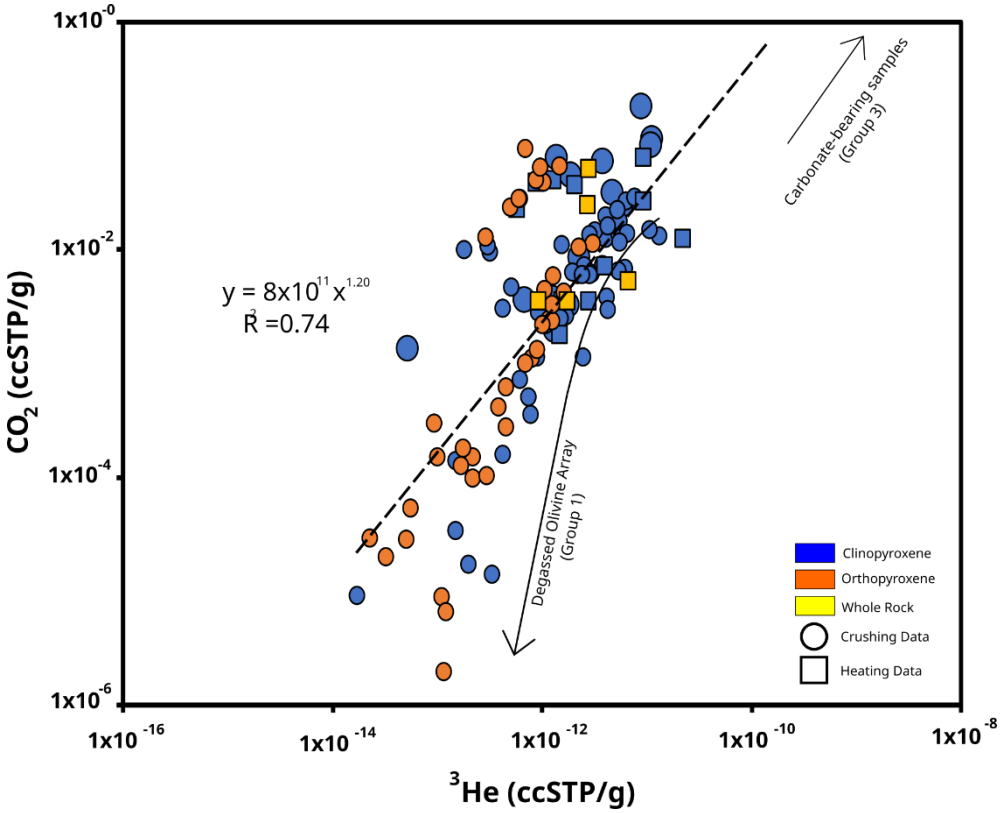

Figure 10.2. Co-variations in of ^3He and CO_2 in 'Group 2' samples described previously. Symbols for the data from this study are larger than those from the published database (Correale et al., 2015; Rizzo et al., 2018; 2021; Halldorson, 2014; Sandoval-Velasquez et al., 2021; Gennaro et al., 2017; Porcelli et al., 1992). Array of 'Group 1' and 'Group 3' samples indicated by arrows.

From this dataset and the ^3He calculations in Chapter 7, the abundance of fluid-inclusion hosted CO_2 and influx rates to the off-craton lithospheric mantle can be determined. A global range of-craton ^3He concentration of 1×10^{-13} to 1×10^{-11} ccSTP/g (Figure 10.1). equates to an off-craton CO_2 concentration of ~8.9×10^{-9} to ~2.2×10^{-6} mol/g. Based on the volume estimate for the global off-craton sub-continental mantle of 1.39×10^{25} g from

Gibson & McKenzie (in review), the bulk CO_2 concentration corresponds to 5.5 x 10^{18} to 1.4 x 10^{21} g.

Based on the flux estimate of ^3He = 3 atoms/s/cm^2 calculated in Chapter 7, together with a $CO_2/^3He$ ratio of 3.2x10^9 (^3He = 1x10^{-12}), the influx of CO_2 to continental off-craton lithospheric mantle corresponds to approximately 1.0x10^{10} atoms/s/cm^2. This equates to 4.1x10^{19} g/million years.

These calculations assume that all of the carbon in the lithospheric mantle is present as CO_2, however mantle carbon may also be present as CO in fluid inclusions (e.g. Andersen *et al.*, 1984). Fortunately, the crushing and heating experiments that have been employed in this work cause any released carbon to be analysed as bulk C and reported as CO_2 (see Appendix C).

$$Bulk\ C = CO_2 \times \frac{Atomic\ Mass\ C}{Molecular\ Mass\ CO2} \qquad \text{Equation 10.1}$$

Where CO_2 can be in any mass or concentration units, the atomic mass of C is 12.01 and the atomic mass of CO_2 is 44.01.

When discussed as bulk C, this equates to an off-craton sub-continental mantle C/^3He of 1.2 x 10^8 (where ^3He = 1 x 10^{-12} ccSTP/g), C concentration from 2.4 x 10^{-9} to 6.1 x 10^{-7} mol/g, and a budgets of 3.4 x 10^{16} to 8.5 x 10^{18} moles. The median C influx of 2.9 x 10^9 atoms/s/cm^2 is equivalent to approximately 6.9 x 10^{12} g/y. This estimate of the C influx to bulk off-craton sub-continental lithospheric mantle falls well within the range for the entire lithospheric mantle (0 to 12.8 mt/y) proposed by Kelemen & Manning (2015).

10.3 $\delta^{13}C$ and $^3He/^4He$ systematics

Having initially formed as melt residue from the convecting upper-mantle, the subcontinental lithospheric mantle has undergone extensive metasomatism by melts and carbonic fluids derived from either the convecting mantle or recycled oceanic lithosphere. The results from this study combined with those from previous investigation may provide insights into the nature of the melt/fluid source using coupled $^3He/^4He$ and $^{12}C/^{13}C$ isotopes. The most striking feature is the wide range in lithospheric mantle $\delta^{13}C$ (-25 to 5‰) and $^3He/^4He$ (4.2 to 13.9 Ra) compositions (Figure 10.3). The large range in $\delta^{13}C$ encompasses that measured in subducted altered oceanic crust (<-20 ‰; e.g. Li *et al.*, 2019 and

references therein), carbonate (0 to 5 ‰; Gradstein *et al.*, 2012) and the MORB-source (-5 ± 2‰ (e.g. Cartigny *et al.*, 2014). Furthermore, the wide range in $^{3}He/^{4}He$ displays affinity with the upper mantle (8 ± 1 Ra; (Allegre *et al.*, 1995) but requires input of melts of primordial material (>10 Ra; e.g. Stuart *et al.*, 2003) and also from a more radiogenic component (<7 Ra), which reflects *in-situ* ^{4}He ingrowth in ambient lithospheric mantle U+Th (see Chapter 9).

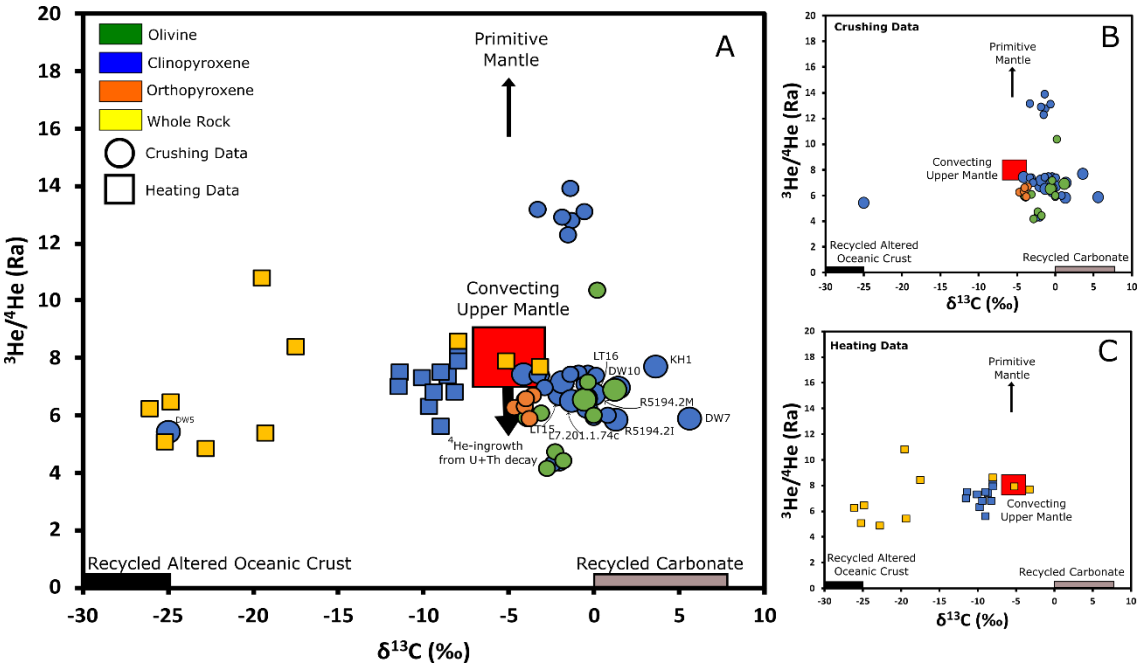

Figure 10.3. $\delta^{13}C$ and $^{3}He/^{4}He$ of olivine, orthopyroxene, clinopyroxene and bulk xenoliths. Reservoir values from Gradstein *et al.* (2012); Li *et al* (2019); Allegre *et al* (1995); and Stuart *et al.* (2003). The symbols for this data from this study are larger than those from the published database. Data sources are the same as Figure 8.1

Figure 10.3 shows a comparison of the $\delta^{13}C$-$^{3}He/^{4}He$ compositions of peridotite and pyroxenite mantle xenoliths together with likely melt/fluid source reservoirs. It is clear from this that the lithospheric mantle displays evidence of interaction of melts/fluids from the convecting upper-mantle, primitive mantle, recycled organic matter and recycled carbonate. The influence of the primitive mantle is best seen in samples from the East African Rift (Halldorson *et al.*, 2014; 2021). Mantle xenoliths from Kilbourne Hole (USA), the Antarctic Peninsula and Southern Patagonia also show evidence of interaction with melts/fluids derived from the convecting upper mantle and recycled carbonate ($\delta^{13}C$ < -3‰), while those from the Tariat Volcanic Field, Hyblean Plateau, Ichinomegata and Poland are dominated by mantle-like $\delta^{13}C$ (-5‰) with lower $^{3}He/^{4}He$ (6-9 Ra; Porcelli *et al.*, 1992; Correale *et al.*, 2015; Rizzo *et al.*, 2018; this study). The xenoliths from Bullenmerri (South East Australia), one from Ichinomegata, N. Tanzania, Geronimo (South West USA), Spain and one from the

West Eifel show an impact from recycled organic carbon ($\delta^{13}C$ > -7‰; Porcelli *et al.*, 1992; Bianchini & Natali, 2017; this study). Interestingly, the lithospheric mantle beneath the Eifel retains evidence for both organic carbon and carbonate. This is displayed by clinopyroxenite DW5 which has very light $\delta^{13}C$ (-25 ‰), and lherzolite samples DW7 and wehrlite DW10 that have heavy $\delta^{13}C$ (5.6 and 1.4‰, respectively). This may indicate that the recent magmatic activity associated with pyroxenite veining in the Eifel has a strong contribution from recycled organic material, while the older metasomatic events (e.g. Witt-Eickschen *et al.*, 2003) recorded by samples DW7 and DW10 retain abundant input from recycled carbonate. This highlights the variable sources of metasomatism within a single location.

Volatiles extracted by crushing techniques tend towards heavier $\delta^{13}C$ compositions than those extracted by heating methods. Of the 56 samples analysed by crushing, all, with the exception of DW5, have $\delta^{13}C$ > -5‰. These heavy $\delta^{13}C$ with variable $^{3}He/^{4}He$ indicate the involvement of carbon of recycled carbonate. The samples analysed by heating methods have lighter $\delta^{13}C$ (-22.8 to -2.6‰) with variable $^{3}He/^{4}He$, implying the involvement of recycled organic carbon reservoirs. Given that crushing methods only release fluid and gaseous phase carbon and heating experiments are dominated by solid carbon species (e.g. Andersen *et al.*, 1984), this may indicate contrasting sources for carbon species in the lithospheric mantle. This is because carbon present in fluid inclusions appears to be predominantly sourced from the mantle and recycled carbonate reservoirs, while solid species (e.g. carbonates) are associated with organic carbon reservoirs. Alternatively, these very light $\delta^{13}C$ signatures could be related to high-temperature fractionation processes (e.g. Cartigny *et al.*, 2001a, 2001b; Mikhail *et al.*, 2014a, 2014b). Recycled organic material, however, represents the favoured source because the degree of fractionation required to produce such light compositions is far beyond experimental constraints (e.g. Mikhail *et al.*, 2019). A cognate origin for fluids/gases and solid inclusions can also not be explained by open-system degassing, because this would result in CO_2 becoming increasingly lighter as opposed to retaining these heavier values.

10.4 Variation of $\delta^{13}C$ with $^{3}He/^{4}He$ and $CO_2/^{3}He$

To further evaluate how the off-craton sub-continental lithospheric mantle is interacting with melts and fluids from different reservoirs in the solid Earth, the $\delta^{13}C$ and $^{3}He/^{4}He$

compositions are compared on Figure 10.4. The database has been filtered to remove olivines that display evidence of CO_2 degassing.

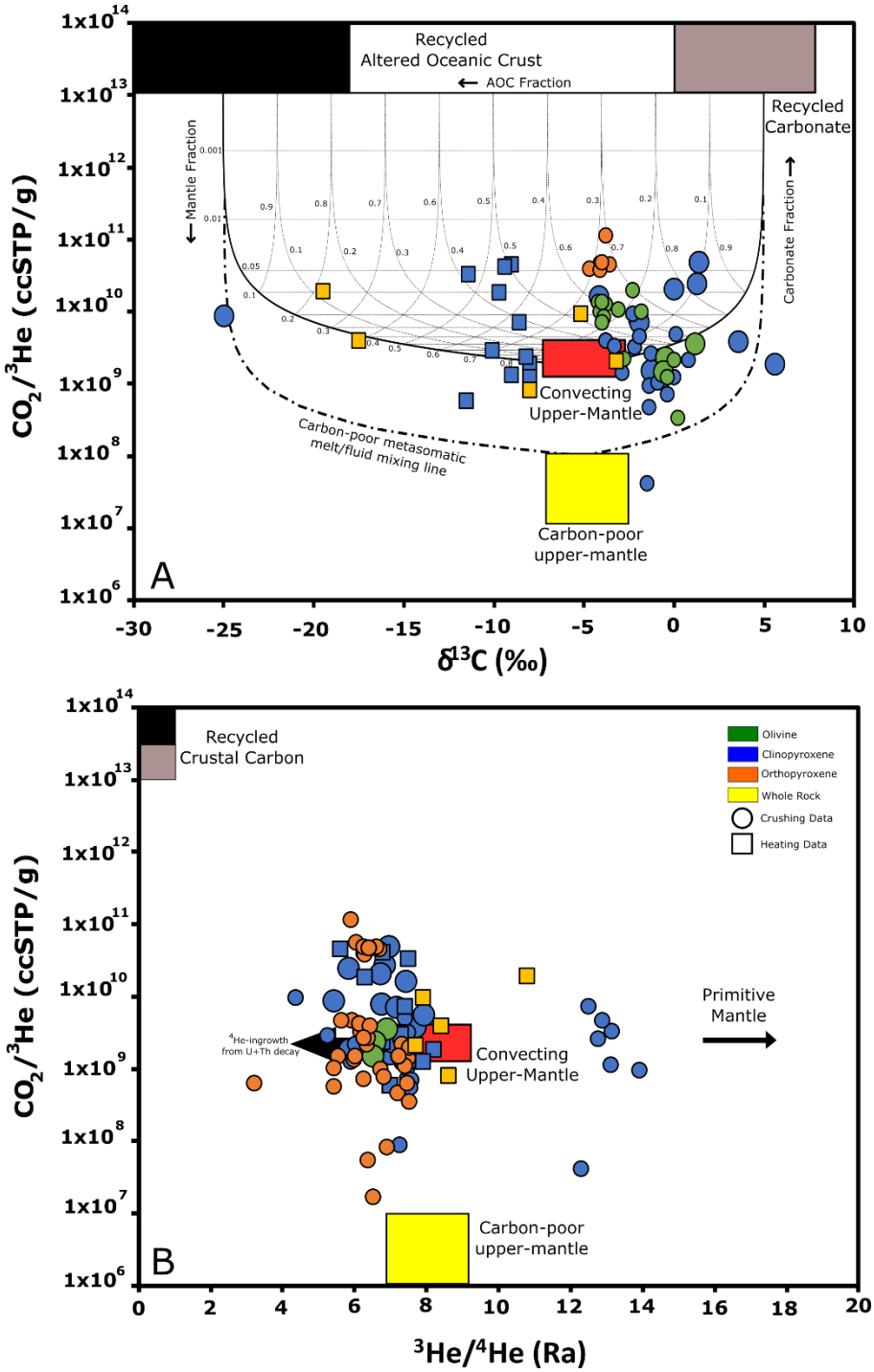

Figure 10.4. Variations of $CO_2/^3He$ in olivine, orthopyroxene, clinopyroxene and calculated whole-rock compositions with: A) $\delta^{13}C$; and B) $^3He/^4He$. Details of reservoir compositions are provided in the main text. The mixing curves in (A) are from Karakuş & Aydin (2017). Symbols for data from this study are larger than those from the published database.

The $\delta^{13}C$ and $CO_2/^3He$ of mantle peridotites and pyroxenites vary greatly (Figure 10.4A), but are dominated by compositions that show the greatest affinity to upper-mantle $\delta^{13}C$ and $CO_2/^3He$ signatures ($\delta^{13}C$ = -5 ± 2‰ and $^3He/^4He$ = 8 ± 1 Ra). Furthermore, the variation of $\delta^{13}C$ and $CO_2/^3He$ can further be explained by the upper-mantle interacting to varying extents with melts of recycled altered oceanic crust and recycled carbonates and then generating melts that are either isotopically light (-7 to -25 ‰) and heavy C (-3 to 0 ‰) with elevated $CO_2/^3He$. This is illustrated on Figure 10.4A by the mixing curves between convecting upper mantle, recycled carbonate and recycled altered oceanic crust (after Karakuş & Aydin, 2017). However, there is a subset of samples that have distinctly heavier $\delta^{13}C$ (>-3 ‰) and lower $CO_2/^3He$ than upper-mantle compositions. A simple explanation for this involves the interaction of a prevalent carbon-poor or ^3He-rich reservoir with heavy $\delta^{13}C$, although current understanding of carbon reservoirs in the Earth's mantle provides no evidence this. Hypothetically, this reservoir could be a deeply recycled carbonate that has undergone significant decarbonation and become enriched by primordial helium – but evidence for this reservoir remains ambiguous. Instead, the heavy $\delta^{13}C$-low $CO_2/^3He$ compositions may indicate the mixing of upper-mantle with melts of recycled carbonates and C-poor upper-mantle (e.g. Le Voyer *et al.*, 2017; Aiuppa *et al.*, 2021). This together with mixing of recycled altered oceanic crust may account for the variation in $\delta^{13}C$ with low $CO_2/^3He$.

Variations in $^3He/^4He$ with $CO_2/^3He$ also show that the convecting upper-mantle may be the dominant source of helium and carbon in the lithospheric mantle as the xenoliths record mantle-like $CO_2/^3He$ compositions (~2.6 x 10^9) and MORB-like $^3He/^4He$ (Figure 10.4B). Importantly, some of these MORB-like $CO_2/^3He$ compositions have slightly lower $^3He/^4He$ (< 7 Ra), which reflects ^4He-ingrowth from U+Th decay. Some mantle xenoliths with $^3He/^4He$ >9 Ra (from Ethopia; Halldorson, 2014) are observed with MORB-like $CO_2/^3He$ and probably reflect the input of high $^3He/^4He$ from the deep mantle. Furthermore, there is also evidence for an for input from recycled crustal sources based on elevated $CO_2/^3He$ and lower $^3He/^4He$ Ra. Unlike $^{13}C/^{12}C$, $^3He/^4He$ cannot be used to distinguish between different crustal carbon reservoirs, so $^3He/^4He$ and $CO_2/^3He$ signatures only identify crustal $CO_2/^3He$ and radiogenic $^3He/^4He$. Finally, mantle xenoliths with relatively low $CO_2/^3He$ also occur with MORB-like $^3He/^4He$ (i.e. 8 ± 1 Ra) and MORB influenced by ^4He-input from ambient U+Th decay

($^3He/^4He$ = 4 to 7). It is most likely that these were produced by the interaction of melts/fluids from the convecting upper-mantle with recycled carbon and a low $CO_2/^3He$ mantle reservoir with mantle-like $^3He/^4He$. This mixing between different reservoirs is further outlined by Figure 10.5, outlining showing that input from recycled reservoirs and radiogenic ingrowth are powerful mechanisms perturbing the CO_2-^3He-^4He signature of the lithospheric mantle.

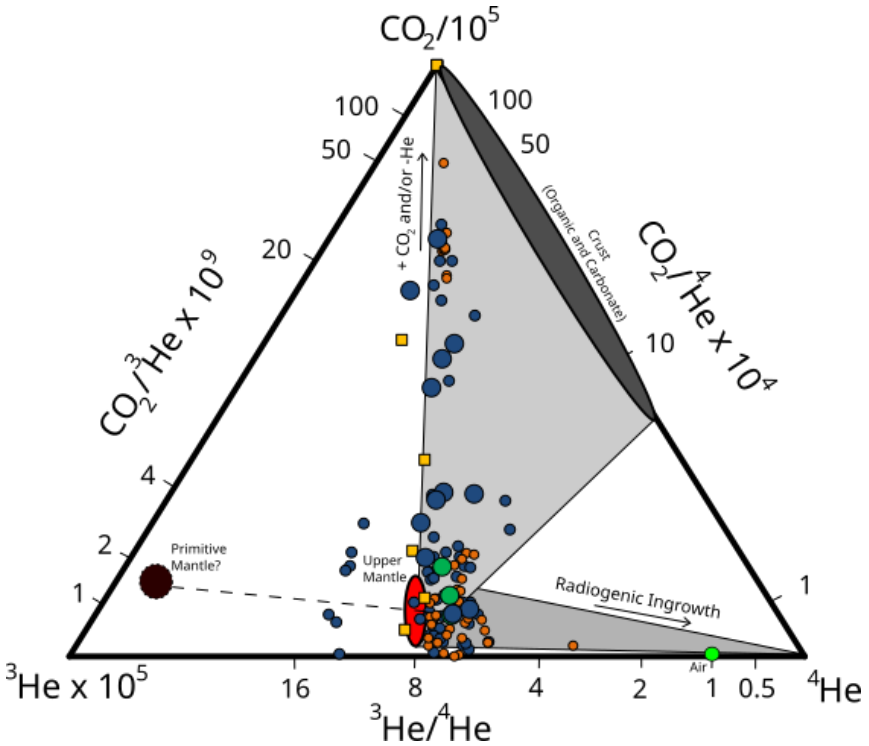

Figure 10.5. Ternary plot adapted from Gilfillan et al. (2019) comparing $CO_2/^3He$, $CO_2/^4He$ and $^3He/^4He$ of peridotite and pyroxenite mantle minerals. Three system component calculated by CO_2+^3He+^4He = 100% and compared to reservoirs from Giggenbach et al. (1993) and those discussed in previous sections.

10.5 Combined carbon and major-trace element systematics

To understand the role of melting and refertilisation on the CO_2 content of the lithospheric mantle, the Mg# (Mg/Mg+Fe) of olivine is compared with the CO_2 content, using data from this study and the published literature (Figure 10.6). Olivine with Mg# >89.5 has highly variable CO_2 contents, ranging from ~1 x 10^{-6} to ~1 x 10^{-1} ccSTP/g, whereas olivine with Mg# <89.5 is limited to higher CO_2 concentrations of ~1 x 10^{-3} to ~1 x 10^{-1} ccSTP/g. This indicates that subcontinental lithospheric mantle with Mg# compositions consistent with forming as a melt residue has varying CO_2 contents. In contrast, lithospheric mantle that has undergone re-fertilisation has high CO_2 contents. These observations highlight that refertilised mantle represents an important and consistently highly concentrated carbon reservoir.

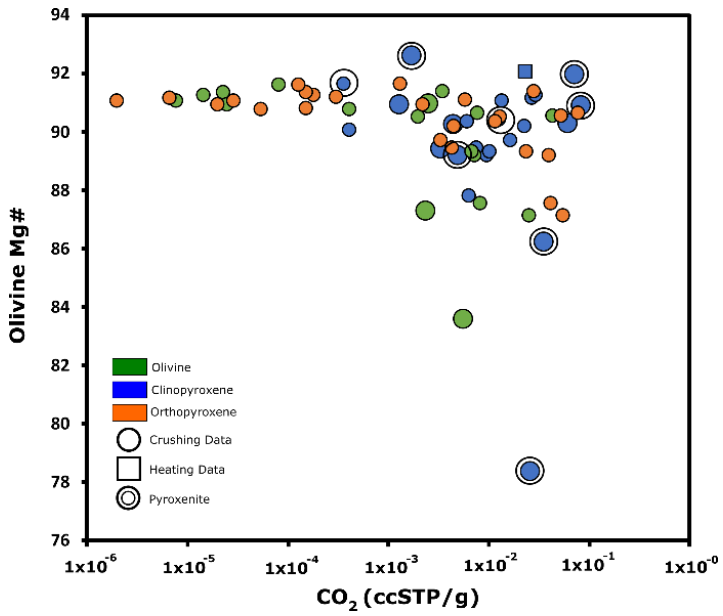

Figure 10.6. Variation of CO_2 (ccSTP/g) with Mg# in corresponding olivine, orthopyroxene and clinopyroxene. Symbols for data from this study larger than those from the published database.

Previous studies have highlighted the relationship between carbon and trace elements in melt inclusions and glasses. Many of these have focused on the use of CO_2/Nb or CO_2/Ba to determine the CO_2 content of the MORB-source mantle (e.g. Cartigny *et al.*, 2008; Le Voyer *et al.*, 2017; Matthews *et al.*, 2021), the OIB-source deep mantle (e.g. Rosenthal *et al.*, 2015) and the lithospheric mantle (e.g. Hudgins *et al.*, 2015). Here, the applications of CO_2/trace-element ratios in melt-inclusions is expanded to include the calculated bulk xenolith trace-element and mineral CO_2 contents. The CO_2/trace-element ratio of mantle peridotite and pyroxenite xenoliths are most statistically significant for CO_2/Nb and CO_2/La (Figure 10.7). These show a CO_2/Nb relationship of CO_2 (ppm) = 95.50 x Nb (ppm) with an R^2 = 0.84, while CO_2/La has a relationship of CO_2 (ppm) = 15.23 x La (ppm) with an R^2 = 0.84. This equates to a CO_2/Nb of 96 and a CO_2/La of 15. These fall within the lower end of the CO_2/Nb observed within melt inclusions found in olivine phenocrysts (CO_2/Nb ≈ 100 to 1000; Matthews *et al.*, 2017). The lower CO_2/Nb and CO_2/La ratios of fluids trapped in the lithospheric mantle relative to melt inclusions in phenocrysts are unsurprising as they are not like-for-like comparisons; in melt-inclusions CO_2, Nb and La occupy the same medium (melts) whereas in peridotites the CO_2 is concentrated in fluid inclusions in very small quantaties and Nb and La are found within crystal lattices at higher quantites.

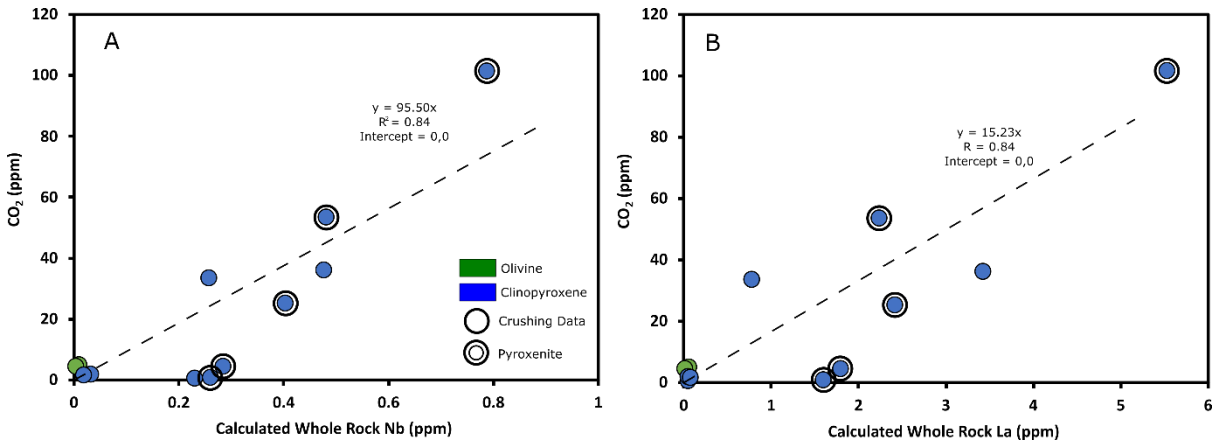

Figure 10.7. CO_2 content of mantle minerals compared to (A) calculated bulk xenolith Nb and (B) La.

Using the results of Figure 10.6, it is possible to calculate the CO_2 content of the off-craton lithospheric mantle based on the calculated bulk xenolith contents of La and Nb. For example, lithospheric mantle with a DMM-like composition (Workman & Hart, 2005) has a Nb content of 0.15 ppm and La of 0.19 ppm. This equates to CO_2 concentrations of 14 ppm and 3 ppm, respectively. More enriched lithospheric mantle, such as that beneath the Eifel, has ~0.5 ppm Nb and ~3 ppm La, which equates to CO_2 concentrations of 47 ppm and 46 ppm, respectively. However, using CO_2/Nb is challenging because: (1) This ratio becomes inaccurate at low ppm relative to La; (2) Nb is very difficult to accurately constrain for mica and amphibole bearing peridotites and pyroxenites, i.e. associated with carbonatite and silicate metasomatism. Therefore, use of CO_2/Nb as a proxy is unreliable for mantle xenoliths.

Current observations of mantle xenoliths suggest that the La content varies from 0.2 ppm at Tariat (e.g. Ionov & Carlson, 2019; Kourim *et al.*, 2021) to ~10 ppm in some pyroxenites (e.g. Witt-Eickschen *et al.*, 2003). This equates to a CO_2 range from 3 ppm to 152 ppm. Additionally, the off-craton lithosphere is dominated by younger, more fertile compositions (e.g. Griffin *et al.*, 2003) and appears to have experienced extensive metasomatic enrichment. As a result, it is reasonable to assume that this reservoir is more enriched in La and CO_2 than the DMM. The average La concentration is taken to be that estimated from 208 spinel peridotite xenoliths (2.6 ppm; McDonough, 1990). This is integrated with La concentrations of pyroxenite (approximately 5 ppm) that are estimated to account for 2-10% of the lithospheric mantle (e.g. Hirschmann & Stolper, 1996; Downes, 2007), to derive the average bulk La of the lithospheric mantle of 2.65 to 2.74 ppm. This equates to an off-

craton lithospheric mantle CO_2 content of 40.3 to 41.7 ppm and a total budget of ~1.84 x 10^{20}g.

10.6 Determining the abundance of carbon in off-craton mantle

The previous sections have discussed two methods to calculate the carbon concentration and total abundance in the off-craton sub-continental mantle, i.e. $CO_2/^3He$ and CO_2/La. These were extrapolated to known ^3He and La concentrations and integrated with the total reservoir mass from Gibson & McKenzie (in review). The median, upper and lower estimates for these methods are presented in Figure 10.8.

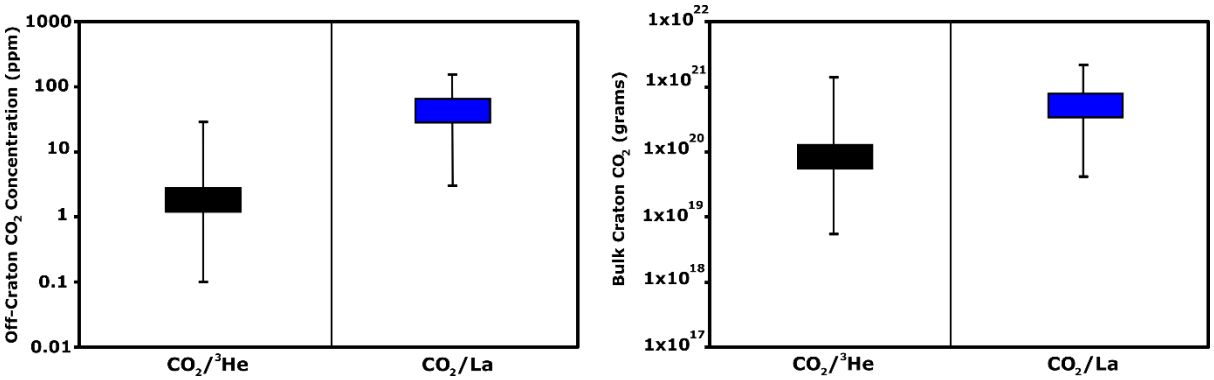

Figure 10.8. Estimates of (A) CO_2 concentrations and (B) CO_2 bulk abundant of the off-craton sub-continental mantle reservoir based on $CO_2/^3He$ and CO_2/La ratios.

Overall, the estimates from these different methods overlap but have key differences. The average concentration of CO_2 is 2 and 41 ppm from $CO_2/^3He$ and CO_2/La methods, respectively. These equate to a bulk CO_2 of 8.6 x 10^{19} g based on $CO_2/^3He$ and 57.0 x 10^{19} g for the total off-craton sub-continental lithospheric mantle. An average of these values shows that the off-craton lithospheric mantle has 21 ppm CO_2 and a bulk content of 3.0x10^{20} g. On balance, the estimates from $CO_2/^3He$ should be more accurate due to the greater number of analyses and supplementation from previous studies. Furthermore, since both ^3He and CO_2 exist in fluid inclusions, and La is hosted in the crystal lattice, it is more likely that $CO_2/^3He$ will remain constant during perturbation. However, both the CO_2/La and $CO_2/^3He$ proxies produce CO_2 concentrations much lower than previous studies (e.g. Foley & Fischer, 2017; CO_2 = 327 ppm). Although the Foley & Fischer (2018) estimate appears to be quite high, the CO_2/La compositions and upper estimates from $CO_2/^3He$ are more akin to the DMM (e.g. Hauri *et al.*, 2017; CO_2 = 53 ± 38 ppm).

10.7 Conclusions

By using CO_2, $\delta^{13}C$ and He-concentrations together with $^3He/^4He$ from both this study and the published literature, it has been possible to improve constraints on the nature, origin and abundance of CO_2 in the off-craton sub-continental mantle. Using clinopyroxene, orthopyroxene and whole-rock data, $CO_2/^3He$ in the off-craton lithospheric mantle is estimated to range from $2x10^9$ to $5x\ 10^9$ with an improved constraint of $CO_2 = 8 \times 10^{11} \times {}^3He^{1.20}$ ($R^2 = 0.74$). Furthermore, it appears that CO_2 is related to La and Nb contents in the off-craton lithospheric mantle, with CO_2 = La x 15.23 ($R^2 = 0.84$) and CO_2 = Nb x 95.50 ($R^2 = 0.84$). Finally, it also appears that off-craton mantle with depleted chemistry (i.e. olivine Mg# > 89.5) has variable CO_2 contents, but re-fertilsed mantle (i.e. olivine < 89.5) exclusively has elevated CO_2 concentrations.

The origin of CO_2 in the off-craton sub-continental mantle has been constrained by $\delta^{13}C$-$^3He/^4He$, $\delta^{13}C$-$CO_2/^3He$ and $^3He/^4He$- $\delta^{13}C$ systematics. These relationships show that samples analysed by heating techniques are dominated by light $\delta^{13}C$, while those analysed by crushing methods are dominated by heavy $\delta^{13}C$. The variations of $\delta^{13}C$ with $^3He/^4He$ show that the subcontinental lithospheric mantle is dominated by convecting upper-mantle-like signatures, with various inputs from primordial, recycled carbonate and recycled altered oceanic crust. These interpretations are supported by variation in $\delta^{13}C$-$CO_2/^3He$ and $^3He/^4He$-$CO_2/^3He$. However, these variations also require a C-poor mantle reservoir. This advances current understanding which has emphasized the involvement of recycled lithosphere on mantle-carbon.

Finally, using parameterisations of $CO_2/^3He$ and CO_2/La together with estimates of volumes for off-craton sub-continental mantle from Gibson & McKenzie (in review) it has been possible to calculate new CO_2 concentrations and budgets for this reservoir based on direct analyses of ultramafic xenoliths. Estimates of CO_2 concentrations for off-craton sub-continental mantle using $CO_2/^3He$ range from 0.1 to 28 ppm (with a median of 2 ppm, where $^3He = 1 \times 10^{-12}$ ccSTP/g) and from using CO_2/La range from 3 to 152 ppm (with an average of 41 ppm, where La = 2.7 ppm). These concentrations equate to a median bulk CO_2 estimates of $3x10^{19}$ and 57×10^{19} g for the total off-craton sub-continental lithospheric mantle based on $CO_2/^3He$ and CO_2/La from this study, respectively.

Chapter 11. Abundance and behaviour of volatiles in the sub-continental lithospheric mantle

11.1 Introduction

Volatile elements are fundamental to many processes in the solid Earth because they influence the temperatures and pressures of melting (e.g. H_2O & F; Gaetani & Grove, 1998; Brey *et al.*, 2009) and also rheology (e.g. Faul *et al.* 2016). Volatiles also impact on biogenic processes at Earth's surface (P & Cl; Broadley *et al.*, 2018; Chen & Chen, 2021) and control ore-petrogenesis (Li; Wang *et al.*, 2020). Recent work by Gibson *et al.* (2020) has: (i) provided typical lithospheric mantle concentrations of H_2O, F and Li; (ii) shown the importance of pyroxenites as H_2O and F hosts; and (iii) highlighted the role of subsolidus equilibration on the distribution of volatile elements between co-existing phases. To further advance the understanding of volatiles in the lithospheric mantle major-, trace- and volatile-element and He and C data for the off-craton lithospheric mantle from Kilbourne Hole, Colorado Plateau, West Eifel Volcanic Field, and Ichinomegata and the disturbed margin of the Tanzania craton is presented. These are combined with the dataset produced by Gibson (2012) and Rooks (2016) from Pali Aike and the Antarctic Peninsula and also include cratonic samples from the Kaapvaal craton from Jackson (2020).

This chapter outlines the different relationships of volatile element (H_2O, Li, B, F, P and Cl) chemistry with lattice (major- and trace-elements) and fluid-hosted (He and C) elements. These relationships are used to (i) outline different mechanisms controlling the abundance in mantle phases and whole rocks; (ii) quantify their abundance in the off-craton mantle; and (iii) provide broad insights to long-term volatile cycles.

11.2 Partitioning of volatiles Between co-existing mantle phases

The partitioning of H, Li, B, F, P and Cl between olivine, orthopyroxene and clinopyroxene using data presented in Chapter 5 in shown in Figure 11.1.

For H_2O, it is apparent that in off-craton lithosphere, orthopyroxene and clinopyroxene are the dominant host with $D_{H_2O}^{cpx-opx}$ between 1.5 and 2. This is consistent with the findings of Demouchy & Bolfan-Casanova (2016) and Gibson *et al.* (2020). This H_2O partitioning is distinct from the on-craton mantle where olivine is an important host for H_2O and $D_{H_2O}^{cpx-opx}$

is to closer to 1 (Jackson, 2020). This is also the case for F which, in off-craton lithosphere has a strong affinity for orthopyroxene and clinopyroxene relative to olivine, with $D_F^{cpx-opx}$ near to 2. This is consistent with the small global F dataset for off-craton mantle published by Urann *et al.* (2017) and Gibson *et al.* (2020). In contrast, the olivine in on-craton lithospheric mantle is a much more important host for F (Jackson, 2020), with D_F^{ol-opx} is closer to 1.

When compared to the results of experiments (Hauri *et al.*, 2006; Dalou *et al.*, 2012; Beyer *et al.*, 2012; Dalou *et al.*, 2014) the $D_{H_2O}^{cpx-opx}$ for off-craton mantle ($D_{H_2O}^{cpx-opx}$ = 1 to 2) is similar to those undertaken at 1200-1500 °C while those for on-craton mantle ($D_{H_2O}^{cpx-opx}$ = 2 to 4) are akin to experiments at 1000-1150 °C. For off-craton xenoliths ($D_F^{cpx-opx}$ = ~1.25), F is inconsistent with experimental partitioning while those from the on-craton ($D_F^{cpx-opx}$ = ~1) have an affinity to experiments undertaken at 1190 to 1430 °C.

Lithium shows distinct partitioning between mantle phases and has the greatest affinity for olivine with D_{Li}^{ol-opx} = 2 with $D_{Li}^{cpx-opx}$ = 1. This is consistent with previous findings for peridotite xenoliths (e.g. Seitz & Woodland, 2000). Phosphorous also has strong affinity for olivine, with D_P^{ol-opx} varying from 2 to 10 and D_P^{ol-cpx} varying from 1 to 6. Clinopyroxene is a more important host for P than orthopyroxene, with $D_P^{cpx-opx}$ ranging from 2 to 6. This broad partitioning between different co-existing mantle phases may be related to the heterogeneous distribution of phosphorous in mantle minerals and slow diffusion after metasomatism (e.g. Mallmann *et al.*, 2009).

Boron appears to show equal affinity for olivine, orthopyroxene and clinopyroxene with $D_B^{cpx-opx}$, D_B^{ol-opx} and D_B^{ol-cpx} =1. This is consistent with previous investigations of mantle xenolith phases (e.g. Kaliwoda *et al.*, 2008). In contrast, Cl appears to have no preferential host. This may relate to the low precision of Cl analyses that produces a wide range in Cl concentrations.

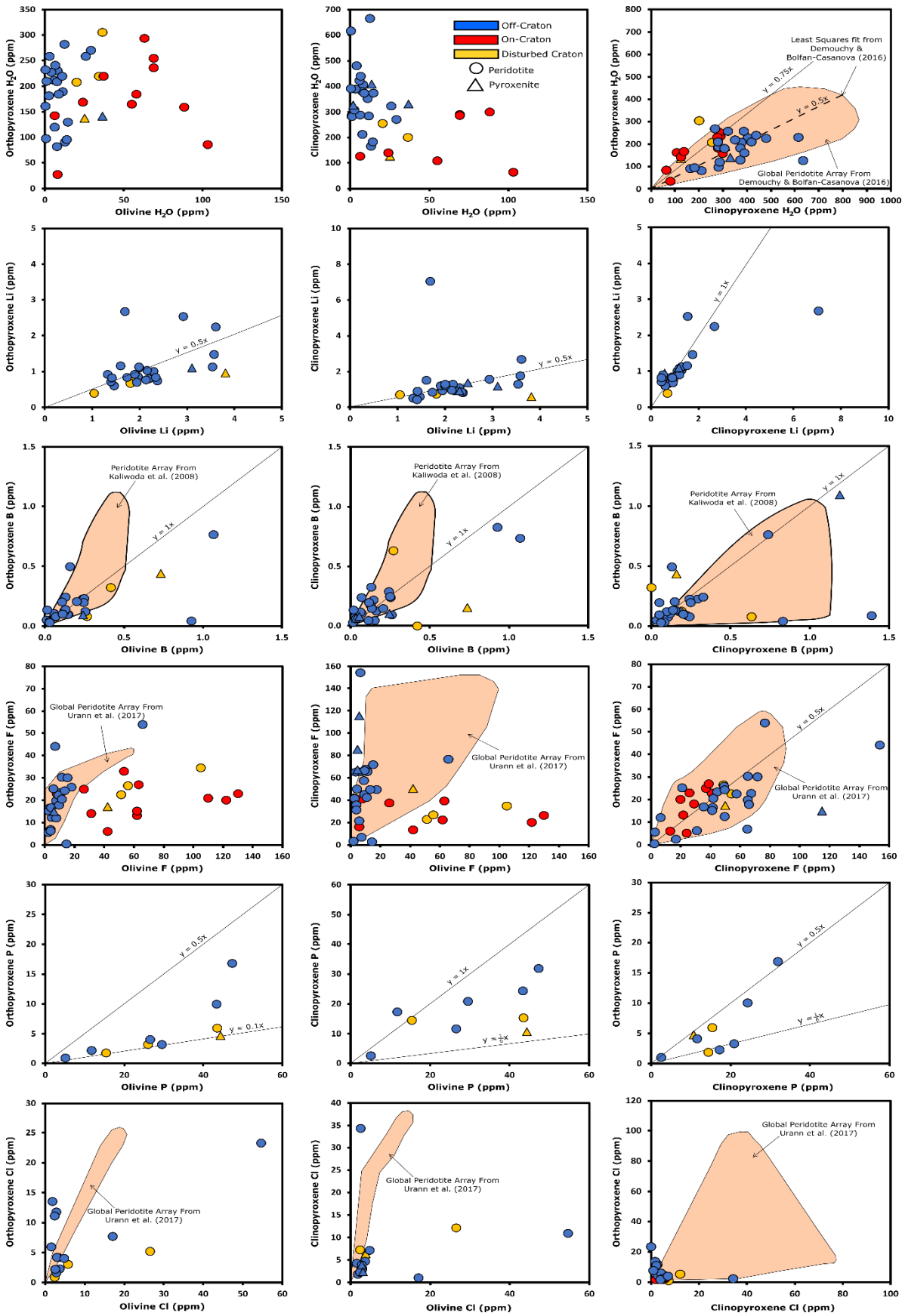

Figure 11.1. Comparison of H_2O, Li, B, F, P and F partitioning between olivine, orthopyroxene and clinopyroxene. Data are from Appendix C Table 14 to 16, Jackson (2020) and Gibson et al. (2020).

11.3 Behaviour of volatile elements

11.3.1 Co-variation of volatile Elements

The concentrations of volatiles (H_2O, Li, B, F, P and Cl) within single minerals and whole-rocks for off-craton peridotite and pyroxenite xenoliths using data from Chapter 5 are shown on a correlation matrix in Figure 11.2. This uses a Pearson's Correlation Coefficient to measure linear relationships of two datasets, and is the ratio between the covariance and their standard deviations (Equation 11.1).

$$P\ X,Y = \frac{cov(X,Y)}{\sigma X \sigma Y} \qquad \text{Equation 11.1}$$

Where: cov = covariance, σX = standard deviation of dataset X and σY = standard deviation of dataset Y

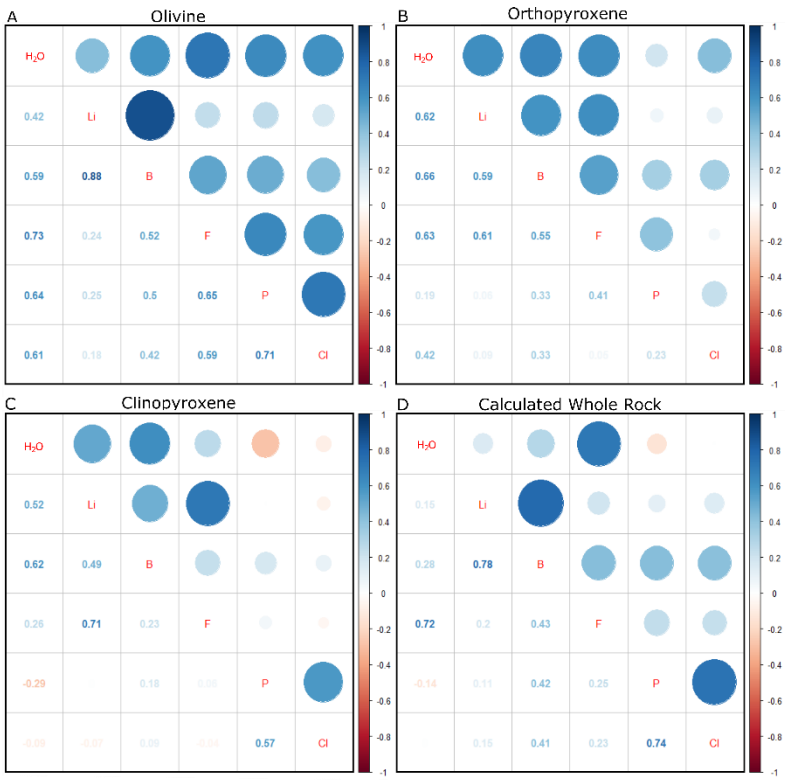

Figure 11.2. Comparison of H_2O, Li, B, F, P and F between A) olivine; B) orthopyroxene; C) clinopyroxene and D) calculated whole-rocks. Colour (scale to right of each plot) and size of circles related to strength of correlation (i.e. bigger = more significant).

The most significant relationships (P>0.7) are observed for Li and B in olivine, orthopyroxene and clinopyroxene and F and H_2O in olivine. This is surprising given how different the ionic properties of these elements are. Furthermore, using calculated bulk xenolith concentrations, it is possible to understand how these volatiles vary on the scale of the off-craton lithospheric mantle. Figure 11.2D shows that the six volatile elements analysed in this

study behave in pairs; i.e. H_2O and F have similar high and low concentrations (P = 0.78), as do Li and B (P = 0.74) and P & Cl (P = 0.74).

11.3.2 Co-behaviour of volatile and major elements

11.3.2.1 H_2O

The concentration of H_2O appears to be related to amounts of Si^{4+} and Al^{3+} in clinopyroxene (Figure 11.3; data in Chapters 4 and 5), where H_2O shows a negative correlation with Si^{4+} but a positive correlation with Al^{3+}. This is likely related to the well-known propensity for H^+ to couple with Al^{3+} during replacement of Si^{4+} (e.g. Stalder & Skogby, 2002) i.e. $Si^{4+} = Al^{3+} + H^+$. Furthermore, there is an observable distinction between on-craton and off-craton H_2O concentrations in clinopyroxene. In off-craton mantle, clinopyroxene has low Si^{4+} (1.8 to 1.97 apfu) but high Al^{3+} (0.05 to 0.15 apfu) with high H_2O (~ 150 to 650 ppmw) and on-craton clinopyroxene has high Si^{4+} (1.97 to 2.00 apfu) and low Al^{3+} (0.01 to 0.06 apfu) and low H_2O (~ 50 to 300 ppm).

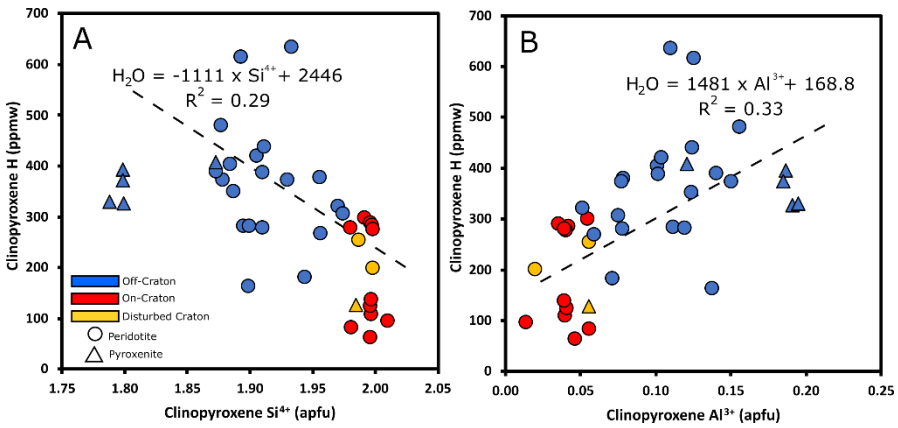

Figure 11.3. Comparison of H_2O with A) clinopyroxene Si^{4+} (apfu) and b) clinopyroxene Al^{3+}.

11.3.2.2 Lithium

Lithium displays moderate correlations with Mg# and SiO_2 in olivine, Mg# in orthopyroxene and clinopyroxene and Ti^{4+} in clinopyroxene (Figure 11.4; data from Chapters 4 and 5). Using the regression lines in Figure 11.5A, C and E, it is possible to calculate the average Li content of the off-craton lithospheric mantle. This is done by combining the relationships of Li with olivine Mg#, orthopyroxene Mg# and clinopyroxene Ti^{4+} relationship with the major element and modal abundances of off-craton mantle (McDonough & Rudnick, 1998). The typical off-craton peridotite olivine has Mg# = 89.6, orthopyroxene has Mg# = 89.3 and clinopyroxene has Ti^{4+} = 0.013 apfu, with 62% olivine, 22% orthopyroxene and 12% clinopyroxene. This

produces a whole-rock Li concentration of 1.77 ppm. Integrated with the off-craton lithosphere reservoir volume estimates of Gibson & McKenzie (in review), this equates to a total Li of 1.3×10^{18} g. While these statistical significance of these estimates are relative poor ($R^2 < 0.5$), they offer an alternative assessment of the Li concentration of the off craton lithospheric mantle.

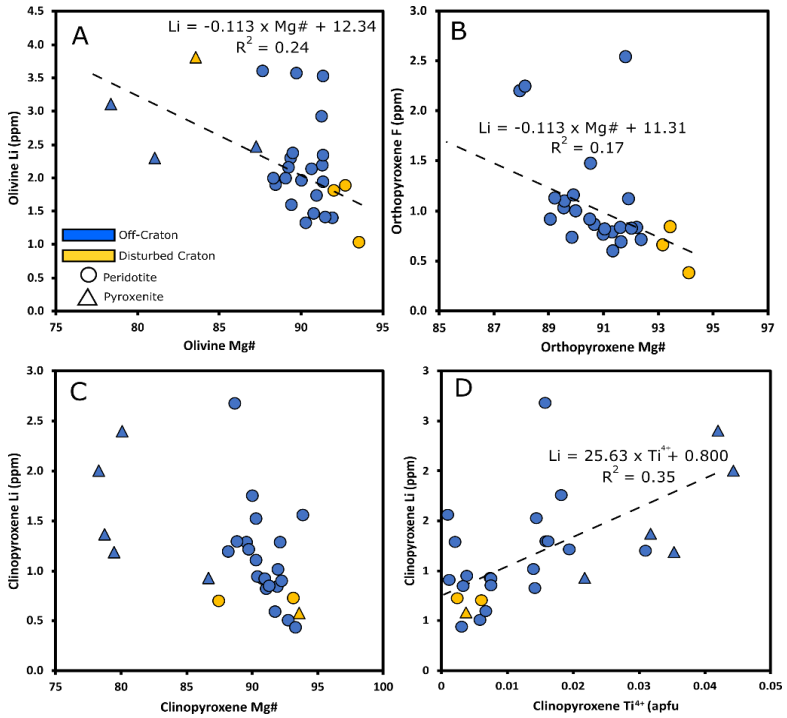

Figure 11.4. Comparison of Li with A) Olivine Mg#; B) Orthopyroxene Mg#; C) Clinopyroxene Mg# and E) Clinopyroxene Ti^{4+} (apfu).

11.3.2.3 Boron

The only clear relationship between B and the major element composition of any mantle mineral is with the Na_2O content of orthopyroxene (Figure 11.5; data in Chapter 4 and 5). This builds and compliments the findings of F variation with Na_2O due to metasomatism (Gibson *et al.*, 2020). Building on this finding, it appears that the B content of orthopyroxene is also sensitive to enrichment. The highest concentrations are in garnet harzburgite TH17 (0.76 ppm) from the Colorado Plateau and pyroxenite BD816 (0.44 ppm) from Northern Tanzania.

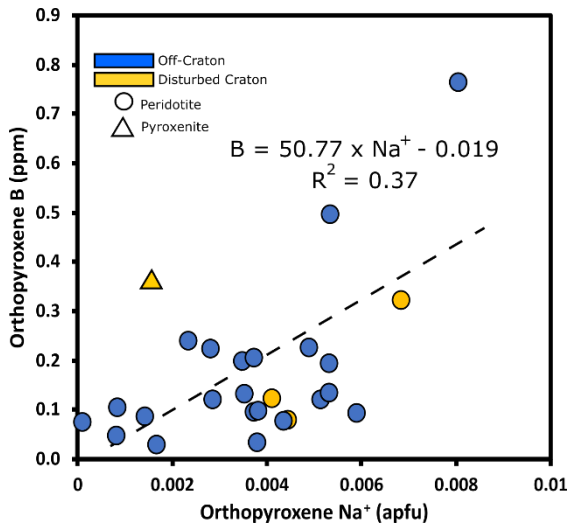

Figure 11.5. Comparison of B (ppm) with Na^+ (apfu).

11.3.2.4 Fluorine

A compositional distinction between off-craton and on-craton mantle is shown by F and Mg# in olivine, orthopyroxene and clinopyroxene (Figure 11.6; data presented in Chapter 4 and 5). The most depleted olivine (on-craton) records higher F concentrations than olivine in off-craton mantle. This contrasts with clinopyroxene which contains less F in on-craton than off-craton lithosphere.

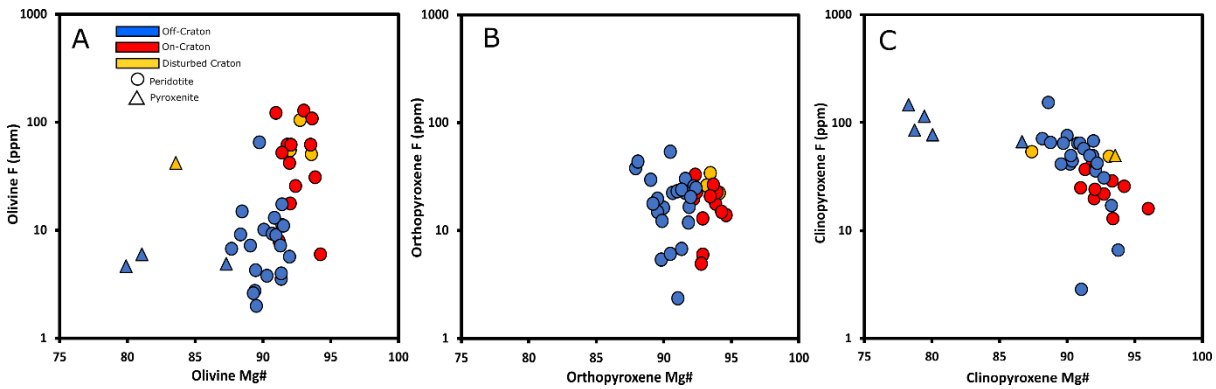

Figure 11.6. Comparison of F with Mg# for A) Olivine; B) Orthopyroxene and C) Clinopyroxene.

Peridotites from the 'disturbed' margins of the Tanzania craton exhibit variations in F and Mg# in olivine and orthopyroxene that are akin to cratonic mantle, while those for clinopyroxene are similar to off-craton lithosphere (Figure 11.6). This suggests that during craton disruption, olivine and orthopyroxene can retain F compositions akin to initial cratonic compositions but the F content of newly introduced clinopyroxene reflects subsequent metasomatic enrichment associated with lithospheric thinning. These

observations are consistent with those for metasomatic clinopyroxene co-existing with highly-refractory olivine, orthopyroxene and garnets at the Tanzanian craton margin (e.g. Gibson *et al.*, 2013).

Olivine, orthopyroxene and clinopyroxene are significant hosts of fluorine in the lithospheric mantle (e.g. Grutzner *et al.*, 2017) and their concentrations vary with major element chemistry (Figure 11.7). In addition to the relationship between F and Na_2O observed by Gibson *et al.* (2020), this study shows the correlation of F with Mn^{+} in olivine (Fig 11.7A), Ti^{4+}, Ca^{2+} and Na^{+} in orthopyroxene (Figure 11.7B, C & D) and Si^{4+}, Ti^{4+} and Ca^{+} in clinopyroxene (Figure 11.7E,F and G).

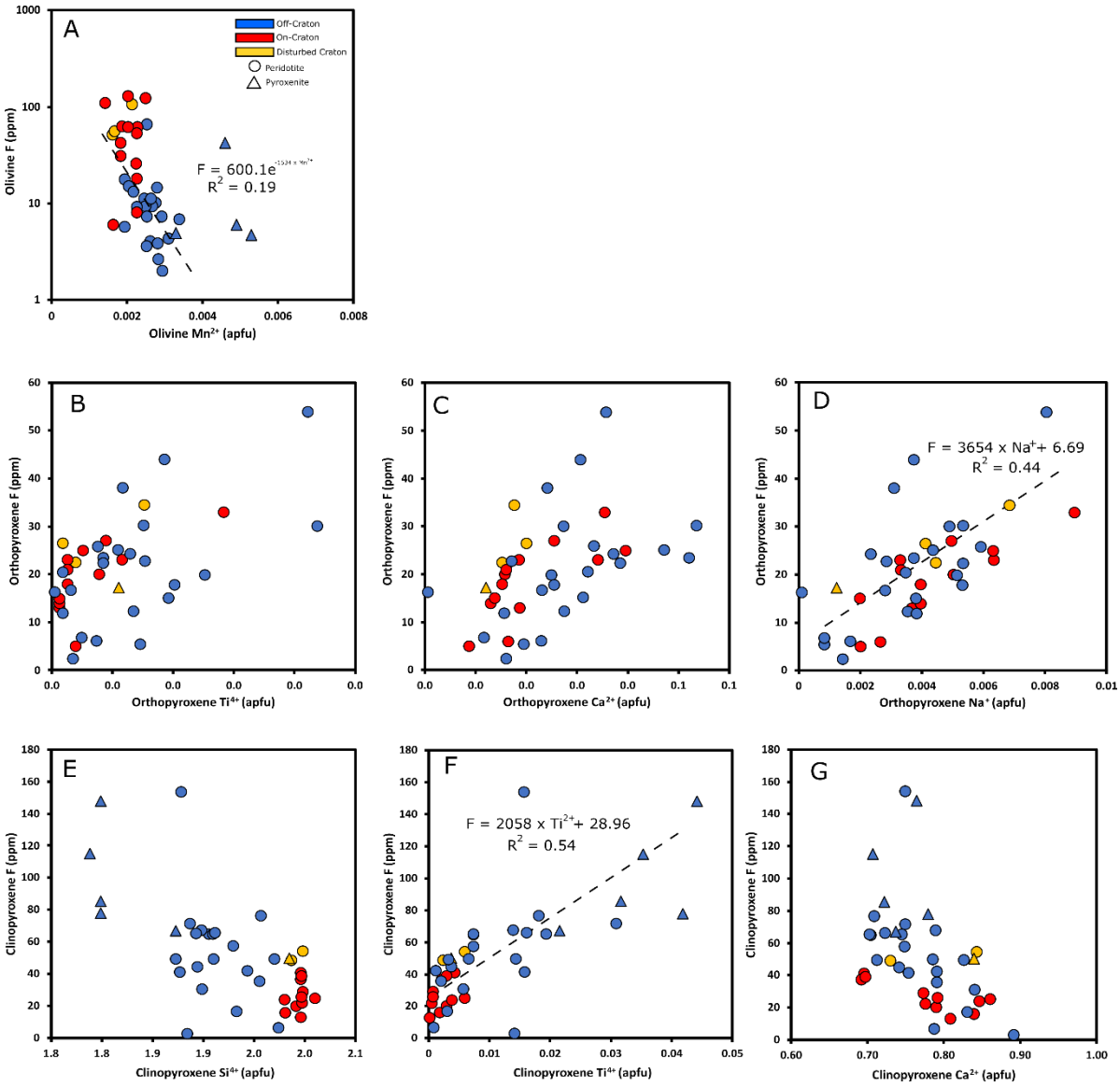

Figure 11.7. Comparison of F with A) Olivine Mn^{+}; B) Orthopyroxene Ti^{2+}; C) Orthopyroxene Ca^{2+}; D) Orthopyroxene Na^{+}; E) Clinopyroxene Si^{4+}; F) Clinopyroxene Ti^{2+}; and G) Clinopyroxene Ca^{2+}.

Using the insights from Figure 11.8, it is possible to calculate an average F content of the off-craton lithospheric mantle. This is done by combining the relationship of F with olivine Mn^{2+}, orthopyroxene Na^{+} and clinopyroxene Ca^{2+} together with off-craton mantle major element data and modal abundances from McDonough & Rudnick (1998). Where, typical off-craton peridotite olivine has Mn^{2+} = 0.003, orthopyroxene has Na^{+} = 0.0044 and clinopyroxene has Ti^{4+} = 0.013, with 62% olivine, 22% orthopyroxene and 12% clinopyroxene. This produces a whole-rock F concentration of 15 ppm. Integrated with the off-craton volume estimates of Gibson & McKenzie (in review), this equates to a total F budget for the off craton mantle of 1.1×10^{19} g.

11.3.3 Whole-Rock Variations in H_2O, Li, B, F and Cl

When comparing calculated whole-rock volatile and major element compositions (Chapter 5 and 6), the most statistically significant relationships are observed between i) boron with Mg# and ii) Cl with Cr_2O_3 (Figure 11.8). Using these insights and comparing them with Mg# (90) and Cr_2O_3 (0.39 wt%; McDonough & Rudnick, 1998), the off-craton lithospheric mantle contains 0.095 ppm B and 5.4 ppm Cl. When integrated with the volume estimates of Gibson & McKenzie (in review), this equates to a bulk B content of 1.2×10^{18} g and a bulk Cl content of 2.1×10^{18} g.

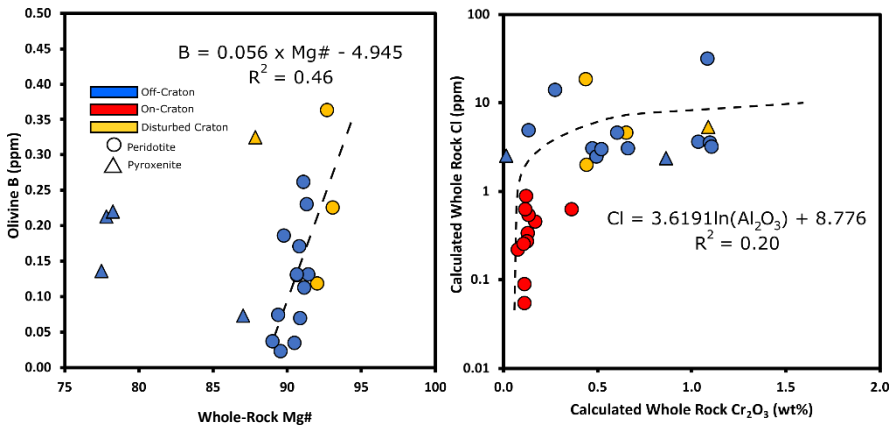

Figure 11.8. A) Whole-rock boron compared with whole-rock Mg# and B) whole-rock Cl compared with whole-rock Cr_2O_3.

The highest bulk B concentration (0.96 ppm) is in garnet harzburgite TH17 from the Colorado Plateau. As outlined in Chapter 2, this location has been associated with metasomatism from the subducted Farallon Plate. The high B concentration may therefore be associated with the release of B-rich fluids from the subducted oceanic lithosphere and enriching the overlying lithospheric mantle.

11.4 Variation in incompatible trace elements and volatile elements

11.4.1 Co-variations of volatile abundance and incompatible trace elements

The Pearson's correlation coefficients for volatile elements and incompatible trace elements in whole-rock peridotites and pyroxenites from the off-craton lithospheric mantle are shown in Figure 11.9 (data presented in Chapter 5). Overall, these show that H_2O has the greatest affinity to Rare-Earth Elements, particularly MREE (Sm-Dy). Furthermore, Li and B shows the greatest affinity to Pb, Th and U and HREE (Tm, Yb and Lu). F shows the greatest affinity to U, Nb and REE while P and Cl show minor relationship with LILE and HREE.

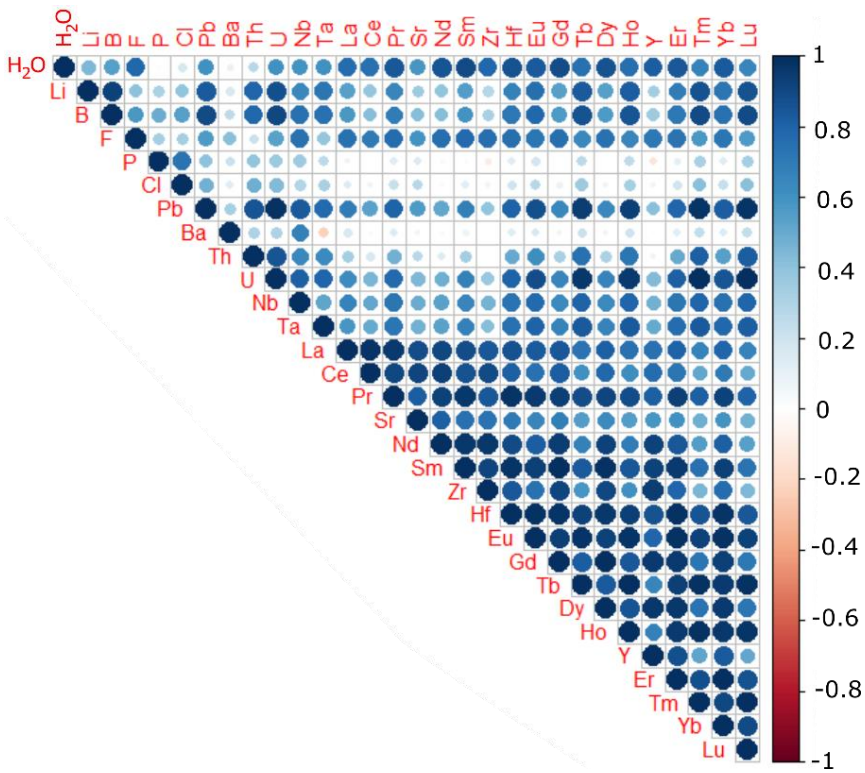

Figure 11.9. Pearson's correlation coefficients for calculated whole rock contents of volatile elements (H, Li, B, F , P and Cl) and incompatible trace elements. All xenoliths are from the off-craton mantle.

The most statistically significant relationships between H_2O, B, F, P and Cl and incompatible trace elements are displayed on Figure 11.10. Using these relationships and the trace-element concentrations for the off-craton lithospheric mantle of McDonough (1990) and Rudnick *et al.* (1998) it is possible to constrain the concentrations of volatiles in this reservoir. Where Gd concentration is 0.6 ppm, H_2O is 100ppm; where U is present at 0.043 ppm, B is 0.22 ppm; where Sm has a concentration of 0.47 ppm, F is 27 ppm; where Er is 0.3 ppm P is 40 ppm; and where Tm is 0.038 ppm Cl is 3.4 ppm. When integrated with the volume of off-craton lithospheric mantle from Gibson & McKenzie (in review), this

generates bulk budgets for H_2O of $1.4x10^{21}$ g, B of $2.8x10^{17}$ g, F of $2.0x10^{19}$ g, P if $5.1x10^{19}$ g and Cl of $1.3x10^{18}$ g.

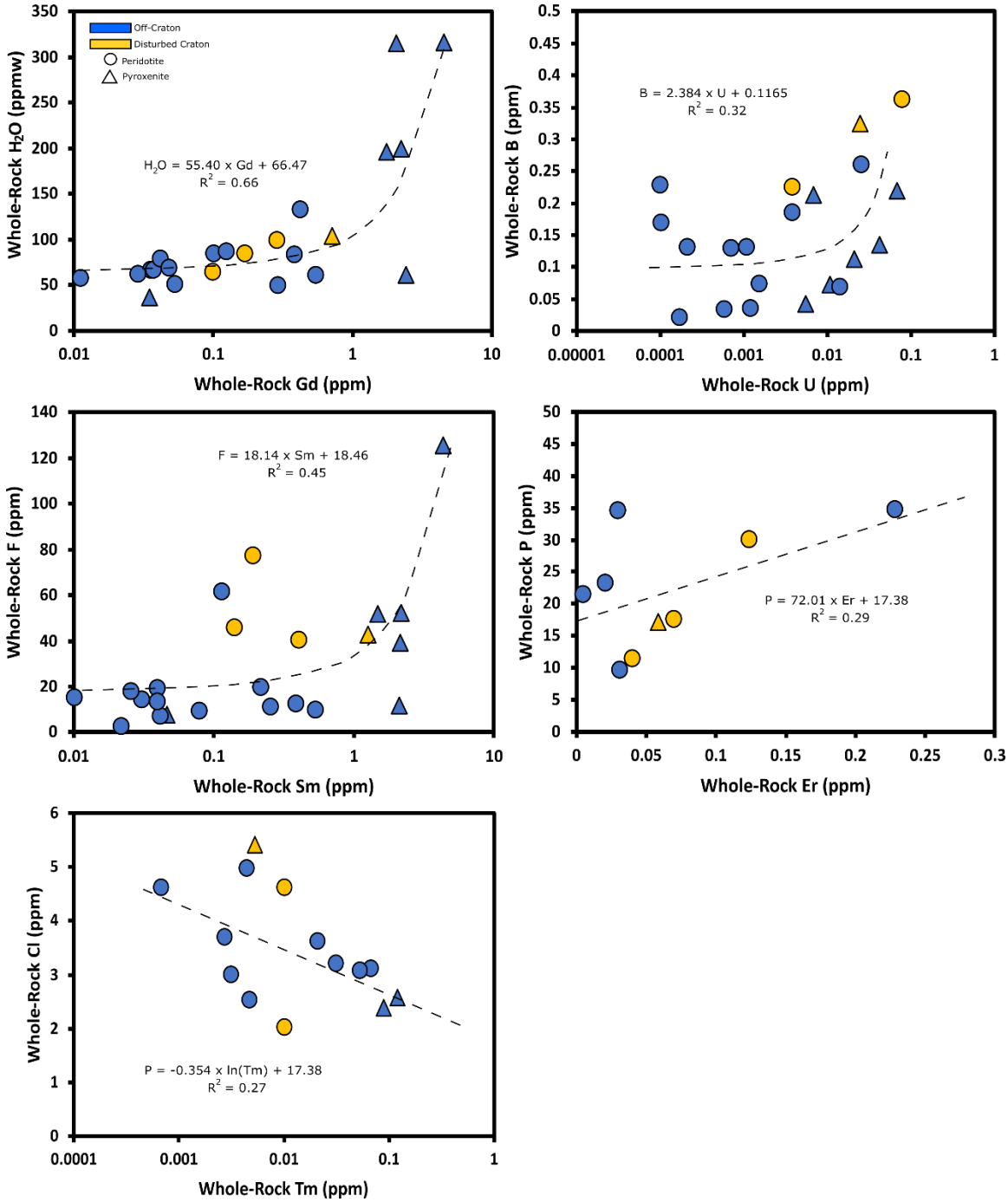

Figure 11.10. A) Gd abundance relative to H_2O; B) U abundance relative to B; C) Sm abundance relative to F; D) Er abundance relative to P and F) Cl abundance relative to Tm.

Furthermore, it is apparent that H_2O and F behave different in the lithospheric mantle than in mantle melts. Typically, in mantle melts H_2O behaves similar to Ce (e.g. Hirschmann, 2018), while F behaves similar to Pr (e.g. Shimizu *et al.*, 2019). However, xenolith data shows that H_2O and F have more affinity to MREEs. This may be related to the bulk-composition or

sub-solidus processes in the lithospheric mantle permitting H_2O to occupy a more stable configuration (e.g. with Al^{3+}; e.g. Gibson *et al.*, 2020).

11.4.2 Metasomatism and volatile abundances

Incompatible trace elements provide vital insights into the nature and extent of metasomatic enrichment, which may not be recorded by major elements. Figure 11.11 shows how B concentrations varies with ratios that are sensitive to metasomatic enrichment (e.g. $[La/Yb]_N$, $[Th/Yb]_N$ and $[Sm/Yb]_N$). As peridotite and pyroxenite xenoliths in the off-craton lithosphere become more metasomatised, the B concentration increases, i.e. as the lithospheric mantle evolves from a depleted residue it becomes an increasingly important reservoir for B.

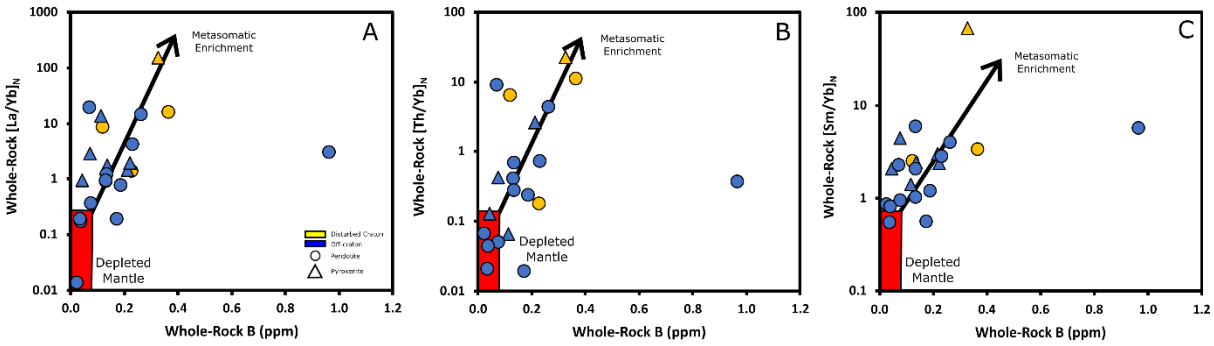

Figure 11.11. Boron (ppm) abundance relative to whole-rock A) $[La/Yb]_N$; B) $[Th/Yb]_N$ and C) $[Sm/Yb]_N$. Reservoir fields are from Workman & Hart (2005) and Marschall et al. (2017).

This is also shown by the positive relationship between Zr/Hf and B concentrations (Figure 11.12). During mantle melting, the residues will have a sub-chondritic Zr/Hf (~40) and the corresponding melts will have supra-chonrdritic Zr/Hf. This is shown by global abyssal peridotites with Zr/Hf of 20-30 and metasomatised lithosphere with Zr/Hf >40 (e.g. Falloon *et al.*, 2006). These systematics are also reflected in Li concentration and indicates a subtle role of metasomatism in Li cycling.

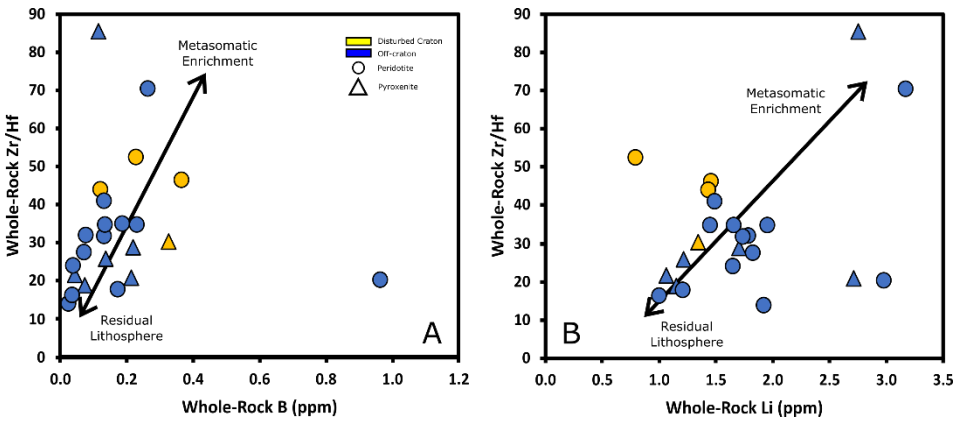

Figure 11.12. Zr/Hf compositions relative to A) B (ppm) and B) Li (ppm).

The composition of metasomatic agents that may be dominantly influencing the cycling of B can be constrained from calculated bulk peridotite and pyroxenite Ti/Eu, $[La/Yb]_N$ and $[Y/Yb]_N$. This is because the co-variation of Ti/Eu and $[La/Yb]_N$ is a sensitive recorder of silicate and carbonatite metasomatism (e.g. Coltorti *et al.*, 2000) whereas Y/Yb_N is sensitive to fluid metasomatism, due to fluid being depleted in Y (see Introduction). From Figure 11.13, it is apparent that B is insensitive to silicate melt metasomatism but is sensitive to $[Y/Yb]_N$, which indicates that B is largely controlled by fluid metasomatism in the lithospheric mantle as opposed to any form of melt metasomatism.

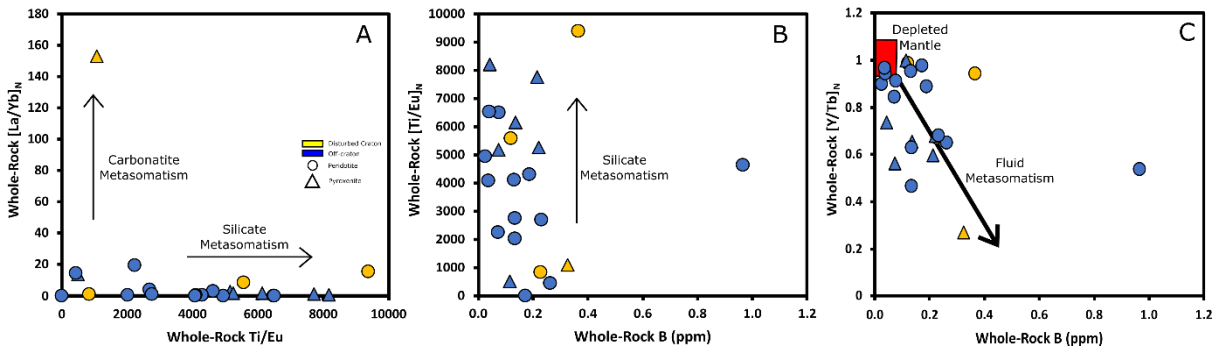

Figure 11.13. A) Ti/Eu relative to La/Yb_N B) Whole-Rock B (ppm) relative to Ti/Eu and C) Whole-Rock B (ppm) relative to Y/Yb_N.

11.5 Volatile elements and bulk xenolith mineralogy

The modal mineralogy of peridotite and pyroxenite xenoliths (presented in Chapter 3) shows an important relationship with the calculated whole-rock H_2O (ppmw; data from Chapter 5). As the modal abundance of olivine increases, the whole-rock H_2O contents decreases, but as the modal amount of clinopyroxene increases, the whole-rock H_2O increases (Figure 11.12). This relationship is quantified by:

Whole-rock H_2O (ppmw) = -2.14 x % olivine abundance + 225 (R^2 = 0.52)

Whole-rock H_2O (ppmw) = 1.99 x % clinopyroxene abundance + 64 (R^2 = 0.53)

This agrees with the relationships in Figure 11.14 because in off-craton lithosphere clinopyroxene and orthopyroxene are the primary hosts for H_2O, while olivine represents a less significant host.

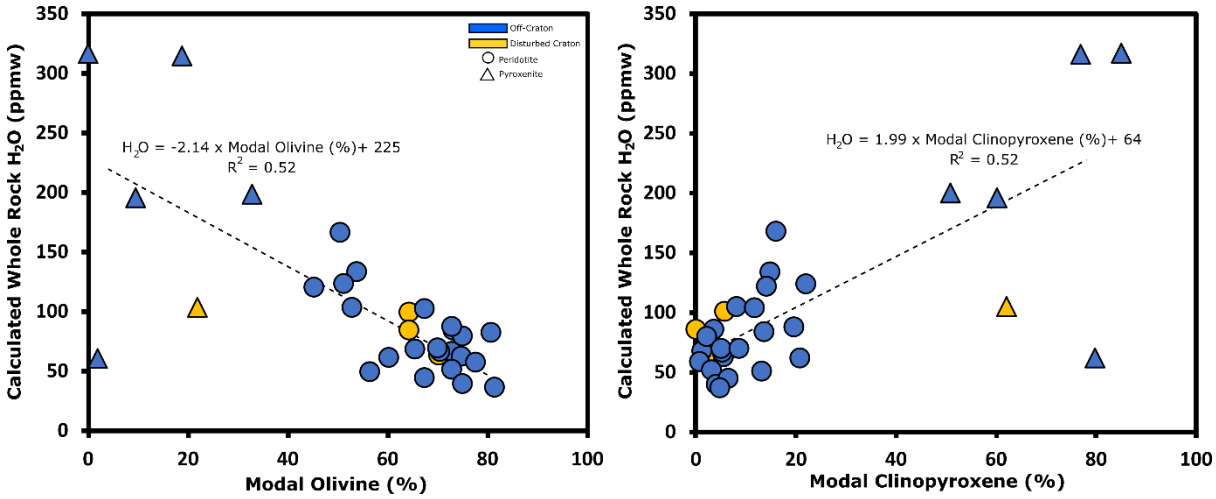

Figure 11.14. Modal olivine and modal clinopyroxene abundances relative to calculated whole-rock H_2O (ppmw) concentrations.

The H_2O content of the continental off-craton lithospheric mantle can be calculated using the relationships between H_2O and modal abundances of olivine and clinopyroxene. This is obtained using the modal mineralogy of McDonough & Rudnick (1998): 62% olivine equates to 92 ppmw H_2O and 11% clinopyroxene equates to 86 ppmw H_2O. The composition of the fertile mantle (e.g. KLB-1; Davis *et al.*, 2009) with 60% olivine corresponds to 97 ppmw H_2O and 14% clinopyroxene at 92 ppmw H_2O. The depleted mantle (Workman & Hart, 2005) has 57% olivine equates to 103 ppmw H_2O and 13% clinopyroxene equates to 90 ppmw H_2O.

11.6 Variations in volatile contents with pressure & temperature

Sections 11.2 and 11.3 show that there are clear distinctions in the H_2O concentrations of olivine and clinopyroxene in off-craton (data from Chapter 5) and cratonic lithospheric mantle (Jackson, 2020). Figure 11.15 highlights the relationship between pressure (see Chapter 7 for estimates) and the H_2O concentrations of olivine, clinopyroxene and bulk xenoliths from this study, and compares them to the global database summarized by Demouchy & Bolfan-Casanova (2016). The mantle xenoliths with the highest final equilibrations pressures record highest H_2O concentrations in olivine and lowest H_2O in

clinopyroxene. Furthermore, the peridotites and pyroxenites with lowest final equilibration pressures have the lowest olivine H_2O but highest clinopyroxene H_2O. However, there is no clear relationship with orthopyroxene or whole rocks.

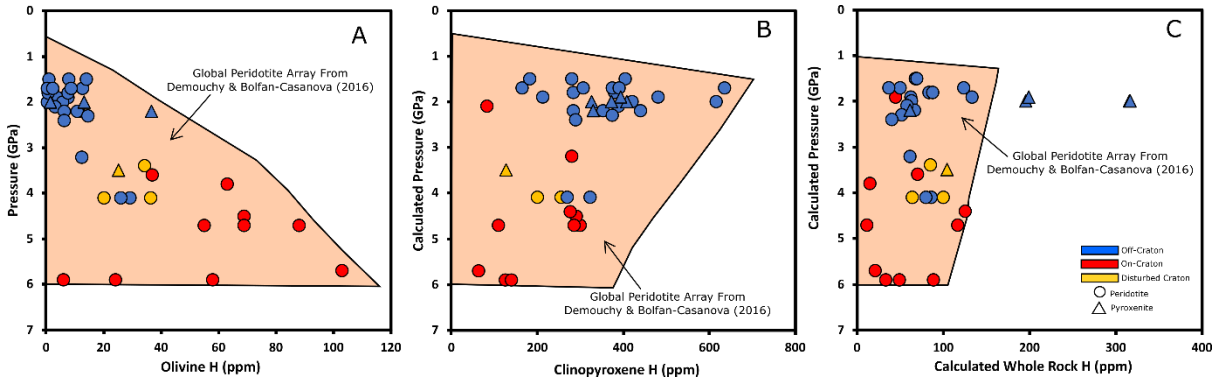

Figure 11.15. Calculated and inferred pressures of spinel and garnet peridotites and pyroxenites compared to A) Olivine H_2O; B) Clinopyroxene H_2O and C) Calculated whole-rock H_2O.

The influence of P and T on the partitioning of H_2O between orthopyroxene and clinopyroxene ($D_{H_2O}^{ol-cpx}$, $D_{H_2O}^{cpx-opx}$ and $D_{H_2O}^{cpx-opx}$) is shown in Figure 11.16. These relationships imply that (i) pressure affects H_2O partitioning, with $D_{H_2O}^{ol-cpx}$ (R^2 = 0.35), $D_{H_2O}^{cpx-opx}$ (R^2 = 0.57) and $D_{H_2O}^{cpx-opx}$ (R^2 = 0.33); (Figure 11.15A, B and C) and (ii) temperature influences $D_{H_2O}^{cpx-opx}$ (Figure 11.16E) and expands the trend of Gibson *et al.* (2020).

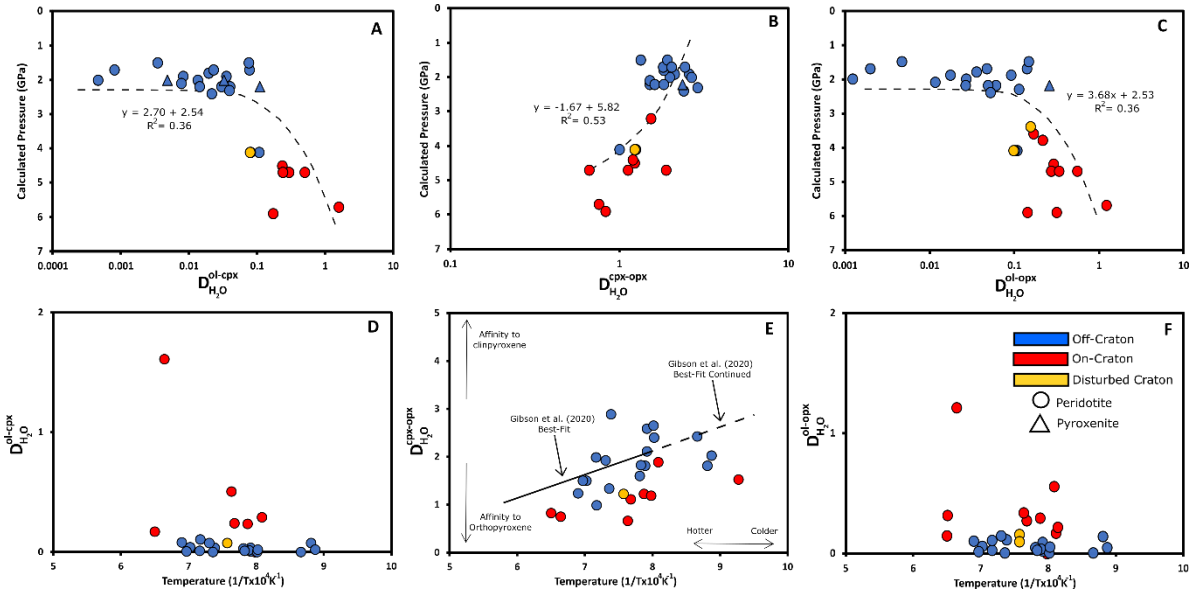

Figure 11.16. Calculated and inferred pressures of spinel and garnet peridotites and pyroxenites compared to H_2O partitioning between A) olivine-clinopyroxene B) Clinopyroxene-orthopyroxene and C) olivine-orthopyroxene). Also shown is temperature compared to H_2O partitioning between D) olivine-clinopyroxene, E) clinopyroxene-orthopyroxene and F) olivine-orthopyroxene.

The temperature dependence of $D_{H_2O}^{cpx-opx}$ is well established experimentally and observed

in natural samples (e.g. Hauri *et al.*, 2006; Gaetani & Grove, 1998; Gibson *et al.*, 2020). This mechanism likely relates to the temperature dependent substitution of Al^{4+} for Si^{4+}, where Al^{3+} increases in orthopyroxene with temperature and is charge balanced by H^+ (e.g. Gasparik & Newton, 1984). The temperature dependent capacity of Al^{3+} in olivine has also been well established, with increasing temperatures corresponding to an increase in Al^{3+} capacity (Bussweiler *et al.*, 2017) and in theory should enable more H^+ incorporation. Therefore, the $D_{H_2O}^{ol-cpx}$ and $D_{H_2O}^{ol-opx}$ should also be temperature dependent. However, this is not necessarily observed in 11.14 and, it may be that clinopyroxene and olivine undergo a pressure dependent H_2O exchange. A possible mechanism is that under higher pressure, the olivine lattice is able to accommodate more H^+ in the form of point defects. With this increased capacity of olivine, H^+ that would otherwise occupy clinopyroxene in lower pressures redistributes and occupies the increased capacity provided by the olivine.

Alternatively, the variability between on-craton and off-craton $D_{H_2O}^{ol-cpx}$ may simply be a function of the different clinopyroxene composition in the two reservoirs. The positive relationship between $D_{H_2O}^{cpx-melt}$ and Al^{3+} (apfu) enables clinopyroxene with increasing Al^{3+} in to store H_2O (O'Leary *et al.*, 2010; Figure 11.16). Therefore, in shallower off-craton lithosphere where clinopyroxene typically has higher Al^{3+}, it can accommodate more H_2O, but in deeper on-craton lithosphere where the clinopyroxene has lower Al^{3+} is less hydrated and H_2O preferentially partitions into the co-existing olivine.

The apparent pressure dependent distribution of H_2O between olivine, orthopyroxene and clinopyroxene may also be related to the lower clinopyroxene and orthopyroxene abundances present in the cratonic mantle (Pearson, 2003). Given clinopyroxene and orthopyroxene can host more H_2O, in more depleted compositions olivine may become a more significant reservoir. However, this seems unlikely as the $D_{H_2O}^{ol-cpx}$ observed in cratons are not reflected by off-craton harzburgites.

Finally, some of the variation between partition of H_2O in olivine and pyroxene may be due to the loss of H_2O during xenolith entrapment and ascent. Studies relevant to conditions in the lithospheric mantle have shown the rapid diffusion of hydrogen for olivine (e.g. Newcombe *et al.*, 2020; $1x10^{-13}$ to $1x10^{-10}$ m^2/s), orthopyroxene (Demers-Roberge *et al.*, 2021; $1x10^{-12}$ to $1x10^{-10.5}$ m^2/s) and clinopyroxene (Ferriss *et al.*, 2016; $1x10^{-13}$ to $1x^{10-9}$

m^2/s). Furthermore, host-magmas typically have high H_2O (>1%) and varying ascent rates that permit varying reequilibration and degassing-induced H-loss. Therefore, it is possible that the rapid eruption rates of kimberlites preserve the original hydrous nature of olivine, orthopyroxene and clinopyroxene while the slower eruption-rates of off-craton magmas may permit degassing-induced H-loss.

11.7 Lattice and fluids hosted volatiles

When comparing lattice-hosted volatile contents (Chapter 4 and 5) with those from fluid-inclusions (Chapter 8), the most significant relationship is between calculated whole-rock B (ppm) and whole-rock $^3He/^4He$ (Figure 11.17). This relationship shows that $^3He/^4He$-B systematics are anchored by depleted upper-mantle signatures (from Allegre *et al.*, 1995 and Marschall *et al.*, 2017) and the observed variations require two different end-members with relative low $^3He/^4He$. One of these has low B concentrations while the other has elevated B concentrations. Given previous constraints on $^3He/^4He$ compositions, this shows that one of the end members is the ambient lithospheric mantle which has maintained low B concentration and undergone ^4He-ingrowth from ^{238}U and ^{232}Th decay. The other represents a B-rich, low $^3He/^4He$ reservoir and is likely to be a metasomatic agent that has experienced input from from recycled lithosphere.

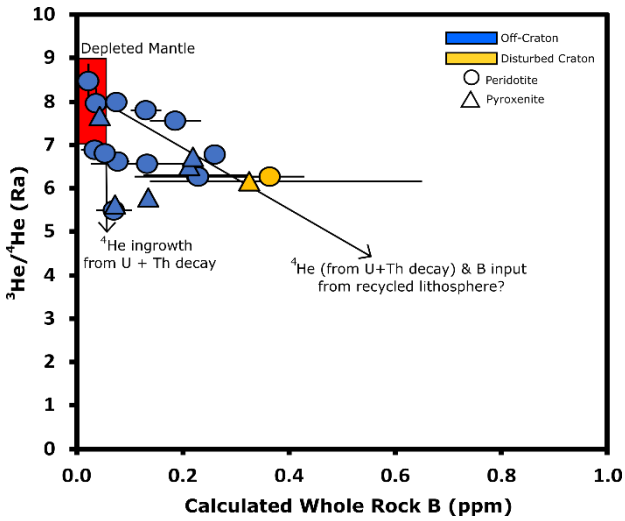

Figure 11.17. Calculated whole-rock B (ppm) compared to calculated whole-rock $^3He/^4He$ (Ra). Horizontal lines show errors and arrows show link between depleted mantle (from Marschall et al., 2017 and Allegre et al., 1995) and hypothetical reservoirs discussed in the main text.

Figure 11.18 integrates information presented by Kobayashi et al. (2019) on the powerful reservoir trace of F/Cl with calculated ^3He-concentrations. This shows that F/Cl compositions increase with greater calculated ^3He and CO_2 concentrations. This implies that the highest

^3He and CO_2 concentrations in the lithospheric mantle are sourced from mantle reservoirs with a limited input of carbon from recycled oceanic lithosphere, such as that sampled by J1 from Ichinomegata. This is somewhat surprising given that the calculated carbon flux from convecting upper mantle is similar to that of subducting oceanic lithosphere. e.g. Kelemen & Manning (2015) suggest that the upper-mantle flux range from 8 to 42 Mt C/y and the flux from recycled oceanic lithosphere is 14 to 66 Mt C/y.

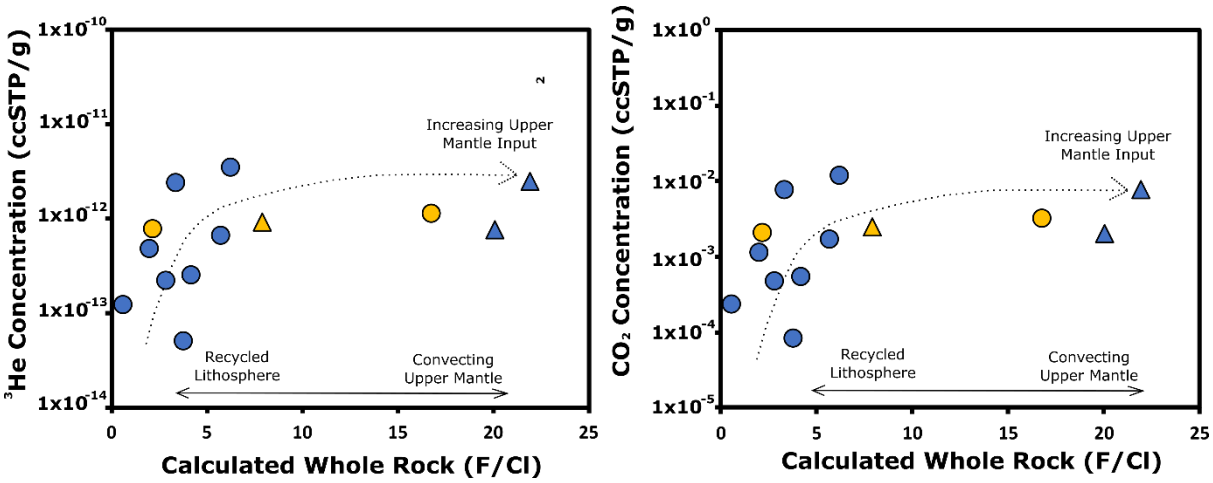

Figure 11.18. Calculated whole-rock F/Cl compared with calculated whole-rock ^3He and inferred CO_2 concentrations using the relationship $CO_2 = {}^3He^{1.2} \times 8x10^{11}$ as calculated in chapter 10.

11.8 Comparison with the volatile content of the MORB-sourced convecting upper mantle

The convecting upper mantle has undergone numerous investigations in order to constrain its volatile composition (e.g. analysis of basaltic lavas, glasses and melt inclusions from mid-ocean ridges; Saal *et al.*, 2004; Salters & Stracke, 2004; Workman & Hart, 2005; Hauri *et al.*, 2017; Kendrick *et al.*, 2017). The calculated concentrations of volatiles for the off-craton sub-continental lithospheric mantle presented in this work are compared to the convecting-upper mantle estimates of Kendrick *et al.* (2017) for H_2O, F and Cl, to Marschall *et al.* (2017) for Li and B and to Salters & Stracke (2004) for P. Marschall *et al.* (2017) suggest that the upper-mantle has 1.2 ppm of Li and 0.08 ppm of B, both lower than the Li and B concentration proposed here (Li = 1.77 ppm and B = 0.09 to 0.22 ppm). Furthermore, Kendrick *et al.* (2017) estimated that the MORB source has 200 ± 100 ppmw of H_2O, 12 ± 2 ppm of F, and 5 ± 2 ppm of Cl. This is lower than the F concentrations (15 to 27 ppm), within the range of calculated Cl (3.4 to 5.4 ppm) and slightly higher than H_2O (86 to 100 ppmw) proposed here. Finally, the P of 41 ppm calculated by Salters & Stracke (2004) is similar to concentrations calculated here (39 ppm).

Overall, this highlights the important role that off-craton lithospheric mantle plays in modulating the flux of different volatiles between the deep Earth and its surface. This is because the sub-continental lithospheric becomes enriched in Li, B and F relative to the convecting upper mantle, thus decreasing the overall flux of these elements between Earth's interior and surface on million-to-billion-year time scales. This is particularly important because B is essential for pre-biotic life (Scorei, 2012) due to its role in ribose synthesis (Ricardo *et al.*, 2004; Furukawa *et al.*, 2013), the thermostability of life biomolecules (Scorei & Cimpoiasu, 2006) and catalytic properties (Saladino *et al.*, 2011). Furthermore, the abundance of boron was potentially scarce in certain ancient microenvironments (Cleaves & Chalmers, 2004). By limiting the flux of B to the Earth's surface, the lithospheric mantle may have had profound effects on the development of life on Earth. Furthermore, the accumulation of F has important consequences if suddenly remobilised during significant volcanic activity (i.e. large igneous provinces; Broadley *et al.*, 2018; Gibson *et al.*, 2020) while Li may represent a significant source in the generation ore-deposits (Wang *et al.*, 2020).

Varying the H_2O content from wet (>150 ppmw) to dry (<150 ppmw) generates approximately 4 orders of magnitude difference in viscosities (Karato, 2010) because increasing water contents decreasing rheological strength (e.g. Faul *et al.*, 2016). The results from this study showing that continental off-craton lithospheric mantle has lower H_2O (86 to 100 ppmw) than the underlying mantle (200 ± 100 ppm; Kenrick *et al.*, 2017) may have important implications for the long-term stability of the lithospheric mantle because it is more resistant to deformation. However, this approach only considers the role of H_2O and ignores the vital effects of pressure and temperature.

11.9 Conclusions

This study highlights the distinct behaviour of H_2O and F in the on- and off-craton mantle. In the on-craton mantle olivine is a major host for these volatile elements but is a less important phase in the off-craton mantle (e.g. Demouchy & Bolfan-Canasova, 2016). This is hypothesized here to be a product of temperature, pressure and compositional dependent distribution of H^+ between clinopyroxene, olivine and melt. Furthermore, this difference highlights how volatiles behave at craton margins. Olivine and clinopyroxene can retain

parental cratonic signatures but the clinopyroxene becomes perturbed and retains recent off-craton signatures (e.g. Gibson *et al.*, 2013).

The concentrations and budgets of H, Li, B, F, P and Cl in the off-craton mantle are obtained using a range of approaches, i.e. through major, trace and mineralogical constraints. The results show that the mean H_2O concentration ranges from 86 to 100 ppmw, Li is 1.77 ppm, B from 0.09 to 0.22 ppm, F from 15 to 27 ppm, P is 40 ppm and Cl from 3.5 to 5.4 ppm. This equates to overall abundances in the off-craton lithosphere of $1.2x10^{21}$ to $1.4x10^{21}$ g of H_2O, $1.3x10^{18}$ g of Li, $1.2x10^{17}$ to $2.8x10^{17}$ g of B, $1.1x10^{19}$ to $2.0x10^{19}$ g of F, $5.1x10^{19}$ g of P and $1.3x10^{18}$ to $2.1x10^{18}$ g of Cl. When compared to these concentrations in the convecting upper mantle, the off-craton lithospheric mantle is more enriched in Li, F and B.

Finally, this study greatly increases the published investigations of B concentrations in ultramafic xenoliths from the sub-continental off-craton lithospheric mantle (e.g. Kaliwoda *et al.*, 2008). The results show that the concentration of B in the off-craton lithospheric mantle is predominantly controlled by melting and metasomatism, particularly by fluid and has implications for B cycling. As the lithosphere becomes metasomatically enriched, it becomes an increasingly significant reservoir for B. The long-term storage of B in the off-craton lithospheric mantle may have important implications for the amount of B cycling from the Earth interior to its surface and ultimately impact on the development of life on Earth.

Chapter 12. Conclusions

12.1 Approach

This study provides the first, fully internally consistent appraisal of the petrography, mineral and calculated whole-rock major, trace and volatile element chemistry together with helium and carbon isotopes of the sub-continental lithospheric mantle. A globally representative set of peridotite and pyroxenite xenoliths from different tectonic settings, varying modal petrology and mineral chemistry reflecting different thermobarometry, melting and metasomatic signatures was analysed

The mantle xenoliths from Colorado Plateau, Ichinomegata, and a subset of samples from the West Eifel have a subduction-zone influence while hose from the Kilbourne Hole, Tariat Volcanic Field and West Eifel Volcanic Field are from present-day intracontinental rift-zones. Moreover, Southern Patagonia is currently in a back-arc setting while the Antarctic Peninsula provides unique insights to a 'slab-window' setting. Finally, samples obtained from Northern Tanzania are from a craton margin and have been variably influenced by cratonic and off-craton melting and metasomatic processes.

The petrography of the mantle xenoliths presented here reflects the highly-variable nature of the sub-continental lithospheric mantle. As outlined in Chapter 3, the ultramafic xenoliths are composed of 23 lherzolites, 13 harzburgites, 6 olivine clinopyroxenites, 1 wehrlite, 1 clinopyroxenite, 1 orthopyroxenite, 1 websterite and 2 composite peridotite-pyroxenite xenoliths. These 37 peridotites reflect variably metasomatized mantle, 9 pyroxenites formed by flow of channelized mantle melts and the other 2 are composite xenoliths.

Barometry presented in Chapter 7 involves the Al-in-orthopyroxene formulation of Nickel & Green (1985) for garnet-bearing ultramafic xenoliths and suggest final equilibration pressures from 21.5 to 41.4 kbar. These pressure constraints are integrated with the two-pyroxene thermometer of Taylor (1998). When inapplicable, the single-pyroxene thermometers of Mercier (1980) are used and corrected to the estimates of Taylor (1998). These have final equilibration temperatures ranging from 850 to 1151 ^{o}C.

Melting regimes for each sample are outlined in Chapter 6 using data presented in Chapter 4 and 5. The degree of melting has been quantified by comparing: coexisting olivine and spinel compositions with the experimental constraints of Jaques & Green (1980); whole-rock

MgO and FeO (wt%) with the models of Herzberg (2004); and whole-rock $[La/Yb]_N$ compositions with the model of Warren (2016). Metasomatic signatures have also been evaluated and are presented in Chapter 6. These are established using the amount of olivine relative to its Mg# content and comparing this to the melting array from Boyd (1989); whole-rock SiO_2 and MgO (wt.%) relative to the melting model of Herzberg (2004); and the abundances of LILE, HFSE, LREE, MREE and HREE relative to known metasomatic agents. Based on these compositions, 4 key groups have been identified.

1. The most 'depleted' peridotites are from Northern Tanzania which have experienced approximately 40% melt extraction yet have highly enriched trace-element signatures. The later indicate interaction by multi-stage metasomatic melts derived from both the convecting upper-mantle and an ancient subduction zone.
2. The most 'fertile' peridotites are from the Kilbourne Hole, Tariat Volcanic Field, and dominated by DMM-like olivines (Mg# = 89.5) that indicate <10% melt extraction. Furthermore, they have the most depleted incompatible trace-element chemistry ($[La/Yb]_N$ = 0.01 to 0.8) which also indicates formation as a residue from the convecting upper-mantle. These xenoliths appear to have undergone minor amounts of metasomatism by low-Mg carbo-silicic high-density fluids.
3. Variable depleted and fertile peridotites occur in the Antarctic Peninsula, Southern Patagonia, West Eifel Volcanic Field and Colorado Plateau. These samples record varying melting regimes within a single location, ranging from ~1% to ~30% melt extraction. They have undergone highly-variable metasomatic enrichment, with signatures indicative of melts and fluids from the convecting upper mantle and recycled lithosphere sources.
4. Pyroxenite samples, which are channelised melts have mineral chemistry more fertile than the DMM and are exclusively formed by crystallisation of volatile-bearing melts and fluids.

The tectonic settings, petrography, thermobarometry, melting and metasomatic signatures of ultramafic xenoliths in this study are exceptionally variable. When combined with previous investigations, these findings provide improved constraints on the following 4 key questions outlined in Chapter 1:

12.2 Why does the $^3He/^4He$ composition of the sub-continental lithospheric mantle vary and what implications does this have on volatile cycles?

To understand why the $^3He/^4He$ composition of the sub-continental lithospheric mantle varies, a large number of major and trace-element analysis of peridotite and pyroxenite xenoliths were used to reconstruct the composition of 50 whole-rocks (Chapter 4, 5 and 8). Whole-rock $^3He/^4He$ ranges from 5.3 ± 0.2 to 8.5 ± 0.4 with ^3He concentrations at $1.4x10^{-14}$ to $1.5x10^{-11}$ ccSTP/g and ^4He concentrations at $1.4x10^{-9}$ to $1.6x10^{-6}$ ccSTP/g. Samples from Kilbourne Hole, Tariat Volcanic Field, Ichinomegata exclusively retain MORB-like $^3He/^4He$ (>7 Ra) whereas other xenoliths have more radiogenic $^3He/^4He$ (<7 Ra).

Chapter 9 shows that major and trace element compositions of olivine and pyroxene are related to the $^3He/^4He$ in their co-existing fluids. Increasing olivine and orthopyroxene Mg# (89.5 to 94), decreasing orthopyroxene Al_2O_3 (0.5 to 6 wt%) and increasing degrees of melt extraction, based on whole-rock MgO and FeO (wt%) and olivine (Mg#) and spinel (Cr#) correlate with decreasing $^3He/^4He$. Furthermore, these systematics outline a distinction between mantle xenoliths sampling on-craton lithosphere (lower $^3He/^4He$ and more depleted chemistry) and the off-craton lithospheric mantle (higher $^3He/^4He$ and less depleted chemistry). To explain these observations, a novel integrative time, temperature and radiogenic ingrowth model of lithospheric mantle formation in the convecting upper-mantle (using insights from Porcelli & Elliott, 2007; Herzberg et al., 2010; Servali & Korenaga, 2018; Day et al., 2015) is developed. These results closely align with the observed xenolith mineral and $^3He/^4He$ compositions and illuminate the dominant mechanisms influencing the variability of $^3He/^4He$ in the sub-continental lithospheric mantle.

Furthermore, there is evidence that $^3He/^4He$ is sensitive to metasomatic processes. This is shown by SiO_2-enriched (modelled after Herzberg, 2004), orthopyroxene-enriched (after Boyd, 1989), elevated $[La/Yb]_N$ and $[Th/Yb]_N$ in samples with relative low $^3He/^4He$ (<7 Ra). This indicates that metasomatic enrichment, particularly that associated with the influence of recycled oceanic lithosphere, may lower the $^3He/^4He$ of the mantle. However, this likely represents a sub-ordinate process.

These insights have particular importance on the long-term storage of fluid-hosted volatiles in the sub-continental lithospheric mantle. The thermal evolution and ingrowth model suggests that the lithospheric mantle may have remained undisturbed on billion-year

timescales unless perturbed by metasomatic processes. This means that important lattice-hosted volatiles (e.g. H, Li, B, F, P and Cl) may remain in the lithospheric mantle on geologically significant cycles, thus removing them from volatile cycling and fluxing from the deep Earth to the atmosphere.

When contextualised with the large number of samples in this study, the most depleted peridotites samples from Northern Tanzania represent the oldest lithosphere which has been most affected by radiogenic ingrowth overprinting the initially higher upper-mantle $^3He/^4He$ (>8). Their $^3He/^4He$ of ~6 Ra is consistent with metasomatism during the past ~1 billion years. The most fertile mantle xenoliths are from Kilbourne Hole, Tariat Volcanic Field and Ichinomegata sample the youngest lithosphere which is likely to have recently formed as a melt residue from the convecting upper mantle. The remaining xenoliths formed in the last billion years and have been variably influenced by metasomatic processes.

Finally, this study shows that the on-craton lithospheric mantle should have a ubiquitously low $^3He/^4He$. This has important implications for understanding melt petrogenesis, particularly that of kimberlites. This is because assimilation of the lithospheric mantle during kimberlite petrogenesis will likely incorporate this low $^3He/^4He$ material. During this assimilation, the theoretically high $^3He/^4He$ of the proto-kimberlite melt would become diluted and lose its original primordial signatures. These observations are consistent with Mg/Si and $^3He/^4He$ mixing models and explain why the pristine primordial mantle hypothesized for proto-kimberlite melts is largely unobserved.

12.3 What is the source of CO_2-bearing fluids in the lithospheric mantle and how much is stored in the off-craton mantle?

To advance the understanding of CO_2 in the off-craton lithospheric mantle, Chapter 10 examines the coupled He and C (concentration and isotope) data presented in Chapter 8 with mineral and whole-rock major and trace elements presented in Chapters 4 and 5.

When filtering the global $CO_2/^3He$ dataset to only record data typical of the off-craton lithospheric mantle, a best fit relationship shows $CO_2 = 8x10^{11} \times {}^3He^{1.2}$ ($R^2 = 0.74$) with a $CO_2/^3He$ range from $2x10^9$ to $5x10^9$ (where $^3He = 1x10^{-13}$ to $1x10^{-11}$). This is slightly higher than the $CO_2/^3He$ of 1.67 to $2.2x10^9$ from Marty & Tolstikhin (1998) and Tucket et al. (2018). When combined with ^3He concentration estimates for the off-craton lithospheric mantle

($1x10^{-13}$ to $1x10^{-11}$), CO_2 is calculated to contain $2.1x10^{-4}$ to $5.1x10^{-2}$ ccSTP/g (0.1 to 28.3 ppm). Using the reservoir volume constraints of Gibson & McKenzie (in review) this equates to a total CO_2 budget of $1.4x10^{21}$ g. Chapter 10 also reveals novel peridotite CO_2-trace element systematics, with CO_2/La and CO_2/Nb ratios of 96 and 15, respectively. These were integrated with geochemical (McDonough, 1990) and petrological constraints (Hirschmann & Stolper, 1996; Downes, 2007) to estimate CO_2 concentrations as 41 ppm and a total budget of 1.84 $x10^{20}$ g. Given the magnitudes of uncertainty associated with ^{3}He concentrations, the CO_2 value produced by CO_2/La is preferred.

The $^3He/^4He$-$^{12}C/^{13}C$ relationships of off-craton mantle xenoliths are discussed in Chapter 10. They show domination and anchoring of upper-mantle signatures with variable affinities to the recycled oceanic lithosphere and primordial mantle reservoirs. These observations are consistent with the $^3He/^4He$-major-trace element systematics presented in Chapter 9 and outline the dominant role that the convecting upper mantle plays influencing the off-craton lithospheric mantle.

12.4 What is the concentration and abundance of H_2O, Li, B, F, P and Cl in the off-craton mantle and what implications do these have to global volatile cycles?

To better constrain the abundance and behaviour of lattice-hosted volatiles in the off-craton lithospheric mantle, the well characterised xenoliths from this study were analysed to constrain their H_2O, Li, B, F, P and Cl by secondary-ion mass spectrometry (SIMS).

The results from this study show that whole-rock H_2O concentrations are sensitive to clinopyroxene Si^{4+} and Al^{3+}, modal mineralogy (olivine and clinopyroxene wt%), and MREE (e.g. Gd). Li correlated with Mg# of olivine, orthopyroxene and clinopyroxene and Ti^{2+} of clinopyroxene. Boron is sensitive to whole-rock Mg# and LILE (e.g. U). Fluorine has many co-varying factors, such as olivine Mn^{2+} and Mg#, orthopyroxene Ti^{2+}, Ca^{2+} and Na^{+}, clinopyroxene Mg#, Si^{4+}, Ti^{2+}, Ca^{2+} and whole-rock MREE and HREE (e.g. Sm). P correlates with the HREE (e.g. Er) while Cl is sensitive to whole-rock Cr_2O_3 and HREE(e.g. Tm). When these observations are integrated with the lithospheric mantle compositions of McDonough (1990) and McDonough & Rudnick (1998) and the mass of Gibson & McKenzie (in review), the calculated bulk off-craton continental lithospheric mantle is estimated to have: 86 to 100 ppmw of H_2O ($1.2x10^{21}$ to $1.4x10^{21}$ g), 1.77 ppm ($1.3x10^{18}$ g), 0.09 to 0.22 ppm of B

($1.2x10^{17}$ to $2.8x10^{17}$ g), 15 to 27 ppm of F ($1.1x10^{19}$ to $2.0x10^{19}$ g), 40 ppm of P ($5.1x10^{19}$g) and 3.5 to 5.4 ppm of Cl ($1.3x10^{18}$ to $2.1x10^{18}$ g).

Compared to the convecting upper-mantle, the sub-continental lithospheric mantle is more highly concentrated in Li, B and F and less concentrated in H_2O. This has important impacts on global volatile cycling and maybe on lithospheric stability. Where, the high concentration of Li, B and F stored in the lithospheric mantle are removed from global volatile cycles between the deep Earth and its surface reservoirs on geologically significant timescales (Chapter 9). Furthermore, the lower H_2O content of the subcontinental off-craton lithospheric mantle relative to the underlying convecting upper mantle may aid rheological contrasts and help the long-term stability of the lithosphere. Conversely, this may also represent extensive loss of H_2O as other models indicate the H_2O content of the lithospheric mantle to be higher than the upper mantle.

When these estimates for average volatile concentrations are applied to the different types of samples identified, the 'depleted' xenoliths have relative low mean H_2O (65 to 105 ppmw), Li (0.8 to 1.5 ppm) and P (11.5 to 30.2 ppm) but high B (0.12 to 0.36 ppm), F (41 to 78 ppm) and Cl (2 to 19 ppm). The fertile xenoliths have relative low Li (1.63 to 1.74 ppm), B (0.04 to 0.13 ppm), F (12 to 14 ppm), P (9.7 ppm) and Cl (3 ppm) below the average estimates but high H_2O (67 to 134 ppm). The remaining peridotites have volatile ranges which encompass those of the depleted and enriched xenoliths.

This study outlies a distinction between the volatile contents of the on-craton and off-craton xenoliths. Where olivine plays an important role in hosting H_2O and F in on-craton samples but is far less significant in off-craton samples. Overall, this shows the importance of pressure, temperature and bulk composition on volatile partitioning. Furthermore, when appraising the evolution of the disturbed cratons, such as that from Northern Tanzania it becomes clear that these regions retain characteristics of on-craton and off-craton settings. Whereby, olivine and orthopyroxene have cratonic H_2O-Mg# and F-Mg# but off-craton clinopyroxene with H_2O-Mg# and F-Mg#.

Finally, this study provides exciting new insights into the origin of ^{3}He and B in the subcontinental lithospheric mantle. The results show that the more ^{3}He-concentrated ultramafic xenoliths have elevated calculated whole-rock F/Cl. Given the power of F/Cl as a

tracer (high = mantle, low = recycled lithosphere), this implies the greatest input from the convecting mantle coincides with the highest ^3He (and therefore CO_2) concentrations.

12.5 Is there a significant distinction between peridotite and pyroxenites in volatile composition and abundance?

Pyroxenites have been recently recognised as an important host for volatiles. This is particularly the case for F and H_2O from Gibson et al. (2020) Here, these observations are expanded.

Firstly, the results outlined in Chapter 8 show peridotites have a ^3He mean = $1x10^{-12} \pm 4x10^{-13}$ and median of $1x10^{-13}$ while pyroxenites have a mean ^3He = $3x10^{-12} \pm 4x10^{-13}$ and a median of $2x10^{-12}$ (where the uncertainty is the standard error). While this may be a slight over-estimate for peridotites (see discussion in section 12.2), this reflects the exclusively high ^3He concentrations of pyroxenites. Using the $CO_2/^3He$ constraint of $CO_2 = 8x10^{11} \times {}^3He^{1.20}$ calculated in Chapter 10, the mean CO_2 concentration of peridotite ($4x10^{-3} \pm 1x10^{-3}$ ccSTP/g; 2.2 ± 0.6 ppm) is lower than the mean CO_2 of pyroxenite ($1x10^{-2} \pm 1x10^{-3}$ ccSTP/g; 5.6 ± 0.6 ppm). This is consistent with CO_2 and La compositions, where pyroxenites are dominated by high CO_2 and La concentrations.

The new constraints from lattice-hosted volatile chemistry also expand insights on H_2O and F (Gibson et al., 2020) to Li and P. This is because major and trace element co-variations outlined in Chapter 11 show that increasing Li and P concentrations are commonly observed in pyroxenites. Where, Li appears sensitive to olivine, orthopyroxene and clinopyroxene Mg#. The lower Mg# mineral compositions typical of pyroxenites have elevated Li concentrations. Additionally, clinopyroxene Ti^{4+} is also positively related to Li concentrations, and pyroxenites commonly contain high-Ti augites. Furthermore, the relationship of P and HREE concentrations would imply that samples with greater whole-rock HREE (e.g. Tm) have higher P. Although individual clinopyroxenes may not have high HREE concentrations, the high modal abundance of clinopyroxene corresponds to higher overall HREE concentrations and therefore hypothetically high P contents.

Overall, this expands our understanding of the importance of pyroxenites as hosts of volatile elements, representing significant reservoirs for ^3He, CO_2, H_2O, F, Li and P. This builds on the findings of Gibson et al. (2020) and shows how pyroxenites may also be important sources

of CO_2 during volcanism associated with large igneous processes and intracontinental rifting (e.g. Wong et al., 2019). Furthermore, pyroxenites may also represent important sources of Li during petrogenesis.

12.6 Future work

This thesis has built on years of exceptional work, by incorporating major and trace element chemistry of ultramafic xenoliths with isotopic analysis of fluid-hosted volatile (He & C) and lattice-hosted volatile (H_2O, Li, B, F, P and Cl). This new data has provided some novel insights and provided future opportunities.

1. Using insights from Chapter 9, this study can explain why kimberlite magmas, which hypothetically come from a pristine deep-mantle source, rarely preserve $^3He/^4He$ indicative of primordial input. Future work could be undertaken on analysing the neon-isotope analysis of these magmas. Currently, one study on the Ne-isotope composition of kimberlites has been undertaken (Sumino et al., 2006) and showed a less nucleogenic composition than that observed for the MORB-source mantle and more akin to samples with 'plume-like' neon isotopes. This evidence for the deep origin of kimberlite magmas should be expanded to incorporate kimberlites of different ages and locations to provide additional insight to their origin.

2. Chapter 10 represents the first integrated CO_2 and whole-rock trace-element analysis of mantle xenoliths. It excitingly produces a positive correlation between CO_2-La and CO_2-Nb, which enables an estimate on the CO_2 concentration within the lithospheric mantle. However, a problem with these findings is that they are limited to 13 samples and extrapolated to the entire off-craton lithospheric mantle. This therefore demands additional analysis to fully appraise this observation and provide tighter constraints on the concentration of CO_2 in the off-craton sub-continental lithospheric mantle.

3. Estimates of the helium concentration of the lithospheric mantle are very inaccurate due to the large range in ultramafic xenoliths (Chapter 8 and 9). Many previous studies are based on the published concentrations of helium in peridotite and pyroxenite xenoliths. However, this likely overestimates the helium concentration in

the continental mantle because of the bias the towards higher values, i.e. it only factors in samples which have high enough concentration to produce accurate $^{3}He/^{4}He$ compositions. As a result, the ^{3}He-concentration commonly used at $1x10^{-11}$ ccSTP/g (e.g. Gautheron & Moriera, 2002), which is higher than the average of published results (approximately $1x10^{-12}$), is an overestimate on the order of 10-100x. This has a significant impact on estimating CO_2 concentrations by $CO_2/^{3}He$ ratios outlined by Chapter 10 and should be addressed in future studies.

4. Chapter 11 has greatly expanded the analysis of boron in ultramafic xenoliths. This has highlighted the importance of metasomatism increasing the B concentration in the sub-continental lithospheric mantle, and how important it is as a long-term reservoir. To advance this understanding, it would be very exciting to constrain the B isotopic composition and how this relates to metasomatic variation. B isotopes are known to be excellent at constraining different Earth reservoirs (e.g. Marshcall, 2018) and by integrating these with metasomatic signatures it may be possible to provide novel insights on the source of B-rich metasomatic processes.

5. Finally, a future opportunity is something that would have formed part of this PhD had it not been impacted by the COVID-19 pandemic. This is the spatial characterisation of volatiles in mantle minerals through characterisation of Atom Probe Tomography (APT). Integration of high-precision analysis of volatile by SIMS with the spatial characterisation using APT would enhance the understanding on the geochemical variability of a sample, where volatiles reside in a crystal structure and the nature of how these volatiles exist through time-of-flight secondary-ion mass spectrometry (TOF-SIMS). Well characterised samples in this study could be funded through the Royce Scheme and prepared at the University of Manchester by Dr. Xiangli Zhong using a transmission electron microscope fitted with a xenon plasma-focused ion-beam (e.g. Halpin et al., 2019) and analysed at the Oxford Atom Probe Facility by Dr. Paul Bagot.

Appendix

Appendix A. Bibliography

Abe, N., Arai, S., Saeki, Y., 1992. Hydration processes in the arc mantle; petrology of the Megata peridotite xenoliths, the Northeast Japan arc. J. Mineral. Petrol. Econ. Geol. 87, 305–317. https://doi.org/10.2465/ganko.87.305

Abe, N., Arai, S., Yurimoto, H., 1998. Geochemical characteristics of the uppermost mantle beneath the Japan island arcs: implications for upper mantle evolution. Phys. Earth Planet. Inter. 107, 233–248. https://doi.org/10.1016/S0031-9201(97)00136-2

Abe, S., Yamamoto, M., 1999. Rb-Sr mineral isochron ages of mantle peridotite xenoliths from Ichinomegata and Kurose, Japan. J. Mineral. Petrol. Econ. Geol. 94, 295–310. https://doi.org/10.2465/ganko.94.295

Ackert, R.P., Singer, B.S., Guillou, H., Kaplan, M.R., Kurz, M.D., 2003. Long-term cosmogenic 3He production rates from 40Ar/39Ar and K-Ar dated Patagonian lava flows at 47°S. Earth Planet. Sci. Lett. 210, 119–136. https://doi.org/10.1016/S0012-821X(03)00134-1

Afonso, J.C., Rawlinson, N., Yang, Y., Schutt, D.L., Jones, A.G., Fullea, J., Griffin, W.L., 2016. 3-D multiobservable probabilistic inversion for the compositional and thermal structure of the lithosphere and upper mantle: III. Thermochemical tomography in the Western-Central U.S. J. Geophys. Res. Solid Earth 121, 7337–7370. https://doi.org/10.1002/2016JB013049

Aiuppa, A., Casetta, F., Coltorti, M., Stagno, V., Tamburello, G., 2021. Carbon concentration increases with depth of meltingin Earth's upper mantle. Nat. Geosci. 2021 149 14, 697–703. https://doi.org/10.1038/s41561-021-00797-y

Alibert, C., 1994. Peridotite xenoliths from western Grand Canyon and The Thumb: a probe into the subcontinental mantle of the Colorado Plateau. J. Geophys. Res. 99, 21605–21620. https://doi.org/10.1029/94jb01555

Allègre, C.J., Moreira, M., Staudacher, T., 1995. 4He/3He dispersion and mantle convection. Geophys. Res. Lett. 22, 2325–2328. https://doi.org/10.1029/95GL02307

An, M., Shi, Y., 2006. Lithospheric thickness of the Chinese continent. Phys. Earth Planet. Inter. 159, 257–266. https://doi.org/10.1016/j.pepi.2006.08.002

An, M., Wiens, D.A., Zhao, Y., Feng, M., Nyblade, A., Kanao, M., Li, Y., Maggi, A., Lévêque, J.J., 2015. Temperature, lithosphere-asthenosphere boundary, and heat flux beneath the Antarctic Plate inferred from seismic velocities. J.

Geophys. Res. Solid Earth 120, 8720–8742. https://doi.org/10.1002/2015JB011917

Andersen, T., Neumann, E.R., 2001. Fluid inclusions in mantle xenoliths. Lithos 55, 301–320. https://doi.org/10.1016/S0024-4937(00)00049-9

Andersen, T., O'reilly, S.Y., Griffin, W.L., 1984. Contributions to Mineralogy and Petrology The trapped fluid phase in upper mantle xenoliths from Victoria, Australia: implications for mantle metasomatism. Contrib Miner. Pet. 88, 72–85.

Anthony, E.Y., Poths, J., 1992. 3He surface exposure dating and its implications for magma evolution in the Potrillo volcanic field, Rio Grande Rift, New Mexico, USA. Geochim. Cosmochim. Acta 56, 4105–4108. https://doi.org/10.1016/0016-7037(92)90022-B

Arai, S., 1994. Characterization of spinel peridotites by olivine-spinel compositional relationships: Review and interpretation. Chem. Geol. 113, 191–204. https://doi.org/10.1016/0009-2541(94)90066-3

Arai, S., Abe, N., Ishimaru, S., 2007. Mantle peridotites from the Western Pacific. Gondwana Res. 11, 180–199. https://doi.org/10.1016/j.gr.2006.04.004

Artemieva, I.M., 2006. Global 1° × 1° thermal model TC1 for the continental lithosphere: Implications for lithosphere secularevolution. Tectonophysics 416, 245–277. https://doi.org/10.1016/j.tecto.2005.11.022

Artemieva, I.M., 2019. Lithosphere structure in Europe from thermal isostasy. Earth-Science Rev. https://doi.org/10.1016/j.earscirev.2018.11.004 Page | iii

Aulbach, S., Rudnick, R.L., 2009. Origins of non-equilibrium lithium isotopic fractionation in xenolithic peridotite minerals: Examples from Tanzania. Chem. Geol. 258, 17–27. https://doi.org/10.1016/j.chemgeo.2008.07.015

Bach, W., Garrido, C.J., Paulick, H., Harvey, J., Rosner, M., 2004. Seawater-peridotite interactions: First insights from ODP Leg 209, MAR 15°N. Geochemistry, Geophys. Geosystems 5, 9–26. https://doi.org/10.1029/2004GC000744

Baker, M.B., Hirschmann, M.M., Ghiorso, M.S., Stolper, E.M., 1995. Compositions of near-solidus peridotite melts from experiments and thermodynamic calculations. Nature 375, 308–311. https://doi.org/10.1038/375308a0

Baker, M.B., Stolper, E.M., 1994. Determining the composition of high-pressure mantle melts using diamond aggregates. Geochim. Cosmochim. Acta 58, 2811–2827. https://doi.org/10.1016/0016-7037(94)90116-3

Ballentine, C.J., Burnard, P.G., 2002. Production, Release and Transport of Noble Gases in the Continental Crust. Rev. Mineral. Geochemistry 47, 481–538. https://doi.org/10.2138/RMG.2002.47.12

Baptiste, V., Tommasi, A., Vauchez, A., Demouchy, S., Rudnick, R.L., 2015. Deformation, hydration, and anisotropy of the lithospheric mantle in an active rift: Constraints from mantle xenoliths from the North Tanzanian Divergence of the East African Rift. Tectonophysics 639, 34–55. https://doi.org/10.1016/J.TECTO.2014.11.011

Baranov, A., Morelli, A., 2013. The Moho depth map of the Antarctica region. Tectonophysics 609, 299-313. https://doi.org/10.1016/j.tecto.2012.12.023

Barfod, D.N., Ballentine, C.J., Halliday, A.N., Fitton, J.G., 1999. Noble gases in the Cameroon line and the He, Ne, and Ar isotopic compositions of high μ (HIMU) mantle. J. Geophys. Res. Solid Earth 104, 29509–29527. https://doi.org/10.1029/1999jb900280

Barry, P.H., Hilton, D.R., Day, J.M.D., Pernet-Fisher, J.F., Howarth, G.H., Magna, T., Agashev, A.M., Pokhilenko, N.P., Pokhilenko, L.N., Taylor, L.A., 2015. Helium isotopic evidence for modification of the cratonic lithosphere during the Permo-Triassic Siberian flood basalt event. Lithos 216–217, 73–80. https://doi.org/10.1016/j.lithos.2014.12.001

Barry, T.L., Ivanov, A. V., Rasskazov, S. V., Demonterova, E.I., Dunai, T.J., Davies, G.R., Harrison, D., 2007. Helium isotopes provide no evidence for deep mantle involvement in widespread Cenozoic volcanism across Central Asia. Lithos 95, 415–424. https://doi.org/10.1016/j.lithos.2006.09.003

Barry, T.L., Saunders, A.D., Kempton, P.D., Windley, B.F., Pringle, M.S., Dorjnamjaa, D., Saandar, S., 2003. Petrogenesis of Cenozoic Basalts from Mongolia: Evidence for the Role of Asthenospheric versus Metasomatized Lithospheric Mantle Sources. J. Petrol. 44, 55–91.

Beccaluva, L., Bianchini, G., Ellam, R.M., Marzola, M., Oun, K.M., Siena, F., Stuart, F.M., 2008. The role of HIMU metasomatic components in the North African lithospheric mantle: Petrological evidence from the Gharyan lherzolite xenoliths, NW Libya. Geol. Soc. Spec. Publ. 293, 253–277. https://doi.org/10.1144/SP293.12

Behr, W.M., Smith, D., 2016. Deformation in the mantle wedge associated with Laramide flat-slab subduction. Geochemistry, Geophys. Geosystems 17, 2643–2660. https://doi.org/10.1002/2016GC006361

Bekaert, D. V., Broadley, M.W., Caracausi, A., Marty, B., 2019. Novel insights into the degassing history of Earth's mantle from high precision noble gas analysis of magmatic gas. Earth Planet. Sci. Lett. 525, 115766. https://doi.org/10.1016/j.epsl.2019.115766

Berkesi, M., Czuppon, G., Szabó, C., Kovács, I., Ferrero, S., Boiron, M.C., Peiffert, C., 2019. Pargasite in fluid inclusions of mantle xenoliths from northeast Australia (Mt. Quincan): evidence of interaction with asthenospheric fluid. Chem. Geol. 508, 182–196. https://doi.org/10.1016/j.chemgeo.2018.06.022

Bernstein, S., Kelemen, P.B., Hanghøj, K., 2007. Consistent olivine Mg# in cratonic mantle reflects Archean mantle melting to the exhaustion of orthopyroxene. Geology 35, 459–462. https://doi.org/10.1130/G23336A.1

Beyer, C., Klemme, S., Wiedenbeck, M., Stracke, A., Vollmer, C., 2012. Fluorine in nominally fluorine-free mantle minerals: Experimental partitioning of F between olivine, orthopyroxene and silicate melts with implications for magmatic processes. Earth Planet. Sci. Lett. 337–338, 1–9. https://doi.org/10.1016/J.EPSL.2012.05.003Page | iv

Bianchini, G., Natali, C., 2017. Carbon elemental and isotopic composition in mantle xenoliths from Spain: Insights on sources and petrogenetic processes. Lithos 272–273, 84–91. https://doi.org/10.1016/J.LITHOS.2016.11.020

Bird, P., Liu, Z., Rucker, W.K., 2008. Stresses that drive the plates from below: Definitions, computational path, model optimization, and error analysis. J. Geophys. Res. Solid Earth 113, 11406. https://doi.org/10.1029/2007JB005460

Boyd, F.R., 1989. Compositional distinction between oceanic and cratonic lithosphere. Earth Planet. Sci. Lett. 96, 15–26. https://doi.org/10.1016/0012-821X(89)90120-9

Bragagni, A., Luguet, A., Fonseca, R.O.C., Pearson, D.G., Lorand, J.P., Nowell, G.M., Kjarsgaard, B.A., 2017. The geological record of base metal sulfides in the cratonic mantle: A microscale 187Os/188Os study of peridotite xenoliths from Somerset Island, Rae Craton (Canada). Geochim. Cosmochim. Acta 216, 264–285. https://doi.org/10.1016/j.gca.2017.04.015

Brandon, A.D., Creaser, R.A., Shirey, S.B., Carlson, R.W., 1996. Osmium recycling in subduction zones. Science (80-.). 272, 861–864. https://doi.org/10.1126/science.272.5263.861

Bräuer, K., Kämpf, H., Niedermann, S., Strauch, G., 2013. Indications for the existence of different magmatic reservoirs beneath the Eifel area (Germany): A multi-isotope (C, N, He, Ne, Ar) approach. Chem. Geol. 356, 193–208. https://doi.org/10.1016/j.chemgeo.2013.08.013

Brey, G.P., Bulatov, V.K., Girnis, A. V., 2008. Geobarometry for Peridotites: Experiments in Simple and Natural Systems from 6 to 10 GPa. J. Petrol. 49, 3–24. https://doi.org/10.1093/PETROLOGY/EGM067

Brey, G.P., Köhler, T., Nickel, K.G., 1990. Geothermobarometry in Four-phase Lherzolites I. Experimental Results from 10 to 60 kb. J. Petrol. 31, 1313–1352. https://doi.org/10.1093/PETROLOGY/31.6.1313

Broadley, M.W., Ballentine, C.J., Chavrit, D., Dallai, L., Burgess, R., 2016. Sedimentary halogens and noble gases within Western Antarctic xenoliths: Implications of extensive volatile recycling to the sub continental lithospheric mantle. Geochim. Cosmochim. Acta 176, 139–156. https://doi.org/10.1016/J.GCA.2015.12.013

Broadley, M.W., Barry, P.H., Ballentine, C.J., Taylor, L.A., Burgess, R., 2018. End-Permian extinction amplified by plumeinduced release of recycled lithospheric volatiles. Nat. Geosci. 2018 119 11, 682–687. https://doi.org/10.1038/s41561-018-0215-4

Brown, R.J., Manya, S., Buisman, I., Fontana, G., Field, M., Niocaill, C. Mac, Sparks, R.S.J., Stuart, F.M., 2012. Eruption of kimberlite magmas: Physical volcanology, geomorphology and age of the youngest kimberlitic volcanoes known on earth (the Upper Pleistocene/Holocene Igwisi Hills volcanoes, Tanzania). Bull. Volcanol. 74, 1621–1643. https://doi.org/10.1007/s00445-012-0619-8

Büchel, G., 2008. Maars of the Westeifel, Germany, in: Paleolimnology of European Maar Lakes. Springer Berlin Heidelberg, pp. 1–13. https://doi.org/10.1007/bfb0117585

Buikin, A., Trieloff, M., Hopp, J., Althaus, T., Korochantseva, E., Schwarz, W.H., Altherr, R., 2005. Noble gas isotopes suggest deep mantle plume source of late Cenozoic mafic alkaline volcanism in Europe. Earth Planet. Sci. Lett. 230, 143–162. https://doi.org/10.1016/J.EPSL.2004.11.001

Burton, K.W., Schiano, P., Birck, J.L., Allègre, C.J., Rehkämper, M., Halliday, A.N., Dawson, J.B., 2000. The distribution and behaviour of rhenium and osmium amongst mantle minerals and the age of the lithospheric mantle beneath Tanzania. Earth Planet. Sci. Lett. 183, 93–106. https://doi.org/10.1016/S0012-821X(00)00259-4

Bussweiler, Y., Brey, G.P., Pearson, D.G., Stachel, T., Stern, R.A., Hardman, M.F., Kjarsgaard, B.A., Jackson, S.E., 2017. The aluminum-in-olivine thermometer for mantle peridotites — Experimental versus empirical calibration and potential applications. Lithos 272–273, 301–314. https://doi.org/10.1016/J.LITHOS.2016.12.015

Campione, M., Malaspina, N., Frezzotti, M.L., 2015. Threshold size for fluid inclusion decrepitation. J. Geophys. Res. Solid Earth 120, 7396–7402. https://doi.org/10.1002/2015JB012086

Cande, S.C., Leslie, R.B., 1986. Late Cenozoic tectonics of the southern Chile Trench. J. Geophys. Res. 91, 471–496. https://doi.org/10.1029/JB091iB01p00471Page | v

Canil, D., O'Neill, H.S.C., Pearson, D.G., Rudnick, R.L., McDonough, W.F., Carswell, D.A., 1994. Ferric iron in peridotites and mantle oxidation states. Earth Planet. Sci. Lett. 123, 205–220. https://doi.org/10.1016/0012-821X(94)90268-2

Carlson, R.W., Ionov, D.A., 2019. Compositional characteristics of the MORB mantle and bulk silicate earth based on spinel peridotites from the Tariat Region, Mongolia. Geochim. Cosmochim. Acta 257, 206–223. https://doi.org/10.1016/j.gca.2019.05.010

Carracedo, A., Rodés, Smellie, J.L., Stuart, F.M., 2019. Episodic erosion in West Antarctica inferred from cosmogenic 3He and 10Be in olivine from Mount Hampton. Geomorphology 327, 438–445. https://doi.org/10.1016/j.geomorph.2018.11.019

Carter, J., 1965. No TitleA geochemical investigation of ultrabasic and basic inclusions in the Kilbourne Hole, New Mexico basalt. Trans. Am. Geophys. Union 46, 186–187.

Cartigny, P., Harris, J.W., Javoy, M., 2001. Diamond genesis, mantle fractionations and mantle nitrogen content: a study of δ13C–N concentrations in diamonds. Earth Planet. Sci. Lett. 185, 85–98. https://doi.org/10.1016/S0012-821X(00)00357-5

Cartigny, P., Palot, M., Thomassot, E., Harris, J.W., 2014. Diamond Formation: A Stable Isotope Perspective. http://dx.doi.org/10.1146/annurev-earth-042711-105259 42, 699–732. https://doi.org/10.1146/ANNUREV-EARTH042711-105259

Cartigny, P., Pineau, F., Aubaud, C., Javoy, M., 2008. Towards a consistent mantle carbon flux estimate: Insights from volatile systematics (H2O/Ce, δD, CO2/Nb) in the North Atlantic mantle (14° N and 34° N). Earth Planet. Sci. Lett. 265, 672–685. https://doi.org/10.1016/J.EPSL.2007.11.011

Chapman, A.D., Riggs, N., Ducea, M.N., Saleeby, J.B., Rautela, O., Shields, J., 2019. Tectonic development of the Colorado Plateau Transition Zone, central Arizona: Insights from lower lithosphere xenoliths and volcanic host rocks. GSA F. Guid. 55, 209–236. https://doi.org/10.1130/2019.0055(09)

Chazot, G., Menzies, M.A., Harte, B., 1996. Determination of partition coefficients between apatite, clinopyroxene, amphibole, and melt in natural spinel lherzolites from Yemen: Implications for wet melting of the lithospheric mantle. Geochim. Cosmochim. Acta 60, 423–437. https://doi.org/10.1016/0016-7037(95)00412-2

Chen, X., Chen, H.Y.H., 2021. Plant mixture balances terrestrial ecosystem C:N:P stoichiometry. Nat. Commun. 2021 121 12, 1–9. https://doi.org/10.1038/s41467-021-24889-w

Chen, Y., Zhang, Y., Graham, D., Su, S., Deng, J., 2007. Geochemistry of Cenozoic basalts and mantle xenoliths in Northeast China. Lithos 96, 108–126. https://doi.org/10.1016/j.lithos.2006.09.015

Chin, E.J., Chilson-Parks, B., Boneh, Y., Hirth, G., Saal, A.E., Hearn, B.C., Hauri, E.H., 2021. The peridotite deformation cycle in cratons and the deep impact of subduction. Tectonophysics 817, 229029. https://doi.org/10.1016/J.TECTO.2021.229029

Class, C., Goldstein, S.L., 2005. Evolution of helium isotopes in the Earth's mantle. Nature 436, 1107–1112. https://doi.org/10.1038/nature03930

Cleaves, H.J., Chalmers, J.H., 2004. Extremophiles May Be Irrelevant to the Origin of Life. https://home.liebertpub.com/ast 4, 1–9. https://doi.org/10.1089/153110704773600195

Cohen, R.S., O'Nions, R.K., Dawson, J.B., 1984. Isotope geochemistry of xenoliths from East Africa: Implications for development of mantle reservoirs and their interaction. Earth Planet. Sci. Lett. 68, 209–220. https://doi.org/10.1016/0012-821X(84)90153-5

Coltorti, M., Beccaluva, L., Bonadiman, C., Salvini, L., Siena, F., 2000. Glasses in mantle xenoliths as geochemical indicators of metasomatic agents. Earth Planet. Sci. Lett. 183, 303–320. https://doi.org/10.1016/S0012-821X(00)00274-0

Coltorti, M., Bonadiman, C., Hinton, R.W., Siena, F., Upton, B.G.J., 1999. Carbonatite metasomatism of the oceanic upper mantle: Evidence from clinopyroxenes and glasses in ultramafic xenoliths of Grande Comore, Indian Ocean. J. Petrol. 40, 133–165. https://doi.org/10.1093/petroj/40.1.133Page | vi

Conrad, C.P., Lithgow-Bertelloni, C., 2006. Influence of continental roots and asthenosphere on plate-mantle coupling. Geophys. Res. Lett. 33. https://doi.org/10.1029/2005GL025621

Correale, A., Martelli, M., Paonita, A., Rizzo, A., Brusca, L., Scribano, V., 2012. New evidence of mantle heterogeneitybeneath the Hyblean Plateau (southeast Sicily, Italy) as inferred from noble gases and geochemistry of ultramafic xenoliths. Lithos 132–133, 70–81. https://doi.org/10.1016/j.lithos.2011.11.007

Correale, A., Paonita, A., Rizzo, A., Grassa, F., Martelli, M., 2015. The carbon-isotope signature of ultramafic xenoliths from the Hyblean Plateau (southeast Sicily, Italy): Evidence of mantle heterogeneity. Geochemistry, Geophys. Geosystems 16, 600–611. https://doi.org/10.1002/2014GC005656

Correale, A., Pelorosso, B., Rizzo, A.L., Coltorti, M., Italiano, F., Bonadiman, C., Giacomoni, P.P., 2019. The nature of the West Antarctic Rift System as revealed by noble gases in mantle minerals. Chem. Geol. 524, 104–118. https://doi.org/10.1016/j.chemgeo.2019.06.020

Correale, A., Rizzo, A.L., Barry, P.H., Lu, J., Zheng, J., 2016. Refertilization of lithospheric mantle beneath the Yangtze craton in south-east China: Evidence from noble gases geochemistry. Gondwana Res. 38, 289–303. https://doi.org/10.1016/j.gr.2016.01.003

Coulson, I.M., Stuart, F.M., MacLean, N.J., 2011. Assessing the link between mantle source and sub-volcanic plumbing in the petrology of basalts from the 2001 and 2002/2003 eruptions of Mount Etna, Sicily: Evidence from geochemical and helium isotope data. Lithos 123, 254–261. https://doi.org/10.1016/j.lithos.2010.11.013

Czuppon, G., Matsumoto, T., Handler, M.R., Matsuda, J. ichi, 2009. Noble gases in spinel peridotite xenoliths from Mt Quincan, North Queensland, Australia: Undisturbed MORB-type noble gases in the subcontinental lithospheric mantle. Chem. Geol. 266, 19–28. https://doi.org/10.1016/j.chemgeo.2009.03.029

D'Orazio, M., Agostini, S., Mazzarini, F., Innocenti, F., Manetti, P., Haller, M.J., Lahsen, A., 2000. The Pali Aike Volcanic Field, Patagonia: Slab-window magmatism near the tip of South America. Tectonophysics 321, 407–427. https://doi.org/10.1016/S0040-1951(00)00082-2

D'Souza, R.J., Canil, D., Coogan, L.A., 2020. Geobarometry for spinel peridotites using Ca and Al in olivine. Contrib. to Mineral. Petrol. 175, 1–12. https://doi.org/10.1007/S00410-019-1647-6/FIGURES/6

Dalou, C., Koga, K.T., Le Voyer, M., Shimizu, N., 2014. Contrasting partition behavior of F and Cl during hydrous mantle melting: implications for Cl/F signature in arc magmas. Prog. Earth Planet. Sci. 1, 1–17. https://doi.org/10.1186/S40645-014-0026-1/FIGURES/5

Davis, F.A., Tangeman, J.A., Tenner, T.J., Hirschmann, M.M., 2009. The composition of KLB-1 peridotite. Am. Mineral. 94, 176–180. https://doi.org/10.2138/AM.2009.2984

Dawson, J.B., 1964. Carbonate Tuff Cones in Northern Tanganyika. Geol. Mag. 101, 129–137. https://doi.org/10.1017/S0016756800048561

Dawson, J.B., 1980. Kimberlite Genesis. pp. 212–224. https://doi.org/10.1007/978-3-642-67742-7_10

Dawson, J.B., 1984. Contrasting types of upper-mantle metasomatism. Kimberlites II Mantle Crust-Mantle Relationships 11, 289–294. https://doi.org/10.1016/b978-0-444-42274-3.50030-5

Dawson, J.B., 1994. Quaternary kimberlitic volcanism on the Tanzania Craton. Contrib Miner. Pet. 116, 473–485.

Dawson, J.B., 2002. Metasomatism and partial melting in upper-mantle peridotite xenoliths from the Lashaine volcano, northern Tanzania. J. Petrol. 43, 1749–1777. https://doi.org/10.1093/petrology/43.9.1749

Dawson, J.B., 2008. The Gregory Rift Valley and Neogene—Recent Volcanoes of Northern Tanzania. Geol. Soc. London, Mem. 33.

Dawson, J.B., Powell, D.G., Reid, A.M., 1970. Ultrabasic xenoliths and lava from the Lashaine Volcano, Northern Tanzania. J. Petrol. 11, 519–548. https://doi.org/10.1093/petrology/11.3.519Page | vii

Dawson, J.B., Smith, J. V, 1988. Metasomatised and veined upper-mantle xenoliths from Pello Hill, Tanzania: evidence for anomalously-light mantle beneath the of the East African Rift Valley Tanzanian sector, Contrib Mineral Petrol.

Dawson, J.B., Smith, J. V., 1973. Alkalic pyroxenite xenoliths from the Lashaine volcano, Northern Tanzania. J. Petrol. 14, 113–131. https://doi.org/10.1093/petrology/14.1.113

Dawson, J.B., Smith, J. V., 1992. Olivine-mica pyroxenite xenoliths from northern Tanzania: metasomatic products of uppermantle peridotite. J. Volcanol. Geotherm. Res. 50, 131–142. https://doi.org/10.1016/0377-0273(92)90041-B

Day, J.M.D., Barry, P.H., Hilton, D.R., Burgess, R., Pearson, D.G., Taylor, L.A., 2015. The helium flux from the contine nts and ubiquity of low-3He/4He recycled crust and lithosphere. Geochim. Cosmochim. Acta 153, 116–133. https://doi.org/10.1016/j.gca.2015.01.008

Day, J.M.D., Hilton, D.R., Pearson, D.G., Macpherson, C.G., Kjarsgaard, B.A., Janney, P.E., 2005. Absence of a high timeintegrated 3He/(U+Th) source in the mantle beneath continents. Geology 33, 733–736. https://doi.org/10.1130/G21625.1

De Ignacio, C., López, I., Oyarzun, R., Márquez, A., 2001. The Northern Patagonia Somuncura plateau basalts: A product of slab-induced, shallow asthenospheric upwelling? Terra Nov. 13, 117–121. https://doi.org/10.1046/j.1365-3121.2001.00326.x

Dean, Presnall, C., 1976. Alumina content of enstatite as a geobarometer for plagioclase and spinel lherzolites. Am. Mineral. 6, 582–588.

Deines, P., 2002. The carbon isotope geochemistry of mantle xenoliths. Earth-Science Rev. 58, 247–278. https://doi.org/10.1016/S0012-8252(02)00064-8

del Valle, R.A., Fourcade, N.H., Medina, F.A., 1983. No TitleInterpretación preliminar de las edades K/Ar y de los analisis químicos de las rocas volcánicas y de los diques de los nunataks Foca, Antártida. Contrib. del Inst. Antártico Argentino, 287.

Demers-Roberge, A., Jollands, M.C., Tollan, P., Müntener, O., 2021. H diffusion in orthopyroxene and the retention of mantle water signatures. Geochim. Cosmochim. Acta 305, 263–281. https://doi.org/10.1016/J.GCA.2021.04.005

Demouchy, S., Bolfan-Casanova, N., 2016. Distribution and transport of hydrogen in the lithospheric mantle: A review. Lithos 240–243, 402–425. https://doi.org/10.1016/J.LITHOS.2015.11.012

Denis, C.M.M., Demouchy, S., Shaw, C.S.J., 2013. Evidence of dehydration in peridotites from Eifel Volcanic Field and estimates of the rate of magma ascent. J. Volcanol. Geotherm. Res. 258, 85–99. https://doi.org/10.1016/j.jvolgeores.2013.04.010

Downes, H., 2007. Origin and significance of spinel and garnet pyroxenites in the shallow lithospheric mantle: Ultramafic massifs in orogenic belts in Western Europe and NW Africa. Lithos 99, 1–24. https://doi.org/10.1016/j.lithos.2007.05.006

Dunai, T.J., Porcelli, D., 2002. Storage and Transport of Noble Gases in the Subcontinental Lithosphere. Rev. Mineral. Geochemistry 47, 371–409. https://doi.org/10.2138/RMG.2002.47.10

Eaton, D.W., Darbyshire, F., Evans, R.L., Grütter, H., Jones, A.G., Yuan, X., 2009. The elusive lithosphere–asthenosphere boundary (LAB) beneath cratons. Lithos 109, 1–22. https://doi.org/10.1016/J.LITHOS.2008.05.009

Embey-Isztin, A., Dobosi, G., Bodinier, J.-L., Bosch, D., Jenner, G.A., Pourtales, S., Bruguier, O., 2014. Origin and significance of poikilitic and mosaic peridotite xenoliths in the western Pannonian Basin: geochemical and petrological evidences. Contrib Miner. Pet. 168, 1054. https://doi.org/10.1007/s00410-014-1054-y

Faccini, B., Rizzo, A.L., Bonadiman, C., Ntaflos, T., Seghedi, I., Grégoire, M., Ferretti, G., Coltorti, M., 2020. Subductionrelated melt refertilisation and alkaline metasomatism in the Eastern Transylvanian Basin lithospheric mantle: Evidence from mineral chemistry and noble gases in fluid inclusions. Lithos 364–365, 105516. https://doi.org/10.1016/j.lithos.2020.105516Page | viii

Falloon, T., Berry, R.F., Robinson, P., Stolz, A.J., 2007. Whole-rock geochemistry of the Hili Manu peridotite, East Timor: implications for the origin of Timor ophiolites ∗. http://dx.doi.org/10.1080/08120090600686793 53, 637–649. https://doi.org/10.1080/08120090600686793

Fan, W.M., Zhang, H.F., Baker, J., Jarvis, K.E., Mason, P.R.D., Menzies, M.A., 2000. On and off the North China Craton: Where is the Archaean keel? J. Petrol. 41, 933–950. https://doi.org/10.1093/petrology/41.7.933

Faul, U.H., Cline, C.J., David, E.C., Berry, A.J., Jackson, I., 2016. Titanium-hydroxyl defect-controlled rheology of the Earth's upper mantle. Earth Planet. Sci. Lett. 452, 227–237. https://doi.org/10.1016/J.EPSL.2016.07.016

Ferriss, E., Plank, T., Walker, D., 2016. Site-specific hydrogen diffusion rates during clinopyroxene dehydration. Contrib. to Mineral. Petrol. 171, 1–24. https://doi.org/10.1007/S00410-016-1262-8/FIGURES/14

Fishwick, S., Bastow, I.D., 2011. Towards a better understanding of African topography: A review of passive-source seismic studies of the African crust and upper mantle. Geol. Soc. Spec. Publ. 357, 343–371. https://doi.org/10.1144/SP357.19

Fitzpayne, A., Giuliani, A., Hergt, J., Phillips, D., Janney, P., 2018. New geochemical constraints on the origins of MARID and PIC rocks: Implications for mantle metasomatism and mantle-derived potassic magmatism. Lithos 318–319, 478–493. https://doi.org/10.1016/j.lithos.2018.08.036

Foley, S.F., Fischer, T.P., 2017. An essential role for continental rifts and lithosphere in the deep carbon cycle. Nat. Geosci. 2017 1012 10, 897–902. https://doi.org/10.1038/s41561-017-0002-7

Francis, D., Patterson, M., 2009. Kimberlites and aillikites as probes of the continental lithospheric mantle. Lithos, 109, 72-80. https://doi.org/10.1016/j.lithos.2008.05.007

Franz, G., Steiner, G., Volker, F., Pudlo, D., Hammerschmidt, K., 1999. Plume related alkaline magmatism in central Africa the Meidob Hills (W Sudan). Chem. Geol. 157, 27–47. https://doi.org/10.1016/S0009-2541(98)00195-8

Frechen, J., 1963. Kristallisation, Mineralbestand, Mineralchemismus und Förderfolge der Mafitite vom Dreiser Weiher in der Eifel. Neues Jahrb. Miner. Monatsh. 205–225.

Frezzotti, M.L., Tecce, F., Casagli, A., 2012. Raman spectroscopy for fluid inclusion analysis. J. Geochemical Explor. https://doi.org/10.1016/j.gexplo.2011.09.009

Frezzotti, M.L., Touret, J.L.R., 2014. CO2, carbonate-rich melts, and brines in the mantle. Geosci. Front. 5, 697–710. https://doi.org/10.1016/J.GSF.2014.03.014

Fuchs, K., Wedepohl, K.H., 1983. Relation of geophysical and petrological models of upper mantle structure of the Rhenish Massif. Plateau uplift Rhenish Shield - a case Hist. 353–363. https://doi.org/10.1007/978-3-642-69219-2_39

Furukawa, Y., Kakegawa, T., 2017. Borate and the Origin of RNA: A Model for the Precursors to Life. Elements 13, 261–265. https://doi.org/10.2138/GSELEMENTS.13.4.261

Gaetani, G.A., Grove, T.L., 1998. The influence of water on melting of mantle peridotite. Contrib. Min. Petrol. 131, 323-346. https://10.1007/s004100050396

Gaffney, A.M., Blicher-Toft, J., Nelson, B.K., Bizzarro, M., Rosing, M., Albarede, F., 2007. Constrains on source-forming processes of West Greenland kimberlites inferred from Hf-Nd isotope systematics. Geochim. Cosmochim. Acta 71, 2820-2836. https://doi.org/10.1016/j.gca.2007.03.009

Gasparik, T., 1984. Two-pyroxene thermobarometry with new experimental data in the system CaO-MgO-Al2O3-SiO2. Contrib. to Mineral. Petrol. 1984 871 87, 87–97. https://doi.org/10.1007/BF00371405

Gasparik, T., Newton, R.C., 1984. The reversed alumina contents of orthopyroxene in equilibrium with spinel and forsterite in the system MgO-Al2O3-SiO2. Contrib. to Mineral. Petrol. 1984 852 85, 186–196. https://doi.org/10.1007/BF00371708

Gautheron, C., Moreira, M., 2002. Helium signature of the sub-continental lithospheric mantle. Earth Planet. Sci. Lett. 199,

39–47. https://doi.org/10.1016/S0012-821X(02)00563-0Page | ix

Gautheron, C., Moreira, M., Allègre, C., 2005. He, Ne and Ar composition of the European lithospheric mantle. Chem. Geol. 217, 97–112. https://doi.org/10.1016/j.chemgeo.2004.12.009

Gennaro, M.E., Grassa, F., Martelli, M., Renzulli, A., Rizzo, A.L., 2017. Carbon isotope composition of CO2-rich inclusions in cumulate-forming mantle minerals from Stromboli volcano (Italy). J. Volcanol. Geotherm. Res. 346, 95–103. https://doi.org/10.1016/J.JVOLGEORES.2017.04.001

Gibson, L., 2012. Antarctic lithosphere architecture and evolution; direct constraints from mantle xenoliths. PhD Thesis. University of Cambridge.

Gibson, S.A. & McKenzie, D.P. On the role of Earth's lithospheric mantle in global volatile cycles (in review). Submitted to Earth & Planetary Science Letters (Sept. 2021)

Gibson, S.A., Malarkey, J., Day., J.A., 2008. Melt depletion and enrichment beneath the Western Kaapvaal Craton: Evidence from Finsch Peridotite Xenoliths. J. Petrol. 49, 1817-1852. https://doi.org/10.1093/petrology/egn048

Gibson, S.A., McMahon, S.C., Day, J.A., Dawson, J.B., 2013. Highly-refractory lithospheric mantle beneath the Tanzanian craton: Evidence from Lashaine pre-metasomatic garnet-bearing peridotites. J. Petrol. 54, 1503–1546. https://doi.org/10.1093/petrology/egt020

Gibson, S.A., Rooks, E.E., Day, J.A., Petrone, C.M., Leat, P.T., 2020. The role of sub-continental mantle as both “sink” and “source” in deep Earth volatile cycles. Geochim. Cosmochim. Acta 275, 140–162. https://doi.org/10.1016/j.gca.2020.02.018

Gibson, S.A., Thompson, R.N., Leonardos, O.H., Dickin, A.P., Mitchell, J.G., 1995. The Late Cretaceous Impact of the Trindade Mantle Plume: Evidence from Large-volume, Mafic, Potassic Magmatism in SE Brazil. J. Petrol. 36, 189–229. https://doi.org/10.1093/PETROLOGY/36.1.189

Giggenbach, W. F., Sano, Y. & Wakita, H. Isotopic composition of helium, and CO2 and CH4 contents in gases produced along the New Zealand part of a convergent plate boundary. Geochimica et. Cosmochimica Acta 57, 3427–3455 (1993). https://doi.org/10.1016/0016-7037(93)90549-C

Gilfillan, S. M. V., Györe, D., Flude, S., Johnson, G., Bond, C. E., Hicks, N., Lister, R., Jones, D. G., Kremer, Y., Haszeldine, R. S., & Stuart, F. M. 2019. Noble gases confirm plume-related mantle degassing beneath southern Africa. Nature Communications, 10(1), 5028– 5027. https://doi.org/10.1038/s41467-019-12944-6.

Giuliani, A., Graham Pearson, D., Soltys, A., Dalton, H., Phillips, D., Foley, S.F., Lim, E., Goemann, K., Griffin, W.L., Mitchell, R.H., 2020. Kimberlite genesis from a common carbonate-rich primary melt modified by lithospheric mantle assimilation. Sci. Adv. 6, eaaz0424. https://doi.org/10.1126/sciadv.aaz0424

Giuliani, A., Koornneef, J.M., Barry, P., Will, P., Busemann, H., Maden, C., Maas, R., Greig, A., Davies, G.R., 2020. A preliminary assessment of the application of Sr, Nd, Pb, He and N isotope analysis to fluid inclusions in kimberlite olivine: A new approach to trace deep-mantle sources. EGUGA 5267.

Godard, G., Martin, S., 2000. Petrogenesis of kelyphites in garnet peridotites: a case study from the Ulten zone, Italian Alps. J. Geodyn. 30, 117–145. https://doi.org/10.1016/S0264-3707(99)00030-7

Goldschmidt, V., 1937. The Principles of Distribution of Chemical Elements in Minerals and Rocks.

Gorring, M.L., Kay, S.M., n.d. Carbonatite metasomatized peridotite xenoliths from southern Patagonia: implications for lithospheric processes and Neogene plateau magmatism. Contrib. Min. Petrol. 140. 55-772. https://10.1007/s004100000164.

Gorring, M.L., Kay, S.M., Zeitler, P.K., Ramos, V.A., Rubiolo, D., Fernandez, M.I., Panza, J.L., 1997. Neogene Patagonian plateau lavas: Continental magmas associated with ridge collision at the Chile Triple Junction. Tectonics 16, 1–17. https://doi.org/10.1029/96TC03368

Graham, D. W., Jenkins, W.J., Kurz, M. D., Batiza, R., 1987. Helium Isotope disequilibrium and geochronology of glassysubmarine basalts. Nature, 326, 384-386. https://doi.org/10.1038/326384a0.

Graham, D.W., 2002. Noble gas isotope geochemistry of mid-ocean ridge and ocean island basalts: Characterization of mantle source reservoirs. Rev. Mineral. Geochemistry 47, 247–317. https://doi.org/10.2138/rmg.2002.47.8

Graham, D.W., Larsen, L.M., Hanan, B.B., Storey, M., Pedersen, A.K., Lupton, J.E., 1998. Helium isotope composition of the early Iceland mantle plume inferred from the Tertiary picrites of West Greenland. Earth Planet. Sci. Lett. 160, 241–255. https://doi.org/10.1016/S0012-821X(98)00083-1Page | x

Graham, D.W., Reid, M.R., Jordan, B.T., Grunder, A.L., Leeman, W.P., Lupton, J.E., 2009. Mantle source provinces beneath the Northwestern USA delimited by helium isotopes in young basalts. J. Volcanol. Geotherm. Res. 188, 128–140. https://doi.org/10.1016/j.jvolgeores.2008.12.004

Green, T.H., Blundy, J.D., Adam, J., Yaxley, G.M., 2000. SIMS determination of trace element partition coefficients between garnet, clinopyroxene and hydrous basaltic liquids at 2–7.5 GPa and 1080–1200°C. Lithos 53, 165–187. https://doi.org/10.1016/S0024-4937(00)00023-2

Grégoire, M., Bell, D., Le Roex, A., 2002. Trace element geochemistry of phlogopite-rich mafic mantle xenoliths: Their classification and their relationship to phlogopite-bearing peridotites and kimberlites revisited. Contrib. to Mineral. Petrol. 142, 603–625. https://doi.org/10.1007/s00410-001-0315-8

Griffin, W.L., O'Reilly, S.Y., Abe, N., Aulbach, S., Davies, R.M., Pearson, N.J., Doyle, B.J., Kivi, K., 2003. The origin and evolution of Archean lithospheric mantle. Precambrian Res. 127, 19–41. https://doi.org/10.1016/S0301-9268(03)00180-3

Griffin, W.L., O'Reilly, S.Y., Afonso, J.C., Begg, G.C., 2009. The Composition and Evolution of Lithospheric Mantle: a Reevaluation and its Tectonic Implications. J. Petrol. 50, 1185–1204. https://doi.org/10.1093/PETROLOGY/EGN033

Grützner, T., Kohn, S.C., Bromiley, D.W., Rohrbach, A., Berndt, J., Klemme, S., 2017. The storage capacity of fluorine in olivine and pyroxene under upper mantle conditions. Geochim. Cosmochim. Acta 208, 160–170. https://doi.org/10.1016/J.GCA.2017.03.043

Hålenius, U., Skogby, H., Edén, M., Nazzareni, S., Kristiansson, P., Resmark, J., 2010. Coordination of boron in nominally boron-free rock forming silicates: Evidence for incorporation of BO3 groups in clinopyroxene. Geochim. Cosmochim. Acta 74, 5672–5679. https://doi.org/10.1016/J.GCA.2010.06.033

Halldorsson, S.A., 2014. Noble gas (He-Ne-Ar) and stable isotope (C-N-O) constraints on volatile sources at convergent and divergent plate boundaries with examples from Indonesia, Iceland and the East African Rift System. PhD Thesis –University of California, San Diego.

Halldõrsson, S.A., Hilton, D.R., Scarsi, P., Abebe, T., Hopp, J., 2014. A common mantle plume source beneath the entire East African Rift System revealed by coupled helium-neon systematics. Geophys. Res. Lett. 41, 2304–2311. https://doi.org/10.1002/2014GL059424

Halpin, J.E., Webster, R.W.H., Gardner, H., Moody, M.P., Bagot, P.A.J., MacLaren, D.A., 2019. An in-situ approach for preparing atom probe tomography specimens by xenon plasma-focussed ion beam. Ultramicroscopy 202, 121–127. https://doi.org/10.1016/J.ULTRAMIC.2019.04.005

Hanger, B.J., 2014. Redox conditions in the cratonic lithosphere and implications for metasomatism. PhD thesis – Australian National University. https://doi.org/10.25911/5D7391230D85D

Hart, S.R., Dunn, T., 1993. Experimental cpx/melt partitioning of 24 trace elements. Contrib. to Mineral. Petrol. 1993 1131 113, 1–8. https://doi.org/10.1007/BF00320827

Harvey, J., Dale, C.W., Gannoun, A., Burton, K.W., 2011. Osmium mass balance in peridotite and the effects of mantlederived sulphides on basalt petrogenesis. Geochim. Cosmochim. Acta 75, 5574–5596. https://doi.org/10.1016/j.gca.2011.07.001

Harvey, J., König, S., Luguet, A., 2015. The effects of melt depletion and metasomatism on highly siderophile and strongly chalcophile elements: S-Se-Te-Re-PGE systematics of peridotite xenoliths from Kilbourne Hole, New Mexico. Geochim. Cosmochim. Acta 166, 210–233. https://doi.org/10.1016/j.gca.2015.06.028

Harvey, J., Yoshikawa, M., Hammond, S.J., Burton, K.W., 2012. Deciphering the trace element characteristics in kilbourne hole peridotite xenoliths: Melt-rock interaction and metasomatism beneath the Rio Grande Rift, SW USA. J. Petrol. 53, 1709–1742. https://doi.org/10.1093/petrology/egs030

Hauri, E.H., Gaetani, G.A., Green, T.H., 2006. Partitioning of water during melting of the Earth's upper mantle at H2Oundersaturated conditions. Earth Planet. Sci. Lett. 248, 715–734. https://doi.org/10.1016/J.EPSL.2006.06.014Page | xi

Hauri, E.H., Maclennan, J., McKenzie, D., Gronvold, K., Oskarsson, N., Shimizu, N., 2018. CO2 content beneath northern Iceland and the variability of mantle carbon. Geology 46, 55–58. https://doi.org/10.1130/G39413.1

Heber, V.S., Brooker, R.A., Kelley, S.P., Wood, B.J., 2007. Crystal-melt partitioning of noble gases (helium, neon, argon, krypton, and xenon) for olivine and clinopyroxene. Geochim. Cosmochim. Acta 71, 1041–1061. https://doi.org/10.1016/j.gca.2006.11.010

Heinonen, J.S., Kurz, M.D., 2015. Low-3He/4He sublithospheric mantle source for the most magnesian magmas of the Karoo large igneous province. Earth Planet. Sci. Lett. 426, 305–315. https://doi.org/10.1016/j.epsl.2015.06.030

Helmstaedt, H., Doig, R., 1975. eclogite nodules from kimberlite pipes of the Colorado Plateau—samples of subducted franciscan-type oceanic lithosphere, in: Physics and Chemistry of the Earth. Elsevier, pp. 95–111. https://doi.org/10.1016/b978-0-08-018017-5.50013-4

Henjes-kunst, F., Altherr, R., 1992. Metamorphic petrology of xenoliths from Kenya and Northern Tanzania and implications for geotherms and lithospheric structures. J. Petrol. 33, 1125–1156. https://doi.org/10.1093/petrology/33.5.1125

Hermann, J., Rubatto, D., 2009. Accessory phase control on the trace element signature of sediment melts in subduction zones. Chem. Geol. 265, 512–526. https://doi.org/10.1016/j.chemgeo.2009.05.018

Herzberg, C., 2004. Geodynamic Information in Peridotite Petrology. J. Petrol. 45, 2507–2530. https://doi.org/10.1093/petrology/egh039

Herzberg, C., Asimow, P.D., 2008. Petrology of some oceanic island basalts: PRIMELT2.XLS software for primary magma calculation. Geochemistry, Geophys. Geosystems 9. https://doi.org/10.1029/2008GC002057

Herzberg, C., Asimow, P.D., Arndt, N., Niu, Y., Lesher, C.M., Fitton, J.G., Cheadle, M.J., Saunders, A.D., 2007. Temperaturesin ambient mantle and plumes: Constraints from basalts, picrites, and komatiites. Geochemistry, Geophys. Geosystems 8, n/a-n/a. https://doi.org/10.1029/2006GC001390

Herzberg, C., Condie, K., Korenaga, J., 2010. Thermal history of the Earth and its petrological expression. Earth Planet. Sci. Lett. 292, 79–88. https://doi.org/10.1016/j.epsl.2010.01.022

Herzberg, C., O'Hara, M.J., 2002. Plume-Associated Ultramafic Magmas of Phanerozoic Age. J. Petrol. 43, 1857–1883. https://doi.org/10.1093/petrology/43.10.1857

Herzberg, C., Rudnick, R., 2012. Formation of cratonic lithosphere: An integrated thermal and petrological model. Lithos 149, 4–15. https://doi.org/10.1016/j.lithos.2012.01.010

Hilton, D.R., Halldórsson, S.A., Barry, P.H., Fischer, T.P., De Moor, J.M., Ramirez, C.J., Mangasini, F., Scarsi, P., 2011. Helium isotopes at Rungwe Volcanic Province, Tanzania, and the origin of East African Plateaux. Geophys. Res. Lett. 38. https://doi.org/10.1029/2011GL049589

Hirschmann, M.M., 2018. Comparative deep Earth volatile cycles: The case for C recycling from exosphere/mantle fractionation of major (H2O, C, N) volatiles and from H2O/Ce, CO2/Ba, and CO2/Nb exosphere ratios. Earth Planet. Sci. Lett. 502, 262–273. https://doi.org/10.1016/J.EPSL.2018.08.023

Hirschmann, M.M., Stolper, E.M., 1996. A possible role for garnet pyroxenite in the origin of the "'garnet signature'" in MORB, Contrib Mineral Petrol. Springer-Verlag.

Hole, M.J., 2021. Chapter 4.1b Antarctic Peninsula: petrology. Geol. Soc. London, Mem. 55, M55-2018–40. https://doi.org/10.1144/m55-2018-40

Horie, S., 1967. Limnological Studies of Lake Yogo-ko. Bull. Disas. Prey. Res. Inst. 17, 1–8.

Howarth, G.H., Barry, P.H., Pernet-Fisher, J.F., Baziotis, I.P., Pokhilenko, N.P., Pokhilenko, L.N., Bodnar, R.J., Taylor, L.A., Agashev, A.M., 2014. Superplume metasomatism: Evidence from Siberian mantle xenoliths. Lithos 184–187, 209–224. https://doi.org/10.1016/j.lithos.2013.09.006Page | xii

Hudgins, T.R., Mukasa, · S B, Simon, · A C, Moore, · G, Barifaijo, · E, 2015. Melt inclusion evidence for CO 2-rich melts beneath the western branch of the East African Rift: implications for long-term storage of volatiles in the deep lithospheric mantle. Contrib Miner. Pet. 169, 46. https://doi.org/10.1007/s00410-015-1140-9

Humphreys, E., Hessler, E., Dueker, K., Farmer, G.L., Erslev, E., Atwater, T., 2003. How laramide-age hydration of North American lithosphere by the farallon slab controlled subsequent activity in the Western United States. Int. Geol. Rev. 45, 575–595. https://doi.org/10.2747/0020-6814.45.7.575

Humphreys, E.D., 1995. Post-Laramide removal of the Farallon slab, western United States. Geology 23, 987–990. https://doi.org/https://doi.org/10.1130/0091-7613(1995)023<0987:PLROTF>2.3.CO;2

Hutchison, R., Dawson, J.B., 1970. Rb, Sr and 87Sr/86Sr in ultrabasic xenoliths and host-rocks, Lashaine volcano, Tanzania. Earth Planet. Sci. Lett. 9, 87–92. https://doi.org/10.1016/0012-821X(70)90030-0

Ionov, D., 2002. Mantle structure and rifting processes in the Baikal-Mongolia region: Geophysical data and evidence from xenoliths in volcanic rocks. Tectonophysics 351, 41–60. https://doi.org/10.1016/S0040-1951(02)00124-5

Ionov, D.A., 2007. Compositional variations and heterogeneity in fertile lithospheric mantle: peridotite xenoliths in basaltsfrom Tariat, Mongolia. Contrib Miner. Pet. 154, 455–477. https://doi.org/10.1007/s00410-007-0203-y

Ionov, D.A., Mukasa, S.B., Bodinier, J.L., 2002. Sr–Nd–Pb Isotopic Compositions of Peridotite Xenoliths from Spitsbergen: Numerical Modelling Indicates Sr–Nd Decoupling in the Mantle by Melt Percolation Metasomatism. J. Petrol. 43, 2261–2278. https://doi.org/10.1093/PETROLOGY/43.12.2261

Ionov, D.A., O'Reilly, S.Y., Griffin, W.L., 1998. A geotherm and lithospheric section for central Mongolia (Tariat region), in: Flower, M.F.J., Chung, S.-L., Lo, C.-H., Lee, T.-Y. (Eds.), Geodynamics Series. American Geophysical Union (AGU), pp. 127–153. https://doi.org/10.1029/gd027p0127

Ionov, D.A., O'Reilly, S.Y., Griffin, W.L., 2011. A geotherm and lithospheric section for central Mongolia (Tariat region). American Geophysical Union (AGU), pp. 127–153. https://doi.org/10.1029/gd027p0127

Irving, A.J., 1980. Petrology and Geochemitry of Composite Ultramafic Xenoliths in Alkalic Basalts and Implications for Magmatic Processes Within the Mantle. Aneruca Hiyrbak if Scuebce 280-A, 389–426.

Ito, E., White, W.M., Göpel, C., 1987. The O, Sr, Nd and Pb isotope geochemistry of MORB. Chem. Geol. 62, 157–176. https://doi.org/10.1016/0009-2541(87)90083-0

Ito, G., Rogers, A.D., Young, K.E., Bleacher, J.E., Edwards, C.S., Hinrichs, J., Honniball, C.I., Lucey, P.G., Piquero, D., Wolfe, B., Glotch, T.D., 2018. Incorporation of Portable Infrared Spectral Imaging Into Planetary Geological Field Work: Analog Studies at Kīlauea Volcano, Hawaii, and Potrillo Volcanic Field, New Mexico. Earth Sp. Sci. 5, 676–696. https://doi.org/10.1029/2018EA000375

Ivanov, A. V., Demonterova, E.I., 2009. Tectonics of the baikal rift deduced from volcanism and sedimentation: a review oriented to the Baikal and Hovsgol lake systems. Prog. Mol. Subcell. Biol. https://doi.org/10.1007/978-3-540-88552-8_2

Iwasaki, T., Levin, V., Nikulin, A., Iidaka, A., 2013. Constraints on the Moho in Japan and Kamchatka. Tectonophysics 609, 184-201. https://doi.org/10.1016/j.tecto.2012.11.023

Jackson, C, G., (2020). Nominally volatile-free mantle minerals: a reservoir for water and fluorine in the Kaapvaal Craton. PhD thesis – University of Cambridge.

Jackson, M.G., Carlson, R.W., Kurz, M.D., Kempton, P.D., Francis, D., Blusztajn, J., 2010. Evidence for the survival of the oldest terrestrial mantle reservoir. Nature 466, 853–856. https://doi.org/10.1038/nature09287

Jalowitzki, T., Sumino, H., Conceição, R. V., Orihashi, Y., Nagao, K., Bertotto, G.W., Balbinot, E., Schilling, M.E., Gervasoni, F., 2016. Noble gas composition of subcontinental lithospheric mantle: An extensively degassed reservoir beneath Southern Patagonia. Earth Planet. Sci. Lett. 450, 263–273. https://doi.org/10.1016/j.epsl.2016.06.034

Jaques, A.L., Green, D.H., 1980. Anhydrous melting of peridotite at 0–15 Kb pressure and the genesis of tholeiitic basalts. Contrib. to Mineral. Petrol. 1980 733 73, 287–310. https://doi.org/10.1007/BF00381447Page | xiii

Jicha, B.R., Rhodes, J.M., Singer, B.S., Garcia, M.O., 2012. 40Ar/39Ar geochronology of submarine Mauna Loa volcano, Hawaii. J. Geophys. Res. Solid Earth 117. https://doi.org/10.1029/2012JB009373

Julia, J., Ammon, C. J., Nyblade, A.A., 2005. Evidence for mafic lower crust in Tanzania, East Africa, from joint inversion of receiver functions and Rayleigh wave dispersion velocities. Geophys. J. Int. 162, 555-569. https://doi.org/10.1111/j.1365-246X.2005.02685.x

Kaliwoda, M., Ludwig, T., Altherr, R., 2008. A new SIMS study of Li, Be, B and δ7Li in mantle xenoliths from Harrat Uwayrid (Saudi Arabia). Lithos 106, 261–279. https://doi.org/10.1016/J.LITHOS.2008.07.009

Kang, J.T., Ionov, D.A., Liu, F., Zhang, C.L., Golovin, A. V., Qin, L.P., Zhang, Z.F., Huang, F., 2017. Calcium isotopic fractionation in mantle peridotites by melting and metasomatism and Ca isotope composition of the Bulk Silicate Earth. Earth Planet. Sci. Lett. 474, 128–137. https://doi.org/10.1016/j.epsl.2017.05.035

Karakuş, H., Aydin, H., n.d. HNC-Plot: an excel VBA for visualization of helium, nitrogen and CO 2 isotope data of crustal and mantle gases. https://doi.org/10.1007/s12145-016-0272-4

Karki, B.B., Ghosh, D.B., Banjara, D., 2020. Mixed incorporation of carbon and hydrogen in silicate melts under varying pressure and redox conditions. Earth Planet. Sci. Lett. 549, 116520. https://doi.org/10.1016/J.EPSL.2020.116520

Kay, S.M., Gorring, M.L., Ramos, V.A., 2004. Magmatic sources, setting and causes of Eocene to Recent Patagonian plateau magmatism (36°S to 52°S latitude). Rev. la Asoc. Geol. Argentina 59, 556–568.

Kelemen, P.B., Hart, S.R., Bernstein, S., 1998. Silica enrichment in the continental upper mantle via melt/rock reaction. Earth Planet. Sci. Lett. 164, 387–406. https://doi.org/10.1016/S0012-821X(98)00233-7

Kelemen, P.B., Manning, C.E., 2015. Reevaluating carbon fluxes in subduction zones, what goes down, mostly comes up. Proc. Natl. Acad. Sci. U. S. A. 112, E3997–E4006. https://doi.org/10.1073/PNAS.1507889112/-/DCSUPPLEMENTAL

Keller, G.R., Morgan, P., Seager, W.R., 1990. Crustal structure, gravity anomalies and heat flow in the southern Rio Grande rift and their relationship to extensional tectonics. Tectonophysics 174, 21–37. https://doi.org/10.1016/0040-1951(90)90382-I

Kempton, P.D., Harmon, R.S., Stosch, H.G., Hoefs, J., Hawkesworth, C.J., 1988. Open-system O-isotope behaviour and trace element enrichment in the sub-Eifel mantle. Earth Planet. Sci. Lett. 89, 273–287. https://doi.org/10.1016/0012-821X(88)90116-1

Kempton, P.D., Hawkesworth, C.J., Lopez-Escobar, L., Pearson, D.G., Ware, A.J., 1999. Spinel±garnet lherzolite xenoliths from Pali Aike: Part 2. Trace element and isotopic evidence bearing on the evolution of lithospheric mantle beneath southern Patagonia, in: Gurney, J.J., Gurney, J.L., Pascoe, M.D., Richardson, S.H. (Eds.), The J.B. Dawson Volume. Proceedings of the International Kimberlite Conference 7. pp. 415–428.

Kempton, P.D., Lopez-Escobar, L., Hawkesworth, C.J., Pearson, D. g., Ware, A.J., 1999. Spinel Garnet Lherzolite Xenoliths from Pali Aike, Part 1: Petrography, Mineral Chemistry and Geothermobarometry, in: Gurney, J.J., Gurney, L.J., Pascoe, M.D., Richardson, S.H. (Eds.), The J.B. Dawson Volume. Proceedings of the International Kimberlite Conference 7. pp. 403–414.

Kendrick, M.A., 2018. Halogens in Seawater, Marine Sediments and the Altered Oceanic Lithosphere 591–648. https://doi.org/10.1007/978-3-319-61667-4_9

Kendrick, M.A., Hémond, C., Kamenetsky, V.S., Danyushevsky, L., Devey, C.W., Rodemann, T., Jackson, M.G., Perfit, M.R., 2017. Seawater cycled throughout Earth's mantle in partially serpentinized lithosphere. Nat. Geosci. 2017 103 10, 222–228. https://doi.org/10.1038/ngeo2902

Kessel, R., Schmidt, M.W., Ulmer, P., Pettke, T., 2005. Trace-element signature of subduction-zone fluids, melts and supercritical liquids at 120-180 km depth. Nature 437, 724–727. https://doi.org/10.1038/nature03971

Kil, Y., Wendlandt, R.F., 2007. Depleted and enriched mantle processes under the Rio Grande rift: spinel peridotite xenoliths. Contrib Miner. Pet. 154, 135–151. https://doi.org/10.1007/s00410-007-0183-yPage | xiv

Kim, K.H., Nagao, K., Tanaka, T., Sumino, H., Nakamura, T., Okuno, M., Lock, J.B., Youn, J.S., Song, J., 2005. He-Ar and Nd-Sr isotopic compositions of ultramafic xenoliths and host alkali basalts from the Korean peninsula. Geochem. J. 39, 341–356. https://doi.org/10.2343/geochemj.39.341

Kinzler, R.J., 1997. Melting of mantle peridotite at pressures approaching the spinel to garnet transition: Application to midocean ridge basalt petrogenesis. J. Geophys. Res. Solid Earth 102, 853–874. https://doi.org/10.1029/96JB00988

Kinzler, R.J., Grove, T.L., 1992. Primary magmas of mid-ocean ridge basalts 1. Experiments and methods. J. Geophys. Res. Solid Earth 97, 6885–6906. https://doi.org/10.1029/91JB02840

Kitamura, S., 1990. Ages of Megata Maars in the Oga Peninsula, Japan. Ann. Tohoku Geogr. Asocciation 42, 161–167. https://doi.org/10.5190/tga1948.42.161

Klöcking, M., White, N.J., Maclennan, J., McKenzie, D., Fitton, J.G., 2018. Quantitative Relationships Between Basalt Geochemistry, Shear Wave Velocity, and Asthenospheric Temperature Beneath Western North America. Geochemistry, Geophys. Geosystems 19, 3376–3404. https://doi.org/10.1029/2018GC007559

Kobayashi, M., Sumino, H., Burgess, R., Nakai, S., Iizuka, T., Nagao, J., Kagi, H., Nakamura, M., Takahashi, E., Kogiso, T., Ballentine, C.J., 2019. Halogen Heterogeneity in the Lithosphere and Evolution of Mantle Halogen Abundances Inferred From Intraplate Mantle Xenoliths. Geochemistry, Geophys. Geosystems 20, 952–973. https://doi.org/10.1029/2018GC007903

Konrad, K., Graham, D.W., Thornber, C.R., Duncan, R.A., Kent, A.J.R., Al-Amri, A.M., 2016. Asthenosphere-lithosphere interactions in Western Saudi Arabia: Inferences from 3He/4He in xenoliths and lava flows from Harrat Hutaymah. Lithos 248–251, 339–352. https://doi.org/10.1016/j.lithos.2016.01.031

Korenaga, J., 2008. Urey ratio and the structure and evolution of Earth's mantle. Rev. Geophys., 46, p. RG2007. https://doi.org/10.1029/2007RG000241

Kourim, F., Wang, K.L., Beinlich, A., Chieh, C.J., Dygert, N., Lafay, R., Kovach, V., Michibayashi, K., Yarmolyuk, V., Iizuka, Y., 2021. Metasomatism of the off-cratonic lithospheric mantle beneath Hangay Dome, Mongolia: Constraints from trace-element modelling of lherzolite xenoliths. Lithos 400–401, 106407. https://doi.org/10.1016/J.LITHOS.2021.106407

Krmíček, L., Halavínová, M., Romer, R.L., Galiová, M.V., Vaculovič, T., 2014. Phlogopite/matrix, clinopyroxene/matrix and clinopyroxene/ /phlogopite trace-element partitioning in a calc-alkaline lamprophyre: new constrains from the Křižanovice minette dyke (Bohemian Massif). J. Geosci. 59, 87–96. https://doi.org/10.3190/jgeosci.160

Kumamoto, K.M., Warren, J.M., Hauri, E.H., 2017. New SIMS reference materials for measuring water in upper mantle minerals. Am. Mineral. 102, 537–547. https://doi.org/10.2138/AM-2017-5863CCBYNCND

Lambart, S., Laporte, D., Provost, A., Schiano, P., 2012. Fate of pyroxenite-derived melts in the peridotitic mantle: Thermodynamic and experimental constraints. J. Petrol. 53, 451–476. https://doi.org/10.1093/petrology/egr068

Laughlin, A.W., Aldrich, M.J., Shafiqullah, M., Husler, J., 1986. Tectonic implications of the age, composition, and orientation of lamprophyre dikes, Navajo volcanic field, Arizona. Earth Planet. Sci. Lett. 76, 361–374. https://doi.org/10.1016/0012-821X(86)90087-7

Le Bas, M.J., Streckeisen, A.L., 1991. The IUGS systematics of igneous rocks. J. Geol. Soc. London. 148, 825–833. https://doi.org/10.1144/gsjgs.148.5.0825

Le Voyer, M., Kelley, K.A., Cottrell, E., Hauri, E.H., 2017. Heterogeneity in mantle carbon content from CO2-undersaturated basalts. Nat. Commun. 2017 81 8, 1–8. https://doi.org/10.1038/ncomms14062

Leat, P.T., Riley, T.R., 2021. Chapter 3.1a Antarctic Peninsula and South Shetland Islands: volcanology. Geol. Soc. London, Mem. 55, M55-2018–52. https://doi.org/10.1144/m55-2018-52

Leat, P.T., Riley, T.R., 2021. Chapter 3.1b Antarctic Peninsula and South Shetland Islands: petrology. Geol. Soc. London, Mem. 55, M55-2018–68. https://doi.org/10.1144/m55-2018-68Page | xv

Lee, C.-T., Rudnick, R.L., McDonough, W.F., Horn, I., 2000. Petrologic and geochemical investigation of carbonates in peridotite xenoliths from northeastern Tanzania. Contrib. to Mineral. Petrol. 2000 1394 139, 470–484. https://doi.org/10.1007/S004100000144

Lee, C.T.A., 2005. Trace element evidence for hydrous metasomatism at the base of the North American lithosphere and possible association with laramide low-angle subduction. J. Geol. 113, 673–685. https://doi.org/10.1086/449327

Li, K., Li, L., Pearson, D.G., Stachel, T., 2019. Diamond isotope compositions indicate altered igneous oceanic crust dominates deep carbon recycling. Earth Planet. Sci. Lett. 516, 190–201. https://doi.org/10.1016/J.EPSL.2019.03.041

Li, Y., Li, J., Song, H., Guo, L., 2002. Helium isotope studies of the mantle xenoliths and megacrysts from the Cenozoic basalts in the Eastern China. Sci. China, Ser. D Earth Sci. 45, 174–183. https://doi.org/10.1007/BF02879794

Li, Z.X.A., Lee, C.T.A., Peslier, A.H., Lenardic, A., Mackwell, S.J., 2008. Water contents in mantle xenoliths from the Colorado Plateau and vicinity: Implications for the mantle rheology and hydration-induced thinning of continental lithosphere.

J. Geophys. Res. Solid Earth 113. https://doi.org/10.1029/2007JB005540Lloyd, F.E., Edgar, A.D., Forsyth, D.M., Barnett, R.L., 1991. The paragenesis of upper-mantle xenoliths from the Quaternary volcanics south-east of Gees, West Eifel, Germany. Mineral. Mag. 55, 95–112. https://doi.org/10.1180/minmag.1991.055.378.08

Lorenz, V., 1984. Explosive Volcanism of the West Eifel Volcanic Field/Germany, in: Developments in Petrology. Elsevier, pp. 299–307. https://doi.org/10.1016/B978-0-444-42273-6.50026-2

Malaspina, N., Poli, S., Fumagalli, P., 2009. The Oxidation State of Metasomatized Mantle Wedge: Insights from C–O–Hbearing Garnet Peridotite. J. Petrol. 50, 1533–1552. https://doi.org/10.1093/PETROLOGY/EGP040

Mallmann, G., O'Neill, H.S.C., 2009. The Crystal/Melt Partitioning of V during Mantle Melting as a Function of Oxygen Fugacity Compared with some other Elements (Al, P, Ca, Sc, Ti, Cr, Fe, Ga, Y, Zr and Nb). J. Petrol. 50, 1765–1794. https://doi.org/10.1093/PETROLOGY/EGP053

Mallmann, G., O'Neill, H.S.C., Klemme, S., 2009. Heterogeneous distribution of phosphorus in olivine from otherwise wellequilibrated spinel peridotite xenoliths and its implications for the mantle geochemistry of lithium. Contrib. to Mineral. Petrol. 158, 485–504. https://doi.org/10.1007/S00410-009-0393-6/FIGURES/9

Marshall, E.W., Barnes, J.D., Lassiter, J.C., 2017. The role of serpentinite-derived fluids in metasomatism of the Colorado Plateau (USA) lithospheric mantle. Geology 45, 1103–1106. https://doi.org/10.1130/G39444.1

Marshall, E.W., Lassiter, J.C., Barnes, J.D., 2018. On the (mis)behavior of water in the mantle: Controls on nominally anhydrous mineral water content in mantle peridotites. Earth Planet. Sci. Lett. 499, 219–229. https://doi.org/10.1016/J.EPSL.2018.07.033

Martelli, M., Bianchini, G, Beccaluva, L., Rizzo, A., 2011. Helium and argon isotopic constraints of mantle xenoliths from Tallante and Calatrava, Spain. Journal of Volcanology and Geothermal Research 200, 18-26. https://doi.org/10.1016/j.jvolgeores.2010.11.015

Marty, B., Tolstikhin, I, N., 1998. CO2 fluxes from mid-ocean ridges, arcs and plumes. Chem. Geol. 145, 233-248. https://doi.org/10.1016/S0009-2541(97)00145-9.

Marty, B., Tolstikhin, I., Kamensky, I.L., Nivin, V., Balaganskaya, E., Zimmermann, J.L., 1998. Plume-derived rare gases in 380 Ma carbonatites from the Kola region (Russia) and the argon isotopic composition in the deep mantle. Earth Planet. Sci. Lett. 164, 179–192. https://doi.org/10.1016/S0012-821X(98)00202-7

Marty, B., Tolstikhin, I.N., 1998. CO2 fluxes from mid-ocean ridges, arcs and plumes. Chem. Geol. 145, 233–248. https://doi.org/10.1016/S0009-2541(97)00145-9

Marty, B., Trull, T., Lussiez, P., Basile, I., Tanguy, J.C., 1994. He, Ar, O, Sr and Nd isotope constraints on the origin and evolution of Mount Etna magmatism. Earth Planet. Sci. Lett. 126, 23–39. https://doi.org/10.1016/0012-821X(94)90240-2

Marty, B., Upton, B. G. J., Ellam, R.M., 1998. Helium isotopes in early Tertiary basalts, northeast Greenland: Evidence for 58 Ma plume activity in the North Atlantic–Iceland volcanic province. Geology 26, 407–410. https://doi.org/ttps://doi.org/10.1130/0091-7613Page | xvi

Mather, K.A., Pearson, D.G., McKenzie, D., Kjarsgaard, B.A., Priestley, K., 2011. Constraints on the depth and thermal history of cratonic lithosphere from peridotite xenoliths, xenocrysts and seismology. Lithos 125, 729–742. https://doi.org/10.1016/J.LITHOS.2011.04.003

Mathez, E.A., 1987. Carbonaceous matter in mantle xenoliths: Composition and relevance to the isotopes. Geochim. Cosmochim. Acta 51, 2339–2347. https://doi.org/10.1016/0016-7037(87)90288-2

Mathez, E.A., Blacic, J.D., Beery, J., Maggiore, C., Hollander, M., 1984. Carbon abundances in mantle minerals determined by nuclear reaction analysis. Geophys. Res. Lett. 11, 947–950. https://doi.org/10.1029/GL011I010P00947

Matsuda, J., Matsumoto, T., Sumino, H., Nagao, K., Yamamoto, J., Miura, Y., Kaneoka, I., Takahata, N., Sano, Y., 2002. The 3He/4He ratio of the new internal He Standard of Japan (HESJ). Geochem. J. 36, 191–195. https://doi.org/10.2343/geochemj.36.191

Matthews, S., Shorttle, O., Maclennan, J., Rudge, J.F., 2021. The global melt inclusion C/Ba array: Mantle variability, melting process, or degassing? Geochim. Cosmochim. Acta 293, 525–543. https://doi.org/10.1016/J.GCA.2020.09.030

Mattsson, H.B., 2012. Rapid magma ascent and short eruption durations in the Lake Natron–Engaruka monogenetic volcanic field (Tanzania): A case study of the olivine melilititic Pello Hill scoria cone. J. Volcanol. Geotherm. Res. 247–248, 16–25. https://doi.org/10.1016/J.JVOLGEORES.2012.07.009

McDonough, W.F., 1990. Constraints on the composition of the continental lithospheric mantle. Earth Planet. Sci. Lett. 101, 1–18. https://doi.org/10.1016/0012-821X(90)90119-I

McDonough, W.F., Rudnick, R.L., 1998. Mineralogy and Composition of the Upper Mantle, in: Ultrahigh Pressure Mineralogy. De Gruyter, pp. 139–164. https://doi.org/10.1515/9781501509179-006

McDonough, W.F., Sun, S. s., 1995. The composition of the Earth. Chem. Geol. 120, 223–253. https://doi.org/10.1016/0009-2541(94)00140-4

McKenzie, D., Bickle, M.J., 1988. The volume and composition of melt generated by extension of the lithosphere. J. Petrol. 29, 625–679. https://doi.org/10.1093/petrology/29.3.625

McKenzie, D., Jackson, J., Priestley, K., 2005. Thermal structure of oceanic and continental lithosphere. Earth Planet. Sci. Lett. 233, 337–349. https://doi.org/10.1016/J.EPSL.2005.02.005

McLennan, S.M., 2018. Lanthanide Rare Earths 1–7. https://doi.org/10.1007/978-3-319-39193-9_96-1

Melchiorre, M., Faccini, B., Grégoire, M., Benoit, M., Casetta, F., Coltorti, M., 2020. Melting and metasomatism/refertilisation processes in the Patagonian sub-continental lithospheric mantle: A review. Lithos 354–355, 105324. https://doi.org/10.1016/j.lithos.2019.105324

Mercier, J.C.C., 1980. Single-pyroxene thermobarometry. Tectonophysics 70, 1–37. https://doi.org/10.1016/0040-1951(80)90019-0

Mercier, J.C.C., Nicolas, A., 1975. Textures and fabrics of upper-mantle peridotites as illustrated by xenoliths from basalts. J. Petrol. 16, 454–487. https://doi.org/10.1093/petrology/16.1.454

Mikhail, S., Crosby, J.C., Stuart, F.M., Dinicola, L., Abernethy, F.A.J., 2019. A secretive mechanical exchange between mantle and crustal volatiles revealed by helium isotopes in 13 C-depleted diamonds. Geochem. Persp. Let 11, 39–43. https://doi.org/10.7185/geochemlet.1923

Mikhail, S., Guillermier, C., Franchi, I.A., Beard, A.D., Crispin, K., Verchovsky, A.B., Jones, A.P., Milledge, H.J., 2014. Empirical evidence for the fractionation of carbon isotopes between diamond and iron carbide from the Earth's mantle. Geochemistry, Geophys. Geosystems 15, 855–866. https://doi.org/10.1002/2013GC005138

Mikhail, S., Verchovsky, A.B., Howell, D., Hutchison, M.T., Southworth, R., Thomson, A.R., Warburton, P., Jones, A.P.,

Milledge, H.J., 2014. Constraining the internal variability of the stable isotopes of carbon and nitrogen within mantle diamonds. Chem. Geol. 366, 14–23. https://doi.org/10.1016/J.CHEMGEO.2013.12.014Page | xvii

Miller, W.G.R., Maclennan, J., Shorttle, O., Gaetani, G.A., Le Roux, V., Klein, F., 2019. Estimating the carbon content of the deep mantle with Icelandic melt inclusions. Earth Planet. Sci. Lett. 523, 115699. https://doi.org/10.1016/J.EPSL.2019.07.002

Mishima, K., Sumino, H., Yamada, T., Ieki, S., Nagakura, N., Otono, H., Oide, H., 2018. Accurate Determination of the Absolute 3He/4He Ratio of a Synthesized Helium Standard Gas (Helium Standard of Japan, HESJ): Toward Revision of the Atmospheric 3He/4He Ratio. Geochemistry, Geophys. Geosystems 19, 3995–4005. https://doi.org/10.1029/2018GC007554

Mollex, G., Füri, E., Burnard, P., Zimmermann, L., Chazot, G., Kazimoto, E.O., Marty, B., France, L., 2018. Tracing helium isotope compositions from mantle source to fumaroles at Oldoinyo Lengai volcano, Tanzania. Chem. Geol. 480, 66–74. https://doi.org/10.1016/j.chemgeo.2017.08.015

Moore, K.R., Wood, B.J., 1998. The Transition from Carbonate to Silicate Melts in the CaO—MgO—SiO2—CO2 System. J. Petrol. 39, 1943–1951. https://doi.org/10.1093/PETROJ/39.11-12.1943

Moreira, M., Rouchon, V., Muller, E., Noirez, S., 2017. The xenon isotopic signature of the mantle beneath Massif Central 6, 28–32. https://doi.org/10.7185/geochemlet.1805

Moucha, R., Forte, A.M., Rowley, D.B., Mitrovica, J.X., Simmons, N.A., Grand, S.P., 2009. Deep mantle forces and the uplift of the Colorado Plateau. Geophys. Res. Lett. 36. https://doi.org/10.1029/2009GL039778

Mundl, A., Ntaflos, T., Ackerman, L., Bizimis, M., Bjerg, E.A., Hauzenberger, C.A., 2015. Mesoproterozoic and Paleoproterozoic subcontinental lithospheric mantle domains beneath southern Patagonia: Isotopic evidence for itsconnection to Africa and Antarctica. Geology 43, 39–42. https://doi.org/10.1130/G36344.1

Muñoz, J., Troncoso, R., Duhart, P., Crignola, P., Farmer, L., Stern, C.R., 2000. La relación de Cinturón Magmático del Terciario-medio del centro-sur de Chile con el incremento de la razón de convergencia de placas en el Oligoceno superior. Rev. Geol. Chile 27, 177–203. https://doi.org/10.4067/S0716-02082000000200003

Naeser, C.W., 1971. Geochronology of the Navajo-Hopi Diatremes, Four Corners Area. J. Geophys. Res. 76, 4978–4985. https://doi.org/10.1029/JB076I020P04978

Nardini, I., Armienti, P., Rocchi, S., Dallai, L., Harrison, D., 2009. Sr-Nd-Pb-He-O isotope and geochemical constraints on the genesis of cenozoic magmas from the West Antarctic Rift. J. Petrol. 50, 1359–1375. https://doi.org/10.1093/petrology/egn082

Newcombe, M.E., Plank, T., Barth, A., Asimow, P.D., Hauri, E., 2020. Water-in-olivine magma ascent chronometry: Every crystal is a clock. J. Volcanol. Geotherm. Res. 398, 106872. https://doi.org/10.1016/J.JVOLGEORES.2020.106872

Nickel, K.G., Green, D.H., 1985. Empirical geothermobarometry for garnet peridotites and implications for the nature of the lithosphere, kimberlites and diamonds. Earth Planet. Sci. Lett. 73, 158–170. https://doi.org/10.1016/0012-821X(85)90043-3

Nimis, P., Grütter, H., n.d. Internally consistent geothermometers for garnet peridotites and pyroxenites. https://doi.org/10.1007/s00410-009-0455-9

Niu, Y., 1997. Mantle Melting and Melt Extraction Processes beneath Ocean Ridges: Evidence from Abyssal Peridotites. J. Petrol. 38, 1047–1074. https://doi.org/10.1093/PETROJ/38.8.1047

Nuccio, P.M., Paonita, A., Rizzo, A., Rosciglione, A., 2008. Elemental and isotope covariation of noble gases in mineral phases from Etnean volcanics erupted during 2001-2005, and genetic relation with peripheral gas discharges. Earth Planet. Sci. Lett. 272, 683–690. https://doi.org/10.1016/j.epsl.2008.06.007

Nybo, J.P., McIntosh, W.C., Semken, S, C., Ar-Ar phlogopite geochronology of the Navajo Volcanic Field and the Ship Rock diatreme of Northwest New Mexico define a 1.4 ma pulse of poteassic magmatism. AGU, Fal Meeting 2011.

O'Connor, T.K., Edgar, A.D., Lloyd, F.E., 1996. origin of glass in ouaternary mantle xenoliths from Meerfeldermaar, West Eifel Germany: implications for enrichment in the lithospheric mantle. Can. Min. 34, 187–200.Page | xviii

O'Leary, J.A., Gaetani, G.A., Hauri, E.H., 2010. The effect of tetrahedral Al3+ on the partitioning of water between clinopyroxene and silicate melt. Earth Planet. Sci. Lett. 297, 111–120. https://doi.org/10.1016/J.EPSL.2010.06.011

O'Nions, R.K., Oxburgh, E.R., 1983. Heat and helium in the earth. Nature 306, 429–431. https://doi.org/10.1038/306429a0

O'Reilly, S.Y., Griffin, W.L., 2013. Mantle metasomatism, in: Lecture Notes in Earth System Sciences. Springer International Publishing, pp. 471–533. https://doi.org/10.1007/978-3-642-28394-9_12

Padovani, E.R., Reid. M.R., 1989. Field guide to Kilbourne Hole maar, Dona Ana County, New Mexico, in: Chapin, C.., Zicek, J.(Eds.), Field Excursions to Volcanic Terranes in the Western United States, Vol. I: Southern Rocky Mountain Region. New Mex. Bur. Mines Min. Res., pp. 174–179.

Pankhurst, R.J., Rapela, C.W., Fanning, C.M., Márquez, M., 2006. Gondwanide continental collision and the origin ofPatagonia. Earth-Science Rev. 76, 235–257. https://doi.org/10.1016/j.earscirev.2006.02.001

Pasyanos, M.E., Masters, T.G., Laske, G., Ma, Z., 2014. LITHO1.0: An updated crust and lithospheric model of the Earth. J. Geophys. Res. Solid Earth 119, 2153–2173. https://doi.org/10.1002/2013JB010626

Pearson, D.G., Carlson, R.W., Shirey, S.B., Boyd, F.R., Nixon, P.H., 1995. Stabilisation of Archaean lithospheric mantle: A ReOs isotope study of peridotite xenoliths from the Kaapvaal craton. Earth Planet. Sci. Lett. 134, 341–357. https://doi.org/10.1016/0012-821X(95)00125-V

Pearson, D.G., Scott, J.M., Liu, J., Schaeffer, A., Wang, L.H., van Hunen, J., Szilas, K., Chacko, T., Kelemen, P.B., 2021. Deep continental roots and cratons. Nat. 2021 5967871 596, 199–210. https://doi.org/10.1038/s41586-021-03600-5

Pearson, D.G., Wittig, N., 2014. The Formation and Evolution of Cratonic Mantle Lithosphere – Evidence from Mantle Xenoliths. Treatise Geochemistry Second Ed. 3, 255–292. https://doi.org/10.1016/B978-0-08-095975-7.00205-9

Pepin, R.O., Porcelli, D., 2002. Origin of Noble Gases in the Terrestrial Planets. Rev. Mineral. Geochemistry 47, 191–246. https://doi.org/10.2138/RMG.2002.47.7

Perkins, D., Anthony, E.Y., 2011. The evolution of spinel lherzolite xenoliths and the nature of the mantle at Kilbourne Hole, New Mexico. Contrib. to Mineral. Petrol. 162, 1139–1157. https://doi.org/10.1007/s00410-011-0644-1

Perkins, G.B., Sharp, Z.D., Selverstone, J., 2006. Oxygen isotope evidence for subduction and rift-related mantle metasomatism beneath the Colorado Plateau-Rio Grande rift transition. Contrib. to Mineral. Petrol. 151, 633–650. https://doi.org/10.1007/s00410-006-0075-6

Pik, R., Marty, B., Hilton, D.R., 2006. How many mantle plumes in Africa? The geochemical point of view. Chem. Geol. 226, 100–114. https://doi.org/10.1016/j.chemgeo.2005.09.016

Pike, J.E.N., Meyer, C.E., Wilshire, H.G., 1980. Petrography and Chemical Composition of a Suite of Ultramafic Xenoliths from Lashaine, Tanzania. J. Geol. 88, 343–352. https://doi.org/10.1086/628512

Planavsky, N., Partin, C., Bekker, A., 2015. Carbon Isotopes as a Geochemical Tracer. Encycl. Astrobiol. 366–371. https://doi.org/10.1007/978-3-662-44185-5_228

Plank, T., Langmuir, C.H., 1998. The chemical composition of subducting sediment and its consequences for the crust and mantle. Chem. Geol. 145, 325–394. https://doi.org/10.1016/S0009-2541(97)00150-2

Porcelli, D., Elliott, T., 2008. The evolution of He Isotopes in the convecting mantle and the preservation of high 3He/4He ratios. Earth Planet. Sci. Lett. 269, 175–185. https://doi.org/10.1016/j.epsl.2008.02.002

Porcelli, D.R., O'nions, R.K., Galer, S.J.G., Cohen, A.S., Mattey, D.P., 1992. Contributions to Mineralogy and Petrology Isotopic relationships of volatile and lithophile trace elements in continental ultramafic xenoliths. Contrib Miner. Pet. 110, 528–538.

Presnall, D.C., 1976. Alumina content of enstatite as a geobarometer for plagioclase and spinel lherzolites | American Mineralogist | GeoScienceWorld. Am. Mineral. 61, 582–588.Page | xix

Preß, S., Wirr, G., Seck, H.A., Eonov, D., Kovalenko, V.I., 1986. Spinel peridotite xenoliths from the Tariat Depression, Mongolia. I: Major element chemistry and mineralogy of a primitive mantle xenolith suite. Geochim. Cosmochim. Acta 50, 2587–2599. https://doi.org/10.1016/0016-7037(86)90212-7

Priestley, K., McKenzie, D., 2013. The relationship between shear wave velocity, temperature, attenuation and viscosity in the shallow part of the mantle. Earth Planet. Sci. Lett. 381, 78–91. https://doi.org/10.1016/j.epsl.2013.08.022

Qi, Y.H., Wu, F., Ionov, D.A., Puchtel, I.S., Carlson, R.W., Nicklas, R.W., Yu, H.M., Kang, J.T., Li, C.H., Huang, F., 2019. Vanadium isotope composition of the Bulk Silicate Earth: Constraints from peridotites and komatiites. Geochim. Cosmochim. Acta 259, 288–301. https://doi.org/10.1016/j.gca.2019.06.008

Ramos, V.A., Kay, S.M., 1992. Southern Patagonian plateau basalts and deformation: Backarc testimony of ridge collisions. Tectonophysics 205, 261–282. https://doi.org/10.1016/0040-1951(92)90430-E

Reid, A.M., Dawson, J.B., 1972. Olivine-garnet reaction in peridotites from Tanzania. LITHOS 5, 115–124. https://doi.org/10.1016/0024-4937(72)90063-1

Reid, A.M., Donaldson, C.H., Brown, R.W., Ridley, W.I., Dawson, J.B., 1975. Mineral Chemistry of Peridotite Xenoliths From the Lashaine Volcano, Tanzania, in: Physics and Chemistry of the Earth. Elsevier, pp. 525–543. https://doi.org/10.1016/b978-0-08-018017-5.50040-7

Reid, M.R., Graham, D.W., 1996. Resolving lithospheric and sub-lithospheric contributions to helium isotope variations in basalts from the southwestern US. Earth Planet. Sci. Lett. 144, 213–222. https://doi.org/10.1016/0012-821x(96)00166-5

Rhodes, J.M., Dawson, J.B., 1975. major and trace element chemistry of peridotite inclusions from the Lashaine volcano, Tanzania, in: Physics and Chemistry of the Earth. Elsevier, pp. 545–557. https://doi.org/10.1016/b978-0-08-018017-5.50041-9

Richter, F.M., 1988. A major change in the thermal state of the Earth at the Archean-Proterozoic Boundary: Consequences for the nature and preservation of continental lithosphere. J. Petrol. Special_Volume, 39–52. https://doi.org/10.1093/petrology/Special_Volume.1.39

Ricketts, J.W., Kelley, S.A., Karlstrom, K.E., Schmandt, B., Donahue, M.S., van Wijk, J., 2016. Synchronous opening of the Rio Grande rift along its entire length at 25-10 Ma supported by apatite (U-Th)/He and fission-track thermochronology, and evaluation of possible driving mechanisms. Bull. Geol. Soc. Am. 128, 397–424. https://doi.org/10.1130/B31223.1

Ridley, W.I., Dawson, J.B., 1975. Lithophile Trace Element Data Bearing on the Origin of Peridotite Xenoliths, Ankaramite and Carbonatite From Lashaine Volcano, N. Tanzania. Phys. Chem. Earth 559–569. https://doi.org/https://doi.org/10.1016/B978-0-08-018017-5.50042-0

Riley, T.R., Leat, P.T., 2021. Chapter 2.2a Palmer Land and Graham Land volcanic groups (Antarctic Peninsula): volcanology. Geol. Soc. London, Mem. 55, M55-2018–36. https://doi.org/10.1144/m55-2018-36

Riley, T.R., Leat, P.T., 2021. Chapter 2.2a Palmer Land and Graham Land volcanic groups (Antarctic Peninsula): volcanology. Geol. Soc. London, Mem. 55, M55-2018–36. https://doi.org/10.1144/m55-2018-36

Riley, T.R., Leat, P.T., 2021. Chapter 2.2b Palmer Land and Graham Land volcanic groups (Antarctic Peninsula): petrology. Geol. Soc. London, Mem. 55, M55-2018–51. https://doi.org/10.1144/m55-2018-51

Riter, J.C., Smith, D., 1996. Xenolith constraints on the thermal history of the mantle below the Colorado Plateau | Geology | GeoScienceWorld. Geology 24, 267–270.

Rizzo, A.L., Faccini, B., Casetta, F., Faccincani, L., Ntaflos, T., Italiano, F., Coltorti, M., 2021. Melting and metasomatism in West Eifel and Siebengebirge Sub-Continental Lithospheric Mantle: Evidence from concentrations of volatiles in fluid inclusions and petrology of ultramafic xenoliths. Chem. Geol. 581, 120400. https://doi.org/10.1016/J.CHEMGEO.2021.120400

Rizzo, A.L., Pelorosso, B., Coltorti, M., Ntaflos, T., Bonadiman, C., Matusiak-Małek, M., Italiano, F., Bergonzoni, G., 2018. Geochemistry of noble gases and co2 in fluid inclusions from lithospheric mantle beneath wilcza góra (Lower silesia, southwest Poland). Front. Earth Sci. 6, 215. https://doi.org/10.3389/FEART.2018.00215/BIBTEXPage | xx

Roden, M.F., Irving, A.J., Murthy, V.R., 1988. Isotopic and trace element composition of the upper mantle beneath a young continental rift: Results from Kilbourne Hole, New Mexico. Geochim. Cosmochim. Acta 52, 461–473. https://doi.org/10.1016/0016-7037(88)90101-9

Roden, M.F., Shimizu, N., 1993. Ion microprobe analyses bearing on the composition of the upper mantle beneath the Basin and Range and Colorado Plateau Provinces. J. Geophys. Res. 98, 91–105. https://doi.org/10.1029/93jb00124

Roden, M.F., Smith, D., McDowell, F.W., 1979. Age and extent of potassic volcanism on the Colorado Plateau. Earth Planet. Sci. Lett. 43, 279–284. https://doi.org/10.1016/0012-821X(79)90212-7

Roden, M.F., Smith, D., Murthy, V.R., 1990. Chemical constraints on lithosphere composition and evolution beneath the Colorado Plateau. J. Geophys. Res. 95, 2811–2831. https://doi.org/10.1029/JB095iB03p02811

Roedder, E., 1984. Volume 12: Fluid inclusions. Rev. Mineral. 12, 1–646.

Rooks, E., 2016. The subcontinental lithospheric mantle evolution of the southern Gondwana margin. University of Cambridge.

Rooney, T.O., Hanan, B.B., Graham, D.W., Furman, T., Blichert-toft, J., Schilling, J.G., 2012. Upper mantle pollution during Afar plume-continental rift interaction. J. Petrol. 53, 365–389. https://doi.org/10.1093/petrology/egr065

Rosenthal, A., Hauri, E.H., Hirschmann, M.M., 2015. Experimental determination of C, F, and H partitioning between mantle minerals and carbonated basalt, CO2/Ba and CO2/Nb systematics of partial melting, and the CO2 contents of basaltic source regions. Earth Planet. Sci. Lett. 412, 77–87. https://doi.org/10.1016/J.EPSL.2014.11.044

Ross, A.J., 2008. . Compositional variability of the mantle beneath West Antarctica and its relationship to terrane tectonics: evidence from mantle xenoliths. University of Cambridge.

Rowe, M.C., Graham, D.W., Smid, E., McGee, L., 2020. Unusually homogeneous helium isotope composition of the Auckland Volcanic Field and its implications for the underlying mantle. Chem. Geol. 545, 119639. https://doi.org/10.1016/j.chemgeo.2020.119639

Ruudnick, R, L., McDonough, W. F., O'Connell, R, J, 1998. Thermal structure, thickness and composition of continental lithosphere. Chem. Geol. 145, 395-411. https://doi.org/10.1016/S0009-2541(97)00151-4

Rudnick, R.L., McDonough, W.F., Chappell, B.W., 1993. Carbonatite metasomatism in the northern Tanzanian mantle: petrographic and geochemical characteristics. Earth Planet. Sci. Lett. 114, 463–475. https://doi.org/10.1016/0012-821X(93)90076-L

Russell, J.K., Porritt, L.A., Lavallé, Y., Dingwell, D.B., 2012. Kimberlite ascent by assimilation-fuelled buoyancy. Nature 481, 352–356. https://doi.org/10.1038/nature10740

Saal, A.E., Hauri, E.H., Langmuir, C.H., Perfit, M.R., 2002. Vapour undersaturation in primitive mid-ocean-ridge basalt and the volatile content of Earth's upper mantle. Nat. 2002 4196906 419, 451–455. https://doi.org/10.1038/nature01073

Saladino, R., Barontini, M., Cossetti, C., Di Mauro, E., Crestini, C., 2011. The Effects of Borate Minerals on the Synthesis of Nucleic Acid Bases, Amino Acids and Biogenic Carboxylic Acids from Formamide. Orig. Life Evol. Biosph. 41, 317–330. https://doi.org/10.1007/S11084-011-9236-3/TABLES/4

Salters, V.J.M., Stracke, A., 2004. Composition of the depleted mantle. Geochemistry, Geophys. Geosystems 5, 5–07. https://doi.org/10.1029/2003GC000597

Saltzman, M.R., Thomas, E., 2012. Carbon Isotope Stratigraphy 11.1. Principles of Carbon Isotope Stratigraphy. https://doi.org/10.1016/B978-0-444-59425-9.00011-1

Sandoval-Velasquez, A., Rizzo, A, L., Frezzotti, M, L., Saucedo, R., Aiuppa, A., 2021. The composition of fluids stored in the central Mexican lithospheric mantle: Inferences from noble gases and CO2 in mantle xenoliths. Chem. Geol. 576, 120270. https://doi.org/10.1016/j.chemgeo.2021.120270.

Sato, Y., Ozawa, K., 2019. Reconstruction of the lithosphere-asthenosphere boundary zone beneath Ichinomegata maar, Northeast Japan, by geobarometry of spinel peridotite xenoliths. Am. Mineral. 104, 1285–1306. https://doi.org/10.2138/am-2019-6858Page | xxi

Satsukawa, T., Godard, M., Demouchy, S., Michibayashi, K., Ildefonse, B., 2017. Chemical interactions in the subduction factory: New insights from an in situ trace element and hydrogen study of the Ichinomegata and Oki-Dogo mantle xenoliths (Japan). Geochim. Cosmochim. Acta 208, 234–267. https://doi.org/10.1016/j.gca.2017.03.042

Saunders, N.J., Barling, J., Harvey, J., Halliday, A.N., 2020. Heterogeneous nickel isotopic compositions in the terrestrial mantle – Part 1: Ultramafic lithologies. Geochim. Cosmochim. Acta 285, 129–149. https://doi.org/10.1016/j.gca.2020.06.029

Savage, P.S., Georg, R.B., Armytage, R.M.G., Williams, H.M., Halliday, A.N., 2010. Silicon isotope homogeneity in the mantle.Earth Planet. Sci. Lett. 295, 139–146. https://doi.org/10.1016/j.epsl.2010.03.035

Scarsi, P., Craig, H., 1996. Helium isotope ratios in Ethiopian Rift basalts. Earth Planet. Sci. Lett. 144, 505–516. https://doi.org/10.1016/s0012-821x(96)00185-9

Schilling, M.E., Carlson, R.W., Tassara, A., Conceição, R.V., Bertotto, G.W., Vásquez, M., Muñoz, D., Jalowitzki, T., Gervasoni, F., Morata, D., 2017. The origin of Patagonia revealed by Re-Os systematics of mantle xenoliths. Precambrian Res. 294, 15–32. https://doi.org/10.1016/j.precamres.2017.03.008

Schmidt, G., Snow, J., 2002. Os isotopes in mantle xenoliths from the Eifel volcanic field and the Vogelsberg (Germany): age constraints on the lithospheric mantle. Contirb Miner. Pet. 143, 694–705. https://doi.org/10.1007/s00410-002-0372-7

Schmidt, G., Witt-Eickschen, G., Palme, H., Seck, H., Spettel, B., Kratz, K.L., 2003. Highly siderophile elements (PGE, Re and Au) in mantle xenoliths from the West Eifel volcanic field (Germany). Chem. Geol. 196, 77–105. https://doi.org/10.1016/S0009-2541(02)00408-4

Schmincke, H.U., 2007. The Quaternary volcanic fields of the East and West Eifel (Germany), in: Mantle Plumes: A Multidisciplinary Approach. Springer Berlin Heidelberg, pp. 241–322. https://doi.org/10.1007/978-3-540-68046-8_8

Schmitt, A.K., Stockli, D.F., Niedermann, S., Lovera, O.M., Hausback, B.P., 2010. Eruption ages of Las Tres Vírgenes volcano (Baja California): A tale of two helium isotopes. Quat. Geochronol. 5, 503–511. https://doi.org/10.1016/j.quageo.2010.02.004

Scorei, R., 2012. Is Boron a Prebiotic Element? A Mini-review of the Essentiality of Boron for the Appearance of Life on Earth. Orig. Life Evol. Biosph. 42, 3–17. https://doi.org/10.1007/S11084-012-9269-2/TABLES/2

Scorei, R., Cimpoiaşu, V.M., 2006. Boron Enhances the Thermostability of Carbohydrates. Orig. Life Evol. Biosph. 2006 361 36, 1–11. https://doi.org/10.1007/S11084-005-0562-1

Seager, W.R., Shafiqullah, M., Hawley, J.W., Marvin, R.F., 1984. New K-Ar dates from basalts and the evolution of the southern Rio Grande rift | GSA Bulletin | GeoScienceWorld [WWW Document]. Geol. Soc. Am. Bull.

Seitz, H.M., Woodland, A.B., 2000. The distribution of lithium in peridotitic and pyroxenitic mantle lithologies — an indicator of magmatic and metasomatic processes. Chem. Geol. 166, 47–64. https://doi.org/10.1016/S0009-2541(99)00184-9

Servali, A., Korenaga, J., 2018. Oceanic origin of continental mantle lithosphere. Geology 46, 1047–1050. https://doi.org/10.1130/G45180.1

Sgualdo, P., Aviado, K., Beccaluva, L., Bianchini, G., Blichert-Toft, J., Bryce, J.G., Graham, D.W., Natali, C., Siena, F., 2015. Lithospheric mantle evolution in the Afro-Arabian domain: Insights from Bir Ali mantle xenoliths (Yemen). Tectonophysics 650, 3–17. https://doi.org/10.1016/j.tecto.2014.11.025

Shannon, R.D., IUCr, 1976. Revised effective ionic radii and systematic studies of interatomic distances in halides and chalcogenides. Acta Crystallogr. 32, 751–767. https://doi.org/10.1107/S0567739476001551

Shaw, A.M., Hilton, D.R., Fischer, T.P., Walker, J.A., de Leeuw, G.A.M., 2006. Helium isotope variations in mineral separates from Costa Rica and Nicaragua: Assessing crustal contributions, timescale variations and diffusion-related mechanisms. Chem. Geol. 230, 124–139. https://doi.org/10.1016/j.chemgeo.2005.12.003Page | xxii

Shaw, C. S. J., Lebert, B, S., Woodland, A. L. 2018. Thermodynamic Modelling of Mantle–Melt Interaction Evidenced by Veined Wehrlite Xenoliths from the Rockeskyllerkopf Volcanic Complex, West Eifel Volcanic Field, Germany. Journal of Petrology 59, 59-86. https://doi.org/10.1093/petrology/egy018

Shaw, C.S.J., 2004. The temporal evolution of three magmatic systems in the West Eifel volcanic field, Germany. J. Volcanol. Geotherm. Res. 131, 213–240. https://doi.org/10.1016/S0377-0273(03)00363-9

Shimizu, K., Ito, M., Chang, Q., Miyazaki, T., Ueki, K., Toyama, C., Senda, R., Vaglarov, B.S., Ishikawa, T., Kimura, J.I., 2019. Identifying volatile mantle trend with the water–fluorine–cerium systematics of basaltic glass. Chem. Geol. 522, 283–294. https://doi.org/10.1016/J.CHEMGEO.2019.06.014

Skewes, M.A. and Stern, C.R., 1979. Petrology and geochemical of alkali basalts and ultramafic inclusions from the Palei-Aike volcanic field in southern Chile and the origin of Patagonia plateau lavas. Journal of Volcanology and Geothermal Research 6(1-2), 3-25. https://doi.org/10.1016/0377-0273(79)90044-1

Smellie, J.L., Hole, M.J., 2021. Chapter 4.1a Antarctic Peninsula: volcanology. Geol. Soc. London, Mem. 55, M55-2018–59. https://doi.org/10.1144/m55-2018-59

Smith, D., 2020. Trace elements in Cr-pyrope from the Navajo volcanic field of the Colorado Plateau, SW USA, and implications for the mantle wedge during low-angle subduction. Lithos 362–363, 105460. https://doi.org/10.1016/j.lithos.2020.105460

Smith, D., Alexis Riter, J.C., Mertzman, S.A., 1999. Water-rock interactions, orthopyroxene growth, and Si-enrichment in the mantle: Evidence in xenoliths from the Colorado Plateau, southwestern United States. Earth Planet. Sci. Lett. 165, 45–54. https://doi.org/10.1016/S0012-821X(98)00251-9

Smith, D., Connelly, J.N., Manser, K., Moser, D.E., Housh, T.B., McDowell, F.W., MacK, L.E., 2004. Evolution of Navajo eclogites and hydration of the mantle wedge below the Colorado Plateau, southwestern United States. Geochemistry, Geophys. Geosystems 5. https://doi.org/10.1029/2003GC000675

Smith, D., Griffin, W.L., 2005. Garnetite xenoliths and mantle - Water interactions below the Colorado Plateau, Southwestern United States. J. Petrol. 46, 1901–1924. https://doi.org/10.1093/petrology/egi042

Smith, D., Levy, S., 1976. Petrology of the Green Knobs diatreme and implications for the upper mantle below the Colorado Plateau. Earth Planet. Sci. Lett. 29, 107–125. https://doi.org/10.1016/0012-821X(76)90031-5

Stachel, T., Aulbach, S., Brey, G.P., Harris, J.W., Leost, I., Tappert, R., Viljoen, K.S., 2004. The trace element composition of silicate inclusions in diamonds: a review. Lithos 77, 1–19. https://doi.org/10.1016/J.LITHOS.2004.03.027

Stalder, R., Skogby, H., 2002. Hydrogen incorporation in enstatite. Eur. J. Mineral. 14, 1139–1144. https://doi.org/10.1127/0935-1221/2002/0014-1139

Starkey, N.A., Stuart, F.M., Ellam, R.M., Fitton, J.G., Basu, S., Larsen, L.M., 2009. Helium isotopes in early Iceland plume picrites: Constraints on the composition of high 3He/4He mantle. Earth Planet. Sci. Lett. 277, 91–100. https://doi.org/10.1016/j.epsl.2008.10.007

Steinberger, B., Becker, T.W., 2018. A comparison of lithospheric thickness models. Tectonophysics 746, 325–338. https://doi.org/10.1016/j.tecto.2016.08.001

Stern, C.R., Kilian, R., Olker, B., Hauri, E.H., Kurtis Kyser, T., 1999. Evidence from mantle xenoliths for relatively thin (< 100 km) continental lithosphere below the Phanerozoic crust of southernmost South America, in: Developments in Geotectonics. Elsevier B.V., pp. 217–235. https://doi.org/10.1016/S0419-0254(99)80013-5

Stosch, H.G., Ionov, D.A., Puchtel, I.S., Galer, S.J.G., Sharpouri, A., 1995. Lower crustal xenoliths from Mongolia and their bearing on the nature of the deep crust beneath central Asia. LITHOS 36, 227–242. https://doi.org/10.1016/0024-4937(95)00019-4

Stosch, H.G., Lugmair, G.W., 1986. Trace element and Sr and Nd isotope geochemistry of peridotite xenoliths from the Eifel (West Germany) and their bearing on the evolution of the subcontinental lithosphere. Earth Planet. Sci. Lett. 80, 281–298. https://doi.org/10.1016/0012-821X(86)90111-1

Stosch, H.G., Lugmair, G.W., Kovalenko, V.I., 1986. Spinel peridotite xenoliths from the Tariat Depression, Mongolia. II: Geochemistry and Nd and Sr isotopic composition and their implications for the evolution of the subcontinental lithosphere. Geochim. Cosmochim. Acta 50, 2601–2614. https://doi.org/10.1016/0016-7037(86)90213-9Page | xxiii

Stosch, H.G., Seck, H.A., 1980. Geochemistry and mineralogy of two spinel peridotite suites from Dreiser Weiher, West Germany. Geochim. Cosmochim. Acta 44, 457–470. https://doi.org/10.1016/0016-7037(80)90044-7

Stroncik, N.A., Trumbull, R.B., Krienitz, M.S., Niedermann, S., Romer, R.L., Harris, C., Day, J.M.D., 2017. Helium isotope evidence for a deep-seated mantle plume involved in South Atlantic breakup. Geology 45, 827–830. https://doi.org/10.1130/G39151.1

Stuart, F.M., Lass-Evans, S., Fitton, J.G., Ellam, R.M., 2003. High 3He/4He ratios in picritic basalts from Baffin Island and the role of a mixed reservoir in mantle plumes. Nature 424, 57–59. https://doi.org/10.1038/nature01711

Su, F., Xiao, Y., He, H., Su, B., Wang, Y., Zhu, R., 2014. He and Ar isotope geochemistry of pyroxene megacrysts and mantle xenoliths in Cenozoic basalt from the Changle-Linqu area in western Shandong. Chinese Sci. Bull. 59, 396–411. https://doi.org/10.1007/s11434-013-0027-2

Sumino, H., Kaneoka, I., Matsufuji, K., Sobolev, A. V., 2006. Deep mantle origin of kimberlite magmas revealed by neon isotopes. Geophys. Res. Lett. 33, 16318. https://doi.org/10.1029/2006GL027144

Sun, C., n.d. Partitioning and Partition Coefficients. https://doi.org/10.1007/978-3-319-39193-9_347-1

Tachibana, Y., Kaneoka, I., Gaffney, A., Upton, B., 2006. Ocean-island basalt-like source of kimberlite magmas from West Greenland revealed by high 3He/4He ratios. Geology 34, 273–276. https://doi.org/10.1130/G22201.1

Takahashi, E., 1980. Thermal history of iherzolite xenoliths—I. Petrology of iherzolite xenoliths from the ichinomegata crater, oga peninsula, northeast Japan. Geochim. Cosmochim. Acta 44, 1643–1658. https://doi.org/10.1016/0016-7037(80)90217-3

Takahashi, E., 1986. Genesis of calc-alkali andesite magma in a hydrous mantle-crust boundary: Petrology of lherzolite xenoliths from the Ichinomegata crater, Oga peninsula, northeast Japan, part II. J. Volcanol. Geotherm. Res. 29, 355–395. https://doi.org/10.1016/0377-0273(86)90051-X

Takeuchi, M., Arai, S., 2015. Upper mantle can in-situ fracture: an implication from a cataclastic peridotite xenolith from Megata, Northeast Japan arc. Mineral. Petrol. 109, 283–294. https://doi.org/10.1007/s00710-015-0365-7

Tamaki, K., 1995. Opening Tectonics of the Japan Sea, in: Backarc Basins. Springer US, pp. 407–420. https://doi.org/10.1007/978-1-4615-1843-3_11

Tanaka, T., Aoki, K., 1981. Petrogenetic implications of REE and Ba data on mafic and ultramafic inclusions from Itinomegata, Japan. J. Geol. 89, 369–390. https://doi.org/10.1086/628597

Taylor, R., W., 1998. An experimental test of some geothermometer and geobaro-meter formulations for upper mantle peridotites with application to the ther-mobarometry of fertile lherzolite and garnet websterite. Neues Jahrb. für Mineral. - Abhandlungen 172, 381–408. https://doi.org/10.1127/NJMA/172/1998/381

Thompson, R.N., Ottley, C.J., Smith, P.M., Pearson, D.G., Dickin, A.P., Morrison, M.A., Leat, P.T., Gibson, S.A., 2005. Source of the Quaternary Alkalic Basalts, Picrites and Basanites of the Potrillo Volcanic Field, New Mexico, USA: Lithosphere or Convecting Mantle? J. Petrol. 46, 1603–1643. https://doi.org/10.1093/PETROLOGY/EGI028

Tiepolo, M., Bottazzi, P., Foley, S.F., Oberti, R., Vannucci, R., Zanetti, A., 2001. Fractionation of Nb and Ta from Zr and Hf at Mantle Depths: the Role of Titanian Pargasite and Kaersutite. J. Petrol. 42, 221–232. https://doi.org/10.1093/PETROLOGY/42.1.221

Tischendorf, G., Rieder, M., Fo¨rsterfo¨fo¨rster, H.-J., Gottesmann, B., Guidotti, C. V, 2004. A new graphical presentation and subdivision of potassium micas. Mineral. Mag. 68, 649–667. https://doi.org/10.1180/0026461046840210

Tolstikhin, I.N., Kamensky, I.L., Marty, B., Nivin, V.A., Vetrin, V.R., Balaganskaya, E.G., Ikorsky, S. V., Gannibal, M.A., Weiss, D., Verhulst, A., Demaiffe, D., 2002. Rare gas isotopes and parent trace elements in ultrabasic-alkaline-carbonatite complexes, Kola Peninsula: Identification of lower mantle plume component. Geochim. Cosmochim. Acta 66, 881–901. https://doi.org/10.1016/S0016-7037(01)00807-9

Tomlinson, E.L., Holland, T.J.B., 2021. A Thermodynamic Model for the Subsolidus Evolution and Melting of Peridotite. J. Petrol. 62. https://doi.org/10.1093/PETROLOGY/EGAB012Page | xxiv

Tucker, J.M., Mukhopadhyay, S., Gonnermann, H.M., 2018. Reconstructing mantle carbon and noble gas contents from degassed mid-ocean ridge basalts. Earth Planet. Sci. Lett. 496, 108–119. https://doi.org/10.1016/J.EPSL.2018.05.024

Urann, B.M., Le Roux, V., Hammond, K., Marschall, H.R., Lee, C.T.A., Monteleone, B.D., 2017. Fluorine and chlorine in mantle minerals and the halogen budget of the Earth's mantle. Contrib. to Mineral. Petrol. 172, 1–17. https://doi.org/10.1007/S00410-017-1368-7/FIGURES/11

Walter, M.J., 2003. Melt Extraction and Compositional Variability in Mantle Lithosphere. Treatise on Geochemistry 2–9, 363–394. https://doi.org/10.1016/B0-08-043751-6/02008-9

Walter, M.J., Sisson, T.W., Presnall, D.C., 1995. A mass proportion method for calculating melting reactions and application to melting of model upper mantle lherzolite. Earth Planet. Sci. Lett. 135, 77–90. https://doi.org/10.1016/0012-821X(95)00148-6

Wang, J., Hattori, K.H., Stern, C.R., 2008. Metasomatic origin of garnet orthopyroxenites in the subcontinental lithospheric mantle underlying Pali Aike volcanic field, southern South America. Mineral. Petrol. 94, 243–258. https://doi.org/10.1007/s00710-008-0017-2

Wang, K., Brodholt, J., Lu, X., 2015. Helium diffusion in olivine based on first principles calculations. Geochim. Cosmochim. Acta 156, 145–153. https://doi.org/10.1016/j.gca.2015.01.023

Wang, K.-L., O'Reilly, S.Y., Griffin, W.L., Pearson, N.J., 2007. In situ Os dating of peridotite xenoliths, Tariat, northern Mongolia High-latitude forcing of in anti-phased precipitat the last glacial-intergl, in: Goldschmidt Conference Abstract. https://doi.org/10.1016/j.gca.2006.06.1495

Wang, Z., Cheng, H., Zong, K., Geng, X., Liu, Y., Yang, J., Wu, F., Becker, H., Foley, S., Wang, C.Y., 2020. Metasomatized lithospheric mantle for Mesozoic giant gold deposits in the North China craton. Geology 48, 169–173. https://doi.org/10.1130/G46662.1

Warren, J.M., 2016. Global variations in abyssal peridotite compositions. Lithos 248–251, 193–219. https://doi.org/10.1016/J.LITHOS.2015.12.023

Wasson, T., J., 1985. Meteorites : their record of early solar-system history, mtre.

Weiss, Y., Kessel, R., Griffin, W.L., Kiflawi, I., Klein-BenDavid, O., Bell, D.R., Harris, J.W., Navon, O., 2009. A new model for the evolution of diamond-forming fluids: Evidence from microinclusion-bearing diamonds from Kankan, Guinea. Lithos 112, 660–674. https://doi.org/10.1016/J.LITHOS.2009.05.038

Wenzel, K.T., Wiedenbeck, M., Gose, J., Rocholl, A., Schmädicke, E., 2021. Water contents of nominally anhydrous orthopyroxenes from oceanic peridotites determined by SIMS and FTIR. Mineral. Petrol. 115, 611–630. https://doi.org/10.1007/S00710-021-00757-9/FIGURES/6

Wernicke, B., 2015. Cenozoic extensional tectonics of the U.S. Cordillera, in: The Cordilleran Orogen. Geological Society of America, pp. 553–17. https://doi.org/10.1130/dnag-gna-g3.553

Weyer, S., Ionov, D.A., 2007. Partial melting and melt percolation in the mantle: The message from Fe isotopes. Earth Planet. Sci. Lett. 259, 119–133. https://doi.org/10.1016/j.epsl.2007.04.033

White, B.S., Wyllie, P.J., 1992. Solidus reactions in synthetic lherzolite-H2O-CO2 from 20–30 kbar, with applications to melting and metasomatism. J. Volcanol. Geotherm. Res. 50, 117–130. https://doi.org/10.1016/0377-0273(92)90040-K

Wiederhold, J.G., 2015. Metal Stable Isotope Signatures as Tracers in Environmental Geochemistry. https://doi.org/10.1021/es504683e

Willcox, A., Buisman, I., Sparks, R.S.J., Brown, R.J., Manya, S., Schumacher, J.C., Tuffen, H., 2015. Petrology, geochemistry and low-temperature alteration of lavas and pyroclastic rocks of the kimberlitic Igwisi Hills volcanoes, Tanzania. Chem. Geol. 405, 82-101. https://doi.org/10.1016/j.chemgeo.2015.04.012.

Willhite, L.N., Jackson, M.G., Blichert-Toft, J., Bindeman, I., Kurz, M.D., Halldórsson, S.A., Harðardóttir, S., Gazel, E., Price, A.A., Byerly, B.L., 2019. Hot and Heterogenous High-3He/4He Components: New Constraints From Proto-Iceland Page | xxvPlume Lavas From Baffin Island. Geochemistry, Geophys. Geosystems 20, 5939–5967. https://doi.org/10.1029/2019GC008654

Williams, W, J, W., 1999. Evolution of Quaternary intraplate mafic lavas detailed using 3He surface exposure and 40Ar/39Ar dating, and elemental He, Sr, Nd, and Pb isotopic signature, Potrillo volcanic field, USA and San Quintin volcanic field, Baja California, Mexico. University of Texas at El Paso.

Witt-Eickschen, G., 2007. Thermal and geochemical evolution of the shallow subcontinental lithospheric mantle beneath the Eifel: Constraints from mantle xenoliths, a review, in: Mantle Plumes: A Multidisciplinary Approach. Springer Berlin Heidelberg, pp. 323–337. https://doi.org/10.1007/978-3-540-68046-8_9

Witt-Eickschen, G., Harte, B., 1994. Distribution of trace elements between amphibole and clinopyroxene from mantle peridotites of the Eifel (western Germany): An ion-microprobe study. Chem. Geol. 117, 235–250. https://doi.org/10.1016/0009-2541(94)90130-9

Witt-Eickschen, G., Kramm, U., 1998. Evidence for the multiple stage evolution of the subcontinental lithospheric mantle beneath the Eifel (Germany) from pyroxenite and composite pyroxenite/peridotite xenoliths. Contrib. to Mineral. Petrol. 131, 258–272. https://doi.org/10.1007/s004100050392

Witt-Eickschen, G., Seck, H.A., Mezger, K., Eggins, S.M., Altherr, R., 2003. Lithospheric mantle evolution beneath the Eifel (Germany): Constraints from Sr-Nd-Pb isotopes and trace element abundances in spinel peridotite and pyroxenite xenoliths. J. Petrol. 44, 1077–1095. https://doi.org/10.1093/petrology/44.6.1077

Wood, B.J., Smythe, D.J., Harrison, T., 2019. The condensation temperatures of the elements: A reappraisal. Am. Mineral. 104, 844–856. https://doi.org/10.2138/AM-2019-6852CCBY

Woodhead, J., Hergt, J., Giuliani, A., Maas, R., Phillips, D., Pearson, D.G., Nowell, G., 2019. Kimberlites reveal 2.5-billion-year evolution of a deep, isolated mantle reservoir. Nature 573, 578–581. https://doi.org/10.1038/s41586-019-1574-8

Workman, R.K., Hart, S.R., 2005. Major and trace element composition of the depleted MORB mantle (DMM). Earth Planet. Sci. Lett. 231, 53–72. https://doi.org/10.1016/j.epsl.2004.12.005

Workman, R.K., Hart, S.R., 2005. Major and trace element composition of the depleted MORB mantle (DMM). Earth Planet. Sci. Lett. 231, 53–72. https://doi.org/10.1016/j.epsl.2004.12.005

Xu, Q., Liu, J., He, H., Zhang, Y., 2019. Nature and evolution of the lithospheric mantle revealed by water contents and He-Ar isotopes of peridotite xenoliths from Changbaishan and Longgang basalts in Northeast China. Sci. Bull. 64, 1325–1335. https://doi.org/10.1016/j.scib.2019.07.006

Xu, Z., Zheng, Y.F., He, H.Y., Zhao, Z.F., 2014. Phenocryst He-Ar isotopic and whole-rock geochemical constraints on the origin of crustal components in the mantle source of Cenozoic continental basalt in eastern China. J. Volcanol. Geotherm. Res. 272, 99–110. https://doi.org/10.1016/j.jvolgeores.2014.01.001

Yamamoto, J., Otsuka, K., Ohfuji, H., Ishibashi, H., Hirano, N., Kagi, H., 2011. Retentivity of CO2 in fluid inclusions in mantle minerals. Eur. J. Mineral. 23 , 805-815. https://doi.org/10.1127/0935-1221/2011/0023-2150.

Yamamoto, M., Kagami, H., Akiyuki, N., Maruyama, T., Kondo, A., Abe, S., Takeda, R., 2013. Sr and Nd isotopic compositions of mafic xenoliths and volcanic rocks from the Oga Peninsula, Northeast Japan Arc: Genetic relationship between lower crust and arc magmas. Lithos 162–163, 88–106. https://doi.org/10.1016/j.lithos.2012.12.002

Yokochi, R., Marty, B., Chazot, G., Burnard, P., 2009. Nitrogen in peridotite xenoliths: Lithophile behavior and magmatic isotope fractionation. Geochim. Cosmochim. Acta 73, 4843–4861. https://doi.org/10.1016/j.gca.2009.05.054

Yoshida, T., Kimura, J.I., Yamada, R., Acocella, V., Sato, H., Zhao, D., Nakajima, J., Hasegawa, A., Okada, T., Honda, S., Ishikawa, M., Ardiansyah Prima, O.D., Kudo, T., Shibazaki, B., Tanaka, A., Imaizumi, T., 2014. Evolution of late cenozoic magmatism and the crust-mantle structure in the NE japan arc. Geol. Soc. Spec. Publ. 385, 335–387. https://doi.org/10.1144/SP385.15

Ziberna, L., Klemme, S., Nimis, P., n.d. Garnet and spinel in fertile and depleted mantle: insights from thermodynamic modelling. https://doi.org/10.1007/s00410-013-0882-5Page | xxvi

Zinngrebe, E., Foley, S.F., 1995. Metasomatism in mantle xenoliths from Gees, West Eifel, Germany: evidence for the genesis of calc-alkaline glasses and metasomatic Ca-enrichment. Contrib. to Mineral. Petrol. 122, 79–96. https://doi.org/10.1007/s004100050114

Appendix B. Methodology

Most of the techniques employed in this study have been previously detailed in the published literature. Therefore, this Appendix gives a brief overview of each method used together with uncertainties. More detailed descriptions are provided where advancements to the analytical techniques have been employed.

Petrographic Constraints

Polished thin sections of the mantle xenoliths were examined at the University of Cambridge to ensure that these rocks are fresh and appropriate for analysis. These were scanned at very high resolution using a digital scanner and subsequently used for determining modal abundance of mineral phases using the JMicroVision image analysis toolbox (www.jmicrovision.com/index.htm, version 1.2.7). A minimum of 500 points for each scan was undertaken to determine modal petrology. These typically comprised olivine, orthopyroxene, clinopyroxene and opaque oxides. However, where applicable amphibole, phlogopite and garnet minerals were also documented. Opaques were determined from EMPA data and where spinel and ilmenite coexisted, the different habit of the minerals were used to determine the differences. Where, spinel has no distinct habit while ilmenite typically shows a tabular habit.

To ensure the sections analysed were representative of the entire sample, the hand specimen was sliced multiple times by a diamond-tipped saw. There we inspected to ensure they appeared similar. However, ensuring a thin section is truly representative of a thin section is a challenge which has faced geologists for generations. This is particularly relevant to coarse-grained rocks because the thin section will contain less total grains than fine-grained rocks. As a result, the point-counting method employed, although on the same surface area, will account for less total minerals comprising a sample.

Mineral Major Element Chemistry by EMPA

In-situ major element analysis was undertaken by electron microprobe (EMPA) analysis at the Micro-Analysis and Micro-Diffraction laboratory in the Department of Earth Sciences at the University of Cambridge. Probe sections and mounts containing olivine, clinopyroxene, orthopyroxene, spinel, garnet, amphibole, and phlogopite analysis were analysed on a Cemeca SX-100 EMPA equipped with five WDS and 1 EDS detector. An accelerating volatage

of 15 keV, and a beam current of 20nA was used with a beam size of 1 µm. Standards for calibration were Na on jadite, K on K-feldspar, Fe on Fayalite, Mn, Ni, and Cr on pure metals, Si and Ca on diopside, Al on corundum, Mg on St Johns olivine, and Ti on rutile. Secondary standards of San Carlos olivine, Aug12214, and VG2 glass were used as secondary standards (Table 23). Matrix effects were corrected using the ZAF correction.

For every sample, a minimum of three grains of each unique mineral present was the subject of spot analysis. These grains had three distinct locations for each analysis which were used to take an average. The data is reported as the average of these analysis with the errors reported as standard deviations.

Mineral Trace Element Chemistry by LA-ICP-MS

In-situ trace element analysis was undertaken by in-situ Laser Ablation Inductively Coupled Plasma Mass Spectrometry (LA-ICP-MS) at the Leading Light Laboratory in the Department of Earth Sciences at the University of Cambridge. Analysis was undertaken on thin sections and mounts using a ESI UP193NC laser ablation system attached to Nexion 350D ICP-MS system. Clinopyroxene and garnets were analysed using CaO and SiO_2 from EMPA analysis as internal standard normalisation. NIST612 was used to calibrate element concentration for all analysis except for Ti in clinopyroxene where NIST610 was used because of the low concentrations of Ti in NIST612. Accuracy was assesed and drift using NIST 614, while BCR-2G, BIR-1, BHVO-2, GOR132-G and in-house clinopyroxene (BD2036) and garnet (BD3736B) were also used. Standard results are reported in Table 24 for August 2019 and November 2021.

Pure helium was used as the ablation gas at 700mL min-1. Ablated sample material was carried in the helium gas which was joined with the argon nebulised gas line from the ICP-MS using a signal homogenised device at 0.8 L min-1 before the ICP-MS torch. The NWR193 is equipped with a TwoVol2 sample chamber and small volume sample cup to quickly and efficiently transfer samples and washout performance.

Data was processed using Glitter software (GEMOC, Australia). Results were checked and filtered for background and melt/mineral inclusions after each analysis to optimise the data. Accuracy is good for data with results between 80% and 140%. Rare-earth elements (REEs) were particularly accurate, with results between 80% and 100% accuracy. During analysis,

suitable replicate spots were analysed and LA-ICP-MS results were averaged. The spots were carefully chosen to avoid contamination from nearby cracks, inclusions, or any overlapping neighbouring phases to ensure only the targeted phase was analysed. For additional details, see Gibson et al., 2020. Errors are calculated as standard deviations of the three grains.

Mineral Volatile Elements by SIMS

The concentrations of H, Li, B, F and Cl (in addition to SiO_2 and CaO for normalization) were determined using a Cameca IMS-7f GEO at the NERC Ion Microprobe Facility at the University of Edinburgh. Data was collected in three analytical sessions (November, 2019, May 2021, and June 2021).

Firstly, peridotites and pyroxenites were mechanically separated to their individual mineral phases. Phases were then optically scanned and those free from melt and mineral inclusions were selected for polishing in the Department of Earth Sciences at the University of Cambridge clean laboratory (Room 007). Minerals were cleaned, mounted in crystal bond, and polished to 1µm. Samples and polishing pads were routinely cleaned in an ultra-sonic bath the minimise contamination. Minerals were mounted into indium mounts and investigated at low vacuum conditions on the SEM to ensure the correct mineral phases had been selected. Mounts were sent to Edinburgh Ion Microprobe Facility (EIMF) and gold coated before being loaded for analysis. SIMS analysis was undertaken before EMPA analysis to avoid contamination and avoid elemental migration under the electron beam.

Analysis was undertaken using a Cameca IMS 7f-Geo over three session. During the first session in November 2019, concentrations of H, Li, B, F and Cl were calculated using the standards glass ALV-519-4-1. H and F calibrations were supplemented by known clinopyroxene and orthopyroxene grains KH03-4, 116610 from Kumamoto et al., 2017 (Table 25). Concentrations of Cl were calculated using ST8.1.A92-2 and background was monitored by analysing an olivine from San Carlos every 2 hours. During the next two sessions in May and June of 2021, the same analytical technique was used for H and F and expanded to include P. The Cl acquisition technique evolved to also include an ALV519-4-1 reference glass from Ben Urann (WHOI) and optical glass herasil with 0.4ppm Cl for background monitoring. This showed consistently low backgrounds for Cl (0.3 to 0.6 ppm),

however ALV519-4-1 was excluded as a calibration as it has too low Cl concentrations (45 ppm) to obtain reliable calibration values (De Hoog, personal communication).

San Carlos olivine was continually analysed multiple times per run (Table 26) as it is considered to have ~0 ppmw (H_2O) and act as an internal reference to asses analytical drift. Particularly high H_2O was recorded on the 31st of May and 1st of June, however these high values were consistent during the analytical run and attributed to an elevated background which could be corrected.

Li concentration in clinopyroxene were determined by LA-ICP-MS and SIMS (Figure A.1). These results show an overall similarity of results between the two methods, but LA-ICP-MS tends to retain slightly higher concentrations than those determined by SIMS.

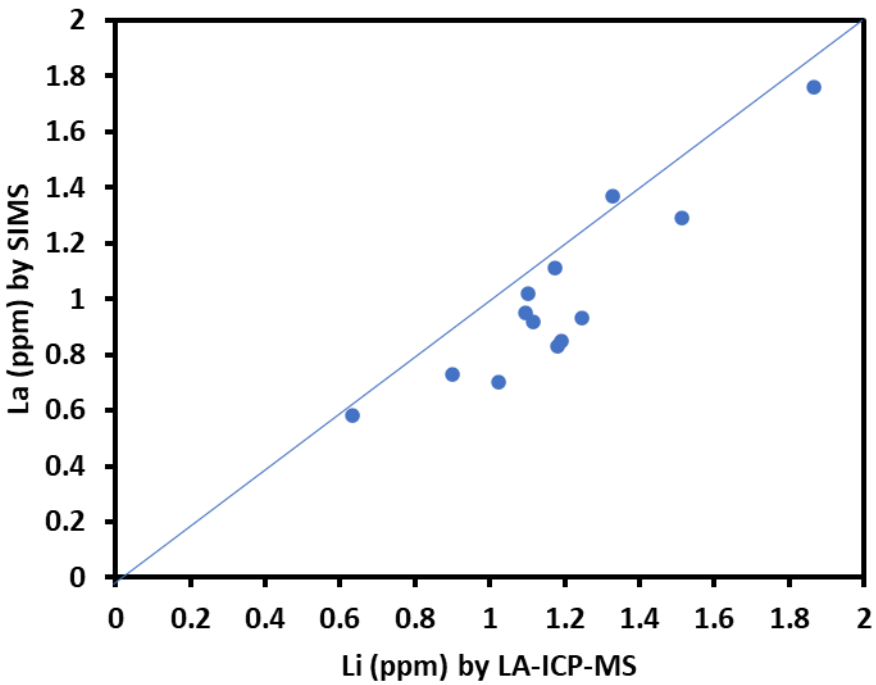

Figure A.1 Showing Li (ppm) determined by LA-ICP-MS compared to Li (ppm) from SIMS in clinopyroxene

Errors were calculated as standard deviations of for the average of the grains analysed and a propagated error of the individual spot analysis.

3.5 Noble Gas Chemistry

$^3He/^4He$ analysis was undertaken using a ThermoFisher Scientific Helix SFT dual collector mass spectrometer at the Scottish Universities Environmental Research Centre following the methods of Carracedo et al. (2019). Approximately 1g of material was loaded into an all-

metal multi-sample pneumatic press. The line was sealed and pumped until it reached an ultra-high vacuum. The gases in fluid inclusions of mineral phases were released by single-step *in vacuo* crushing and purified in an all-metal, ultra-high-vacuum line equipped with two heated (250 ^{o}C) SAES GP50 getters and one activated charcoal finger (cooled to approximately -196 ^{o}C using liquid nitrogen). ^{3}He was analysed by a copper beryllium ion counting electron multiplier while ^{4}He was analysed by an electrically suppressed Faraday detector.

Determination of mass spectrometer sensitivity and ratio reproducibility was performed by measuring HESJ standard gas (Matsuda et al., 2002) with $^{3}He/^{4}He = 20.63 \pm 0.10\ R_A$. ($R_A$ being the $^{3}He/^{4}He$ of air at 1.34×10^{-6} (Mishima et al., 2018)). Blank analysis were performed frequently to obtain a well constrained background ^{3}He and ^{4}He. The average blank levels for these analysis were $^{3}He = 1.76 \times 10^{-15} \pm 3.92 \times 10^{-17}$ cm^{3}, and $^{4}He = 1.72 \times 10^{-10} \pm 4.42 \times 10^{-11}$ cm^{3}.

After crushing and bulk ^{3}He and ^{4}He abundances were determined, each sample was sieved and material finer than 300 µm was weighed, assuming all gases had been released from this material. This was then used to calculate the concentration of ^{3}He and ^{4}He in each mineral phase. Samples with multiple mineral analysis were then processed to obtain a xenolith $^{3}He/^{4}He$ signatures and concentrations. This was done using a weighted average outlined in Chapter 8.

When comparing samples analysed in this study which had previously been analysed by heating methods, the crushing method has slightly lower ^{3}He and ^{4}He concentrations than that from heating. The crushing method is likely more representative of the $^{3}He/^{4}He$ of the sampled mantle as the elevated signatures from the heating method is likely sampling cosmogenic ingrowth from ^{3}He while at the surface (as discussed in the main body of text). However, this may have important implications for concentration calculations and how it influences bulk CO_2 concentrations.

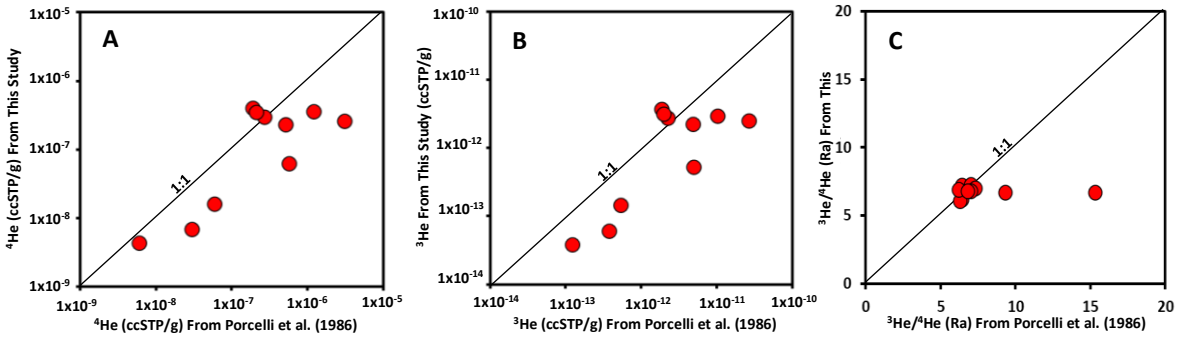

Figure A.2 a) ^{4}He-concentration (ccSTP/g), b) ^{3}He-concentration (ccSTP/g), c) ^{3}He/^{4}He (Ra) of whole-rock and mineral compositions of BD128, BD738, BD816, and BD3847 from this study and Porcelli et al. (1986). Analytical errors are smaller than the symbols.

The minimum threshold for determining if a sample was to be included for interpretation was based on the ^{3}He and ^{4}He concentrations measured during this analytical process. Martelli et al. (2011) use the arbitrary cut-off value of ^{4}He = 3.x10^{-9} cm^{3}STP/g. However, this value is inconsistent with the data produced here when comparing analytical ^{3}He/^{4}He with ^{3}He and ^{4}He concentration. Instead, this data indicates a more suitable cut-off value of ^{4}He = 5x10^{-9} cm^{3}STP/g and ^{3}He = 3x10^{-14}.

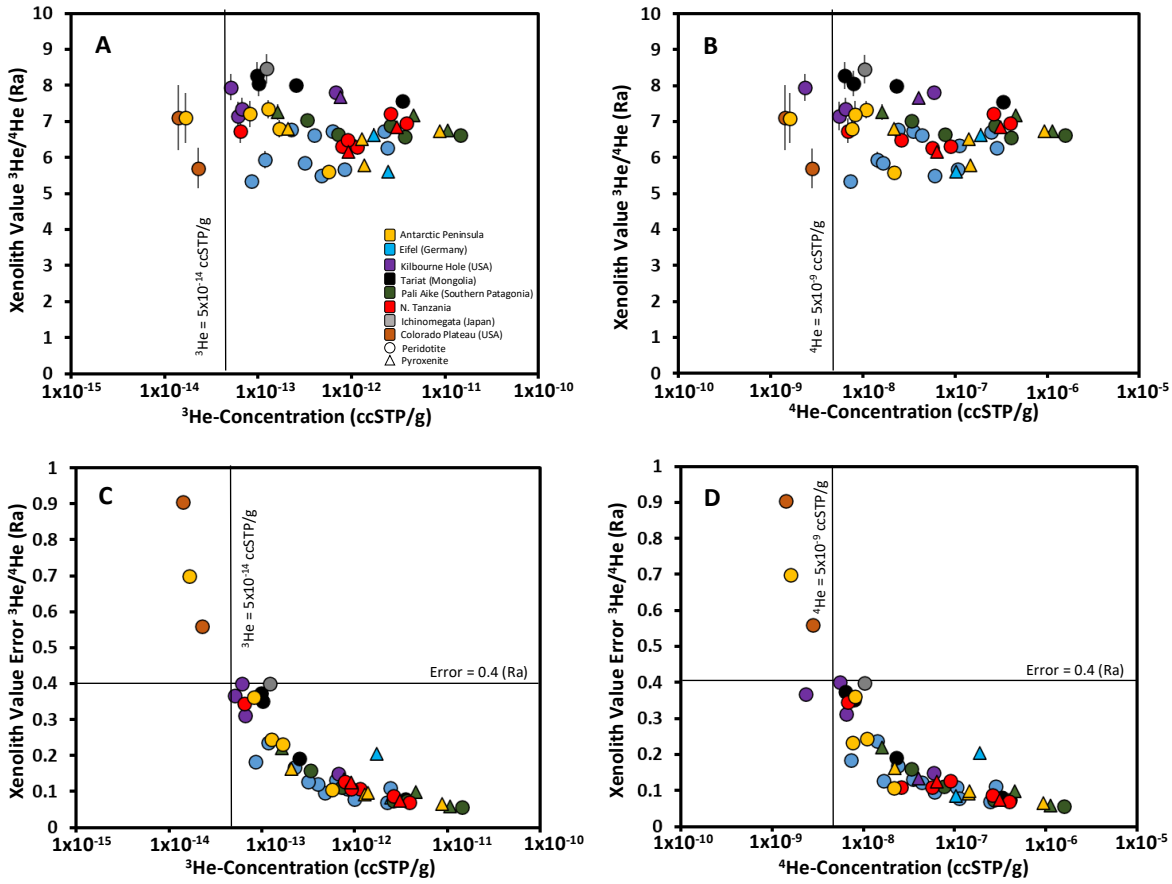

Figure A.3 showing xenolith value ^{3}He/^{4}He (Ra) compared to a) xenolith value ^{3}He-concentration and b) xenolith value ^{4}He-concentration, and xenolith value ^{3}He/^{4}He (Ra) error compared to c) xenolith value ^{3}He-concentration and b) xenolith value ^{4}He-concentration. Error bars are displayed for A + B and key for symbols displayed in A.

Carbon Chemistry

Carbon concentration and isotope compositions were determined by Feargus Abernethy using the FINESSE static-vacuum mass spectrometry system at the Open University which are detailed in Verchovsky et al. (1998, 2002).

To be internally consistent with ^{3}He and ^{4}He determinations, carbon abundance and isotope compositions were also determined using a crushing technique. Carbon was released from the fluid inclusions using a stepped crushing technique and measured at 0, 20, 40, 80, 160, 320, 640 and 1280 strokes or until all carbon has been released.

Following a cleaning processes outlined in Appendix B section 3.5, mineral separates are loaded into the crusher and heated to remove surface adsorbed carbon. Following crushing, gases are passed through a liquid nitrogen-cooled cold finger array and a molecular sieve for purification. Carbon abundance is determined by a 1 Torr MKS Baratron capacitance

manometer and expanded into a triple-collected mass spectrometer operating in static mode to determine ^{12}C and ^{13}C. C abundance is accurate to <5 % and $\delta^{13}C$ is accurate to <0.5 ‰.

Appendix C. Data Tables

Table 1. Olivine Major Element Composition (wt. % oxide).

Sample	SiO2	st.dev	TiO2	st.dev	Al2O3	st.dev	Cr2O3	st.dev	FeO	st.dev	MnO	st.dev	NiO	st.dev	MgO	st.dev	CaO	st.dev	Na2O	st.dev	Mg#
KG3610.10A	41.53	0.13			0.01	0.00	0.01	0.01	8.52	0.17	0.12	0.01	0.42	0.02	49.89	0.13	0.03	0.00			91.26
KG3609.21	41.11	0.39			0.02	0.01	0.01	0.02	8.98	0.19	0.13	0.03	0.40	0.02	49.81	0.39	0.09	0.03			90.82
KG3719.25	41.00	0.19			0.02	0.01	0.00	0.00	10.05	0.22	0.15	0.02	0.39	0.03	48.94	0.25	0.07	0.01			89.67
L7.201.1.41	40.48	0.30			0.02	0.00	0.02	0.00	10.32	0.24	0.15	0.01	0.39	0.01	49.00	0.16	0.07	0.01			89.43
BN	41.03	0.24			0.01	0.01	0.00	0.02	10.45	0.18	0.16	0.02	0.37	0.03	48.88	0.18	0.05	0.01			89.29
DW3	41.36	0.07			0.02	0.00	0.02	0.01	8.24	0.05	0.14	0.01	0.39	0.01	50.96	0.06	0.05	0.00			91.69
DW7	40.76	0.17			0.06	0.01	0.05	0.02	8.89	0.11	0.14	0.03	0.36	0.03	49.81	0.21	0.14	0.02			90.90
DW8	40.82	0.23			0.02	0.01	0.01	0.02	8.62	0.13	0.14	0.03	0.36	0.03	50.30	0.14	0.04	0.01			91.23
DW10	40.52	0.13			0.03	0.01	0.02	0.02	10.32	0.20	0.22	0.04	0.32	0.18	48.90	0.13	0.09	0.01			89.41
MM5	40.89	0.15			0.05	0.01	0.04	0.02	8.70	0.05	0.13	0.03	0.40	0.03	50.14	0.13	0.14	0.06			91.13
MM8	40.77	0.26			0.07	0.04	0.07	0.01	8.40	0.09	0.12	0.02	0.34	0.07	50.27	0.18	0.13	0.00			91.43
MM11	40.52	0.31			0.02	0.00	0.01	0.02	9.43	0.11	0.14	0.02	0.35	0.02	49.69	0.13	0.06	0.00			90.38
G17	41.18	0.12			0.02	0.00	0.05	0.00	8.44	0.14	0.12	0.02	0.39	0.02	49.89	0.07	0.06	0.01			91.33
G18	40.59	0.18			0.02	0.01	0.01	0.02	8.72	0.20	0.14	0.03	0.35	0.05	49.82	0.28	0.04	0.04			91.06
KH2	40.92	0.27			0.03	0.01	0.01	0.02	10.48	0.12	0.15	0.03	0.39	0.03	48.47	0.24	0.07	0.01			89.18
KH3D	40.44	0.28			0.00	0.00	0.04	0.01	8.93	0.04	0.13	0.02	0.37	0.02	50.16	0.08	0.13	0.00			90.92
KH4	41.00	0.12			0.02	0.01	0.01	0.01	10.43	0.05	0.14	0.01	0.37	0.01	48.62	0.16	0.06	0.09			89.26
KH5	41.07	0.16			0.03	0.01	0.01	0.02	10.40	0.11	0.15	0.03	0.39	0.09	48.61	0.03	0.07	0.01			89.29
TM1	40.11	0.25			0.01	0.01	0.01	0.02	10.15	0.13	0.13	0.02	0.42	0.04	49.20	0.12	0.03	0.01			89.63
TM2	41.03	0.17			0.02	0.01	0.02	0.02	10.29	0.09	0.15	0.03	0.30	0.26	49.07	0.27	0.07	0.01			89.47
TM3	40.98	0.16			0.04	0.02	0.01	0.01	10.84	0.10	0.15	0.04	0.47	0.40	48.47	0.22	0.07	0.01			88.86
TM4	41.14	0.29			0.04	0.07	0.01	0.01	9.53	0.13	0.13	0.04	0.45	0.19	49.52	0.32	0.05	0.01			90.26
CP31																					
CP33	41.04	0.10			0.02	0.01	0.02	0.04	9.89	0.15	0.12	0.02	0.37	0.05	48.88	0.25	0.06	0.03			89.80
LT1	40.94	0.20			0.05	0.11	0.01	0.02	9.33	0.09	0.13	0.02	0.41	0.01	48.71	0.24	0.03	0.02			90.30
LT16	40.99	0.14			0.04	0.01	0.04	0.02	8.72	0.09	0.11	0.01	0.40	0.02	49.16	0.17	0.09	0.02			90.95
PA3-5	41.28	0.17			0.05	0.01	0.05	0.02	7.72	0.07	0.09	0.04	0.40	0.05	49.56	0.20	0.11	0.01			91.96
CP62																					
BD730	41.01	0.17			0.01	0.14	0.01	0.07	8.80	0.12	0.11	0.02	0.42	0.01	50.49	0.22	0.03	0.03			91.09
BD738	41.10	NA							7.72	NA	0.09	NA			50.30	NA	0.03	NA			92.07
BD794	41.34	0.33			0.01	0.11	0.04	0.10	7.82	0.11	0.08	0.01	0.40	0.39	50.62	0.25	0.03	0.09			92.02
BD797	41.02	0.10			0.01	0.00	0.05	0.01	7.44	0.10	0.10	0.01	0.44	0.02	51.30	0.26	0.09	0.02			92.48
BD822	41.40								7.50		0.08				51.75		0.04				92.48
TH17	40.56	0.31			0.02	0.01	0.05	0.02	9.92	0.22	0.12	0.02	0.41	0.01	48.66	0.12	0.08	0.01			89.74
BP1	40.65	0.35			0.00	0.00	0.00	0.00	9.32	0.25	0.13	0.02	0.43	0.04	49.25	0.22	0.02	0.01			90.40
TH33	40.93	0.40			0.02	0.00	0.08	0.01	8.39	0.19	0.09	0.01	0.39	0.06	49.78	0.18	0.08	0.01			91.36
J1	40.95	0.19			0.02	0.00	0.03	0.00	10.14	0.18	0.14	0.02	0.36	0.04	48.53	0.20	0.06	0.02			89.51
KG3619.7	39.15	0.23			0.02	0.00	0.00	0.02	19.24	0.13	0.21	0.03	0.32	0.03	41.50	0.23	0.09	0.01			79.35
L7201.1.74c	38.86	0.36			0.07	0.01			17.90	0.22	0.23	0.01	0.11	0.00	43.02	0.46	0.20	0.01			81.07
R5194.2I	38.78	0.16			0.04	0.00			19.92	0.30	0.26	0.01	0.09	0.01	40.49	0.17	0.11	0.01			78.37
R5194.2M																					
MM6	40.41	0.17			0.05	0.01	0.04	0.02	11.29	0.23	0.17	0.02	0.27	0.09	48.07	0.19	0.15	0.01			88.36
DW5	40.50	0.26			0.06	0.05	0.04	0.02	12.23	0.21	0.16	0.03	0.29	0.19	47.04	0.18	0.15	0.02			87.28
KH1	39.18	0.18			0.06	0.04	0.01	0.00	18.75	0.22	0.25	0.04	0.05	0.04	41.83	0.19	0.16	0.02			79.91
LT14																					
LT15	39.88	0.12				0.01	0.01	0.03	15.53	0.19	0.22	0.03	0.14	0.04	44.42	0.22	0.04	0.05			83.60
BD816	39.40	0.02			0.00	0.00	0.04	0.01	15.48	0.15	0.21	0.03	0.35	0.02	44.17	0.21	0.05	0.01			83.57
BD3847	39.60	NA							16.90	NA					43.30	NA	0.22	NA			82.04

Table 2. Orthopyroxene Major Element Chemistry (wt.% oxide).

Sample	SiO2	st.dev	TiO2	st.dev	Al2O3	st.dev	Cr2O3	st.dev	FeO	st.dev	MnO	st.dev	NiO	st.dev	MgO	st.dev	CaO	st.dev	Na2O	st.dev	Mg#
KG3610.10A	56.87	0.45	0.01	0.00	2.55	0.77	0.55	0.17	5.46	0.16	0.14	0.01	0.09	0.01	34.28	0.42	0.43	0.04	0.12	0.02	91.80
KG3609.21	57.28	0.50	0.00	0.00	2.05	0.07	0.49	0.03	5.66	0.13	0.12	0.02			34.18	0.33	0.66	0.03	0.05	0.01	91.50
KG3719.25	55.48	0.24	0.09	0.00	4.24	0.08	0.39	0.03	6.29	0.15	0.15	0.02			32.90	0.10	0.77	0.02	0.10	0.01	90.31
L7.201.1.41	55.07	0.22	0.10	0.01	4.28	0.03	0.45	0.03	6.61	0.21	0.16	0.01	0.10	0.01	32.90	0.20	0.75	0.03	0.11	0.01	89.88
BN	55.51	0.37	0.13	0.01	4.09	0.05	0.27	0.03	6.71	0.12	0.15	0.02			32.78	0.25	0.56	0.02	0.10	0.01	89.70
DW3	56.60	0.22	0.03	0.00	2.79	0.06	0.44	0.03	5.36	0.02	0.14	0.01	0.11	0.01	34.84	0.12	0.64	0.04	0.08	0.01	92.06
DW7	54.33	0.17	0.09	0.00	4.61	0.03	0.88	0.04	5.69	0.04	0.17	0.03	0.25	0.25	32.60	0.14	1.38	0.07	0.12	0.01	91.08
DW8	55.89	0.26	0.04	0.01	2.93	0.08	0.35	0.04	5.62	0.07	0.13	0.02	0.08	0.06	34.38	0.08	0.46	0.03	0.04	0.01	91.60
DW10																					
MM5	55.79	0.52	0.10	0.02	3.35	0.27	0.60	0.08	5.68	0.05	0.14	0.01	0.10	0.02	33.84	0.28	0.86	0.04	0.10	0.02	91.39
MM8	55.15	0.16	0.12	0.01	3.67	0.06	1.01	0.04	5.32	0.07	0.13	0.03	0.07	0.19	33.04	0.10	1.45	0.02	0.15	0.01	91.71
MM11	55.32	0.21	0.01	0.01	3.44	0.27	0.45	0.07	6.05	0.10	0.15	0.03	0.10	0.06	33.62	0.26	0.72	0.10	0.07	0.02	90.83
G17	56.73	0.30	0.04	0.01	2.24	0.23	0.31	0.04	5.82	0.04	0.13	0.01	0.06	0.01	34.32	0.18	0.32	0.01	0.02	0.01	91.31
G18	55.68	0.76	0.09	0.03	2.87	0.76	0.46	0.21	5.98	0.14	0.14	0.04	0.08	0.16	34.36	0.33	0.32	0.03	0.02	0.02	91.10
KH2	55.03	0.24	0.13	0.01	4.88	0.07	0.37	0.03	6.63	0.10	0.16	0.02	0.10	0.03	32.37	0.18	0.82	0.04	0.11	0.01	89.69
KH3D	54.73	0.42	0.06	0.01	4.31	0.04	0.85	0.03	5.61	0.01	0.13	0.01	0.12	0.02	32.97	0.07	1.43	0.02	0.10	0.00	91.29
KH4	54.52	0.14	0.15	0.00	4.92	0.07	0.40	0.05	6.65	0.09	0.14	0.05	0.09	0.02	31.88	0.14	0.84	0.03	0.11	0.01	89.53
KH5	54.93	0.59	0.09	0.01	4.89	0.18	0.35	0.04	6.93	1.66	0.16	0.07	0.10	1.19	32.08	0.02	0.83	0.03	0.11	0.01	89.20
TM1	54.37	0.73	0.12	0.01	4.35	0.20	0.34	0.04	6.40	0.12	0.16	0.02	0.10	0.03	33.25	0.23	0.43	0.04	0.07	0.01	90.26
TM2	55.29	0.13	0.15	0.02	4.73	0.10	0.34	0.04	6.45	0.12	0.15	0.03	0.09	0.12	32.84	0.15	0.74	0.06	0.13	0.02	90.07
TM3	54.95	0.47	0.15	0.01	4.90	0.15	0.31	0.05	6.66	0.15	0.13	0.04	0.07	0.14	32.26	0.33	0.69	0.03	0.14	0.02	89.62
TM4	55.87	0.30	0.12	0.01	4.00	0.40	0.40	0.08	5.98	0.07	0.17	0.03	0.04	0.13	33.45	0.32	0.52	0.03	0.09	0.01	90.89
CP31																					
CP33	55.82	0.06	0.18	0.00	3.50	0.02	0.42	0.03	6.20	0.18	0.14	0.02	0.08	0.04	33.02	0.06	0.70	0.03	0.16	0.02	90.47
LT1	54.98	0.31	0.06	0.02	4.52	0.17	0.56	0.07	6.17	0.11	0.13	0.02			32.90	0.35	0.62	0.31	0.05	0.02	90.48
LT16	55.67	0.10	0.07	0.02	2.75	0.03	0.84	0.04	5.43	0.08	0.12	0.02			33.22	0.49	1.04	0.04	0.16	0.01	91.60
PA3-5	55.14	0.39	0.08	0.01	2.86	0.05	0.99	0.01	4.89	0.06	0.13	0.02			33.14	0.12	1.26	0.01	0.13	0.02	92.35
BD730	57.82	0.29	0.04	0.00	1.08	0.04	0.32	0.01	5.30	0.17	0.11	0.00	0.11	0.01	35.33	0.15	0.55	0.02			92.24
BD738	57.90	NA	0.15	NA	1.10	NA	0.19	NA	4.62	NA	0.10	NA			34.50	NA	0.42		0.11	NA	93.01
BD794	58.21	0.65	0.01	0.00	1.01	0.02	0.42	0.01	4.64	0.25	0.12	0.00		0.02	35.32	0.21	0.55	0.01	0.12		93.14
BD797	57.68	0.40	0.04	0.05	1.27	0.14	0.57	0.08	4.33	0.09	0.11	0.01	0.10	0.01	35.71	0.35	0.41	0.05			93.63
BD822	57.80	NA	0.09	NA	1.78	NA	0.31	NA	4.49	NA	0.10	NA			36.15	NA	0.45	NA	0.08	NA	93.49
TH17	55.56	0.43	0.32	0.01	1.63	0.04	0.64	0.03	6.09	0.09	0.11	0.03			32.56	0.14	0.95	0.04	0.24	0.02	90.51
BP1	54.38	0.44	0.03	0.00	4.53	0.20	0.58	0.05	5.95	0.27	0.14	0.05			32.01	0.35	0.74	0.07	0.05	0.01	90.56
TH33	57.51	0.28	0.06	0.02	1.52	0.07	0.80	0.08	5.14		0.13				34.08	0.40	0.91	0.08	0.18	0.01	92.20
J1	55.30	0.18	0.11	0.02	3.40	0.27	0.41	0.04	6.64	0.25	0.16	0.03	0.09	0.02	32.93	0.33	0.53	0.07	0.02	0.01	89.84
KG3619.7	53.28	0.27	0.32	0.01	4.95	0.10	0.23	0.03	11.87	0.19	0.19	0.04	0.00	0.02	28.36	0.24	0.99	0.02	0.15	0.01	80.98
L7201.1.74c																					
R5194.2I																					
R5194.2M																					
MM6	54.45	0.12	0.28	0.02	4.08	0.06	0.77	0.03	6.95	0.11	0.16	0.04	0.06	0.04	31.91	0.05	1.43	0.02	0.13	0.01	89.11
DW5																					
KH1																					
LT14	55.87	0.46	0.06	0.01	3.86	0.52	0.34	0.06	5.86	0.16	0.09	0.03	0.14	0.03	33.31	0.30	0.47	0.03	0.11	0.01	91.02
LT15																					
CP62	55.29	0.23	0.31	0.04	3.42	0.19	0.25	0.06	8.24	0.18	0.12	0.03	0.13	0.03	31.77	0.18	0.66	0.02	0.11	0.01	87.30
BD816	56.80	0.52	0.09	0.01	0.39	0.03	0.12	0.03	9.95	0.14	0.24	0.02	0.03	0.00	32.10	0.66	0.36	0.03	0.04	0.01	85.19

Table 3. Clinopyroxene Major Element Chemistry (wt.% oxide).

Sample	SiO2	st.dev	TiO2	st.dev	Al2O3	st.dev	Cr2O3	st.dev	FeO	st.dev	MnO	st.dev	NiO	st.dev	MgO	st.dev	CaO	st.dev	Na2O	st.dev	Mg#	Cr#
KG3610.10A	54.59	0.35	0.03	0.02	3.50	0.43	1.31	0.11	1.86	0.07	0.07	0.01	0.04	0.01	15.83	0.23	20.31	0.23	2.03	0.12	93.82	20.00
KG3609.21	54.40	0.27	0.01	0.00	2.16	0.11	0.77	0.09	2.20	0.06	0.09	0.02			17.47	0.21	22.34	0.15	0.57	0.04	93.39	19.33
KG3719.25	52.36	0.29	0.43	0.03	6.12	0.25	0.94	0.06	2.75	0.13	0.07	0.02			15.34	0.10	20.55	0.15	1.46	0.03	90.86	9.34
L7.201.1.41	51.57	0.41	0.53	0.11	6.53	0.38	1.04	0.08	2.91	0.12	0.10	0.01	0.05	0.01	15.17	0.22	20.19	0.19	1.82	0.07	90.29	9.68
BN	52.42	0.20	0.61	0.02	6.41	0.10	0.64	0.04	2.65	0.07	0.09	0.02			14.79	0.15	20.22	0.13	1.87	0.01945	90.87	6.30
DW3	53.96	0.53	0.08	0.01	3.64	0.54	0.74	0.20	2.56	0.02	0.07	0.00	0.04	0.00	16.74	0.43	20.37	0.14	1.28	0.099894	92.11	12.04
DW7	51.81	0.31	0.21	0.01	5.46	0.03	1.39	0.04	3.30	0.07	0.10	0.04	0.03	0.02	17.50	0.08	18.45	0.08	1.01	0.15	90.44	14.60
DW8	52.40	0.21	0.16	0.01	3.71	0.15	0.76	0.07	2.47	0.07	0.06	0.02	0.05	0.08	16.26	0.13	22.08	0.14	0.95	0.033272	92.14	12.01
DW10	52.39	0.71	0.20	0.09	3.84	0.41	1.22	0.35	2.93	0.19	0.08	0.04	BDL	NA	16.29	0.34	21.05	0.26	1.06	0.152929	90.84	17.52
MM5	51.88	0.50	0.47	0.17	5.17	0.50	1.38	0.31	2.88	0.15	0.11	0.03	0.04	0.02	16.55	0.27	19.51	0.44	1.27	0.127386	91.10	15.18
MM8	52.03	0.33	0.26	0.01	4.60	0.04	1.78	0.04	3.10	0.05	0.08	0.02	0.04	0.19	17.69	0.05	18.12	0.09	1.20	0.018694	91.06	20.65
MM11	52.31	0.64	0.07	0.01	4.86	0.43	0.90	0.20	2.98	0.08	0.10	0.03	0.01	0.16	16.26	0.31	20.16	0.33	1.29	0.053285	90.67	11.10
G17	52.52	0.37	0.27	0.01	4.84	0.15	1.70	0.11	3.17	0.02	0.10	0.02	0.06	0.01	17.48	0.05	18.11	0.14	1.20	0.035694	90.77	19.12
G18	52.48	1.04	0.35	0.21	3.35	1.36	1.01	0.33	2.66	0.33	0.08	0.02	0.04	0.15	17.16	0.89	21.31	1.47	0.76	0.117391	92.01	16.83
KH2	51.95	0.27	0.54	0.02	7.11	0.14	0.81	0.04	3.07	0.09	0.11	0.04	0.04	0.03	14.97	0.09	19.70	0.20	1.67	0.051373	89.69	7.06
KH3D	51.82	0.58	0.13	0.00	5.13	0.02	1.38	0.02	3.17	0.04	0.09	0.02	0.07	0.02	17.45	0.10	19.21	0.16	0.90	0.025497	90.75	15.25
KH4	51.59	0.10	0.58	0.01	7.24	0.13	0.82	0.04	3.07	0.07	0.08	0.04	0.05	0.02	14.77	0.07	19.34	0.19	1.76	0.043159	89.55	7.05
KH5	52.08	0.27	0.40	0.01	7.19	0.11	0.77	0.06	2.98	0.08	0.11	0.03	0.04	0.08	14.98	0.05	19.44	0.10	1.74	0.044244	89.97	6.73
TM1	51.52	0.25	0.59	0.02	6.59	0.37	0.71	0.05	2.44	0.06	0.11	0.02	0.02	0.03	14.79	0.22	20.43	0.29	1.82	0.099504	91.54	6.78
TM2	51.99	0.20	0.62	0.02	6.89	0.17	0.75	0.05	2.89	0.09	0.09	0.03	0.05	0.21	15.01	0.13	19.30	0.16	1.77	0.040452	90.26	6.81
TM3	52.22	0.12	0.67	0.02	7.14	0.12	0.69	0.05	3.12	0.06	0.11	0.04	0.09	0.16	15.03	0.10	18.97	0.16	1.94	0.036164	89.55	6.12
TM4	52.54	0.19	0.53	0.03	6.49	0.24	1.00	0.07	2.28	0.07	0.09	0.04	0.05	0.14	14.68	0.17	20.32	0.10	1.93	0.088501	92.00	9.40
CP31																						
CP33	52.91	0.15	0.66	0.04	5.76	0.14	1.02	0.16	2.99	0.11	0.07	0.04	0.04	0.04	15.29	0.13	18.79	0.09	2.12	0.056598	90.13	10.62
LT1	52.18	0.34	0.21	0.02	5.55	0.41	1.10	0.06	2.14	0.19	0.10	0.02			15.38	0.76	21.55	0.79	1.20	0.07	92.75	11.75
LT16	52.83	0.54	0.27	0.22	3.57	0.35	1.61	0.16	2.94	0.23	0.09	0.02			17.24	0.37	19.13	0.15	1.27	0.25	91.25	23.28
PA3-5																						
BD730	54.79	0.21	0.11	0.02	2.29	0.20	1.33	0.02	2.16	0.11	0.07	0.01	0.05	0.01	17.25	0.13	20.55	0.25	1.56	0.113519	93.44	28.02
BD738	55.10	NA	0.42	NA	3.51	NA	1.11	NA	2.17	NA	0.09	NA			16.00	NA	18.40	NA	2.21	NA	92.93	17.50
BD794	54.48	0.59	0.09	0.08	2.56	0.51	2.11	0.25	2.15	0.59	0.07	0.04			16.39	1.03	18.68	0.65	2.13	0.511224	93.14	35.61
BD797																						
BD822																						
TH17	53.67	0.41	0.66	0.02	2.72	0.03	2.01	0.08	3.31	0.05	0.10	0.02			16.71	0.16	18.15	0.15	1.90	0.0494	90.00	33.16
BP1	52.37	0.45	0.09	0.01	5.73	0.18	1.04	0.08	2.41	0.05	0.11	0.02			15.83	0.18	20.50	0.12	1.24	0.05	92.14	10.86
TH33	53.71	0.36	0.12	0.06	2.35	0.33	2.35	0.14	2.71	0.07	0.09	0.01			17.27	0.28	18.11	0.09	1.57	0.07	91.91	40.08
J1	50.93	0.55	0.51	0.02	4.61	0.22	1.02	0.12	2.73	0.08	0.09	0.02	0.04	0.01	15.61	0.18	22.49	0.22	0.50	0.03	91.06	12.95
KG3619.7	50.44	0.11	1.26	0.02	7.31	0.11	0.40	0.04	6.02	0.14	0.14	0.01	0.00	0.00	13.85	0.09	18.62	0.02	1.67	0.019551	80.40	3.52
L7201.1.74c	48.64	0.44	1.28	0.10	8.97	0.58			6.77	0.36	0.16	0.01	0.04	0.01	14.69	0.21	17.93	0.99	1.24	0.28	79.47	
R5194.2I	48.40	0.67	1.50	0.27	8.51	0.52	0.20	0.17	5.98	0.40	0.14	0.02	0.01	0.01	13.45	0.21	19.56	0.62	1.02	0.14	80.04	1.56
R5194.2M	48.26	0.25	1.58	0.09	8.42	0.33	0.13	0.03	6.59	0.43	0.17	0.01	0.02	0.01	13.30	0.29	19.14	0.46	1.11	0.16	78.26	1.06
MM6	51.27	0.26	0.67	0.03	5.33	0.11	1.23	0.20	4.13	0.10	0.11	0.02	0.02	0.10	16.97	0.15	18.46	0.24	1.04	0.038445	87.99	13.37
DW5	51.22	0.49	0.79	0.08	5.59	0.55	1.13	0.15	4.48	0.23	0.11	0.03	0.04	0.18	16.33	0.50	18.80	0.64	0.97	0.07	86.67	11.90
KH1	48.48	0.35	1.14	0.20	8.74	0.32	0.02	0.01	6.85	0.25	0.17	0.03	0.02	0.01	14.19	0.29	18.15	0.45	1.11	0.23	78.70	0.13
LT14	52.66	0.48	0.34	0.04	7.21	0.70	0.71	0.05	2.46	0.07	0.07	0.02	0.07	0.02	14.26	0.40	19.45	0.14	2.32	0.100275	91.18	6.16
LT15	51.47	0.42	0.27	0.01	4.66	0.29	0.44	0.05	3.87	0.33	0.12	0.03	0.00	0.04	15.26	0.59	22.71	0.87	0.44	0.038039	87.56	5.92
CP62																						
BD816	54.03	0.39	0.14	0.11	2.25	0.93	1.72	0.75	2.03	0.22	0.06	0.03	0.02	0.00	16.53	1.39	19.69	.1.14	1.62	0.63	93.55	33.93
BD3847	52.70	NA	1.04	NA	2.27	NA	0.06	NA	5.06	NA	0.12	NA			15.30	NA	21.10	NA	1.04	NA	84.35	1.74

Table 4. Spinel Major Element Chemistry (wt.% oxide)

Sample	SiO2	st.dev	TiO2	st.dev	Al2O3	st.dev	Cr2O3	st.dev	FeO	st.dev	MnO	st.dev	NiO	st.dev	MgO	st.dev	CaO	st.dev	Na2O	st.dev	Mg#	Cr#
KG3610.10A	0.06	0.03	0.02	0.01	22.68	5.18	48.49	5.63	10.32	1.22	2.19	0.49	0.13	0.02	16.08	1.22	0.18	0.03	0.03	0.02	73.52	58.92
KG3609.21	0.04	0.01	0.02	0.01	30.26	0.34	39.32	0.49	13.60	0.20	0.15	0.02			15.74	0.13					67.36	46.57
KG3719.25	0.05	0.01	0.11	0.01	55.45	0.36	12.19	0.15	10.74	0.17	0.09	0.02			19.80	0.27	0.01	0.00	0.01	0.00	76.67	12.85
L7.201.1.41	0.05	0.01	0.13	0.01	51.71	0.67	15.29	0.69	9.48	0.34	2.78	0.33	0.34	0.02	19.53	0.23	0.01	0.00			78.59	16.55
BN	0.05	0.01	0.13	0.01	58.22	0.17	8.82	0.10	10.84	0.15	0.10	0.03			20.44	0.11		0.01			77.07	9.23
DW3	0.04	0.01	0.08	0.00	33.90	0.98	33.55	1.33	13.92	0.32	0.15	0.03		0.03	17.33	0.43		0.01			68.93	39.90
DW7	0.14	0.02	0.31	0.09	39.54	1.04	26.78	1.06	13.21	0.35	0.12	0.05		0.03	18.76	0.17		0.01			71.68	31.24
DW8	0.06	0.01	0.08	0.01	44.73	0.27	21.12	0.15	13.58	0.13	0.14	0.05		0.03	18.82	0.15		0.01			71.18	24.06
DW10	0.06		0.32		30.67		33.84		18.14		0.21				15.83						60.86	42.53
MM5	0.09	0.06	0.44	0.13	36.44	2.07	30.03	2.15	13.27	0.30	0.14	0.02		0.02	18.11	0.26		0.04			70.88	35.60
MM8	0.13	0.01	0.57	0.12	29.90	0.72	36.67	0.30	14.34	0.41	0.12	0.06		0.03	17.14	0.16		0.01			68.05	45.14
MM11	0.05	0.02	0.03	0.01	42.14	0.62	23.94	0.27	14.21	0.13	0.14	0.04		0.03	17.97	0.22		0.01			69.27	27.60
G17	0.05	0.01	0.09	0.00	34.02	0.09	30.39	0.28	17.76	0.21	0.16	0.03		0.04	16.29	0.15		0.01			62.05	37.47
G18																						
KH2	0.08	0.04	0.09	0.02	58.13	1.30	9.55	0.36	11.31	0.44	0.07	0.11		0.17	20.76	0.52		0.02			76.59	9.93
KH3D	0.11	0.01	0.14	0.01	39.80	0.16	26.92	0.15	12.62	0.16	0.12	0.01		0.01	18.72	0.07		0.01			72.56	31.21
KH4	0.06	0.04	0.12	0.00	58.59	1.05	9.94	0.42	11.26	0.42	0.08	0.03		0.07	21.19	0.39		0.02			77.03	10.22
KH5	0.07	0.05	0.10	0.04	59.06	3.14	8.67	1.07	10.34	4.38	0.16	0.10		2.12	20.83	0.16		0.11			78.22	8.96
TM1	0.04	0.01	0.09	0.01	58.12	0.08	8.98	0.14	10.20	0.13	0.11	0.02		0.04	20.53	0.10		0.01			78.21	9.39
TM2	0.11	0.05	0.26	0.15	57.09	1.82	10.18	1.80	10.66	0.17	0.09	0.04		0.07	21.14	0.13		0.02			77.95	10.68
TM3	0.09	0.01	0.19	0.00	58.34	0.14	8.27	0.09	11.01	0.22	0.09	0.05		0.03	20.55	0.13		0.01			76.90	8.69
TM4	0.05	0.02	0.12	0.01	54.90	0.18	12.54	0.27	10.33	0.13	0.06	0.02		0.05	20.19	0.14		0.03			77.70	13.29
CP31																						
CP33	0.06	0.01	0.58	0.01	40.26	0.19	25.30	0.29	14.70	0.33	0.10	0.03		0.03	17.48	0.13		0.01		0.01	67.95	29.66
LT1	0.17	0.12	0.11	0.10	48.48	2.55	15.77	0.11	12.16	0.15	0.10	0.06			18.01	1.37					72.52	17.91
LT16	0.09	0.01	0.65	0.01	24.67	0.08	41.14	0.14	15.48	0.17	0.16	0.02			16.08	0.10					64.94	52.80
PA3-5	0.13	0.05	0.50	0.08	23.45	0.23	44.08	0.17	13.86	0.17	0.14	0.03			15.91	0.14					67.17	55.78
BD730	0.15	0.14	0.09	0.07	55.83	1.23	12.59	1.29	10.29	0.26	0.20	0.02			20.74	0.19					78.22	13.14
BD738																						
BD794																						
BD797			1.51	NA	14.50	NA	53.90	NA	15.90	NA	0.18	NA			15.10	NA					62.86	71.38
BD822			0.98	NA	13.70	NA	54.90	NA	15.50	NA	0.25	NA			15.20	NA					63.61	72.89
TH17																						
BP1	0.02	0.01	0.12	0.02	47.70	0.25	17.39	0.15	13.82	0.17	0.13	0.02	0.34	0.04	18.75	0.14					70.75	19.65
TH33	0.15	0.03	0.65	0.03	12.69	0.22	54.59	0.45	16.67	0.19	0.22	0.02	0.15	0.03	13.90	0.19					59.79	74.27
J1																						
KG3619.7																						
L7201.1.74c	0.17	0.00	0.57	0.02	61.35	0.12	0.03	0.00	13.22	0.19	6.62	0.27	0.16	0.01	19.18	0.08	0.11	0.01			72.10	0.03
R5194.2l	0.08	0.01	0.39	0.22	60.27	1.23	0.68	0.10	14.20	1.39	5.73	0.77	0.12	0.01	17.86	0.87	0.13	0.01			69.15	0.75
R5194.2M	0.07	0.01	0.49	0.00	58.05	0.09	1.55	0.07	16.19	0.15	6.50	0.32	0.12	0.01	16.36	0.16	0.15	0.01			64.29	1.76
MM6	0.11	0.01	1.15	0.02	36.15	0.47	26.18	0.50	18.14	0.22	0.16	0.04	0.25	0.03	16.89	0.12						
DW5																						
KH1	0.12	0.01	0.52	0.05	59.58	1.13	0.00	0.00	20.21	0.60	0.13	0.03	0.09	0.02	17.73	0.19					61.00	0.00
LT14	0.04	0.01	0.12	0.00	43.69	0.75	23.23	0.66	13.00	0.35	0.11	0.04		0.04	17.55	0.32					70.64	26.29
LT15																						
CP62	0.07	0.02	1.38	0.05	41.44	0.70	19.35	0.51	19.96	0.54	0.11	0.02			15.88	0.32					58.65	23.85
BD816																						
BD3847			13.00	NA	4.98	NA	13.00	NA	32.00	NA	0.20	NA			7.70	NA					30.02	63.65

Table 5. Garnet Major Element Chemistry (wt.% oxide)

Sample	SiO2	st.dev	TiO2	st.dev	Al2O3	st.dev	Cr2O3	st.dev	FeO	st.dev	MnO	st.dev	NiO	st.dev	MgO	st.dev	CaO	st.dev	Na2O	st.dev	Mg#	Cr#
CP31	42.68	NA	0.17	NA	23.02	NA	0.97	NA	7.40	NA	0.32	NA	0.01	NA	20.49	NA	4.81	NA	0.01	NA	83.15	2.75
CP33	42.52	0.17	0.19	0.01	22.91	0.14	1.25	0.15	7.72	0.10	0.32	0.03	0.01	0.02	20.91	0.13	4.77	0.07	0.03	0.01	82.84	3.54
BD730	42.33	0.17	0.10	0.01	21.92	0.14	3.09	0.07	7.52	0.12	0.37	0.02			20.76	0.22	5.25	0.03	0.02	0.01	83.11	8.65
BD738	42.90	NA	0.42	NA	22.30	NA	2.18	NA	7.04	NA	0.32	NA			21.40	NA	4.53	NA	0.05	NA	84.42	6.15
BD794	42.33	0.33	0.04	0.04	21.09	0.11	4.60	0.10	6.50	0.11	0.32	0.01			21.33	0.25	5.20	0.09			85.40	12.76
BD797	41.50	NA	0.19	NA	20.70	NA	4.49	NA	6.15	NA	0.33	NA			21.90	NA	4.39	NA	0.05	NA	86.39	12.70
TH17	41.49	0.77	0.73	0.03	19.51	0.26	4.49	0.19	7.77	0.36	0.33	0.02			20.25	0.35	5.31	0.15	0.07	0.02	82.29	13.38
TH33	40.99	0.55	0.19	0.02	16.93	0.18	7.49	0.22	6.45	0.24	0.31	0.03	0.01	0.00	21.00	0.19	6.24	0.34	0.06	0.01	85.30	22.89
CP62	41.94	0.13	0.28	0.02	22.74	0.13	0.87	0.24	10.31	0.23	0.34	0.03			19.54	0.12	4.45	0.05	0.03	0.01	77.16	2.51

Table 6. Amphibole Major Element Chemistry (wt.% oxide)

Sample	SiO2	st.dev	TiO2	st.dev	Al2O3	st.dev	Cr2O3	st.dev	FeO	st.dev	MnO	st.dev	NiO	st.dev	MgO	st.dev	CaO	st.dev	Na2O	st.dev	Mg#	Cr#
L7.201.1.41	42.18	0.50	2.29	0.03	14.36	0.19	1.45	0.05	4.18	0.13	0.07	0.02	0.13	0.04	16.63	0.25	10.97	0.08	3.15	0.08	87.64	6.34
DW10	43.20	0.24	0.93	0.02	13.15	0.12	1.85	0.04	4.13	0.12	0.10	0.08	0.12	0.03	17.86	0.17	11.13	0.04	2.87	0.08	88.52	8.63
MM11	42.66	0.28	0.39	0.02	14.21	0.13	1.84	0.09	4.03	0.08	0.07	0.06	0.12	0.04	17.86	0.05	10.89	0.05	3.00	0.05	88.77	8.01
BD3847	43.20	NA	3.58	NA	10.60	NA	0.15	NA	7.42	NA	0.11	NA			16.40	NA	11.00	NA	3.19	NA	79.76	0.94

Table 7. Mica Major Element Chemistry (wt.% oxide)

Sample	SiO2	st.dev	TiO2	st.dev	Al2O3	st.dev	Cr2O3	st.dev	FeO	st.dev	MnO	st.dev	NiO	st.dev	MgO	st.dev	CaO	st.dev	Na2O	st.dev	K2O	st.dev	Mg#	Cr#
L7.201.1.41	37.31	0.33	3.57	0.05	16.81	0.17	1.29	0.03	4.43	0.05	0.02	0.02	0.22	0.01	20.92	0.06	0.13	0.02	0.89	0.02	9.44	0.05	89.37	4.90
TM2	37.87	0.01	5.77	0.05	16.54	0.12	0.88	0.00	4.41	0.10	0.05	0.01	0.25	0.05	19.93	0.13	0.03	0.01	0.04	0.01	10.07	0.09	88.96	3.45
TH17	40.17	0.29	3.26	0.03	13.60	0.07	1.33	0.07	4.30	0.12	0.03	0.03	0.23	0.02	23.06	0.08	0.03	0.02	0.20	0.04	10.45	0.18		
BD738	40.00	NA	9.13	NA	13.50	NA	0.71	NA	3.57	NA	0.04	NA	0.24	NA	18.70	NA			0.06	NA	9.64	NA	90.33	3.41
CP62	38.49	0.49	5.04	0.06	15.52	0.17	0.52	0.03	5.63	0.17	0.02	0.05			20.21	0.20	0.09	0.02	0.68	0.05	9.53	0.30	86.48	2.20
BD816	39.60	NA	3.53	NA	11.60	NA	0.42	NA	5.39	NA	0.04	NA			21.90	NA			0.19	NA	10.60	NA	87.87	2.37
BD3847	37.20	NA	4.18	NA	14.20	NA	0.11	NA	7.51	NA	0.06	NA			20.10	NA			1.14	NA	9.03	NA	82.67	0.52

Table 8. Ilmenite Major Element Chemistry (wt.% oxide)

Sample	SiO2	st.dev	TiO2	st.dev	Al2O3	st.dev	Cr2O3	st.dev	FeO	st.dev	MnO	st.dev	NiO	st.dev	MgO	st.dev	CaO	st.dev	Na2O	st.dev	Mg#	Cr#
TH17	0.04	0.01	48.97	4.70	1.68	1.25	9.28	4.95	26.43	1.53	0.21	0.06	0.30	0.05	13.57	0.54	0.03	0.03			47.79	0.01

Table 9. Clinopyroxene Trace Element chemistry of concentration (ppm wt%) and Standard deviation in (ppm wt%) for KH1, KH2, KH3D, KH4, KH5, BP1, TH17 and TH33.

	KH1		KH2		KH3D		KH4		KH5		BP1		TH17		TH33	
Element	**Concentration**	**StDev**	**Concentration**	**StDev**	**Concentration**	**StDev**	**Concentration**	**StDev**	**Concentration**	**StDev**	**Concentration**	**StDev**	**Concentration**	**StDev**	**Concentration**	**StDev**
Li7	1.3267	0.1732	1.5606	0.0660			1.5117	0.0520	2.2389	0.4285	7.6167	2.7642			1.1911	0.4462
Al27	46678	628	45202	1905			46147	1143	43622	364	39829	1322				
Si29	210751	5934	225738	7319	241900	3338	222559	4568	211835	1717	260262	5323	252417	0	279959	26378
K39					43.1533	3.5506							157.6878	5.3905		
Ca43	125073	0	140796	0	134120	2351	139367	0	138938	0	157234	0	118814	1222	129456	2190
Sc45	56.0178	0.9576	67.9989	2.5105	47.1425	0.4995	69.5133	1.1778	67.2922	1.9963	55.6900	3.5557	20.8944	0.3484	20.3744	1.8763
Ti47	7269	312	4102	58	836	38	4611	68	2796	49	678	43	4035	120	648	201
V51	323.0133	11.0193	257.6522	4.7035	204.7033	1.8720	256.9633	0.9876	249.8167	3.1891	219.8911	7.1657	314.1978	9.5247	269.8367	14.5838
Fe57	48064	1550	15624	625	16360	1457	15114	321	16913	221	14189	185	18031	816	17159	906
Co59	37	2	21	1	27	0	20	0	21	1	24	1	24	0	12299	1751
Ni60	74.4978	3.1046	307.1689	6.9246	430.8225	3.7465	311.0456	6.5386	332.4489	7.2681	375.3622	10.3961	409.1600	5.3158	30.0022	1.4776
Sr88	57.1400	0.9241	17.9822	1.1399	25.6350	0.9588	45.2267	1.0764	17.6356	2.1699			138.0733	3.4591	501.3478	30.6881
Rb85															87.8644	12.9759
Y89	14.1122	0.1500	18.9933	0.4397	5.7842	0.0554	20.4856	0.5762	19.2100	0.2916	7.9456	0.2249	3.5478	0.2420	0.8489	0.6100
Zr90	27.6578	0.7893	14.2244	0.3455	8.4442	0.4033	26.1333	0.4251	10.8700	0.2368	0.0899	0.0434	30.5400	0.2938	8.5944	2.8919
Nb93	0.2844	0.0266			0.6142	0.0233			0.2300	0.0283			0.1828	0.0154	0.4828	0.3544
Ba137	0.1335	0.0692	0.0769	0.0165	0.8881	0.2637	0.1229	0.0456	0.1468	0.0193	0.0814	0.0267	0.1702	0.0173	5.7622	10.3163
La139	1.7889	0.0310	0.2476	0.0850	0.8100	0.0674	0.5844	0.0283	0.2173	0.0599	0.0079	0.0046	2.4044	0.0455	1.7456	1.1646
Ce140	6.7411	0.1667	0.9522	0.0535	2.4983	0.0741	2.4878	0.0491	0.5431	0.1071			10.1422	0.2708	6.3667	3.2281
Pr141	1.2522	0.0038	0.3170	0.0118	0.3972	0.0146	0.5733	0.0153	0.1436	0.0044	0.0037	0.0014	1.7852	0.0423	0.9500	0.4397
Nd143	7.4078	0.2392	2.5900	0.0874	2.0217	0.0573	3.7911	0.0905	1.3533	0.0338	0.0428	0.0157	9.5800	0.3312	4.7444	2.1422
Sm147	2.4589	0.0643	1.4344	0.0707	0.5512	0.0530	1.7189	0.1262	1.0500	0.0404	0.0682	0.0222	2.4400	0.0769	1.0267	0.5137
Eu153	0.8878	0.0624	0.6089	0.0236	0.1947	0.0081	0.7089	0.0366	0.4970	0.0292	0.0520	0.0093	0.7892	0.0137	0.2613	0.1253
Gd157	2.9367	0.1185	2.4844	0.0901	0.7341	0.0360	2.8689	0.1720	2.0733	0.1235	0.4178	0.0417	1.9444	0.0051	0.5644	0.3264
Tb159	0.4400	0.0200	0.4689	0.0204	0.1323	0.0108	0.4989	0.0334	0.4418	0.0106	0.1287	0.0088	0.2332	0.0163	0.0553	0.0292
Dy163	2.9678	0.2310	3.4967	0.2065	0.9966	0.0331	3.8844	0.0849	3.4211	0.0448	1.1756	0.1385	1.1441	0.0447	0.2796	0.1604
Ho165	0.5711	0.0158	0.7633	0.0240	0.2276	0.0065	0.8567	0.0578	0.7778	0.0212	0.3081	0.0283	0.1522	0.0159	0.0294	0.0174
Er166	1.4733	0.0833	2.2500	0.0736	0.6835	0.0193	2.3833	0.0649	2.2744	0.0517	1.0111	0.0860	0.2977	0.0335	0.0716	0.0377
Tm169	0.2006	0.0112	0.3378	0.0150	0.1022	0.0043	0.3633	0.0100	0.3456	0.0146	0.1583	0.0125	0.0285	0.0015	0.0100	0.0069
Yb172	1.2789	0.0905	2.1678	0.0888	0.6890	0.0189	2.2789	0.0342	2.2756	0.0255	1.1578	0.0250	0.1430	0.0164	0.0513	0.0393
Lu175	0.1672	0.0114	0.2991	0.0078	0.0955	0.0043	0.3356	0.0077	0.3321	0.0175	0.1761	0.0050	0.0141	0.0023	0.0064	0.0045
Hf178	1.2767	0.0145	0.7056	0.0077	0.2567	0.0095	1.0800	0.0524	0.5389	0.0559	0.0103	0.0056	1.6706	0.0675	0.5200	0.1748
Ta181	0.0570	0.0085	0.0051	0.0031	0.0417	0.0038	0.0202	0.0016	0.0178	0.0049	0.0026	0.0014	0.0140	0.0010	0.0322	0.0162
Pb208	0.0755	0.0416	0.0298	0.0108	0.0290	0.0095	0.0156	0.0162	0.0350	0.0182	0.0102	0.0089	0.1368	0.0160	0.2295	0.0867
Th232	0.0333	0.0060	0.1769	0.1181	0.0542	0.0030	0.0206	0.0116	0.0146	0.0053			0.0304	0.0011	0.1307	0.2178
U238	0.0093	0.0023	0.0270	0.0030	0.0160	0.0034	0.0083	0.0066	0.0037	0.0007			0.0073	0.0015	0.0303	0.0361

Table 10. Clinopyroxene Trace Element chemistry of concentration (ppm wt%) and Standard deviation in (ppm wt%) for TM1, TM2, TM3, TM4, DW3, DW5, DW7 and DW8

	TM1		TM2		TM3		TM4		DW3		DW5		DW7		DW8	
Element	**Concentration**	**StDev**	**Concentration**	**StDev**	**Concentration**	**StDev**	**Concentration**	**StDev**	**Concentration**	**StDev**	**Concentration**	**StDev**	**Concentration**	**StDev**	**Concentration**	**StDev**
Li7			1.1744	0.0605	1.4022	0.0670					1.2456	0.2350	0.8700	0.0467	0.6744	0.0652
Al27			40261	1206	41607	827							31435	388	20894	129
Si29	240731	0	224672	8196	213233	4702	240731	0	250703	2399	23501	292	223717	4130	235166	1690
K39	0.9950	0.3323					2.9667	3.4231	9.7022	2.6780						
Ca43	136561	6705	137937	0	135793	0	91849	77589	131363	10295	13439	144	131505	0	157234	0
Sc45	61.6333	2.3146	67.7844	5.1224	67.6700	0.8894	45.5500	27.9052	68.7622	2.6434	54.3848	1.0981	48.7600	2.2292	75.2300	2.6376
Ti47	3549	96	4440	227	4648	51	2618	1614	479	51	4964	269	1398	18	1093	19
V51	267.7717	11.3585	263.5522	17.5733	265.4078	8.5160	210.1278	100.1647	211.5911	12.0573	285.1429	2.5721	212.9667	2.9198	212.3433	2.9450
Fe57	17236	886	15431	713	17223	715	24442	12496	25572	2557	8080	1202	20057	845	16147	309
Co59	17	0	22	2	22	1	28	20	21	2	23332	581	27	0	18	1
Ni60	282.4883	12.2730	347.9011	17.0412	371.1267	39.3314	393.7111	192.8389	358.9567	25.9286	36.1111	1.3560	449.9833	13.4649	315.6144	6.9101
Sr88	58.1250	1.8880	79.6256	3.2052	95.5767	4.4767	38.8441	33.4222	319.4922	10.9385	394.7651	3.9440	43.1200	7.9805	172.2689	2.8565
Rb85											47.7916	4.9776				
Y89	16.1900	0.0990	20.0611	0.8885	19.6767	0.3868	10.9994	8.9906	10.5611	1.3210	9.0407	0.5908	8.7511	0.2030	7.7878	0.1422
Zr90	22.4867	0.0707	34.8056	2.7209	36.7344	0.6599	15.2599	12.5172	38.8256	6.9694	25.9904	1.5677	7.6444	0.3762	11.7411	0.7270
Nb93	0.2572	0.0243	0.2162	0.0550	0.6700	0.1033	0.1819	0.1315	0.8428	0.1896	0.6253	0.2877	0.4893	0.0339	0.4161	0.0490
Ba137	0.0175	0.0016	0.0486	0.0222	0.1218	0.0965	0.0280	0.0183	0.1266	0.0194	4.2291	3.3916	0.1964	0.0478	0.0833	0.0169
La139	0.7728	0.0412	1.1433	0.1213	1.8811	0.1655	0.5165	0.4450	22.1456	1.3492	2.9010	0.3706	1.9089	0.5209	20.6411	0.6234
Ce140	2.7850	0.1108	4.0200	0.1762	5.4656	0.2560	1.8629	1.5990	59.7756	2.6545	10.3710	1.1369	5.3633	1.0196	32.2300	0.6240
Pr141	0.4847	0.0198	0.7589	0.0269	0.9244	0.0575	0.3236	0.2794	6.7167	0.2924	1.8011	0.1294	0.6909	0.1276	2.9222	0.0453
Nd143	3.0417	0.0354	4.5744	0.1059	5.2767	0.1157	2.0316	1.7497	24.2356	2.1374	9.6060	0.4697	3.1278	0.1314	9.9267	0.1244
Sm147	1.3817	0.0401	1.8500	0.0862	2.0133	0.0186	0.9257	0.7903	3.8544	0.3870	2.8229	0.2584	0.8378	0.0587	1.7022	0.0790
Eu153	0.5863	0.0066	0.7178	0.0102	0.7767	0.0633	0.3936	0.3339	1.1047	0.1144	0.9606	0.0505	0.3148	0.0219	0.5052	0.0228
Gd157	2.1067	0.0141	2.6500	0.1073	2.7678	0.0631	1.4132	1.2011	2.8100	0.3520	2.6867	0.2387	1.1533	0.0418	1.5222	0.0367
Tb159	0.3872	0.0082	0.5043	0.0451	0.5157	0.0088	0.2602	0.2200	0.3729	0.0380	0.3684	0.0259	0.2322	0.0091	0.2218	0.0123
Dy163	2.8250	0.0448	3.6633	0.2052	3.7667	0.0555	1.9080	1.5886	2.1333	0.2292	2.2090	0.1865	1.6867	0.0115	1.5022	0.0574
Ho165	0.6170	0.0009	0.7911	0.0336	0.7911	0.0190	0.4185	0.3438	0.3972	0.0290	0.3661	0.0187	0.3662	0.0198	0.3071	0.0065
Er166	1.8700	0.0141	2.2422	0.0383	2.3111	0.0301	1.2790	1.0237	1.0831	0.0850	0.9154	0.0676	1.0856	0.0417	0.8489	0.0403
Tm169	0.2703	0.0038	0.3254	0.0175	0.3486	0.0049	0.1873	0.1438	0.1517	0.0162	0.1162	0.0045	0.1384	0.0091	0.1197	0.0035
Yb172	1.8517	0.0401	2.0778	0.0734	2.2567	0.0814	1.2902	0.9729	1.0217	0.1608	0.6837	0.0998	0.9856	0.0763	0.8356	0.0171
Lu175	0.2685	0.0082	0.3022	0.0138	0.3212	0.0082	0.1921	0.1324	0.1372	0.0206	0.0886	0.0049	0.1386	0.0151	0.1224	0.0044
Hf178	0.7270	0.0325	1.0833	0.1272	1.1744	0.0647	0.4957	0.4013	0.5496	0.1469	1.3701	0.1181	0.3409	0.0270	0.3239	0.0527
Ta181	0.0233	0.0014	0.0146	0.0051	0.0158	0.0026	0.0161	0.0124	0.1072	0.0192	0.0570	0.0028	0.0616	0.0245	0.1529	0.0148
Pb208	0.0465	0.0016	0.1198	0.0411	0.2293	0.0047	0.0339	0.0218	0.4187	0.0429	0.1512	0.0334	0.0501	0.0201	1.1967	0.0570
Th232	0.0231	0.0011	0.0209	0.0029	0.1047	0.0153	0.0157	0.0128	0.9240	0.1343	0.0598	0.0191	0.0789	0.0229	2.4800	0.0666
U238	0.0099	0.0000	0.0057	0.0012	0.0314	0.0066	0.0070	0.0050	0.1911	0.0234	0.0142	0.0095	0.0174	0.0081	0.6289	0.0434

Table 11. Clinopyroxene Trace Element chemistry of concentration (ppm wt%) and Standard deviation in (ppm wt%) for DW10, MM5, MM6, MM8, MM11, G17, G18 and KG3610.10.

	DW10		MM5		MM6		MM8		MM11		G17		G18		KG3610.10A	
Element	Concentration	StDev	Concentration	StDev	Concentration	StDev	Concentration	StDev	Concentration	StDev	Concentration	StDev	Concentration	StDev	Concentration	StDev
Li7					1.1922	0.0084	1.4783	0.5789	1.3789	0.2635	1.4554	0.2995	0.8650	0.2428		
Al27	19486	1112			30035	1036			28719	5973			22448	660		
Si29	224574	10770	242757	2699	227437	8025	26898	211	222283	5212	25483	330	263926	1818		
K39			10.3017	6.0087												
Ca43	150087	0	138380	2062	132220	0	12954	25	144370	0	12943	14	160093	0		
Sc45	44.0833	2.3432	62.2800	0.6416	49.4911	1.0699	52.4140	0.9235	70.9956	0.8540	52.2617	1.1064	90.6783	7.4364		
Ti47	1146	14	2777	246	4479	241	1971	26	534	170	1917	32	2607	217		
V51	189.8444	9.5895	299.9267	24.2150	250.9356	1.8072	256.0130	1.6065	171.2178	27.5798	245.1814	5.1013	220.3900	20.3222		
Fe57	15375	1095	21254	688	24099	682	13315	201	15591	662	11927	483	16749	1978		
Co59	21	1	21	1	30	0	16216	65	22	1	16194	401	21	3		
Ni60	308.2544	11.1403	366.3389	19.0554	387.8067	25.4645	36.7515	0.0757	351.5256	18.7372	37.2741	2.4053	357.5750	43.7157		
Sr88	377.1256	27.0936	177.6178	3.4070	82.3289	6.9301	662.7875	14.5445	285.8456	11.4977	833.9872	423.7905	103.2233	26.2195	212.8364	109.6387
Rb85							90.7595	1.9057			80.0632	2.0662			1.3358	1.7800
Y89	11.8678	0.3742	15.1911	0.4423	7.1422	0.3900	11.7132	0.5018	10.3744	2.1637	11.7948	0.2493	8.8167	0.3158	4.7127	3.0469
Zr90	61.0778	5.3337	53.8422	2.7360	19.5500	1.8366	34.4195	0.1308	31.0678	11.4572	27.0079	1.8018	31.3200	10.6679	6.1936	5.8648
Nb93	1.5078	0.1421	0.7409	0.0848	0.3059	0.0502	0.8650	0.0754	1.4744	0.2362	0.8172	0.2326	0.2625	0.0686	0.3584	0.5310
Ba137	0.5084	0.4504	0.0492	0.0259	0.1098	0.0249	0.6700	0.5218	0.9588	0.6714			9.9733	1.1172	1.7023	3.0087
La139	11.1378	0.5698	11.4289	0.5201	2.7333	0.3673	5.8425	0.1567	20.9289	1.4047	4.9548	0.2011	12.4483	4.8484	14.7118	5.8977
Ce140	41.4367	2.1055	42.6511	2.1317	9.3722	0.9741	14.7388	0.2025	59.9233	4.9152	12.0241	0.8176	21.5133	9.5554	24.2682	11.8995
Pr141	6.2111	0.2367	6.6500	0.2411	1.5100	0.1172	2.0238	0.1402	7.9056	0.9425	1.5877	0.1168	1.5917	0.6010	2.2116	1.4162
Nd143	28.0211	1.1555	31.4500	0.8758	8.2722	0.7367	9.6085	0.3029	30.4744	4.6430	7.7491	0.3389	4.5500	1.3105	6.7427	4.9765
Sm147	5.6022	0.4784	6.1856	0.1761	2.3767	0.1049	2.6103	0.0962	4.3400	0.8150	2.1107	0.1092	0.9183	0.0259	0.9777	0.7726
Eu153	1.7222	0.0241	1.8389	0.0453	0.7422	0.0570	1.0147	0.1735	1.1978	0.2154	0.7277	0.0901	0.3437	0.0061	0.3918	0.3024
Gd157	4.3944	0.2388	4.6433	0.1475	2.1211	0.1022	2.5570	0.0519	2.8978	0.5401	2.3378	0.2857	1.1517	0.0684	0.7414	0.5650
Tb159	0.5567	0.0433	0.5857	0.0218	0.3101	0.0284	0.3877	0.0080	0.3674	0.1033	0.3662	0.0215	0.2188	0.0101	0.1086	0.0830
Dy163	3.1433	0.0684	3.3367	0.1136	1.8344	0.1049	2.5550	0.0434	2.2211	0.5210	2.7372	0.1721	1.6167	0.0424	0.7567	0.5435
Ho165	0.5378	0.0302	0.5709	0.0096	0.3139	0.0179	0.5075	0.0601	0.4033	0.1016	0.4867	0.0224	0.3347	0.0189	0.1604	0.1004
Er166	1.3456	0.0934	1.5189	0.0535	0.8189	0.1052	1.2032	0.1143	1.1500	0.2364	1.2911	0.0665	0.9933	0.0141	0.5548	0.3136
Tm169	0.1674	0.0135	0.2007	0.0035	0.0953	0.0033	0.1365	0.0016	0.1736	0.0410	0.1533	0.0025	0.1403	0.0071	0.0964	0.0491
Yb172	1.1278	0.1018	1.2811	0.0414	0.6100	0.0203	0.8417	0.0184	1.1167	0.2028	0.8030	0.0135	0.9683	0.0165	0.7416	0.3444
Lu175	0.1496	0.0088	0.1617	0.0090	0.0747	0.0115	0.1090	0.0104	0.1668	0.0307	0.1303	0.0091	0.1325	0.0111	0.1189	0.0514
Hf178	0.6822	0.0888	1.3711	0.2000	0.9756	0.0283	0.9798	0.0238	0.5372	0.2166	0.8550	0.0965	1.1033	0.3818	0.0725	0.0234
Ta181	0.2452	0.0122	0.1558	0.0183	0.0534	0.0237	0.1332	0.0139	0.3657	0.0615	0.1130	0.0155	0.0049	0.0003	0.0118	0.0061
Pb208	0.1728	0.0547	0.1946	0.0854	0.0917	0.0146	0.0610	0.0863	0.4256	0.0310	0.2212	0.2372	0.7233	0.0896	0.2788	0.0605
Th232	0.3118	0.0112	0.4112	0.0588	0.0483	0.0123	0.1278	0.0068	0.8689	0.1767	0.1341	0.0246	1.4967	0.4337		
U238	0.0584	0.0068	0.0951	0.0223	0.0098	0.0048	0.0351	0.0074	0.1504	0.0336	0.0339	0.0137	0.7050	0.1485	0.4574	0.0553

Table 12. Clinopyroxene Trace Element chemistry of concentration (ppm wt%) and Standard deviation in (ppm wt%) for KG3609.21, KG3719.25, L7.201.1.41, BN, L7.201.1.74c, R5194.I, R5194.M and CP33

	z		KG3719.25		L7.201.1.41		BN		L7.201.1.74c		R5194.I		R5194.M		CP33	
Element	Concentration	StDev	Concentration	StDev	Concentration	StDev	Concentration	StDev	Concentration	StDev	Concentration	StDev	Concentration	StDev	Concentration	StDev
Li7	0.6616	3.0800	1.3678	0.0320			1.3611	0.2287							1.1422	0.1183
Al27																
Si29	18449	263126	235972	14631			223860	12148							241997	6173
K39																
Ca43	0	159664	146871	0			144513	0							134292	0
Sc45	3.8289	73.1622	67.9089	2.2282			69.5289	2.1773							29.3167	1.4837
Ti47	17	49	2973	356			3789	259							3598	194
V51	10.3698	227.0833	285.6289	9.2165			286.2911	10.1770							319.0678	6.0991
Fe57	213	5470	5834	386			3765	154							6375	1267
Co59	3509	25304	31211	1943			37339	3546							18679	2427
Ni60	1.0876	25.5211	22.9178	0.9823			20.2078	0.2615							21.1256	0.8300
Sr88	16.0401	454.1900	358.5211	15.9333	137.2200	10.8794	325.8233	7.8120	66.4350	2.0140	81.5658	5.5871	85.4342	10.6723	346.7478	10.1824
Rb85	8.5499	127.8500	44.1544	4.2136	0.0129	0.0035	42.3556	3.3656	0.0043	0.0019	0.0183	0.0150	0.0676	0.0492	90.3233	0.6894
Y89	0.2849	1.1567	15.5567	1.0817	19.9180	1.6757	19.2044	0.6408	11.7733	0.4554	19.4533	1.5425	24.8708	2.0406	3.4178	0.1651
Zr90	0.6070	1.0478	18.3133	1.1543	62.9573	17.5003	23.4711	0.2497	32.2108	2.6982	54.2592	7.0351	79.8283	13.3320	22.4344	1.6608
Nb93	0.0802	0.3241	0.1738	0.0272	0.5361	0.1470	0.2029	0.0336	0.3268	0.0364	0.7924	0.0695	0.9264	0.2949	1.0622	0.1583
Ba137	0.0442	0.1148	0.0470	NA	0.0691	0.0356	0.7607	0.8077	0.0655	0.0608	0.0298	0.0170	0.0304	0.0128	0.1140	0.0583
La139	0.3510	4.1456	0.7772	0.0912	9.5320	0.4484	0.4421	0.0573	2.0033	0.1371	4.7525	0.9464	6.5017	1.9670	2.2756	0.1522
Ce140	1.1117	8.9667	2.8811	0.2525	22.6813	1.3867	2.0278	0.0367	7.6008	0.4942	15.0508	1.8041	20.9225	4.7847	6.2033	0.3025
Pr141	0.2239	0.8069	0.5268	0.0297	3.3940	0.2380	0.4838	0.0277	1.4958	0.0980	2.5852	0.2005	3.3067	0.4950	0.8822	0.0589
Nd143	0.5951	2.5478	3.1878	0.1750	15.0980	1.7125	3.6978	0.0336	8.5700	0.5618	13.9200	0.9690	17.2958	1.7572	4.2878	0.2344
Sm147	0.0379	0.1992	1.1978	0.0823	3.6747	0.5768	1.5622	0.1524	2.6458	0.1722	4.1692	0.2740	5.0642	0.2891	1.3944	0.1800
Eu153	0.0317	0.1030	0.5573	0.0480	1.1520	0.1858	0.6977	0.0452	0.9904	0.0722	1.4651	0.0948	1.7994	0.0911	0.5157	0.0602
Gd157	0.0465	0.1257	1.9944	0.2476	3.4893	0.7089	2.4756	0.0668	3.0400	0.1549	4.4192	0.3093	5.3883	0.4390	1.3533	0.2093
Tb159	0.0030	0.0132	0.3591	0.0201	0.5741	0.0937	0.4793	0.0270	0.4549	0.0264	0.6846	0.0455	0.8416	0.0799	0.2122	0.0005
Dy163	0.0207	0.1401	2.8689	0.2505	3.9127	0.5307	3.4556	0.2509	2.7742	0.1455	4.3042	0.3127	5.2842	0.4904	0.8722	0.0847
Ho165	0.0060	0.0454	0.6301	0.0384	0.7713	0.0815	0.7620	0.0495	0.4963	0.0386	0.8037	0.0772	0.9843	0.0789	0.1320	0.0324
Er166	0.0385	0.1172	1.7889	0.0765	2.2507	0.1658	2.1167	0.1155	1.1917	0.0669	2.1242	0.2071	2.6867	0.2691	0.3391	0.0216
Tm169	0.0053	0.0255	0.2390	0.0244	0.3123	0.0384	0.3184	0.0250	0.1494	0.0201	0.2784	0.0342	0.3528	0.0285	0.0290	0.0043
Yb172	0.0239	0.2201	1.5433	0.0994	2.0867	0.1725	1.8622	0.1103	0.9450	0.0903	1.8325	0.2121	2.3008	0.2292	0.1358	0.0188
Lu175	0.0099	0.0480	0.2221	0.0302	0.2921	0.0294	0.2914	0.0075	0.1174	0.0107	0.2356	0.0213	0.3174	0.0319	0.0217	0.0088
Hf178	0.0029	0.0212	0.6500	0.0260	1.4808	0.7576	0.9033	0.0555	1.5358	0.1046	2.1058	0.3925	2.7758	0.4372	0.9300	0.0441
Ta181	0.0089	0.0303	0.0150	0.0057	0.1503	0.0526	0.0052	0.0025	0.0655	0.0113	0.1608	0.0471	0.1914	0.0718	0.0204	0.0045
Pb208	0.0738	0.3639	0.2800	0.2135	0.1699	0.0356	0.3478	0.1331	0.1001	0.0876	0.1180	0.0321	0.1093	0.0321	0.2635	0.1303
Th232	0.0268	0.1977	0.0191	0.0020	0.6699	0.0698	0.0649	0.0137	0.5080	1.1144					0.1278	0.0202
U238	0.0035	0.1004	0.0172	0.0094	0.1831	0.0265	0.0651	0.0193	0.0088	0.0026	0.0847	0.0313	0.0820	0.0639	0.0431	0.0152

Table 13. Clinopyroxene Trace Element chemistry of concentration (ppm wt%) and Standard deviation in (ppm wt%) for CP62, LT1, LT16, LT14, LT15, BD730, BD794, BD816 and J1.

	CP62		LT1		LT16		LT14		LT15		BD730		BD794		BD816		J1	
Element	Concentration	StDev	Concentration	StDev	Concentration	StDev	Concentration	StDev	Concentration	StDev	Concentration	StDev	Concentration	StDev	Concentration	StDev	Concentration	StDev
Li7	1.6867	0.0330					14.0611	21.0176	0.8078	0.2045					0.6344	0.2467	1.1811	0.3287
Al27																		
Si29	295334	735					1165747	1536649	260155	5413					290654	15384	24416	685
K39																		
Ca43	4717	0					139009	NA	165811	NA					140748	8472	16071	102
Sc45	10.8633	0.0189	49.2495	2.9055	50.1442	3.7319	149.4089	157.0916	83.3722	1.6880					25.3567	15.8704	87.9624	2.8602
Ti47	2669	166	1058	74	988	126	4072	3610	1727	74					587	93	3274	63
V51	108.7017	1.3506	262.0170	10.0873	196.6450	11.0801	951.1389	1108.8636	263.8833	2.9550	49.0500	NA	39.5200	NA	368.5289	93.1748	417.4868	13.6502
Fe57	1694	1					20159	26381	3008	177					13881	7431	7866	207
Co59	99847	12202					394768	625224	31164	2000	109	NA	125	NA	12810	375	16128	1140
Ni60	85.5983	2.5809	352.6295	50.6713	445.5617	23.6826	487.5767	789.0963	28.1600	2.9653	2002.2002	NA	2256.0000	NA	24.4589	3.7804	23.7568	2.1805
Sr88	1196.7650	13.1923	9.0425	1.0380	26.0825	5.4976	7036.2344	11386.6125	138.0344	14.9734	44.1200	NA	10.7800	NA	449.1656	55.6980	386.0471	19.0303
Rb85			0.0265	0.0153	0.2495	0.0884	69.3189	2.4243	36.1322	1.3173	12.3200	NA	2.9500	NA	187.1078	68.1991	1.3134	0.0465
Y89	0.5167	0.0990	8.4210	0.5751	5.6942	0.4908	56.3722	57.8919	8.1322	0.1705	2.0700	NA	0.4300	NA	1.2711	0.6478	23.1469	2.5432
Zr90	12.0583	0.0024	2.6530	0.8754	56.3483	7.0601	26.7400	12.0107	5.8422	NA	14.2400	NA	3.5300	NA	35.6522	42.0986	12.5669	0.8540
Nb93			0.0432	0.0182	0.1517	0.0471	3.0456	4.4466	0.1800		5.6600	NA	1.1900	NA	0.4123	0.2175		
Ba137	0.4000		0.1003	0.1103	0.2901	0.0804	5.6500	2.2816			78.0300	NA	25.2400	NA	0.4310	0.0800		
La139	0.0303	0.0104	0.2830	0.0444	0.3272	0.0936	2.4489	0.9277	0.5079	0.0599	3.4600	NA	0.7600	NA	7.1878	6.9305		
Ce140	0.0341	0.0400	0.9874	0.0551	1.4750	0.2001	4.2689	1.4163	2.0900	0.0971	6.5600	NA	1.3100	NA	24.0511	22.9322	0.4656	0.0323
Pr141	0.0275	0.0241	0.1522	0.0211	0.3508	0.0575	0.6606	0.2492	0.4349	0.0127	0.7900	NA	0.1800	NA	2.6944	2.0342	0.2443	0.0174
Nd143	0.0850		0.9395	0.1363	2.4167	0.5167	3.8222	1.3373	2.4744	0.1800	2.9600	NA	0.6800	NA	9.9644	6.0846	2.6464	0.4013
Sm147	0.0610		0.5179	0.1079	1.2983	0.1488	1.7761	0.2483	1.0856	0.1172	0.5200	NA	0.1400	NA	2.0244	1.6185	1.8242	0.1298
Eu153	0.0231	0.0027	0.2596	0.0350	0.4881	0.0760	0.9233	0.4919	0.3956	0.0084	0.1500	NA	0.0400	NA	0.5457	0.4917	0.6631	0.1136
Gd157	0.0595	0.0092	0.8324	0.0913	1.7625	0.1608	4.0633	2.6426	1.3233	0.1656	0.4100	NA	0.1000	NA	1.1619	1.0066	2.9977	0.4342
Tb159	0.0086	0.0011	0.2001	0.0216	0.2808	0.0403	1.3167	1.4096	0.2354	0.0114	0.0600	NA	0.0100	NA	0.1085	0.1162	0.5913	0.0748
Dy163	0.0838	0.0144	1.4190	0.1105	1.5658	0.1569	8.7744	8.9026	1.5233	0.0693	0.3200	NA	0.0700	NA	0.4673	0.3405	4.5383	0.4179
Ho165	0.0165	0.0043	0.3377	0.0310	0.2421	0.0331	1.8730	1.7444	0.3334	0.0393	0.0700	NA	0.0100	NA	0.0557	0.0277	0.9564	0.0967
Er166	0.0422	0.0007	0.9485	0.1014	0.5342	0.0637	7.0178	6.9995	0.8589	0.0476	0.2000	NA	0.0400	NA	0.0952	0.0258	2.8889	0.3043
Tm169	0.0093	0.0059	0.1388	0.0143	0.0560	0.0087	0.8564	0.7787	0.1313	0.0072	0.0300	NA	0.0100	NA	0.0084	0.0016	0.3736	0.0301
Yb172	0.0442	0.0120	1.0005	0.1122	0.2345	0.0612	5.5778	5.1964	0.7222	0.0703	0.2300	NA	0.0600	NA	0.0320	0.0099	2.2769	0.3277
Lu175	0.0084	0.0011	0.1354	0.0179	0.0301	0.0119	0.8222	0.7554	0.1102	0.0163	0.0380	NA	0.0110	NA	0.0048	0.0027	0.3229	0.0329
Hf178	0.7583	0.0966	0.1618	0.0447	1.3725	0.1346	0.9578	0.3947	0.3066	0.0868	0.3200	NA	0.0800	NA	1.1766	1.4168	0.8971	0.1072
Ta181	0.0062	0.0025	0.0067	0.0055	0.0291	0.0112	0.0465	0.0212	0.0095	0.0039	0.3400	NA	0.1100	NA	0.0623	0.0495		
Pb208	0.0980	NA	0.0630	0.0323	0.0545	0.0225	0.3188	0.1644	0.3052	0.0634	0.6700	NA	0.2100	NA	0.9091	0.4716	0.0493	0.0065
Th232	0.0045	0.0001	0.0042	0.0023	0.0136	0.0079	0.1927	0.0512	0.0223	0.0087	0.4100	NA	0.0800	NA	0.1478	0.1856	0.0312	0.0044
U238	0.0073	0.0051	0.0039	0.0022	0.0070	0.0045	0.3426	0.5112	0.0191	0.0114	0.0900	NA	0.1400	NA	0.0407	0.0519	0.0147	0.0059

Table 14. Garnet Trace Element chemistry of concentration (ppm wt%) and Standard deviation in (ppm wt%).

	TH17		TH33		CP33		CP62		BD794		BD730	
Element	Concentration	StDev	Concentration	StDev	Concentration	StDev	Concentration	StDev	Concentration	StDev	Concentration	StDev
Li7			0.9200	0.6788	0.2555	0.0654	0.2411	0.0535	0.2053	0.0525	0.1733	0.0354
Al27												
Si29	191416	1653	185524	16684	226993	14759	211648	24076				
K39												
Ca43	33206	2011	46456	0	34091	0	31804	0				
Sc45	75	1	177	8	115	5	109	5	99	5		
Ti47	4432	34	1416	57	1378	117	2304	80	237	28	558	13
V51	227	2	295	26	99	4	92	7	205	6	191	6
Fe57	36695	982	42389	2270	9166	439	3749	518				
Co59	39.9	0.5	110801	15755	62574	6925	109284	14236				
Ni60	69.6733	1.3576	43.5550	2.0105	47.1300	3.7464	54.0922	3.4613	52.9833	2.0006	41.4000	1.0819
Sr88	0.4035	0.0337	112.9833	29.9295	59.2322	1.7287	69.1933	6.0276	0.8333	1.0640		
Rb85			1.3433		0.8300		3.6700		1.7333	0.9790	0.2933	0.0849
Y89	26.7550	0.3559	10.5000	2.0318	34.3611	1.3066	31.3700	1.4607	2.3700	0.1819	7.4167	0.2828
Zr90	64.7450	0.1296	55.5900	12.0114	24.7311	0.3181	162.8167	18.2206	6.5333	2.5702	8.1700	0.4313
Nb93	0.1513	0.0066	0.5000	0.1838	0.2750	0.0427	0.1305	0.0148	0.4700	0.1039	0.2967	0.0000
Ba137	0.0273	0.0018	0.6800		0.1915	0.2242	0.0693	0.0218	3.7200	4.8888	0.3733	0.0354
La139	0.0223	0.0083	0.1357	0.0297	0.0204	0.0048	0.0187	0.0025	0.2067	0.1060	0.0333	0.0000
Ce140	0.3052	0.0087	0.6082	0.1120	0.0825	0.0100	0.0398	0.0039	0.4667	0.1159	0.2400	0.0000
Pr141	0.1258	0.0035	0.1772	0.0163	0.0322	0.0053	0.0204	0.0093	0.1533	0.0153	0.0900	0.0141
Nd143	1.4317	0.0306	1.5300	0.3300	0.3753	0.0659	0.2386	0.0191	1.6533	0.0208	0.8000	0.0283
Sm147	1.3997	0.0618	1.0567	0.0283	0.6400	0.1450	0.4789	0.1254	0.4933	0.0115	0.4800	0.0495
Eu153	0.7213	0.0151	0.4843	0.0523	0.3786	0.0235	0.3173	0.0124	0.1467	0.0306	0.1767	0.0141
Gd157	2.9800	0.0471	1.6967	0.0141	1.9233	0.1214	1.7000	0.0882	0.2667	0.0987	0.5600	0.0707
Tb159	0.6167	0.0094	0.3547	0.0801	0.5333	0.0240	0.5356	0.0164	0.0433	0.0058	0.1033	0.0071
Dy163	4.7950	0.1014	2.0550	0.5586	4.7589	0.2898	5.0756	0.4696	0.3100	0.0458	0.9833	0.0849
Ho165	1.0605	0.0332	0.4415	0.0940	1.3167	0.1153	1.3211	0.1367	0.0867	0.0058	0.2733	0.0071
Er166	2.9650	0.0165	1.0717	0.2051	4.6233	0.1563	4.0411	0.3667	0.3267	0.0115	0.9633	0.0071
Tm169	0.4343	0.0179	0.1743	0.0396	0.6989	0.0369	0.5911	0.0369	0.0700	0.0000	0.1833	0.0071
Yb172	2.8517	0.0259	1.0750	0.0071	4.7622	0.1012	3.7344	0.3639	0.7033	0.0252	1.5033	0.0212
Lu175	0.3850	0.0179	0.1928	0.0106	0.8511	0.0184	0.5822	0.0369	0.1367	0.0153	0.2667	0.0071
Hf178	1.3662	0.0186	1.2917	0.0731	0.3444	0.0513	3.9156	0.7748	0.1067	0.0208	0.1433	0.0212
Ta181	0.0054	0.0022	0.0292	0.0115	0.0052	0.0006	0.0142	0.0050	0.0367	0.0058	0.0200	0.0000
Pb208	0.0095	0.0078	0.1620	0.1527	0.0785	0.0276	0.0765	0.0389	2.0900	3.4729	0.3533	0.2899
Th232	0.0033	0.0004	0.0168	0.0061	0.0042	0.0022	0.0076	NA	0.0100		0.0333	0.0071
U238	0.0056	0.0009	0.0275	0.0134	0.0137	0.0048	0.0114	0.0117	0.0800	0.0608	0.0367	0.0071

Table 15. Amphibole trace-element chemistry (ppm wt%)

	MM11		DW10	
	Concentration	StDev	Concentration	StDev
Li7			0.4800	0.0424
Al27	87269	3506	11637	804
Si29	184206	5230	117466	5956
K39				
Ca43	77902	0	79332	0
Sc45	60.0667	2.0953	22.0733	0.5877
Ti47	2726.4	58.4	669.7	74.2
V51	297.4833	6.0785	107.3600	4.6215
Fe57	20572	519	8563	609
Co59	38.4322	1.3026	10.9800	0.4498
Ni60	843.4289	28.0941	164.4667	4.8916
Sr88	588.8167	17.9841	200.9700	7.2683
Rb85	15.2878	6.6985		
Y89	13.8844	0.1746	6.5500	0.1058
Zr90	60.5300	1.1837	34.0733	0.5876
Nb93	157.7478	10.8763	1.3333	0.3940
Ba137	309.6522	85.9334	0.6767	0.1818
La139	27.7022	2.2625	6.2500	0.1311
Ce140	77.3067	4.7164	23.5100	0.1873
Pr141	10.3700	0.4441	3.4967	0.0723
Nd143	40.5789	0.2921	15.5700	0.2193
Sm147	5.8156	0.2665	3.1200	0.0361
Eu153	1.4578	0.0707	0.9733	0.0666
Gd157	3.9389	0.1350	2.4967	0.0850
Tb159	0.4789	0.0154	0.3037	0.0222
Dy163	2.8656	0.0534	1.7400	0.0600
Ho165	0.5178	0.0135	0.2877	0.0025
Er166	1.4544	0.1194	0.7100	0.0265
Tm169	0.1994	0.0160	0.0997	0.0095
Yb172	1.3433	0.0448	0.6033	0.0115
Lu175	0.2030	0.0090	0.0867	0.0121
Hf178	1.2033	0.0639	0.3900	0.0100
Ta181	11.9933	1.0317	0.1773	0.0294
Pb208	1.3044	0.0139	0.1453	0.0641
Th232	0.9367	0.1841	0.2073	0.0075
U238	0.1849	0.0247	0.0450	0.0026

Table 16. Mica trace-element chemistry (ppm wt%)

	CP62	
	Concentration	StDev
Li7	1.2706	0.5429
Al27		
Si29	207153	108353
K39		
Ca43	714.7	NA
Sc45	4.8194	2.4952
Ti47	49888.6333	26504.0056
V51	305.1594	154.6706
Fe57	4118.0883	1995.5655
Co59	113666.7622	68939.7233
Ni60	91.6194	46.1872
Sr88	2567	1307
Rb85	68.8144	42.1579
Y89		
Zr90	30.6294	16.2654
Nb93	26.8272	13.4571
Ba137	1234.2200	755.4459
La139	0.4044	0.5715
Ce140	0.1750	0.2442
Pr141	0.0926	0.0988
Nd143	0.3413	0.3856
Sm147		
Eu153	0.0611	0.0174
Gd157		
Tb159	0.0102	0.0096
Dy163	0.0738	0.0717
Ho165		
Er166	0.0394	0.0198
Tm169		
Yb172	0.0349	0.0217
Lu175		
Hf178	1.3528	0.7423
Ta181	2.5883	1.3510
Pb208	0.2089	0.1183
Th232	0.0055	0.0053
U238	0.0089	0.0110

Table 17. Whole-Rock Powder Trace Element Chemistry (Data from Gibson et al., 2013 as wt % ppm.)

	Li	V	Ni	Co	Pb	Ba	Th	U	Nb	Ta	La	Ce	Pr	Sr	Nd	Sm	Zr	Hf	Eu	Ti	Gd	Tb	Dy	Ho	Y	Er	Tm	Yb	Lu
BD730					0.67	78.03	0.41	0.09	5.66		3.46	6.56	0.79	44.12	2.96	0.52	14.24	0.32	0.15	973	0.41	0.06	0.32	0.07	2.07	0.20	0.03	0.23	0.04
BD794					0.21	25.24	0.08	0.14	1.18		0.76	1.31	0.18	10.78	0.68	0.14	3.53	0.08	0.04	223	0.10	0.01	0.07	0.01	0.43	0.04	0.01	0.06	0.01
BD797					0.26	24.02	0.14	0.08	1.94		1.40	2.01	0.33	24.42	1.22	0.19	6.04	0.13	0.05	469	0.17	0.02	0.14	0.03	0.82	0.07	0.01	0.06	0.01
BD822					0.68	18.38	0.14	0.09	1.52		1.04	1.60	0.23	19.98	0.74	0.12	3.25	0.07	0.03	378	0.09	0.01	0.06	0.01	0.30	0.02	0.00	0.02	0.00
BD3847						766.00			26.00		6.70	16.40	2.51	183.00	10.60	2.28	87.00		0.71	24520	2.20		1.38	0.25	7.00	0.58		0.35	0.05

Table 18. Olivine Volatile Element Chemistry (ppm; H is H_2O wt.% ppm)

Date	Sample	H	Error	Li	Error	B	Error	F	Error	P	Error	Cl	Error
Nov-19	TM2	8	1	2.30	0.02	0.07	0.00	2.8	0.1			3.0	1.8
Nov-19	J1	8	1	2.37	0.07	0.01	0.01	2.0	0.5			2.8	1.9
Nov-19	KH4	4	1	2.16	0.04	0.03	0.00	2.6	0.3			1.6	0.5
Nov-19	KH1	2	0	2.47	0.02	0.03	0.01	4.7	0.2			2.9	0.9
Nov-19	G17	6	3	2.19	0.28	0.06	0.03	3.6	0.9			1.8	0.1
Nov-19	DW3	7	3	3.54	0.27	0.24	0.01	4.1	0.5			2.4	0.7
Nov-19	DW5	13	3	2.30	0.08	0.05	0.01	4.9	0.5			3.1	0.6
May-21	TH17	29	9	3.58	0.30	1.07	0.27	65.8	8.8	43.3	1.6	17.1	8.7
May-21	BP1	12	4	1.69	0.09	0.93	0.89	14.5	9.0	5.1	5.4	54.7	63.2
May-21	BD730	36	11	1.04	0.09	0.27	0.10	51.3	3.7	43.5	1.5	26.6	25.1
May-21	BD816	25	22	3.82	0.20	0.74	0.13	42.0	9.7	44.3	15.4	3.8	1.8
May-21	BD797	34	7	1.89	0.07	0.42	0.07	105.1	5.7	25.9	1.8	5.9	5.2
Jun-21	TM4	13	3	1.96	0.06	0.26	0.07	10.2	1.1	47.3	4.3	3.7	2.8
Jun-21	KH3D	11	9	2.14	0.02	0.15	0.03	9.3	1.1	11.7	1.1	2.8	1.3
Jun-21	BD794	20	2	1.81	0.06	0.13	0.03	55.7	2.5	15.4	0.3	2.4	2.1
Jun-21	MM8	3	2	1.94	0.03	0.16	0.02	11.2	0.2	26.6	2.1	4.8	2.4
Jun-21	TH33	26	10	2.35	0.05	0.14	0.03	17.6	1.2	29.5	0.9	2.5	1.9

Table 19. Orthopyroxene Volatile Chemistry (ppm; H is H_2O wt.% ppm)

Date	Sample	H	Error	Li	Error	B	Error	F	Error	P	Error	Cl	Error
Nov-19	KH4	227	21	1.02	0.02	0.03	0.01	15.1	0.9			5.9	0.6
Nov-19	J1	230	35	0.73	0.07	0.05	0.02	5.4	1.5			11.8	5.1
Nov-19	DW3	208	16	1.12	0.02	0.22	0.02	16.7	0.8			11.1	2.4
Nov-19	G17	212	10	0.78	0.01	0.10	0.04	6.8	1.7			13.5	5.4
Nov-19	BD816	101	14	0.94	0.04	0.22	0.13	14.9	1.8			10.5	9.2
Nov-19	TM2	82	40	1.00	0.03	0.07	0.02	16.3	1.1			4.2	2.2
May-21	TH17	270	19	1.47	0.43	0.76	0.24	53.9	17.9	10.01	6.13	7.7	7.5
May-21	BP1	281	18	2.67	0.45	0.04	0.01	0.4	0.8	0.96	0.14	23.2	35.3
May-21	BD730	305	39	0.38	0.05	0.08	0.05	22.5	5.4	5.94	3.27	5.1	5.8
May-21	BD816	137	37	0.95	0.05	0.44	0.27	17.2	6.6	4.74	5.05	4.2	3.1
May-21	BD797	219	45	0.84	0.06	0.32	0.07	34.5	2.0	3.22	0.24	3.0	1.4
Jun-21	TM4	90	7	0.86	0.07	0.12	0.02	22.7	1.0	16.83431	15.22417	2.2	1.4
Jun-21	KH3D	188	7	0.76	0.03	0.10	0.02	23.4	0.8	2.196011	0.330221	1.6	1.2
Jun-21	BD794	208	10	0.66	0.03	0.12	0.05	26.5	1.3	1.7923	0.151925	0.8	0.8
Jun-21	MM8	258	22	0.69	0.01	0.50	0.51	30.2	1.7	4.073611	0.319065	4.0	0.5
Jun-21	TH33	258	37	0.83	0.05	0.09	0.03	25.9	1.5	3.226311	0.307152	2.2	2.0

Table 20. Clinopyroxene Volatile Chemistry (ppm; H is H_2O wt.% ppm)

Date	Sample	H	Error	Li	Error	B	Error	F	Error	P	Error	Cl	Error
Nov-19	TM2	212	24	1.11	0.01	0.11	0.02	41.6	0.8			3.0	0.2
Nov-19	KH1	326	27	1.37	0.01	0.07	0.00	85.5	1.0			3.8	0.7
Nov-19	KH4	481	31	1.29	0.04	0.08	0.02	41.2	1.9			4.2	0.1
Nov-19	J1	405	36	0.83	0.10	0.03	0.01	2.8	0.9			2.6	1.7
Nov-19	DW5	408	14	0.93	0.06	0.08	0.02	67.1	3.8			2.4	0.1
Nov-19	DW3	379	7	1.29	0.05	0.29	0.02	35.6	2.4			2.2	1.1
Nov-19	G17	421	14	0.93	0.01	0.12	0.02	64.9	2.4			1.7	0.2
May-21	TH17	269	116	1.76	0.52	0.74	0.25	76.6	13.0	24.35	6.86	12.3	5.8
May-21	BP1	665	84	7.06	1.17	0.83	0.60	2.3	0.7	2.56	0.89	10.9	2.3
May-21	BD730	201	73	0.70	0.09	0.63	0.46	54.3	15.0	15.36	10.47	12.1	3.7
May-21	BD816	127	70	0.58	0.44	0.16	0.19	50.1	8.5	10.68	3.13	6.4	1.2
Jun-21	TM4	164	14	1.02	0.08	0.09	0.02	67.5	4.5	31.87	6.56	4.6	1.5
Jun-21	KH3D	284	6	0.95	0.02	0.05	0.02	44.7	1.8	17.23	21.71	3.9	1.9
Jun-21	BD794	255	47	0.73	0.10	0.19	0.10	48.9	4.4	14.45	7.33	7.2	6.6
Jun-21	MM8	389	47	0.92	0.05	0.13	0.01	65.1	3.3	11.57	1.45	7.1	2.9
Jun-21	TH33	322	92	0.85	0.10	0.22	0.27	49.4	6.1	20.88	15.89	34.3	41.5

Table 21. Calculated Whole Rock Volatile Element Chemistry (ppm; H is H_2O wt.% ppm)

Date	Sample	Location	H	Error	Li	Error	B	Error	F	Error	P	Error	Cl	Error
Nov-19	J1	Ichinomegata	67	10	1.92	0.07	0.02	0.01	2.8	0.8			5.0	2.7
Nov-19	KH4	Kilbourne Hole	134	11	1.63	0.03	0.04	0.01	11.6	0.7			3.1	0.4
Nov-19	TM2	Tariat Volcanic Field	62	12	1.78	0.02	0.07	0.01	13.0	0.4			3.1	1.5
Nov-19	DW3	West Eifel	84	5	3.17	0.23	0.26	0.02	10.2	0.8			3.6	1.0
Nov-19	G17	West Eifel	63	5	1.82	0.21	0.07	0.03	7.4	1.1			3.7	1.0
May-21	BP1	Colorado Plateau	61	5	1.38	0.13		0.46	7.4	4.7	2.8	2.7	32.3	39.0
May-21	TH17	Colorado Plateau	86	14	2.98	0.33		0.25	61.8	10.6	34.6	2.7	14.1	8.1
May-21	BD730	Northern Tanzania	100	19	0.79	0.07	0.23	0.10	40.9	4.4	30.2	2.2	18.9	17.6
May-21	BD797	Northern Tanzania	85	18	1.46	0.06	0.36	0.07	77.7	4.3	17.6	1.2	4.6	3.8
Jun-21	TH33	Colorado Plateau	80	17	1.95	0.05	0.13	0.04	19.7	1.3	23.2	1.0	3.0	2.7
Jun-21	KH3D	Kilbourne Hole	67	9	1.74	0.02	0.13	0.03	14.4	1.1	9.7	2.0	2.5	1.3
Jun-21	BD794	Northern Tanzania	65	5	1.43	0.05	0.12	0.04	46.0	2.1	11.5	0.4	2.0	1.8
Jun-21	TM4	Tariat Volcanic Field	50	5	1.45	0.06	0.19	0.05	20.0	1.4	34.8	6.9	3.2	2.1
Jun-21	MM8	West Eifel	58	6	1.66	0.03	0.23	0.12	15.4	0.5	21.6	1.7	4.6	2.0

Table 22. Calculated Whole Rock Major Element Chemistry (wt. %)

Sample	Location	Lithology	SiO2	TiO2	Al2O3	Cr2O3	FeO	MnO	NiO	MgO	CaO	Na2O		Total		Mg#
KG3610.10A	Antarctic Peninsula	Peridotite	42.94	0.00	0.96	1.20	7.89	0.17	0.35	45.71	1.03	0.11		100.36		91.18
KG3609.21	Antarctic Peninsula	Peridotite														
KG3719.25	Antarctic Peninsula	Peridotite														
L7.201.1.41	Antarctic Peninsula	Peridotite	43.61	0.08	3.04	0.64	8.79	0.22	0.28	41.46	2.04	0.19		100.35		89.37
BN	Antarctic Peninsula	Peridotite														
DW3	West Eifel	Peridotite	47.84	0.02	1.91	1.21	8.10	0.14	0.33	48.34	2.89	0.18		110.97		91.40
DW7	West Eifel	Peridotite	46.60	0.05	2.83	0.84	7.32	0.15	0.30	40.54	1.37	0.09		100.09		90.80
DW8	West Eifel	Peridotite	43.39	0.02	2.72	0.98	7.71	0.13	0.26	43.06	1.70	0.08		100.06		90.87
DW10	West Eifel	Peridotite	43.27	0.09	2.10	1.10	8.14	0.17	0.21	37.84	6.54	0.39		99.86		89.23
MM5	West Eifel	Peridotite	44.55	0.07	1.84	0.79	7.61	0.13	0.29	43.14	1.82	0.12		100.37		90.99
MM8	West Eifel	Peridotite	43.50	0.03	1.11	0.60	7.79	0.13	0.28	46.24	0.51	0.04		100.24		91.36
MM11	West Eifel	Peridotite	45.14	0.03	3.06	0.80	7.65	0.14	0.23	39.53	2.91	0.32		99.80		90.20
G17	West Eifel	Peridotite	43.26	0.02	1.61	1.03	7.97	0.12	0.31	44.55	1.09	0.07		100.04		90.87
G18	West Eifel	Peridotite	43.52	0.03	0.81	0.14	7.68	0.13	0.26	43.95	0.24	0.02		96.78		91.07
KH2	Kilbourne Hole	Peridotite	43.62	0.12	4.49	0.60	8.55	0.14	0.26	38.70	3.61	0.31		100.41		88.97
KH3D	Kilbourne Hole	Peridotite	44.11	0.02	1.56	0.49	7.87	0.13	0.29	44.20	1.43	0.07		100.17		90.92
KH4	Kilbourne Hole	Peridotite	44.45	0.13	4.92	0.66	8.37	0.13	0.23	37.96	3.09	0.29		100.23		89.00
KH5	Kilbourne Hole	Peridotite	45.30	0.08	3.69	0.41	8.41	0.15	0.26	38.76	3.13	0.29		100.48		89.15
TM1	Tariat Volcanic Field	Peridotite	42.94	0.10	3.95	0.51	8.39	0.13	0.28	40.41	2.78	0.25		99.75		89.57
TM2	Tariat Volcanic Field	Peridotite	44.74	0.16	3.54	0.46	8.13	0.14	0.21	38.69	4.14	0.39		100.59		89.45
TM3	Tariat Volcanic Field	Peridotite	43.61	0.17	5.52	0.65	8.52	0.14	0.29	37.21	4.01	0.42		100.53		88.62
TM4	Tariat Volcanic Field	Peridotite	43.39	0.10	5.50	1.07	7.79	0.13	0.27	39.18	2.79	0.27		100.50		89.96
CP31	Southern Patagonia	Peridotite														
CP33	Southern Patagonia	Peridotite	45.10	0.20	3.32	0.60	7.74	0.12	0.24	37.23	5.10	0.56		100.21		89.55
LT1	Southern Patagonia	Peridotite	45.19	0.05	3.54	0.80	7.48	0.13	0.23	38.52	3.42	0.19		99.55		90.17
LT16	Southern Patagonia	Peridotite	44.48	0.03	0.95	0.56	7.82	0.11	0.29	44.26	0.88	0.07		99.46		90.98
PA3-5	Southern Patagonia	Peridotite	41.99	0.02	0.84	0.68	6.91	0.10	0.30	43.96	0.33	0.03		95.15		91.90
BD730	Northern Tanzania	Peridotite	45.51	0.02	2.23	0.41	7.57	0.13	0.30	42.85	1.74	0.09		100.84		90.99
BD738	Northern Tanzania	Peridotite	44.11	0.20	2.35	0.27	6.90	0.11	0.00	43.55	1.44	0.14		99.08		91.84
BD794	Northern Tanzania	Peridotite	45.31	0.01	1.53	0.44	6.93	0.10	0.28	44.83	0.88	0.09		100.40		92.02
BD797	Northern Tanzania	Peridotite	45.12	0.03	1.45	0.63	6.41	0.11	0.31	44.49	0.39	0.00		98.94		92.52
BD822	Northern Tanzania	Peridotite	41.68	0.01	0.26	0.26	6.91	0.08	0.00	47.90	0.08	0.01		97.19		92.52
TH17	Colorado Plateau	Peridotite	43.13	0.12	0.56	0.27	8.66	0.12	0.30	42.93	0.92	0.13		97.13		89.84
BP1	Colorado Plateau	Peridotite														
TH33	Colorado Plateau	Peridotite	44.59	0.02	0.71	0.52	7.57	0.11	0.29	45.24	0.72	0.08		99.86		91.41
J1	Ichinomegata	Peridotite	44.13	0.03	0.91	0.13	9.07	0.14	0.29	43.72	0.44	0.02		98.89		89.57
KG3619.7	Antarctic Peninsula	Pyroxenite														
L7201.1.74c	Antarctic Peninsula	Pyroxenite	39.56	1.12	18.37	0.00	8.18	1.34	0.03	16.11	14.28	0.99		99.99		77.82
R5194.2l	Antarctic Peninsula	Pyroxenite														
R5194.2M	Antarctic Peninsula	Pyroxenite														
MM6	West Eifel	Pyroxenite	45.29	0.35	2.84	0.66	7.25	0.14	0.13	30.63	9.48	0.54		97.31		88.28
DW5	West Eifel	Pyroxenite	46.99	0.61	4.31	0.87	5.75	0.12	0.08	21.43	14.47	0.74		95.37		86.92
KH1	Kilbourne Hole	Pyroxenite	32.93	0.84	23.30	0.01	12.05	0.16	0.04	17.94	10.91	0.67		98.85		72.64
LT14	Southern Patagonia	Pyroxenite	52.93	0.20	6.50	1.05	4.27	0.08	0.10	23.16	10.21	1.24		99.75		90.62
LT15	Southern Patagonia	Pyroxenite	50.34	0.25	4.20	0.40	5.01	0.13	0.02	18.12	20.49	0.39		99.34		86.57
CP62	Southern Patagonia	Pyroxenite	48.59	0.36	7.99	0.75	8.45	0.15	0.09	27.30	1.37	0.10		95.15		85.21
BD816	Northern Tanzania	Pyroxenite	51.09	0.13	1.57	1.10	6.21	0.12	0.09	25.00	12.27	1.01		98.60		87.77
BD3847	Northern Tanzania	Pyroxenite														

Table 23. Calculated Whole Rock Trace Element Chemistry (ppm)

	Location	Pb	Ba	Th	U	Nb	Ta	La	Ce	Pr	Sr	Nd	Sm	Zr	Hf	Eu	Ti	Gd	Tb	Dy	Ho	Y	Er	Tm	Yb	Lu
KH1	Kilbourne Hole	0.05	0.08	0.020	0.006	0.17	0.03	1.07	4.04	0.75	34.28	4.44	1.48	16.59	0.77	0.53	4362	1.76	0.26	1.78	0.34	8.47	0.88	0.12	0.77	0.100
KH2	Kilbourne Hole	0.01	0.01	0.008	0.005		0.00	0.04	0.17	0.06	3.13	0.45	0.25	2.48	0.12	0.11	714	0.43	0.08	0.61	0.13	3.30	0.39	0.06	0.38	0.052
KH3D	Kilbourne Hole	0.00	0.04	0.003	0.001	0.03	0.00	0.04	0.14	0.02	1.49	0.09	0.03	0.45	0.01	0.01	42	0.04	0.01	0.05	0.01	0.29	0.03	0.00	0.03	0.004
KH4	Kilbourne Hole	0.00	0.02	0.003	0.001	0.05	0.00	0.09	0.36	0.08	6.60	0.55	0.25	3.82	0.16	0.10	673	0.42	0.07	0.57	0.13	2.99	0.35	0.05	0.33	0.049
KH5	Kilbourne Hole	0.01	0.02	0.002	0.001	0.03	0.00	0.03	0.08	0.02	2.61	0.20	0.16	1.61	0.08	0.07	414	0.31	0.07	0.51	0.12	2.84	0.34	0.05	0.34	0.049
BP1	Colorado Plateau	0.01		0.000	0.000	0.02		0.00			0.20	0.00	0.01		0.00	0.01	71	0.06	0.01	0.14	0.04	0.98	0.12	0.02	0.12	0.019
TH17	Colorado Plateau	0.01	0.03	0.002	0.000	0.00	0.00	0.10	0.44	0.08	5.67	0.42	0.11	1.76	0.09	0.04	171	0.10	0.01	0.07	0.01	0.31	0.03	0.00	0.02	0.003
TH33	Colorado Plateau	0.01	0.13	0.003	0.001	0.02	0.00	0.04	0.14	0.02	1.78	0.12	0.04	1.17	0.03	0.01	38	0.04	0.01	0.04	0.01	0.21	0.02	0.00	0.02	0.004
TM1	Tariat Volcanic Field	0.01	0.00	0.003	0.001	0.03	0.00	0.10	0.36	0.06	7.61	0.40	0.18	2.95	0.10	0.08	465	0.28	0.05	0.37	0.08	2.12	0.24	0.04	0.24	0.035
TM2	Tariat Volcanic Field	0.03	1.26	0.004	0.002	0.06	0.00	0.24	0.83	0.16	16.47	0.94	0.38	7.18	0.22	0.15	960	0.55	0.10	0.75	0.16	4.13	0.46	0.07	0.43	0.062
TM3	Tariat Volcanic Field	0.05	0.02	0.021	0.006	0.14	0.00	0.38	1.11	0.19	19.40	1.07	0.41	7.46	0.24	0.16	944	0.56	0.10	0.76	0.16	3.99	0.47	0.07	0.46	0.065
TM4	Tariat Volcanic Field	0.02		0.009	0.004	0.10	0.00	0.22	0.65	0.11	11.48	0.58	0.22	3.73	0.11	0.09	400	0.29	0.05	0.36	0.08	2.05	0.23	0.03	0.19	0.031
DW3	West Eifel	0.06	0.02	0.126	0.026	0.11	0.01	3.01	8.13	0.91	43.45	3.30	0.52	5.28	0.07	0.15	65	0.38	0.05	0.29	0.05	1.44	0.15	0.02	0.14	0.019
DW5	West Eifel	0.12	3.25	0.046	0.011	0.48	0.04	2.23	7.96	1.38	36.70	7.38	2.17	19.96	1.05	0.74	3812	2.06	0.28	1.70	0.28	6.94	0.70	0.09	0.53	0.068
DW7	West Eifel	0.00	0.01	0.003	0.001	0.02	0.01	0.07	0.20	0.03	1.60	0.12	0.03	0.28	0.01	0.01	52	0.04	0.01	0.06	0.01	0.32	0.04	0.01	0.04	0.005
DW8	West Eifel	0.08	0.01	0.176	0.045	0.03	0.02	1.46	2.29	0.21	12.21	0.70	0.12	0.83	0.02	0.04	77	0.11	0.02	0.11	0.02	0.55	0.06	0.01	0.06	0.009
DW10	West Eifel	0.05	0.17	0.097	0.018	0.48	0.08	3.44	12.79	1.92	116.10	8.64	1.73	18.84	0.21	0.53	354	1.36	0.17	0.97	0.17	3.66	0.41	0.05	0.35	0.046
MM5	West Eifel	0.02	0.00	0.032	0.007	0.06	0.01	0.89	3.33	0.52	13.85	2.45	0.48	4.20	0.11	0.14	217	0.36	0.05	0.26	0.04	1.18	0.12	0.02	0.10	0.013
MM6	West Eifel	0.05	0.06	0.025	0.005	0.16	0.16	1.39	4.76	0.77	41.82	4.20	1.21	9.93	0.50	0.38	2275	1.08	0.16	0.93	0.16	3.63	0.42	0.05	0.31	0.038
MM8	West Eifel	0.00	0.00	0.001	0.000	0.00	0.00	0.02	0.06	0.01	0.71	0.04	0.01	0.13	0.00	0.00	10	0.01	0.00	0.01	0.00	0.05	0.01	0.00	0.00	0.001
MM11	West Eifel	0.11	16.67	0.141	0.026	8.59	0.68	3.66	10.38	1.38	61.29	5.35	0.76	6.48	0.12	0.20	201	0.51	0.08	0.38	0.07	1.82	0.20	0.03	0.19	0.028
G17	West Eifel	0.05	0.12	0.037	0.014	0.00	0.00	0.56	1.14	0.11	8.26	0.31	0.04	0.31	0.01	0.01	27	0.03	0.00	0.03	0.01	0.15	0.02	0.00	0.02	0.003
G18	West Eifel	0.00	0.06	0.009	0.004	0.00	0.00	0.07	0.13	0.01	0.62	0.03	0.01	0.19	0.01	0.00	16	0.01	0.00	0.01	0.00	0.05	0.01	0.00	0.01	0.001
KG3610.10A	Antarctic Peninsula	0.01	0.08	0.0005	0.021	0.02	0.00	0.69	1.14	0.10	10.00	0.32	0.05	0.29	0.00	0.02	9	0.03	0.01	0.04	0.01	0.22	0.03	0.00	0.03	0.006
KG3609.21	Antarctic Peninsula																									
KG3719.25	Antarctic Peninsula																									
L7.201.1.41	Antarctic Peninsula	0.02	0.01	0.060	0.016	0.05	0.01	0.86	2.04	0.31	12.35	1.36	0.33	5.67	0.13	0.10	284	0.31	0.05	0.35	0.07	1.79	0.20	0.03	0.19	0.026
BN	Antarctic Peninsula																									
L7201.1.74c	Antarctic Peninsula	0.08	0.05	0.404	0.007	0.26	0.05	1.59	6.05	1.19	52.88	6.82	2.11	25.64	1.22	0.79	6094	2.42	0.36	2.21	0.40	9.37	0.95	0.12	0.75	0.093
R5194.2I	Antarctic Peninsula	0.06	0.02		0.043	0.40	0.08	2.41	7.63	1.31	41.35	7.06	2.11	27.51	1.07	0.74	4556	2.24	0.35	2.18	0.41	9.86	1.08	0.14	0.93	0.119
R5194.2M	Antarctic Peninsula	0.09	0.03		0.070	0.79	0.16	5.52	17.76	2.81	72.53	14.68	4.30	67.77	2.36	1.53	8028	4.57	0.71	4.49	0.84	21.12	2.28	0.30	1.95	0.269
CP33	Southern Patagonia	0.07	0.03	0.036	0.015	0.27	0.01	0.58	1.57	0.23	22.86	1.09	0.36	5.68	0.24	0.13	910	0.35	0.06	0.22	0.04	0.87	0.09	0.01	0.04	0.009
LT1	Southern Patagonia	0.01	0.02	0.001	0.001	0.01	0.00	0.04	0.15	0.02	1.36	0.14	0.08	0.40	0.02	0.04	159	0.12	0.03	0.21	0.05	1.26	0.14	0.02	0.15	0.020
LT16	Southern Patagonia	0.00	0.01	0.000	0.000	0.00	0.00	0.01	0.04	0.01	0.78	0.07	0.04	1.69	0.04	0.01	30	0.05	0.01	0.05	0.01	0.17	0.02	0.00	0.01	0.001
CP62	Southern Patagonia	0.02	0.02	0.004	0.004	0.03	0.00	0.01	0.01	0.01	0.74	0.05	0.10	32.57	0.79	0.07	461	0.34	0.11	1.02	0.27	6.28	0.81	0.12	0.75	0.119
LT14	Southern Patagonia	0.16	2.07	0.084	0.024	0.25	0.02	0.98	2.61	0.41	34.92	2.32	0.85	10.20	0.38	0.33	1025	1.32	0.26	1.95	0.48	12.61	1.67	0.23	1.56	0.231
LT15	Southern Patagonia	0.28		0.020	0.017	0.16	0.01	0.46	1.89	0.39	32.59	2.23	0.98	5.27	0.28	0.36	1557	1.19	0.21	1.37	0.30	7.34	0.77	0.12	0.65	0.099
BD730	Northern Tanzania	0.16	1.03	0.006	0.004	0.04	0.00	0.31	1.89	0.35	50.89	1.78	0.40	1.44	0.03	0.14	118	0.29	0.04	0.20	0.04	1.09	0.12	0.02	0.15	0.026
BD794	Northern Tanzania	0.21	25.24	0.080	0.140	1.18		0.76	1.31	0.18	10.78	0.68	0.14	3.53	0.08	0.04	223	0.10	0.01	0.07	0.01	0.43	0.04	0.01	0.06	0.011
BD797	Northern Tanzania	0.26	24.02	0.140	0.080	1.94		1.40	2.01	0.33	24.42	1.22	0.19	6.04	0.13	0.05	469	0.17	0.02	0.14	0.03	0.82	0.07	0.01	0.06	0.009
BD822	Northern Tanzania	0.68	18.38	0.140	0.090	1.52		1.04	1.60	0.23	19.98	0.74	0.12	3.25	0.07	0.03	378	0.09	0.01	0.06	0.01	0.30	0.02	0.00	0.02	0.002
BD816	Northern Tanzania	0.56	0.27	0.092	0.025	0.26	0.04	4.46	14.91	1.67	116.01	6.18	1.26	22.10	0.73	0.34	364	0.72	0.07	0.29	0.03	0.79	0.06	0.01	0.02	0.003
J1	Ichinomegata	0.00	0.01	0.000	0.000			0.00	0.01	0.00	0.02	0.03	0.02	0.15	0.01	0.01	39	0.04	0.01	0.05	0.01	0.27	0.03	0.00	0.03	0.004

Table 24. Mineral Helium Isotope Chemistry

Sample	Location	Rock type	Mineral	Mass (g)	R/Ra	±	3He ccSTP/g	error	4He ccSTP/g	error
Bruce Nunatac	Antarctica	Peridotite	olivine	0.5845	7.9	0.4	8.84E-14	4.21E-15	8.02E-09	7.57E-11
Bruce Nunatak	Antarctica	Peridotite	orthopyroxene	1.2808	7.1	0.2	1.65E-13	3.97E-15	1.67E-08	3.47E-11
KG3609.21	Antarctica	Peridotite	orthopyroxene	1.471	6.8	0.8	9.11E-15	9.86E-16	9.62E-10	3.01E-11
KG3609.21	Antarctica	Peridotite	olivine	0.7194	7.4	0.6	4.89E-14	4.20E-15	4.75E-09	6.17E-11
KG3610.10A	Antarctica	Peridotite	orthopyroxene	0.7038	7.4	0.4	9.22E-14	4.65E-15	8.91E-09	6.30E-11
KG3610.10A	Antarctica	Peridotite	olivine	0.7168	7.0	0.3	7.38E-14	3.52E-15	7.51E-09	6.17E-11
KG3719.25	Antarctica	Peridotite	orthopyroxene	0.5328	5.3	0.1	1.65E-12	1.45E-14	2.22E-07	8.58E-11
KG3719.25	Antarctica	Peridotite	olivine	0.5296	7.3	0.4	1.15E-13	6.09E-15	1.13E-08	8.30E-11
L7.201.1.41	Antarctica	Peridotite	orthopyroxene	0.5121	6.3	0.6	3.51E-14	3.20E-15	3.97E-09	8.35E-11
L7.201.1.41	Antarctica	Peridotite	olivine	0.5533	6.9	0.1	9.07E-13	1.77E-14	9.38E-08	8.79E-11
KG3619.7	Antarctica	Pyroxenite	clinopyroxene	0.8625	6.8	0.2	2.07E-13	4.67E-15	2.18E-08	8.03E-11
L7201.1.74c	Antarctica	Pyroxenite	clinopyroxene	0.5481	6.5	0.1	1.28E-12	1.53E-14	1.41E-07	8.18E-11
R5194.2I	Antarctica	Pyroxenite	olivine	0.3225	5.7	0.1	8.56E-13	2.10E-14	1.08E-07	1.39E-10
R5194.2I	Antarctica	Pyroxenite	clinopyroxene	0.4602	5.8	0.1	1.84E-12	1.86E-14	2.26E-07	1.05E-10
R5194.2M	Antarctica	Pyroxenite	clinopyroxene	0.3903	6.7	0.1	8.79E-12	5.44E-14	9.33E-07	1.49E-10
DW10	Eifel	Peridotite	olivine	0.7526	6.0	0.3	1.67E-13	6.93E-15	1.99E-08	5.90E-11
DW10	Eifel	Peridotite	clinopyroxene	0.8308	7.0	0.1	1.35E-12	1.07E-14	1.39E-07	7.39E-11
DW3	Eifel	Peridotite	olivine	0.6594	6.8	0.2	2.25E-13	5.06E-15	2.39E-08	8.57E-11
DW8	Eifel	Peridotite	clinopyroxene	0.6382	5.9	0.2	1.18E-13	4.55E-15	1.42E-08	9.77E-12
G16	Eifel	Peridotite	clinopyroxene	0.7831	5.7	0.1	8.34E-13	1.36E-14	1.06E-07	8.59E-11
G17	Eifel	Peridotite	orthopyroxene	1.3	5.5	0.1	5.96E-13	7.58E-15	7.73E-08	4.10E-11
G17	Eifel	Peridotite	olivine		5.5	0.1	3.70E-13	6.98E-15	4.85E-08	6.06E-11
G18	Eifel	Peridotite	orthopyroxene	1.5238	5.5	0.1	2.10E-13	4.43E-15	2.71E-08	2.93E-11
G18	Eifel	Peridotite	olivine	1.1581	4.8	0.4	2.78E-14	2.05E-15	4.24E-09	3.31E-11
MM11	Eifel	Peridotite	olivine	0.6083	6.6	0.1	4.03E-13	6.74E-15	4.35E-08	7.53E-11
MM5	Eifel	Peridotite	clinopyroxene	0.727	6.7	0.1	2.23E-12	1.65E-14	2.45E-07	6.33E-11
MM6	Eifel	Peridotite	olivine	0.666	6.3	0.1	9.85E-13	9.74E-15	1.11E-07	6.95E-11
MM8	Eifel	Peridotite	orthopyroxene	0.6244	6.1	0.1	2.39E-12	2.42E-14	2.80E-07	1.09E-10
MM8	Eifel	Peridotite	clinopyroxene	0.1373	6.6	0.2	3.22E-12	6.87E-14	3.46E-07	3.28E-10
MM8	Eifel	Peridotite	olivine	0.5773	6.3	0.1	2.13E-12	2.57E-14	2.43E-07	1.44E-10
DW7	Eifel	Peridotite	clinopyroxene	0.6766	5.9	0.1	1.77E-12	2.06E-14	2.15E-07	8.33E-11
DW7	Eifel	Peridotite	olivine	0.752	5.8	0.3	6.97E-14	3.52E-15	8.59E-09	5.89E-11
DW5	Eifel	Pyroxenite	olivine	0.6708	6.1	0.2	4.54E-13	1.09E-14	5.30E-08	6.68E-11
DW5	Eifel	Pyroxenite	clinopyroxene	0.9681	5.4	0.1	1.11E-11	4.71E-14	1.47E-06	3.54E-10
MM6	Eifel	Pyroxenite	clinopyroxene	0.229	6.6	0.2	1.75E-12	5.24E-14	1.88E-07	2.03E-10
KH2	Kilbourne Hole	Peridotite	clinopyroxene	0.7533	6.9	0.4	5.09E-14	2.65E-15	5.31E-09	5.87E-11
KH2	Kilbourne Hole	Peridotite	orthopyroxene	0.5491	7.5	0.6	3.66E-14	2.72E-15	3.47E-09	8.06E-11
KH2	Kilbourne Hole	Peridotite	olivine	0.4496	7.2	0.3	1.38E-13	6.19E-15	1.41E-08	5.18E-11
KH3D	Kilbourne Hole	Peridotite	clinopyroxene	0.4906	7.9	0.1	6.71E-13	1.10E-14	6.05E-08	9.22E-11
KH3D	Kilbourne Hole	Peridotite	orthopyroxene	0.5977	7.8	0.2	4.76E-13	1.05E-14	4.36E-08	7.47E-11
KH3D	Kilbourne Hole	Peridotite	olivine	1.1358	7.7	0.1	9.04E-13	1.26E-14	8.44E-08	5.52E-11
KH4	Kilbourne Hole	Peridotite	clinopyroxene	1.1284	8.0	0.2	1.54E-13	4.17E-15	1.37E-08	3.93E-11
KH4	Kilbourne Hole	Peridotite	olivine	0.776	7.5	1.0	1.35E-14	1.52E-15	1.29E-09	8.15E-11
KH5	Kilbourne Hole	Peridotite	olivine	1.3958	7.3	0.3	4.77E-14	1.94E-15	4.67E-09	3.17E-11
KH5	Kilbourne Hole	Peridotite	clinopyroxene	0.5605	7.4	0.3	1.10E-13	4.49E-15	1.07E-08	1.00E-10
KH1	Kilbourne Hole	Pyroxenite	olivine	0.4437	7.6	0.3	2.37E-13	7.52E-15	2.23E-08	9.99E-11
KH1	Kilbourne Hole	Pyroxenite	clinopyroxene	0.7379	7.7	0.1	2.24E-12	2.09E-14	2.08E-07	6.96E-11
TM1	Mongolia	Peridotite	orthopyroxene	0.4617	7.8	0.6	4.41E-14	3.48E-15	4.03E-09	9.59E-11
TM1	Mongolia	Peridotite	clinopyroxene	0.6433	8.5	0.3	1.82E-13	5.43E-15	1.54E-08	6.89E-11
TM2	Mongolia	Peridotite	clinopyroxene	1.1806	8.4	0.2	2.46E-13	5.15E-15	2.09E-08	3.78E-11
TM2	Mongolia	Peridotite	olivine	0.6137	7.7	0.2	2.71E-13	6.21E-15	2.53E-08	1.04E-10
TM2	Mongolia	Peridotite	orthopyroxene	0.6919	7.8	0.2	2.54E-13	5.83E-15	2.31E-08	6.43E-11
TM3	Mongolia	Peridotite	olivine	0.6921	8.4	0.4	5.66E-14	2.89E-15	4.85E-09	6.39E-11
TM3	Mongolia	Peridotite	clinopyroxene	0.4357	7.9	0.3	2.24E-13	7.87E-15	2.05E-08	1.29E-10
TM4	Mongolia	Peridotite	clinopyroxene	0.8765	7.4	0.1	3.72E-12	2.32E-14	3.58E-07	1.15E-10
TM4	Mongolia	Peridotite	olivine	0.8644	7.7	0.1	3.30E-12	1.83E-14	3.06E-07	6.99E-11
TM4	Mongolia	Peridotite	orthopyroxene	0.686	7.5	0.1	3.59E-12	2.75E-14	3.41E-07	9.76E-11
CP31	South America	Peridotite	garnet	0.9614	6.2	0.1	5.36E-13	7.85E-15	6.22E-08	4.82E-11
CP31	South America	Peridotite	olivine	0.513	7.1	0.1	7.21E-13	1.36E-14	7.28E-08	9.13E-11
CP31	South America	Peridotite	orthopyroxene	0.6864	6.8	0.1	1.03E-12	1.30E-14	1.08E-07	6.65E-11
CP33	South America	Peridotite	olivine	0.5264	7.0	0.2	3.32E-13	7.06E-15	3.38E-08	8.44E-11
LT1	South America	Peridotite	olivine	0.4704	6.9	0.1	2.60E-12	1.98E-14	2.70E-07	1.02E-10
LT16	South America	Peridotite	olivine	0.5571	6.6	0.1	3.68E-12	3.16E-14	4.00E-07	9.45E-11
PA3-5	South America	Peridotite	orthopyroxene	0.4099	6.7	0.1	1.54E-11	6.62E-14	1.63E-06	1.23E-09
PA3-5	South America	Peridotite	olivine	0.9163	6.5	0.1	1.38E-11	4.77E-14	1.52E-06	1.27E-09
CP62	South America	Pyroxenite	clinopyroxene	0.1182	7.2	0.1	4.58E-12	5.33E-14	4.56E-07	4.11E-10
LT14	South America	Pyroxenite	clinopyroxene	1.0814	7.3	0.2	1.63E-13	4.76E-15	1.61E-08	4.11E-11
LT15	South America	Pyroxenite	clinopyroxene	0.771	6.7	0.1	1.07E-11	4.55E-14	1.13E-06	5.59E-10
BD128A	Tanzania	Peridotite	orthopyroxene	0.4174	7.2	0.1	2.97E-12	2.86E-14	2.96E-07	1.24E-10
BD128A	Tanzania	Peridotite	olivine	0.7988	7.3	0.1	2.37E-12	2.22E-14	2.34E-07	1.04E-10
BD730	Tanzania	Peridotite	clinopyroxene	0.4864	6.3	0.1	7.88E-13	1.49E-14	8.93E-08	9.26E-11
BD738	Tanzania	Peridotite	clinopyroxene	0.4884	6.8	0.3	1.51E-13	7.22E-15	1.59E-08	9.06E-11
BD738	Tanzania	Peridotite	olivine	0.8013	6.7	0.4	4.01E-14	2.08E-15	4.31E-09	5.61E-11
BD797	Tanzania	Peridotite	orthopyroxene	0.10728	6.3	0.1	1.16E-11	1.00E-13	1.31E-06	5.20E-10
BD797	Tanzania	Peridotite	olivine	0.4963	6.1	0.2	2.48E-13	8.64E-15	2.89E-08	9.03E-11
BD822	Tanzania	Peridotite	orthopyroxene	0.7489	6.4	0.1	3.55E-12	2.29E-14	3.94E-07	1.47E-10
BD822	Tanzania	Peridotite	olivine	0.5004	6.8	0.4	1.26E-13	6.80E-15	1.34E-08	8.85E-11
BD3847	Tanzania	Peridotite	olivine	0.5389	7.0	0.1	3.88E-12	2.64E-14	3.99E-07	1.16E-10
BD3847	Tanzania	Pyroxenite	vein	0.821	6.8	0.1	3.34E-12	2.54E-14	3.49E-07	7.58E-11
BD3847	Tanzania	Pyroxenite	clinopyroxene	0.3556	6.7	0.1	2.21E-12	1.94E-14	2.34E-07	1.44E-10
BD816	Tanzania	Pyroxenite	clinopyroxene	0.541	6.2	0.1	3.07E-12	3.45E-14	3.56E-07	8.84E-11
BD816	Tanzania	Pyroxenite	olivine	0.3441	6.4	0.3	2.44E-13	9.89E-15	2.71E-08	1.29E-10
BD816	Tanzania	Pyroxenite	orthopyroxene	0.3713	6.0	0.1	1.08E-12	2.07E-14	1.28E-07	1.24E-10
Japan 86394	Japan	Peridotite	olivine	0.6088	8.5	0.4	1.22E-13	5.64E-15	1.03E-08	7.27E-11

Table 25. Calculated Whole-Rock Helium Isotope Composition

Sample	Location	Rock Type	Value	Error	3He ccSTP	error	4He ccSTP	error
Bruce Nunatac	Antarctica	Peridotite	7.3	0.2	1.28E-13	1.95E-14	1.08E-08	7.57E-11
KG3609.21	Antarctica	Peridotite	7.1	0.7	1.67E-14	3.98E-15	1.60E-09	3.01E-11
KG3610.10A	Antarctica	Peridotite	7.2	0.4	8.17E-14	1.87E-14	8.15E-09	6.30E-11
KG3719.25	Antarctica	Peridotite	5.6	0.1	5.70E-13	1.24E-13	2.16E-08	8.58E-11
L7.201.1.41	Antarctica	Peridotite	6.8	0.2	1.69E-13	2.04E-14	7.62E-09	8.35E-11
KG3619.7	Antarctica	Pyroxenite	6.8	0.2	2.07E-13	4.67E-15	2.18E-08	8.03E-11
L7201.1.74c	Antarctica	Pyroxenite	6.5	0.1	1.28E-12	1.53E-14	1.41E-07	8.18E-11
R5194.2l	Antarctica	Pyroxenite	5.8	0.1	1.38E-12	9.44E-14	1.46E-07	1.39E-10
R5194.2M	Antarctica	Pyroxenite	6.7	0.1	8.79E-12	5.44E-14	9.33E-07	1.49E-10
DW10	West Eifel	Peridotite	6.7	0.1	6.30E-13	3.62E-14	3.48E-08	5.90E-11
DW3	West Eifel	Peridotite	6.8	0.2	2.25E-13	5.06E-15	2.39E-08	8.57E-11
DW8	West Eifel	Peridotite	5.9	0.2	1.18E-13	4.55E-15	1.42E-08	9.77E-12
G16	West Eifel	Peridotite	5.7	0.1	8.34E-13	1.36E-14	1.06E-07	8.59E-11
G17	West Eifel	Peridotite	5.5	0.1	4.78E-13	3.13E-14	5.96E-08	4.10E-11
G18	West Eifel	Peridotite	5.3	0.2	8.53E-14	2.31E-14	7.34E-09	2.93E-11
MM11	West Eifel	Peridotite	6.6	0.1	4.03E-13	6.74E-15	4.35E-08	7.53E-11
MM5	West Eifel	Peridotite	6.7	0.1	2.23E-12	1.65E-14	2.45E-07	6.33E-11
MM6	West Eifel	Peridotite	6.3	0.1	9.85E-13	9.74E-15	1.11E-07	6.95E-11
MM8	West Eifel	Peridotite	6.3	0.1	2.41E-12	3.55E-14	2.84E-07	1.82E-10
DW7	West Eifel	Peridotite	5.9	0.1	3.17E-13	1.23E-13	1.65E-08	8.33E-11
DW5	West Eifel	Pyroxenite	5.6	0.1	2.46E-12	5.50E-14	1.02E-07	6.68E-11
MM6	West Eifel	Pyroxenite	6.6	0.2	1.75E-12	5.24E-14	1.88E-07	2.03E-10
KH2	Kilbourne Hole	Peridotite	7.1	0.4	6.07E-14	4.12E-15	5.48E-09	6.93E-11
KH3D	Kilbourne Hole	Peridotite	7.8	0.2	6.71E-13	1.15E-14	5.84E-08	7.58E-11
KH4	Kilbourne Hole	Peridotite	7.9	0.4	5.12E-14	2.74E-14	2.35E-09	3.93E-11
KH5	Kilbourne Hole	Peridotite	7.3	0.3	6.66E-14	7.77E-15	6.50E-09	3.17E-11
KH1	Kilbourne Hole	Pyroxenite	7.7	0.1	7.68E-13	3.83E-14	4.03E-08	9.99E-11
TM1	Tariat	Peridotite	8.3	0.4	9.79E-14	1.69E-14	6.39E-09	9.59E-11
TM2	Tariat	Peridotite	8.0	0.2	2.56E-13	5.72E-15	2.30E-08	6.65E-11
TM3	Tariat	Peridotite	8.1	0.4	1.02E-13	1.21E-14	7.84E-09	6.39E-11
TM4	Tariat	Peridotite	7.6	0.1	3.51E-12	2.31E-14	3.34E-07	9.30E-11
CP31	Pali Aike	Peridotite	6.6	0.1	7.22E-13	1.12E-14	7.67E-08	6.77E-11
CP33	Pali Aike	Peridotite	7.0	0.2	3.32E-13	7.06E-15	3.38E-08	8.44E-11
LT1	Pali Aike	Peridotite	6.9	0.1	2.60E-12	1.98E-14	2.70E-07	1.02E-10
LT16	Pali Aike	Peridotite	6.6	0.1	3.68E-12	3.16E-14	4.00E-07	9.45E-11
PA3-5	Pali Aike	Peridotite	6.6	0.1	1.45E-11	2.65E-13	1.57E-06	1.23E-09
CP62	Pali Aike	Pyroxenite	7.2	0.1	4.58E-12	5.33E-14	4.56E-07	4.11E-10
LT14	Pali Aike	Pyroxenite	7.3	0.2	1.63E-13	4.76E-15	1.61E-08	4.11E-11
LT15	Pali Aike	Pyroxenite	6.7	0.1	1.07E-11	4.55E-14	1.13E-06	5.59E-10
BD128A	Tanzania	Peridotite	7.2	0.1	2.63E-12	1.14E-13	2.61E-07	1.24E-10
BD730	Tanzania	Peridotite	6.3	0.1	7.88E-13	1.49E-14	8.93E-08	9.26E-11
BD738	Tanzania	Peridotite	6.7	0.3	6.50E-14	2.89E-14	6.78E-09	9.06E-11
BD797	Tanzania	Peridotite	6.3	0.1	1.15E-12	5.38E-13	5.65E-08	5.20E-10
BD822	Tanzania	Peridotite	6.5	0.1	9.11E-13	1.83E-13	2.59E-08	1.47E-10
BD3847	Tanzania	Peridotite	7.0	0.1	3.88E-12	2.64E-14	3.99E-07	1.16E-10
BD3847	Tanzania	Pyroxenite	6.9	0.1	3.05E-12	2.39E-14	3.11E-07	1.17E-10
BD816	Tanzania	Pyroxenite	6.2	0.1	9.28E-13	2.59E-14	6.32E-08	1.26E-10
Japan 86394	Japan	Peridotite	8.5	0.4	1.22E-13	5.64E-15	1.03E-08	7.27E-11
BP1	Colorado Plateau	Peridotite	7.1	0.9	1.41E-14	1.05E-14	1.42E-09	6.79E-11
TH17	Colorado Plateau	Peridotite	5.7	0.6	2.28E-14	1.67E-14	2.81E-09	8.40E-11

Table 26. Carbon Isotope Composition

Sample	Rock Type	Mineral	Mass (mg)	Carbon (ppm)	CO2 (ppm)	δ13C (‰)	±
KH1	Pyroxenite	Clinopyroxene	247.35	1.3	4.77	3.6	1
KH2	Peridotite	Clinopyroxene	240.2	0.21	0.77		
KH3D	Peridotite	Clinopyroxene	217.08	0.56	2.06		
TM4	Peridotite	Clinopyroxene	279.91	9.17	33.65	-4.14	1
DW7	Peridotite	Clinopyroxene	241.81	0.45	1.65	5.6	1.4
DW10	Peridotite	Clinopyroxene	272.79	9.9	36.33	1.4	1.4
DW5	Pyroxenite	Clinopyroxene	243.95	14.61	53.62	-24.99	1.4
LT1	Peridotite	Olivine	244.48	1.4	5.14	1.2	1
LT16	Peridotite	Olivine	263.85	1.3	4.77	-0.5	1
PA3-5	Peridotite	Olivne	264.31	3.1	11.38	-0.6	1
LT15	Pyroxenite	Clinopyroxene	239.3	12.7	46.61	-2	1
CP62	Pyroxenite	Clinopyroxene	268.2	4.9	17.98	-1.9	1.2
R5194.2M	Pyroxenite	Clinopyroxene	279.4	27.7	101.66	0	1
R5194.2I	Pyroxenite	Clinopyroxene	235.32	6.9	25.32	1.3	1.2
L7.201.1.74C	Pyroxenite	Clinopyroxene	277.62	0.3	1.10	-1.3	1

Table 27. Secondary Standard Results From EMPA Analysis

Sample	VG2			Augite_122142			Ilmenite			San Carlos		
Element	Wt. %	Error	Del Lim (ppm)	Wt. %	Error	Del Lim (ppm)	Wt. %	Error	Del Lim (ppm)	Wt. %	Error	Del Lim (ppm)
SiO2	50.26	0.22	464	50.48	0.22	459	0.01	0.02	201	40.98	0.20	436
Na2O	2.64	0.11	432	1.34	0.07	375	0.02	0.03	344	0.02	0.03	294
Al2O3	13.59	0.11	322	8.25	0.08	281	-0.07	0.02	279	0.03	0.01	94
K2O	0.20	0.03	245	0.00	0.01	142	0.00	0.01	153			
Cr2O3	0.03	0.04	478	0.14	0.06	645	-0.02	0.08	967	0.03	0.05	571
MnO	0.17	0.11	1169	0.13	0.07	701	4.45	0.23	1419	0.12	0.05	593
FeO	11.77	0.46	1268	6.28	0.34	1110	46.20	0.88	1921	9.24	0.41	1167
NiO	0.03	0.05	609	0.04	0.08	887	0.01	0.09	1023	0.42	0.10	869
CaO	10.90	0.24	580	15.88	0.20	485	0.04	0.02	169	0.13	0.01	112
TiO2	1.88	0.05	282	0.87	0.02	156	47.08	0.46	559	-0.01	0.01	181
MgO	6.87	0.10	364	16.16	0.16	487	0.32	0.03	287	49.64	0.30	760

Table 28. Standards used in LA-ICP-MS analysis

Date	**GeoReM**	Aug-19	Nov-21	**GeoReM**	Nov-21	**GeoReM**	Aug-19	Nov-21	**GeoReM**	Aug-19	Nov-21	**GeoReM**	Aug-19	Nov-21
Standard	**BCR-2G**	BCR-2G	BCR-2G	**BHVO-2G**	BHVO-2G	**NIST614**	NIST614	NIST614	**NIST612**	NIST612	NIST6612	**NIST610**	NIST610	NIST610
Li7	**13.9**	9.39	10.35	**4.4**	7.65	**1.69**	1.88	1.65	**40.2**	41.92	40.28	**468**	460.19	471.91
Sc45	**33**	37.65	37.17	**33**	35.02	**0.74**	2.34	2.03	**39.9**	41.61	40.76	**455**	491.99	492.81
Ti47	**14100**	17585.34	15435.12	**16300**	18620.37	**3.61**	5.00	6.68	**44**	51.09	44.54	**452**	547.18	491.79
V51	**425**	435.93	458.53	**308**	323.86	**1.01**	1.18	0.99	**38.8**	39.65	39.14	**450**	441.04	449.59
Co59	**38**	38.03	41.09	**44**	44.79	**0.79**	0.69	0.74	**35.5**	35.52	35.75	**410**	382.07	412.12
Ni60	**13**	11.97	14.09	**116**	119.12	**1.1**	1.18	1.38	**38.8**	38.84	39.49	**458.7**	425.80	466.46
Sr88	**342**	325.10	339.20	**396**	394.21	**45.8**	45.98	46.39	**78.4**	76.64	78.94	**515.5**	488.40	527.96
Y89	**35**	36.06	34.88	**26**	25.31	**0.79**	0.98	0.74	**38.3**	38.64	39.64	**462**	476.80	482.33
Zr90	**184**	181.00	188.39	**170**	171.45	**0.848**	1.02	0.81	**37.9**	36.52	38.73	**448**	431.00	467.15
Nb93	**12.5**	12.14	13.36	**18.3**	19.13	**0.824**	0.81	0.81	**38.9**	38.15	39.34	**465**	445.45	478.58
Ba137	**683**	648.08	670.59	**131**	128.14	**3.2**	2.95	3.34	**39.3**	38.63	39.79	**452**	416.84	450.23
La139	**24.7**	26.06	25.71	**15.2**	15.38	**0.72**	0.77	0.72	**36**	36.86	36.98	**440**	441.40	445.56
Ce140	**53.3**	53.67	52.02	**37.6**	36.08	**0.813**	0.76	0.78	**38.4**	39.57	38.66	**453**	431.66	438.96
Pr141	**6.7**	6.70	6.70	**5.35**	5.25	**0.768**	0.80	0.76	**37.9**	38.35	38.22	**448**	426.93	449.11
Nd143	**28.9**	29.57	29.58	**24.5**	24.90	**0.752**	0.85	0.69	**35.5**	36.28	36.11	**430**	441.08	449.08
Sm147	**6.59**	6.71	7.14	**6.1**	6.47	**0.754**	0.83	0.77	**37.7**	38.00	38.34	**453**	464.44	471.38
Eu153	**1.97**	1.96	2.02	**2.07**	2.10	**0.77**	0.79	0.78	**35.6**	35.47	36.12	**447**	434.72	447.92
Gd157	**6.71**	7.06	6.56	**6.16**	5.98	**0.763**	0.81	0.69	**37.3**	38.09	38.03	**449**	458.60	455.16
Tb159	**1.02**	1.07	1.06	**0.92**	0.91	**0.739**	0.86	0.73	**37.6**	37.10	38.55	**437**	443.53	459.44
Dy163	**6.44**	6.91	6.52	**5.28**	5.27	**0.746**	0.87	0.70	**35.5**	37.03	36.69	**437**	466.75	450.29
Ho165	**1.27**	1.41	1.39	**0.98**	0.98	**0.749**	0.90	0.73	**38.3**	38.98	39.43	**449**	470.08	471.59
Er166	**3.7**	3.90	3.93	**2.56**	2.68	**0.74**	0.83	0.72	**38**	38.68	38.90	**455**	478.19	473.21
Tm169	**0.51**	0.56	0.54	**0.34**	0.31	**0.732**	0.86	0.68	**36.8**	38.84	37.85	**435**	465.55	453.91
Yb172	**3.39**	3.87	3.14	**2.01**	1.91	**0.777**	0.90	0.68	**39.2**	41.26	36.09	**450**	501.43	434.21
Lu175	**0.503**	0.56	0.52	**0.279**	0.28	**0.732**	0.88	0.71	**37**	39.05	38.05	**439**	476.34	465.68
Hf178	**4.84**	5.16	5.21	**4.32**	4.37	**0.711**	0.75	0.73	**36.7**	36.08	37.62	**435**	439.91	451.35
Ta181	**0.78**	0.87	0.79	**1.15**	1.15	**0.808**	0.92	0.78	**37.6**	41.03	38.56	**446**	494.76	471.47
Pb208	**11**	11.67	11.24	**1.7**	1.75	**2.3**	2.27	2.13	**38.57**	40.29	38.40	**426**	425.86	411.80
Th232	**5.9**	6.48	6.35	**1.22**	1.29	**0.748**	0.81	0.74	**37.79**	38.69	38.51	**457.2**	470.53	473.23
U238	**1.69**	1.73	1.80	**0.403**	0.43	**0.823**	0.79	0.84	**37.38**	38.34	37.37	**461**	436.59	452.79

For each date specified, each sample was subjected to a minimum of 15 individual analysis

Table 29. Standards used for SIMS calibration

Standard	H2O (ppmw)	Li (ppm)	B (ppm)	F (ppm)	P (ppm)	Cl (ppm)
ALV-519-4-1	1700	3.6	0.5	95	302	
OPX-KH03-4-3	216			25	10.6	
OPX-116610-3	128			17.4	0.5	
CPX-KH03-4-1	427			64.8		
CPX-SC-J1-1	62			26	30.9	
CPX-SMC31139-1	5			0.5		
ST8.1.A92-2						2026.1

Table 30. Sand Carlos Olivine Variation through SIMS analysis (ppm; H is H_2O (wt.% ppm)

Sample	Date	H	Li	B	F	P	Cl
San Carlos	19-Nov-19	-6.11	1.88	0.02	2.34		2.26
San Carlos	19-Nov-19	-6.23	1.98	0.02	2.50		3.80
San Carlos	19-Nov-19	-5.92	1.95	0.02	2.90		2.27
San Carlos	19-Nov-19	-6.77	2.02		2.66		2.30
San Carlos	19-Nov-19	-6.11	1.95	0.02	2.22		2.28
San Carlos	19-Nov-19	-6.09	2.01	0.01	3.73		3.02
San Carlos	20-Nov-19	-6.15	1.92	0.04	3.05		2.28
San Carlos	20-Nov-19	-5.11	1.92	0.02	2.30		
San Carlos	20-Nov-19	-4.87	2.06	0.15	9.53		27.16
San Carlos	20-Nov-19	-5.05	1.92	0.04	3.96		4.19
San Carlos	20-Nov-19	-4.18	2.06	0.16	15.25		32.95
San Carlos	21-Nov-19	-5.17	2.07	0.01	5.09		5.57
San Carlos	21-Nov-19	-5.09	2.04	0.02	2.79		
San Carlos	21-Nov-19	-5.09	1.98	0.01	2.10		5.73
San Carlos	21-Nov-19	-4.88	2.04	0.01	3.96		2.80
San Carlos	21-Nov-19	-5.41	1.96	0.03	2.23		2.16
San Carlos	21-Nov-19	-5.15	2.00	0.03	3.38		1.42
San Carlos	21-Nov-19	-5.08	2.04	0.04	2.37		1.52
San Carlos	04-May-21	15.50	1.97	0.10	7.30	8.61	
San Carlos	04-May-21	-8.45	1.95	0.10	6.86	7.79	5.52
San Carlos	04-May-21	1.47	2.13	0.08	7.96	9.59	6.67
San Carlos	04-May-21	19.42	2.15	0.44	8.61	8.87	26.07
San Carlos	04-May-21	-2.73	2.07	0.05	6.36	8.73	1.66
San Carlos	04-May-21	12.56	2.12	0.07	9.81	9.43	2.64
San Carlos	05-May-21	0.90	2.11	0.06	3.28	9.18	1.95
San Carlos	05-May-21	2.71	2.05	0.05	1.81	9.08	2.93
San Carlos	05-May-21	1.50	1.97	0.07	2.11	8.34	4.87
San Carlos	05-May-21	4.69	1.99	0.07	3.95	8.78	2.93
San Carlos	05-May-21	3.10	2.06	0.09	4.52	8.31	2.90
San Carlos	05-May-21	1.78	2.06	0.05	2.00	8.49	4.87
San Carlos	06-May-21	2.10	1.97	0.14	3.75	7.14	10.94
San Carlos	06-May-21	-2.04	1.97	0.15	5.62	8.21	5.98
San Carlos	06-May-21	0.12	2.03	0.15	5.15	8.39	11.91
San Carlos	06-May-21	-12.76	2.04	0.09	4.83	7.72	3.94
San Carlos	06-May-21	3.06	2.03	0.15	5.13	8.08	7.01
San Carlos	31-May-21	43.18	2.02	0.09	5.23	8.73	4.79
San Carlos	31-May-21	42.34	1.91	0.17	5.50	8.82	0.81
San Carlos	31-May-21	40.59	2.02	0.14	5.13	8.44	
San Carlos	31-May-21	42.83	1.96	0.16	5.37	9.19	3.11
San Carlos	31-May-21	40.36	1.97	0.11	6.50	9.03	3.13
San Carlos	31-May-21	43.23	2.02	0.14	4.76	9.41	1.56
San Carlos	01-Jun-21	28.44	2.04	0.06	8.24	8.68	1.82
San Carlos	01-Jun-21	26.69	2.14	0.08	9.26	9.15	2.77
San Carlos	01-Jun-21	24.82	2.12	0.06	9.82	8.52	0.90
San Carlos	01-Jun-21	27.38	2.07	0.12	10.42	9.05	6.32
San Carlos	01-Jun-21	25.14	2.01	0.02	9.26	9.27	2.74
San Carlos	01-Jun-21	28.39	2.09	0.05	8.72	9.25	1.82
San Carlos	02-Jun-21	4.19	2.32	0.22	3.34	7.90	2.07
San Carlos	02-Jun-21	3.87	2.13	0.18	3.93	8.14	5.20
San Carlos	02-Jun-21	2.62	2.14	0.14	4.99	8.43	8.27
San Carlos	02-Jun-21	4.46	2.11	0.15	4.83	8.13	5.11
San Carlos	02-Jun-21	5.13	2.15	0.22	3.31	8.78	4.11
San Carlos	02-Jun-21	1.37	2.10	0.19	3.00	8.23	2.12